Design and Chiroptical Properties of Chirally Substituted Indolenine Squaraine Mono-, Oligo- and Polymers

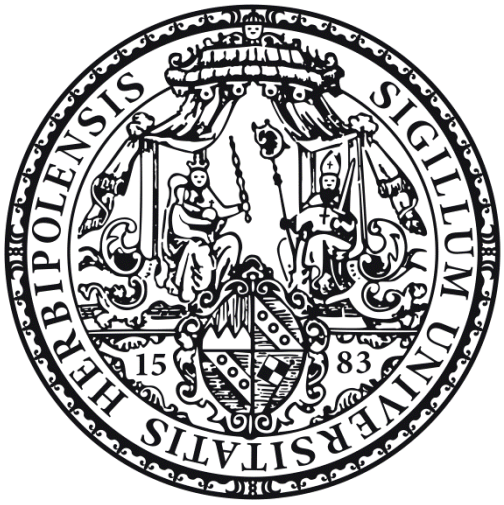

Dissertation zur Erlangung

des naturwissenschaftlichen Doktorgrades der

Julius-Maximilians-Universität Würzburg

vorgelegt von

Joshua Selby

aus Schwäbisch-Hall

Würzburg 2022

Eingereicht bei der Fakultät für Chemie und Pharmazie am

Gutachter der schriftlichen Arbeit

1. Gutachter: Prof. Dr. Christoph Lambert

2. Gutachter: Prof. Dr. Dr. h.c. Gerhard Bringmann

Prüfer des öffentlichen Promotionskolloquiums

1. Prüfer: Prof. Dr. Christoph Lambert

2. Prüfer: Prof. Dr. Dr. h.c. Gerhard Bringmann

3. Prüfer:

Datum des öffentlichen Promotionskolloquiums

Doktorurkunde ausgehändigt am

Für meine Eltern und Großeltern

Die experimentellen Arbeiten wurden vom Januar 2017 bis September 2021 am Institut für Organische Chemie der Universität Würzburg durchgeführt.

Mein besonderer Dank gilt

Herrn Prof. Dr. Christoph Lambert

für die Vergabe des vielseitigen und interessanten Themas,
den damit verbundenen aufschlussreichen Diskussionen, dem Vertrauen und
den Freiheiten bei dessen Bearbeitung.

“To achieve great things, two things are needed: a plan, and not quite enough time.”

—— Leonard Bernstein

“Sometimes science is more art than science. A lot of people don’t get that.”

—— Rick Sanchez

COPYRIGHT

The following theses were supervised during the time of this work:

1. *Synthese und Charkterisierung von chiralen Squarain-Polymeren*, Manuel Buckel, *Bachelor Thesis*, Julius-Maximilians-Universität, Würzburg, **2018**.
2. *Synthese und Charkterisierung von chiralen cis-Indolenin Squarain Polymeren*, Silas Gröger, *Bachelor Thesis*, Julius-Maximilians-Universität, Würzburg, **2018**.

TABLE OF CONTENTS

ABBREVIATIONS

CD	Circular dichroism
CPL	Circularly polarized luminescence
CP	Circularly polarized
DCM	Dichloromethane
DEF	*N*,*N*-diethylformamide
DFT	Density functional theory
DMF	*N*,*N*-dimethylformamide
DMP	2,2-Dimethoxypropane
DMPC	1,2-dimyristoyl-*sn*-glycero-3-phosphocholine
EA	Ethyl acetate
EM	Electromagnetic
FGI	Functional group interconversion
FWHM	Full width at half maximum
GPC	Gel permeation chromatography
HPLC	High performance liquid chromatography
NMR	Nuclear magnetic resonance
NOESY	Nuclear Overhauser enhancement spectroscopy
PCM	Polarizable continuum model
RT	Room temperature
TA	Transient absorption
TD	Time dependent
TIPBS	2,4,6-triisopropylbenzenesulfonyl
XPhos-Pd-G2	Chloro(2-dicyclohexylphosphino-2',4',6'-triisopropyl-1,1'-biphenyl)[2-(2'-amino-1,1'-biphenyl)]palladium(II)
XRD	X-ray diffractometry

1 INTRODUCTION

One central domain of organic chemistry has always been the design and synthesis of functional dyes and chromophores. Due to their inherent optical properties, which stem from their ability to interact with electromagnetic radiation, they have been incorporated into a plethora of applications all throughout history.[1] These range from medical applications, such as imaging dyes,[2-3] to advanced technological applications, e.g., organic photovoltaics (OPV)[4] or organic light emitting diodes (OLEDs).[5-6] Specifically, this aforementioned interaction is foremost that of the chromophore with the electric field component of the electromagnetic (EM) wave.[7-9] In order for there to be an interaction with the magnetic field component, which is perpendicular to the electric field, certain criteria for the molecular symmetry must be met – specifically the absence of an improper rotation axis.[10-14] This leads to the molecule being chiral, meaning that its mirror images are not superimposable.[15]

Chirality can be found all throughout nature, as the essential building blocks of life mostly consist of chiral compounds.[16-18] This inspired many scientific efforts to study molecular chirality, since the development of chiral compounds with the ability to specifically interact with living organisms has led to major advances in medicine and thus the improvement of civilization.[19-20] Apart from this vast field of applications, due to the aforementioned ability to facilitate an interaction with the magnetic field component of EM radiation, chirality may also be of interest for the incorporation into organic chromophores. This is in order to improve upon existing or generate novel types of applications,[10, 21] such as in second-harmonic microscopy,[22] as colorimetric molecular sensors,[23] catalysts in photochemical reactions,[24] chiroptical sensors,[25-26] molecular switches, as well as in organic electronics (OPV[27] and CP-OLEDs).[28-29]

As of now, many different types of chiral chromophores have been studied, including PBIs (perylene bisimides),[25, 30-31] coronenes,[32] BODIPYs (boron-dipyrrins),[33-35] porphyrins,[24, 36-40] phthalocyanines,[41-42] helicenes,[28-29, 43-44] merocyanines,[45] and cyanines.[46] Furthermore, chiral chromophores can be used in their monomeric form,[47] as supramolecular aggregates or polymeric foldamers,[48-51] further diversifying the range of potential applications. An especially promising and interesting class of chromophores are squaraines, which possess a great diversity of chemical structures and whose already remarkable optical properties can be

tailored by numerous methods. Yet, surprisingly, only few examples of chiral squaraines have been reported in the scientific literature thus far.[26, 52-60]

1.1 Squaraines

1.1.1 General description

Squaraines constitute a subtype of polymethine dyes, meaning they are essentially a system consisting of an odd number of repeating methine (-CH-) units with conjugated double bonds. More specifically, they are the 1,3-di-condensation product of squaric acid derivatives with nucleophiles. The name "squaraine" is a combination of the terms "squaric" and "betaine", thus referring to their zwitterionic structure, as can be seen in Figure 1, where the general structure along with the resulting two main resonance structures are depicted.[61] Typically, the nucleophiles (Nu in Figure 1) used are electron rich (hetero)aromatic compounds, such as anilines, phenols, pyrroles, indolenines, quinolines, and benzothiazoles,[62] to name selected examples. This results in a donor-acceptor-donor (D-A-D) structure with the central squaric acid core as the electron-deficient acceptor moiety, which can further be derivatized by introducing additional electron-withdrawing substituents (X in Figure 1). [62-68]

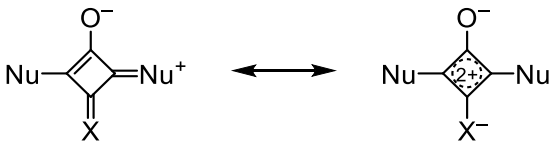

Figure 1. General structure of squaraine dyes (two main types of resonance structures).

Owing to this general structure, squaraines possess many advantageous optical properties, such as a sharp and intense absorption in the red-to-NIR spectral region (see Figure 2), as well as high fluorescence quantum yields along with small Stokes-shifts,[62, 64, 67-68] as the Huang-Rhys factors are generally quite small, indicating a very similar geometry of the ground and electronically excited state.[69-71] This is in contrast to the structurally similar class of merocyanines, which typically exhibit a broader absorption due to pronounced charge-transfer interactions because of their inherent dipolar structure.[72]

As previously mentioned, these optical properties can be fine-tuned using different approaches. One possible way of achieving this would be the alteration of the substitution by using different donor and acceptor groups, where an increase in donor or acceptor strength

leads to a spectral red-shift of the absorption. This can also be achieved by extension of the π-system, for example by using quinoline as the donor moiety, as this also leads to a red-shift, although the donor strength is comparable to that of indolenine. [62-68] A comparison of the absorption properties of differently substituted squaraines is shown in Figure 2.

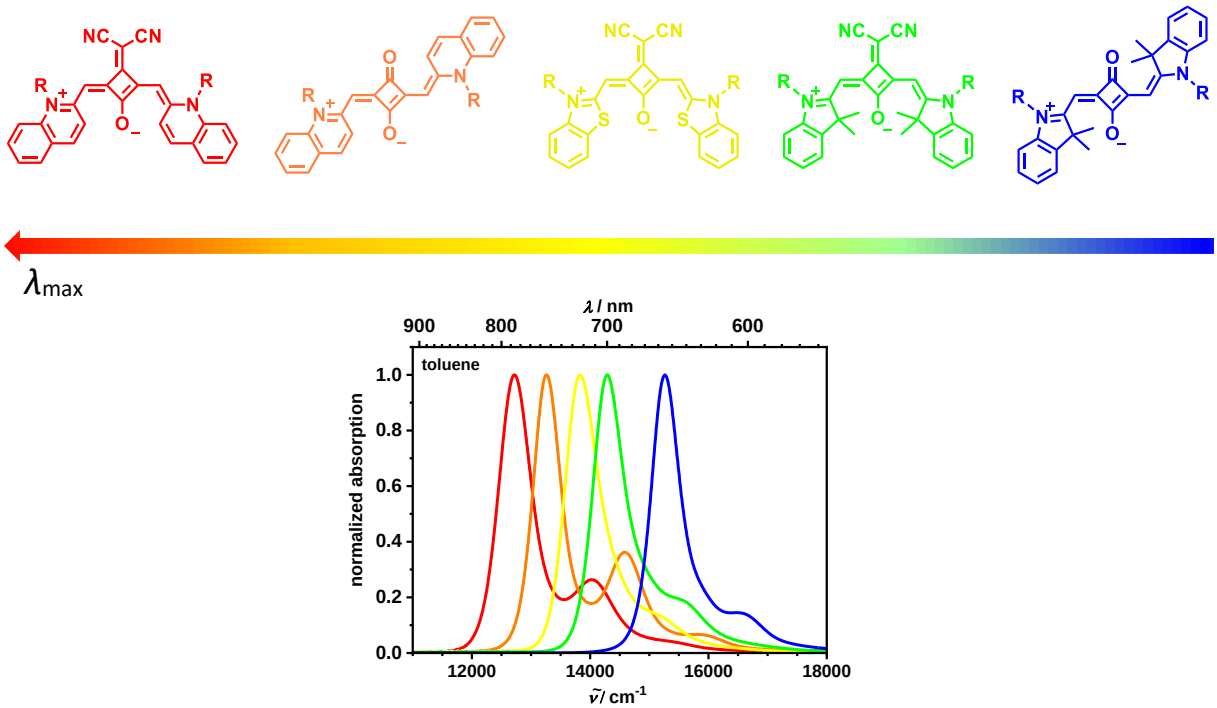

Figure 2. Examples of differently substituted squaraines and their corresponding absorption spectrum.[63, 73]

Another method to manipulate the optical properties is the coupling of monomeric chromophores, where the excitonic interactions of the individual monomeric units lead to an overall bathochromic or hypsochromic shift and usually a broadening of the main absorption band due to structural disorder,[74-76] the latter effect being especially beneficial for photovoltaic applications, since a larger portion of the sunlight can therefore be absorbed.[77] The coupling of the squaraine chromophores can be realized in two ways – either by supramolecular aggregation, where the monomeric units aggregate due to intermolecular interactions (such as dipole-dipole interactions or π-stacking),[52, 54-60, 77-84] or the covalent linking of chromophores to create oligo- and polymers.[85-97] Examples for these two cases are shown in Figure 3.

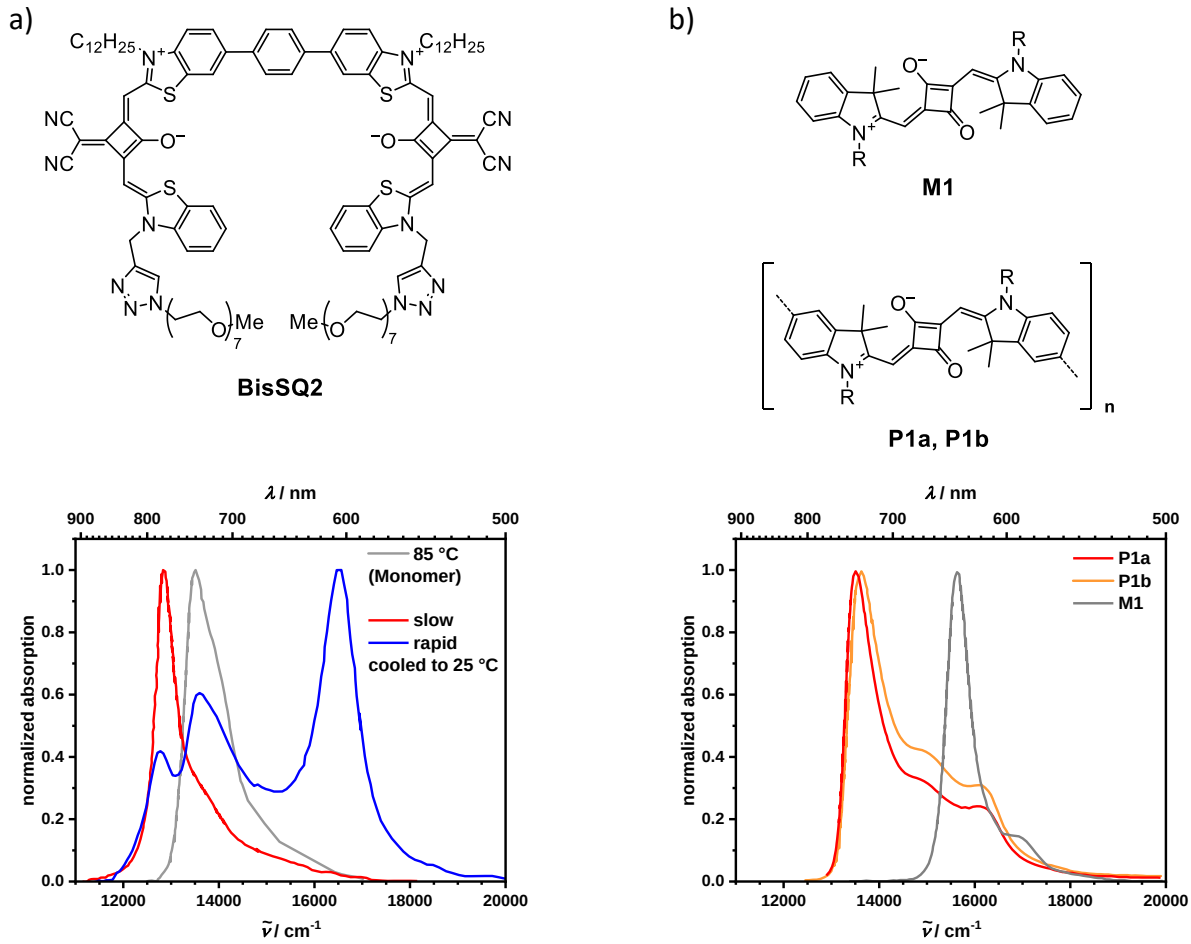

Figure 3. Examples of excitonically coupled squaraines. a) Intermolecular squaraine aggregate of **BisSQ2** (top) and corresponding absorption spectra in toluene/TCE 98:2 (bottom). Grey: 85 °C (monomeric species), blue: rapid-cooled to 25 °C, red: slow-cooled to 25 °C, recreated from ref.[78] b) Squaraine polymers **P1a** and **P1b** (different chain lengths) with corresponding monomer **M1** (top) and respective absorption spectra (bottom) in DCM, recreated from ref.[96]

BisSQ2 constitutes an example for intermolecular aggregation via π-stacking of the individual monomer units, which leads to a bathochromic or hypsochromic shift of the main absorption band depending on the respective aggregation type, which can be controlled by the cooling rate of the hot monomer solution (see Figure 3a). The inolenine squaraine polymer **P1**, on the other hand, consists of covalently linked monomeric building blocks, where an overall approximate head-to-tail arrangement of the transition dipole moments leads to a red-shift of the absorption compared to that of the monomer **M1** (see Figure 3b).

Due to these interesting and tunable optical properties, as well as the structural alterability and chemical and photochemical stability, squaraines have successfully been employed in a diverse range of applications, such as ion sensing,[98-101] bioimaging,[102-106] as photoconductors for xerographic processes,[107-108] as absorbers for optical data storage,[109-110] as materials for non-linear optics (NLO),[64, 89, 111-113] in OLEDs[114-116] and OPV,[94, 117-120] as well as in organic thin-film transistors.[121]

1.1.2 Chiral squaraines

Despite the aforementioned advantages that squaraines offer, examples of chiral squaraine (systems) found in the scientific literature are only relatively scarce in number, and this research exclusively focused on the use of chiral peripheral side chains or residues to facilitate supramolecular aggregation. The first ever chiral squaraine aggregate was reported by Whitten et al. This consisted of the asymmetric aniline squaraine **cSQ1** (Figure 4), which, when dispersed in enantiomerically pure DMPC (1,2-dimyristoyl-*sn*-glycero-3-phosphocholine) vesicles, showed a bisignate CD signal coinciding with the H-band of the aggregate absorption spectrum.[54]

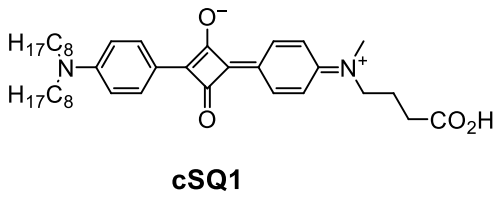

cSQ1

Figure 4. Structure of the monomeric squaraine **cSQ1**.[54]

In this example, the chiral induction was not due to the chirality of the monomer units, but rather was achieved by using a chiral host. Expanding on these findings, the authors then designed the similar aniline-squaraine **cSQ2**,[56, 59] where a cholesterol unit was attached to the squaraine chromophore. This approach was later also chosen by Ramaiah et al., who selected a quinoline squaraine as the parent chromophore (**cSQ3**).[57] These two examples are shown in Figure 5.

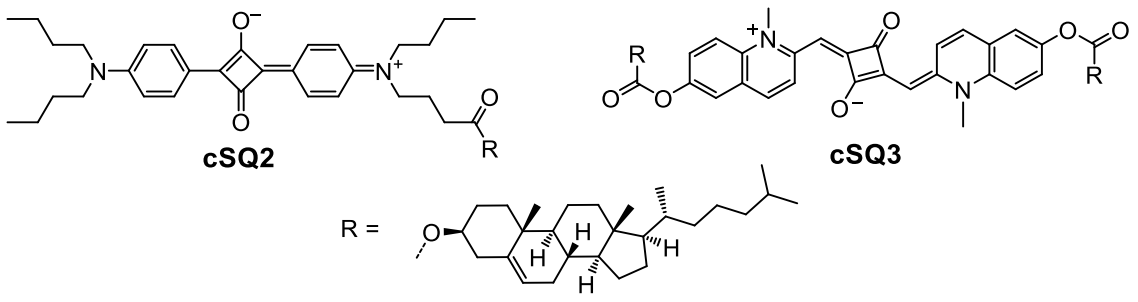

Figure 5. Structures of **cSQ2** and **cSQ3**.[56-57, 59]

In both cases, the cholesterol unit is a crucial factor in the aggregation process, since in both cases reference squaraines lacking the cholesterol moiety displayed an entirely different aggregation behavior. The study of **cSQ2** mainly focused on its ability to form organogels[56] and Langmuir-Blodgett films,[59] while the aggregation of **cSQ3** was studied in solution, as well

as in thin films. Here, an interesting observation was made, where the chirality of the supramolecular assembly was inverted (sign change of the excitonic CD signal) by, e.g., variation of temperature (see Figure 6). The authors explained this by the two enantiomeric stacks being either the result of thermodynamic or kinetic control of the aggregation process, where factors such as solvation and solvent polarity determined the handedness of the helical assembly. Studying the chiroptical properties and morphologies of thin films prepared from different solvent compositions revealed the ability to also form kinetically trapped supramolecular assemblies, which were distinct in terms of their chiroptical properties.[57]

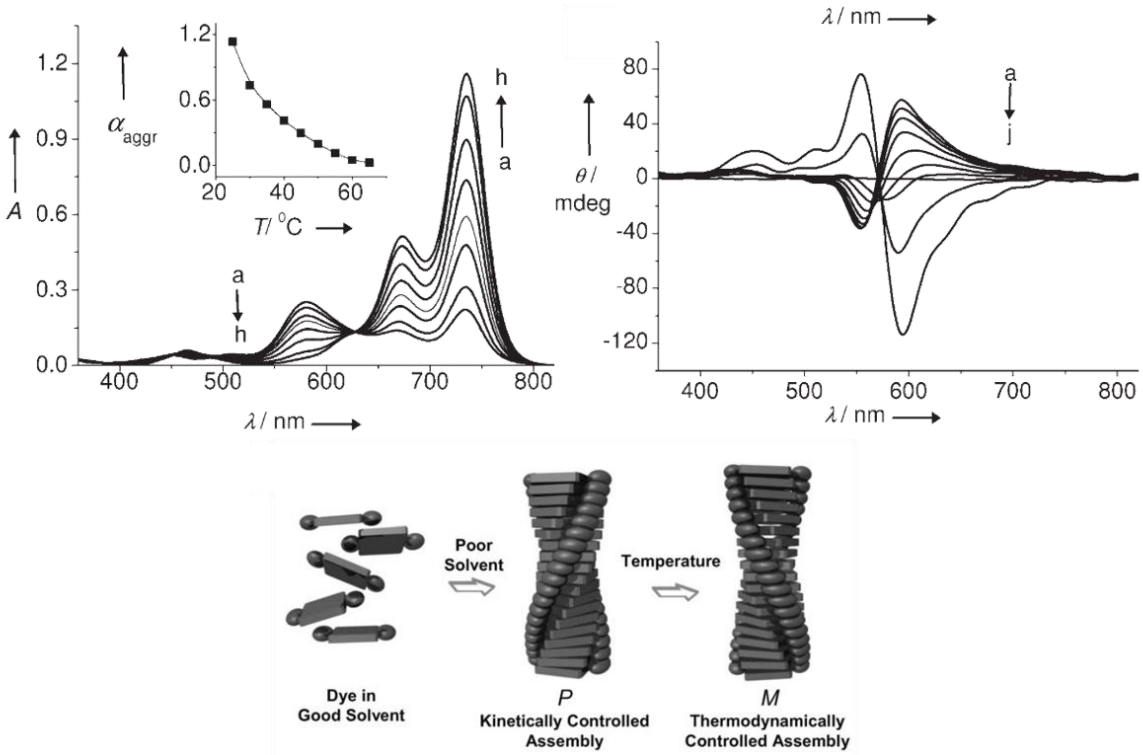

Figure 6. Absorption (top left) and CD (top right) of **cSQ3** in $CHCl_3$/MeCN (1:1). The temperature was increased from a) to h) from 25 °C to 60 °C in 5 °C increments. i) and j) are the CD spectra after slow cooling for 10 or 20 min, respectively. The inset of the absorption spectrum represents the aggregation ratio α_{agg} = monomer/aggregate. Bottom: schematic representation of the aggregation under kinetic or thermodynamic conditions. Reproduced with permission from *Chiral Supramolecular Assemblies of a Squaraine Dye in Solution and Thin Films: Concentration-, Temperature-, and Solvent-Induced Chirality Inversion*, K. Jyothish, M. Hariharan, D. Ramaiah, Copyright © (2007) John Wiley and Sons.[57]

Another approach in order to obtain chiral squaraine assemblies was the use of monomers bearing chiral side chains. Ajayaghosh et al. designed the tripodal squaraine **cSQ4**,[52, 55] which is shown in Figure 6.

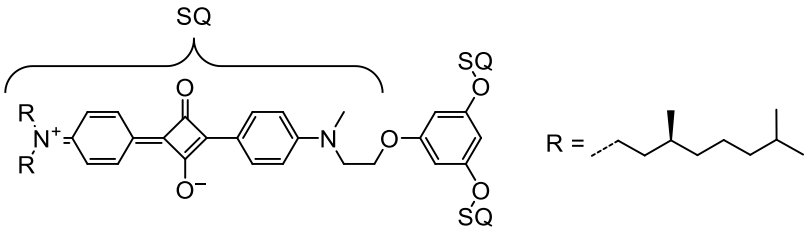

cSQ4

Figure 7. Structure of the tripodal squaraine **cSQ4**.[52, 55]

The squaraine **cSQ4** was part of a larger series of squaraines each bearing different side chains. In certain solvent mixtures, these squaraines formed aggregates, as apparent in the respective UV-Vis-NIR spectra through the emergence of an H-band. Interestingly, the homoaggregate comprised of **cSQ4** did not exhibit any significant CD signal, indicating the formation of a non-defined aggregate lacking a helical twist. However, upon addition of alkaline earth metal ions (especially Ca^{2+} and Mg^{2+}), a strong excitonic CD couplet was observed, which was the result of an obvious change in morphology. AFM measurements further elucidated this, as the morphology changed from spherical to helical as the result of the interaction with the metal ion, where the length of the helical segments correlated with the observed CD effect. While in the absence of these metal ions the primary interaction leading to the aggregation was the π-stacking of two central phenyl moieties, the complexation precluded this interaction due to electrostatic repulsion of the positive charges. Instead, linear, hollow dimers bound through side-chain interactions were formed, which further form a helical assembly possessing a preferred handedness due to the side chains acting as a chiral handle.[52, 55]

A system that has also been extensively studied by Hecht and Schiek et al. was the proline-derived chiral squaraine **cSQ5**,[26, 58, 60] which is shown in Figure 8.

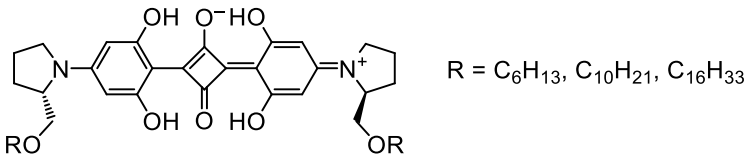

cSQ5

Figure 8. Structure of the proline-derived squaraine **cSQ5**.[26, 58, 60]

This squaraine displayed a solvent and temperature dependent aggregation behavior, where the rise of the H- and J-band coincided with an increase of the excitonic CD signal. Interestingly, the CD signal coincided with either the J-[60] or H-band,[58] depending on the side chain and solvent system used (see Figure 9), which points towards a different aggregation

behavior under these respective conditions. Furthermore, a unique arrangement in a self-templating manner was observed on highly oriented pyrolytic graphite surfaces, which has previously not been observed for other (achiral) squaraines. This observation was explained by the chiral alkyl side chains interacting with the graphite surface and thus directing the self-assembly of the squaraine chromophores.[60]

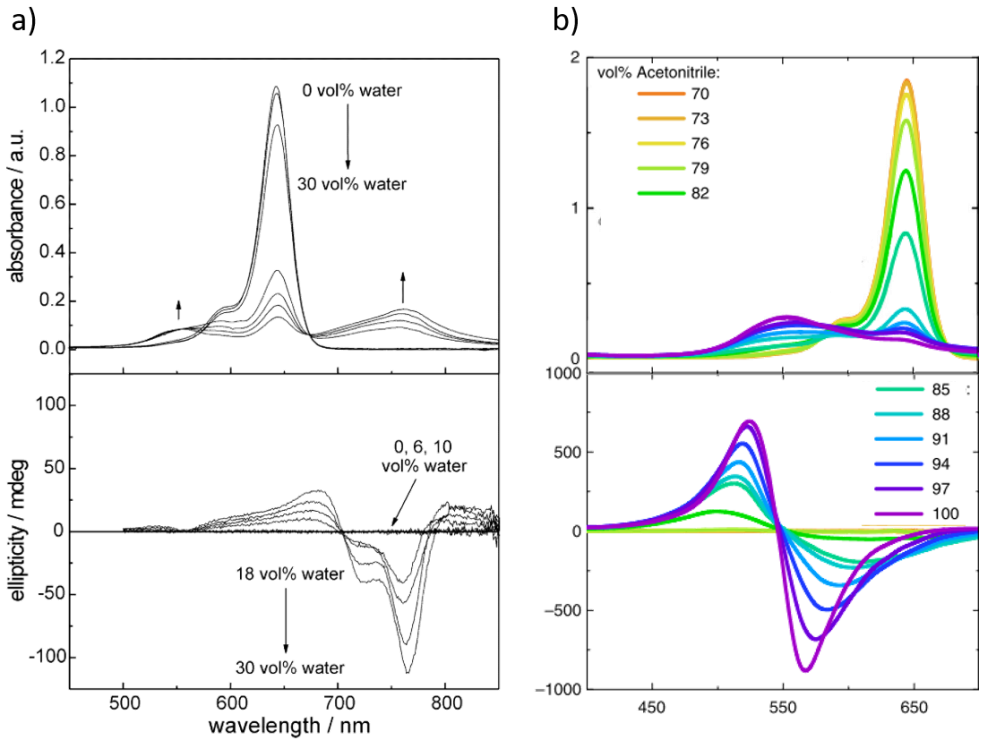

Figure 9. Absorption (top) and CD spectra (bottom) of (*S*,*S*)-**cSQ5** bearing different side chains in different solvent systems. a) R = $C_{10}H_{21}$, MeCN/H_2O. Reproduced with permission from *Synthesis of a Novel Chiral Squaraine Dye and Its Unique Aggregation Behavior in Solution and in Self-Assembled Monolayers*, R. S. Stoll, N. Severin, J. P. Rabe and S. Hecht, Copyright © (2006) John Wiley and Sons[60] b) R = $C_{16}H_{33}$, $CHCl_3$/MeCN. Adapted from ref.[58] (open access).

Furthermore, thin films of **cSQ5** were prepared for the study of their chiroptical properties using Mueller-Matrix spectroscopy, which allows the determination of the various parameters of the dielectric function and thus can be used for the investigation of the chiroptical properties of anisotropic samples.[122] After annealing, the films exhibited J-aggregate behavior with a bathochromic shift of the main absorption band, which coincided with a strong CD signal with dissymmetry factors ranging up to 0.75. It was further concluded, that the large dissymmetry factor does not stem from mesoscopic ordering, which would lead to artifacts arising from linear dichroism and Bragg reflection, but rather is the result of the large oscillator strength due to the strong excitonic coupling. To further demonstrate this, similar measurements on a structurally similar reference system were performed, where the excitonic coupling was weak, which led to *g*-values that were roughly two orders of magnitude

lower compared to those of **cSQ5**.[58] This type of supramolecular architecture comprising **cSQ5** has also been successfully incorporated into organic photodiodes.[26]

Most recently, Schiek et al. have also reported a novel type of chiral squaraine **cSQ6**, which was studied in an analogous manner using similar methods.[53] The chemical structure of **cSQ6** is shown in Figure 10.

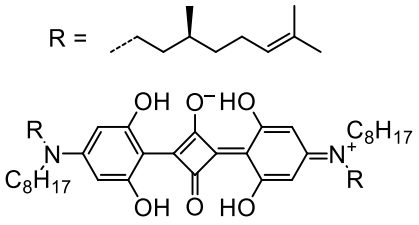

cSQ6

Figure 10. Left: Structure of **cSQ6**, right: dissymmetry factor of thin films of **cSQ6** at different thicknesses.[53]

In this work, the authors also found that monomeric indolenine squaraines bearing chiral 3,7-dimethyloctyl side chains (SQA type, see Figure 22a in chapter 2) neither formed aggregates in solution, nor in thin films, which was also reported in other studies in the past.[84] The dissymmetry factor obtained for thin films of **cSQ6** was also quite remarkable, as values of up to 0.2 were obtained.[53]

1.2 Interaction of light with chiral matter

1.2.1 Circular dichroism

As already previously stated, the optical properties of chromophores mainly stem from the interaction with the electric field component of the EM radiation, as matter is comprised of positively charged atomic nuclei and negatively charged electrons. This interaction can be modeled classically as a dampened harmonic oscillator, where the electric field periodically displaces the charges within a molecule. The response of the medium is governed by its susceptibility $\chi(\omega)$, which is related to the index of refraction $n'(\omega)$. This is a complex quantity and is defined as:

$$n'(\omega) = n(\omega) - i\, l(\omega) \tag{1}$$

where $n(\omega)$ is the real part of the complex refraction index and $l(\omega)$ is the imaginary part, essentially the absorption coefficient.[7-9, 123] These two quantities are dependent of one another and can be interconverted using the Kramers-Kroning relations.[124-127] In chiral media, due to the symmetry of the molecule, it interacts differently with left and right circularly polarized light – meaning that $n'(\omega)$, and therefore $n(\omega)$ and $l(\omega)$, is different for these two polarization states. This gives rise to two chiroptical phenomena, namely ORD (optical rotation dispersion) and CD (circular dichroism), which are the direct results of the aforementioned differences of these quantities, respectively.[12-13, 128]

ORD, which describes the rotation of the polarization plane of linearly polarized light, has been widely used to characterize organic compounds in the past. Its most notable use was as an essential tool for the determination of the absolute configurations of sugars by Emil Fischer, which had earned him the Nobel Prize for chemistry in 1902.[129] In the domain of dye chemistry, CD spectroscopy, which is the difference of the absorption between left and right circularly polarized light, is widely employed for the study of chiral chromophores. Because of its use as a central method in this work, key quantities will be defined and derived in this following section as performed by Schellman.[13]

The general method for the quantum mechanical description is in terms of time dependent perturbation theory. Specifically regarding the 0→m transition, the general expression obtained hereby is:

$$\frac{da_{\mathrm{m}}}{dt} = \frac{1}{i\hbar} W_{\mathrm{m0}} \tag{2}$$

with the perturbation matrix element

$$W_{\mathrm{m0}} = \langle \Psi_{\mathrm{m}} | \widehat{W} | \Psi_0 \rangle = \exp\left[\frac{i(E_{\mathrm{i}} - E_0)t}{\hbar}\right] \langle \psi_{\mathrm{m}} | \widehat{W} | \psi_0 \rangle = \exp[i\omega_{\mathrm{m0}} t] \langle \psi_{\mathrm{m}} | \widehat{W} | \psi_0 \rangle \tag{3}$$

Where a_{m} is the coefficient of the wavefunction in the excited state m, $\hbar$ the reduced Planck's constant, Ψ the wavefunction of the perturbed system, $\widehat{W}$ the perturbation operator, E the energy, ψ the wavefunction of the unperturbed system, t the time and ω_{m0} the circular frequency of the transition. This contains the assumption, that because the system is in the initial state 0, the corresponding coefficients a_0 is set to one while all the others are set to zero.

The perturbation can be separated in a time dependent and independent (V) component, representing an oscillating field with its circular frequency ω.

$$W = V\cos(\omega t) = \frac{1}{2}\left[V e^{i\omega t} + V^* e^{-i\omega t}\right] \tag{4}$$

Inserting this expression into eq. (2) leads to:

$$\frac{da_{\mathrm{m}}}{dt} = \frac{1}{2i\hbar}\{\exp[i(\omega_{\mathrm{m0}} + \omega)t] V_{\mathrm{m0}} + \exp[i(\omega_{\mathrm{m0}} - \omega)t] V_{\mathrm{m0}}^*\} \tag{5}$$

Integrating with the boundary conditions $a_{\mathrm{m}} = 0$ and $a_0 = 1$ at $t = 0$ and neglecting terms with $(\omega_{\mathrm{m0}} + \omega)$ in the denominator, since these are vanishingly small compared to the second term, since $\omega \approx \omega_{\mathrm{m0}}$, leads to the following expression:

$$\begin{aligned} a_{\mathrm{m}} &= \frac{1}{2i\hbar}\int_0^t \exp[i(\omega_{\mathrm{m0}} + \omega)t'] V_{\mathrm{m0}} dt' + \frac{1}{2i\hbar}\int_0^t \exp[i(\omega_{\mathrm{m0}} - \omega)t'] V_{\mathrm{m0}}^* dt' \\ &= \frac{V_{\mathrm{m0}}}{2i\hbar}\left\{\frac{\exp[i(\omega_{\mathrm{m0}} + \omega)t] - 1}{i(\omega_{\mathrm{m0}} + \omega)}\right\} + \frac{V_{\mathrm{m0}}^*}{2i\hbar}\left\{\frac{\exp[i(\omega_{\mathrm{m0}} + \omega)t] - 1}{i(\omega_{\mathrm{m0}} - \omega)}\right\} \\ &\cong \frac{V_{\mathrm{m0}}^*}{2\hbar}\frac{\exp[i(\omega_{\mathrm{m0}} - \omega)t] - 1}{(\omega_{\mathrm{m0}} - \omega)} \end{aligned} \tag{6}$$

The probability of a photon to promote the system to the state m is given by the square of its corresponding coefficient.

$$a_{\mathrm{m}}a_{\mathrm{m}}^{*} = \frac{|V_{0\mathrm{m}}|^2}{4\hbar^2}\frac{\{\exp[i(\omega_{\mathrm{m}0}-\omega)t]-1\}\{\exp[-i(\omega_{\mathrm{m}0}-\omega)t]-1\}}{(\omega_{\mathrm{m}0}-\omega)^2}$$
$$= \frac{|V_{0\mathrm{m}}|^2}{4\hbar^2}\left[\frac{\sin^2\left(\frac{\omega_{\mathrm{m}0}-\omega}{2}\right)t}{(\omega_{\mathrm{m}0}-\omega)^2}\right] = \frac{\pi}{4}\frac{|V_{0\mathrm{m}}|^2}{\hbar^2}t\delta\left(\frac{\omega_{\mathrm{m}0}-\omega}{2}\right) \quad (7)$$

Deriving this expression with respect to *t* then gives the transition rate, and multiplication by $\hbar\omega$ further represents the energy absorbed per molecule per second.

$$u_{\mathrm{m}} = \hbar\omega\,\frac{d|a_{\mathrm{m}}|^2}{dt} = \frac{\pi\omega|V_{0\mathrm{m}}|^2}{2\hbar}\delta(\omega_{\mathrm{m}0}-\omega) \quad (8)$$

Since larger systems usually consist of multiple states arising from rotational and vibrational degrees of freedom, it is useful to discuss the band shape by defining a weighing function representing the transition density $\rho_{\mathrm{m}}(\omega_{\mathrm{m}0})$, which describes the probability of an electronic transition taking place at $\omega_{\mathrm{m}0}$. This weighing function possesses the shape of the absorption band and can be described either by theoretical considerations or an empirical function. Further integrating over $\omega_{\mathrm{m}0}$ then results in the following expression:

$$u_{\mathrm{m}}(\omega) = \frac{\pi\omega\rho_{\mathrm{m}}(\omega)|V_{0\mathrm{m}}|^2}{2\hbar} \quad (9)$$

This constitutes the basis for the theoretical description of molecular spectroscopy, and through the appropriate selection of *V* can enable the discussion of all types of optical phenomena encountered in this matter.

In absorption spectroscopy, the primary interaction is the interaction with the electric field component, so

$$V_{0m} = -\boldsymbol{\mu}\boldsymbol{E} = E_0\boldsymbol{v}_{\mathrm{e}}\cdot\boldsymbol{\mu}_{0\mathrm{m}} \quad (10)$$

where E_0 is the electric field strength, v_{e} the polarization unit vector and μ_{0m} the transition dipole moment. Inserting this into eq. (9) and substituting E_0^2 with the equivalent definition of the intensity (see eq. (73) in the appendix) leads to

$$u_{\mathrm{m}}(\omega) = \frac{\pi\omega\rho_{\mathrm{m}}(\omega)|\boldsymbol{v}_{\mathrm{e}}\mu_{0\mathrm{m}}E_0|^2}{2\hbar} = \frac{4\pi^2\omega\rho_{\mathrm{m}}(\omega)|\boldsymbol{v}_{\mathrm{e}}\mu_{0\mathrm{m}}|^2 I}{\hbar nc} \quad (11)$$

where *c* is the speed of light in vacuum and *n* the refractive index. This expression can then be inserted into the Beer-Lambert law (see eq. (72) in the appendix), and after averaging over all orientations ($|\mu_x|^2 = |\mu_y|^2 = \frac{1}{3}|\boldsymbol{\mu}|^2$) to account for the random orientation of the molecules, and application of the Lorentz local field correction,[130] the following equation for the

absorption coefficient ε is obtained (the index 0m is exchanged for eg, representing the ground and excited state, respectively):

$$\varepsilon = \frac{4\pi\omega\rho_{\mathrm{m}}(\omega)N_{\mathrm{A}}\beta^2}{3(2303)\hbar nc}\,\mu_{\mathrm{eg}}^2 \tag{12}$$

Where $\beta = (n^2+2)/3$ is the factor introduced by the aforementioned local field correction.

For the description of circular dichroism, the potential must be expanded to include the magnetic interaction, therefore (in eq. 9) $V = -\boldsymbol{\mu E} - \boldsymbol{mB}$. It is necessary to decompose the linear components into circularly polarized components, since linear polarization itself is a linear combination of two opposite states of circular polarization of the same magnitude and vice versa. Therefore, the electric and magnetic dipole components can be written as follows:

$$\mu_+ = \frac{\mu_x+i\mu_y}{\sqrt{2}},\ \mu_- = \frac{\mu_x-i\mu_y}{\sqrt{2}},\ \mu_x = \frac{\mu_++\mu_-}{\sqrt{2}},\ \mu_y = \frac{\mu_+-\mu_-}{\sqrt{2}i} \tag{13}$$

$$m_+ = \frac{-im_x+m_y}{\sqrt{2}},\ m_- = \frac{im_x+m_y}{\sqrt{2}},\ m_x = \frac{-m_+-m_-}{\sqrt{2}i},\ m_y = \frac{m_++m_-}{\sqrt{2}} \tag{14}$$

The vectors for the electric and magnetic dipole moments can therefore be expressed by the following equations, neglecting the component in the direction of propagation (z-component):

$$\boldsymbol{\mu} = \mu_x\boldsymbol{v_x} + \mu_y\boldsymbol{v_y} = \mu_-\boldsymbol{e}_+ + \mu_+\boldsymbol{e}_- \tag{15}$$

$$\boldsymbol{m} = m_x\boldsymbol{v_x} + m_y\boldsymbol{v_y} = m_-\boldsymbol{b}_+ + m_+\boldsymbol{b}_- \tag{16}$$

Because of orthonormality relations of the unit vectors e_+ and e_- (CP), and v_x and v_y (LP), the interaction with left and right circularly polarized light becomes:

$$V_\pm = -\mu_\pm E_0 - m_\pm B_0 \tag{17}$$

In order to evaluate the squared matrix element V_{m0}^2, as it appears in eq. (9), a substitution of m in eq. 12 is made, where $\boldsymbol{g} = -i\,\boldsymbol{m}$. This is in order to enable the rearrangement of later terms. Performing this substitution and inserting eq. (13) and eq. (14) into eq. (17), the following expression is obtained for V_{0m}:

$$(V_\pm)_{0\mathrm{m}} = [(\mu_x)_{0\mathrm{m}}E_0 \pm (g_x)_{0\mathrm{m}}B_0] - i\left[\pm(\mu_y)_{0\mathrm{m}}E_0 + (g_y)_{0\mathrm{m}}B_0\right] \tag{18}$$

Squaring eq. (18), which can be done using $(a+ib)^2 = a^2+b^2$ and averaging over all orientations ($a_xb_x = a_yb_y = \frac{1}{3}(\boldsymbol{a}\cdot\boldsymbol{b})$) results in the following expression:

$$(V_{\pm})_{0m}^{2} = \frac{\mu_{\mathrm{eg}}^{2}}{3} E_0^2 + \frac{m_{\mathrm{eg}}^{2}}{3} B_0^2 \mp \frac{2}{3} R_{\mathrm{eg}} E_0 B_0 \tag{19}$$

With the squared electric transition moment μ_{eg}^{2}, squared magnetic transition moment m_{eg}^{2} and the rotational strength R_{eg}, which is defined as the imaginary part of the scalar product of the electric and magnetic transition moment.

$$R_{\mathrm{eg}} = -\mu_{0\mathrm{m}} \cdot g_{0\mathrm{m}} = \mathrm{Im}(\mu_{0\mathrm{m}} \cdot m_{\mathrm{m}0}) \tag{20}$$

The first term in eq. (18) describes the electric dipole interaction as previously derived in eq.(12). The second term represents the magnetic dipole interaction. This is usually only observed in very distinct cases and is several orders of magnitude smaller than the former, which is why this term will be omitted from the following discussion. The last term represents the interaction between these two components and is the basis for circular dichroism. Using the respective definitions for the intensity (see eq. (73) in the appendix), applying the Lorentz correction and introducing the respective transition density functions, before inserting eq. (19) into the expression for the transition rate (eq. (9)) and subsequently into the Beer-Lambert law (see eq. (72) in the appendix), an expression for the absorption coefficients for right and left CP light is obtained:

$$\varepsilon_{\pm} = \frac{4\pi^2 N_{\mathrm{A}}}{3(2303)\hbar c} \left[\frac{\beta^2}{n} \rho_{\mathrm{m}}(\omega) \mu_{\mathrm{eg}}^{2} \mp 2\beta \sigma_{\mathrm{m}}(\omega) R_{\mathrm{eg}} \right] \tag{21}$$

If the incident beam is linearly polarized, essentially being the equal mixture of left and right CP light, or the molecule is achiral (R_{eg} = 0) the CD term cancels out and eq. (21) becomes eq. (11). As CD ($\Delta\varepsilon$) is the defined as the difference of left and right CP light, the analogous expression for CD is:

$$\Delta\varepsilon = \varepsilon_{\mathrm{l}} - \varepsilon_{\mathrm{r}} = \frac{16\omega\pi^2 N_{\mathrm{A}} \beta \sigma_{\mathrm{m}}(\omega)}{3(2303)\hbar c} R_{\mathrm{eg}} \tag{22}$$

The quantitative comparison of CD data is usually done in terms of the dissymmetry factor g_{abs},[14, 131-132] which is defined as the ratio of $\Delta\varepsilon$ to ε. Substituting eq. 10 and eq. 21 into this definition leads to the following expression:

$$g_{\mathrm{abs}} = \frac{\Delta\varepsilon}{\varepsilon} = \frac{4n}{\beta} \frac{\sigma_{\mathrm{m}}(\omega)}{\rho_{\mathrm{m}}(\omega)} \frac{R_{\mathrm{eg}}}{\mu_{\mathrm{eg}}^{2}} \approxeq \frac{4R_{\mathrm{eg}}}{\mu_{\mathrm{eg}}^{2}} \tag{23}$$

The approximation can be made, since the absorption and CD bands usually possess the same shape ($\frac{\sigma_{\mathrm{m}}(\omega)}{\rho_{\mathrm{m}}(\omega)} = 1$) and due to the cancellation of the intrinsic effect of the refractive index by

the internal field dependence ($\frac{n}{\beta} = 1$). In terms of SI units, the individual components ($\Delta\varepsilon$ and ε, R_{eg} and μ_{eg}^2) are not comparable, due to the interactions arising from magnetic or electric fields, respectively. This is why cgs units are used for the calculation of these quantities, as this symmetric system uses the same dimension for electric and magnetic fields (dielectric constant in vacuum $\varepsilon_0 = 1$, magnetic permeability in vacuum $\mu_0 = 1$),[133] which leads to the dissymmetry factor overall being dimensionless in terms of cgs units (here, both μ and m are in the dimension of $cm^{5/2}\ g^{1/2}\ s^{-1}$).[132-135] Because the right side expression for g_{abs} in eq. (23) is energy-independent, it allows for the comparison of experimental data with quantum chemical calculations. In general, there are two equivalent forms of R_{eg} used for quantum chemical calculations:[136]

$$R_{\mathrm{eg}} = \frac{e^2\hbar}{2mc}\langle g|\sum_{\mathrm{k}}\hat{r}_{\mathrm{k}}|e\rangle\langle e|\sum_{\mathrm{k}}\hat{r}_{\mathrm{k}}\times\hat{\nabla}_{\mathrm{k}}|g\rangle \tag{24}$$

$$R'_{\mathrm{eg}} = \frac{e^2\hbar^3}{2m^2c\omega_{\mathrm{e}}}\langle g|\sum_{\mathrm{k}}\hat{\nabla}_{\mathrm{k}}|e\rangle\langle e|\sum_{\mathrm{k}}\hat{r}_{\mathrm{k}}\times\hat{\nabla}_{\mathrm{k}}|g\rangle \tag{25}$$

where e is the elemental charge, m the mass of an electron, c the speed of light, ω_e the excitation energy, $\hat{r}_{\mathrm{k}}$ the position operator, $\hat{\nabla}_{\mathrm{k}}$ the gradient operator, and e and g denote the wavefunctions for the ground and excited state, respectively. Here, the top expression (eq. (24)) is the rotational strength in the dipole-length form and the bottom one (eq. (25)) the dipole velocity form. If the wavefunctions used are exact solutions to the model Hamiltonian, these two expressions are identical. While R_{eg} fulfils the sum rule, stating that the sum of all rotational strengths is zero, R'_{eg} is origin independent. In practice, however, the values obtained by using R'_{eg} are more reliable and better comparable because of the independence of origin, leading to its widespread use for the calculation of rotational strengths in literature.[132, 136-137]

As can be seen in eq. (22), the CD effect is directly proportional to the rotational strength R_{eg}. When using the alternative definition of the scalar product with ϑ being the angle between the two vectors,

$$R_{\mathrm{eg}} = |\boldsymbol{\mu}_{\mathrm{eg}}||\boldsymbol{m}_{\mathrm{eg}}|\cos\vartheta \tag{26}$$

it can be seen that the CD does not only depend on the magnitude of the individual vectors, but also on their mutual orientation. This leads to colinear arrangements (ϑ = 0°, 180°)

resulting in large CD signals and dissymmetry factors, while angles close to 90° result in a vanishing CD signal.

Similar to fluorescence being a radiative de-excitation mechanism of molecules, CPL is its chiroptical analogue. In contrast to CD, CPL gives insight into the structural dynamics of the excited state, thus being a complementary probe for the study of chiral molecules in different electronic states. As for CD spectroscopy, CPL is usually discussed in terms of the luminescence dissymmetry factor g_{lum}:[131, 138-139]

$$g_{\mathrm{lum}} = \frac{\Delta I}{I} = \frac{I_{\mathrm{l}} - I_{\mathrm{R}}}{\frac{1}{2}(I_{\mathrm{l}} + I_{\mathrm{R}})} \cong \frac{4R_{\mathrm{eg,fl}}}{\mu^2_{\mathrm{eg,fl}}} \tag{27}$$

Where *I* is the fluorescence intensity and ΔI the difference in intensity between left and right CP light. As for CD, the same orientation dependence as described in eq. (26) holds true.

Another factor, which contributes to large values for g_{lum}, is its dependency on the number of coherently coupled chromophores. This effect was described by Spano et al.,[140-143] who argued that the luminescence anisotropy was strongly sensitive towards long-range excitonic coupling, which enabled the use of CPL spectroscopy as a probe for structural order, since a higher degree of order results in a more strongly delocalized exciton. This correlation was described by the following equation:[143]

$$g_{\mathrm{lum}} \propto \sum\nolimits_{\mathrm{n,s}} J_{\mathrm{n,n+s}}\, s\, \sin(\varphi s) \tag{28}$$

where $J_{\mathrm{n,n+s}}$ denotes the coupling between molecules separated by *s* lattice spacing and φ is the pitch angle between two adjacent chromophores.

Occasionally, CPL is also discussed in terms of CPL brightness B_{CPL}:[144]

$$B_{\mathrm{CPL}} = \varepsilon \phi_{\mathrm{fl}} \frac{g_{\mathrm{lum}}}{2} \tag{29}$$

Where ϕ_{fl} is the fluorescence quantum yield.

1.2.2 Exciton chirality[145-148]

As previously stated, a system comprised of multiple chromophores possesses spectral properties that differ from those of the individual monomeric units. More specifically, the individual subunits are coupled via dipole-dipole interactions, which leads to a visible red- or

blue-shift of the main absorption band. This was first described by Kasha et al. among others in terms of exciton coupling theory.[74-76] Considering a homodimer with two identical chromophores 1 and 2, the Hamiltonian is

$$H = \hat{H}_1 + \hat{H}_2 + \hat{H}_{12} \tag{30}$$

where H_1 and H_2 represent the Hamiltonians of the subgroups 1 and 2 and H_{12} the interaction between the two. Solving the secular equation

$$\begin{pmatrix} H_{11} & H_{21} \\ H_{12} & H_{22} \end{pmatrix} \begin{pmatrix} c_1 \\ c_2 \end{pmatrix} = E \begin{pmatrix} c_1 \\ c_2 \end{pmatrix} \tag{31}$$

where H_{ij} are the Hamiltonian matrix elements using the wavefunctions for the excited states

$$\psi_{\mathrm{e}} = c_1 \varphi_{10} \varphi_{2\mathrm{a}} + c_2 \varphi_{1\mathrm{a}} \varphi_{20} \tag{32}$$

where a denotes the excited state and 0 the ground state, leads to the following energies and wavefunctions for the 2 solutions obtained for E:

$$\psi_{\pm} = \frac{1}{\sqrt{2}} (\varphi_{10} \varphi_{2\mathrm{a}} \pm \varphi_{1\mathrm{a}} \varphi_{20}) \tag{33}$$

$$E_{\pm} = E_{\mathrm{a}} \pm J \tag{34}$$

where J is the interaction potential, which constitutes a dipole-dipole interaction approximated by the point-dipole approximation:

$$J = \langle \varphi_{10} \varphi_{2\mathrm{a}} | H_{12} | \varphi_{1\mathrm{a}} \varphi_{20} \rangle = \frac{1}{\boldsymbol{R}_{12}} \left[\boldsymbol{\mu}_1 \boldsymbol{\mu}_2 - \frac{3(\boldsymbol{\mu}_1 \cdot \boldsymbol{R}_{12})(\boldsymbol{\mu}_2 \cdot \boldsymbol{R}_{12})}{\boldsymbol{R}_{12}^2} \right] \tag{35}$$

Where $\boldsymbol{\mu}_1$ and $\boldsymbol{\mu}_2$ are the transition moment vectors of the monomer units and $\boldsymbol{R}_{12}$ the interchromophore distance vector. As seen in eq. (12), the intensity of the absorption band associated with the transition is directly proportional to the squared transition moment μ_{eg}^2. The corresponding transition moment for this system is

$$\boldsymbol{\mu}_{\pm} = \langle \psi_{\pm} | \boldsymbol{\mu} | \psi_0 \rangle = \frac{\boldsymbol{\mu}_1 \pm \boldsymbol{\mu}_2}{\sqrt{2}} \tag{36}$$

When regarding CD, the intensity of the CD band is proportional to the rotational strength R_{eg}. This can be seen in eq. (22) and was first described by Rosenfeld, which is why its definition in eq. (20) is also commonly referred to as the Rosenfeld equation. In order to derive an

expression for the dimer, its electric and magnetic transition moments must be inserted into eq. (20). The definition for the magnetic transition moment of a given subunit n is

$$\boldsymbol{m}_{\mathrm{n}} = \frac{e^2}{2mc}\langle\psi_{\mathrm{n}a}|\hat{\boldsymbol{r}} \times \hat{\boldsymbol{p}}|\psi_{\mathrm{n}0}\rangle \tag{37}$$

where $\hat{\boldsymbol{p}}$ is the linear momentum and $\hat{\boldsymbol{r}}$ the position operator. The position vector can be split into two individual terms:

$$\boldsymbol{r} = \boldsymbol{R}_{\mathrm{n}} + \boldsymbol{r}'_{\mathrm{n}} \tag{38}$$

Where $\boldsymbol{R}_{\mathrm{n}}$ is the position vector of the chromophore center and $\boldsymbol{r}'_{\mathrm{n}}$ the vector connecting the center of the subunit n and the electron. Substituting eq. (38) into eq. (37) then leads to the following expression:

$$\begin{aligned}\boldsymbol{m}_{\mathrm{n}} &= \frac{e^2}{2mc}\langle\psi_{\mathrm{n}a}|\boldsymbol{R}_{\mathrm{n}} \times \hat{\boldsymbol{p}}|\psi_{\mathrm{n}0}\rangle + \frac{e^2}{2mc}\langle\psi_{\mathrm{n}a}|\hat{\boldsymbol{r}}_{\mathbf{n}} \times \hat{\boldsymbol{p}}|\psi_{\mathrm{n}0}\rangle \\ &= \frac{e^2}{2mc}\boldsymbol{R}_{\mathrm{n}} \times \langle\psi_{\mathrm{n}a}|\hat{\boldsymbol{p}}|\psi_{\mathrm{n}0}\rangle + \boldsymbol{m}'_{\mathrm{n}}\end{aligned} \tag{39}$$

As the shape of the wavefunctions are independent of $\boldsymbol{R}_{\mathrm{n}}$, this quantity can be factored out of the integral. The second term $\boldsymbol{m}'_{\mathrm{n}}$ then describes contribution of the rotational strength of the monomer subunit which is independent of its location within the dimer. Substitution of the gradient operator in $\hat{\boldsymbol{p}}$ with the commutator relation $\left[\hat{H}, \hat{\mu}\right] = -\frac{\hbar^2 e}{m}\hat{\nabla}$ yields

$$\langle\psi_{\mathrm{n}a}|\hat{\boldsymbol{p}}|\psi_{\mathrm{n}0}\rangle = \frac{-2\pi i m c}{e\lambda_{\mathrm{eg}}}\langle\psi_{\mathrm{n}a}|\hat{\boldsymbol{\mu}}|\psi_{\mathrm{n}0}\rangle = \frac{-2\pi i m c}{e\lambda_{\mathrm{eg}}}\boldsymbol{\mu}_{\mathrm{eg}} \tag{40}$$

where λ_{eg} is the wavelength of the monomer transition, leading to the following expression for the magnetic transition moments of the excitonic transitions in the dimer.

$$\begin{aligned}\boldsymbol{m}_{\pm} = \langle\psi_{\pm}|\boldsymbol{m}|\psi_0\rangle &= \frac{\boldsymbol{m}_1 \pm \boldsymbol{m}_2}{\sqrt{2}} \\ &= \frac{(\boldsymbol{m}'_1 \pm \boldsymbol{m}'_2)}{\sqrt{2}} - \left(\frac{i\pi}{\sqrt{2}\lambda_{eg}}\right)[\boldsymbol{R}_1 \times \boldsymbol{\mu}_1 \pm \boldsymbol{R}_2 \times \boldsymbol{\mu}_2]\end{aligned} \tag{41}$$

Inserting eq. (36) and eq. (41) into eq. (20) then ultimately leads to the following expression for the rotational strength of the dimer:[1]

[1] The factor -1 is due to the complex conjugation of m_{eg}: $\boldsymbol{m}_{0\mathrm{m}} = -\boldsymbol{m}^*_{\mathrm{m}0}$

$$
\begin{aligned}
R_{\mathrm{eg}\pm} &= -\mathrm{Im}\left(\boldsymbol{\mu}_{\mathrm{eg}\pm} \cdot \boldsymbol{m}_{\mathrm{eg}\pm}\right) \\
&= -\frac{1}{2}\mathrm{Im}(\boldsymbol{m}_1' \cdot \boldsymbol{\mu}_1 + \boldsymbol{m}_2' \cdot \boldsymbol{\mu}_2) \mp \frac{1}{2}\mathrm{Im}(\boldsymbol{m}_1' \cdot \boldsymbol{\mu}_2 + \boldsymbol{m}_2' \cdot \boldsymbol{\mu}_1) \\
&\pm \frac{\pi}{2\lambda_{\mathrm{eg}}} \boldsymbol{R}_{12} \cdot (\boldsymbol{\mu}_2 \times \boldsymbol{\mu}_1) = -R_{\mathrm{mon}} \mp R_{\mathrm{e-m}} \pm R_{\mathrm{ex}}
\end{aligned}
\tag{42}
$$

The rotational strength of the dimer is comprised of three individual contributions. The first term, R_{mon}, describes the sum of the individual rotational strengths of the monomer subunits. It is independent their mutual orientations and is only non-zero if they are also chiral. $R_{\mathrm{e\text{-}m}}$, the second term, describes the coupling of the electric transition moment of one monomer subunit with the magnetic transition moment of the other (electric-magnetic coupling). The last term, R_{ex}, usually constitutes the dominating contribution in electrically allowed transitions, since the magnitude of the cross product of the electric transition moments is larger than the terms involving the magnetic transition moments. It is directly proportional to the scalar triple product of $\boldsymbol{\mu}_1$, $\boldsymbol{\mu}_2$ and $\boldsymbol{R}_{12}$ and therefore possesses the following angle-dependency:

$$
R_{\mathrm{ex}} = \frac{\pi}{2\lambda_{\mathrm{eg}}} |\boldsymbol{R}_{12}||\boldsymbol{\mu}_1||\boldsymbol{\mu}_2| \sin\theta \cos\varphi \tag{43}
$$

Where θ is the angle between $\boldsymbol{\mu}_1$ and $\boldsymbol{\mu}_2$ and φ the angle between $\boldsymbol{R}_{12}$ and the cross product of $\boldsymbol{\mu}_1$ and $\boldsymbol{\mu}_2$. This arrangement is shown in Figure 11.

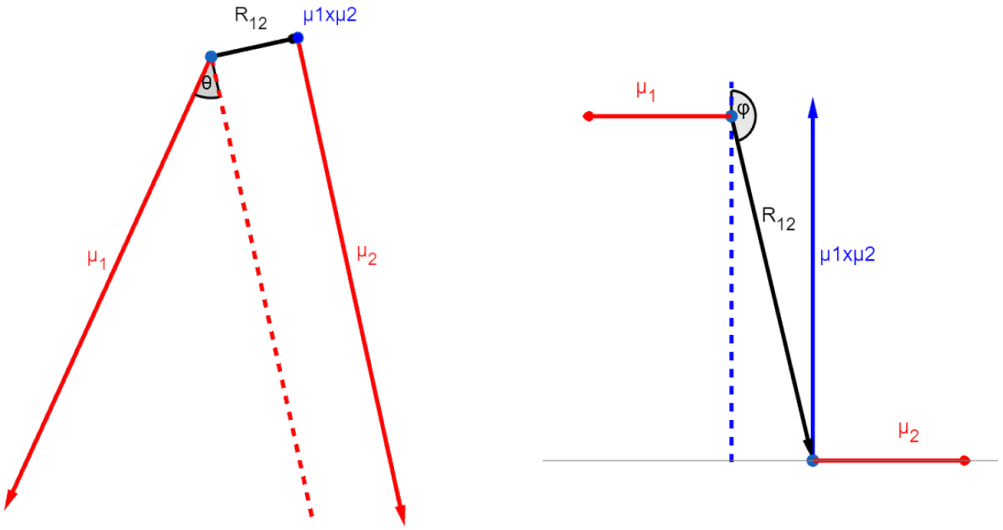

Figure 11. Geometrical arrangement of the vector quantities used for the calculation of R_{ex}. Left: top view, right: front view.

Unlike R_{mon} and $R_{\mathrm{e\text{-}m}}$, it is not required for one of the monomers to be optically active in order for R_{ex} to be non-zero, but the term vanishes if two of the three vectors are parallel or all three vectors are in the same plane. Such an arrangement can be described as achiral, and therefore

such systems will only exhibit CD if the individual monomers are chiral themselves (due to the orthogonality of the electric and magnetic transition moment in achiral molecules), since R_{mon} and $R_{e\text{-}m}$ then remain non-zero. These two cases are further illustrated in Figure 12.

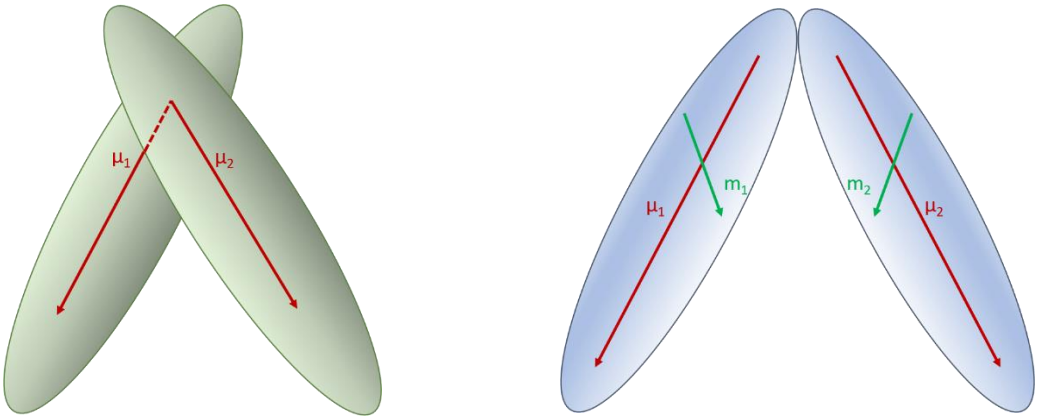

Figure 12. Left: twisted (chiral) arrangement of chromophores where $R_{ex} \neq 0$, right: planar (achiral) arrangement of chiral chromophores (***μ*** and ***m*** not orthogonal). The magnitude of ***m*** is exaggerated for demonstration purposes.

In general, the individual respective contributions of $R_{e\text{-}m}$ and R_{ex} to the overall rotational strength are of the same magnitude, but opposite in sign for the two excitonic states, leading to a CD spectrum comprised of two bands of equal intensities and opposite signs, where the zero-crossing coincides with the absorption maximum. This is commonly referred to as an excitonic couplet. Since it was first discovered by Cotton in 1895,[149] it is also often referred to as the Cotton-effect.[150] An example for a such a spectrum is shown in Figure 13. In this case, where the rotational strengths are balanced, the resulting CD spectrum is called conservative. If there are significant contributions from R_{mon}, or mixing with other excited states, leading to unequal intensities of the excitonic CD bands, the spectrum is called nonconservative. In a conservative CD spectrum, its integration over the frequency from 0 to ∞ must give zero. This is referred to as the sum rule and means that the sum of all individual components of the total rotational strength is zero.

$$\sum_k R_k = 0 \tag{44}$$

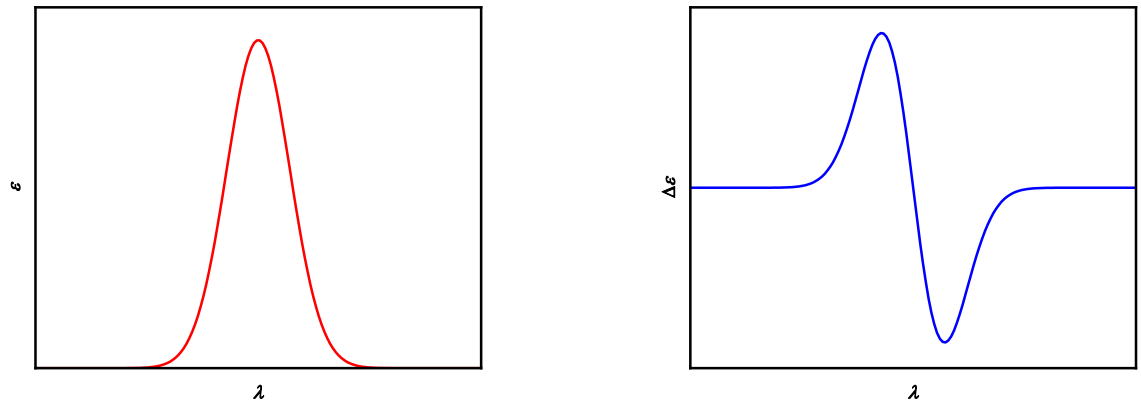

Figure 13. Schematic illustration of the absorption (left) and CD (right) spectrum of an excitonically coupled homodimer. A Gauss-function and its derivative was used for the construction of the two spectra.

Multiple systems have been used for the experimental and theoretical study of exciton chirality. One simple system suitable for these investigations are binaphthyls, where the variation of the substitution manipulates the dihedral angle, which in turn influences the CD spectrum (width, amplitude and energetic separation of the excitonic CD bands).[151-152] Another system, which nicely demonstrates the orientation and distance dependence of the rotational strength was described by Harada and Nakanishi et al., who functionalized cholesterol derivatives with benzoate groups.[153-157] Due to the polycyclic structure of the steroid scaffold and the thereby generated conformational rigidity, this system is suited for such systematic studies regarding geometrical parameters. Additionally, the chiroptical properties are dominated by the excitonic interactions of the benzoate groups and the contributions of the steroid core are negligible.

A selected example series of such p-dimethylaminobenzoate-substituted cholesterol derivatives **C1-C6** is shown in Figure 15, the corresponding spectra are shown in Figure 16. When comparing **C1** to **C2** (spectra not shown), both compounds exhibit an absorption band centered at 308-309 nm, where the absorption coefficient of **C2** is roughly twice as large. This can be ascribed to the charge transfer band of the dimethylaminobenzoate groups. In contrast to this rather unremarkable observation, the CD spectra differ markedly. While **C1** only has a very weak positive CD band ($\Delta\varepsilon$ = 2.9) following the absorption band, **C2** displays an intense bisignate CD signal in this region. This is due to excitonic coupling of the dimethylaminobenzoate units and nicely demonstrates that excitonic interactions can result in an overall amplification of the CD effect.

Using a Gaussian transition weighing function $\sigma(\omega)$ and inserting the expression for the rotational strength according to eq. (42) into eq. (22) followed by a Taylor expansion against $\frac{\omega_i}{\Delta\omega}$ around $\frac{\omega_0}{\Delta\omega}$, the following relation can be derived for such dimeric dibenzoate-substituted cholesterol systems:[153, 155]

$$\Delta\varepsilon(\omega) = \frac{4\sqrt{\pi}{\omega_0}^2}{2.296 \times 10^{-39}\Delta\omega^2}\frac{\omega_0 - \omega}{\Delta\omega}\exp\left[-\left(\frac{\omega_0 - \omega}{\Delta\omega}\right)^2\right] \cdot \{[\boldsymbol{R}_{12} \cdot (\boldsymbol{\mu}_1 \times \boldsymbol{\mu}_2)] \cdot J\} \propto \frac{1}{|\boldsymbol{R}_{12}|^2} \quad (45)$$

where ω_0 is the wavenumber of the monomer transition, ω_i the wavenumber of the *i*-th excitonic transition and $\Delta\omega$ the standard deviation of the Gaussian distribution. The second term in eq. (45) (marked in blue) is also referred to as the quadrupole term, which is indirectly proportional to the square of the interchromophoric distance and possesses an angle dependency as shown in Figure 14. If the quadrupole term is positive, then the exciton chirality is termed positive (positive Cotton effect), while for negative values it is vice versa. This enables a qualitative estimate of the absolute configuration, if the sign of *J* is known (assignment of the two exciton bands).

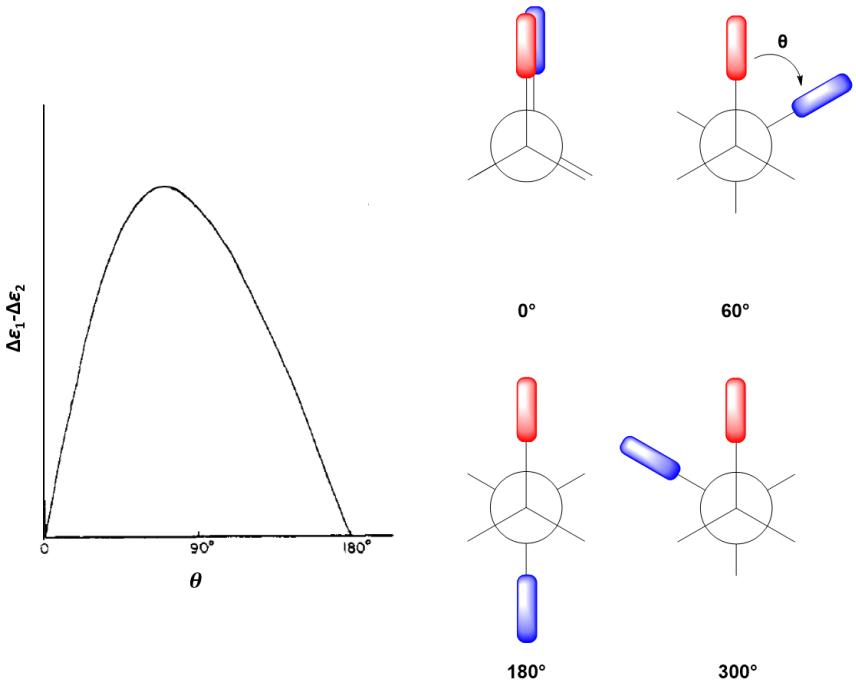

Figure 14. Left: Angle dependency of the CD amplitude (difference of the Δε values of the two CD bands) on the dihedral angle θ, Reproduced with permission from *Quantitative definition of exciton chirality and the distant effect in the exciton chirality method*, N. Harada, S.-M. L. Chen, K. Nakanishi, Copyright © (1975) American Chemical Society.[155] right: schematic illustrations of different dihedral angles.

As seen in Figure 14, the maximum amplitude is not at θ = 90° as would be expected according to eq. (43), but rather at 70°. This is due to the spectral width of the CD bands and angle dependency of J.[152-153, 155] Due to the anti-symmetric nature of the sine function, angles between 180-360° lead to a sign change in the CD spectrum while the shape of the angle dependency function shown is mirrored.

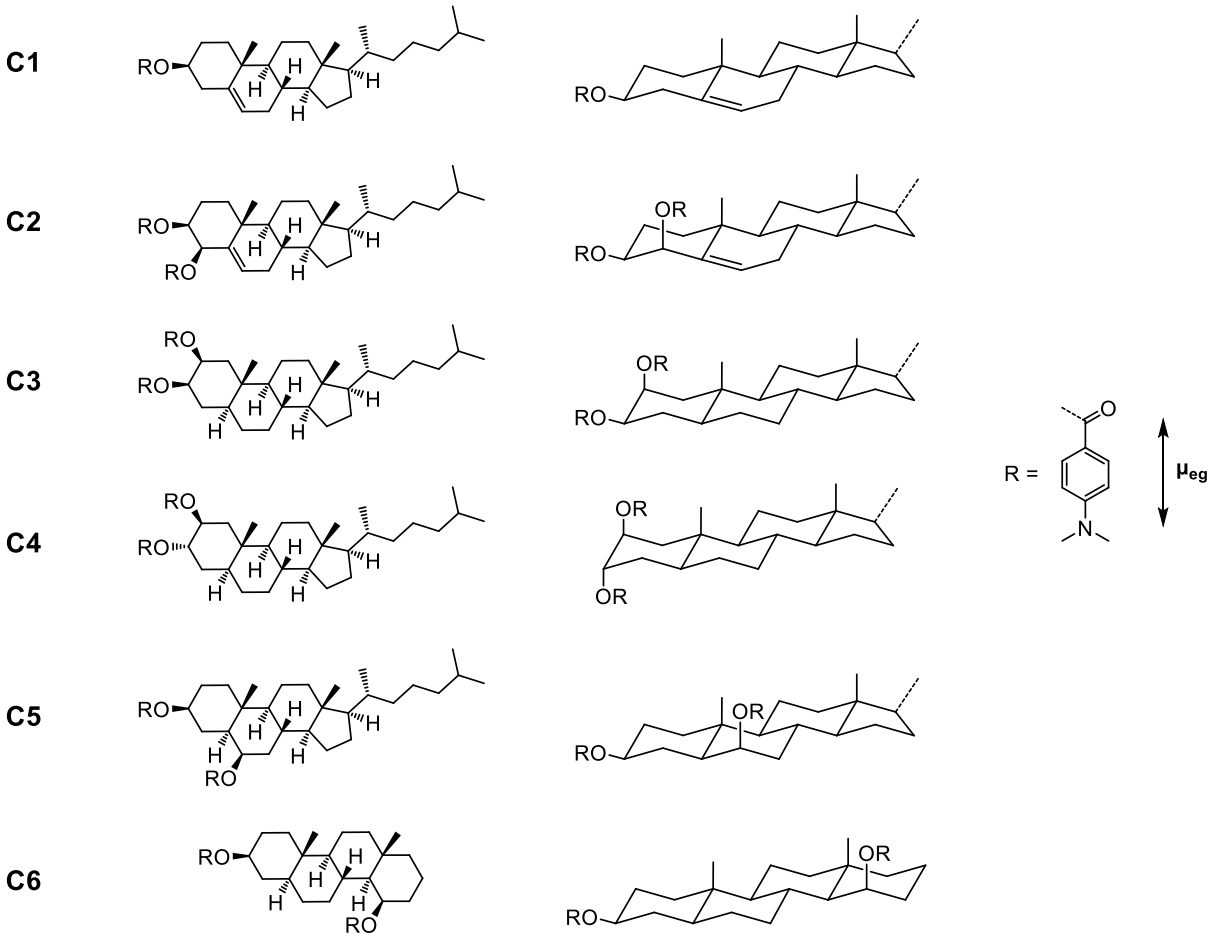

Figure 15. Structures of the dimethylaminobenzoate-substituted cholesterol derivatives (planar and 3D drawings), as well as the dimethylaminobenzoate group with its transition moment $\boldsymbol{\mu}_{\mathbf{eg}}$.

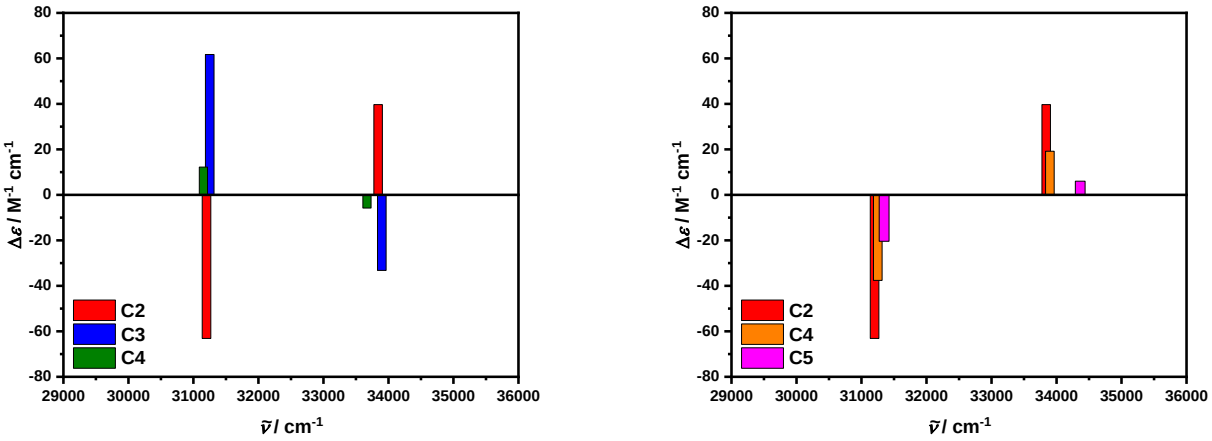

Figure 16. Excitonic CD bands (shown as sticks) of compounds **C2-C6** corresponding to CT-bands of the dimethylaminobenzoate moiety. Values taken from ref.[153]

When comparing the excitonic CD spectra **C2**, **C3** and **C4**, it can be seen that the CD bands nicely adhere to the above-described angle dependence. Here, **C2** and **C3** roughly possess the same relative angle, leading to a similar magnitude of the CD bands. However, the direction ("screw sense") is opposite, comparable to the 60° and 300° conformations shown in Figure 14, leading to a sign change of the spectrum. **C4**, on the other hand, possesses a trans-diaxial arrangement of the two dimethylaminobenzoate groups, thus leading to a dihedral angle close to 180°, which causes the CD signal to nearly vanish. The comparison of **C2**, **C5** and **C6** illustrates the distance dependency of the CD signal. While the dihedral angle remains approximately constant, the interchromophoric distance increases, resulting in a progressively diminishing CD signal.

1.2.3 Chiral helical aggregates

One special case that is of particular interest is the helical arrangement of chromophores. Due to the widespread occurrence of this type of structure, the understanding of the (chiroptical) properties of these systems has therefore been a significant field of research in the past, where several models were constructed and refined over the years.[127, 158-164]

An example for such a model was developed by Knoester et al.,[162] who modelled the helix as a cylindrical aggregate as shown in Figure 17. The geometry can be described by the basis vectors a_1 and a_2. Rolling the lattice perpendicular to the helix direction z along *C*, which is the vector connecting the two outer monomer units and perpendicular to the helix direction z,

results in the cylinder as depicted on the right-hand side of Figure 17. The absolute value of *C* is given by $2\pi R$, where *R* is the radius of the cylinder. It connects two lattice points, so *C* can be described as a linear combination of the two basis vectors $C = c_1a_1 + c_2a_2$. When rolled, the aggregate becomes a set of N_1 rings, each containing N_2 subunits and separated by the distance *h*. Furthermore, each ring is twisted by the angle *γ* with respect to the previous one. For the individual position of a subunit, n_1 describes the ring of the stack in which it is located in and n_2 the position within the ring, so that connecting each subunit with the same n_2 essentially describes a helix wrapped around the cylinder. As can be seen on the right-hand side of Figure 17, each subunit possesses a transition moment *μ* with equal magnitudes and orientations, that make an angle *β* with the cylinder axis and an its projection on the *xy* plane an angle *α* with the tangent of the ring.

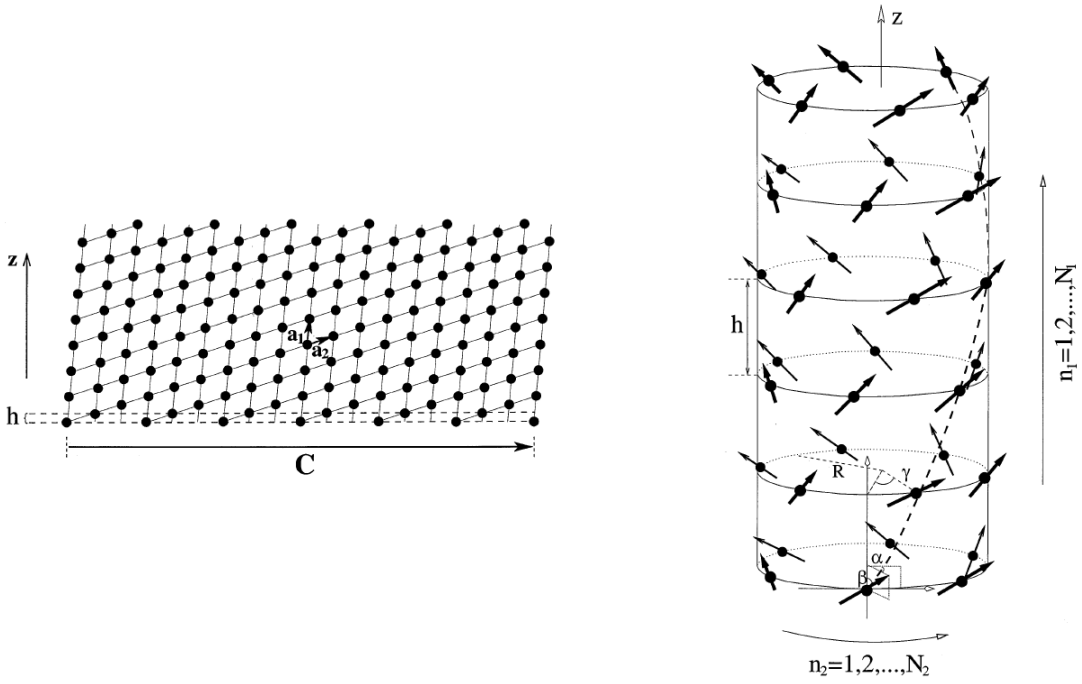

Figure 17. Left: 2D-lattice of the aggregate. Each dot represents a subunit. Right: Construction of the aggregate by rolling around *C*. The arrows describe dipole moments. Reproduced with permission from *Optical Properties of Helical Cylindrical Molecular Aggregates: The Homogeneous Limit*, C. Didraga, J. A. Klugkist, J. Knoester, Copyright © (2002) American Chemical Society.[162]

Using a Frenkel exciton Hamiltonian and a transformation following Bloch's theorem,[165] an expression for the rotational strength of the aggregate can be derived:

$$R = \frac{1}{3}\frac{\pi}{2\lambda}\sum_{nm}\varphi_{\mathrm{k}}(n)\varphi_{\mathrm{k}}^{*}(m)\boldsymbol{R}_{12}\cdot(\boldsymbol{\mu}_{\mathrm{n}}\times\boldsymbol{\mu}_{\mathrm{m}}) \tag{46}$$

This resembles the expression for R_{ex} derived in equation (42). φ_k are the Bloch-wavefunctions of the exciton eigenstates. Further imposing periodic boundary conditions and convolution with a line shape function $F(\omega)$ gives the final result for the CD spectrum of a helical aggregate:

$$CD(\omega) = \frac{N|\mu|^2\pi R}{6\lambda}\sin 2\beta \cos\alpha[F(\omega - E_0) - F(\omega - E_h)] + \frac{N|\mu|^2\pi h}{6\lambda}\sin^2\beta \frac{dF(\omega - E_h)}{d\omega}\sum_n n_1 J(n)\sin\left(\gamma n_1 + \frac{2\pi}{N_2}n_2\right) \quad (47)$$

where J describes the coupling, E_0 is the energy of the absorption peak corresponding to the excitation parallel to the helix axis z, and E_h the energy of the band polarized perpendicular to the helix axis. In this equation, the term $[F(\omega - E_0) - F(\omega - E_h)]$ represents transition arising from the isolated ring of molecules (ring contribution), whereas the second term describes contributions of the aforementioned helix wrapped around the cylinder (helix contribution). The ring contribution is made up of two separate parts of opposite signs located at E_0 and E_h, respectively. The helix contribution is exclusively located at E_h and has a dispersive shape, where the group velocity (sum in eq. (47)) plays an important role. The various negative and positive bands often overlap, resulting in a CD spectrum that is very sensitive towards the variation of geometrical parameters (length N_1, circumference N_2, angles α and β). Examples for such CD spectra are shown in Figure 18, where the parameter N_1 is varied.

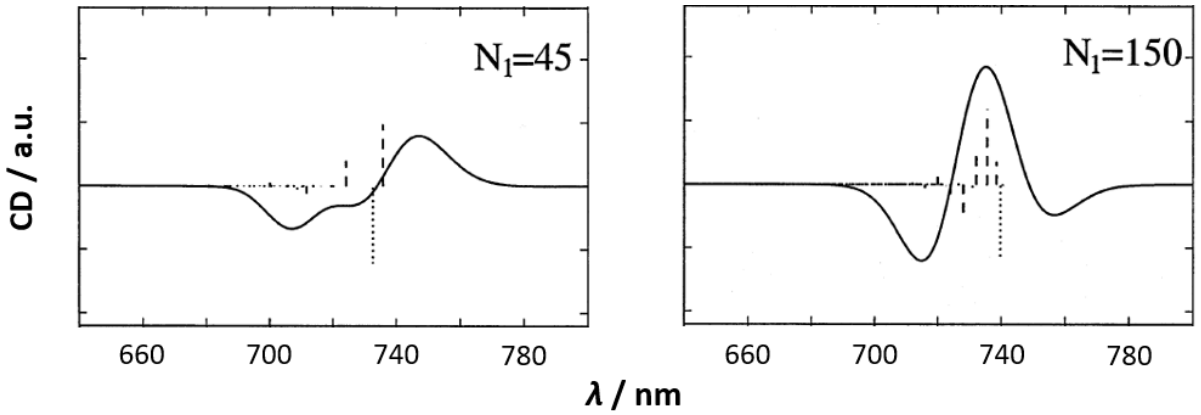

Figure 18. Examples for CD spectra of the above-described aggregation type with different lengths N_1. Left: N_1 = 45, right: N_1 = 150. Chlorosomes were used as the model system for these calculations. Reproduced with permission from *Optical Properties of Helical Cylindrical Molecular Aggregates: The Homogeneous Limit*, C. Didraga, J. A. Klugkist, J. Knoester, Copyright © (2002) American Chemical Society.[162]

1.3 Chiral polymeric foldamers

1.3.1 Helix vs. random coil conformations in foldamers

Throughout nature, the helix is a frequently occurring structural motif. It was first discovered in the form of helical sections (α-helix) in proteins as their secondary structure by Pauling et al.[16] Due to the primary structure of the amino acid chains, where the individual building blocks differ in their characteristic residues, the folding into various types of conformations is facilitated.[166] Inspired by this, many artificial polymeric foldamers (covalently linked intramolecular aggregates), as well as intermolecular aggregates, have been constructed and characterized using a wide variety of different monomer species.[48-51, 167-171]

In such foldamers, the individual monomer units usually possess a certain degree of conformational freedom, e.g., the rotation around the connecting covalent bonds, enabling the formation of different conformations of the polymer strand. This situation is usually described by an equilibrium between a random coil and a more ordered helical conformation as shown in Figure 19.[172-175] Depending on the type of parent monomer structure used, many different methods are employed to induce the folding into a helical conformation, such as a change in solvent,[91-92, 176-177] temperature,[91, 178] pH-value,[179-181] or the addition of template (guest molecules/ions inducing the formation of a helix).[182-186]

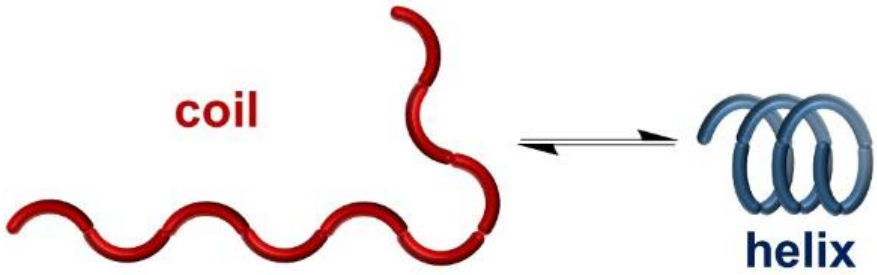

Figure 19. Schematic representation of the helix-coil equilibrium in foldamers. Reproduced from ref.[91] (open access).

Adding an element of chirality in these systems may result in the helix possessing an excess of one twist sense (twist bias). To this date, a plethora of artificial homohelical polymers consisting of different classes of parent monomer structures have been described in the literature, including phenylene ethynylenes,[187-196] thiophenes,[178, 197-201] indolocarbazoles,[202] aromatic amides,[203-206] porphyrins,[207] synthetic peptides,[208-209] bi-[210-211] and tripyridines,[212] terphenyls,[213-214] isocyanates,[215-219] isocyanides,[220-222] silanes,[223-224] and acetylenes.[225-227] The homohelicity in these systems can be achieved by various

methods of chiral induction, which will be showcased using various examples in the following section.

1.3.2 Examples for chiral induction in homohelical foldamers

A rather obvious method to realize chiral induction is the use of intrinsically chiral molecules to construct the main chain. One example are covalently linked binaphthyls, which form a helical conformation through rotation around the connecting bond and therefore exhibit an increased CD signal.[228-229] In many cases, the incorporation of chiral units into the main chain[189, 192-193] or the use of chiral terminal groups[223, 227, 230-231] is also sufficient for an induction of twist sense bias in the resulting helical conformation. One example for this was the use of chiral initiators for the polymerization of polyacrylates reported by Yuki et al.[230] The use of external stimuli, such as chiral guest molecules[187-188, 206, 232] or chiral solvents,[216] were also successful at achieving this goal. This was demonstrated by Green et al., who used chiral 2-substituted chloroalkanes as a solvent for achiral polyisocyanates (**P1** in Figure 20), which led to a visible CD signal.[216] If the helix is sufficiently conformationally stable, homohelicity can also be achieved by asymmetric polymerization[222, 233] or even chiral resolution. [205, 210, 212] One example for this is the resolution of double-stranded Cu(I)-helicates by diastereomeric salt formation and subsequent precipitation.[210]

Among the most established method, however, is the use of chiral side chains, which enable the folding into a homohelical conformation through cooperative interactions.[234] Green et al. was one of the first to demonstrate this using polyisocyanates bearing chiral side chains,[215-219] which are shown in Figure 20.

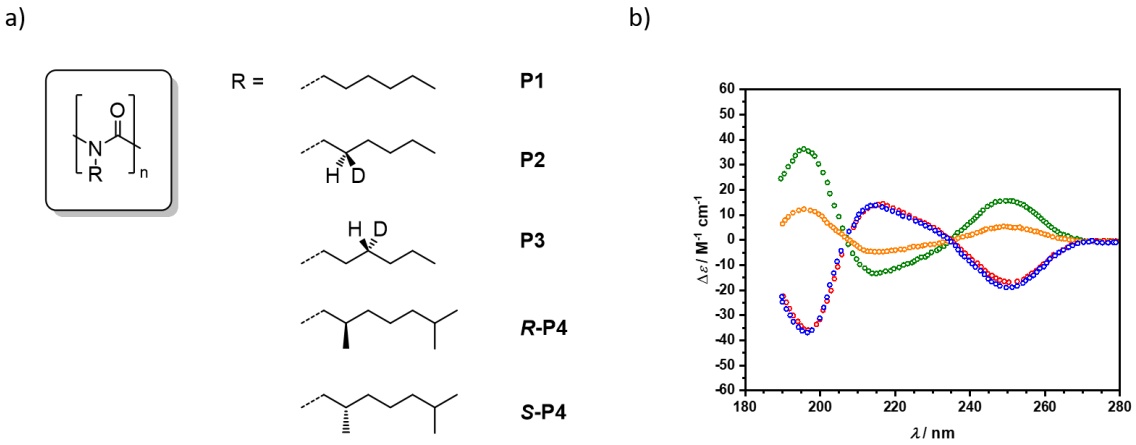

Figure 20. Chiral polyisocyanates studied by Green et al. a) Structures of **P1**-**P4** b) CD spectra of *R*-**P4** (blue circles), *S*-**P4** (green circles), *R*-**P4**/*S*-**P4** 49:51 (orange circles) and *R*-**P4**/*S*-**P4** 56:44 (red circles), recreated from ref.[215]

The depicted polyisocyanates generally adopt helical conformations depending on their main chain length, where longer polymer strands tend to increasingly adopt random-coil-like structures due to factors such as bending of the stiff helix or helix reversals.[235] While the achiral derivative **P1** forms a racemic mixture of *M*- and *P*-helices in achiral solvents, it was shown that the introduction of a chiral perturbation led to a visible CD signal and therefore an excess in twist bias of the resulting helix. This was even achieved when merely substituting one hydrogen atom of the *n*-hexyl chain with deuterium in **P2** and **P3**, which possess opposite preferred screw senses. Using temperature dependent chiroptical spectroscopy, the authors were able to derive a model using statistical thermodynamics enabling the explanation of this phenomenon. It was concluded, that this was due to the large conformational reversal barrier, which led to the tiny energy difference being amplified by the formation of long helical sequences, which in turn governed the chiroptical properties. Further studies of *R*/*S*-**P4** confirmed this model, as even a seemingly negligible amount (~ 0.01%) of chiral side chains used along achiral side chains ('Sergeants-and-Soldiers' principle), or the use of a mixture of *R*- and *S*-**P4** with a very low enantiomeric excess ('Majority Rule') induces an observable excess in helical screw sense, which is shown in Figure 21b. Here, an ee-value of 2% was sufficient to achieve nearly complete homohelicity.

Another example system, which has been extensively studied by Moore et al., are phenylene-ethynylene oligomers.[177, 187-195, 236-237] In such systems, many of the aforementioned methods have proven successful in forming a helical conformation possessing an excess in screw sense. The general structure, as well as the methods used for the chiral induction, are shown in Figure 21.

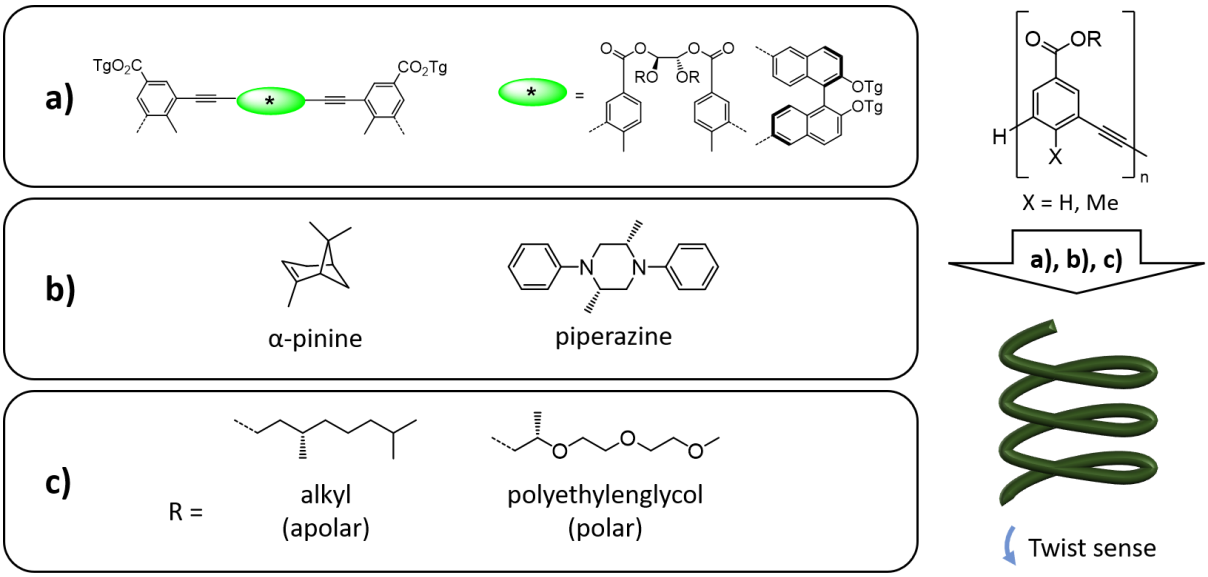

Figure 21. Structure and methods of chiral induction of phenylene-ethynylene oligomers by Moore et al.[177, 187-195, 236-237] a) Incorporation of chiral groups directly into the main chain, b) addition of chiral guests, c) use of chiral side chains.

After the initial discovery, that these phenylene-ethynylene oligomers generally undergo a cooperative solvent or temperature dependent helix-coil transition,[177, 236] multiple methods of chiral induction in these systems were subsequently established. The first reported homohelical foldamer of this type was one containing an enantiomerically pure binaphthyl moiety incorporated directly into the main chain as depicted in Figure 21a.[192] This outcome was later also realized when exchanging the binaphthyl unit with a helicene[189] unit or a tartaric acid derived tether.[193] In these examples, the incorporated moiety acts as a template that allows the folding of the helix to be unidirectional. A different approach was the addition of a chiral guest molecule, such as (-)-α-pinene (Figure 21b), was able to generate a twist-sense bias, as the guest molecule bound in the helical cavity.[188, 237] This was studied in acetonitrile/water mixtures of various compositions. When adding 100 equivalents of α-pinene, the use of shorter side chains (triethyleneglycol) led to the emergence of a CD signal at a water content of 10%, while no CD signal was observed for analogous oligomers bearing longer hexaethyleneglycol side chains for water contents of up to 50%. It was therefore concluded, that at lower water contents the binding of the side chains inside the helical cavity was preferred and further increase of the water content led to the solvation of the side chains, thus enabling the binding of the guest molecule in its place. In precedent studies, the use of chiral side chains as shown in Figure 21c has also led to a preferred screw sense of the resulting helix.[190-191, 194-195] As in the case of the aforementioned polyisocyanates, the folding was also in a cooperative manner as demonstrated using varying amounts of chiral side chains

following the Sergeant-and-Soldier principle, as the relationship of the fraction of chiral side chains and the observed CD intensity was non-linear.[190] Furthermore, it was found that these helically twisted oligomers underwent cooperative intermolecular aggregation (stacking of one helix on top of the other) as well, where the chirality was transferred from a chiral helix (oligomer bearing chiral side chains) to an analogous achiral derivative.[195]

2 SCOPE OF THE WORK

This work follows the work of S. Völker,[86, 92-94, 96] H. Ceymann,[238] M. Schreck[73, 85, 88, 90] and A. Turkin,[86, 91] who synthesized various oligo- and polymers using the indolenine squaraines **SQA** and **SQB** (Figure 22a) as the two main monomer species. These oligo- and polysquaraines possessed altered optical properties compared to the respective monomers, which were explained in terms of Kasha's exciton coupling theory. Perhaps most interestingly, higher oligomers (n > 6) and polymers of **SQB** showed a pronounced solvent and temperature dependent J- or H-type behavior, which was ascribed to the formation of a random coil and loosely wound helical conformation (Figure 22b) through rotation around the connecting biaryl axis.

a)

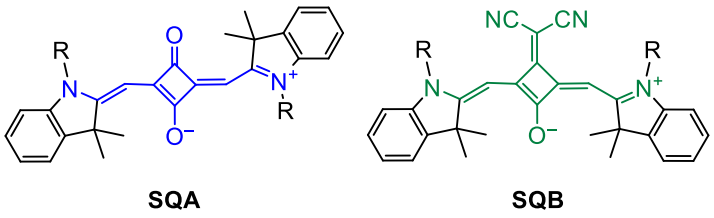

b)

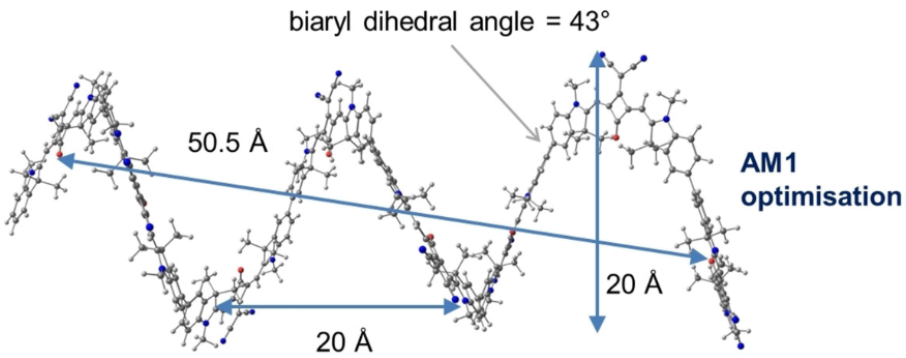

Figure 22. a) Structures of the two types of indolenine squaraine parent structures used in this and preceding work. b) AM1-optimized model helix structure of the SQB-octamer showing highlighted geometrical parameters. Reproduced from ref.[91] (open access).

As outlined in the introduction, the addition of an element of chirality can prove beneficial for potential applications of organic chromophores due to the interaction with CP light. As the literature on chiral squaraines is rather limited, the question arose if these squaraine systems would constitute a suitable system for the incorporation of chirality. This can best be achieved either by the introduction of chiral side chains (R* in Figure 23), or by altering the substitution at the 3-position (quaternary C-atom) of the indolenine subunit (A in Figure 23). Oligo- and polymerization of such chiral monomers may then enable the interpretation of the chiroptical

properties in terms of exciton chirality and potentially lead to an enhanced CD effect. Furthermore, as described in chapter 1.3, both main chain and side chain chirality have successfully induced a twist-sense bias in helical polymers. As **SQB** oligo- and polymers adopt a helical conformation, the monomer chirality may be used as conformational control in this case as well.

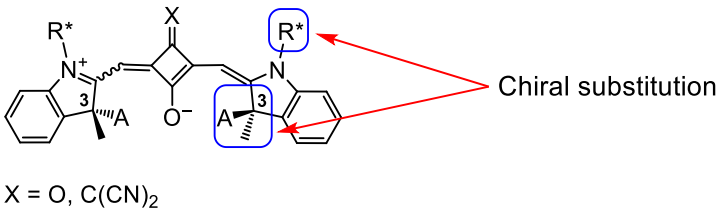

Figure 23. General structure and possibilities for the incorporation of chirality in the investigated indolenine squaraines.

In the first part of this work, the synthetic methodology for the preparation of C(3)-chiral indolenine squaraines with varying substitution (*n*-propyl and phenyl) and chiral alkyl side chains will be presented. The resulting monomeric squaraines will then be discussed in terms of their geometrical structure, as well as their optical and chiroptical properties.

In the following chapter, the synthesis and characterization of SQB-homopolymers bearing different chiral side chains will be discussed. As in the previous studies, the focus will be set on their solvent and temperature dependent (chir)optical properties, in order to gain insight into the conformation of the polymers in solution.

This section is then followed by the analogous discussion of polymers containing the C(3)-chiral phenyl substituted **SQB*** – specifically **SQA-SQB*** and **SQB-SQB*** copolymers, and **SQB*** homopolymers. Additionally, analogous di- and trimers of comprising these structural motifs are prepared as model systems in order to assist the interpretations of the findings for the polymers. The hereby obtained experimental results for these oligomers are then further compared to theoretical calculations (cooperation with D. Fischermeier, Mitric group University of Würzburg) and discussed in terms of exciton chirality.

The last chapter then deals with the synthesis and characterization of the **Pr-SQB***-homopolymer in the same fashion as the phenyl-substituted analogues in the previous chapter.

3 CHIRAL INDOLENINE SQUARAINE MONOMERS[1]

3.1 C(3)-chiral monomers

In a previous attempt by Schreck et al. to alter the substitution at the quaternary carbon at the 3-position of the indolenine subunit by replacing the methyl groups with phenyl groups (**TPh-SQB** in Figure 24), it was found that this resulted in an inverted structure, where the phenyl groups faced away from the squaric acid core due to steric repulsion. Polymers comprised of **TPh-SQB** showed an exclusive formation of elongated J-type zigzag conformations.[90] This inspired the idea to introduce a chiral center at this position, which is well suited due to its vicinity to the central chromophore. The aim of this is the investigation of the impact on the geometrical structure and (chir)optical properties of the monomers, while also further retaining the goal of selective conformational control of polymers comprising this type of chiral building blocks. This led to the initial idea of replacing only one methyl group with a phenyl group, resulting in **Ph-SQB***, as well as different other derivatives, which is also shown in Figure 24.

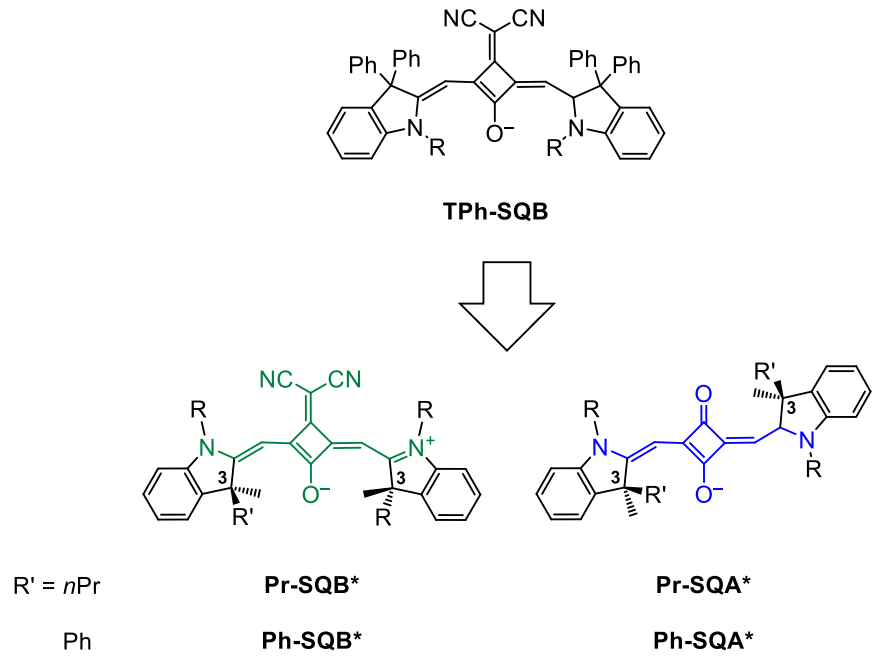

Figure 24. Structures of **TPh-SQB** and the target C(3)-chiral squaraines**.**

[1] a) Partially reprinted (adapted) with permission from *Chiroptical Properties of Indolenine Squaraines with a Stereogenic Center at Close Proximity*, J. Selby, M. Holzapfel, B. K. Lombe, D. Schmidt, A.-M. Krause, F. Würthner, G. Bringmann, C. Lambert *J. Org. Chem.* **2020**, *85*, 12227-122242. © 2020 American Chemical Society.
b) Partially reprinted (adapted) with permission from *Polymeric Indolenine-Squaraine Foldamers with a Preferred Helix Twist Sense and their Chiroptical Absorption and Emission Properties*, J. Selby, M. Holzapfel, K. Radacki, A. Swain, H. Braunschweig, C. Lambert *Macromolecules* **2022**, *55*, 421-436. © 2022 American Chemical Society.

Furthermore, as outlined in chapter 1.1.2, all of the research conducted on chiral squaraines exclusively focused on the use of chiral peripheral groups or side chains. This was done in order to study supramolecular aggregation. Therefore, the incorporation of a chiral center directly into the backbone of the chromophore may enable the study of the chirality of the monomers themselves, as the chiral perturbation is now in sufficient vicinity to the central chromophore and therefore may lead to a significant CD signal.

3.1.1 Synthesis

The synthetic route for symmetric indolenine squaraines has been well established. In this standard approach, the deprotonated indolium salt reacts as a nucleophile with a squaric acid (ester). Therefore, in this case, the synthetic challenge lies in the synthesis of the enantiomerically pure indolium salt. There are two possible strategies to achieve this goal, which are illustrated in Figure 25. The first method (I) is the direct alkylation of the indolenine via an S_N2-reaction with an alkyl iodide in a polar aprotic solvent, while the second method (II) consists of the nucleophilic addition of MeMgBr to the carbonyl group of an *N*-alkylated oxindole followed by the acidic elimination of water. The choice of the method employed depended on the desired substitution at the chiral center at the 3-position of the indolenine subunit.

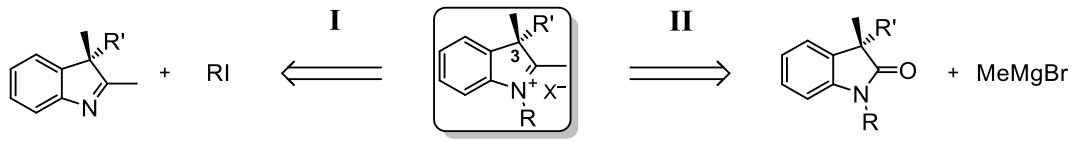

Figure 25. Two approaches for the synthesis of the C(3)-chiral indolium salts.

3.1.1.1 Synthesis of the phenyl-substituted C(3)-chiral indolium salts via pathway II

A method for the asymmetric synthesis of 3-aryl-3-alkyl substituted oxindoles was previously developed by Smith et al.[239] Thus, pathway II was chosen for the synthesis of the phenyl-substituted derivatives. First, the chiral auxiliary **4** was synthesized *ex* chiral pool starting from either *L*- or *D*-serine methyl ester hydrochloride and is shown in Scheme 1. For clarity, only the synthesis of the *S*-enantiomer is shown, the influence of the configuration at the stereogenic center is indicated when appropriate.

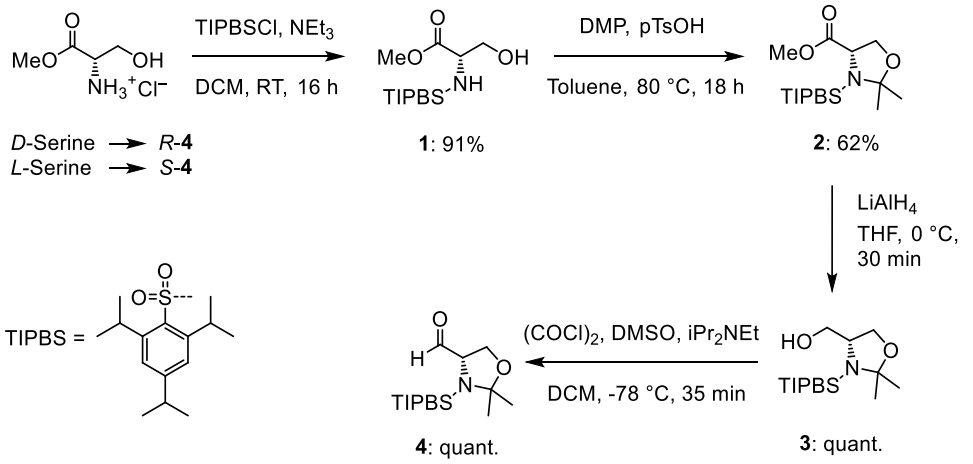

Scheme 1. Synthesis of the aldehyde **4** (chiral auxiliary).

The first step is the introduction of the 2,4,6-triisopropylbenzenesulfonyl (TIPBS) moiety, which will later act as the stereodirecting group. Subsequently, compound **1** is treated with dimethoxypropane (DMP) under acidic catalysis and the acetal **2** is formed. The ester function is then converted to the corresponding aldehyde **4** by reduction to the alcohol **3** using $LiAlH_4$, followed by a Swern oxidation. The overall yield of this reaction sequence was 56%.

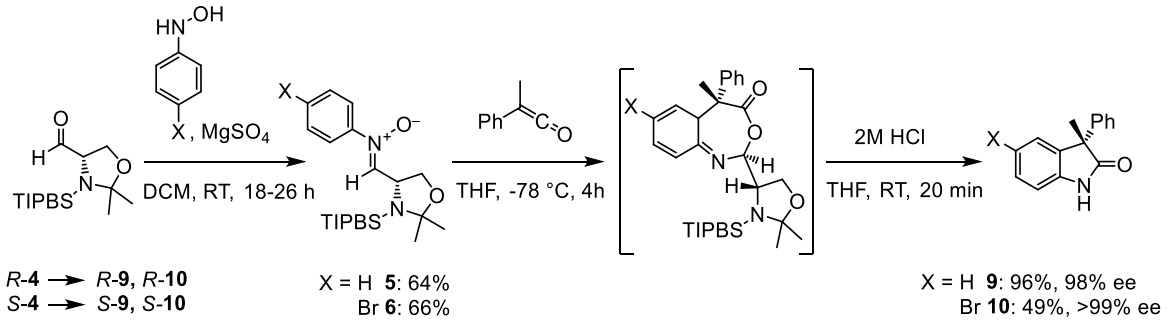

Scheme 2. Synthesis of the chiral oxindoles **9** and **10**.

The oxindoles were then prepared using the aldehyde **4** as a chiral auxiliary and is shown in Scheme 2. In an addition-elimination reaction, the nitrones **5** (using phenylhydroxylamine) and **6** (using 5-bromophenylhydroxylamine) were formed in moderate yields of 64% and 66%, respectively. These were then treated with phenylmethylketene **8** under kinetic conditions, whereupon a [3+2] cycloaddition took place followed by a [3,3] sigmatropic rearrangement. The selectivity of this transformation stems from the TIPS group blocking one face of the π-system and enabling a favorable orientation of the ketene during its attack on the π-system, which can be seen in the calculated transition state of this reaction in Figure 26.[239]

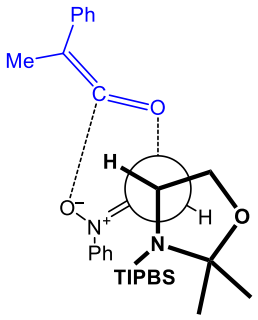

Figure 26. Structure of the favored transition state of the initial cycloaddition.[239]

Further acidic hydrolysis of the hereby formed intermediate resulted in the oxindoles **9** and **10**, which were obtained in high yields of up to 96%. While recrystallization of **9** was not possible, **10** was able to be recrystallized from MeCN/H_2O, thus further increasing the enantiomeric excess to ≥ 99%. Nevertheless, the enantiomeric purity of **9** was also sufficient and ranged from 94-98% (see analytical HPLC chromatograms in the appendix). Theoretically, it should be possible to reuse the auxiliary for further batches, but the aldehyde **4** was neither stable on silica nor neutral alumina, and therefore only trace amounts were isolated.

Phenylmethylketene **8** was priorly synthesized as shown in Scheme 3. 3-Phenylpropionic acid was converted to the corresponding acid chloride **7** using thionyl chloride. The ketene was then synthesized by elimination of HCl using NEt_3. Here, the use of a cryostat for an overnight reaction and performing a distillation under an inert atmosphere and reduced pressure, instead of the widely reported Kugelrohr distillation, reliably led to greatly improved yields of up to 68% compared to those reported in the literature (30-45%).[240-241]

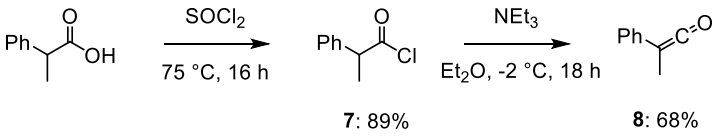

Scheme 3. Synthesis of phenylmehtylketene **8**.

The alkylation of the oxindoles **9** and **10** (Scheme 4) was carried out via prior deprotonation with K_2CO_3 in DMF followed by treatment with the alkyl iodides in an S_N2-reaction. Depending on the side chain used, the obtained yields varied greatly, ranging from 41% for compound **19a** to 95% for compound **20b**.

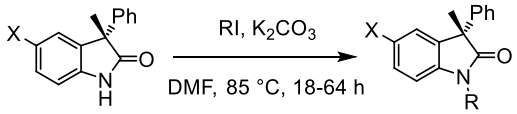

X = H, R = *n*-Bu **19a**: 41%
X = H, R = *n*-Hex **19b**: 84%
X = H, R = $C_{16}H_{33}$ **19c**: 88%
X = Br, R = *n*-Hex **20a**: 91%
X = Br, R = $C_{16}H_{33}$ **20b**: 95%

Scheme 4. Alkylation of the oxindoles **19** and **20**.

The synthesis of the racemic alkylated oxindoles, which were used for the preparation of the diastereomeric mixtures of the target squaraines, is similar compared to that of the previously reported diphenyl-substituted analogues and is shown in Scheme 5.

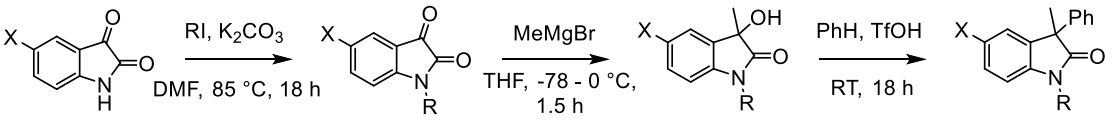

X = H, R = *n*-Bu **15a**: 98%
X = H, R = *n*-Hex **15b**: 50%
X = H, R = $C_{16}H_{33}$ **15c**: 16%
X = Br, R = *n*-Hex **16a**: 28%
X = Br, R = $C_{16}H_{33}$ **16b**: 54%

X = H, R = *n*-Bu **17a**: 71%
X = H, R = *n*-Hex **17b**: 67%
X = H, R = $C_{16}H_{33}$ **17c**: 70%
X = Br, R = *n*-Hex **18a**: quant
X = Br, R = $C_{16}H_{33}$ **18b**: 80%

X = H, R = *n*-Bu **19a**: 45%
X = H, R = *n*-Hex **19b**: 98%
X = H, R = $C_{16}H_{33}$ **19c**: 33%
X = Br, R = *n*-Hex **20a**: 68%
X = Br, R = $C_{16}H_{33}$ **20b**: 86%

Scheme 5. Racemic synthesis of the 3-phenyl substituted oxindoles **19** and **20**.

The first step is the alkylation of either isatin or 5-bromoisatin using the same method as previously described for the chiral oxindoles. These alkylated isatin derivatives **15** and **16** are then treated with MeMgBr at -78 °C, where the methyl group is selectively added to the more reactive keto group to form the alcohols **17** and **18**. These are then in turn treated with the superacid TfOH and benzene, where the hydroxy group is protonated leading to the elimination of water, whereupon the resulting cation acts as an electrophile in an S_EAr-reaction with benzene to form the racemic oxindoles *rac*-**19** and *rac*-**20**.

Finally, the indolium salts are synthesized by nucleophilic addition of MeMgBr to the lactams **19** and **20**, followed by subsequent acidic elimination using HCl in MeOH, which is shown in Scheme 6. The use of HCl in MeOH (as compared to HCl in H_2O) proved to be crucial, since the following steps were unsuccessful otherwise. Due to the tendency of these indolium salts to decompose under ambient conditions,[90, 242] they were used directly for further synthesis and without further purification or characterization. The yields were assumed to be quantitative.

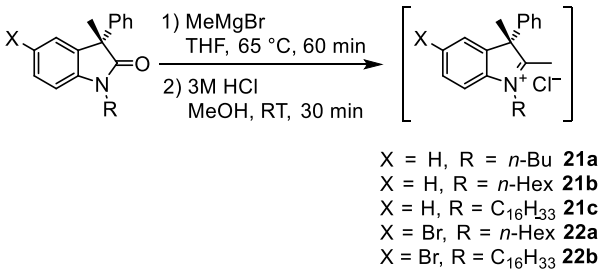

Scheme 6. Synthesis of the 3-phenyl substituted indolium salts.

3.1.1.2 Synthesis of the n-propyl-substituted C(3)-chiral indolium salts via pathway I

Because the above-described method only yields satisfying results for 3-aryl-3-alkyl substituted oxindoles, an alternative method is required in order to obtain the 3,3-dialkyl-substituted analogues. Therefore, the indolenines **13** and **14** were prepared racemically and then resolved using a kinetic resolution by asymmetric hydrogenation as developed by Fan et al.[243] The racemic synthetic pathway, which is illustrated in Scheme 7, consisted of a Fischer-indole synthesis of the indoles **11** and **12** starting from (5-bromo)phenylhydrazine hydrochloride and 2-hexanone, followed by a nucleophilic substitution of the deprotonated indoles with methyl iodide to form the target indolenines **13** and **14**.[244]

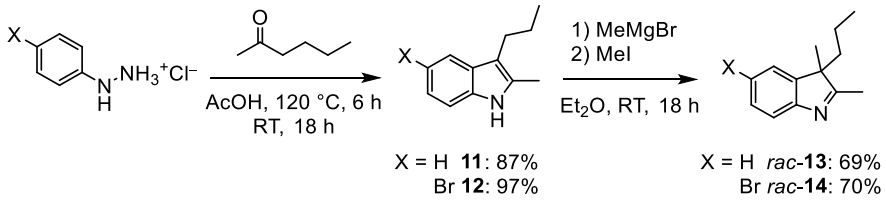

Scheme 7. Racemic synthesis of the indolenines **13** and **14**.

The chiral ruthenium catalyst **Cat*** used in the asymmetric hydrogenation was prepared as shown in Scheme 8.[243, 245-247] In the first step, (*R*,*R*)-1,2-diphenylethane-1,2-diamine was treated with p-(trifluoromethyl)benzenesulfonic acid chloride to form the sulfonic acid amide **15** in an addition-elimination reaction. Upon treatment with the dichloro-(p-cymene)-ruthenium(II) dimer the chiral mononuclear ruthenium complex **16** is obtained. In the final step, the chloride anion is exchanged for a triflate ion using silver triflate to form the desired complex **Cat***.

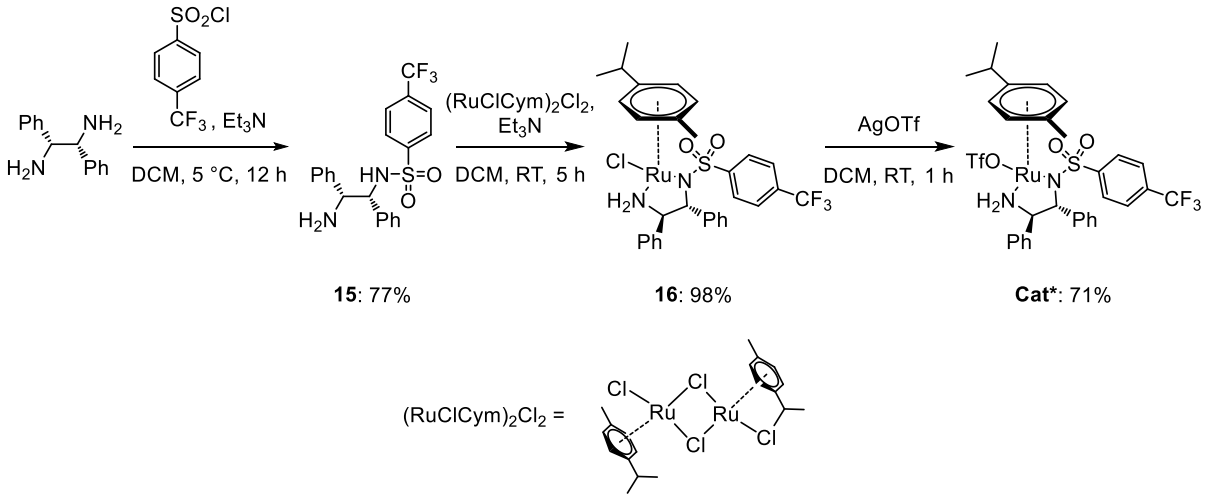

Scheme 8. Synthesis of the chiral Ru-catalyst **Cat***.

In the asymmetric hydrogenation (Scheme 9), one enantiomer of **13** or **14** was preferably hydrogenated, meaning the reaction rate of the hydrogenation of the favorable reaction (k_{fast}) was greater compared to that of the disfavored case (k_{slow}). The mechanism of this reaction was proposed to include the in-situ formation of the superacid TfOH, which protonates the indolenine nitrogen to form the corresponding iminium salt. The selectivity is believed to originate from the CH/π activation between the η^6-arene ligand at the ruthenium and the fused benzene ring of the indolenine, and the formation of a 10-membered-ring transition state, which is shown in Figure 27.[243, 245-247]

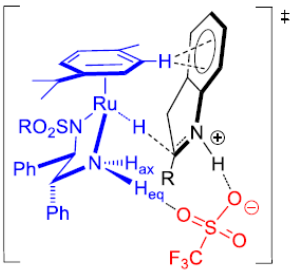

Figure 27. Proposed transition state of the asymmetric hydrogenation of indolenines. Reproduced with permission from *Highly Enantioselective Synthesis of Indolines: Asymmetric Hydrogenation at Ambient Temperature and Pressure with Cationic Ruthenium Diamine Catalysts*, Z. Yang, F. Chen, Y. He, N. Yang, and Q.-H. Fan, Copyright © (2016) John Wiley and Sons.[243]

In such kinetic resolutions, there is always a tradeoff of purity versus yield. This becomes more significant, the less selective the reaction is. The longer the reaction takes place, the higher the conversion becomes, the more the yield of the unreacted substrate (target product) will decrease and its purity increase. One way to quantify this is the use of the selectivity factor *S*,[248] which is defined as the ratio of the two rate constants for the hydrogenation reactions

of the two enantiomers and is calculated using eq. (48). The calculated selectivity factors for various kinetic resolutions are summarized in Table 1.

$$S = \frac{k_{\text{fast}}}{k_{\text{slow}}} = \frac{ln[(1-c)(1-ee)]}{ln[(1-c)(1+ee)]} \tag{48}$$

Where *c* is the conversion and *ee* the enantiomeric excess of the unreacted target compound.

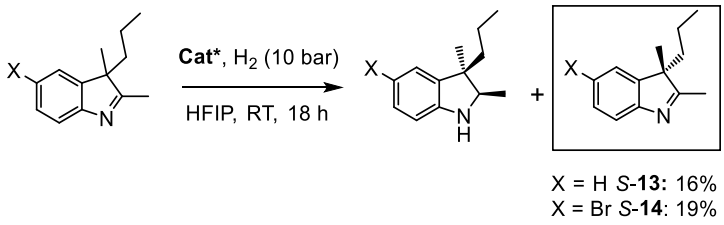

Scheme 9. Kinetic resolution by asymmetric hydrogenation of indolenines **13** and **14**.

Table 1. Conversion *c*, enantiomeric excess *ee* and selectivity factors *S* of different kinetic resolutions of **13** and **14**.

	c	***ee***	***S***
***S*-13_1**	64%	79%	5.86
***S*-13_2**	82%	97%	5.20
***S*-13_3**	81%	98%	5.82
***S*-14_1**	44%	40%	4.48
***S*-14_2**	80%	98%	5.99

For the unbrominated indolenine **13** the average selectivity factor was 5.63, while for the brominated derivative **14** it was 5.23, showing no significant impact of the bromine atom on the selectivity of the reaction. Generally, the selectivity was quite low compared to other kinetic resolutions reported in the literature,[249-252] which meant higher conversions had to be employed in order to achieve a sufficient enantiomeric purity. Fortunately, the synthesis of the racemic indolenines was unproblematic and possible on a gram scale, and up to 1.5 g of the indolenine could be used for one hydrogenation reaction.

Another possible method to obtain the indolenines in an enantiomerically pure form would be the use of preparative HPLC on a chiral stationary phase. This was done with ***rac*-14**, where the chromatogram of the resolution is shown in Figure 28.

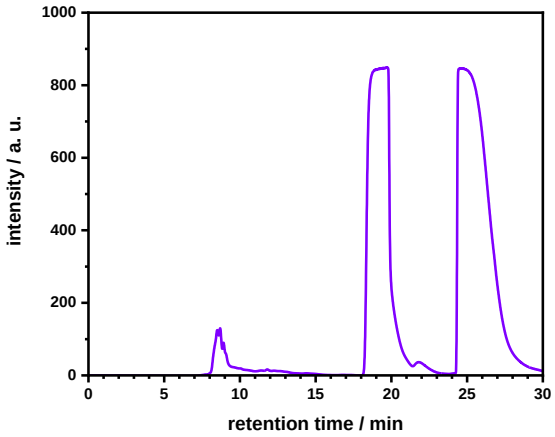

Figure 28. Chromatogram of the resolution of ***rac*-14** via preparative HPLC (Phenomenex LUX cellulose-2, *n*-Hex/*i*PrOH 99:1, 10 mL min^{-1}). The peak centered around a retention time of 19 min corresponds to the *R*-enantiomer, the one at 25 min to the *S*-enantiomer.

In general, this method is also viable, as it theoretically offers quantitative yields of *both* enantiomers in near complete enantiomeric purity (for compound ***S*-14** see analytical HPLC chromatogram in Figure 77 in the appendix) depending on the quality of the resolution. This eliminates the necessity of an elaborate asymmetric synthesis or alternative chiral resolution, albeit with the drawback of the time-intensive separation process, as only small quantities can be separated per run. Additionally, the preparative HPLC-columns are usually very expensive.

The final step was the alkylation of the enantioenriched indolenines with the alkyl iodide to form the indolium salts **23** and **24**, which is shown in Scheme 10.

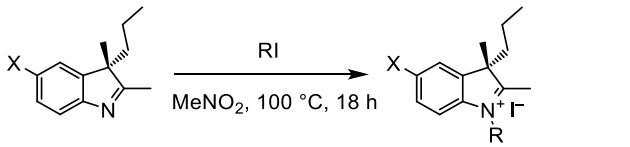

X = H, R = *n*-Bu **23:** quant.
X = Br, R = 7-methyloctyl **24**: 74%

Scheme 10. Alkylation of the enantioenriched indolenines to form the indolium salts **23** and **24**.

While **24** was purified by precipitation from Et_2O, **23** remained a viscous oil. Due to the aforementioned tendencies for these indolium salts to decompose under ambient conditions, **23** was used crude without further purification and the yield was assumed to be quantitative.

3.1.1.3 Synthesis of the symmetric C(3)-chiral squaraines

With the chiral indolium salts in hands, the synthesis of the symmetric C(3)-chiral indolenine squaraine monomers proceeded according to the standard synthetic route for symmetric indolenine squaraines and is depicted in Scheme 11.

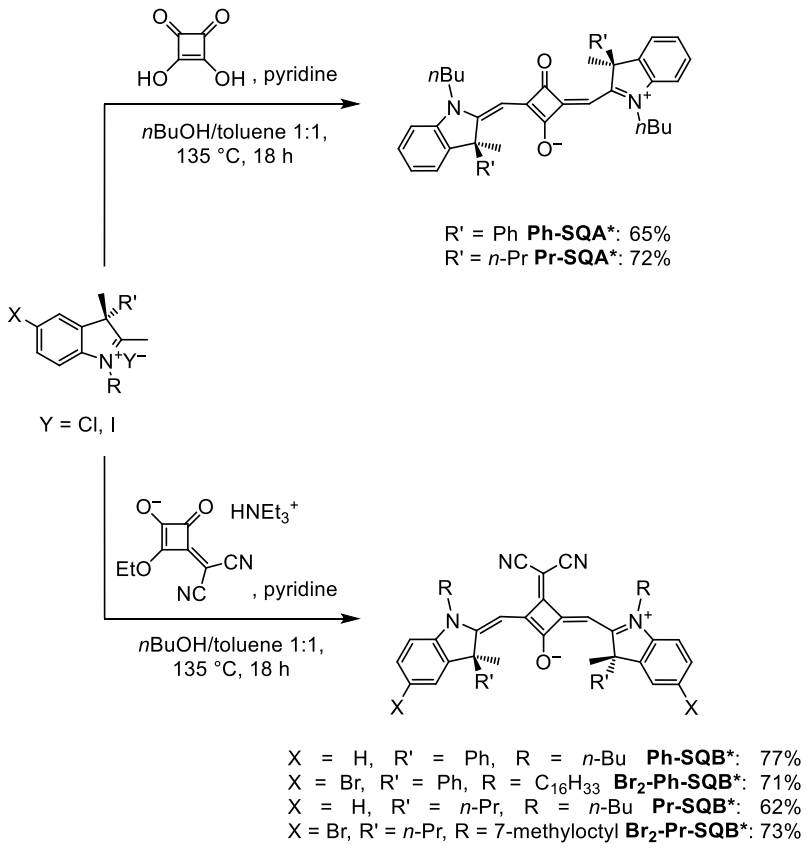

Scheme 11. Synthesis of the symmetric squaraine monomers **Pr-SQA***, **Ph-SQA***, **Pr-SQB***, **Br$_2$-Pr-SQB***, **Ph-SQB*** and **Br$_2$-Ph-SQB***.

The deprotonated indolium salts reacted with either triethylammonium 3-(dicyanomethylene)-2-ethoxy-4-oxocyclobut-1-en-1-olate **CN** (for the SQB-type squaraines) or squaric acid (for the SQA-type squaraines) in a dicondensation reaction under azeotropic removal of water to form the target squaraine monomers in satisfying yields ranging from 62-75%. The unbrominated derivatives were further recrystallized in order to increase the stereochemical purity. In a statistical distribution according to eq. (49)-(51) (binomial distribution), the achiral *R*,*S* meso-form arising from the small *R*-impurity in the indolium salts should constitute the major impurity (ca. 5%), while the *R*,*R*-enantiomer should only be formed in negligible amounts. This distribution can be assumed, since using racemic indolium salts roughly leads to a 1:2:1 ratio of the *S*,*S*-, *R*,*S*- and *R*,*R*-diastereomers, respectively.

Comparing the expected purity to that determined by chiral analytical HPLC proved that recrystallization is an effective method for the purification of the target compounds.

$$P(\mathrm{RS}) = 2 \times p\mathrm{R} \times p\mathrm{S} \tag{49}$$

$$P(\mathrm{SS}) = p\mathrm{S}^2 \tag{50}$$

$$P(\mathrm{RR}) = p\mathrm{R}^2 \tag{51}$$

where *P* denotes the probability of the formation of a diastereomer and *p* is the relative amount of the enantiomer in the starting material.

For symmetrical squaraines, the *RS* and *SR* isomers are identical, and, as previously stated, achiral (*meso*-form). This is because for the SQB-type squaraines both residues are on the same side of the planar chromophore, leading to the existence of a mirror plane perpendicular to the chromophore plane along the central molecular axis dividing the squaric acid ring (C_s-symmetry). For the SQA-type squaraines the residues are on the opposite side, thus leading to the molecule having the centroid of the squaric acid ring plane as an inversion center (C_i-symmetry). If the squaraine is asymmetric, such as the monobrominated derivatives presented in chapter 5, the aforementioned elements of symmetry are no longer present, therefore leading to the *RS* and *SR* isomers being two enantiomers of a chiral molecule (C_1-symmetry). The structures of the aforementioned isomers of the non-brominated squaraine monomers **SQA*** and **SQB***, along with their respective symmetry elements and point group labels are summarized in Figure 29.

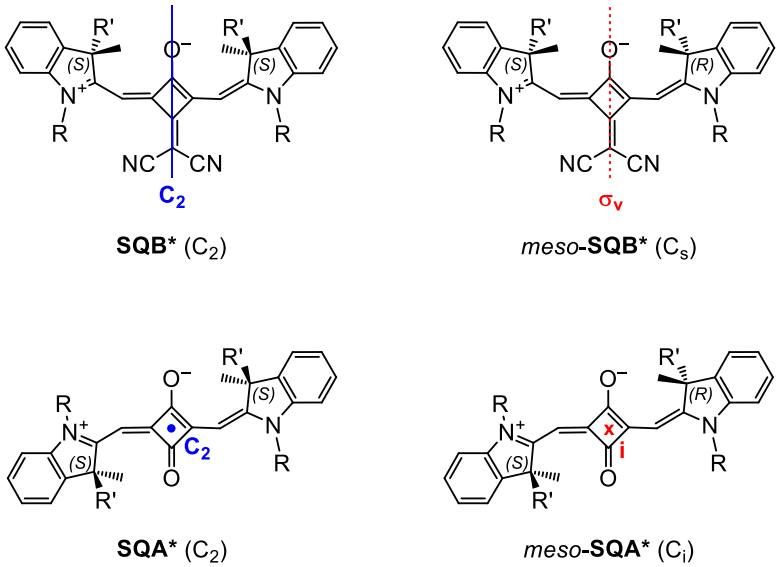

Figure 29. General structures of the non-brominated squaraine monomers (**SQA*** and **SQB***, chiral and achiral *meso*-diastereomers). Chirality-retaining symmetry elements are marked in blue, chirality-breaking symmetry elements in red.

3.1.2 Structural elucidation

Single crystals were grown for **Pr-SQA***, **Pr-SQB*** and **Ph-SQB***, from which X-ray crystallographic data were able to be collected. The crystal structures are shown in Figure 30, a general illustration containing the numbering scheme along with definitions of selected planes is shown in Figure 95 in the appendix. Angles between selected planes are summarized in Table 2.

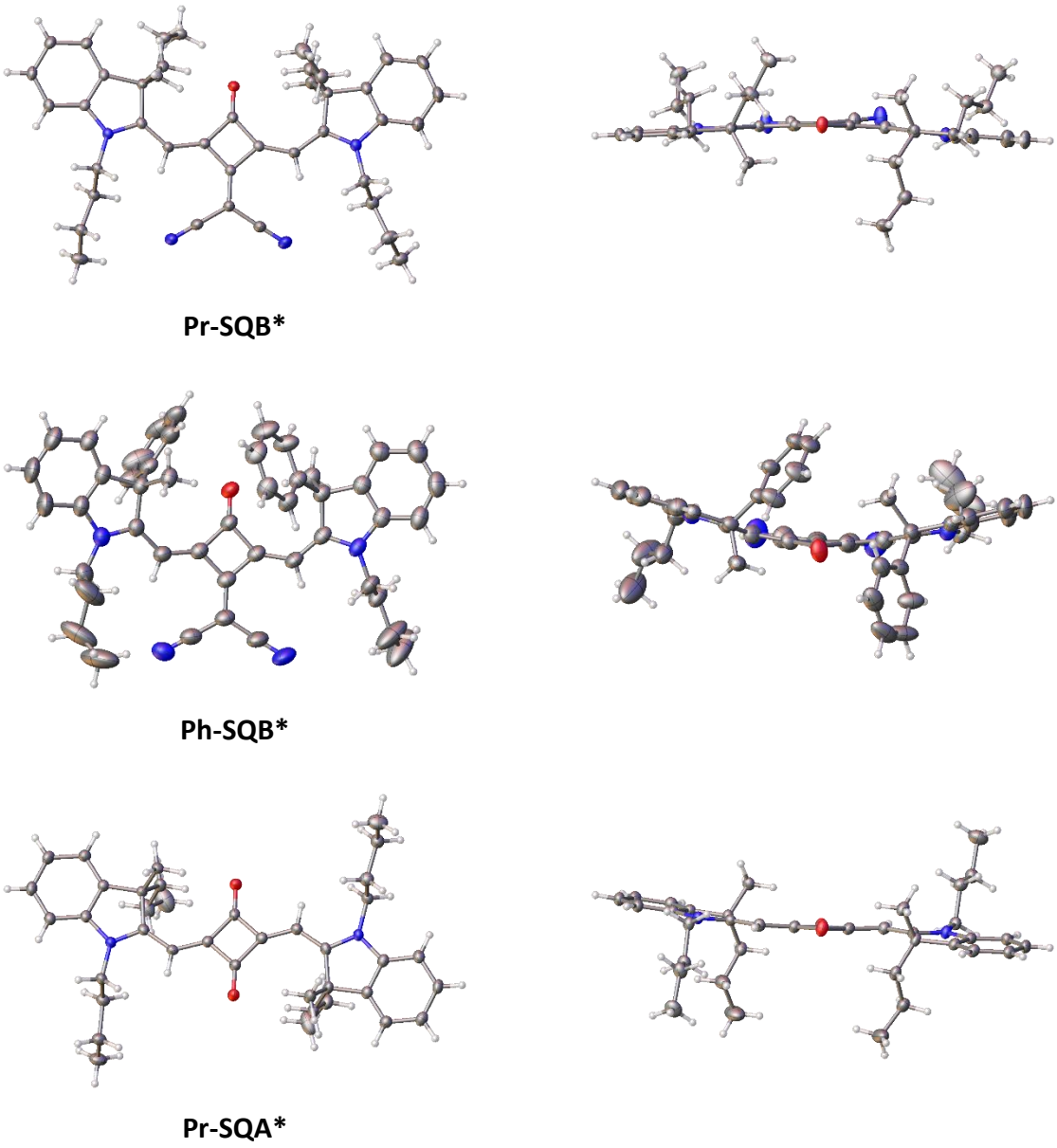

Figure 30. X-ray structures of **Pr-SQB*** (top), **Ph-SQB*** (middle) and **Pr-SQA*** (bottom). Left: top view, right: front view. Thermal ellipsoids at 50% probability level. Red: oxygen, grey: carbon, blue: nitrogen, white: hydrogen.

In the case of **Pr-SQB***, the chromophore was nearly planar, with dihedral angles between the two central planes comprising one half of the central squaric acid ring and the adjacent carbon atom (A_1 and A_2 in Figure 95) of 3.7°. The indolenine planes (I_1 and I_2 in Figure 95) were also nearly in plane with their adjacent central planes, with angles of 2.4° and 2.2°, respectively. This planar geometry was also observed in the achiral dimethyl-substituted **SQB**.[63, 65] Comparison of the bond lengths of the polymethine chain (N1-(C1-7)-N2) of **SQB** and **Pr-SQB*** revealed minor deviations (Table 40 in the appendix).

On the contrary, the crystal structure of **Ph-SQB*** showed a bent, U-shaped geometry (referring to the curvature of the chromophore when viewed from the front, see Figure 30). This was mainly due to the central squaric acid moiety not being planar, with an angle between planes A_1 and A_2 of 11.7°. Furthermore, the indolenine planes were also slightly twisted out of plane, with an angle of 12.4° between planes I_1 and A_1 and 10.0° between planes I_2 and A_2. Surprisingly, the bond lengths matched those of **SQB** more closely than in the case of **Pr-SQB***, even though the geometry varied significantly. The structure of **Ph-SQB*** was also optimized at the B3LYP/6-31G* level of theory,[1] which is also shown in Figure 31. For this calculation, the N-alkyl side chains were replaced by methyl groups. Interestingly, the optimized structure differed significantly from the crystal structure, with an energy difference of ca. 55 kJ mol^{-1} (0.57 eV) (calculated at the same level as the geometry optimization, all C-H bonds in the X-ray structure were stretched to 1.08 Å for the calculation), leading to the conclusion that the DFT structure was more representative of the actual structure present in solution. In this optimized structure, the central squaric acid ring is planar with an angle of 0.0° between the planes A_1 and A_2. The indolenine units were also slightly twisted out of plane, but in opposite directions, with an angle of -15.0° between planes I_1 and A_1 and 15.0° between planes I_2 and A_2, leading to an S-shaped chromophore.

[1] Theoretical calculations performed by Dr. M. Holzapfel

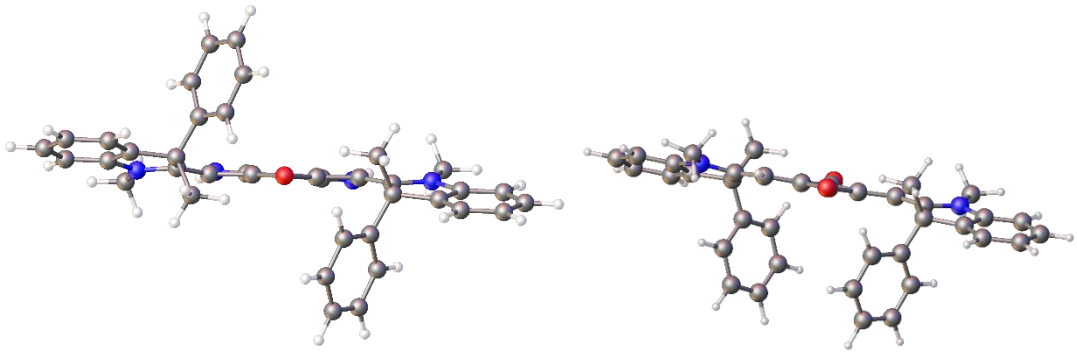

Figure 31. Front view of the B3LYP/6-31G* optimized structures of **Ph-SQB*** (left) and **Ph-SQA*** (right).

The reason for this discrepancy remains unclear, but one possible explanation could be an attractive dispersion interaction of the methyl group of one indolenine with the phenyl group of the other, leading to the observed bent, U-shaped geometry of the experimental crystal structure of **Ph-SQB***. Overall, the deviation of the expected planarity may be caused by the steric strain imposed by the large phenyl groups. In **TPh-SQB**, this led to a strongly twisted inverted structure, which can be seen in Figure 32.

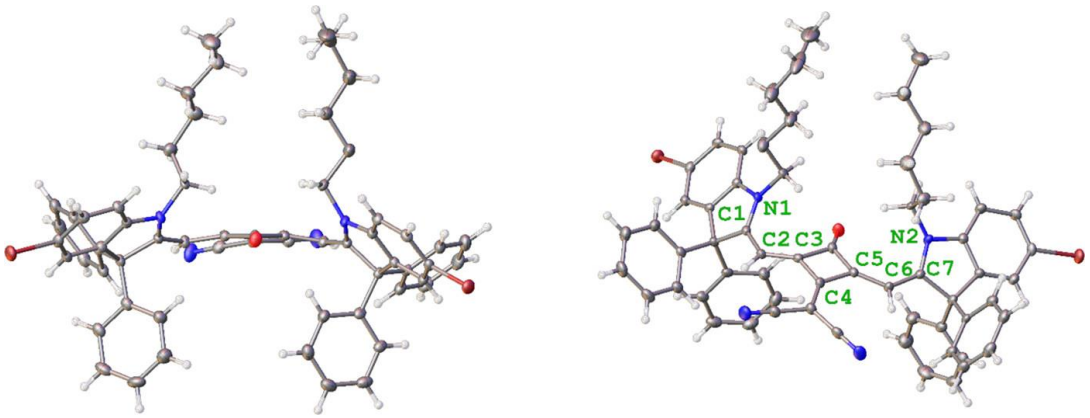

Figure 32. Front view (left) and top view (right) of the crystal structure of **TPh-SQB**.[90] Thermal ellipsoids at 50% probability level. Red: oxygen, grey: carbon, blue: nitrogen, white: hydrogen, burgundy: bromine.

When analyzing the crystal structure of **Pr-SQA***, it can be seen that while the central squaric acid ring is planar with an angle of 3.7° between A_1 and A_2, the indolenine rings are slightly twisted out of plane by 10.0° and -7.8° relative to the respective ajacent half of the central squaric acid ring. The bond lengths also only exhibited minuscule differences that were non-systematic. As the *n*-propyl groups in the 3-position of the indolenine moiety are not sufficiently large to produce structural torsion as apparent in the nearly planar structure of **Pr-SQB***, and DFT-calculations of **Pr-SQA*** showed the chromophore to be planar, this observation is unexpected. Furthermore, due to the transoid structure of the SQA-type squaraines, substituents in this position are expected to possibly have a lesser impact on the

overall geometry of the chromophore. Regarding the data of the achiral, dimethyl-substituted **SQA** (bearing unbranched, *n*-alkyl chains with varying lengths),[253-255] a certain degree of non-planarity is also observed in some cases and appears not to be inherent to the substitution of the chromophore backbone. Indeed, such deviations were also observed for SQB-type squaraines, where one indolenine ring was twisted out of plane. [117, 255] Unfortunately, no single crystals of **Ph-SQA*** were obtained, but nevertheless, DFT-calculations revealed a slightly twisted geometry comparable to the case of **Ph-SQB***, where the indolenine rings are twisted out of plane by 14.2° with respect to the quasi planar central squaric acid moiety. In order to confirm the postulated structure (phenyl groups facing towards the squaric acid core as opposed to facing outward as in **TPh-SQB**), NOESY-NMR experiments were performed and are presented in section 11.4 in the appendix.

Table 2. Angles between selected planes of indolenine squaraines.

	$\measuredangle(A_1 - A_2)$	$\measuredangle(A_1 - I_1)$	$\measuredangle(A_2 - I_2)$
SQA-C4[253]	9.6°	7.9°	5.1°
SQA-C6[254]	0.0°	10.9°	10.9°
SQA-C8[255]	0.0°	4.0°	4.0°
Pr-SQA*	2.0°	10.0°	-7.8°
Ph-SQA* DFT	0.2°	14.2°	14.2°
Pr-SQB*	3.7°	2.4°	2.2°
Ph-SQB*	11.7°	12.4°	10.0°
Ph-SQB* DFT	0.0°	15.0°	-15.0°

In all cases, no π/π-interactions were found in the solid state, which is due to the steric shielding caused by the substituents in the 3-position of the indolenine subunit. Even when only methyl groups are attached in this position, this steric hindrance is present to a small extent[253] and may be the reason why such indolenine squaraines do not form aggregates in organic solvents.[84]

For all the chiral squaraines, the Flack-parameter was sufficiently close to zero within two times the respective standard deviation (**Pr-SQA***: 0.07(7), **Pr-SQB***: 0.00(5), **Ph-SQB***: 0.05(5)), although the standard deviation in **Pr-SQA*** was rather large and therefore

theoretically precludes a definitive statement. [256-258] Since all compounds were proven to be optically pure, the crystal structures enable the verification of the absolute configuration.

3.1.3 Absorption and fluorescence spectroscopy

The UV-Vis-NIR and fluorescence spectra of the unbrominated C(3)-chiral monomers are shown in Figure 33 and the data are summarized in Table 3.

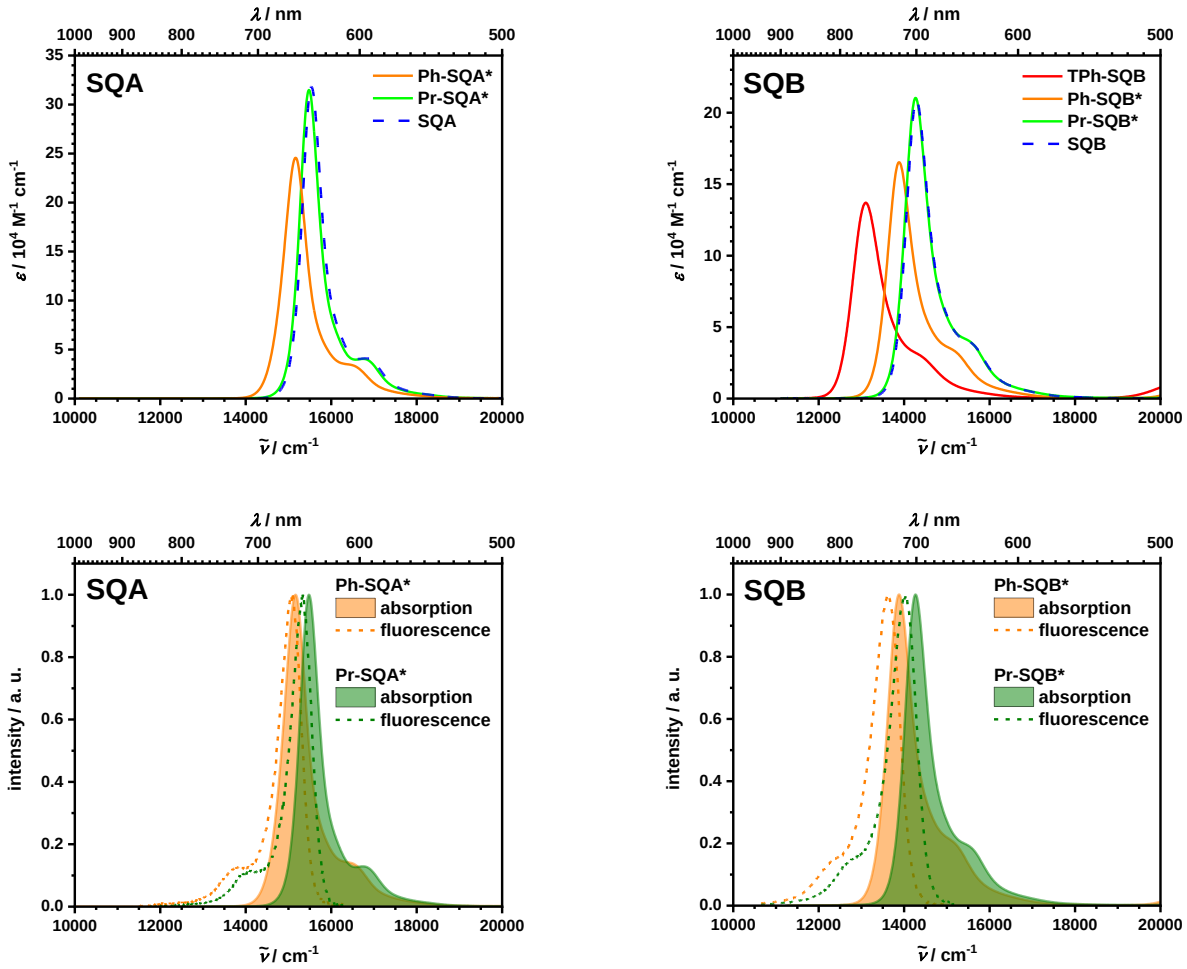

Figure 33. Linear optical spectra of **SQA**, **Pr-SQA***, **Ph-SQA***, **SQB**, **Pr-SQB***, **Ph-SQB***and **TPh-SQB**[73, 90] in toluene. Left: **SQA**-type squaraines, right: **SQB**-type squaraines; top: UV/vis spectra, bottom: normalized absorption and fluorescence spectra.

All compounds showed the typical absorption behavior of squaraine dyes, that is a sharp and intense absorption maximum in the red-to-NIR spectral region (13 100-15 500 cm^{-1}), with a vibronic shoulder at the high-energy side. In both the **SQA**- and **SQB**-type squaraines, the chiral *n*-propyl-substituted derivatives and the achiral dimethyl-substituted derivatives possessed nearly identical optical properties, whereas the phenyl-substituted derivatives differed from the aforementioned cases. The absorption maxima of **Ph-SQA*** and **Ph-SQB***

were red-shifted by 300 cm^{-1} and 400 cm^{-1}, respectively. Additionally, the introduction of phenyl groups led to a decrease of the absorption coefficient and a broadening of the absorption band. The corresponding squared transition moments μ_{eg}^2, which were determined by integration of the main absorption band and calculated according to eq. (74), decreased by 13.3 D^2 for **Ph-SQB*** (85.1 D^2) and 8.6 D^2 for **Ph-SQA*** (103.3 D^2) compared to 98.4 D^2 for **Pr-SQB*** and 111.9 D^2 for **Pr-SQA***. In the case of **TPh-SQB**, with four phenyl groups, these features became even more extreme, with the absorption band being bathochromically shifted by 1200 cm^{-1} and the squared transition moment being 81.6 D^2, corresponding to a reduction by 16.8 D^2 compared to that of **Pr-SQB*** (98.4 D^2). Since this seemed to be a systematic trend, the question of its origin arose. Since X-ray crystallography and DFT calculations both revealed a non-planar structure for the phenyl-substituted derivatives, it was postulated that the twisting of the chromophore caused the observed red-shift, such as previously reported for non-planar porphyrins by Smith et al.[1, 259] Therefore, in order to support this claim, TD-DFT calculations[1] using various geometries and substitution patterns of the **Ph-SQB*** chromophore were performed, which is shown in Figure 34.

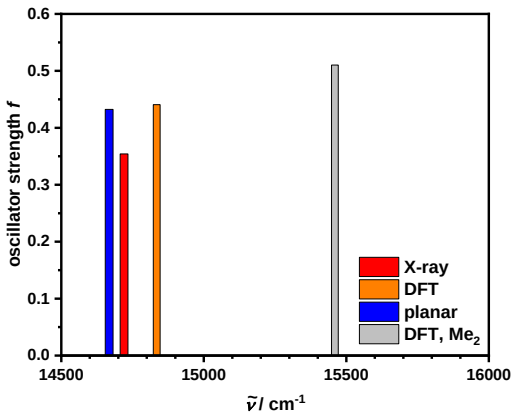

Figure 34. TD-DFT calculations (B3LYP/6-31G*) of the oscillator strengths of the HOMO-LUMO transition in **Ph-SQB*** using different geometries and substitution patterns. Blue: **Ph-SQB*** with enforced planarity of the π-system, grey: DFT-optimized structure of **Ph-SQB*** with methyl groups instead of phenyl groups (non-planar SQB), red: X-ray structure of **Ph-SQB*** as shown in Figure 30, orange: DFT-optimized structure of **Ph-SQB*** as shown in Figure 31.

Surprisingly, the calculations falsified this postulation, as merely enforcing the planarity of the π-system did not lead to the observed red-shift, while replacing the phenyl groups with methyl groups yielded the correct result. Thus, the changes of optical properties of **Ph-SQA*** and

[1] Theoretical calculations performed by Dr. M. Holzapfel

Ph-SQB* compared to their parent compounds are caused by electronic effects exerted by the two phenyl groups, rather than being an effect of structural torsion.

In all cases, the fluorescence and absorption spectra showed mirror symmetry with a Stokes shift of 60-140 cm^{-1} for the **SQA** derivatives and 200-240 cm^{-1} for the SQB analogues. Again, the *n*-propyl-substituted squaraines displayed emission properties nearly identical to those of their achiral dimethyl-substituted counterparts – specifically the Stokes shifts, fluorescence lifetimes, and quantum yields. The Stokes shift of **Ph-SQA*** was significantly reduced by 80 cm^{-1} compared to that of the planar **SQA** derivatives. For the **SQB** derivatives, the Stokes shift of **Ph-SQB*** was 10 cm^{-1} lager than that of the planar derivatives, whereas **TPh-SQB** possessed a Stokes shift that was 30 cm^{-1} smaller than that of **SQB** and **Pr-SQB***. Regarding the fluorescence lifetimes, the alkyl-substituted squaraines all exhibited a monoexponential decay with the lifetime of the SQA-type squaraines (ca. 1.7 ns) being roughly half as long as those of the SQB type (ca. 3.4 ns). All diphenyl-substituted squaraines displayed a biexponential decay with an additional shorter component <1 ns and a long component of ca. 1.1 ns for **Ph-SQA*** and ca. 4 ns for **Ph-SQB***. Such biphasic decays had frequently been observed for indolenine squaraines.[260] Examining the quantum yields, that of **Ph-SQA*** (0.24) was decreased by 0.37 compared to **SQA** (0.61). In the case of **Ph-SQB*** (0.60), the quantum yield was slightly reduced by 0.15 compared to **SQB** (0.75). For **Ph-SQA***, this went along with a significantly shorter lifetime, indicating that the phenyl substituents promote nonradiative decay channels.

Table 3. Spectroscopic data (absorption maxima $\tilde{\nu}_{abs}$, extinction coefficients ε_{max}, squared transition moments μ_{eg}^2, fluorescence maxima $\tilde{\nu}_{em}$, quantum yields Φ_{fl}, fluorescence lifetimes τ_{fl} and mean fluorescence lifetimes $\overline{\tau}_{fl}$) of **SQA**, **Pr-SQA***, **Ph-SQA***, **SQB**, **Pr-SQB***, **Ph-SQB***, and **TPh-SQB**[73, 90] in toluene.

	$\tilde{\nu}_{abs}$ (λ_{abs}) / cm^{-1} (/ nm)	ε_{max} / M^{-1} cm^{-1}	μ_{eg}^2 [a] / D^2	$\tilde{\nu}_{em}$ (λ_{em}) / cm^{-1} (/ nm)	Φ_{fl}	τ_{fl} [b] / ns	$\overline{\tau}_{fl}$ [c] / ns
SQA	15 500 (644)	3.18×10^5	113	15 400 (651)	0.61	1.68	1.68
Pr-SQA*	15 500 (646)	3.15×10^5	111	15 300 (652)	0.60	1.64	1.64
Ph-SQA*	15 200 (660)	2.46×10^5	103	15 100 (662)	0.24	0.19 (0.05) 1.13 (0.95)	1.12
SQB	14 300 (699)	2.10×10^5	98.4	14 000 (714)	0.75	3.45	3.45
Pr-SQB*	14 300 (701)	2.10×10^5	98.4	14 000 (712)	0.74	3.39	3.39
Ph-SQB*	13 900 (720)	1.65×10^5	85.1	13 600 (733)	0.60	0.62 (0.02) 3.95 (0.98)	3.93
TPh-SQB	13 100 (763)	1.37×10^5	81.6	12 900 (755)	0.04	0.21 (0.90) 2.94 (0.10)	1.87

[a] determined by integration of the main absorption band and calculated using eq. (74) in the appendix. [b] Determined by TCSPC, decay curves fitted with a (multi-)exponential fit, amplitudes are given in parantheses. Excitation was at 15 200 cm^{-1} (656 nm). [c] Intensity-weighed mean fluorescence lifetime calculated according to eq. (77) in the appendix.

3.1.4 CD spectroscopy

The CD spectra of the C(3)-chiral squaraines are depicted in Figure 35, the data are summarized in Table 4. An overlay plot of the normalized absorption and CD spectra is shown in Figure 101 in the appendix.

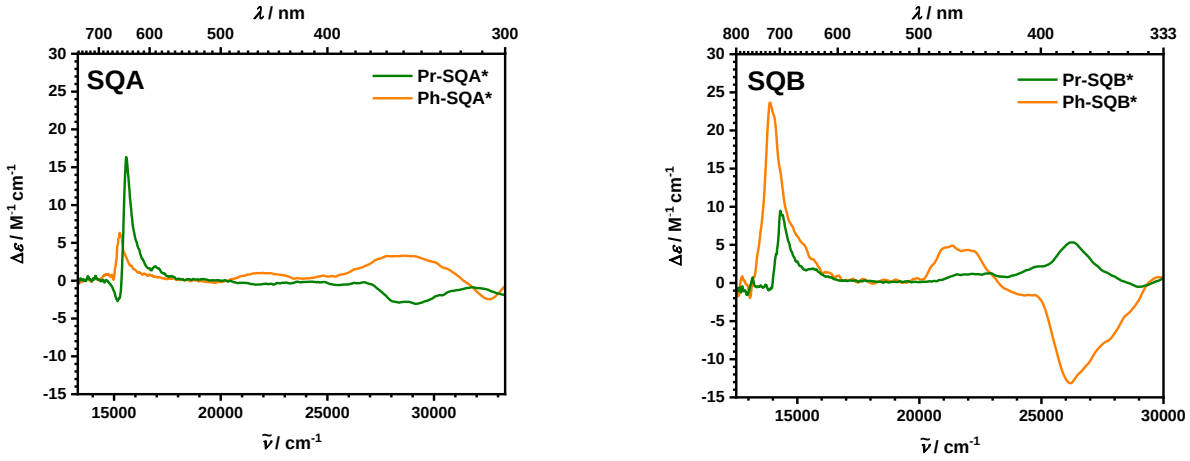

Figure 35. CD spectra of the chiral squaraines in toluene. Left: **SQA**-type squaraines, right: **SQB**-type squaraines.

Table 4. Summary of the chiroptical data (CD peaks $\tilde{\nu}_{CD}$, difference of absorption $\Delta\varepsilon$, experimentally determined rotational strengths R_{exp}, dissymmetry factors g_{abs}) of **Pr-SQA*, Ph-SQA*, Pr-SQB*,** and **Ph-SQB*** in toluene**.**

	$\tilde{\nu}_{CD}$ (λ_{CD}) / cm^{-1} (/ nm)	$\Delta\varepsilon$ / M^{-1} cm^{-1}	R_{exp} [b] / 10^{-40} cgs	$\lvert g_{abs}(\tilde{\nu}_{max})\rvert$ [a] / cgs
Pr-SQA*	15 200 (658)	-2.7	- [c]	2.2 × 10^{-5}
	15 600 (641)	16	- [c]	6.4 × 10^{-5}
	29 100 (344)	-3.1	-7	5.7 × 10^{-4}
Ph-SQA*	15 300 (654)	6.3	- [c]	3.1 × 10^{-5}
	21 700 (461)	1.0	2	1.1 × 10^{-3}
	28 600 (350)	3.3	11	6.0 × 10^{-4}
Pr-SQB*	14 300 (699)	8.6	11	5.1 × 10^{-5}
	26 200 (381)	5.1	- [c]	1.6 × 10^{-4}
Ph-SQB*	13 900 (719)	24	42	1.5 × 10^{-4}
	21 400 (467)	4.9	10	2.6 × 10^{-4}
	26 200 (382)	-13	-30	4.9 × 10^{-4}

[a] $\Delta\varepsilon(\tilde{\nu}_{max})/\varepsilon(\tilde{\nu}_{max})$. [b] determined by integration of the CD band and calculated using eq. (75) in the appendix. [c] not determinable due to superposition of transitions.

All of the C(3)-chiral squaraines displayed a significant CD signal in the region of the lowest-energy absorption. All squaraines exhibited a positive signal coinciding with the main absorption band, and additional bands in the higher energy region, where the signs for the *n*-propyl- and phenyl-substituted derivatives were opposite for the most prominent high energy bands. As can be seen in Figure 36, the CD and absorption spectra of **Ph-SQB*** are largely solvent-independent, which is expected for such squaraines, since the reported solvatochromism is generally quite low.[128] Furthermore, the CD spectra of the two enantiomers possess the expected mirror-image relationship.

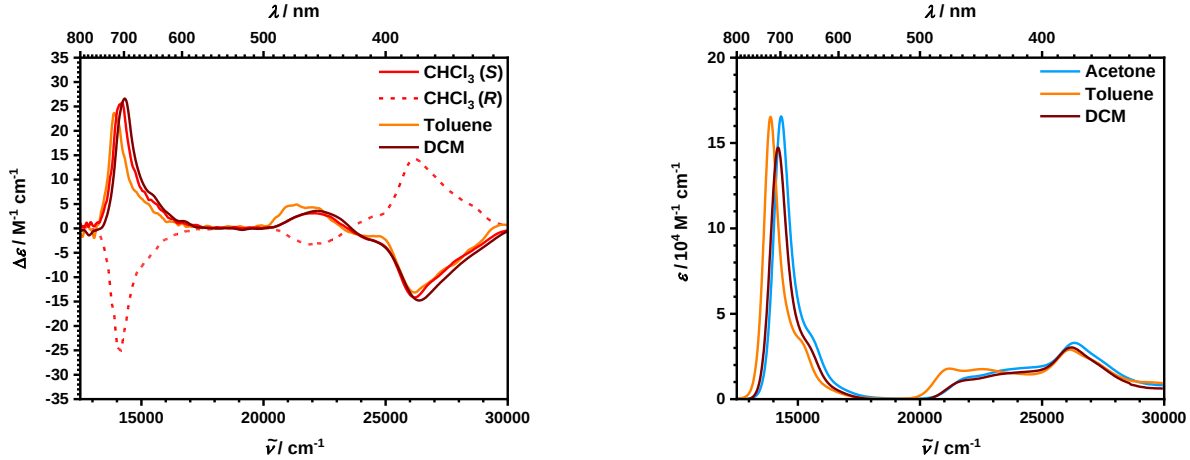

Figure 36. CD (left) and absorption (right) spectra of **Ph-SQB*** in different solvents.

To further assist the interpretation of these findings, time-dependent density functional theory (TD-DFT) calculations were performed at B3LYP/6-31G* level in the gas phase.[1] The calculated CD spectra are shown in Figure 39 and the data are summarized in Table 5. As in the case with the absorption spectra, the influence of the chromophore geometry was unclear, which is why analogous calculations of the rotatory strength of **Ph-SQB*** were performed. The results are shown in Figure 37. Because the non-planarity by itself does not yield a significant rotatory strength, whereas an enforced planar geometry of **Ph-SQB*** does, the same conclusions can be drawn that the geometry of the chromophore does not affect the chiroptical properties.

[1] Theoretical calculations performed by Dr. M. Holzapfel

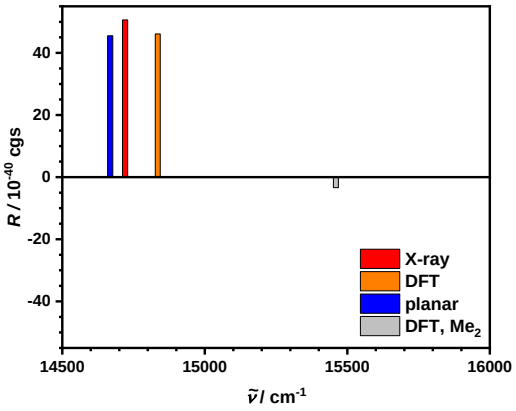

Figure 37. TD-DFT calculations (B3LYP/6-31G*) of the rotatory strengths of the HOMO-LUMO transition in **Ph-SQB*** using different geometries and substitution patterns. Blue: **Ph-SQB*** with enforced planarity of the π-system, grey: DFT-optimized structure of **Ph-SQB*** with methyl groups instead of phenyl groups (non-planar SQB), red: X-ray structure of **Ph-SQB*** as shown in Figure 30, orange: DFT-optimized structure of Ph-SQB* as shown in Figure 31.

For both **SQA**-type squaraines, the positive CD signal largely followed the main absorption band at the high-energy side, but dropped off steeply at the low-energy side. For **Pr-SQA***, a small but distinctly visible negative signal was observed at 15 200 cm^{-1}. When closely examining the absorption spectra (see logarithmic plot in Figure 100 in the appendix), a very weak band at ca. 13 800 cm^{-1} becomes visible. Indeed, the TD-DFT calculation of the absorption spectra of achiral **SQA** also showed this weak band (with formally zero intensity) at somewhat lower energy than the main absorption band (Figure 38) yielded two almost equally intense CD signals. The one at lower energy (the HOMO-LUMO transition) had a negative sign, the one at higher energy (the n-π* transition) had a positive one. This contrasted the experimental results, where the assignment was opposite. A similar observation was made for **Ph-SQA***. Again, the computed CD spectra in the low-energy region around 15 000-16 000 cm^{-1} showed an intense negative signal at slightly lower energy than the positive CD signal (Figure 39). The orbital contributions to these two transitions did not allow a specific assignment, they were both mixtures of a HOMO-LUMO transition and an n-π* transition. In the experimental CD spectra there was no negative CD signal visible here, but the positive signal dropped off very steeply at the low-energy side indicating an overlap with a negative CD signal in that energy region. Regarding the higher-energy region, the calculated CD spectrum of **Ph-SQA*** showed two additional HOMO-LUMO+n transitions, which roughly matched the observed signals in the experimental spectrum in both energy and intensity ratio, although the calculations significantly overestimated the values for *R*. Even though a negative

signal was visible for **Pr-SQA*** in the same region, the calculated spectrum did not show these transitions as pronounced as in the case of **Ph-SQA***.

For the main low-energy absorption band, the experimental g_{abs} was larger for the *n*-propyl-substituted derivative (6.4×10^{-5} cgs) than for the phenyl-substituted derivative (3.1×10^{-5} cgs). These obtained values are typical of achiral chromophores in a chiral environment.[14, 131] However, the superposition of two signals with opposing signs in this region precluded an accurate determination of R and g_{abs}. For the lower-energy transitions, the DFT computations yielded angles between the electric and magnetic transition moments close to 90°, which led to lower values for R and therefore g_{abs}. The experimental values for g_{abs} for the higher-energy transitions were roughly one order of magnitude larger than those for the main absorption bands, reaching up to 1.1×10^{-3} cgs for the transition at 21 700 cm^{-1} in **Ph-SQA***. These relatively high values were due to the transition being only weakly allowed (low absorption coefficient ε), while possessing a pronounced CD signal, possibly due to the magnetic and electronic transition moments being collinear ($\vartheta = 0°$). The DFT computations (see Figure 39) indeed showed such HOMO-LUMO+n transitions with ($\vartheta = 0°$), albeit at higher energy. The value for g_{abs} obtained for the higher-energy band in **Pr-SQA*** (6.0×10^{-4} cgs) was nearly identical to that of **Ph-SQA*** (5.7×10^{-4} cgs), although the sign of the CD signal was exchanged.

The situation for the **SQB** derivatives was somewhat different. The TD-DFT calculations did not show any additional band besides the main absorption band at around 14 000 cm^{-1}. This is because there is only one oxygen in the squaric acid moiety and the main absorption band is shifted to lower energy. Thus, the possible n-π* excitation did not overlap with the lowest-energy absorption, but was presumably at higher energy. For **Ph-SQB*** the band shape of the positive CD signal followed the absorption spectra, whereas the signal for **Pr-SQB*** fell off steeper at the low-energy side. For both **Pr-SQB*** and **Ph-SQB***, the DFT computations gave the correct sign of the CD signal. Due to the absence of additional transitions in the region of the main absorption band, it was possible to compare the experimentally determined rotatory strength R_{exp} (by integration of $\Delta\varepsilon/\tilde{\nu}$, see Table 4) with the calculated one R_{theo} (see Table 5). For **Ph-SQB***, the obtained experimental value was 42×10^{-40} cgs and for **Pr-SQB*** 11×10^{-40} cgs. With 46×10^{-40} cgs and 25×10^{-40} cgs, the computed values were in rather good agreement. The corresponding experimental anisotropy factors g_{abs} for these transitions were 5.1×10^{-5} cgs for **Pr-SQB*** and 1.5×10^{-4} cgs for **Ph-SQB***, which were lower than the

calculated values g_{theo} of 1.5×10^{-4} cgs and 3.1×10^{-4} cgs by a factor of 2 to 3. Even more interesting were the experimental CD spectra in the region between 23 000 and 34 000 cm^{-1}. Although the absorption spectra were very similar in this region, the CD spectra differed significantly. From fluorescence excitation anisotropy measurements of **SQB**, it is known that the band around 27 000 cm^{-1} is polarized along the C_2-axis of **SQB**.[261] This band is associated with a HOMO to LUMO+1 excitation (Figure 38). The TD-DFT calculations of the CD spectra of both **Pr-SQB*** and **Ph-SQB*** indicated this transition to possess a negative rotatory strength with an angle of 180° between the electric and magnetic transition moment, which was consistent with the anisotropy measurements mentioned above for **SQB**. However, the experimental CD spectrum of **Ph-SQB*** only showed this negative signal at ca. 26 000 cm^{-1}, while **Pr-SQB*** has a strong positive signal in the spectral region. This suggests that in **Pr-SQB*** the negative CD signal was overlaid by an even stronger positive signal, which could be due to an n-π* excitation. Although the TD calculations showed an n-π* excitation in that spectral region, its intensity was weak and its sign was negative. As in the case of the **SQA** derivatives, where multiple signals overlapped in the region of the main HOMO-LUMO transition, a determination of R_{exp} was not possible. Also, the g_{abs} values for the bands in the higher-energy region were markedly larger than the ones for the HOMO-LUMO transitions, possibly due to the collinearity of the electric and magnetic transition moment vectors (ϑ = 180°).

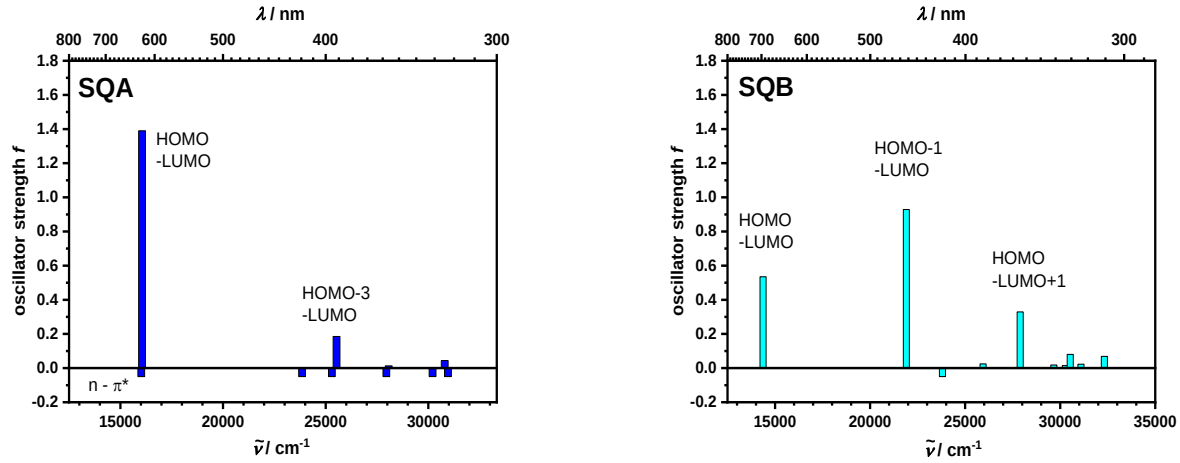

Figure 38. TD-DFT calculated oscillator strengths of the parent structures **SQA** (shifted by -2636 cm^{-1}) and **SQB** (shifted by -1223 cm^{-1}) at B3LYP/6-31G* level. Transitions with zero intensity are given as small negative bars.

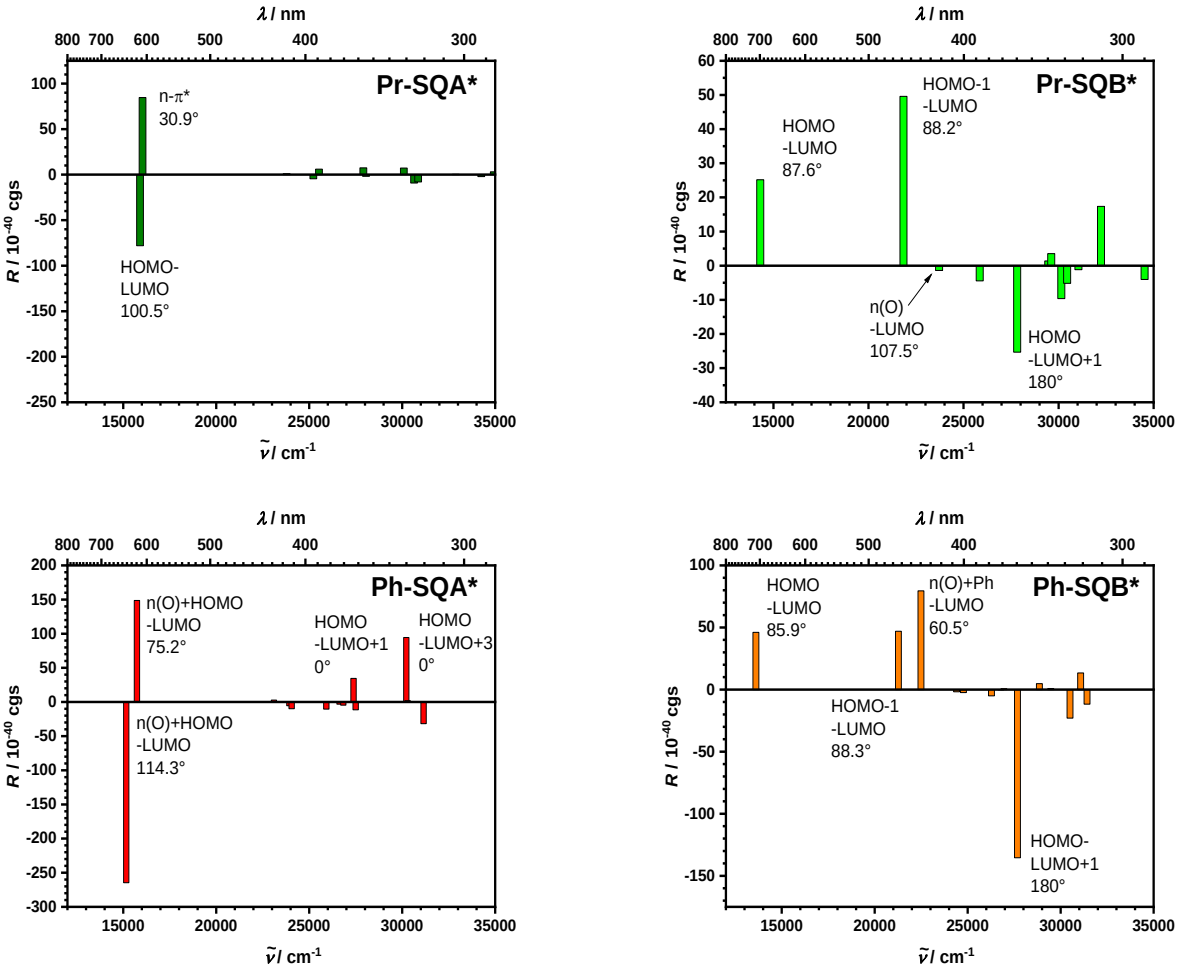

Figure 39. Calculated rotatory strengths of the C(3)-chiral squaraines **Pr-SQA***, **Ph-SQA***, **Pr-SQB*** and **Ph-SQB***. The angles given for the transitions are the ones between the electronic and the magnetic dipole moments. The energetic positions of the signals are shifted in the same way as those of the linear absorption spectra in Figure 38.

Table 5. Calculated electronic μ_{el} and magnetic m_{mag} transition moments, the angle ϑ and its cosine between them, as well as the calculated rotatory strength R_{theo} and anisotropy factors g_{theo} of **Pr-SQA***, **Ph-SQA***, **Pr-SQB***, and **Ph-SQB***. Calculations were performed using a B3LYP/6-31G* optimized geometry and TDDFT. For the SQA derivatives, the transition energies were shifted by 2636 cm^{-1} and for the SQB derivatives by 1223 cm^{-1}.

	$\tilde{\nu}_{CD}$ / cm^{-1}	$\lvert\mu_{el}\rvert$ / a.u.[a]	$\lvert m_{mag}\rvert$ / a.u.	ϑ / deg	cos ϑ	R_{theo} / 10^{-40} cgs	g_{theo}[b] / cgs
Pr-SQA*	15 900	0.390	0.394	100.5	-0.182	-78.0	-2.3×10^{-4}
	16 040	0.081	0.437	30.9	0.858	84.6	5.8×10^{-3}
Ph-SQA*	15 160	0.283	0.782	114.3	-0.412	-264	-1.4×10^{-3}
	15 740	0.243	0.851	75.2	0.256	149	1.1×10^{-3}
	27 380	0.015	1.310	0.0	1.000	34.5	0.17
	30 220	0.031	1.917	0.0	1.000	94.4	0.14
Pr-SQB*	14 310	0.230	0.796	87.6	-0.042	25.2	1.5×10^{-4}
	21 840	0.358	1.984	88.2	0.031	49.6	2.7×10^{-4}
	23 710	0.008.	0.289	107.5	-0.301	-1.39	-1.8×10^{-2}
	27 820	0.242	0.059	180.0	-1.000	-25.3	-4.7×10^{-4}
Ph-SQB*	13 610	0.204	0.904	85.9	0.072	46.1	3.1×10^{-4}
	21 280	0.337	2.090	88.3	0.030	47.0	2.8×10^{-4}
	22 490	0.096	0.771	60.5	0.492	79.5	6.2×10^{-3}
	27 680	0.226	0.335	180.0	-1.000	-135	-2.9×10^{-3}

[a] Transition velocity, where (in a.u.) μ_{vel}=-$\Delta E \cdot \mu_{dip}$ [b] $4R_{theo}/\mu_{el}^2$.

In general, the DFT calculations proved to be not always fully reliable in terms of the sign, energy, as well as the magnitude of the rotatory strength. This was mainly due to the fact that n-π* excitations, which overlapped other transitions in multiple cases, are not well described by DFT methods and squaraine excited states are inherently difficult to be described by DFT methods.[262-264] Moreover, due to the rotatory strength depending on the cosine of the angle ϑ between the electric and magnetic transition moments, slight deviations may have caused a change in sign, since many of the reported angles were around 90°. Other tested functionals and methods (CAM-B3LYP, BHandHLYP, M06, M06L and ZINDO) yield slightly varying but no better results. Nevertheless, these calculations proved to be useful in gaining insights into the origin of the observed CD and produced sufficiently accurate results for the HOMO-LUMO transition in the SQB derivatives.

3.2 SQB monomers bearing chiral side chains

As stated earlier, the alternative site for chiral functionalization is the alkyl side chain as indicated in Figure 23. The main intention for the use of chiral side chains was the construction of SQB-homopolymers in order to possibly form helical polymers with a twist-sense bias. Therefore, dibrominated dimethyl-substituted monomers bearing different chiral side chains are necessary target compounds. For the chiral side chains, the 3,7-dimethyloctyl chain was selected as a starting point, as all previous research was conducted using this side chain to ensure comparability. The size and position of the substituent at the chiral center was systematically varied, as shown in Figure 40, which enabled the systematic study of the resulting influence on the conformation of the polymers in solution.

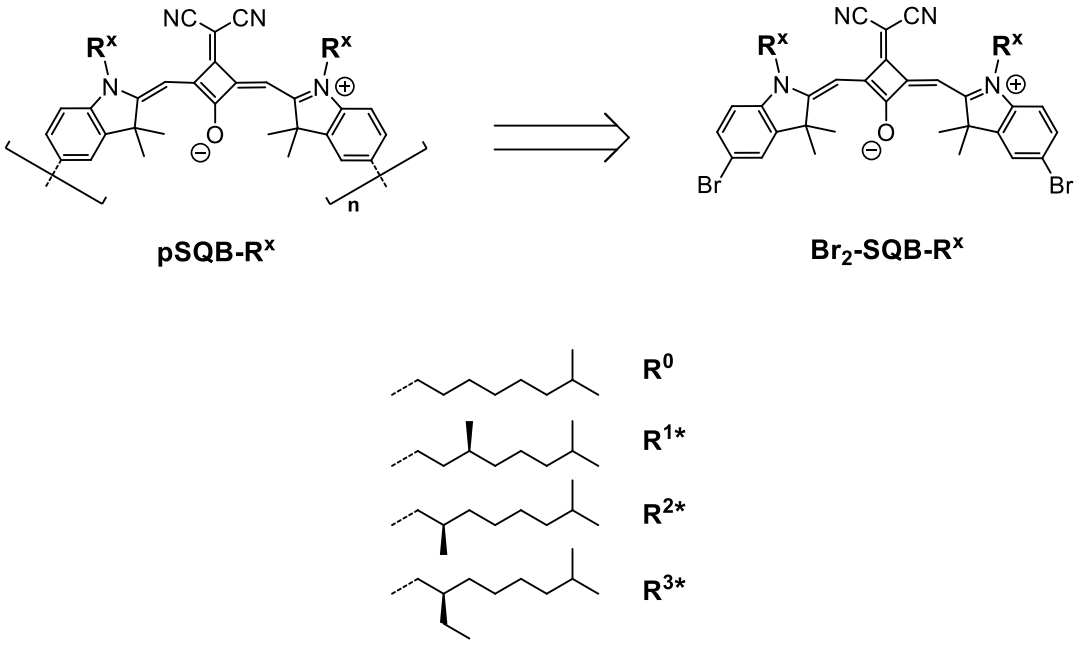

Figure 40. Structure of the SQB-polymers and necessary monomer building blocks bearing chiral side chains.

Furthermore, the study of the structure and chiroptical properties of the monomeric compounds is essential for the confirmation of the obtained results of the polymers. Also, the comparison with the previously described C(3)-chiral squaraines may further provide useful insights. This series can be viewed as having an increasing steric demand of the alkyl group due to its size and the vicinity of the chiral center on the respective side chain to the chromophore. While **R^0** bears no chiral center, **R^{1*}** has a methyl group at the 3-position. In **R^{2*}**, this methyl group is moved closer to the central chromophore at the 2-position. Finally, in **R^{3*}** this methyl group is replaced by an ethyl group, thus increasing the bulkiness.

3.2.1 Synthesis

In the usual synthetic route for indolenine squaraines, the alkyl pendant chain is usually attached to the indolenine via an S_N2-reaction, where an alkyl iodide acts as the electrophile. The iodo-substituent is usually introduced in an Appel-type reaction, where the hydroxy group of the primary alcohol is substituted by iodine.[265-266] While enatiomerically pure *S*-3,7-dimethyloctanol (**R^{1*}-OH**) is commercially available, the other two alcohols *R*-2,7-dimethyloctanol and *R*-2-ethyl-7-methyloctanol (**R^{2*}-OH 30a** and **R^{3*}-OH 30b**) were synthesized by a selective asymmetric alkylation. Since primary alcohols and their analogous carboxylic acid derivatives are readily interconvertible, the asymmetric alkylation developed by Evans et al.[267-268] was chosen for the synthesis of these alkyl chains. The retrosynthetic analysis is summarized in Figure 41.

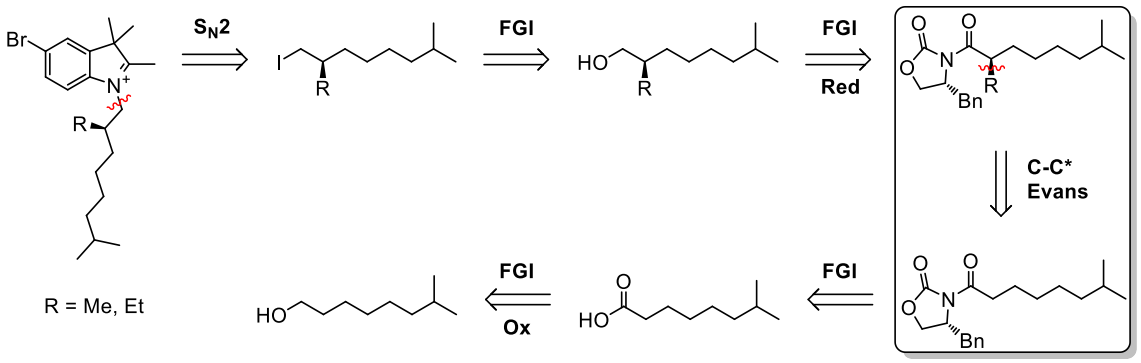

Figure 41. Retrosynthetic analysis of the chiral side chains **R^{2*}** and **R^{3*}**, with the Evans asymmetric alkylation highlighted as the key step.

The synthesis of the imide **28** is shown in Scheme 12. The initial step was the oxidation of 7-methyloctanol **R^{0}-OH (25)**, which was previously synthesized in a copper-catalyzed S_N2-reaction with isopropylmagnesium bromide and sodium 6-bromohexanoate and subsequent immediate reduction with $LiAlH_4$ according to a procedure reported in the literature.[269] Here, a method for the oxidation of primary alcohols to their corresponding carboxylic acid with NaOCl using KBr/4-MeO-TEMPO as the main catalyst system under phase-transfer catalysis as reported by Quici et al. was chosen,[270] which afforded 7-methyloctanoic acid **26** in a nearly quantitative yield of 92%. In order to enhance the reactivity towards nucleophiles, the acid **26** was converted to the corresponding acid chloride **27** with thionyl chloride, before the Evans-auxiliary was attached via an S_N2t reaction with the deprotonated carbamate (auxiliary) to form the desired imide **28**.

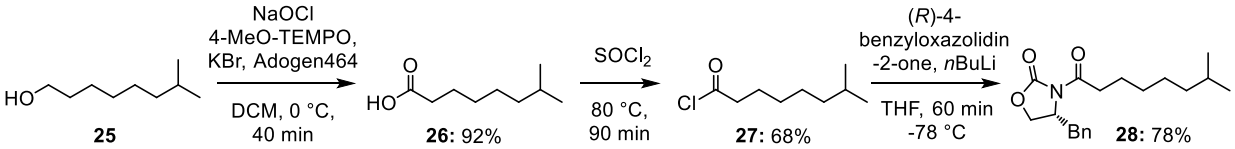

Scheme 12. Synthesis of the imide **28**.

The key synthetic step was the Evans asymmetric alkylation and is shown in Scheme 13.

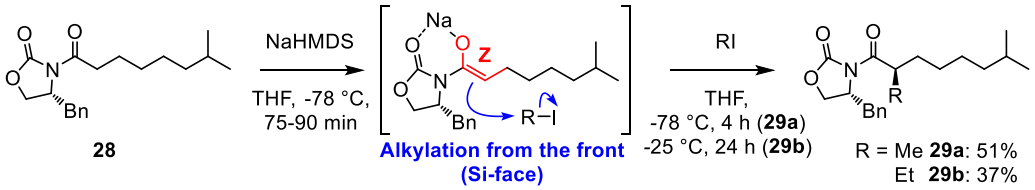

Scheme 13. Evans asymmetric alkylation of **28** to form **29a** and **29b**.

First, the imide **28** is quantitatively deprotonated by the sterically hindered strong base sodium hexamethyldisilazide (NaHMDS). This is done under kinetic conditions to selectively form the *Z*-enolate, and the selectivity is further enhanced by rigidification through chelation with sodium.[268] The enolate is then alkylated with MeI (to form **29a**) or EtI (to form **29b**). Here, the large benzyl moiety acts as the stereodirecting group, that selectively blocks one face of the carbonyl group, leading to the alkylation proceeding on the opposite side (*Si*-face). At a reaction temperature of -78 °C, this reaction is highly selective and only one diastereomer was obtained, which was also reported by Williams et al. for similar substrates.[271] When using EtI, the reaction rate decreased drastically due to the decreased reactivity of the electrophile. This required an increase of the reaction temperature by 53 °C to accelerate the reaction to a sufficient level. Nevertheless, only one diastereomer was obtained in this case as well.

Compounds **29a** and **29b** were then reduced to the corresponding alcohols **R^{2}*-OH** (**30a**) and **R^{3}*-OH** (**30b**) using $LiBH_4$. This is possible due to the leaving group being stabilized by the carbonyl group in the α-position of the nitrogen, thus leading to the formation of the alcohol rather than the carbamate. Along with **R^{0}-OH** and **R^{1}*-OH**, the primary alcohols were then all converted to the corresponding alkyl iodides **R^{0}-I** (**31a**), **R^{1}*-I** (**31b**), **R^{2}*-I** (**31c**), and **R^{3}*-I** (**31d**) in the aforementioned Appel-type reaction. These two steps are shown in Scheme 14.

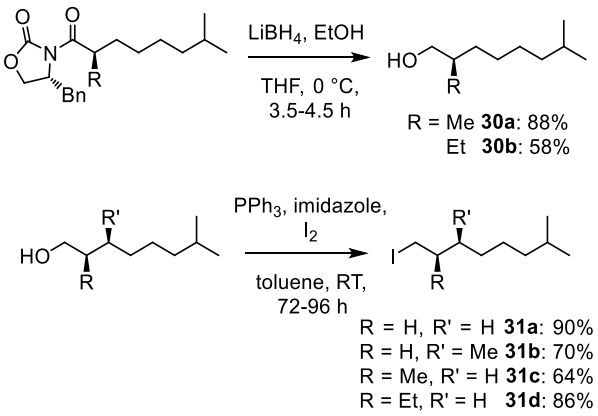

Scheme 14. Reduction of **29** (top) and conversion of the alcohols **30** to the corresponding alkyl iodides **31** (bottom).

The *N*-alkylated indolium salts **34** are usually synthesized by direct alkylation of the indolenine (Scheme 15 lower pathway, I in section 3.1.1). For the alkyl iodides **R^0-I** (**31a**) and **R^{1*}-I** (**31b**), this approach was sufficiently successful and provided the respective indolium salts **34a** and **34b** in yields of 63-71%. When using **R^{2*}-I** (**31c**), this reaction was very slow and only trace amounts of the corresponding indolium salt were isolated. This observation can be explained by the decreased reactivity of the electrophile, since moving the methyl group closer to the leaving group increases the steric hindrance and thus slows the rate of this S_N2-reaction, similar to the case when using a neopentyl-residue.[272] To circumvent this problem, the alternative pathway II as described in section 3.1.1 was selected, as the deprotonated oxindole constitutes a superior nucleophile compared to the neutral indolenine. 5-Bromo-3,3-dimethylindolin-2-one (**32**), which was priorly prepared by bromination of 3,3-dimethylindolin-2-one with elemental bromine,[273] was alkylated with **31c** and **31d** to form the *N*-alkylated oxindoles **33a** and **33b**, respectively. This was done at slightly elevated temperatures compared to the previous cases described in section 3.1.1.1, and only moderate yields of 29-55% were achieved. These were then further treated with MeMgBr and subsequently with HCl in MeOH to afford the indolium salts **34c** and **34d** (Scheme 15, upper pathway).

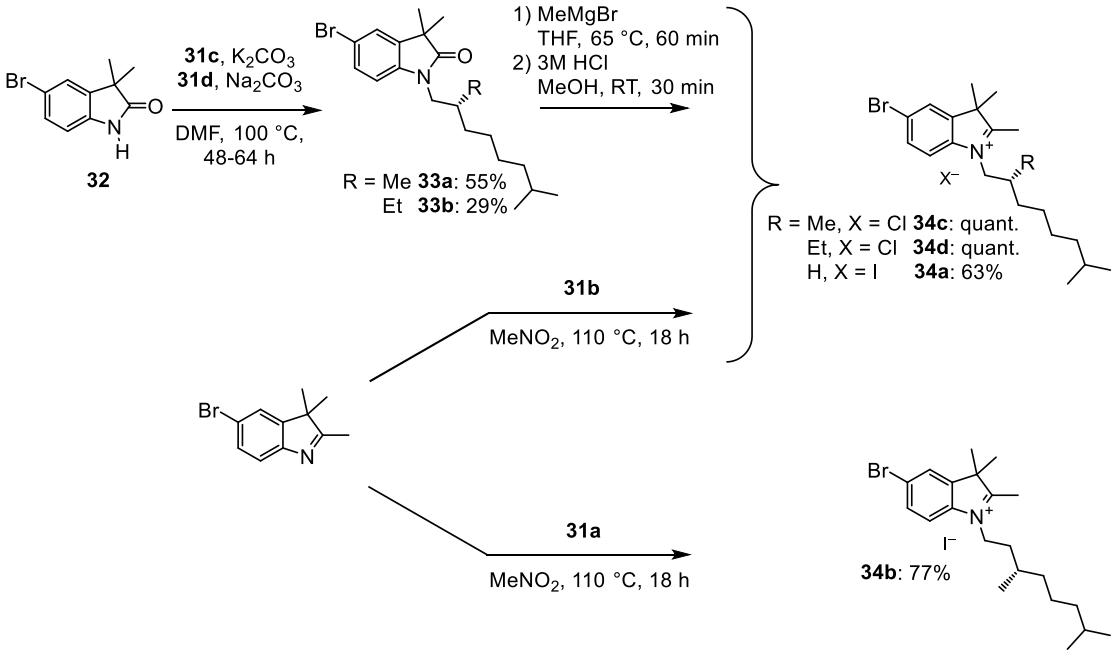

Scheme 15. Synthesis of the indolium salts **34**.

The final dicondensation reaction with triethylammonium 3-(dicyanomethylene)-2-ethoxy-4-oxocyclobut-1-en-1-olate **CN** under azeotropic removal of water then gave the target dibrominated SQB-monomers **Br_2-SQB-R^0**, **Br_2-SQB-R^{1}***, **Br_2-SQB-R^{2}*** and **Br_2-SQB-R^{3}*** in good to excellent yields of 63-94%, which is depicted in Scheme 16.

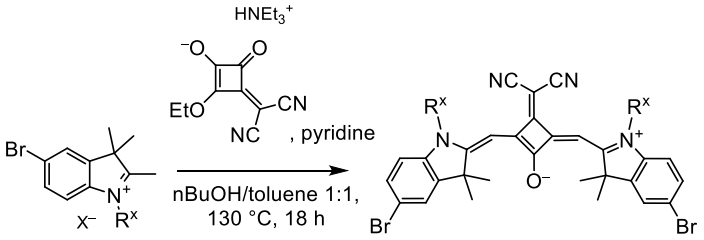

Scheme 16. Synthesis of the dibrominated squaraine monomers **Br_2-SQB-R^0**, **Br_2-SQB-R^{1}***, **Br_2-SQB-R^{2}*** and **Br_2-SQB-R^{3}***.

3.2.2 X-ray crystallography

Single crystals of these dibrominated monomers bearing chiral side chains were also grown from which X-ray crystallographic data were able to be collected. The resulting crystal structures are shown in Figure 42.

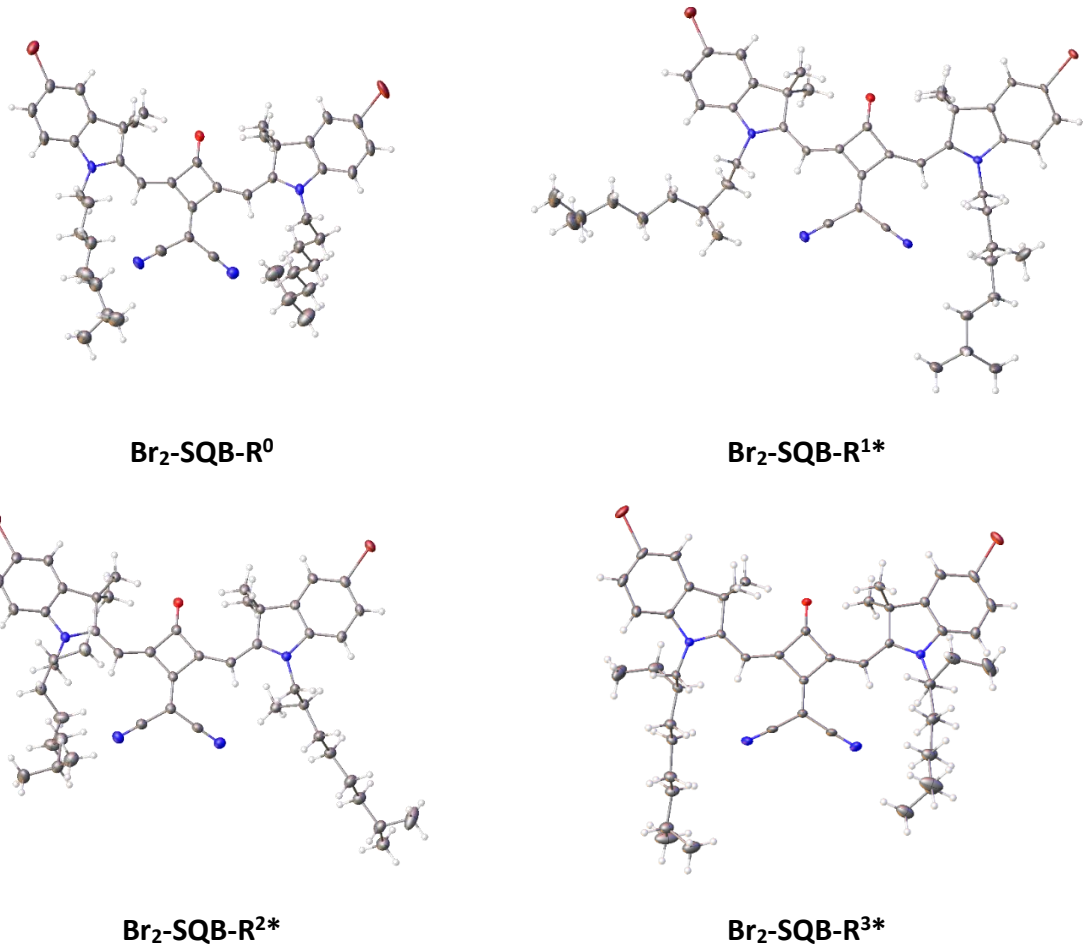

Br_2-SQB-R^0 **Br_2-SQB-R^{1*}**

Br_2-SQB-R^{2*} **Br_2-SQB-R^{3*}**

Figure 42. Crystal structures of the dibrominated squaraine monomers. Thermal ellipsoids at 50% probability level. Grey: carbon, white: hydrogen, red: oxygen, blue: nitrogen, burgundy: bromine.

In all cases, the absolute configuration of the stereocenter on the chiral side chains was able to be verified, since the Flack-parameter and its standard deviation (**Br_2-SQB-R^{1*}**: 0.006(8), **Br_2-SQB-R^{2*}**: -0.017(6), **Br_2-SQB-R^{3*}**: -0.037(7)) were sufficiently small (zero within three times the standard deviation). [256-258]

For **Br_2-SQB-R^0**, **Br_2-SQB-R^{2*}**, and **Br_2-SQB-R^{3*}** the expected nearly planar geometry of the central squaric acid ring and the indolenine moieties was observed, while in **Br_2-SQB-R^{1*}** both indolenine rings were slightly twisted out of plane compared to the central ring. This unexpected observation was also previously made for similar indolenine squaraines. In all cases, the bond angles and lengths within the polymethine chain (green in Figure 96) were

similar and showed no systematic deviations (see Table 41-Table **43**) containing all relevant bond angles and dihedral angles between selected planes).

3.2.3 CD spectroscopy

The CD spectra of the dibrominated squaraine monomers are shown in Figure 43, the corresponding chiroptical data are summarized in Table 6.

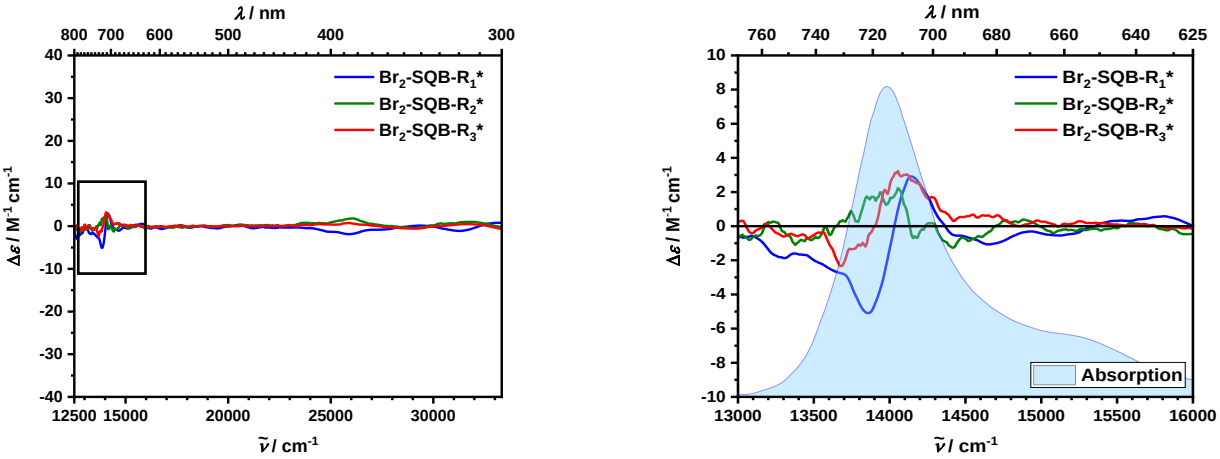

Figure 43. CD spectra of the **Br_2-SQB-R^1*, Br_2-SQB-R^2*** and **Br_2-SQB-R^3*** in toluene**.** Left: full range (12 500-33 300 cm^{-1}), right: magnified section (13 000-16 000 cm^{-1}).

Table 6. Summary of the chiroptical data (CD peaks $\tilde{\nu}_{CD}$, difference of absorption $\Delta\varepsilon$, dissymmetry factors g_{abs}) of **Br_2-SQB-R^1*, Br_2-SQB-R^2*** and **Br_2-SQB-R^3*** in toluene.

	$\tilde{\nu}_{CD}$ (λ_{CD}) / cm^{-1} (/ nm)	$\Delta\varepsilon$ / M^{-1} cm^{-1}	$\lvert g_{abs}(\tilde{\nu}_{max})\rvert$ [a] / cgs
Br_2-SQB-R^1*	13 900 (722)	-5.09	-3.54×10^{-5}
	14 100 (707)	2.91	1.59×10^{-5}
Br_2-SQB-R^2*	14 000 (716)	1.40	6.54×10^{-6}
Br_2-SQB-R^3*	13 700 (730)	-2.14	-1.92×10^{-5}
	14 100 (712)	3.11	1.79×10^{-5}

[a] $\Delta\varepsilon(\tilde{\nu}_{max})/\varepsilon(\tilde{\nu}_{max})$.

All of the dibrominated monomers with the chiral information located on the peripheral side chains only exhibit a very weak CD signal ($\Delta\varepsilon < 5\ M^{-1}\ cm^{-1}$) with small g_{abs} values of ca. $6.5 \times 10^{-6} – 3.5 \times 10^{-5}$ cgs. This is in accordance with the findings reported for other enantiomerically pure squaraines bearing chiral side chains, which generally exhibited no notable CD signal.[52, 55, 57-58, 60] A close examination of the CD spectra reveals a sharp signal, that does not follow the absorption band at either side (see overlay plot in Figure 43). For **Br_2-SQB-R^1*** this signal is bisignate and with equal intensities, possessing its zero-crossing at the same energy as that of the main absorption band at 14 000 cm^{-1}, while **Br_2-SQB-R^2*** only exhibits one positive band with its maximum matching that of the absorption band. For **Br_2-SQB-R^3*** the situation seems to be similar to that of **Br_2-SQB-R^1***, only that the two bands are of different intensities, leading to neither the zero crossing (13 910 cm^{-1}) nor the respective maxima of the CD bands at 13 700 cm^{-1} and 14 050 cm^{-1} being aligned with the absorption maximum. Since it has been shown that in the C(3)-chiral squaraines the angle between the electric and magnetic transition moments were usually close to 90° for the HOMO-LUMO transitions, it is speculated that this bisignate signal may originate from vibronic coupling, where certain vibrational modes may cause slight deviations of this angle from 90° and therefore lead to the observed small, sharp signal. Nevertheless, this effect is negligible and all further results in the polymers can be attributed to supramolecular chirality.

3.3 Conclusions

The employed synthetic methodology was successful for the synthesis of squaraine monomers with a stereogenic center at the 3-position of the indolenine subunit or on the alkyl side chain in satisfying optical purity. Using the described methods, a plethora of differently substituted derivatives may be synthesized, e.g., by using different alkyl groups or differently substituted aromatic residues. All monomers were investigated in terms of their geometrical structure, using X-ray crystallography and/or DFT-calculations. It was found that the alkyl-substituted C(3)-chiral monomers, as well as the analogues bearing chiral side chains, all possessed the expected nearly planar geometry, albeit with a few non-systematic deviations (**Pr-SQA*** and **Br_2-SQB-R^1***). On the other hand, the phenyl-substituted C(3)-chiral derivatives exhibited a twisted geometry, which was also observed for the tetraphenyl-substituted derivative **TPh-SQB**. This was concluded, since for both **Ph-SQA*** and **Ph-SQB***, DFT optimized

geometries showed the indolenine rings twisted slightly out of plane, and the crystal structure of **Ph-SQB*** was also significantly bent.

While the *n*-alkyl substituted C(3)-chiral squaraines possessed the same linear optical properties as their achiral tetramethyl-substituted counterparts, the introduction of two phenyl groups led to a bathochromic shift with a concomitant decrease in squared transition moment, along with a broadening of the main absorption band. The emission properties were also affected, with a decrease in Stokes shift, fluorescence quantum yield, and, in the case of **Ph-SQA***, fluorescence lifetime. DFT-calculations further showed this effect to be the results of the substitution itself, rather than that of structural torsion.

All compounds exhibited a CD signal, which was generally much more significant for the C(3)-chiral squaraines. For the main HOMO-LUMO transition, the obtained dissymmetry factors ranged from $3.1 \times 10^{-5} – 1.5 \times 10^{-4}$ cgs for the C(3)-chiral squaraines, while the values obtained for the monomers bearing chiral side chains were roughly one order of magnitude smaller ($6.5 \times 10^{-6} – 3.5 \times 10^{-5}$ cgs). This phenomenon was described by Moscowitz and Snatzke, who classified chiral chromophores according to the distance of the chiral perturbation to the main chromophore (subdivision into “spheres” around the central chromophore), where an increasing distance led to smaller dissymmetry factors, and thus enabled the use of this quantity as a means of classification.[12, 14, 274] As the chiral perturbation in the C(3)-chiral squaraines is in closer proximity compared to that on the remote side chains, the reported findings are in accordance with this theory. TD-DFT calculations proved to be useful in gaining superficial insights into the origin of the chiroptical properties, and revealed an angle close to 90° between the electric and magnetic transition moments. Overall, the chiroptical properties heavily depended on the type of chromophore (SQA vs. SQB), as well as the substitution. By variation of the substitution and/or the main chromophore type in future studies design strategies could be established for this type of chiral chromophore.

4 POLYMERIC SQB FOLDAMERS BEARING CHIRAL SIDE CHAINS [1]

As stated in previous chapters, the SQB-homopolymer was shown to exhibit a solvent and temperature dependent equilibrium between a random coil and a helix conformation.[73, 86, 92] In order to further elucidate the precise structure of the helical conformation, as well as to possibly find the origin of this phenomenon, a series of monodisperse oligomers **SQB$_{1\text{-}9}$** was synthesized and spectroscopically studied by A. Turkin.[91, 275-276]

While shorter oligomers of a chain length of n ≤ 3 showed no noteworthy solvent-dependent behavior, the larger oligomers with n ≥ 4 displayed a strong tendency to form helices in certain solvents. By screening 18 different solvents, it was found that the tendency to form helices correlated with the Hansen solubility dispersion index,[277] where a value smaller than 17.4 promoted the formation of a helix through a change in mutual orientation of the banana-bent **SQB** chromophores, which became apparent by a hypsochromically shifted main absorption band (H-type behavior in terms of Kasha's exciton coupling theory)[75-76]. In contrast, in solvents with a large Hansen solubility dispersion index, a bathochromic shift of the main absorption band was observed (J-type behavior). Further temperature-dependent absorption spectroscopic studies in PhCN enabled the determination of the thermodynamic parameters of the helix folding, where a stepwise increase of Δ*H* and Δ*S* were observed for each helix turn (consisting of roughly three monomers) from the tetramer to the nonamer. The average value of Δ*G* per monomer was determined to be 3.62 kJ mol^{-1} and does not fall within the usual range of typical intermolecular interactions, such as *π*-stacking,[278] hydrogen bonding,[279] or dipole-dipole interactions.[280]

Therefore, theoretical calculations were performed, which revealed a large helical pitch (2 nm) and a dihedral angle of 43°, as shown in Figure 22b. This geometry was then further confirmed by experimental studies using DOSY-NMR and small-angle neutron scattering (SANS). Furthermore, due to the large distance between the two chromophores, the aforementioned interaction types could be ruled out. This led to the postulation that the solvent molecules may be encapsulated between two parallel oriented squaraine units, thus forming a type of clathrate, as a similar type of ordering involving solvent molecules has

[1] Partially reprinted (adapted) with permission from *Polymeric Indolenine-Squaraine Foldamers with a Preferred Helix Twist Sense and their Chiroptical Absorption and Emission Properties*, J. Selby, M. Holzapfel, K. Radacki, A. Swain, H. Braunschweig, C. Lambert *Macromolecules* **2022**, *55*, 421-436. © 2022 American Chemical Society.

previously been reported for polymeric hydrocarbons[281] or helical coronene aggregates.[32] Force-field calculations of the octamer **SQB$_8$** in an acetone box showed the solvent molecules to interact with the SQB units, thus acting as a type of adhesive for the respective sheets of the helix, which is shown in Figure 44.

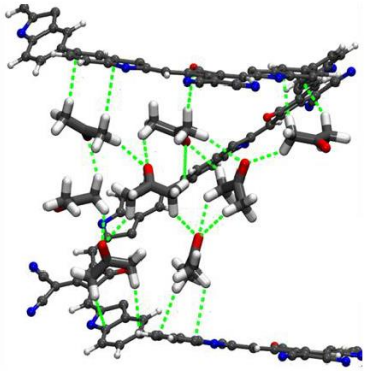

Figure 44. Optimized snapshot of the **SQB$_8$**-acetone clathrate. Reproduced from ref.[91] (open access).

As previously mentioned, the use of chiral side chains in this system may lead to the helical conformation possessing an excess in twist bias. Moreover, the side chains may have an impact on the folding of the polymers, which can perhaps be evaluated due to the systematic nature of the variation of the structure of the side chains as shown in Figure 40.

4.1 Synthesis

Succeeding the successful synthesis of the dibrominated squaraine monomers, the next step was their polymerization. Here, the Ni-mediated Yamamoto-homocoupling reaction was utilized, which is depicted in Scheme 17.

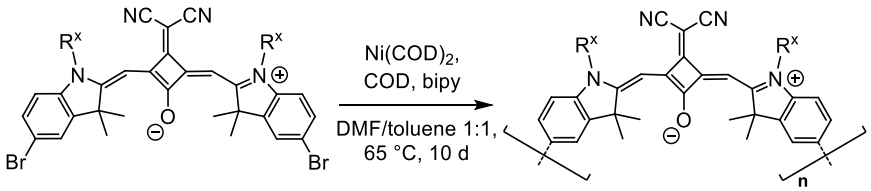

Br$_2$-SQB-R^0
Br$_2$-SQB-R^{1*}
Br$_2$-SQB-R^{2*}
Br$_2$-SQB-R^{3*}

p(SQB-R^0)
p(SQB-R^{1*})
p(SQB-R^{2*})
p(SQB-R^{3*})

Scheme 17. Polymerization of the dibrominated squaraine monomers **Br$_2$-SQB-R^0**, **Br$_2$-SQB-R^{1*}**, **Br$_2$-SQB-R^{2*}** and **Br$_2$-SQB-R^{3*}** via Yamamoto-homocoupling.

The obtained crude polymers were successively washed in a Soxhlet-extractor using diverse solvents, before being fractionated by preparative GPC. The molecular weight distributions of the individual polymer fractions were then determined by analytical GPC, where the aforementioned series of monodisperse oligomers (**SQB-R^1)$_{1\text{-}9}$** were used as the standard for the GPC calibration. Even though the molecular weights of the respective oligomers were quite small (M_n < 10 000), it has previously been shown that extrapolation of GPC data yields reliable results.[282] The data obtained by analytical GPC, as well as the chromatograms of the analytical and preparative runs, are presented in section 11.1.2 in the appendix.

When examining the obtained data, the first obvious trend is that the average degree of polymerization X_n becomes larger when increasing the steric demand (as specified in section 3.2) of the side chains from **p(SQB-R^0)** (22.8) to **p(SQB-R^{3*})** (65.3), while the corresponding polydispersity index (*PDI*) remained within a similar range (1.3-1.5). The same observation also holds true for the shorter fractions (F2), although here the *PDI* values possessed a greater degree of variance. This trend can be explained by the differences in solubility, since the polymers start to precipitate from the reaction mixture once a certain main chain length is reached. This fact was previously exploited in the synthesis of SQA-homopolymers, where different solvent compositions for the polymerization led to polymers of different lengths, thus hereby enabling control of the overall degree of polymerization.[94] In the present case, the control stems from the fact that differently branched alkyl chains affect the solubility in most organic solvents.[283] The shortest fraction (F3) contained significant amounts of shorter oligomer and monomer species in all cases and was therefore omitted from any further investigation.

4.2 Absorption spectroscopy

In order to gain insights into the polymer conformations in different solvents, absorption spectra were recorded in DMF (*N*,*N*-dimethylformamide), DEF (*N*,*N*-diethylformamide), PhCN (benzonitrile), toluene and $CHCl_3$ (chloroform). This allowed the observation of the pure H-type (helix) and J-type (random coil) behavior, as well as mixtures of both. The spectra of the F1 fraction are shown in Figure 45, the corresponding data are summarized in Table 7. The analogous spectra and data for the F2 fraction can be found in section 11.5 in the appendix.

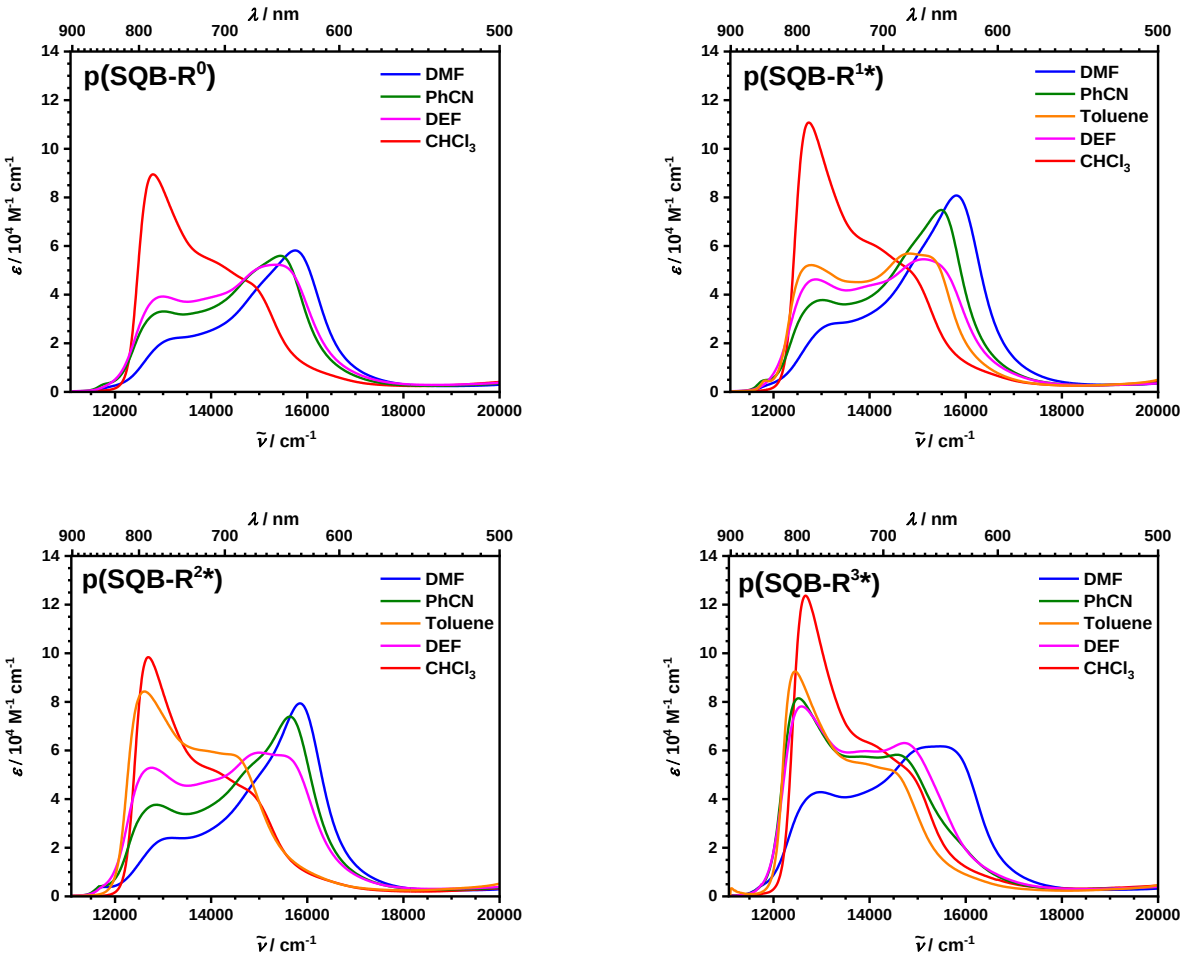

Figure 45. UV-Vis-NIR absorption spectra of **p(SQB-R^0)**, **p(SQB-R^{1*})**, **p(SQB-R^{2*})** and **p(SQB-R^{3*})** (F1) in various solvents. Absorption coefficients are reported per monomer unit. Measurement for **p(SQB-R^0)** in toluene omitted due to solubility issues.

In accordance with the precedent studies, a similar solvent dependent J- or H-type behavior was observed in this case as well for all polymers, where the absorption maximum was either bathochromically of hypsochromically shifted compared to that of the parent monomer **SQB** (14 300 cm^{-1}). The spectra can generally be described as a mixture (linear combination) of those of the pure J- or H-type species. The J-band is located at ca. 12 900 cm^{-1} and is most pronounced in $CHCl_3$, which leads to the assumption that the random coil structure is predominant in this solvent. On the other hand, the H-band is between 15 400 and 15 900 cm^{-1} and is most intense in DMF, where a helix is formed. The other tested solvents constitute intermediate cases, were a mixture of varying content of either helix or random coil conformations are present. Interestingly, an additional very weak band at ca. 11 800 cm^{-1} was observed, where the intensity correlated with that of the main H-band. This was assigned to be the lowest-lying excitonic transition of the helix, which is electronically weakly allowed and polarized along the helix axis.

Regarding the longest fraction (F1), the spectra of **p(SQB-R^0)**, **p(SQB-R^1*)**, and **p(SQB-R^2*)** are very similar with the exception of toluene. In this case, a mixture of variable amounts of H- and J-type behavior is found for **p(SQB-R^0)** and **p(SQB-R^1*)**, while **p(SQB-R^2*)** shows an exclusive J-type behavior. For **p(SQB-R^1*)**, this contradicts the results obtained for the respective nonamer with racemic side chains **(SQB-R^1)$_9$**, which did not display any H-type behavior in toluene. However, the polymer **p(SQB-R^1)** described by M. Schreck also exhibited this type of behavior in toluene.[73] In consequence, it can be concluded that the folding may also be dependent on the polymer main chain length in certain cases. This also means that the required chain length for the (partial) helix folding in toluene is greater than that of the nonamer. Since **p(SQB-R^1*)** and **p(SQB-R^2*)** possess a similar degree of polymerization (Table 33 and Table 34), it can be concluded that the observed differences can solely be ascribed to the influence of the side chain. Concerning **p(SQB-R^3*)**, it is obvious that in this case the increased size of the substituent on the side chain has a major impact on the formation of a helix, as in all of the tested solvents, apart from DMF, a random coil conformation is strongly favored. When comparing the different polymers, the spectral positions of the absorption maxima of the H- and J-band vary somewhat. When increasing the steric influence of the side chain, the spectral shifts of the respective aggregation type become larger in the majority of cases (see Table 7). For example, the absorption maximum of **p(SQB-R^3*)** in chloroform is red-shifted by 120 cm^{-1} compared to that of **p(SQB-R^0)**. This can be explained by an increased exciton delocalization length,[284] which in this case is likely due to an increasing degree of structural order within the J-type superstructure,[275, 285-287] since for the oligomers bearing racemic side chains **R^1** the red-shift of the main absorption band in $CHCl_3$ reaches its maximum at a relatively short chain length of roughly n = 8.[91] This is also further apparent when comparing the shape of the respective spectra of the investigated polymers in $CHCl_3$, where the main absorption band becomes narrower and more intense compared to the higher-energy shoulders between 13 600 cm^{-1} and 15 100 cm^{-1} when increasing the steric influence of the side chains. This trend also holds true for the H-type spectra in DMF (excluding **p(SQB-R^3*)**), where the absorption band of **p(SQB-R^2*)** is narrower and hypsochromically shifted by 100 cm^{-1} compared to that of **p(SQB-R^0)**, although this can also be explained by an increased main chain length, which was also previously observed when comparing the nonamer **(SQB-R^1)$_9$** to the corresponding polymer **p(SQB-R^1)**.[73, 91] This trend can be visualized by a comparison of the normalized absorption spectra in DMF and $CHCl_3$, which is shown in

Figure 46. Although clearly discernable, this effect is only minor when compared to other cases in the literature, such as the polymer **p(SQA-SQB)**[93] and BODIPY-oligomers by Wertz et al., where an ethyl group acted as a conformational anchor by fixation through dispersion interactions.[286]

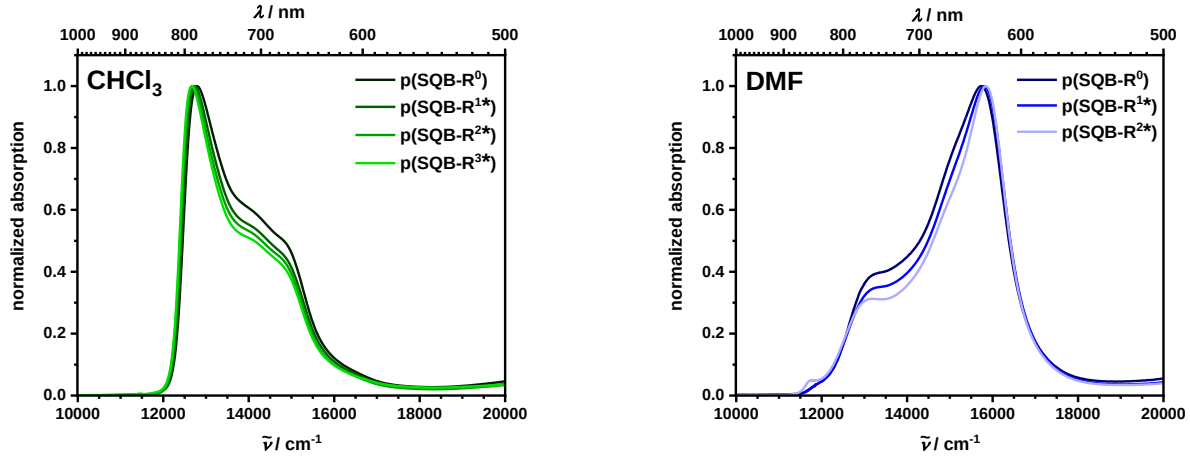

Figure 46. Overlay plot of the normalized absorption spectra of **p(SQB-R^0)**, **p(SQB-R^1*)**, **p(SQB-R^2*)** and **p(SQB-R^3*)** in $CHCl_3$ (left) and DMF (right). Spectrum of **p(SQB-R^3*)** in DMF omitted due to deviating spectral shape.

The spectra of the shorter polymer fractions (F2) generally only differ slightly from those of F1 for most solvents (see Figure 103 and Table 46) with exception of PhCN. Here, the spectra of the F2 fractions show a larger deviation from those of the longer fractions. Generally, the tendency to form helices with H-type behavior appears to be lower in the F2 fraction when compared to the longer polymer fraction (F1), which becomes obvious when regarding the spectra in DMF. Furthermore, the spectral shifts of the polymers compared to the monomer species in $CHCl_3$ seem to decrease markedly in the F2 set of polymers compared to those of F1, where the F2 fraction of **p(SQB-R^2*)** is blue-shifted by 120 cm^{-1} compared to the F1 fraction. Since the polydispersity values for the F2 fraction tended to be rather large (up to 2.11 for **p(SQB-R^2*)**, see Table 1), all these findings can be explained by the presence of significant amounts of shorter oligomers ($n < 8$) in F2, whose spectra overlap with those of the longer polymers. Since the predominant formation of a helix with H-type behavior requires at RT a main chain length of at least four in acetone or DMF, and six in PhCN,[91] this explains the larger impact on the spectra in PhCN compared to those in DMF. Furthermore, due to the limit for the red-shift of the J-type species being reached at relatively small main chain lengths, the smaller red-shift of the F2 set of polymers in $CHCl_3$ compared to that of the F1 fraction can also be seen as a proof for the presence of shorter oligomers.

It can therefore be concluded, that even small changes in the alkyl side chain (size, branching and position of the stereogenic center) may influence the degree of random coil vs. helix folding and have a minor impact on the exact structure of these conformations as well. This is remarkable, since the alkyl chains cannot interact across helix turns, as they are much too distant.

Table 7. Optical spectroscopic data (absorption maxima $\tilde{\nu}_{abs}$, extinction coefficients ε_{max}, squared transition moments μ_{eg}) of the F1 fraction of **p(SQB-R⁰)**, **p(SQB-R¹*)**, **p(SQB-R²*)** and **p(SQB-R³*)**.

		$\tilde{\nu}_{abs}$ (λ_{abs}) [a] / cm^{-1} (/ nm)	ε_{max} [a b] / M^{-1} cm^{-1}	μ_{eg}^2 [b d] / D²
p(SQB-R⁰)	$CHCl_3$	12 800 (782)	8.95×10^4	102
	toluene	12 800 (783)	-[c]	-[c]
	DEF	15 300 (653)	5.23×10^4	90.8
	PhCN	15 400 (648)	5.60×10^4	78.2
	DMF	15 800 (635)	5.82×10^4	74.6
p(SQB-R¹*)	$CHCl_3$	12 700 (785)	1.11×10^5	120
	toluene	14 800 (675)	5.69×10^4	96.2
	DEF	15 100 (661)	5.46×10^4	99.0
	PhCN	15 500 (646)	7.48×10^4	95.2
	DMF	15 800 (633)	8.08×10^4	99.7
p(SQB-R²*)	$CHCl_3$	12 700 (788)	9.84×10^4	104
	toluene	12 600 (793)	8.43×10^4	108
	DEF	15 000 (667)	5.91×10^4	115
	PhCN	15 600 (640)	7.39×10^4	97.4
	DMF	15 900 (631)	7.94×10^4	92.3
p(SQB-R³*)	$CHCl_3$	12 700 (789)	1.24×10^5	129
	toluene	12 500 (803)	9.50×10^4	106
	DEF	12 600 (795)	7.81×10^4	127
	PhCN	12 500 (799)	8.14×10^4	114
	DMF	15 500 (646)	6.17×10^4	110

[a] values for global maximum. [b] values per monomer unit. [c] not determined due to insufficient solubility. [d] determined by integration of the main absorption band and calculated using eq. (74) in the appendix.

4.3 CD spectroscopy

To evaluate, whether or not the formed helices indeed possess a twist-sense bias, CD spectroscopy was performed in the same solvents as used for the absorption spectroscopy. described in the previous chapter. As the monomers are nearly CD silent (see section 3.2.3), it can be concluded that the CD signal of the polymers solely stems from the helical superstructure. Due to the spectra of the shorter fractions (F2) essentially being identical in shape to those of the longer fractions (F1), but smaller in magnitude due to the presence of shorter, non-helical, CD-silent oligomers, the discussion will focus on the latter. The CD spectra of the F2 fractions are shown in section 11.5 in the appendix (Figure 104). Those of the F1 fractions are shown in Figure 47, the corresponding chiroptical data are summarized in Table 8.

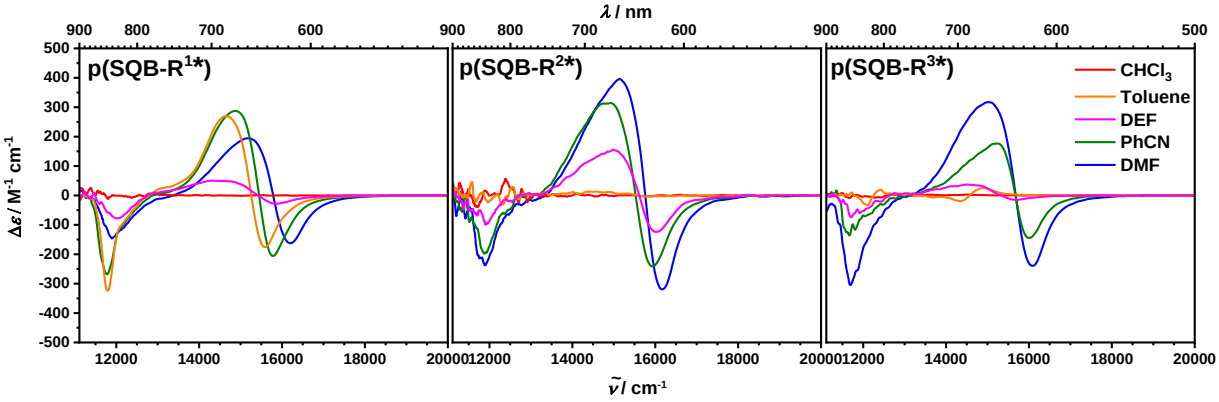

Figure 47. CD spectra of **p(SQB-R^{1}*)**, **p(SQB-R^{2}*)** and **p(SQB-R^{3}*)** in various solvents. Values for Δε are reported per monomer unit.

All spectra possess the same overall shape in DMF, PhCN, and DEF, that is a negative-positive-negative sequence of CD bands on going from lower to higher energy. In all cases, the sum of all rotational strengths is zero, which is in accordance with the sum rule (eq. (44) in section 1.2.2) and expected for the CD signals of an exciton manifold. In $CHCl_3$, where all polymers adopt a random coil conformation, no CD signal is visible, since this is an achiral arrangement of practically achiral chromophores. This also holds true for **p(SQB-R^{2}*)** and **p(SQB-R^{3}*)** in toluene, while for **p(SQB-R^{1}*)**, which undergoes partial helix formation in toluene, a strong CD signal as in the case of DMF and PhCN is visible. As expected, **p(SQB-R^{0})** is CD-inactive. Here, the use of a chiral solvent, which facilitates the folding into a homohelical conformation, such as (*S*)-1-methylbutanol, did not lead to a visible CD signal, as also observed when using racemic side chains as opposed to the purely achiral analogues used in this work.[91]

Table 8. Chiroptical data (CD bands $\tilde{\nu}_{CD}$, difference in absorption $\Delta\varepsilon$, rotational strengths R_{exp} and dissymetry factors g_{abs}) of **p(SQB-R¹*)**, **p(SQB-R²*)**, and **p(SQB-R³*)** (F1 fractions) in various solvents. Solvents, where no H-type behavior was found, are omitted.

		$\tilde{\nu}_{CD}$ (λ_{CD}) / cm^{-1} (/ nm)	$\Delta\varepsilon$ / M^{-1} cm^{-1} [a]	R_{exp} / 10^{-40} cgs [a d]	$\lvert g_{abs}(\tilde{\nu}_{max})\rvert$ / cgs [a b]
p(SQB-R¹*)	DMF	11 900 (840)	-147	-225	4.30 × 10^{-2} [c]
		15 200 (660)	194	386	2.94 × 10^{-3}
		16 200 (617)	-163	-186	2.57 × 10^{-3}
	PhCN	11 800 (849)	-268	-306	6.46 × 10^{-2}
		14 900 (672)	287	528	4.84 × 10^{-3}
		15 800 (634)	-206	-219	3.73 × 10^{-3}
	toluene	11 800 (848)	-324	-293	6.92 × 10^{-2}
		14 600 (683)	269	479	5.21 × 10^{-3}
		15 600 (642)	-176	-183	4.59 × 10^{-3}
	DEF	12 000 (832)	-77.7	-106	5.92 × 10^{-2}
		14 500 (692)	49.6	130	9.49 × 10^{-4}
		15 900 (631)	-28.6	-35.5	7.20 × 10^{-4}
p(SQB-R²*)	DMF	11 900 (841)	-237	-336	5.80 × 10^{-2}
		15 100 (661)	396	827	7.78 × 10^{-3}
		16 200 (619)	-319	-355	5.72 × 10^{-3}
	PhCN	11 900 (841)	-198	-251	4.75 × 10^{-2}
		14 900 (670)	314	673	7.00 × 10^{-3}
		15 900 (628)	-241	-282	5.40 × 10^{-3}
	DEF	11 900 (840)	-100	-119	1.76 × 10^{-2}
		15 000 (668)	155	333	3.08 × 10^{-3}
		16 000 (624)	-124	-142	3.61 × 10^{-3}
p(SQB-R³*)	DMF	11 700 (855)	-305	-410	7.86 × 10^{-2}
		15 000 (666)	317	679	5.12 × 10^{-3}
		16 100 (622)	-239	-266	5.09 × 10^{-3}
	PhCN	11 700 (857)	-136	-167	4.44 × 10^{-2} [c]
		15 200 (656)	176	337	4.28 × 10^{-3}
		16 000 (625)	-145	-143	5.86 × 10^{-3}
	DEF	11 700 (854)	-72.4	-146	1.90 × 10^{-2}
		14 500 (690)	37.3	83.1	5.85 × 10^{-4}
		15 700 (637)	-15.2	-16.5	5.47 × 10^{-4}

[a] values per monomer unit. [b] $\Delta\varepsilon(\tilde{\nu}_{max})/\varepsilon(\tilde{\nu}_{max})$. c values for $\varepsilon(\tilde{\nu}_{max})$ taken from absorption measurements due to unreliable values obtained from the CD spectrometer. [d] determined by integration of the CD band and calculated using eq. (75) in the appendix.

Semiempirical ZINDO calculations[1] of the rotatory strength of a helical octamer model structure with left-handed screw sense yields a CD spectrum that is in qualitative agreement with the experiment, see Figure 48. The lowest energy negative CD signal refers to the tiny absorption peak at ca. 11 800 cm^{-1} visible in the absorption spectra of all polymers in DMF. According to the ZINDO calculations, the electric transition moment of this absorption is polarized along the helix axis and is parallel to the associated magnetic transition moment, which results in the strong CD signal. The electric and magnetic dipole moments of the other two CD signals are polarized perpendicularly to the helix axis. As described in section 1.2.3, this lowest-energy transition can be interpreted as the ring contribution at E_0 of eq. (47), whereas the higher-energy bands are a superposition of the ring contribution at E_h, and the helical contribution. The experimental spectra qualitatively also resemble the calculated spectra depicted in Figure 18 (right hand side), thus further proving the described model to be sufficient for the discussion of the CD spectra of these systems.[162] Overall, this type of CD spectrum can be described as the CD "fingerprint" of the SQB-helix.

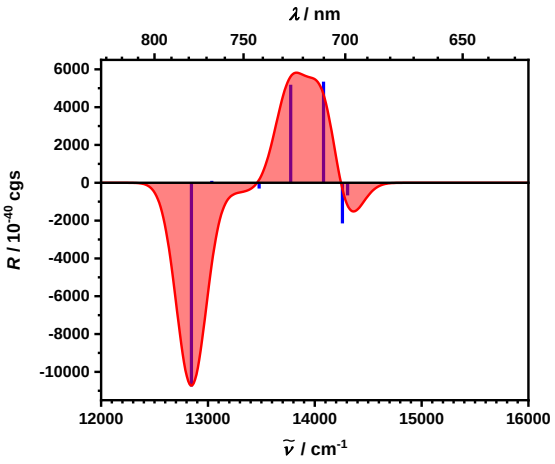

Figure 48. ZINDO calculated CD spectrum of a model octamer helix **SQ_8** optimized with the AM1 hamiltonian. The stick spectrum was convoluted with Gaussian function with a FWHM of 330 cm^{-1}.

Apart from the dependence on the relative amount of helical sections within the polymer strand, the CD signal also correlates with the excess of the preferred helical screw sense. Comparing the CD spectra to the respective absorption spectra, for **p(SQB-R^{2}*)** and **p(SQB-R^{3}*)**, the CD intensity seems to correlate with the H-type character, while in **p(SQB-R^{1}*)** this is not the case. Here, the CD signal is much larger in toluene compared to that in DMF,

[1] Theoretical calculations performed by Dr. M. Holzapfel

even though it displays a stronger H-type character in the latter solvent. This indicates that in DMF the excess of the preferred helical screw sense is smaller than in toluene.

The obtained dissymmetry factors g_{abs} (see Table 8) must be interpreted with care, since the absorption spectra might be a superposition of the H- and J-type spectra, while the CD spectra are that of the pure helix. Nevertheless, the obtained values allow the approximate comparison with other classes of chiral compounds.[14, 131] For the lowest energy band, g_{abs} reaches values of up to 7.86×10^{-2} cgs for **p(SQB-R^{3}*)** in DMF. As the ZINDO-calculations indicated, this is an electronically weakly allowed transition with its electric and magnetic transition moment colinear, leading to a large value for R and therefore g_{abs} (magnetically allowed transition).[14] The obtained dissymmetry factors for the bands associated with the other transitions are similar, ranging up to 7.78×10^{-3} cgs for **p(SQB-R^{3}*)** in DMF. Comparing these to the values obtained for the C(3)-chiral monomers discussed in section 3.1.4, these are roughly 1-2 orders of magnitude larger in the present case. Furthermore, these values are comparable to other intrinsically chiral chromophores,[14] such as helicenoids[44, 288] or axially chiral biaryls.[289-290] Regarding helical polymers, Suginome et al. reported homohelical poly(quinoxaline-2,3-diyl)s with dissymmetry factors on the same order of magnitude.[291]

4.4 Temperature dependent absorption spectroscopy

It was apparent in the previously discussed UV-Vis absorption spectra, that the side chains had a marked influence on the helix-coil equilibrium of the polymers (especially in toluene). To further quantify these effects, temperature dependent UV-Vis-NIR absorption measurements were performed in PhCN, as this solvent has proven to be suitable for these types of measurements due to the advantageous thermodynamics (high degree of reversibility, small ΔG) of the helix-coil equilibrium in this solvent.[91, 276] The temperature dependent spectra are shown in Figure 49, the corresponding optical data are summarized in Table 47 in the appendix.

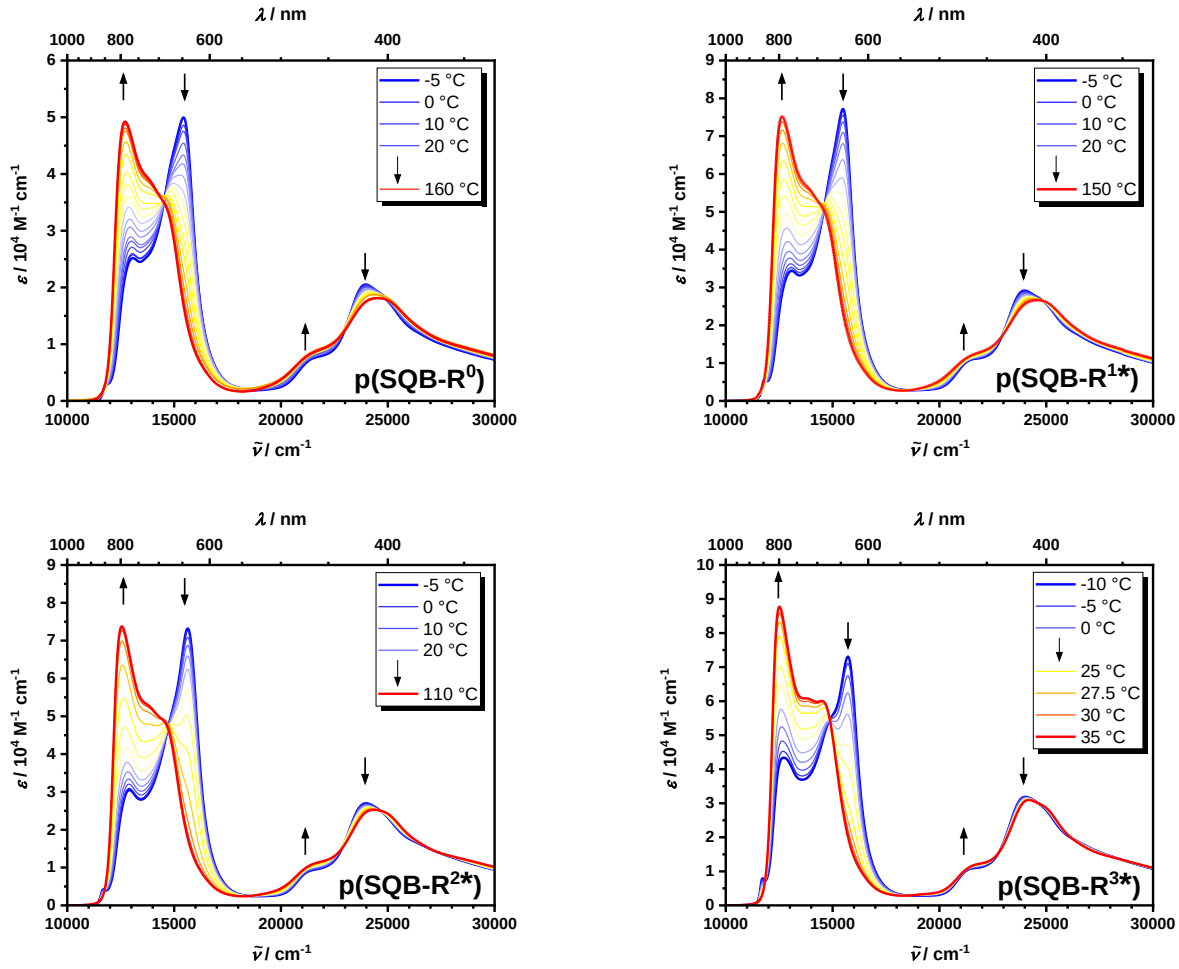

Figure 49. Temperature dependent UV-Vis-NIR spectra of **p(SQB-R^0)**, **p(SQB-R^1*)**, **p(SQB-R^2*)** and **p(SQB-R^3*)** (F1 fraction) in benzonitrile. Arrows indicate an increase or decrease in intensity with increasing temperature.

In all cases, the polymers display an increasing H-type behavior at lower temperatures, which, upon heating, reversibly transforms into J-type behavior. For all compounds, a prominent isosbestic point can be identified between 14 600 and 14 900 cm^{-1}, with additional isosbestic points at higher and lower energies, thus indicating the presence of only two structures in equilibrium.

When examining the spectra at the extreme temperatures more closely, it can be seen that the individual spectral features become more pronounced when increasing the steric demand of the side chains on going from **p(SQB-R^0)** to **p(SQB-R^3*)**. This can be seen especially for the J-type spectra, where the main absorption peak at around 12 500 - 12 700 cm^{-1} becomes narrower and more intense compared to its higher-energy shoulders. This narrowing of the spectral features is also observed in the H-type spectra to an extent, where for **p(SQB-R^2*)** and **p(SQB-R^3*)** an additional lower-energy shoulder at 14 800 cm^{-1} becomes visible. This can possibly be explained by the conformational restriction caused by the steric demand of the

side chains, therefore leading to a superstructure with a higher degree of order, e.g. a more elongated coil or a more perfect helix, which in turn leads to narrower and more distinct spectral features.[285-287] Additionally, this structural perfection is also visible through the isosbestic points which are more ideal on going from **p(SQB-R^0)** to **p(SQB-R^3*)**. Inspecting the location of absorption maxima of the J-band at high temperatures, this trend becomes further apparent. Whereas **p(SQB-R^0)** possesses its maximum at 12 700 cm^{-1}, those of **p(SQB-R^1*)**, **p(SQB-R^2*)** and **p(SQB-R^3*)** are shifted to lower energies by 70 cm^{-1}, 140 cm^{-1} and 180 cm^{-1}, respectively. Since the red-shift of the absorption maximum due to excitonic coupling is dependent on the exciton delocalization, this observation could be explained by an increasing exciton delocalization length due to a more ordered structure as previously described.[275, 284] A similar trend is obvious for the H-band, where the absorption maximum is progressively blue-shifted, but this can also be due to a larger degree of polymerization, since merely increasing the main chain length was also shown to cause such a blue shift when comparing **p(SQB-R^1*)** to the respective nonamer. This was not the case for the J-type spectra, since the spectra in chloroform were nearly identical.[91]

In order to determine the thermodynamic parameters of the folding process, the temperature-dependent extinction coefficient of the H-band (ε_H) was fitted using a two-state cooperative equilibrium model,[172, 177]

$$\frac{OD(\lambda)}{cd} = \frac{K}{1+K}\varepsilon_H + \frac{1}{1+K}\varepsilon_C \qquad \text{with} \qquad K = \exp\left(-\frac{\Delta H}{RT} + \frac{\Delta S}{R}\right) \tag{52}$$

where ε_C is the absorption coefficient of the random coil at the same wavenumber and K is the equilibrium constant of the helix-coil equilibrium, with ΔH being the enthalpy and ΔS the entropy of this process. These fits are shown in Figure 50, the obtained parameters are summarized in Table 9.

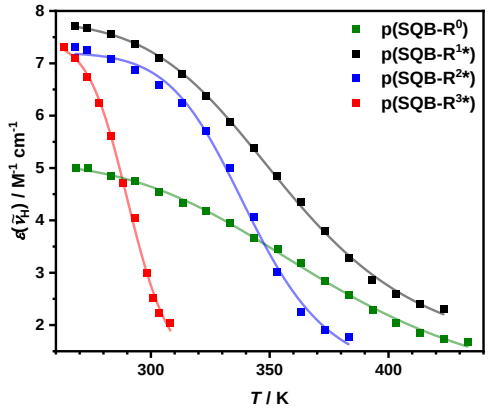

Figure 50. Fits of the temperature dependent extinction coefficients of the H-band with eq. (52) for the polymers **p(SQB-R⁰)**, **p(SQB-R¹*)**, **p(SQB-R²*)** and **p(SQB-R³*)**. For the exact wavenumber, see Table 48 in the appendix. Data points are shown as squares with the fitting curve shown as lines.

Table 9. Thermodynamic parameters (difference in enthalpy Δ*H*, difference in entropy Δ*S*, difference in Gibbs free energy at RT ΔG_{298}) obtained from the fits of the temperature dependent absorption data in PhCN of the polymers using eq. (52).

	ΔH / kJ mol^{-1}	ΔS / J K^{-1} mol^{-1}	ΔG_{298} / kJ mol^{-1} [a]
(SQ-R¹)₉	-31.9	-95.6	-3.4
pSQ-R⁰	-26.7	-71.3	-5.5
pSQ-R¹*	-35.7	-99.9	-5.9
pSQ-R²*	-56.7	-166.2	-7.2
pSQ-R³*	-80.1	-275.4	+2.0

[a] Calculated using eq. (79) in the appendix.

Comparison of the obtained values of **p(SQB-R¹*)** for Δ*H* and Δ*S* to those obtained for the respective nonamer[91] reveals similar values for these parameters, even though the chain length is significantly larger, thus leading to the assumption that these values converge to this specific limit on going from smaller oligomers to the polymer. This is in contrast to the findings for polymeric phenyl ethynylenes reported by Moore et al., where the values for Δ*G* were directly proportional to the main chain length, which would also be expected for an increasing amount of helical turns.[177] For the oligomeric counterparts **(SQB-R¹)ₙ** of **p(SQB-R¹*)** a step-wise increase of $|\Delta H|$ and $|\Delta S|$ from the tetramer to the nonamer for each helix turn was observed.[91] This indicates that sections within the polymer strand of **p(SQB-R¹*)** behave independently and these sections are, on average, only slightly larger than a nonamer, which is illustrated in Figure 51. This also means that coil sections and helix section may be present

at the same time within a polymer strand, an interpretation that was also derived from time resolved transient absorption studies on **p(SQB-R^1)** with racemic side chains in the past.[86] Since the main chain lengths of all polymers are significantly larger than that of the nonamer and it can therefore be concluded that all the obtained values represent the respective convergence limit, the differences in the thermodynamic values on going from **p(SQB-R^0)** to **p(SQB-R^3*)** can solely be ascribed to the effect of the substitution on the side chains and not to the polymer length.

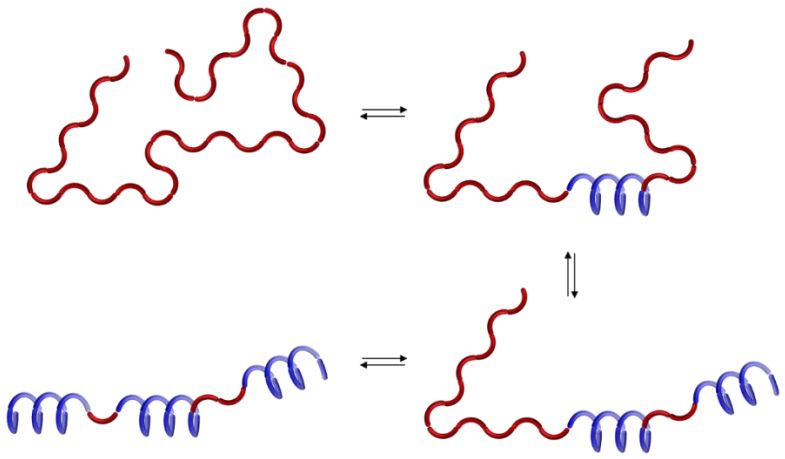

Figure 51. Independent folding of random coil sections into helical sections.

Regarding the obtained values for Δ*H* and Δ*S*, the absolute values of these quantities increase throughout the series on going from **p(SQB-R^0)** to **p(SQB-R^3*)**. While the obtained values for **p(SQB-R^0)** and **p(SQB-R^1*)** are comparable, the increase becomes especially significant when moving the chiral center closer to the SQB-chromophore in **p(SQB-R^2*)** and again when further increasing the size of the substituent at this position in **p(SQB-R^3*)**. The increasing entropic disfavorment is compensated by enthalpy, but to varying degrees, which is why the concrete temperature dependence of the helix-coil equilibrium and denaturing temperature (temperature where all helices are unfolded) are different for each polymer. The calculated values for Δ*G* at 298 K also describe the situation as it was apparent by the UV-Vis-NIR spectra in PhCN at RT (Figure 45), since the polymers possessing a negative value show a predominant H-type behavior, while **p(SQB-R^3*)**, which has a positive value for Δ*G*, mainly displays a J-type behavior. As the above-described spectral features (spectral narrowing, bathochromic/hypsochromic shifts and more ideal isosbestic points) are only minor, the differences in the obtained thermodynamic parameters do not likely solely stem from an

increased structural perfection, but rather may be the result of the formed helical segments (as indicated in Figure 51) being longer in **p(SQB-R^{2}*)** and **p(SQB-R^{3}*)**.

4.5 Temperature dependent CD spectroscopy

4.5.1 Thermodynamic model

In the previous section, it was described how the type of side chain influences the equilibrium between the helical and random coil conformation of the main polymer strand. Since the use of enantiomerically pure side chains led to a visible CD signal, and, upon closer examination, the magnitude of the CD effect did not always directly correlate with the intensity of the H-band, this led to the assumption that the polymers do not adopt exclusively homohelical conformations, but rather only lead to an excess of one helix enantiomer. This situation can be represented by the following model, which describes the equilibrium between the *M*-helix, random coil and *P*-helix conformations:

$$M \rightleftharpoons C \rightleftharpoons P$$

where *M* is the *M*-helix, *C* the random coil and *P* the *P*-helix with the respective equilibrium constants K_M and K_P. Disregarding stereochemistry, this equilibrium becomes the simple helix-coil equilibrium:

$$C \rightleftharpoons H$$

with *H* being the helical conformation and K_H its corresponding equilibrium constant. The following statements also hold true:

$$[H] + [C] = c_0 \tag{53}$$

$$[M] + [P] = [H] \tag{54}$$

where c_0 is the overall concentration. Using the definition of the equilibrium constants, it can be shown that

$$K_M + K_P = K_H \tag{55}$$

The CD intensity *CD* is directly proportional to the excess of one helix enantiomer. Arbitrarily assuming that *M* is the predominant helical screw sense, the CD intensity can therefore be expressed as:

$$CD = \Delta\varepsilon_M \left([M] - [P]\right) \tag{56}$$

Where $\Delta\varepsilon_{\mathrm{M}}$ is the difference in absorption for the pure *M*-helix. Substituting the respective equilibrium constants into eq. (56), then rearranging eq. (55) to obtain an expression for K_{M} and further inserting this into the equation leads to the following expression:

$$CD = \Delta\varepsilon_{\mathrm{M}}\,[C](2K_{\mathrm{M}} - K_{\mathrm{H}}) \tag{57}$$

Since $[H] = K_{\mathrm{H}}[C]$, eq. (53) can be rearranged as follows

$$[C] = \frac{c_0}{1 + K_{\mathrm{H}}} \tag{58}$$

Finally inserting eq. (58) into eq. (57) leads to the following expression:

$$\Delta\varepsilon_{\mathrm{obs}} = \Delta\varepsilon_{\mathrm{M}}\,\frac{2K_{\mathrm{M}} - K_{\mathrm{H}}}{1 + K_{\mathrm{H}}} \tag{59}$$

With $\Delta\varepsilon_{\mathrm{obs}} = {}^{\mathrm{CD}}/_{\mathrm{c}_0}$. Substituting the definition for *K* in eq. (52) into eq. (59) then enables the determination of the thermodynamic parameters of the equilibrium between the random coil and *M*-helix conformation by fitting the temperature dependent CD data, which would constitute a quantitative measure of the twist bias of the helical polymers. Because *M* was defined as the predominant screw sense, K_{M} must be larger than K_{P}. Since eq. (55) holds true, the allowed values for K_{M} are:

$$\frac{1}{2}K_{\mathrm{H}} \leq K_{\mathrm{M}} \leq K_{\mathrm{H}}$$

In the case of $K_{\mathrm{M}} = \frac{1}{2}K_{\mathrm{H}}$, which describes the situation where there is no twist bias at all, eq. (59) becomes zero, which is expected for a racemic mixture. On the other hand, when $K_{\mathrm{M}} = K_{\mathrm{H}}$, only one helical configuration is formed. Substituting this into eq. (59) leads to this becoming

$$\Delta\varepsilon_{\mathrm{obs}} = \Delta\varepsilon_{\mathrm{M}}\,\frac{K_{\mathrm{H}}}{1 + K_{\mathrm{H}}} \tag{60}$$

Because the random coil conformation is CD silent ($\Delta\varepsilon_{\mathrm{C}} = 0$), eq. (60) is essentially identical to eq. (52) and therefore yields the same temperature dependency as the absorption data, which is to be expected.

In practice, this means that the thermodynamic parameters of the overall helix-coil equilibrium must be determined prior to using this model for fitting the temperature dependent CD data. This also means, that it is only possible for solvents and measuring setups which have a sufficiently large accessible temperature range and therefore allow the

observation of the full helix folding and unfolding. Furthermore, the fitting of such data may be complicated and require well developed fitting routines and precise measuring equipment, especially if the spectroscopic changes are dominated by the helix unfolding itself.

4.5.2 Experimental results

In order to assess the degree of homohelicity, temperature dependent CD spectra of the polymers were recorded (see Figure 52). The temperature-dependent CD and absorption data were then plotted together, where the minimum and maximum values on the axes were set to the corresponding minimum and maximum values for ε and $\Delta\varepsilon$, respectively, in order to make the data comparable (see Figure 53).

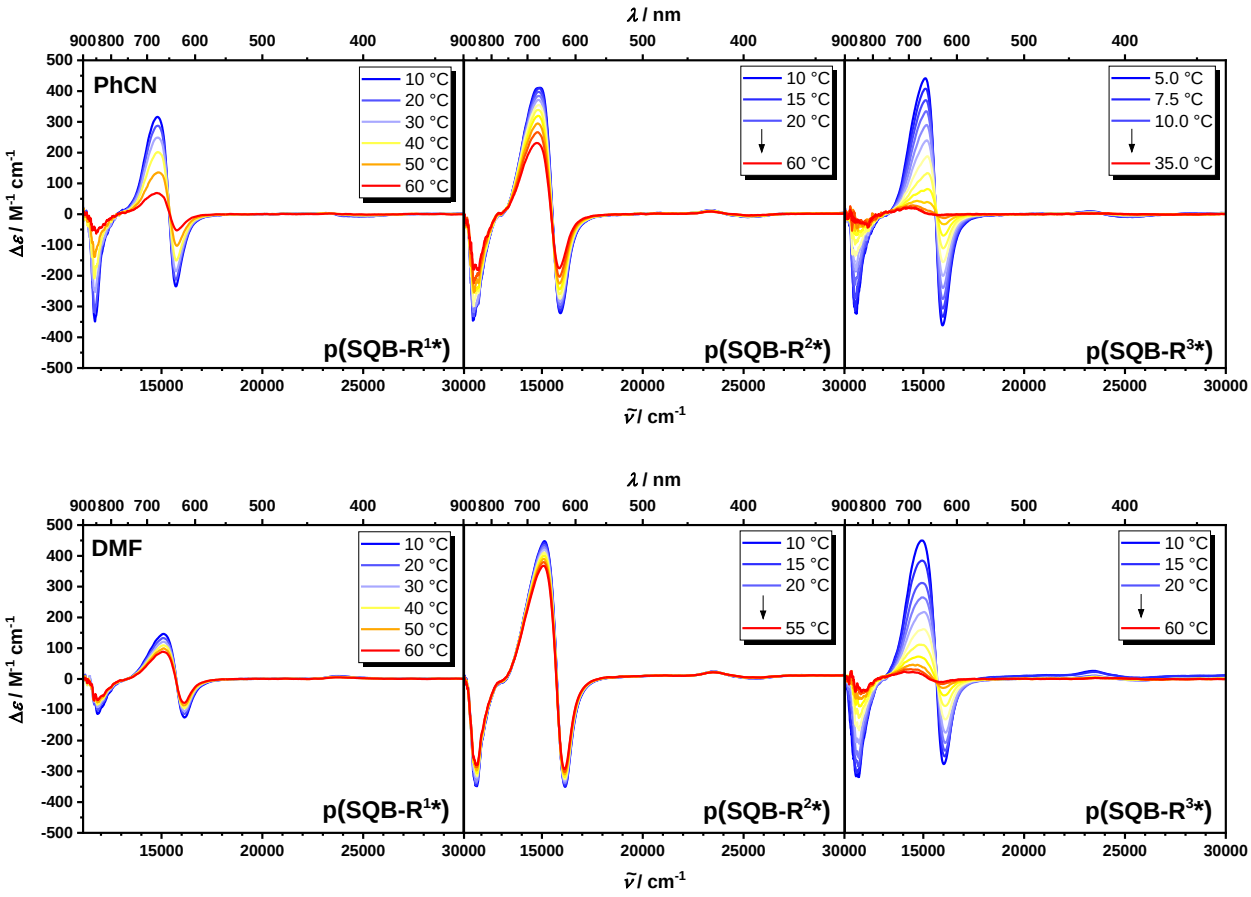

Figure 52. Temperature-dependent CD spectra of **p(SQB-R^1*)**, **p(SQB-R^2*)**, and **p(SQB-R^3*)** (F1 fraction) in PhCN (top) and DMF (bottom).

In all cases, the CD signal diminishes upon heating, which demonstrates the unfolding of the helix, as the random coil conformation is CD silent. In PhCN, the CD and the absorption data are identical (within experimental error), which leads to the conclusion that all of the investigated polymers are nearly completely homohelical in this solvent, since this is expected

in the above-described limit where $K_H = K_M$. In DMF, on the other hand, this is only the case for **p(SQB-R²*)**. In **p(SQB-R³*)** a minor deviation of these trends is observed, although this is only the case for temperatures between 35-60 °C. This can possibly be explained by the presence of other conformations, as the isosbestic point in the temperature dependent absorption spectra (see Figure 105 in the appendix) is less ideal and the shape of the J-type spectra differ significantly compared to those previously discussed in section 4.4. Another explanation could be the loss of complete homohelicity at higher temperatures close to that of the complete unfolding of the helix, leading to the quicker diminishing of the CD signal compared to that of the absorption. On the other hand, for **p(SQB-R¹*)** there is a marked difference of the temperature dependencies of CD and absorption, which seems to be clearly systematic. This can be seen as further evidence for an incomplete homohelicity, which was initially postulated in section 4.3, as the CD signal did not correlate with the H-type character when comparing its CD spectra in different solvents. Unfortunately, the accessible temperature range (limited by the measuring equipment) does not allow the extraction of the amount of preferred helicity by fitting the data using eq. (59).

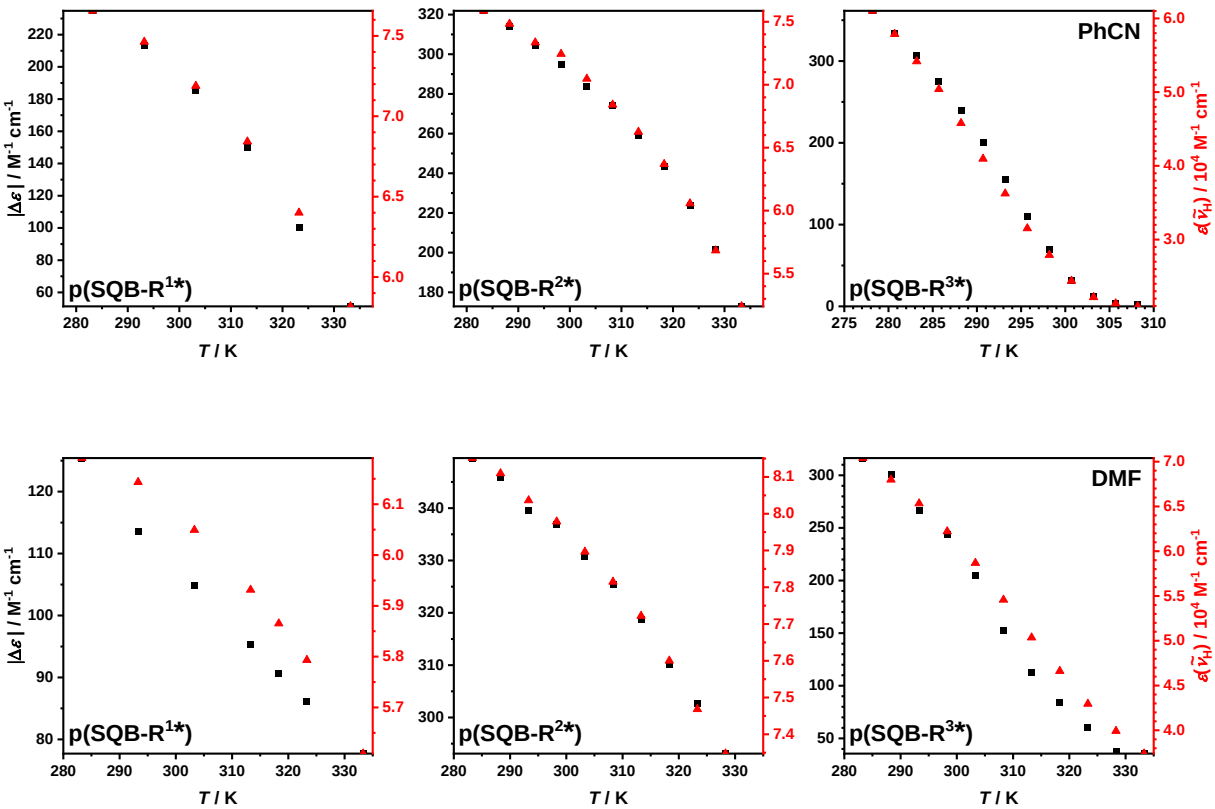

Figure 53. Overlay plots of the temperature-dependent absorption coefficients of the H-band (red) and the absolute value of the difference in absorption (black) for **p(SQB-R¹*)**, **p(SQB-R²*)**, and **p(SQB-R³*)**. For the exact wavenumbers, see Table 48 in the appendix. Top: PhCN, bottom: DMF.

4.6 Emission spectroscopy

4.6.1 Fluorescence spectroscopy

Previous studies on the fluorescence properties of **SQB** oligomers showed that these are non-fluorescent in solvents where helix formation predominates the superstructure. Thus, fluorescence spectra were recorded of the longest fractions (F1) of all polymers in $CHCl_3$, where a random coil is expected, and in toluene, where mixtures with helix are present. This behavior is expected, because non-radiative decay from the upper to the lower excitonic state results in subsequent non-radiative decay to the ground state due to the optically forbidden nature of this transition.[74-76, 292] The spectra in toluene in comparison with the absorption are shown in Figure 54, an overlay of all fluorescence spectra in chloroform and toluene in Figure 55. The corresponding data are summarized in Table 10. Due to insufficient solubility, the data for **p(SQB-R^0)** in toluene must be interpreted with care.

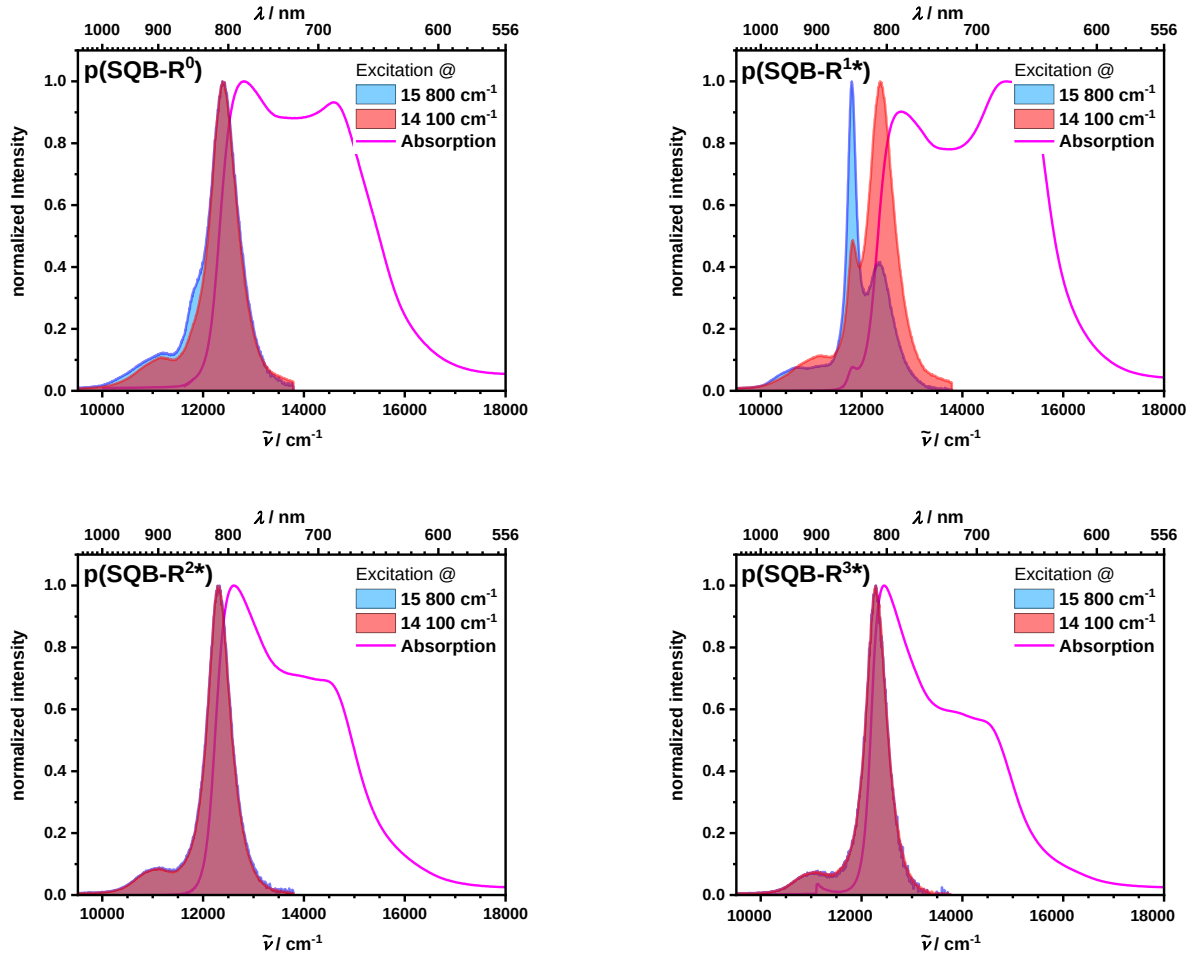

Figure 54. Normalized fluorescence (excitation at 15 800 cm^{-1} (635 nm) and 14 100 cm^{-1} (710 nm)) and absorption spectra of **p(SQB-R^0)**, **p(SQB-R^{1}*)**, **p(SQB-R^{2}*)** and **p(SQB-R^{3}*)** in toluene.

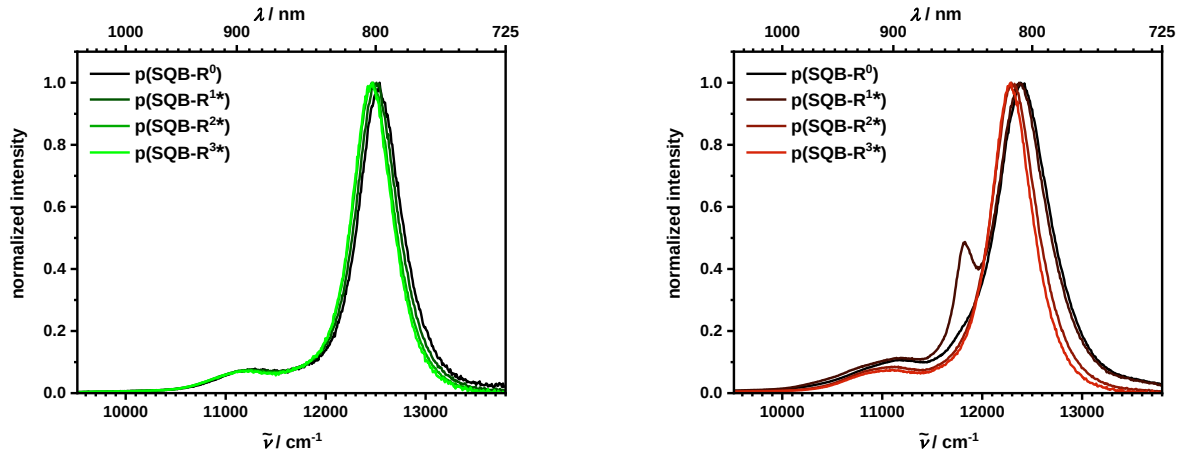

Figure 55. Overlay plot of the normalized fluorescence spectra of **p(SQB-R^0)**, **p(SQB-R^{1}*)**, **p(SQB-R^{2}*)** and **p(SQB-R^{3}*)** in $CHCl_3$ (left) and toluene (right). Excitation at 14 100 cm^{-1} (710 nm).

In $CHCl_3$, the fluorescence spectra are narrow with a vibronic progression which demonstrates emission from the lowest exciton state of the random coil structure in all cases. The quantum yield ranges from 0.16 for **p(SQB-R^0)** to 0.21 for **p(SQB-R^{2}*)**, and the fluorescence exhibits a similar biphasic decay with a dominating longer (ca. 1.0 ns) and a shorter component (ca. 0.4 ns), leading to a mean fluorescence lifetime of roughly 1 ns. The spectral widths decrease slightly from 500 cm^{-1} to 480 cm^{-1} on going from **p(SQB-R^0)** to **p(SQB-R^{3}*)**. This went along with a concomitant red-shift of 80 cm^{-1} throughout this series. In toluene, **p(SQB-R^{2}*)** and **p(SQB-R^{3}*)** show similar fluorescence behavior as in $CHCl_3$, that is, a narrow emission band with a fluorescence quantum yield of 0.26 and a biphasic decay with an average lifetime of ca. 2 ns. However, for **p(SQB-R^{1}*)**, and to a lesser extent for **p(SQB-R^0)**, an excitation wavelength dependent emission was observed. For **p(SQB-R^{1}*)**, excitation at 14 100 cm^{-1} into the J-type band produces an emission at 12 400 cm^{-1} accompanied by a much weaker band at 11 800 cm^{-1}. In this case, the decrease of spectral widths and red-shift of the emission band centered around 12 400 cm^{-1} was to a significantly higher extent, as the *FWHM* decreased by 180 cm^{-1} and the emission wavenumber by 90 cm^{-1} on going from **p(SQB-R^0)** to **p(SQB-R^{3}*)**.

The spectral narrowing is caused by an increase of effective exciton delocalization length N_{eff} and can be estimated by the following equation:[293]

$$\sqrt{N_{\mathrm{eff}}} = \frac{FWHM(\mathrm{monomer})}{FWHM(\mathrm{polymer})} \tag{61}$$

where *FWHM* denotes the spectral full width at half maximum. With *FWHM* =787 cm^{-1} ($CHCl_3$), 727 cm^{-1} (toluene) for the monomer, N_{eff} slightly increases from 2.48 to 2.69 on going from **p(SQB-R^0)** to **p(SQB-R^{3}*)** in $CHCl_3$ and from 1.17 to 2.20 in toluene. As stated in the previous

sections, this increase in exciton delocalization length leads to a red-shift and spectral narrowing of the emission band and is the result of a higher degree of structural order.[275] In the present case, this could mean a higher ordered J-type structure, such as a more elongated coil. Also, since this effect reaches its limit at relatively short main chain lengths, this leads to the conclusion that the type of side chain is the sole cause for this observation.

Interestingly, excitation of **p(SQB-R^{1}*)** at the H-type band at 15 800 cm^{-1} reverses the intensity ratio of the two emission bands. This clearly indicates that a mixture of random coil and helix structures are formed in toluene, and that depending on the excitation wavenumber, either the coil fluoresces at 12 400 cm^{-1} or the helix at 11 800 cm^{-1} (for excitation spectra and emission spectra measured at different excitation wavelengths of **p(SQB-R^{1}*)** see Figure 102 in the appendix). A closer look at the absorption spectra shows that the helix emission is associated with the small absorption peak at ca. 11 800 cm^{-1} which is also better discernable in the CD spectrum. The width of the fluorescence signal is 230 cm^{-1}, which is surprisingly small. This yields with eq. (71) N_{eff} = 10.0. Thus, owing to the higher order in the helix compared to the random coil, the effective delocalization length is much larger than in the latter, where we found N_{eff} = 1.37 from the peak width of the emission at 12 400 cm^{-1}. In solvents such as PhCN or DMF, where the pure helix is formed, no fluorescence was observed at all.

Table 10. Summary of the fluorescence data (excitation wavenumber $\tilde{\nu}_{ex}$, emission wavenumber $\tilde{\nu}_{em}$, spectral full width at half maximum *FWHM*, Stokes-shift $\Delta\tilde{\nu}$, fluorescence quantum yield Φ_{fl}, fluorescence lifetimes τ_{fl}, mean fluorescence lifetime $\bar{\tau}_{fl}$) of the **p(SQB-R^0)**, **p(SQB-R^1*)**, **p(SQB-R^2*)** and **p(SQB-R^3*)** in $CHCl_3$ and toluene.

		$\tilde{\nu}_{ex}$ (λ_{ex}) / cm^{-1} (/ nm)	$\tilde{\nu}_{em}$ (λ_{em}) / cm^{-1} (/ nm)	*FWHM* / cm^{-1}	$\Delta\tilde{\nu}$ / cm^{-1}	Φ_{fl}	τ_{fl} [a] / ns	$\bar{\tau}_{fl}$ [b] / ns
p(SQB-R^0)	toluene	14 100 (710)	12 400 (807)	670	390	0.22	1.06 (0.23) 2.43 (0.77)	2.27
		15 800 (635)	11 800 (847)	-	-	0.15	-	-
	$CHCl_3$	14 600 (685)	12 500 (798)	500	250	0.16	0.43 (0.25) 0.99 (0.75)	0.92
p(SQB-R^1*)	toluene	14 100 (710)	12 400 (809)	620	390	0.12	0.54 (0.06) 1.73 (0.50) 3.26 (0.44)	2.65
		15 800 (635)	11 800 (847)	230	-	0.10	1.19 (0.13) [c] 3.26 (0.87)	3.15
	$CHCl_3$	14 600 (685)	12 500 (800)	490	240	0.17	0.41 (0.27) 0.95 (0.73)	0.87
p(SQB-R^2*)	toluene	14 100 (710)	12 300 (814)	540	330	0.26	1.06 (0.19) 2.27 (0.81)	2.15
	$CHCl_3$	14 600 (685)	12 500 (802)	490	230	0.21	0.43 (0.22) 1.02 (0.78)	0.96
p(SQB-R^3*)	toluene	14 100 (710)	12 300 (814)	490	160	0.26	0.79 (0.14) 2.11 (0.86)	1.93
	$CHCl_3$	14 600 (685)	12 500 (802)	480	210	0.20	0.47 (0.21) 1.07 (0.79)	1.01

[a] Determined by TCSPC, decay curves fitted with a (multi-)exponential fit, amplitudes are given in parantheses. Excitation was at 15 240 cm^{-1} (656 nm), fluorescence signal at 12 500 cm^{-1} (800 nm) was measured unless stated otherwise. [b] Intensity-weighed mean fluorescence lifetime calculated according to eq. (77) in the appendix. [c] Fluorescence at 11 800 cm^{-1} (850 nm).

4.6.2 CPL spectroscopy

To further elucidate the origin of the observed emission from the helix foldamer of **p(SQB-R^{1}*)** in toluene CPL spectra were recorded in toluene, which is exemplarily shown in Figure 56 for a sample absorbance of 0.9 at the absorption maximum of 14 800 cm^{-1}. Additionally, CPL spectra using varying sample concentrations were measured and subsequently corrected for self-absorption as further verification that the observed CPL is indeed a genuine effect of this system. These results, along with the detailed description of the self-absorption correction following a procedure developed by Castiglioni et al.[139, 294] are presented in section 11.6 in the appendix.

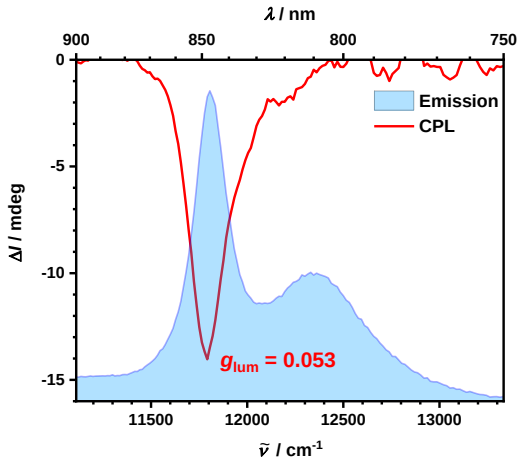

Figure 56. CPL-spectrum of **p(SQB-R^{1}*)** in toluene (OD($\tilde{\nu}_{max}$) = 0.9) with superimposed emission spectrum (excitation at 15 800 cm^{-1} (635 nm). The measured spectrum was further corrected for self-absorption as mentioned above. The CPL spectrum is somewhat broadened compared to the fluorescence because of larger slit widths of the CPL spectrometer.

Since the helical structure has a preference in twist sense, which is obvious by the CD signal exhibited in toluene, a non-zero CPL signal is also expected. Indeed, such a signal was observed, which is seen in Figure 15 where it is superimposed on the fluorescence spectrum. A CPL signal is only seen for the sharp emission at 11 800 cm^{-1} but not for the emission at 12 400 cm^{-1}. This further proves that the sharp low energy emission stems from the chiral helix but the high energy emission from the random coil. The dissymmetry factor g_{lum} of the CPL signal was 0.053 (OD($\tilde{\nu}_{max}$) = 0.9), which is similar to the corresponding dissymmetry factor of the absorption g_{abs} of the lowest energy transition at 11 800 cm^{-1} (0.069). These values are correlated and the value of g_{lum} is usually slightly smaller or equal compared to that of g_{abs}.[131] Because this transition is magnetic-dipole allowed and electric-dipole suppressed, the magnitude of the dissymmetry factors are relatively large.[138] Both g_{lum} and g_{abs} are apparent values as they only refer to the excess of chiral helix with the preferred helix twist sense.

Unfortunately, this means that a discussion in terms of the CPL brightness (eq. (29)) is not possible, since the quantum yield of the pure helix is not known. As stated in section 1.2.1 in eq. (28), the value of g_{lum} was also found to be proportional to the number of coherently coupled chromophores. As the exciton is strongly delocalized in the present case, such a large value for g_{lum} would be the consequence of this relation. This further proves, that this emission band corresponds to the weak absorption band at around 11 800 cm^{-1}, and that this originates from the highly ordered helical structure.

4.7 Conclusions

The dibrominated monomers were polymerized via Yamamoto-homocoupling and subsequently fractionized by GPC, which yielded polymers with polymerization degrees X_n between 23 and 65 for the longer fraction with similar corresponding PDI values of 1.3 – 1.4. As previously reported for analogous oligomers **(SQB-R^1)$_{1\text{-}9}$** with racemic side chains,[91] these polymers displayed solvent-dependent UV-Vis-NIR spectra, which could generally be described as a linear combination of the pure H- and J-type spectra, which are associated with a helix foldamer and a random coil structure, respectively. It became apparent that with increasing steric demand of the alkyl side chains the equilibrium between random coil and helix is shifted towards the former at RT, which is especially apparent in toluene, where only J-type spectra were observed for **p(SQB-R^2*)** and **p(SQB-R^3*)**. CD spectroscopy revealed that the helical H-type foldamers possessed a preferred twist sense, with $\Delta\varepsilon$ values of up to 396 M^{-1} cm^{-1} for **p(SQB-R^2*)** in DMF and a large g_{abs}-value of up to 0.079 cgs for **p(SQB-R^3*)** in DMF. All polymers displayed the typical fluorescence from the lowest lying excitonic state of the random coil conformation in $CHCl_3$ and toluene, where a progressive red-shift and narrowing of the emission band was observed, along with a concomitant decrease in Stokes-shift and increase in quantum yield on going from **p(SQB-R^0)** to the **p(SQB-R^3*)**. Interestingly, a very narrow emission band at 11 800 cm^{-1} was observed for the helix foldamer of **p(SQB-R^1*)** in toluene, from which an average coherence length N_{eff} of ca. 10 could be estimated. In agreement with CD spectroscopy, CPL spectroscopy revealed a large g_{lum}-value of 0.053 cgs.

Closely examining the spectral features indicated a slightly higher degree of structural order, that is, a more perfect helix or elongated coil in certain solvents when increasing the steric demand of the side chains. This became apparent in the UV-Vis-NIR and fluorescence spectra,

where the spectral widths decreased, while the spectral shifts of the respective aggregation type increased, which is generally the result of a greater exciton delocalization length in higher-ordered systems. Although these trends were clearly observable, these effects were only minor.

Analogous to the series of oligomers **(SQB-R^1)$_{1\text{-}9}$**, the quantification of the thermodynamics of the helix-coil equilibrium was achieved by temperature dependent absorption spectroscopy in PhCN. Along this series, a decrease of entropy and enthalpy was observed, which was especially significant when moving the branching point on the alkyl side chain closer to the chromophore and when increasing the size of the substituent in this position. As the obtained values for **p(SQB-R^{1*})** were comparable to that of the respective nonamer **(SQB-R^1)$_9$**, it was concluded that the polymer independently folds into helical segments, rather than completely folding into a single large helix, which also means that both helical and open-chain sections are present within one polymer strand. Therefore, these helical sections likely comprise ca. 10 monomer units, which is also in agreement with the coherence length determined by fluorescence spectroscopy. As the aforementioned increased structural perfection is only minor, the decrease in entropy and enthalpy likely stems from the length of these helical segments increasing with a larger degree of perturbation on the side chain from **p(SQB-R^0)** to **p(SQB-R^{3*})**.

As the magnitude of the CD effect scales with the degree of homohelicity, the development of a thermodynamic model enabled the assessment of the twist sense bias using temperature dependent CD spectroscopy. When comparing the temperature dependent absorption and CD data, it was found that all of the investigated polymers were nearly completely homohelical in PhCN, while **p(SQB-R^{1*})** and possibly **p(SQB-R^{3*})** showed a deviation in these two data trends in DMF, leading to the conclusion of an incomplete degree of homohelicity. Unfortunately, fitting the data using the developed model did not yield any results.

5 PH-SQB* OLIGO AND -POLYMERS

5.1 Introduction

In an attempt to further tailor the optical properties of such indolenine squaraine polymers, various (co)polymers comprising different types of parent monomer structures were designed and studied by Lambert et al, such as the SQA-SQB copolymer **p(SQA-SQB)** (Figure 57a).[73, 87, 93] For the better interpretation of the hereby obtained results, shorter oligomers, such as dimers and trimers, were synthesized comprising these same building blocks. This also enabled the systematic study in terms of exciton coupling theory, e.g., by inserting various spacers in between two squaraine units to vary the degree of coupling between them (Figure 57b),[73, 88, 295] or to fixate the interchromophoric dihedral angle (Figure 57c).[260]

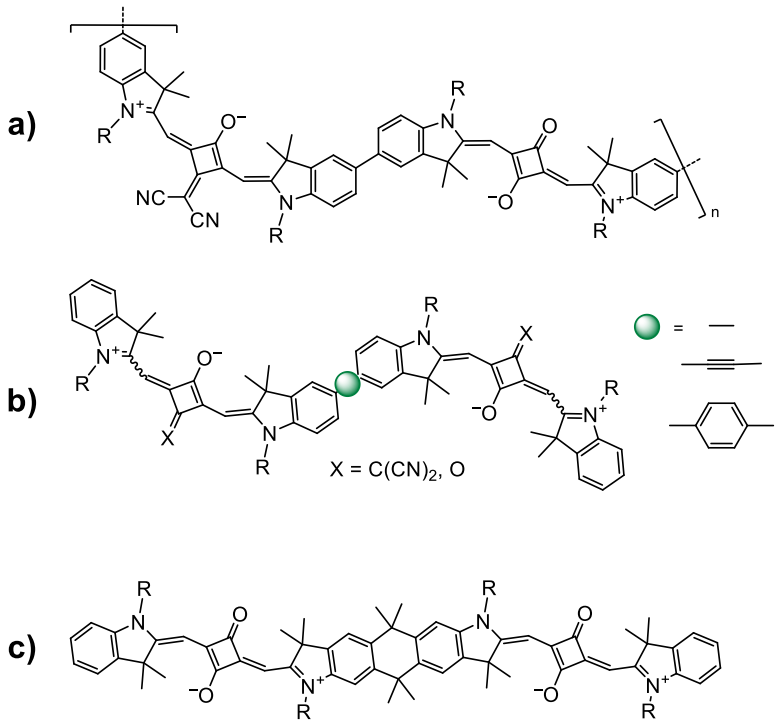

Figure 57. Examples of (co)oligo- and polymeric squaraines. a) SQA-SQB copolymer, b) homo/heterodimers with varying spacer units, c) Anthracene-bridged SQA dimer.

In order to describe these systems, the model derived in section 1.2.2 must be generalized. For any given n-mer, the matrix in the secular equation (eq. (31)) is of the dimension n×n. Assuming the interactions of non-adjacent chromophores are small compared to those of two adjacent chromophores, they can be neglected in terms of the nearest-neighbor approximation.[93] Also neglecting Van-der-Waals interactions, this results in the following matrix eigenvalue problem:[238, 296]

$$\begin{pmatrix} H_{11} & J & 0 \\ J & \ddots & J \\ 0 & J & H_{\mathrm{nn}} \end{pmatrix} \begin{pmatrix} c_1 \\ \vdots \\ c_{\mathrm{n}} \end{pmatrix} = E \begin{pmatrix} c_1 \\ \vdots \\ c_{\mathrm{n}} \end{pmatrix} \tag{62}$$

Following the same principles as in the case of the homodimer, the Hamiltonian and the wavefunctions of the singly excited states are:[1]

$$\psi_{\mathrm{e}} = \prod_{\mathrm{i}=1}^{\mathrm{n}} \varphi_{\mathrm{i}0} \sum_{\mathrm{j}=1}^{\mathrm{n}} \frac{c_{\mathrm{j}} \varphi_{\mathrm{j}a}}{\varphi_{\mathrm{j}0}} \tag{63}$$

$$H = \sum_{\mathrm{i}=1}^{\mathrm{n}} H_{\mathrm{i}} + \sum_{\mathrm{i}=1}^{\mathrm{n}} \sum_{\mathrm{j}>\mathrm{i}}^{\mathrm{n}} V_{\mathrm{ij}} \tag{64}$$

To obtain the eigenvalues *E*, the secular determinant det(**H** - *E*) is set to zero, resulting in a n-degree polynomial equation, which is then solved for *E*. By inserting the hereby obtained solutions into eq. (62), the coefficients of the specific wavefunctions (eigenvector) for the excited states are obtained. These are mainly dependent on the geometry of the n-mer, as well as the energetic spacing between the individual chromophore units. This then enables the calculation of the electric and magnetic transition moments, and in turn the rotational strength.

The simplest model, which illustrates the concept of exciton coupling in AB co-aggregates and enables the discussion of the obtained results, is of course the AB dimer. For this system, the obtained solutions are:[93, 153, 238, 296-298]

$$E_{\pm} = \bar{E} \pm \sqrt{\Delta E^2 + J^2} \tag{65}$$

$$\boldsymbol{\mu}_{+} = c_1^{+} \boldsymbol{\mu}_1 + c_2^{+} \boldsymbol{\mu}_2 = \boldsymbol{\mu}_1 \cos\theta + \boldsymbol{\mu}_2 \sin\theta \tag{66}$$

$$\boldsymbol{\mu}_{-} = c_1^{-} \boldsymbol{\mu}_1 + c_2^{-} \boldsymbol{\mu}_2 = \boldsymbol{\mu}_1 \sin\theta + \boldsymbol{\mu}_2 \cos\theta \tag{67}$$

[1] For polymers, the excited states are described as a linear combination of multiple chromophore excitations. Using the Bloch theorem and imposing periodic boundary conditions, the energies and wavefunctions can then be obtained for such systems.

$$\begin{aligned} R_{\pm} &= -\mathrm{Im}\left(\boldsymbol{c_1^{\pm 2}}\boldsymbol{m}_1' \cdot \boldsymbol{\mu}_1 + \boldsymbol{c_2^{\pm 2}}\boldsymbol{m}_2' \cdot \boldsymbol{\mu}_2\right) \mp \mathrm{Im}\left(\boldsymbol{c_1^{\pm}}\boldsymbol{c_2^{\pm}}\boldsymbol{m}_1' \cdot \boldsymbol{\mu}_2 + \boldsymbol{c_1^{\pm}}\boldsymbol{c_2^{\pm}}\boldsymbol{m}_2' \cdot \boldsymbol{\mu}_1\right) \\ &\quad - \boldsymbol{c_1^{\pm}}\boldsymbol{c_2^{\pm}}\pi\sqrt{E_1E_2}\boldsymbol{R}_{12} \cdot (\boldsymbol{\mu}_2 \times \boldsymbol{\mu}_1) \\ &= R_{\mathrm{mon}} \mp R_{\mathrm{e-m}} \pm \frac{\pi J\sqrt{E_1E_2}}{\sqrt{4\Delta E^2 + 4J^2}}\boldsymbol{R}_{12} \cdot (\boldsymbol{\mu}_2 \times \boldsymbol{\mu}_1) \end{aligned} \tag{68}$$

where $\Delta E = \frac{(E_2 - E_1)}{2}$ is half of the energetic separation of the monomer excited states and $\bar{E} = \frac{(E_2 + E_1)}{2}$ the average monomer excited state energy (often set to zero) ($E_2 > E_1$). θ is defined so that

$$\tan 2\theta = \frac{J}{2\Delta E} \tag{69}$$

This means, that for the perfect parallel (H-dimer) or head-to-tail arrangement (J-dimer), both the transitions to the upper and lower excitonic state are allowed. Also, as the coefficients *c* are not equal, the excitonic states are mainly localized on the A or B unit, respectively, as compared to the homodimer where $c_1 = \pm c_2$, meaning that both excitonic states are fully delocalized over both chromophores. As can be seen in eq. (68), the rotational strength for both excitonic transitions is equal in magnitude and opposite in sign, leading to the sum rule being fulfilled as well.

Since the use of chiral side chains for the induction of homohelicity in SQB-homopolymers was successful as described in chapter 4, the use of main-chain chirality to achieve analogous results is also to be tested. Therefore, **Ph-SQB*** (henceforward only referred to as **SQB*** when deemed appropriate) was selected as the core chiral monomer building block, which was used to synthesize an SQB-SQB* copolymer and an SQB* homopolymer. As a similar solvent dependent conformational change was also observed in the SQA-SQB copolymer, an analogous SQA-SQB* copolymer was prepared as well. To further facilitate the interpretation of the results in terms of exciton coupling and chirality, various di- and trimers were also prepared as model systems. The target compounds are shown in Figure 58.

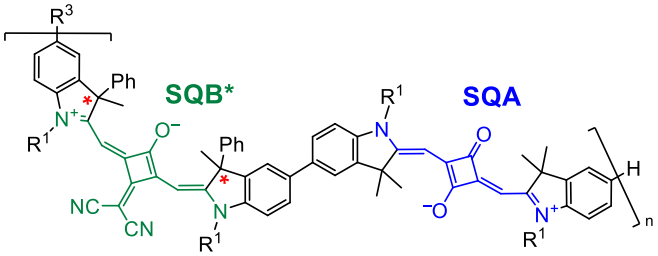

S-**SQA-SQB***: * = *(S)*, R^1 = *n*Hex, R^3 = H, n = 1
R-**SQA-SQB***: * = *(R)*, R^1 = $C_{16}H_{33}$, R^3 = H, n = 1
S-**SQA-SQB*-SQA**: * = *(S)*, R^1 = $C_{16}H_{33}$, R^3 = SQA, n = 1
R-**SQA-SQB*-SQA**: * = *(R)*, R^1 = $C_{16}H_{33}$, R^3 = SQA, n = 1
p(SQA-SQB*): * = *(S)*, R^1 = $C_{16}H_{33}$, R^3 = H, n ~ 10

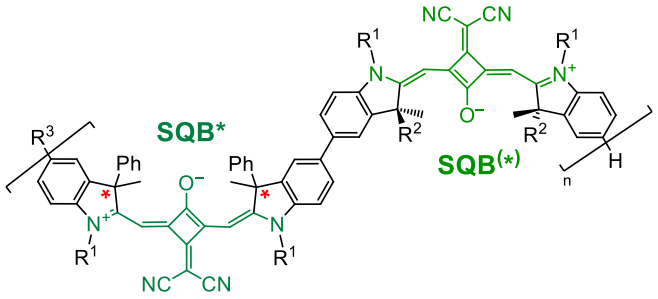

S-**SQB-SQB***: * = *(S)*, R^1 = *n*Hex, R^2 = Me, R^3 = H, n = 1
R-**SQB-SQB***: * = *(R)*, R^1 = $C_{16}H_{33}$, R^2 = Me, R^3 = H, n = 1
S-**SQB-SQB*-SQB**: * = *(S)*, R^1 = $C_{16}H_{33}$, R^2 = Me, R^3 = SQB, n = 1
R-**SQB-SQB*-SQB**: * = *(R)*, R^1 = $C_{16}H_{33}$, R^2 = Me, R^3 = SQB, n = 1
p(SQB-SQB*): * = *(S)*, R^1 = $C_{16}H_{33}$, R^2 = Me, R^3 = H, n ~ 10
dSQB*: * = *(S)*, R^1 = $C_{16}H_{33}$, R^2 = Ph, R^3 = H, n = 1
tSQB*: * = *(S)*, R^1 = $C_{16}H_{33}$, R^2 = Ph, R^3 = SQB, n = 1
pSQB*: * = *(S)*, R^1 = $C_{16}H_{33}$, R^2 = Ph, R^3 = H, n ~ 13

Figure 58. Structures of the target indolenine squaraine oligo- and polymers.

5.2 Synthesis

As briefly indicated in section 3.1.1.3, the synthesis of asymmetric, monobrominated derivatives of **Ph-SQB***, as well as achiral tetramethyl-substituted analogues, are required for the construction of the target di- and trimers. These monobrominated derivatives are then linked together using a Suzuki cross-coupling reaction. Their syntheses follow the well-described semisquaraine route as reported in the literature.[91, 96, 260, 299-300] For the two mixed dimers *S*-**SQA-SQB*** and *S*-**SQB-SQB***, shorter *n*-hexyl side chains were chosen in order to potentially grow single crystals for X-ray crystallography, but this was to no avail. The use of different side chains may also possibly affect the conformation of the dimer in solution, which can hereby be tested.

The first step was the synthesis of the semisquaraine ethyl esters **37** and **40**. Here, the unbrominated indolium salts were deprotonated with NEt_3 and treated with squaric acid diethyl ester in a condensation reaction to form the desired semisquaraine esters in moderate yields ranging from 42% to 52%. For the synthesis of the SQB-type derivatives, these were then treated with malonic acid dinitrile and NEt_3 to form the corresponding salts **39** and **41** in a Knoevenagel-type reaction (Scheme 18, upper and middle pathway), while the further synthesis of the SQA-type derivatives required the saponification of the ethyl ester to form the semisquaraine acids **38** (Scheme 18, lower pathway).

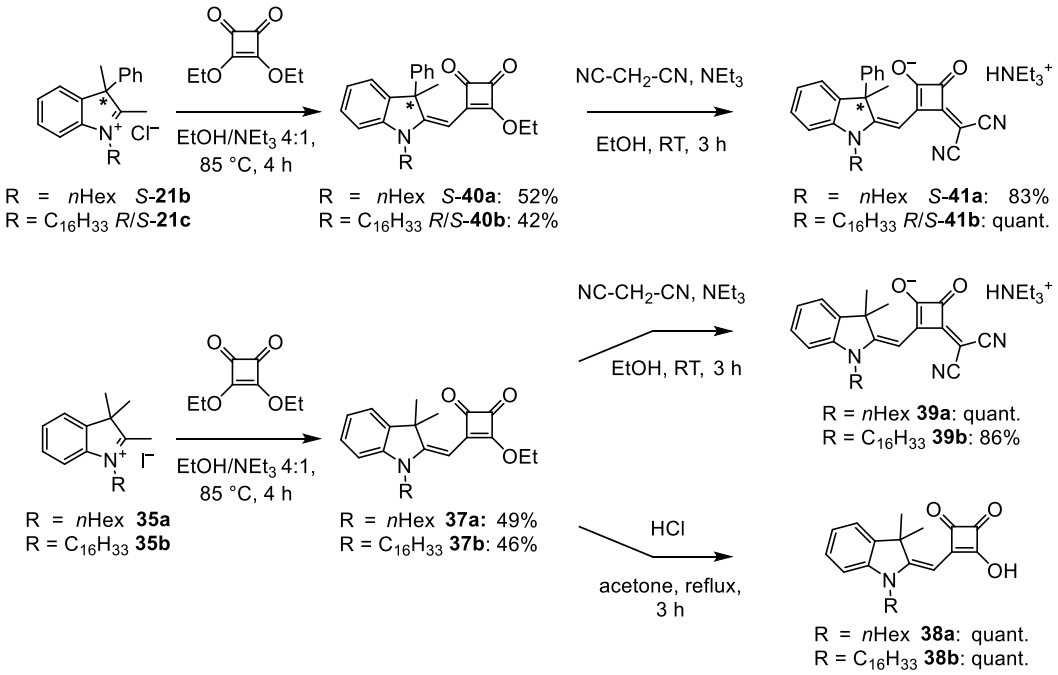

Scheme 18. Synthesis of the semisquaraine salts **39** and **41**, as well as the semisquaraine acids **38**.

These compounds were then treated with the respective brominated indolium salt (**22** and **36**) to form the desired asymmetric, monobrominated squaraines in a further condensation reaction, as shown in Scheme 19.

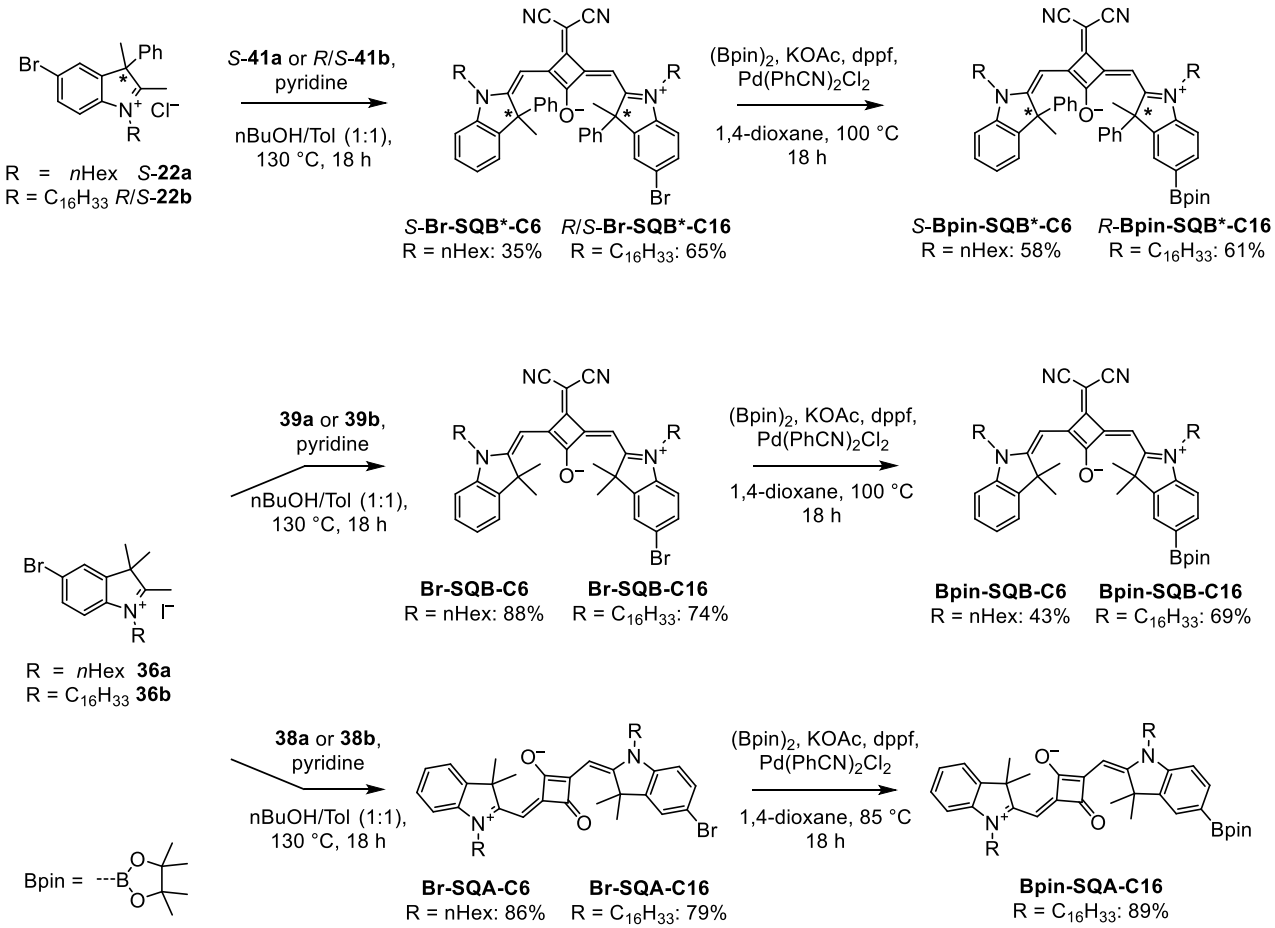

Scheme 19. Synthesis of the asymmetric, monobrominated squaraine monomers.

The reaction proceeded under the azeotropic removal of water in the case of the achiral dimethyl-substituted derivatives, or under an inert gas atmosphere for the diphenyl-substituted derivatives (similar to the symmetrical analogues in chapter 3), in order to avoid debromination as previously reported in the synthesis of **TPh-SQB***.[90] Interestingly, the dibrominated and non-brominated derivatives were isolated in various reactions as well, regardless of using a Dean-Stark trap or performing the reaction in a closed system. This 'scrambling' is therefore postulated to be the result of a deprotonated indolenine nucleophilically attacking the central squaric acid ring, as this moiety is electron deficient and has previously been shown to act as an electrophile.[101, 301] Following the nucleophilic attack, the previously attached indolenine is then eliminated as its methylene base form, thus resulting in the formation of the aforementioned symmetrical derivatives. Separation via

column chromatography only proved to be sufficiently successful for the derivatives bearing *n*-hexadecyl side chains, as the R_f-values of the *n*-hexyl substituted analogues were too similar. Unfortunately, precipitation/recrystallization, GPC or HPLC on silica also did not yield satisfactory results in this case as well. The monobrominated squaraines were then converted to their corresponding boronic acid esters using the Pd-catalyzed Miyaura-borylation reaction as also shown in Scheme 19. As the R_f-values of the monoborylated derivatives were sufficiently different from those of their symmetrical analogues, this enabled their chromatographic purification.

Finally, the borylated and brominated monomers were coupled using a Suzuki cross-coupling reaction as shown in Scheme 20 (details summarized in Table 11). Here, the second-generation XPhos (XPhos-Pd-G2) catalyst was chosen in combination with $CsCO_3$ as the base, as these conditions were proven to be well suited for these systems.[91] Using an excess of the borylated component ensured the complete conversion of the monobrominated derivative, along with its potential dibrominated impurity, thus enabling the separation of hereby formed oligomeric side products via preparative GPC and affording the target compound in satisfying purity.

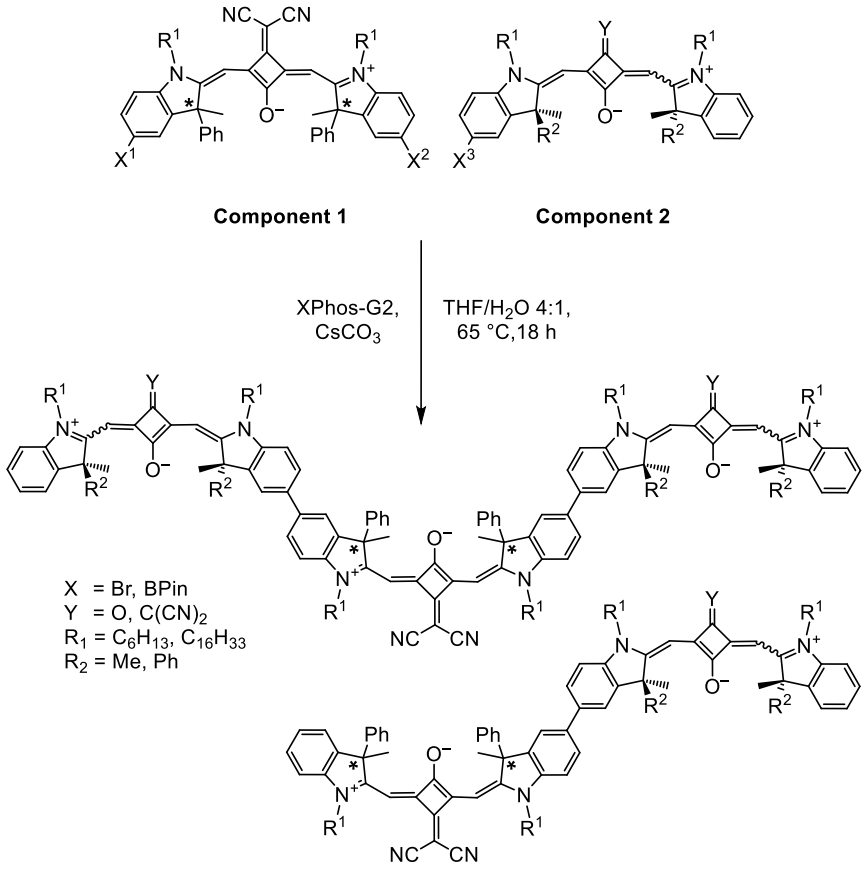

Scheme 20. General scheme of the synthesis of the target squaraine di- and trimers via Suzuki cross coupling.

Table 11. Monomers used for the synthesis of the target di- and trimers, along with the obtained yields.

Component 1	Component 2	Product	Substituents	Yield
***S*-Bpin-SQB*-C6**	**Br-SQA-C6**	***S*-SQA-SQB***	X^1 = H, X^2 = Bpin, X^3 = Br, Y = O, R^1 = *n*Hex, R^2 = Me	27%
***R*-Br-SQB*-C16**	**Bpin-SQA-C16**	***R*-SQA-SQB***	X^1 = H, X^2 = Br, X^3 = Bpin, Y = O, R^1 = $C_{16}H_{33}$, R^2 = Me	43%
***S*-Br-SQB*-C6**	**Bpin-SQB-C6**	***S*-SQB-SQB***	X^1 = H, X^2 = Br, X^3 = Bpin, Y = $C(CN)_2$, R^1 = *n*Hex, R^2 = Me	57%
***S*-Br-SQB*-C16**	**Bpin-SQB-C16**	***R*-SQB-SQB***	X^1 = H, X^2 = Br, X^3 = Bpin, Y = $C(CN)_2$, R^1 = *n*Hex, R^2 = Me	58%
***S*-Br-SQB*-C16**	***S*-Bpin-SQB*-C16**	**dSQB***	X^1 = H, X^2 = Br, X^3 = Bpin, Y = $C(CN)_2$, R^1 = $C_{16}H_{33}$, R^2 = Ph	81%
S*-Br_2-Ph-SQB	**Bpin-SQA-C16**	***S*-SQA-SQB*-SQA**	X^1 = Br, X^2 = Br, X^3 = Bpin, Y = O, R^1 = $C_{16}H_{33}$, R^2 = Me	74%
R*-Br_2-Ph-SQB	**Bpin-SQA-C16**	***R*-SQA-SQB*-SQA**	X^1 = Br, X^2 = Br, X^3 = Bpin, Y = O, R^1 = $C_{16}H_{33}$, R^2 = Me	77%
S*-Br_2-Ph-SQB	**Bpin-SQB-C16**	***S*-SQB-SQB*-SQB**	X^1 = Br, X^2 = Br, X^3 = Bpin, Y = $C(CN)_2$, R^1 = $C_{16}H_{33}$, R^2 = Me	55%
R*-Br_2-Ph-SQB	**Bpin-SQB-C16**	***R*-SQB-SQB*-SQB**	X^1 = Br, X^2 = Br, X^3 = Bpin, Y = $C(CN)_2$, R^1 = $C_{16}H_{33}$, R^2 = Me	42%
S*-Br_2-Ph-SQB	***S*-Bpin-SQB*-C16**	**tSQB***	X^1 = Br, X^2 = Br, X^3 = Bpin, Y = $C(CN)_2$, R^1 = $C_{16}H_{33}$, R^2 = Ph	77%

The copolymers **p(SQA-SQB*)** and **p(SQB-SQB*)** were also synthesized via Suzuki cross-coupling of the respective dibrominated (**Br_2-Ph-SQB***) and diborylated monomers (**$Bpin_2$-SQA** and **$Bpin_2$-SQB**), while the **p(SQB*)** homopolymer was synthesized via Yamamoto homocoupling of **Br_2-Ph-SQB*** as analogously described in the case of the SQB-polymers bearing chiral side chains in section 4.1. Both of these reactions are depicted in Scheme 21. The required diborylated, achiral derivatives **$Bpin_2$-SQA** and **$Bpin_2$-SQB** were synthesized via their respective dibrominated counterparts **Br_2-SQA** and **Br_2-SQB** using a Miyaura-borylation reaction as described above for the asymmetric dericatives (not shown, see section 8.2.4 or ref.[96] for details regarding their synthesis).

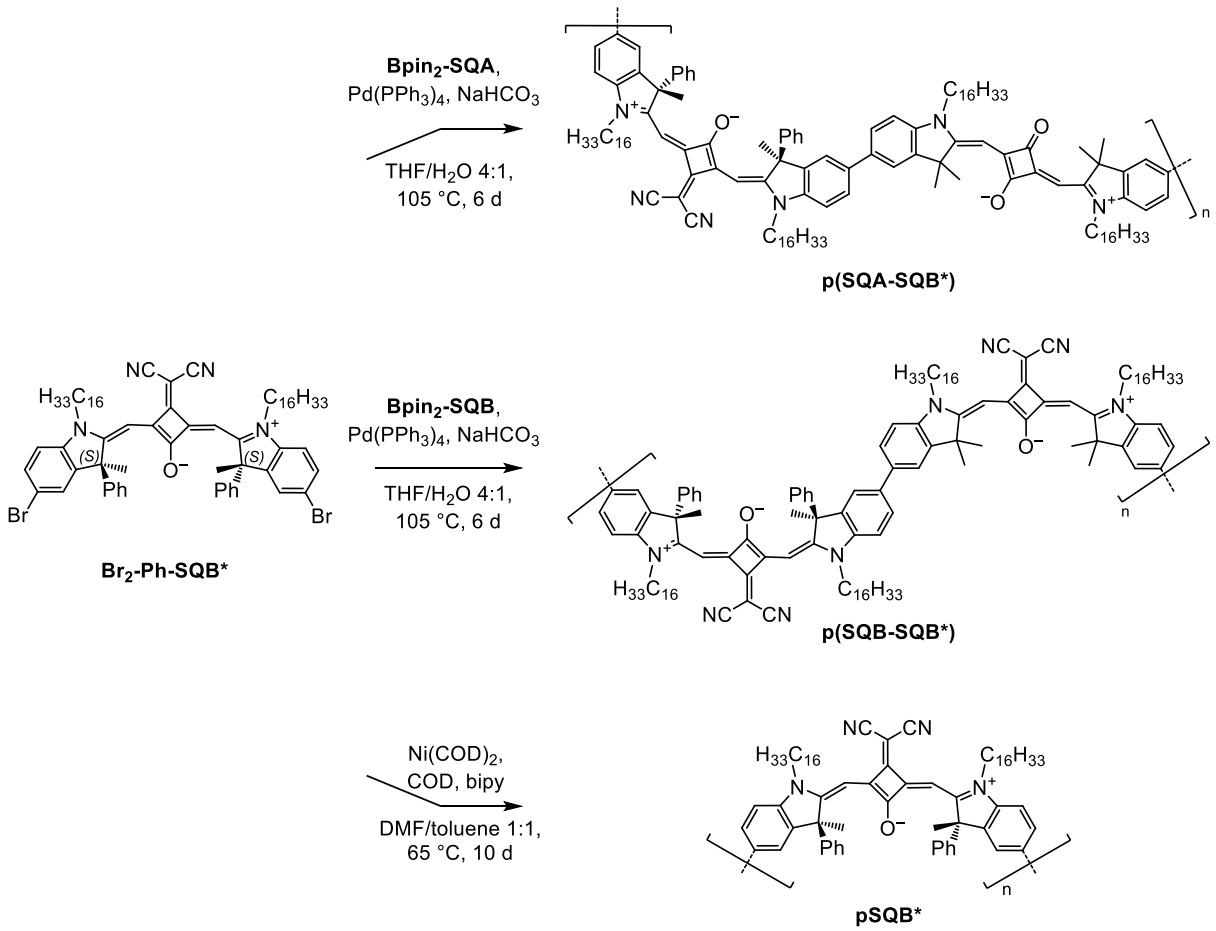

Scheme 21. Synthesis of **p(SQA-SQB*)**, **p(SQB-SQB*)** and **pSQB***.

In all cases, the crude product was washed successively in a Soxhlet-extractor using various solvents, before being fractionated by preparative GPC. The individual fractions were then characterized regarding their molecular weight distribution, the results alongside the respective chromatograms of the analytical and preparative runs are shown in section 11.1.2.2 in the appendix. Regarding the longest fractions (F1), the number average molecular weight was comparable in all cases, ranging from 18 000 (**p(SQA-SQB*)**) to 23 000 (**p(SQB-SQB*)**) for the copolymers and 26 000 for the homoplymer **p(SQB*)**, thus resulting in the main chains roughly being comprised of the same number of squaraine units. While **p(SQB*)** and **p(SQB-SQB*)** possessed a similar *PDI* value of roughly 1.5, the value obtained for **p(SQA-SQB*)** (2.0) was significantly larger. Due to the shorter fractions being relatively heterogenous (as described in chapter 4), only the longest fractions of the respective polymers were investigated in this work.

5.3 SQA-SQB-type heterooligomers and copolymer

5.3.1 Absorption and fluorescence spectroscopy

The UV-Vis-NIR and fluorescence spectra of the investigated compounds alongside those of their achiral analogues are shown in Figure 59, and the corresponding data are summarized in Table 12. For absorption spectra in various solvents, see Figure 106 in the appendix.

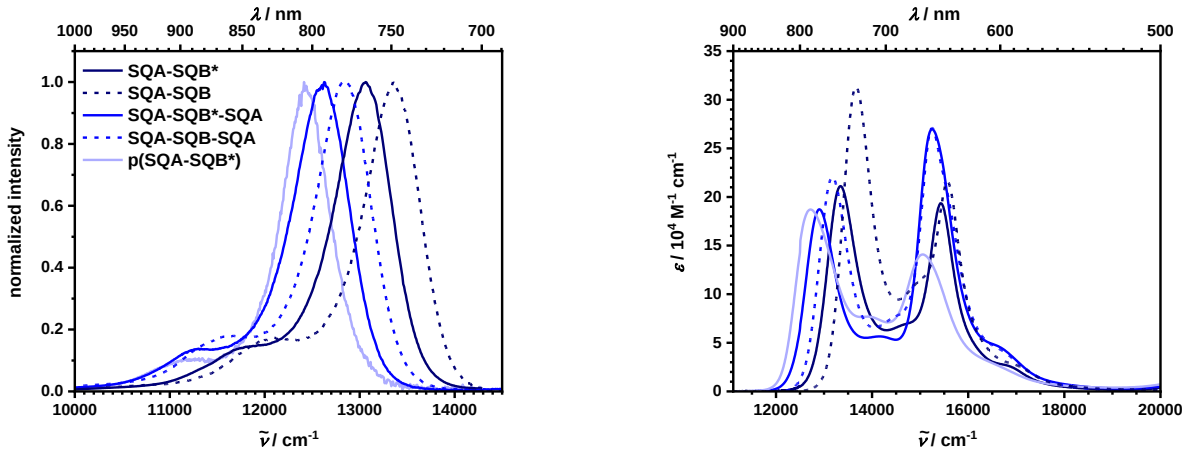

Figure 59. Normalized fluorescence (left) and absorption (right) spectra of **SQA-SQB***, **SQA-SQB*-SQA** and **p(SQA-SQB*)** (solid lines), along with the achiral analogues **SQA-SQB**[73] and **SQA-SQB-SQA**[73] (dashed lines) in toluene.

In general, the absorption spectra of the chiral di- and trimers are similar to those of their achiral analogues, while the achiral **p(SQA-SQB)**, contrarily to **p(SQA-SQB*)**, exhibits a pronounced solvent-dependent absorption behavior (Figure 60). In all cases, the spectra are the result of excitonic coupling of two different types of chromophores (SQA and SQB), where the excited states are largely localized on the respective moieties. This results in two main absorption maxima at 12 700-13 700 cm^{-1} and 15 000-15 800 cm^{-1}, corresponding to the upper and lower transition of the exciton manifold, respectively. The splitting of these two states can generally be described by the exciton bandwidth δE:[1]

$$\delta E = 2\sqrt{\Delta E^2 + 2^n J^2} \tag{70}$$

where $n = 0$ yields the result for the dimer, $n = 1$ for the ABA trimer and $n = 2$ for the polymer.[93, 296] This means, that for an increasing number of coupled chromophores the energetic separation increases as well when assuming a constant excitonic coupling J, which is also observed on going from the dimer (2070 cm^{-1}) to the trimer (2300 cm^{-1}) to the polymer

[1] The factor 2^n is not the result of the derivation, but rather a convenient expression to generalize the results obtained for the dimer, the trimer and the polymer.

(2390 cm^{-1}) in chloroform, although it has been shown that the excitonic coupling for this type of system decreases slightly when adding additional chromophore units.[73, 93] Examining the oligomer spectra more closely, it can be seen that while the high-energy absorption maximum (location and absorption coefficient) is nearly identical when comparing the spectra of the respective chiral and achiral derivatives, the lower-energy maximum is bathochromically shifted by 200-400 cm^{-1} and less intense in the chiral derivatives. This was previously also observed in the monomer itself (see section 3.1.3), and in all cases the total squared transition moment is, within experimental error, roughly the sum of the squared transition moments of the monomeric compounds (monomer values see Table 3; values per monomer unit within the same range, see Table 12), thus obeying the Kuhn sum rule.[145]

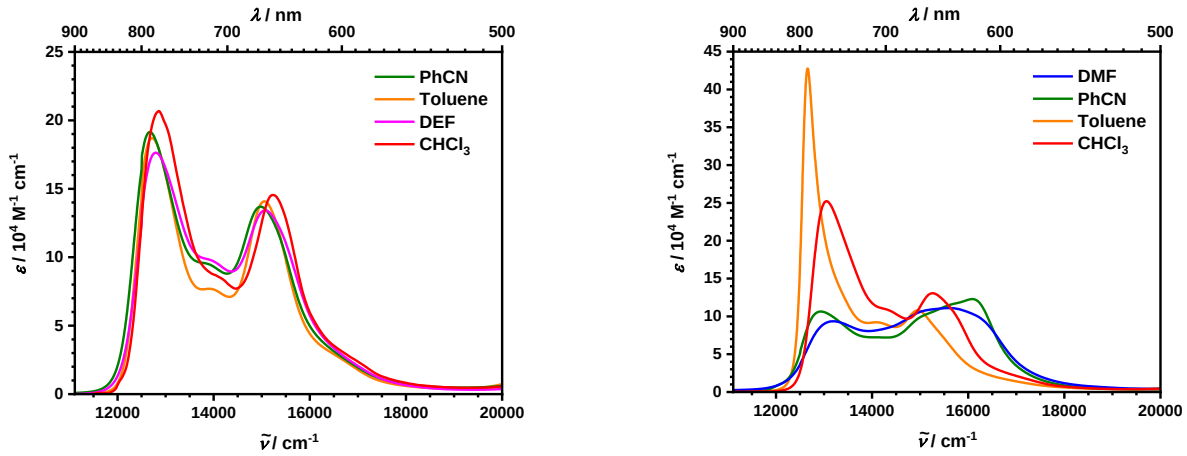

Figure 60. Absorption spectra of **p(SQA-SQB*)** (left) and **p(SQA-SQB)**[87, 276] (right) in various solvents. Absorption coefficients are reported per monomer unit.

The solvent-dependent absorption of **p(SQA-SQB)** can be ascribed to changes in conformation in solution, as previously discussed in chapter 4 for the SQB-homopolymers. Here, the higher energy band is more pronounced in solvents such as DMF or PhCN, where a helix-like structure is postulated, whereas in $CHCl_3$ and toluene the lower-energy band is more pronounced. In toluene, this leads to a narrowing and intensification of this band, which is caused by a coherent excitation of multiple chromophores analogous to the exchange narrowing reported for J-aggregates.[293, 302] This in turn can be explained by the formation of a higher-ordered, more elongated conformation in this particular solvent.[87, 93] In the chiral polymer **p(SQA-SQB*)**, on the other hand, the absorption spectra are relatively solvent-independent. This means that here the conformation is similar in all of the tested solvents. In this case it is speculated that the phenyl groups prevent the formation of higher-ordered conformations,

possibly by preventing the solvent molecules from interacting with the squaraine chromophores as described for the pure SQB-helix.[91]

Regarding the fluorescence spectra, all compounds exclusively display fluorescence from the lowest-lying excitonic state according to Kasha's rule.[292] In all cases, the fluorescence spectra are narrow with a vibronic progression on the low-energy side and are reminiscent of those of the monomer species. Just as in the case of the absorption spectra, the fluorescence spectra of the chiral diphenyl-substituted derivatives are bathochromically shifted – specifically by ca. 300 cm^{-1} compared to their respective achiral analogues. This observation goes alongside a reduced quantum yield in toluene, whereas in chloroform all values are comparably minute. This is most likely due to the impact of the phenyl substituents, which has also produced similar effects in the monomers as described in section 3.1.3. Further comparison of the other quantities and characteristics (FWHM, Stokes-shifts, fluorescence lifetimes) does not reveal any systematic deviations. CPL measurements were attempted, but no signal was detected for all of the chiral compounds.

Using the data obtained from fluorescence spectroscopy eq. (61), as these were found to correlate with those obtained from the absorption data, the coherence length in **p(SQA-SQB*)** was determined to be 1.45 in toluene, meaning the exciton is delocalized over roughly 3 squaraine units. This value is considerably smaller compared to that obtained for the purely tetramethyl-substituted **p(SQA-SQB)**, which was found to be ca. 3.9. As previously stated, this points towards the formation of a superstructure with a high degree of structural order in the latter, where this trend correlated with an increasing main chain length.[87] Even though the degree of polymerization was smaller and the polydispersity relatively high when comparing the obtained results to the previously reported cases of **p(SQA-SQB)**,[87, 93] it is believed that the observed differences most likely mainly stem from the effect of the substitution, rather than being the result of a smaller main chain length or higher polydispersity.

Table 12. Summary of the optical data (wavenumber $\tilde{\nu}_{abs}$ and corresponding absorption coefficients ε_{max} of absorption maxima 1 and 2, squared transition moments μ_{eg}^2, emission maxima $\tilde{\nu}_{em}$, full width at half maximum of the emission spectra *FWHM*, Stokes-shifts $\Delta\tilde{\nu}$, quantum yields Φ_{fl}, fluorescence lifetimes τ_{fl}, mean fluorescence lifetimes $\bar{\tau}_{fl}$) of **SQA-SQB**[73], **SQA-SQB***, **SQA-SQB-SQA**[73], **SQA-SQB*-SQA**, and **p(SQA-SQB*)** in chloroform and toluene.

		$\tilde{\nu}_{abs}$ (λ_{abs}) 1 / cm^{-1} (/ nm)	ε_{max} 1 [a] / M^{-1} cm^{-1}	$\tilde{\nu}_{abs}$ (λ_{abs}) 2 / cm^{-1} (/ nm)	ε_{max} 2 [a] / M^{-1} cm^{-1}	μ_{eg}^2 [a b] / D^2	$\tilde{\nu}_{em}$ (λ_{em}) / cm^{-1} (/ nm)	FWHM / cm^{-1}	$\Delta\tilde{\nu}$ / cm^{-1}	Φ_{fl}	τ_{fl} [c] / ns	$\bar{\tau}_{fl}$ [d] / ns
SQA-SQB	$CHCl_3$	13 900 (719)	3.09×10^5	15 800 (634)	2.03×10^5	261	13 600 (735)	- [e]	300	0.05	1.82	1.82
	toluene	13 700 (730)	3.13×10^5	15 600 (643)	2.15×10^5	248	13 400 (746)	710	290	0.69	1.80 (0.51) 2.41 (0.49)	2.14
SQA-SQB*	$CHCl_3$	13 500 (739)	2.32×10^5	15 600 (641)	2.14×10^5	242	13 300 (753)	860	250	0.06	0.24 (0.93) 1.22 (0.07)	0.51
	toluene	13 300 (750)	2.11×10^5	15 400 (649)	1.93×10^5	191	13 100 (765)	720	280	0.44	1.15 (0.10) 2.41 (0.90)	2.34
SQA-SQB-SQA	$CHCl_3$	13 400 (748)	3.44×10^5	15 400 (649)	4.06×10^5	280	13 100 (763)	830	260	0.10	0.22	0.22
	toluene	13 200 (759)	2.20×10^5	15 200 (656)	2.71×10^5	251	12 900 (775)	720	270	0.73	1.88 (0.99) 2.84 (0.01)	1.89
SQA-SQB*-SQA	$CHCl_3$	13 100 (763)	2.79×10^5	15 400 (649)	4.06×10^5	269	12 800 (782)	780	320	0.08	0.19 (0.45) 0.47 (0.55)	0.40
	toluene	12 900 (775)	1.87×10^5	15 200 (656)	2.71×10^5	241	12 600 (792)	720	280	0.39	1.76 (0.72) 2.43 (0.28)	1.99
p(SQA-SQB*)	$CHCl_3$	12 900 (778)	2.07×10^5	15 200 (656)	1.45×10^5	255	12 600 (796)	610	290	0.03	0.17 (0.76) 0.42 (0.24)	0.28
	toluene	12 700 (786)	1.87×10^5	15 000 (665)	1.41×10^5	218	12 400 (806)	600	320	0.25	0.87 (0.22) 1.79 (0.78)	1.68

[a] Values per monomer unit. [b] determined by integration of the main absorption band and calculated using eq. (74) in the appendix. [c] Determined by TCSPC, decay curves fitted with a (multi-)exponential fit, amplitudes are given in parantheses. Excitation was at 15 240 cm^{-1} (656 nm). [e] Intensity-weighed mean fluorescence lifetime calculated according to eq. (77) in the appendix. [e] no data available.

5.3.2 CD spectroscopy

The CD spectra of the chiral SQA-SQB-type di-, tri- and polymers in $CHCl_3$ and toluene are shown in Figure 61, the chiroptical data are summarized in Table 13. For CD spectra in various solvents, see Figure 107 in the appendix.

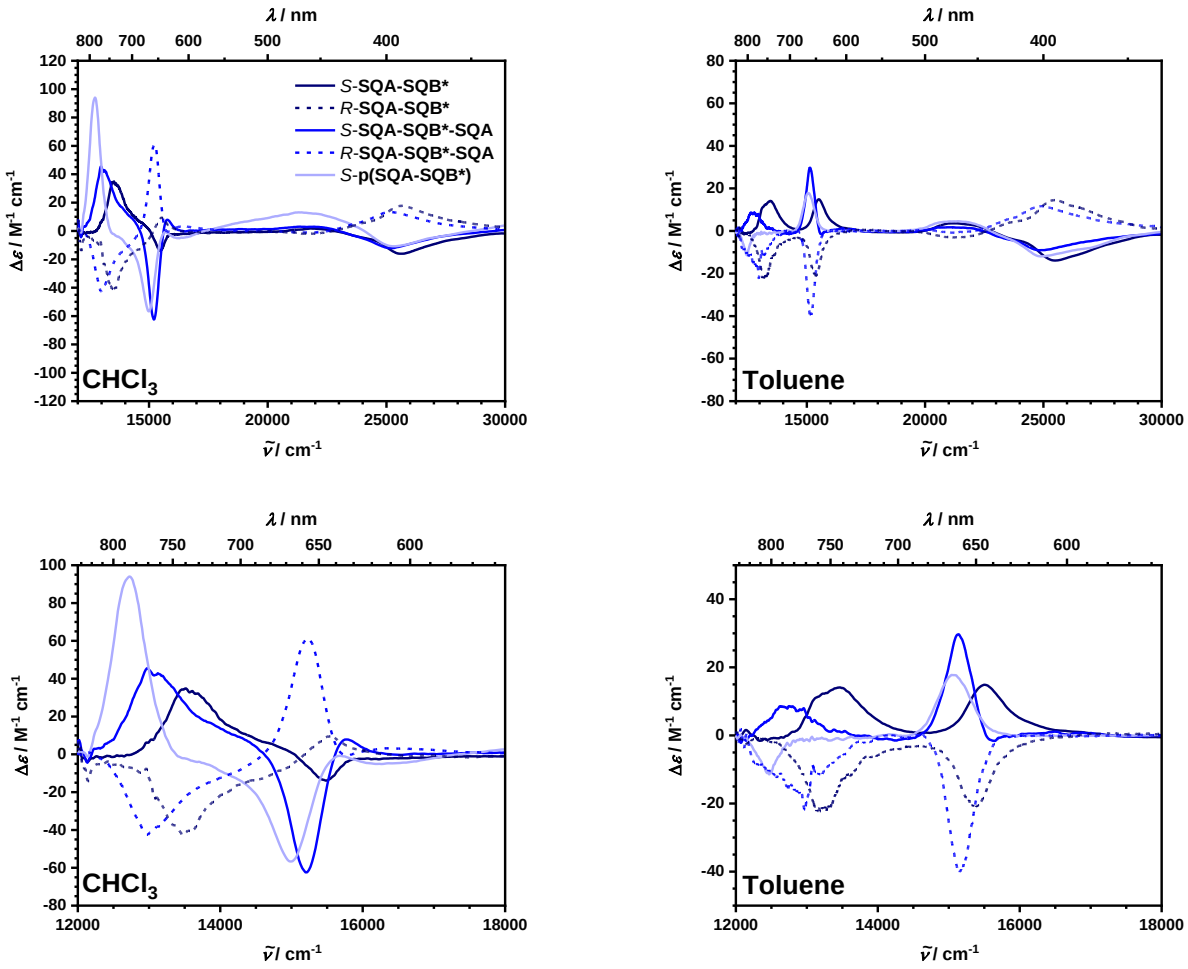

Figure 61. CD spectra of **SQA-SQB***, **SQA-SQB*-SQA** and **p(SQA-SQB*)** in chloroform (left) and toluene (right). Top: full range (12 000-30 000 cm^{-1}), bottom: magnified section (12 000-18 000 cm^{-1}). Values for Δε are reported per monomer unit. Slight differences in the spectra of *R*-**SQA-SQB*** and *S*-**SQA-SQB*** obtained in toluene may be due to the measurements being performed on different spectrometers.

As expected, all CD spectra of enantiomeric compounds behave like mirror images of one another. Due to the enantiomers of **SQA-SQB*** bearing different side chains (*n*-hexyl vs. *n*-hexadecyl), the conclusion can be made that the side chain does not affect the (chir)optical properties and therefore also the underlying geometrical arrangement of these systems, regardless of the solvent. The slightly lower values of Δε obtained for the *S*-enantiomer likely stem from ***S*-Br-SQB*-C6** being of slightly lower stereochemical purity compared to that of ***R*-Br-SQB*-C16**, (see section 11.1.1 in the appendix).

All spectra (*S*-enantiomers) share a vaguely similar general structure with a CD band corresponding to the lower excitonic transition between 13 000-13 500 cm^{-1}, and one to the upper transition between 15 100-15 500 cm^{-1}. In general, all systems exhibit a strong solvent dependency, where the signs and intensity of the CD bands vary when changing the solvent from chloroform to toluene. This is in stark contrast to the absorption spectra, which are not significantly solvent dependent. The CD signal generally becomes less intense in toluene compared to that in chloroform, as the absolute values for $\Delta\varepsilon$ and *R* are significantly decreased in the former. Additionally, the shape of the CD spectrum in toluene is unexpected, as both transitions possess a positive sign instead of the anticipated bisignate exciton coupled. The obtained g_{abs} values for these compounds range from 5.41×10^{-5} cgs for the lowest-energy transition of **SQA-SQB*-SQA** at 12 700 cm^{-1} in toluene to 4.34×10^{-4} cgs for the lower excitonic transition at 12 700 cm^{-1} of **p(SQA-SQB*)** in chloroform, and are therefore in the same order of magnitude as the C(3)-chiral monomers described in chapter 3.1. For the energetically lowest-lying transition, the CD band becomes narrower and more intense with an increasing number of coupled chromophores in $CHCl_3$, as the $\Delta\varepsilon$ values increase from 34.8 M^{-1} cm^{-1} for the dimer to 94.1 M^{-1} cm^{-1} for the polymer, possibly the result of an increased conformational chiral discrimination in longer oligomers.

As the monomer CD spectra are solvent invariant towards the solvent (see Figure 36), the reason for this solvent dependency most likely does not stem from intrinsic effects, but rather originates from different conformations of the oligo- and polymers in different solvents. Therefore, the obtained dissymmetry factors are not representative, as multiple conformations possessing different CD spectra may be present at the same time.

Table 13. Summary of the chiroptical data (CD bands $\tilde{\nu}_{CD}$, difference in absorption $\Delta\varepsilon$, rotational strengths R_{exp} and dissymetry factors g_{abs}) of ***S*-SQA-SQB*, *S*-SQA-SQB*-SQA and p(SQA-SQB*-SQA)** in toluene and chloroform.

		$\tilde{\nu}_{CD}$ (λ_{CD}) / cm^{-1} (/ nm)	$\Delta\varepsilon$ / M^{-1} cm^{-1} [a]	R_{exp} / 10^{-40} cgs [a c]	$\lvert g_{abs}(\tilde{\nu}_{max})\rvert$ / cgs [a b]
SQA-SQB*	$CHCl_3$	13 500 (740)	34.8	56.8	1.51×10^{-4}
		15 500 (646)	-13.9	-14.4	7.24×10^{-5}
	toluene	13 500 (743)	14.1	21.1	7.19×10^{-5}
		15 500 (645)	14.9	17.3	8.03×10^{-5}
SQA-SQB*-SQA	$CHCl_3$	13 000 (771)	45.5	82.3	2.66×10^{-4}
		15 200 (658)	-62.4	-41.4	3.15×10^{-4}
	toluene	12 700 (785)	8.58	10.9	5.41×10^{-5}
		15 100 (660)	29.7	18.9	1.16×10^{-4}
p(SQA-SQB*)	$CHCl_3$	12 700 (786)	94.1	96.1	4.34×10^{-4}
		15 000 (667)	-56.7	-71.5	4.38×10^{-5}
	toluene	12 500 (802)	-11.4	-9.27	7.38×10^{-5}
		15 000 (665)	17.7	15.4	1.18×10^{-4}

[a] values per monomer unit. [b] $\Delta\varepsilon(\tilde{\nu}_{max})/\varepsilon(\tilde{\nu}_{max})$. [c] determined by integration of the CD band and calculated using eq. (75) in the appendix.

5.3.3 TD-DFT calculations[1]

To further elucidate the origin of the solvent-dependency of the CD spectra, TD-DFT calculations were performed on the **SQA-SQB*** dimer on the CAM-B3LYP/def2-SVP level. Here, the dihedral angle θ was systematically varied, and geometry optimizations revealed four major conformations A-D (θ_A = 36°, θ_B = 144°, θ_C = 216° = -36°, θ_D = 324° = -144° as local minima in terms of energy), which are shown in Figure 62. The absolute values are similar to the ones previously reported in the literature for covalently linked squaraine oligomers.[91, 303] Henceforward, the conformers A and C will be referred to as '*cis*' and B and D as '*trans*' – describing the relative orientation of the squaraine chromophores to one another. Regarding the orientation with respect to the adjacent phenyl group of the SQB*-unit, conformers A and B will be referred to as '*syn*', while C and D as '*anti*'.

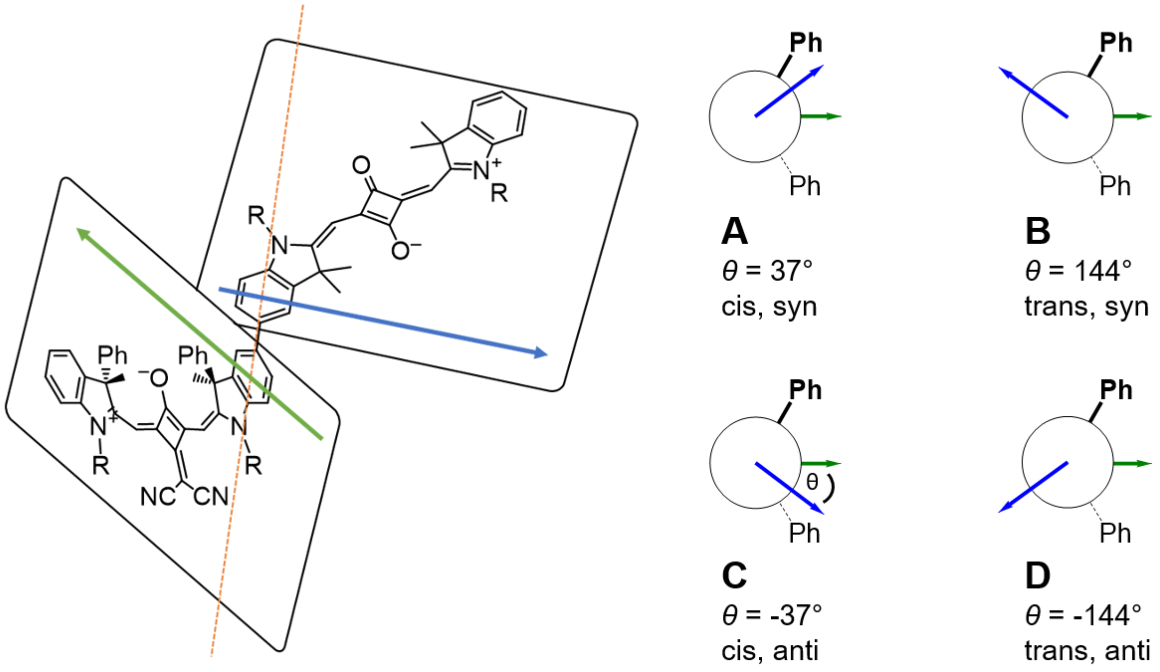

Figure 62. Geometrical arrangement of the squaraine dimers. Left: general structure (conformer B) with planes containing the squaraine chromophores and plane vectors (green and blue arrows) connected by the dihedral axis (orange dotted line), right: corresponding schematic representation of the conformers A-D with varying interchromophoric dihedral angles θ. The adjacent phenyl group used as the reference point is displayed as bold. Y = O, $C(CN)_2$; R^2 = Me, Ph.

To account for fluctuations of the dihedral angle at RT, ensemble CD and UV-Vis-NIR spectra were calculated (see Figure 63), where the dihedral angle θ was set to $\theta_X \pm 18°$ (the index *X* referring to the respective conformers A-D as described above) and varied in increments of 9°. All of the resulting angles were seen as equally probable and the corresponding spectra

[1] Theoretical calculations performed by D. Fischermeier (Mitric group, University of Würzburg)

were simply combined, as no statistical weighing was considered. All calculations were executed using a polarizable continuum model (PCM) with either chloroform or toluene as the solvent. It was found that aside from minor spectral shifts the results were nearly identical, indicating the origin of this effect not being the solvation itself. Therefore, all of the depicted results are those using chloroform as the solvent unless stated otherwise.

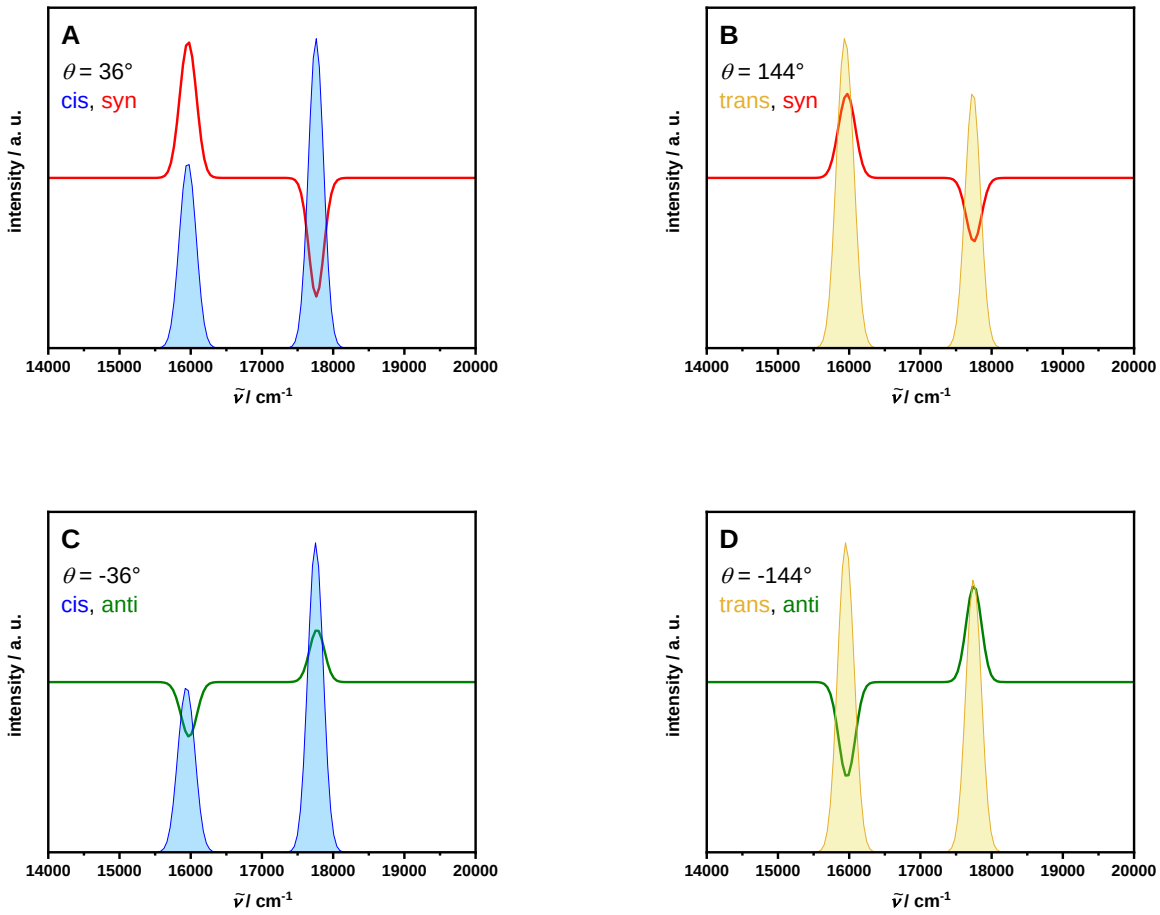

Figure 63. Calculated ensemble spectra of **SQA-SQB*** (CD: red (syn) or green (anti) line, absorption: blue (cis, H-type) or orange (trans, J-type) area) of conformers A-D convoluted with a Gaussian function with a FWHM of 100 cm^{-1}. Absorption spectra are normalized, while the CD spectra are to scale.

The absorption properties are almost exclusively governed by the mutual orientation of the two squaraine units and therefore the respective electric transition moments. This results in the *cis* conformers A and C displaying an H-type behavior, where the higher-energy band is more intense than the lower-energy band, whereas the *trans* conformers B and D exhibit a J-type behavior where the intensity ratio is vice versa. The CD spectra are the result of the corresponding rotational strengths for the two transitions being of opposite signs according to $R_{e\text{-}m}$ and R_{ex} in eq. (68) (and also eq. (42)). As the rotational strength is usually dominated by R_{ex}, which is proportional to the sine of the interchromophoric dihedral angle θ, as specified

by eq. (43), the overall sign of the CD spectrum is expected to undergo a change after the dihedral angle exceeds 180°, leading to the spectra of the anti (C, D) and syn (A, B) conformers being approximate mirror-images of one another, thus possessing a quasi-enantiomeric relationship (this is similar to the case of the dimethylaminobenzoate-substituded cholesterol derivatives **C2** and **C3** showcased in section 1.2.2 in the introduction). As the absolute value of the hereby calculated rotational strengths of the respective upper and lower excitonic transitions are not completely equal (sum rule not fulfilled), these CD spectra can be classified as non-conservative. Additionally, the magnitude of the rotational strength does not strictly adhere to the dependency on the sine of the dihedral angle θ, thus leading to the assumption that the contributions from the $R_{e\text{-}m}$ term in eq. (68) is significant and R_{ex} alone does not sufficiently describe the dependency of the rotational strength on θ. Unfortunately, the employed methods did not allow for an extraction of the individual monomer components of μ and m, thus precluding a further analysis of the individual contributions to the overall rotational strength.

Comparing the calculated spectra to the experimentally obtained spectra, it can be seen that a *trans*-conformation and thus a J-type arrangement seems to be *slightly* favored in all of the tested solvents, as the J- and H-band are nearly identical in intensity with the J-band being marginally more intense. This leads to the assumption of them roughly being equally probable and populated, which was also previously concluded for both **dSQB** and **dSQA**.[303] Furthermore, no systematic trends in the absorption and fluorescence data indicate the situation to be different in the present case. As the absorption spectra are largely independent of the relative orientation with respect to the adjacent phenyl group, this explains the invariancy of the experimentally obtained absorption spectra towards a change of solvent. Regarding the CD spectra, on the other hand, the situation is opposite. Here, the solvent dependency of the experimentally obtained spectra suggest a different relative orientation towards the adjacent phenyl groups, which in turn means that the chiral discrimination in terms of the dihedral angle θ specifically is dependent on the solvent. This chiral discrimination describes the preference for the adoption of either the *syn*- or *anti*-conformations as “dihedral enantiomers”, which are identical and therefore equally probable when no chiral center is present.

In general, the experimental CD spectra can be approximated by combining the calculated *syn* and *anti*-conformer ensemble spectra, where respective *cis* (A+C) and *trans* (B+D) ratio is fixed

at 1:1 due to the aforementioned similarity in energies. A comparison of CD spectra with a varying relative amount of the *anti*-conformers is shown in Figure 64a, whereas a comparison of selected calculated spectra with the experimental data is shown in Figure 64b.

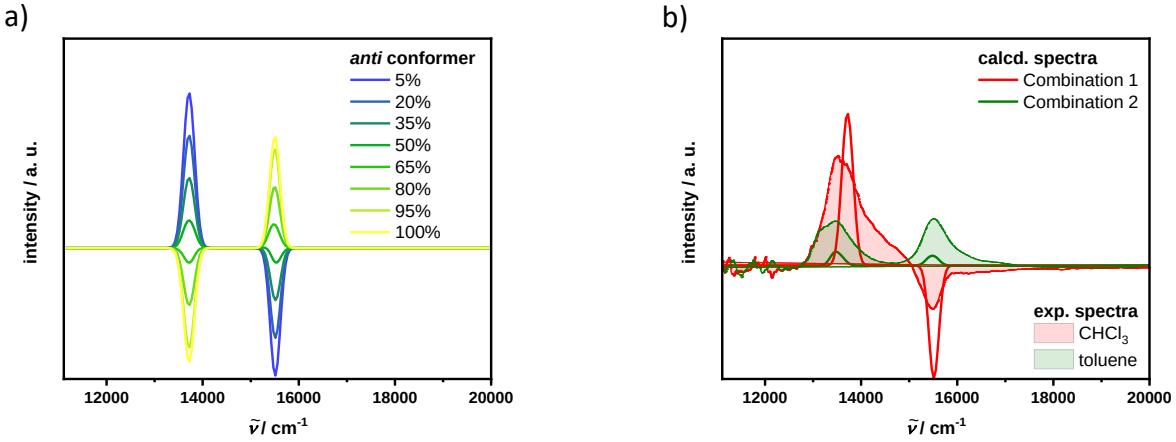

Figure 64. a) Combined calculated CD spectra (shifted by -2250 cim^{-1}) with varying relative amounts of the *anti*-conformer, where the degree of chiral discrimination is identical for the *syn* and *anti*-conformers, b) comparison of the experimental spectra in chloroform and toluene with the combined calculated CD spectra comprising 35% *anti*-conformer (identical chiral discrimination, combination 1, $CHCl_3$ PCM, shifted by -2250 cm^{-1}), as well as varying amounts of conformers A-D with a varying low degree of chiral discrimination (combination 2: A: 17%, B: 25%, C: 33%, D: 25%, toluene PCM, shifted by -2000 cm^{-1}).

As can be seen in Figure 64b, the experimental data obtained in chloroform are qualitatively in good agreement with a combination of calculated CD spectra where the conformation is predominately *syn* (65%), which can also be deduced from the sign of the CD spectrum itself. It can therefore be concluded, that chloroform promotes the adoption of a *syn*-conformation, regardless of the overall mutual orientation of the squaraine chromophores (*cis* vs. *trans*). This is unexpected, since the steric hindrance is believed to be higher in the *cis*-conformers. However, using the same approach for the experimental data in toluene does not yield the correct spectral shape, as the signs of both transitions are identical, which contradicts the description in terms of exciton chirality. This means that the chiral discrimination (*syn* vs. *anti*) appears to be different in the *cis* and *trans* conformers. Therefore, to generate the experimental spectra, the chiral discrimination in the *trans*-conformers was assumed to be non-existent, i.e., conformers B and D being equally probable, as these conformations are likely less affected by the steric strain caused by the adjacent phenyl groups. In the *cis*-conformations, the *anti*-conformer C is then slightly favored, as the ratio of A and C which ultimately led to the generation of a CD spectrum that was in qualitative agreement with the experimentally obtained data was roughly 1:2. This overall lower degree of chiral discrimination is also intuitive, as the CD effect is greatly reduced when compared to that in

chloroform. Unfortunately, these calculations do not reveal the exact reason for this solvent-dependent behavior.

When increasing the number of coupled chromophores, the overall spectral shape is largely conserved compared to that of the dimer, indicating the same preferences of chiral discrimination, which in turn means that the CD spectra of the trimer and polymer can also be explained by the same underlying principles.

5.4 SQB-type homooligo- and polymers

5.4.1 Absorption and fluorescence spectroscopy

The UV-Vis-NIR and fluorescence spectra of the investigated compounds alongside those of their achiral analogues are shown in Figure 65, and the corresponding data are summarized in Table 14. For absorption spectra in various solvents, see Figure 108 in the appendix.

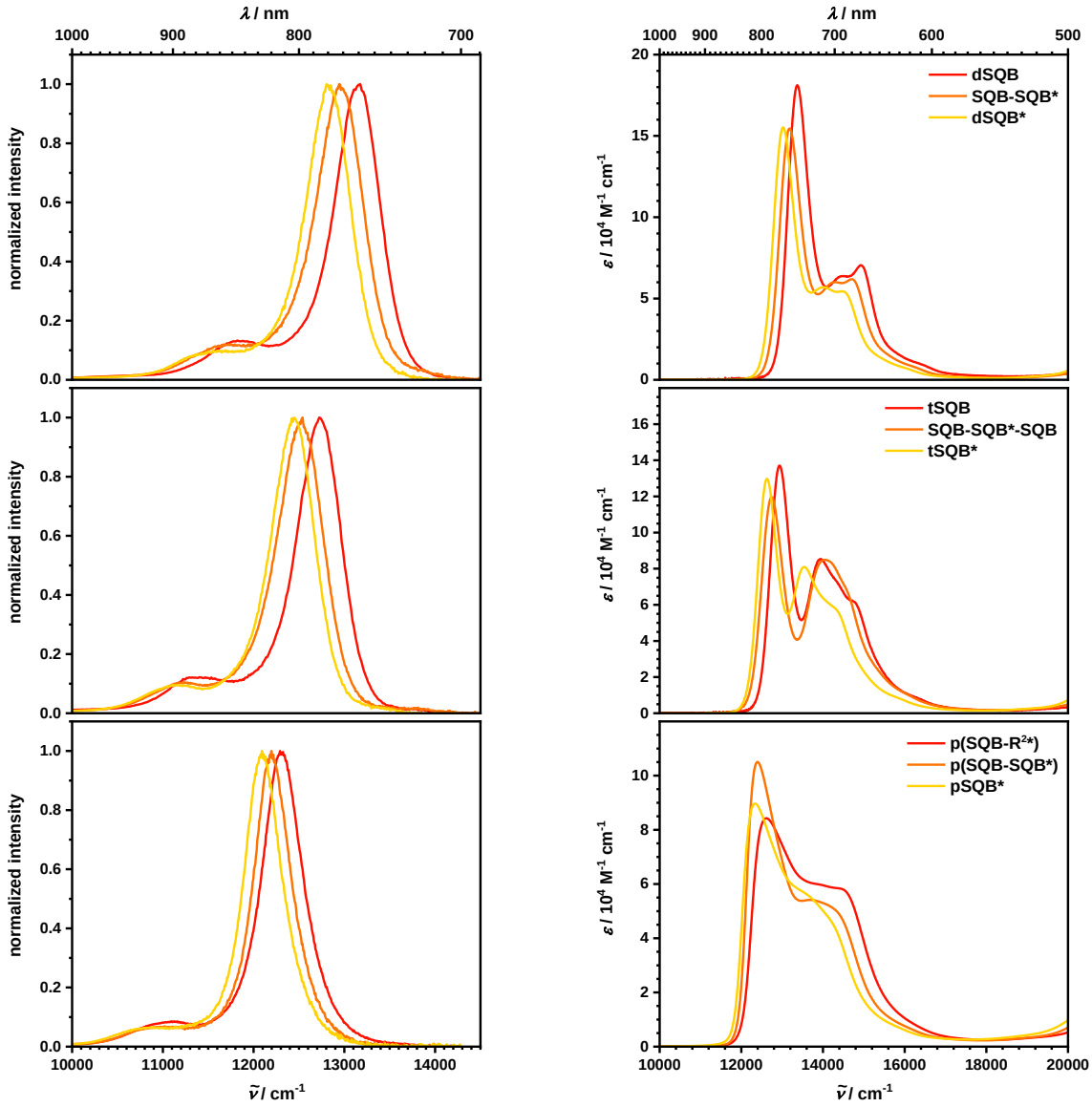

Figure 65. Comparison of the normalized fluorescence spectra (left) and UV-Vis-NIR absorption spectra (right) of the dimers **dSQB**[73], **SQB-SQB*** and **dSQB*** (top), trimers **tSQB**[73], **SQB-SQB*-SQB** and **tSQB*** (middle) and polymers **p(SQB-R2*)**, **p(SQB-SQB*)** and **pSQB*** (bottom) in toluene. Values of ε reported per monomer unit.

As in the previous case of the SQA-SQB-type heterooligomers, the absorption spectra of the chiral derivatives mostly resemble those of their achiral analogues, where the main absorption band is progressively more red-shifted when replacing **SQB** units with chiral **SQB*** units (by ca. 300 cm^{-1} per **SQB*** unit regarding the dimers). Due to the differences of **Ph-SQB*** and **SQB**

only being miniscule, all of these systems can be viewed as homooligo- and polymers in terms of exciton coupling theory. Therefore, the spectra are the result of a predominant J-type coupling, which leads to the main absorption band being red-shifted compared to that of the monomer. Higher-energy shoulders between 14 000 cm^{-1} and 16 000 cm^{-1} are observed in all cases as well, which point towards a deviation from the perfect J-type geometry, where all the transition moments are in a linear head-to-tail arrangement.[88, 91] Additionally, theoretical studies of **dSQB** performed by Spano et al. have shown the simultaneous presence of different conformers, where the dihedral angle between the two SQB chromophore units was either 37° (cis) or 142° (trans), leading to the emergence of an additional higher-energy H-type band at ca. 15 000 cm^{-1}.[303] Interestingly, when examining the spectra obtained in toluene of the dimer series more closely, this aforementioned higher-energy peak at 14 900 cm^{-1} diminishes when going from **dSQB** to **SQB-SQB*** to **dSQB***, which seems to indicate an increased conformational restriction when partially replacing the methyl groups in the 3-position by bulkier phenyl groups in this solvent, although this trend may be less pronounced when regarding the data obtained in other solvents (see Figure 108 in the appendix).

While tetramethyl-substituted SQB-polymers as described in chapter 4 show a unique and pronounced solvent-dependent behavior, the main-chain chiral analogues **p(SQB-SQB*)** and **pSQB*** lack this solvent dependency (see Figure 108 in the appendix) and exclusively exhibit a J-type absorption behavior in all of the tested solvents. This can be explained by the bulky phenyl groups preventing the folding into a helical structure. Because the expected helical pitch is very large, as discussed in detail in chapter 4 for the dimethyl-substituted analogues, and the chromophore interaction should therefore be minimal, this leads to the conclusion that the substitution at this position influences the ability of the solvent molecules to interact with the SQB units and arrange themselves in a favorable manner to enable the folding into a helical conformation. Interestingly, even the use of smaller amounts (10-20%) of **Ph-SQB*** as a dopant in SQB-homopolymers (see section 11.6 in the appendix) similar to a Sergeants-and-Soldiers experiment completely prevented the folding into a helical conformation.

The fluorescence spectra are again the result of an exclusive emission from the energetically lowest-lying state following Kasha's rule in all cases.[292] They are narrow with a vibronic shoulder on the low-energy side and roughly mirror the monomer absorption spectrum. As observed in the case of the SQA-SQB-type cooligomers, the introduction of phenyl groups leads to a progressive bathochromic shift by roughly 100-200 cm^{-1} per replaced SQB unit.

Contrary to the previous case (section 5.3.1), the quantum yields are largely unaffected by this change in substitution. This is unexpected, since the introduction of phenyl groups promotes non-radiative decay and thus leads to lower quantum yields as priorly observed. As previously found for the monomer **Ph-SQB***, the phenyl substituents lead to a longer fluorescence lifetime in toluene, which can be seen when comparing the dimers and trimers, e.g., **tSQB*** possessing a mean fluorescence lifetime which is 0.50 ns longer compared to that of **tSQB** (see Table 14). Additionally, the Stokes-shifts and spectral widths of the di- and trimers decrease slightly when increasing the degree of chiral substitution. This, alongside the higher quantum yield, points towards an increased structural order, which was also apparent in the absorption spectra of the dimer series in toluene. Here, the higher-energy band at 14 900 cm^{-1}, which is ascribed to the presence of the *cis*-conformer, was reduced in intensity, likely being the result of a higher degree of conformational restriction caused by the phenyl groups.

For the polymers, these above-described trends are not clearly obvious, as their extent is relatively small in magnitude and compensated by the higher number of degrees of freedom and/or the heterogeneity of their composition. Using eq. (61), the coherence length was determined to be 2.42 for **p(SQB-SQB*)** and 2.45 for **pSQB*** in toluene (the values calculated for $CHCl_3$ were nearly identical with 2.41 and 2.46, respectively), indicating a similarity of the superstructures present in solution.[1] Moreover, these values are slightly higher but comparable to those of the purely tetramethyl-substituted analogues in chloroform, while for toluene the comparability is reduced due to the formation of helical sections in certain cases. These higher values also indicate a greater degree of structural order compared to the purely methyl-substituted counterparts, possibly caused by the structural restriction exerted by the large phenyl groups.

As with the SQA-SQB-type compounds, no CPL signal was detected for any of the SQB-type analogues as well.

[1] For the calculation of N_{eff} of **pSQB*** the FWHM of **Ph-SQB*** (766 cm^{-1}) was used and for that of **p(SQB-SQB*)** the average FWHM of **Ph-SQB*** and **SQB** (747 cm^{-1}).

Table 14. Summary of the optical data (wavenumber $\tilde{\nu}_{abs}$ and corresponding absorption coefficients ε_{max} of absorption maxima 1 and 2, squared transition moments μ_{eg}^2, emission maxima $\tilde{\nu}_{em}$, full width at half maximum of the emission spectra *FWHM*, Stokes-shifts $\Delta\tilde{\nu}$, quantum yields Φ_{fl}, fluorescence lifetimes τ_{fl}, mean fluorescence lifetimes $\bar{\tau}_{fl}$) of **dSQB**[73], **SQB-SQB***, **dSQB***, **tSQB**[73], **SQB-SQB*-SQB**, **tSQB***, **p(SQB-R²*)**, **p(SQB-SQB*)** and **pSQB*** in chloroform and toluene.

		$\tilde{\nu}_{abs}$ (λ_{abs}) / cm^{-1} (/ nm)	ε_{max} [a] / M^{-1} cm^{-1}	μ_{eg}^{2} [a b] / D²	$\tilde{\nu}_{em}$ (λ_{em}) / cm^{-1} (/ nm)	FWHM / cm^{-1}	$\Delta\tilde{\nu}$ / cm^{-1}	Φ_{fl}	τ_{fl} [c] / ns	$\bar{\tau}_{fl}$ [d] / ns
dSQB	$CHCl_3$	13 600 (736)	1.69×10^5	118	13 300 (751)	740	270	0.20	0.31 (0.21) 1.00 (0.79)	0.95
	toluene	13 400 (748)	1.81×10^5	113	13 100 (761)	640	230	0.68	2.49 (0.83) 4.08 (0.17)	2.89
SQB-SQB*	$CHCl_3$	13 400 (747)	1.49×10^5	118	13 100 (762)	690	260	0.20	0.46 (0.26) 0.96 (0.74)	0.89
	toluene	13 200 (759)	1.55×10^5	101	13 000 (772)	620	220	0.66	1.62 (0.19) 3.15 (0.81)	2.99
dSQB*	$CHCl_3$	13 200 (756)	1.51×10^5	104	13 000 (770)	670	240	0.16	0.41 (0.42) 0.97 (0.58)	0.84
	toluene	13 000 (768)	1.55×10^5	96.9	12 800 (780)	590	200	0.57	1.64 (0.30) 3.34 (0.70)	3.04
tSQB	$CHCl_3$	13 200 (760)	1.34×10^5	127	12 900 (775)	700	250	0.20	0.90 (0.84) 1.30 (0.16)	0.99
	toluene	12 900 (774)	1.37×10^5	113	12 700 (786)	610	200	0.58	2.12 (0.89) 4.26 (0.11)	2.54
SQB-SQB*-SQB	$CHCl_3$	12 900 (774)	1.12×10^5	119	12 700 (789)	680	250	0.24	0.59 (0.31) 1.37 (0.69)	1.24
	toluene	12 700 (785)	1.20×10^5	111	12 500 (798)	610	210	0.64	1.81 (0.48) 3.10 (0.52)	2.65
tSQB*	$CHCl_3$	12 800 (781)	1.30×10^5	116	12 600 (794)	640	180	0.17	0.44 (0.41) 0.95 (0.59)	0.83
	toluene	12 600 (792)	1.29×10^5	105	12 400 (804)	570	190	0.57	1.64 (0.30) 3.34 (0.70)	3.04
p(SQB-R²*)	$CHCl_3$	12 700 (788)	9.84×10^4	104	12 500 (802)	490	230	0.21	0.43 (0.22) 1.02 (0.78)	0.96
	toluene	12 600 (793)	8.43×10^4	108	12 300 (814)	540	330	0.26	1.06 (0.19) 2.27 (0.81)	2.15
p(SQB-SQB*)	$CHCl_3$	12 500 (797)	1.19×10^5	117	12 300 (810)	510	200	0.13	0.22 (0.20) 0.78 (0.80)	0.74
	toluene	12 400 (807)	1.05×10^5	105	12 200 (820)	480	200	0.32	0.82 (0.16) 1.94 (0.84)	1.86
pSQB*	$CHCl_3$	12 500 (801)	1.17×10^5	125	12 200 (819)	510	270	0.10	0.23 (0.26) 0.60 (0.74)	0.56
	toluene	12 300 (811)	8.97×10^4	98.5	12 100 (827)	490	240	0.33	0.93 (0.21) 2.06 (0.79)	1.94

[a] Values per monomer unit. [b] determined by integration of the main absorption band and calculated using eq. (74) in the appendix. [c] Determined by TCSPC, decay curves fitted with a (multi-)exponential fit, amplitudes are given in parantheses. Excitation was at 15 240 cm^{-1} (656 nm). [e] Intensity-weighed mean fluorescence lifetime calculated according to eq. (77) in the appendix.

5.4.2 CD spectroscopy

The CD spectra of the chiral SQB-type di-, tri- and polymers in $CHCl_3$ and toluene are shown in Figure 66, the chiroptical data are summarized in Table 15. For CD spectra in various solvents, see Figure 109 in the appendix.

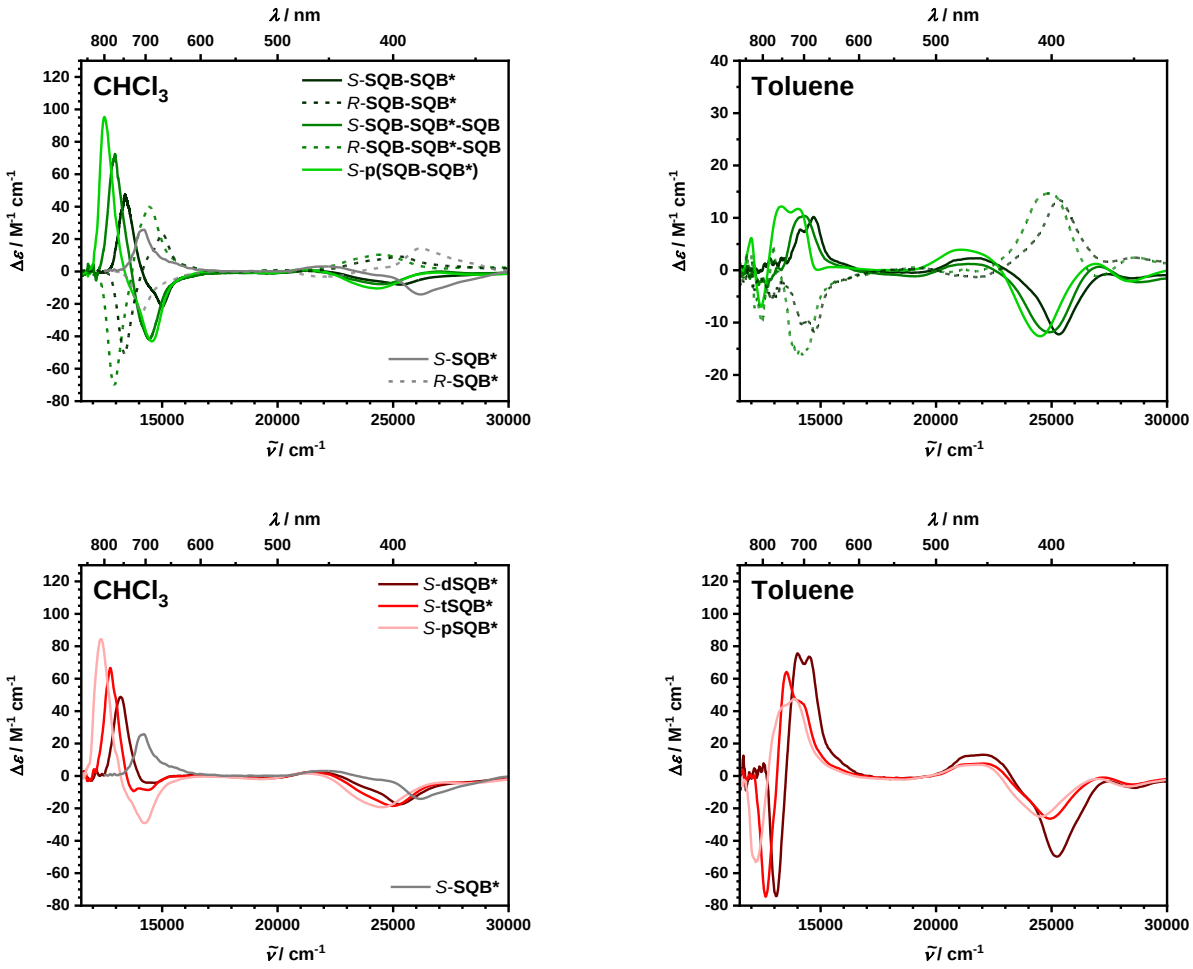

Figure 66. CD spectra of the mixed oligo- and polymers (**SQB-SQB***, **SQB-SQB*-SQB**, **p(SQB-SQB*)**, top) and the SQB* homooligo and -polymers (**dSQB***, **tSQB*** and **pSQB***, bottom) in $CHCl_3$ (left) and toluene (right). Values for Δε reported per monomer unit.

As expected, all CD spectra of enantiomeric compounds behave like mirror images of one another. Due to the enantiomers of **SQB-SQB*** bearing different side chains (*n*-hexyl vs. *n*-hexadecyl), the conclusion can be made that the side chain does not affect the (chir)optical properties and therefore also the underlying geometrical arrangement of these systems, regardless of the solvent. The slightly lower values of Δε obtained for the *S*-enantiomer likely stem from ***S*-Br-SQB*-C6** being of slightly lower stereochemical purity compared to that of ***R*-Br-SQB*-C16**, (see section 11.1.1 in the appendix).

Regarding the CD spectra (only the *S*-enantiomers are regarded for this discussion) in chloroform, all compounds exhibit resembling CD-characteristics, that is a positive band coinciding with the main absorption band between 12 200 and 13 400 cm^{-1}, that increases in intensity with increasing main chain length and a negative band in the region of the higher-energy shoulders of the absorption between 13 900 and 15 000 cm^{-1}. While the rotational strength of the low energy band is comparable regarding the respective di-, tri- and polymers, the rotational strength of the higher-energy band is generally smaller in the pure SQB*-type compounds compared to the mixed SQB-SQB* analogues. As previously described for the SQA-SQB*-type systems, the increased rotational strength of the main S_0-S_1 transition likely is the result of the excitonic coupling, as the arrangement of the individual chromophores is not in plane (dihedral angle $\theta \neq 0°$), thus leading to the R_{ex}-term in eq. (42) being non-zero. Also, the contributions from the $R_{e\text{-}m}$-term are likely significant in this case as well. The g_{abs} value is therefore also roughly five to six times (and therefore nearly one order of magnitude) larger than that of the monomer, reaching values of up to 9.19×10^{-4} cgs for **pSQB***.

In toluene, on the other hand, the situation is different comparing the mixed SQB-SQB* systems to their pure SQB*-type counterparts. While the latter exhibit CD spectra that are somewhat reminiscent of the mirror-image relationship of enantiomers when comparing them to those obtained in $CHCl_3$ (signs of the CD bands exchanged) with similar g_{abs} values, the CD spectra of the former differ markedly. Here, the obtained values for R and $\Delta\varepsilon$ are generally substantially smaller, similar to those of the SQA-SQB-type systems, leading to the g_{abs}-values being roughly one order of magnitude lower compared to those obtained in $CHCl_3$. Surprisingly, no CD signal corresponding to the main low-energy band is visible at all.

As in the previously described case of the SQA-SQB-type systems, the assumption can be made that this solvent dependency most likely stems from the presence of different conformations in solution.

Table 15. Summary of the chiroptical data (CD bands $\tilde{\nu}_{CD}$, difference in absorption $\Delta\varepsilon$, rotational strengths R_{exp} and dissymetry factors g_{abs}) of ***S*-SQB*, *S*-SQB-SQB*, dSQB*, *S*-SQB-SQB*-SQB, tSQB*, p(SQB-SQB*)** and **pSQB*** in toluene and chloroform.

		$\tilde{\nu}_{CD}$ (λ_{CD}) / cm^{-1} (/ nm)	$\Delta\varepsilon$ / M^{-1} cm^{-1} [a]	R_{exp} / 10^{-40} cgs [a c]	$\lvert g_{abs}(\tilde{\nu}_{max})\rvert$ / cgs [a b]
SQB*	$CHCl_3$	14 200 (704)	25.8	49.4	1.81×10^{-4}
	toluene	13 900 (719)	23.6	41.7	1.48×10^{-4}
SQB-SQB*	$CHCl_3$	13 400 (747)	47.5	54.5	3.20×10^{-4}
		15 000 (666)	-21.5	-33.1	3.19×10^{-4}
	toluene	-	-	-	-
		14 700 (660)	10.2	20.4	3.33×10^{-4}
dSQB*	$CHCl_3$	13 200 (758)	48.8	63.2	3.27×10^{-4}
		14 500 (689)	-4.15	-6.30	7.42×10^{-5}
	toluene	13 100 (765)	-37.1	-31.3	2.43×10^{-4}
		14 000 (715)	37.8	83.2	6.64×10^{-4}
SQB-SQB*-SQB	$CHCl_3$	13 000 (772)	72.5	87.0	6.09×10^{-4}
		14 400 (693)	-41.9	-76.8	4.61×10^{-4}
	toluene	-	-	-	-
		14 300 (698)	9.94	18.0	9.78×10^{-5}
tSQB*	$CHCl_3$	12 700 (785)	66.7	80.3	5.55×10^{-4}
		13 800 (727)	-9.39	-17.9	1.22×10^{-4}
	toluene	12 600 (793)	-74.5	-71.2	6.50×10^{-4}
		13 500 (740)	64.1	135	8.06×10^{-4}
p(SQB-SQB*)	$CHCl_3$	12 500 (800)	95.3	115	7.88×10^{-4}
		14 600 (687)	-43.0	-83.8	9.07×10^{-4}
	toluene	-	-	-	-
		13 300 (752)	12.2	30.7	2.31×10^{-4}
pSQB*	$CHCl_3$	12 400 (808)	84.3	115	9.19×10^{-4}
		14 200 (702)	-29.0	-59.7	6.51×10^{-4}
	toluene	12 200 (820)	-53.0	-61.1	6.58×10^{-4}
		13 900 (722)	47.5	129	9.04×10^{-4}

[a] values per monomer unit. [b] $\Delta\varepsilon(\tilde{\nu}_{max})/\varepsilon(\tilde{\nu}_{max})$. [c] determined by integration of the CD band and calculated using eq. (75) in the appendix.

5.4.3 TD-DFT calculations[1]

As performed for **SQA-SQB***, TD-DFT calculations with a varying dihedral angle as depicted in Figure 62 (conformations A-D) were performed using the same procedure for **SQB-SQB*** and **dSQB***, which are shown in Figure 67 and Figure 68, respectively.

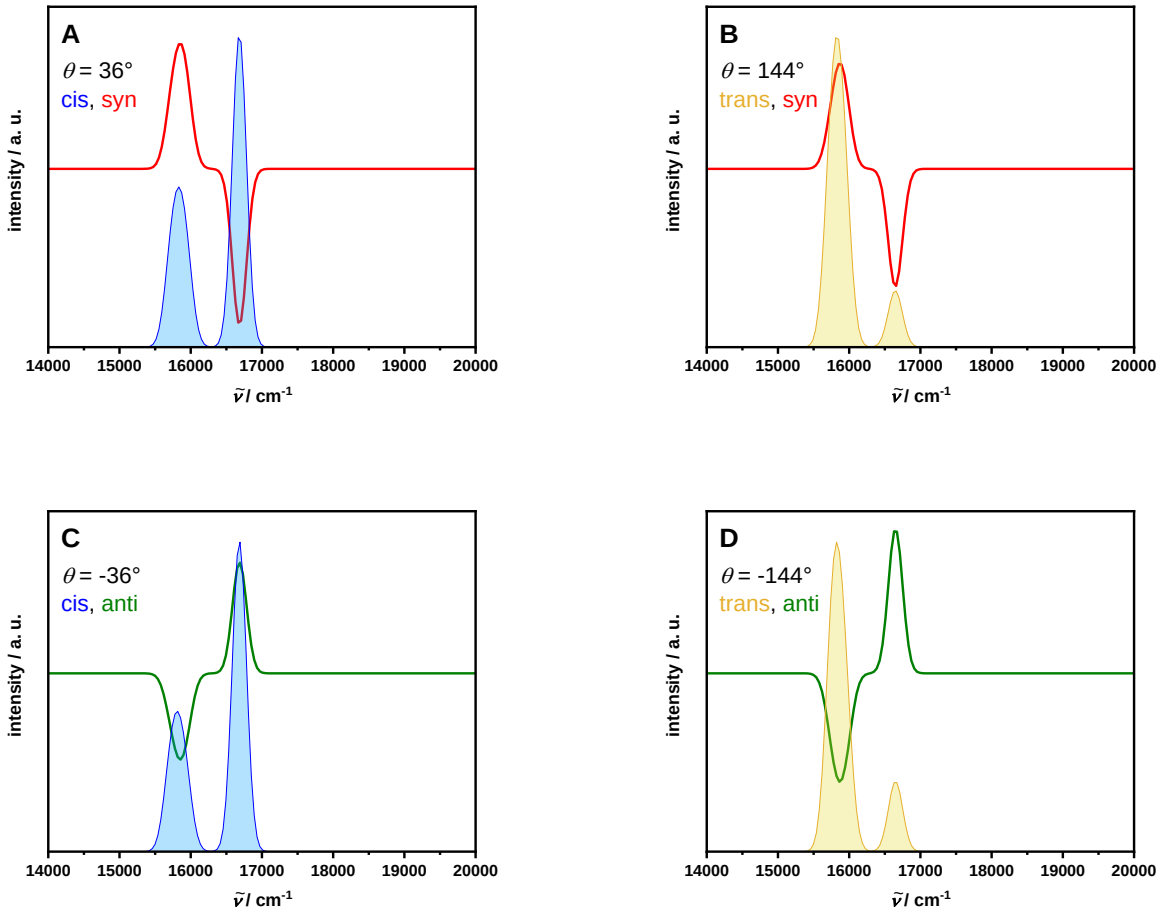

Figure 67. Calculated ensemble spectra of **SQB-SQB*** (CD: red (syn) or green (anti) line, absorption: blue (cis, H-type) or orange (trans, J-type) area) of conformers A-D convoluted with a Gaussian function with a FWHM of 100 cm^{-1}. Absorption spectra are normalized, while the CD spectra are to scale.

[1] Theoretical calculations performed by D. Fischermeier (Mitric group, University of Würzburg)

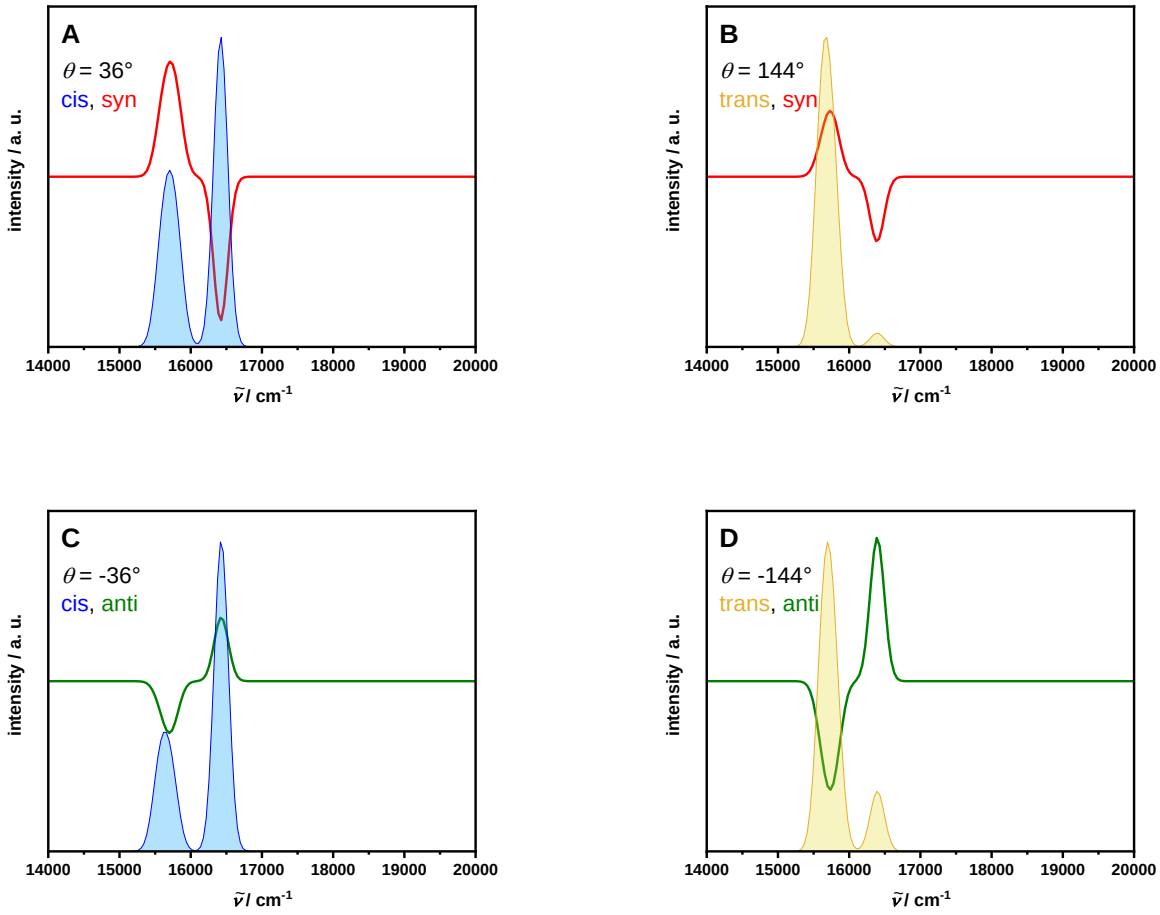

Figure 68. Calculated ensemble spectra of **dSQB*** (CD: red (syn) or green (anti) line, absorption: blue (cis, H-type) or orange (trans, J-type) area) of conformers A-D convoluted with a Gaussian function with a FWHM of 100 cm^{-1}. Absorption spectra are normalized, while the CD spectra are to scale.

As in the previously discussed case of **SQA-SQB***, the UV-Vis-NIR absorption is largely the result of the geometrical arrangement of the electric transition moments and thus the mutual orientation of the SQB-chromophores. For both **SQB-SQB*** and **dSQB***, a *cis*-arrangement results in an H-type behavior with a hypsochromic shift of the main absorption band, whereas a *trans*-arrangement leads to a J-type behavior with a respective bathochromic shift. As can be seen in the absorption spectra of the dimer series **dSQB**, **SQB-SQB*** and **dSQB*** in toluene (Figure 65), the relative amount of the *cis*-conformers decreases when successively replacing SQB units with SQB* analogues, as the higher-energy peak at 14 900 cm^{-1} was reduced in intensity. This trend was also discernable in the fluorescence data in both $CHCl_3$ and toluene, as the spectral widths were decreased in **SQB-SQB*** and **dSQB*** when compared to **dSQB**. For **SQB-SQB***, the *cis-trans* ratio was assumed to be 1:1 as well, while for **dSQB*** it was arbitrarily assumed to be 3:7 based on the aforementioned findings in the experimental absorption and fluorescence data.

Using these ratios as a constraint, the experimental CD spectra were reconstructed by the combination of the respective *syn* and *anti* ensemble spectra (Figure 69b). Combinations comprising an increasing amount of the anti-conformers assuming an identical chiral discrimination for both the *cis* and *trans* conformations are shown in Figure 69a.

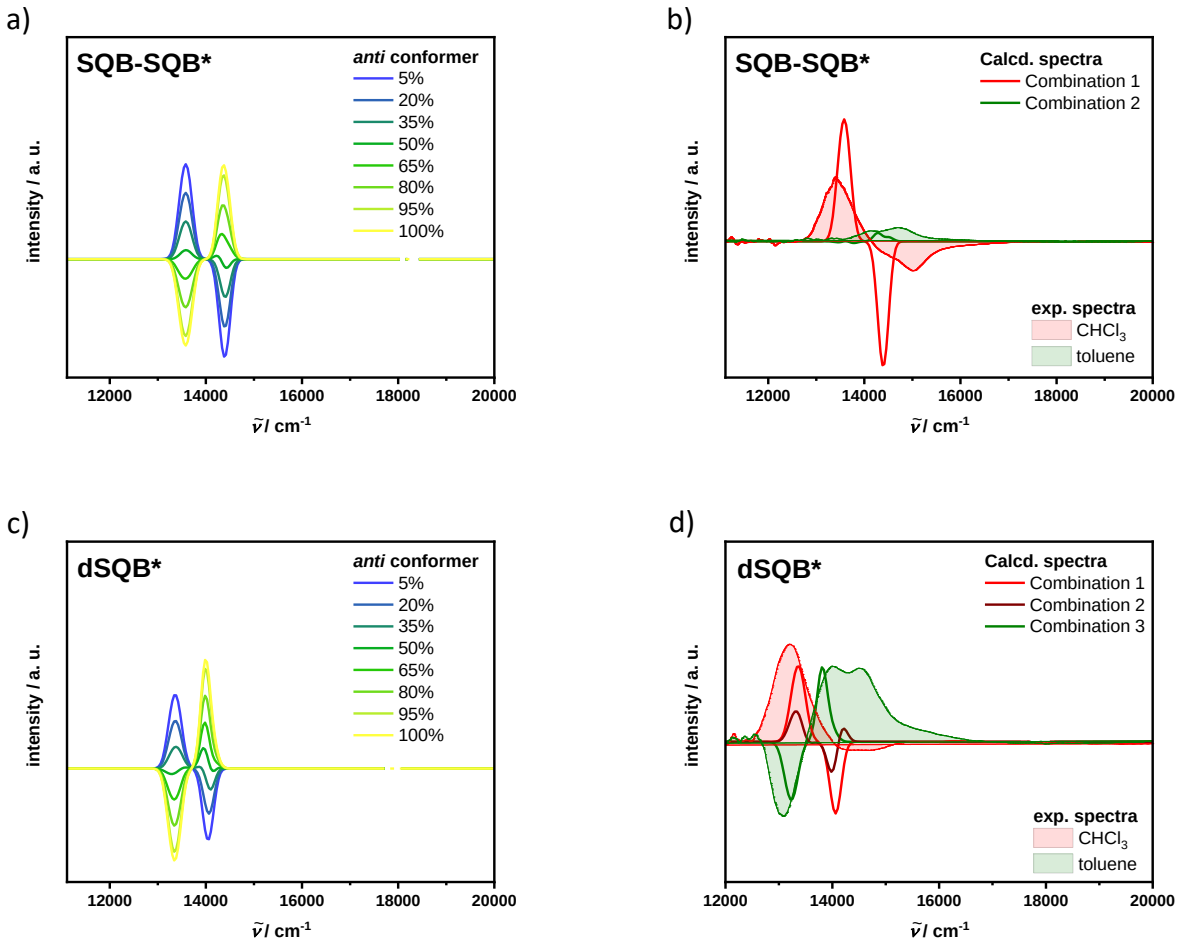

Figure 69. Left: Combined calculated CD spectra of a) **SQB-SQB*** (top, shifted by -2250 cm^{-1}) and c) **dSQB*** (bottom, shifted by -2325 cm^{-1}) with varying relative amounts of the *anti*-conformer, where the chiral discrimination is identical for the *syn* and *anti*-conformers. Right: comparison of the experimental spectra in chloroform and toluene of b) **SQB-SQB*** with the combined calculated CD spectra comprising 20% *anti*-conformer (identical degree of chiral discrimination, combination 1, $CHCl_3$ PCM, shifted by -2250 cm^{-1}), as well as varying amounts of conformers A-D with a low degree of chiral discrimination (combination 2: A: 20.5%, B: 25.0%, C: 29.5%, D: 25.0%, toluene PCM, shifted by -1750 cm^{-1}), and d) **dSQB*** with the combined calculated CD spectra comprising 20% *anti*-conformer (identical degree of chiral discrimination, combination 1, $CHCl_3$ PCM, shifted by -2325 cm^{-1}), 65% of the anti-conformer (identical degree of chiral discrimination, combination 3, toluene PCM, shifted by -2000 cm^{-1}), as well as varying amounts of conformers A-D with a different degree of chiral discrimination for the *cis* and *trans* conformers (combination 2: A: 5.0%, B: 57.0%, C: 13.0%, D: 25.0%, $CHCl_3$ PCM, shifted by -2325 cm^{-1}).

As previously described for **SQA-SQB***, the CD spectra are mostly dependent on the sine of the interchromophoric dihedral angle θ according to eq. (43), and thus show a quasi-enantiomeric relationship for the *syn*- and *anti*-conformers. Again, a larger than expected deviation from the aforementioned sine-dependency of the rotational strength was observed for **dSQB***, leading to the conclusion that the rotational strength is also non-negligibly dependent on the $R_{e\text{-}m}$ and R_{mon}-terms in eq. (42).

For **SQB-SQB***, the same conclusions can be drawn as for **SQA-SQB***. Regarding the obtained experimental spectra in chloroform, these can be approximated using a combination of predominately *syn*-conformer CD spectra. The experimental data in toluene can be approximately reproduced when assuming no chiral discrimination in the *trans*-conformers and a *syn* to *anti* ratio of 2:3 in the cis conformers, thus leading to an overall small CD effect, where no signal corresponding to the main absorption band is visible at all.

For **dSQB*** the situation is somewhat different. Here, the experimental spectra in chloroform also indicate an overall bias towards the adoption of *syn*-conformers, but the chiral discrimination seems to be somewhat lower as in the previous cases (**SQA-SQB*** and **SQB-SQB***). This becomes apparent by the greatly reduced rotational strength of the higher-energy CD band at 14 500 cm^{-1} in **dSQB*** (-6.30×10^{-40} cgs) compared to that of **SQB-SQB*** (-33.1×10^{-40} cgs). Assuming a large degree of steric hindrance in conformer A, as the two phenyl groups are in closer proximity to each other in this conformation, this could lead to a stronger favoring of the corresponding analogous *anti*-conformation C. As this steric strain is not as significant in the *trans*-conformers B and D, the adoption of the *syn*-conformer B is likely still favored. When assuming a 1:5 ratio of conformers A and C and roughly 11:5 for conformers B and D (combination 2 in Figure 69b), this leads to the main positive CD peak at 13 200 cm^{-1} still being prominent while the higher energy band at 14 500 cm^{-1} becomes vanishingly small.

In toluene, on the other hand, the experimentally obtained spectrum qualitatively matches well with a combination of calculated spectra of predominately *anti*-conformers, hence explaining the overall sign change of the CD spectrum and therefore the quasi-enantiomeric relationship of the two types of spectra. Contrary to the previous cases (**SQA-SQB*** and **SQB-SQB***), where toluene led to an overall small chiral bias of the resulting conformers, the overall large magnitude of the CD effect, as well as the clearly defined spectral shape, lead to the assumption that this is opposite in this case. The reason for this might be the influence of

the phenyl groups, possibly by exerting a larger degree of steric strain on the system and thus leading to a larger degree of chiral discrimination.

For both the SQB-SQB*- and pure SQB*-type systems, increasing the main chain length and therefore the number of coupled chromophores does not lead to a difference in spectral shape, meaning that the CD spectra of the higher oligomers can be explained by the same underlying principles.

5.5 Conclusions

The standard methodology for the synthesis of squaraine oligo- and polymers, which was employed in this work, was successful and all the target compounds were obtained in sufficient yields and satisfying (stereochemical) purity. The absorption and fluorescence properties of the chiral squaraine oligo- and polymers containing the **Ph-SQB*** moiety mostly resembled those of their purely tetramethyl-substituted analogues. Here, the main difference that was observed in all cases, was a bathochromic shift of the respective main lowest-energy absorption band (J-band) by ca. 100-300 cm^{-1}, which was also analogously observed for the corresponding fluorescence spectra. For the SQA-SQB-type cooligomers, this went alongside a reduction in intensity of the J-band, as well as in fluorescence quantum yield in toluene. While the achiral polymer **p(SQA-SQB)** exhibited a solvent-dependent absorption behavior, which can be explained by the formation of different conformations in different solvents similar to the SQB-homopolymers discussed in chapter 4, the chiral counterpart **p(SQA-SQB*)** completely lacked this type of behavior. It is assumed that this was due to the introduction of a bulky phenyl group at the 3-position of the SQB-unit, which precluded a favorable interaction with the solvent molecules and thus the formation of different conformers.

For the SQB-type homooligomers and -polymers, a slightly higher degree of structural order was observed when successively replacing SQB units with the chiral **Ph-SQB*** derivative. This became apparent in the UV-Vis-NIR absorption spectra (especially in the dimer series in toluene), where the higher-energy shoulders between 14 000 and 16 000 cm^{-1} decreased in intensity. This claim was further strengthened by the fluorescence data, as a higher degree of C(3)-chiral phenyl substitution led to reduced spectral widths and Stokes-shifts, as well as higher-than-expected quantum yields in toluene. The polymers **p(SQB-SQB*)** and **pSQB***, in contrast to their purely tetramethyl counterparts discussed in chapter 4, displayed an

exclusive J-type absorption behavior that was invariant towards a change of solvent, indicating the absence of helical conformations. Interestingly, SQB-homopolymers comprising only 10-20% of **Ph-SQB*** also did not fold into a helical conformation.

Contrary to the absorption spectra, the CD spectra of all of the investigated chiral oligo- and polymers containing the **Ph-SQB*** moiety exhibited a pronounced solvent-dependent behavior. In chloroform, the situation was similar for both the SQA-SQB- and purely SQB-type oligo- and polymers. All of the CD spectra of the investigated compounds displayed a positive-negative band sequence (positive exciton chirality) corresponding to the lower- and higher-energy transitions of their respective exciton manifolds. The rotational strength of the main S_0-S_1 transition was increased compared to that of the **Ph-SQB*** monomer due to the excitonic coupling of the individual electric and magnetic transition moments ($R_{e\text{-}m}$ and R_{ex} in eqs. (42) and (68)), thus leading to g_{abs}-values of up to 9.04×10^{-4} cgs for the low-energy transition of **pSQB*** at 12 400 cm^{-1}, which is almost one order of magnitude higher than the value obtained for the monomer (1.81×10^{-4} cgs). As this effect is increased when increasing the main chain length, it is concluded that the degree of chiral discrimination also increases in higher oligomers and polymers. TD-DFT calculations of the respective dimers **SQA-SQB***, **SQB-SQB*** and **dSQB***, where the dihedral angle was systematically varied, further revealed that the CD spectra were the result of a conformational bias towards a *syn*-conformation, where the squaraine chromophore was oriented on the same side as the adjacent phenyl group, thus resulting in the experimentally obtained CD spectra possessing this particular spectral shape.

In toluene, the situation was vastly different compared to that in chloroform. Here, the CD effect was of much smaller magnitude in the mixed systems comprising the **Ph-SQB*** and the achiral **SQA** or **SQB** moieties, whereas the purely SQB*-type oligo- and polymers possessed CD spectra roughly being mirror images of those obtained in chloroform. For the mixed systems, this resulted in g_{abs}-values of roughly the same order of magnitude or lower compared to that of the **Ph-SQB*** monomer (~10^{-4} cgs). In the purely SQB*-type substituted derivatives, on the other hand, a similar amplification of the rotational strength was observed with g_{abs}-values ranging up to 9.04×10^{-4} cgs for the higher-energy transition of **pSQB*** in toluene at 13 900 cm^{-1}. Analogous TD-DFT-calculations revealed the preference of the *anti*-conformation, where the adjacent phenyl group was on the opposite side compared to the connected squaraine unit. For the mixed (chiral and achiral) systems, this bias was very weak and the overall degree of chiral discrimination was considerably lower compared to that in

chloroform. In the **dSQB***-dimer, possibly owing to the increase in steric strain, this did not seem to be the case. Here the calculations revealed a clear preference towards the *anti*-conformations, thus leading to the mirror-image relationship of the CD spectra to those obtained in chloroform.

Unfortunately, although these calculations did reveal the origin of the shape of the observed CD spectra and elucidated the underlying principles regarding the relationship of the conformation and the resulting (chir)optical properties, no explanation can be found as to why certain solvents favor the adoption of different conformations. Because the favoring of the *cis*-conformation in $CHCl_3$ is counter-intuitive due to the larger degree of steric strain, it is speculated that the solvent may act as an adhesive in this case as well, similar to the SQB helix.[91] In principle, every experimentally obtained CD spectrum can be generated by arbitrarily combining the CD spectra of the conformers A-D in Figure 62, where the corresponding absorption spectrum acts as an overall constraint. Due to the fact that the origin of this solvent-dependency remains unknown, a more precise and systematic approach is precluded in this case. Furthermore, due to this being a complex equilibrium of multiple conformers, an experimental characterization, e.g., by performing titration experiments with different solvent compositions, may not be successful at quantifying the exact ratio of the adopted conformers.

6 Pr-SQB* HOMOPOLYMER

As the introduction of a phenyl group at the 3-position of the indolenine subunit completely prevented the adoption of a helical conformation of the SQB-type homopolymers, an analogous polymer exclusively comprising the **Pr-SQB*** building block **p(Pr-SQB*)** was prepared in order to possibly achieve chiral induction via main-chain chirality. This was done because the smaller *n*-propyl group may possess a lesser extent of steric strain (compared to the analogous phenyl-substituted derivatives) and thus may possibly allow for a folding of the polymer strand into a helical conformation.

6.1 Synthesis

The dibrominated *n*-propyl substituted squaraine monomer **Br_2-Pr-SQB***, which was priorly synthesized using the HPLC-resolved *n*-propyl-substituted indolenine *S*-**14** as described in sections 3.1.1.2 and 3.1.1.3, was polymerized using a Ni-mediated Yamamoto homocoupling reaction as shown in Scheme 22.

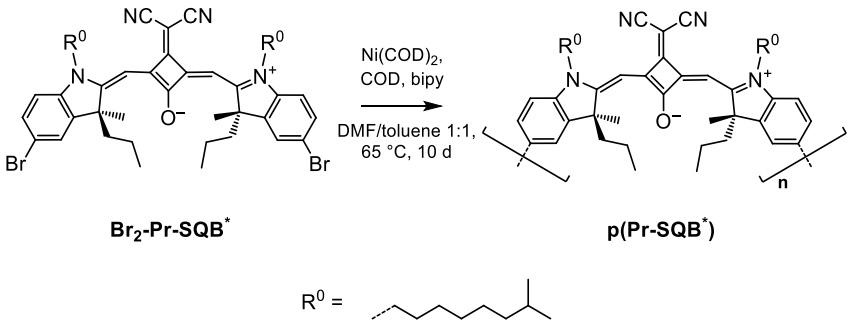

Scheme 22. Polymerization of the dibrominated squaraine monomer **Br_2-Pr-SQB*** via Yamamoto-homocoupling.

As done with all previously described polymers, the obtained crude polymer **p(Pr-SQB*)** was successively washed with different solvents in a Soxhlet-extractor, before being fractionated by preparative GPC using DCM as the eluent. The molecular weight distributions of the individual polymer fractions were then determined by analytical GPC and the results, along with the chromatograms of the analytical and preparative runs are shown in section 11.1.2.2 in the appendix.

The obtained degree of polymerization X_n, as well as the polydispersity index (PDI) was comparable to the values obtained for the tetramethyl-substituted derivatives presented in chapter 4. The value obtained for the degree of polymerization of the F1 fraction (32.4) falls between that of **p(SQB-R^0)** (22.8) and **p(SQB-R^1*)** (38.5), and thus the explanation presented in section 4.1, that the main chain length is governed by the solubility in the solvent used for the polymerization, is likely also valid in this case as well due to similar solubility in the tested solvents. As with the previous polymers, only the F1 fraction was used for further studies.

6.2 Absorption and fluorescence spectroscopy

The UV-Vis-NIR absorption spectra of **p(Pr-SQB*)** in different solvents, as well as the normalized fluorescence and absorption spectra in toluene, are shown in Figure 70. The corresponding data are summarized in Table 16 (absorption) and Table 17 (fluorescence).

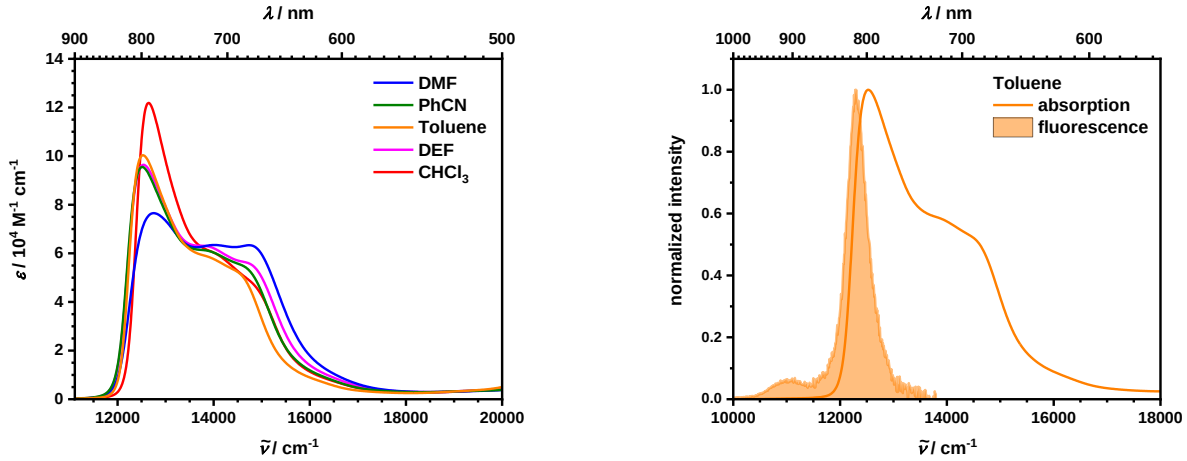

Figure 70. UV-Vis-NIR absorption spectra of **p(Pr-SQB*)** in various solvents (left) and comparison of the normalized absorption and emission spectra of **p(Pr-SQB*)** in toluene (left). Values for ε reported per monomer unit.

Table 16. Optical spectroscopic data (absorption maxima $\tilde{\nu}_{abs}$, extinction coefficients ε_{max}, squared transition moments μ_{eg}^2) of **p(Pr-SQB*)** in various solvents.

solvent	$\tilde{\nu}_{abs}$ (λ_{abs})[a] / cm^{-1} (/ nm)	ε_{max}[a b] / M^{-1} cm^{-1}	μ_{eg}^2[b c] / D²
DMF	12 800 (784)	7.65×10^4	123
PhCN	12 500 (799)	9.55×10^4	114
Toluene	12 500 (799)	1.00×10^5	109
DEF	12 500 (798)	9.64×10^4	127
$CHCl_3$	12 600 (791)	1.22×10^5	123

[a] values for global maximum. [b] values per monomer unit. [c] determined by integration of the main absorption band and calculated using eq. (74) in the appendix.

In contrast to the tetramethyl-substituted analogues discussed in chapter 4, **p(Pr-SQB*)** exclusively exhibits a J-type behavior in all of the tested solvents, which was also observed for **pSQB*** and **p(SQB-SQB*)** as discussed in section 5.4.1. For all of the tested solvents apart from DMF, the spectral shape and the corresponding optical data is virtually identical, and can be described as that of the pure J-type structure with the main absorption maximum being located at ca. 12 500-12 600 cm^{-1} possessing shoulders at the high-energy side between 13 500 and 15 000 cm^{-1}. In DMF, the absorption band is significantly broadened and the intensity ratio of the main absorption peak and its corresponding shoulders is greatly reduced, along with being hypsochromically shifted by ca. 200-300 cm^{-1} compared to the other tested solvents. Nevertheless, the observed absorption spectrum in DMF is still completely void of the characteristic H-type features, specifically the main H-band between 15 500 and 15 800 cm^{-1}, as well as the electronically weakly allowed low-energy peak 11 800 cm^{-1} corresponding to the transition of the ring contribution at E_0 of the squaraine helix.

As for all of the discussed squaraine polymers, the fluorescence results from the lowest-lying state of the exciton manifold and is in accordance with Kasha's rule. It is narrow with a vibronic shoulder on the low-energy side and mirrors that of the monomer. Comparing the obtained fluorescence data to those of the tetramethyl-substituted analogous polymers in section 4.6.1, it can be seen that the data are largely comparable to those of **p(SQB-R^2*)** and **p(SQB-R^3*)**, specifically in terms of the positions of the emission maxima, spectral widths, Stokes-shifts and fluorescence lifetimes. This points towards a comparable degree of conformational order within the superstructures of the aforementioned polymers in the discussed solvents. Consequently, a similar effective coherence length according to eq. (61) of 2.37 in toluene and 2.40 in chloroform was obtained for **p(Pr-SQB*)**, which were furthermore also comparable to those calculated for **pSQB*** and **p(SQB-SQB*)**. Interestingly, the obtained quantum yield in toluene was slightly higher (37%) compared to those of all the previously discussed SQB-type homopolymers (**p(SQB-R^2*)** and **p(SQB-R^3*)**: 26%, **p(SQB-SQB*)**: 32%, **pSQB***: 33%). Further CPL-measurements did not yield any signal in this case as well.

Table 17. Summary of the fluorescence data (emission maxima $\tilde{\nu}_{em}$, full width at half maximum of the emission spectra *FWHM*, Stokes-shifts $\Delta\tilde{\nu}$, quantum yields Φ_{fl}, fluorescence lifetimes τ_{fl}, mean fluorescence lifetimes $\bar{\tau}_{fl}$) of **Pr-SQB*** and **p(Pr-SQB*)** in chloroform and toluene.

		$\tilde{\nu}_{em}$ (λ_{em}) / cm^{-1} (/ nm)	*FWHM* / cm^{-1}	$\Delta\tilde{\nu}$ / cm^{-1}	Φ_{fl}	τ_{fl} [a] / ns	$\bar{\tau}_{fl}$ [b] / ns
Pr-SQB*	toluene	14 000 (712)	720	230	0.74	3.39	3.39
	$CHCl_3$	14 200 (702)	750	350	0.54	2.50	2.50
p(Pr-SQB*)	toluene	12 300 (813)	470	220	0.37	1.03 (0.18) 2.09 (0.82)	1.99
	$CHCl_3$	12 400 (804)	480	200	0.23	0.31 (0.16) 0.99 (0.84)	0.95

[a] Determined by TCSPC, decay curves fitted with a (multi-)exponential fit, amplitudes are given in parantheses. Excitation was at 15 200 cm^{-1} (656 nm), fluorescence signal at 12 500 cm^{-1} (800 nm) was measured unless stated otherwise. [b] Intensity-weighed mean fluorescence lifetime calculated according to eq. (77) in the appendix.

6.3 CD spectroscopy

The CD spectra of **p(Pr-SQB*)** in different solvents are shown in Figure 71 and the corresponding data are summarized in Table 18.

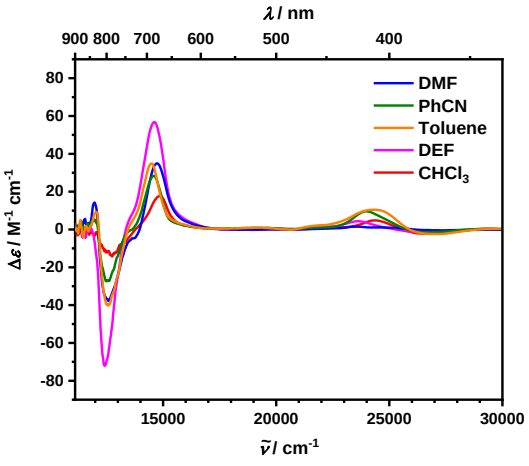

Figure 71. CD spectra of **p(Pr-SQB*)** in various solvents. Values for $\Delta\varepsilon$ reported per monomer unit.

The overall shape of all the experimentally obtained CD spectra is roughly identical and consists of an excitonic couplet with a negative band corresponding to the lower excitonic transition and thus the main absorption band between 12 400 and 12 600 cm^{-1}, as well as a

higher-energy positive band between 14 500 and 14 900 cm^{-1}. Although the shape of the obtained spectra is similar in all of the tested solvents, the magnitude varies greatly, as $\Delta\varepsilon$-values for the low-energy transition range from -14.3 in chloroform to -72.0 in DEF. As the absolute values of the experimentally obtained rotational strengths are roughly equal (see Table 18), these CD spectra can be deemed as approximately conservative. Comparing the spectra in different solvents reveals an additional sharp CD signal at 12 000 cm^{-1} in certain cases, which is especially pronounced in DMF and may be the result of either the contribution of additional states in the polymer or the presence of other conformers. The obtained g_{abs}-values lie within the range between 1.38×10^{-4} cgs for the lower-energy transition in $CHCl_3$ and 1.03×10^{-3} cgs for the higher-energy transition in DEF, which is 1-2 orders of magnitude larger compared to that of the monomer (5.1×10^{-5} cgs). As in the case of the other SQB-type homopolymers described in section 5.4.2, this is the result of an increased rotational strength due to excitonic coupling via the $R_{e\text{-}m}$ and R_{ex} terms in eq. (42). Also, the adoption of different conformations possessing different CD spectra leads to the requirement of the g_{abs}-values being interpreted with care.

Even though the CD spectra are reminiscent of the ones obtained for the helical polymers described in section 4.3 at first glance, there are several crucial differences. Firstly, the position of the CD bands is different, as the absorption spectra are those of a different aggregation type, thus leading to the observed bands corresponding to different states overall. Additionally, the spectra of the helical polymers possess an additional CD signal corresponding to a magnetically allowed and electronically quasi-forbidden low-energy (11 800 cm^{-1}) transition, which is polarized along the helix axis (ring contribution at E_0, see section 1.2.3), which is completely absent in the present case. Lastly, the obtained dissymmetry factors and rotational strengths for the electronically allowed transitions are even larger (by a factor of up to 7) due to the signal originating from the chiral superstructure itself.

Table 18. Chiroptical data (CD bands $\tilde{\nu}_{CD}$, difference in absorption $\Delta\varepsilon$, rotational strengths R_{exp} and dissymetry factors g_{abs}) of **p(Pr-SQB*)** in various solvents.

	$\tilde{\nu}_{CD}$ (λ_{CD}) / cm^{-1} (/ nm)	$\Delta\varepsilon$ / M^{-1} cm^{-1} [a]	R_{exp} / 10^{-40} cgs [a c]	$\lvert g_{abs}(\tilde{\nu}_{max})\rvert$ / cgs [a b]
DMF	12 600 (795)	-37.8	-61.9	5.55×10^{-4}
	14 700 (679)	35.0	59.6	6.16×10^{-4}
PhCN	12 500 (798)	-27.3	-37.8	3.13×10^{-4}
	14 600 (686)	28.4	44.4	5.33×10^{-4}
Toluene	12 600 (795)	-40.2	-56.0	4.62×10^{-4}
	14 500 (691)	34.9	56.9	7.40×10^{-4}
DEF	12 400 (806)	-72.0	-97.3	7.92×10^{-4}
	14 600 (685)	56.8	109	1.03×10^{-3}
$CHCl_3$	12 700 (785)	-14.3	-27.1	1.38×10^{-4}
	14 900 (673)	17.7	30.5	4.05×10^{-4}

[a] values per monomer unit. [b] $\Delta\varepsilon(\tilde{\nu}_{max})/\varepsilon(\tilde{\nu}max)$. [c] determined by integration of the CD band and calculated using eq. (75) in the appendix.

6.4 TD-DFT calculations[1]

In order to better understand the experimental observations, theoretical calculations were performed on the AM1 level of theory and summarized in Figure 72.

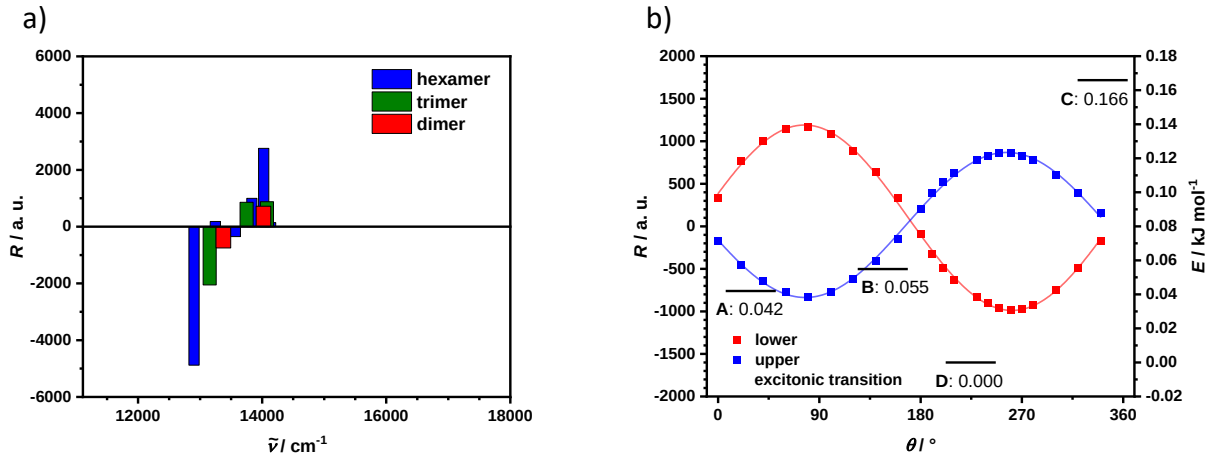

Figure 72. a) Calculated rotational strengths for an AM1-optimized **Pr-SQB*** dimer, trimer and hexamer. b) Calculated rotational strengths (squares) dependent on the dihedral angle of the upper (blue) and lower (red) excitonic transitions fitted with a sine function (lines). Relative energies of the conformations depicted in Figure 62 (conformer D is set as zero energy) are shown as black bars labeled with their corresponding relative energies in kJ/mol.

The calculated CD spectra of the dimer, trimer and hexamer shown in Figure 72a are similar in shape, which was also analogously observed when comparing the **Ph-SQB*** oligomers and polymers in chapter 5, thus leading to the dimer being a sufficient model system for the explanation of the underlying effects. The dependency of the rotational strength of the dimer on the dihedral angle θ is shown in Figure 72b for both transitions and nicely adheres to the expected sine dependency. This observation, alongside the consideration that the rotational strength of the monomeric building block is rather small, leads to the assumption that the R_{ex} term of eq. (42) constitutes the main contribution to the overall rotational strength.

As in the case of the **Ph-SQB*** oligo- and polymers, geometry optimizations revealed the same four local minima in terms of energy (conformations A-D see Figure 62). Therefore, it is assumed that the dihedral angle mainly adopts one of these values and the variation in magnitude does not stem from a change in preferred dihedral angle in different solvents, but rather a different degree of chiral discrimination. Contrary to the former case, the shapes of all CD spectra are similar in all solvents. As the exciton chirality is negative in this case, it can be concluded that in all of the tested solvents the conformation is predominately *anti*. This

[1] Theoretical calculations performed by Dr. M. Holzapfel

can possibly be explained by the preference for the *trans*-conformation, where the *anti*-conformation (D) is slightly more stable compared to the analogous *syn*-conformation (B), although the difference in energy is nearly negligible (0.055 kJ mol^{-1}). Perhaps specific interactions with solvent molecules similar to the case of the SQB helix described in chapter 4 may be the cause for this conformational preference. Nevertheless, this trend is clearly obvious and can also intuitively be explained by the steric hindrance present in the respective conformers A-D, although the employed methodology was not able to fully and definitively explain the underlying origins of this observation in this case as well.

6.5 Conclusions

The synthesis of **p(Pr-SQB*)** was straightforward and consisted of the polymerization of its respective monomeric building block **Br_2-Pr-SQB*** via Yamamoto-homocoupling. After fractionization via preparative GPC, the obtained polydispersity and degree of polymerization were comparable to those obtained for the tetramethyl-substituted analogues discussed in chapter 4.

The linear optical properties (absorption and fluorescence) of **p(Pr-SQB*)** showed the exclusive formation of a J-type conformation in all of the tested solvents, and closely examining the respective absorption and fluorescence data pointed towards a relatively high degree of conformational order when compared to the series of polymers bearing different chiral side chains (similar to the case of **p(SQB-R^3*)**). Furthermore, the obtained data was similar to those obtained for the **Ph-SQB*** containing homopolymers **p(SQB-SQB*)** and **pSQB***. Interestingly, a higher-than-expected quantum yield was observed for **p(Pr-SQB*)**, hinting at an influence of the propyl groups on the fluorescence properties in the polymer.

As expected, due to the lack of a helical conformation, the CD spectra did not bear the characteristic CD “fingerprint” of the SQB-helix. In this case, the CD spectra could be described as a negative exciton couplet, where the spectral shape was preserved when changing the solvent, which was in stark contrast to the solvent-dependent CD spectra of the **Ph-SQB***-containing SQA-SQB-type cooligo- and polymers, as well as the analogous SQB-type homooligo- and polymers. Similar to the latter cases, the rotational strength was increased here as well due to excitonic coupling of the monomer electric and magnetic transition

moments according to eq. (42), leading to g_{abs}-values of up to 1.03×10^{-3} cgs observed for the upper excitonic transition in DEF.

Theoretical calculations on the AM1 level of theory revealed a universal bias towards the *anti*-conformations as apparent by the sign of the CD spectra – specifically the *trans*-conformer D as this possessed the lowest calculated energy, although the differences in relative energies of the four main conformations were negligibly small (< 0.16 kJ mol^{-1}). The reason for the chiral bias is speculated to be specific interactions with solvent molecules. As previously stated, this is in contrast to the **Ph-SQB*** oligo- and polymers discussed in chapter 5, where using different solvents resulted in different spectral shapes and thus preferred conformations, where a clear favoring of the *cis*-conformations was apparent in chloroform for all the investigated compounds. Unfortunately, the underlying reason for the chiral/conformational discrimination remains not fully understood.

7 CONCLUSIONS AND OUTLOOK

7.1 English

In this work, various chirally substituted indolenine squaraine monomers of the SQB-type were successfully synthesized and utilized for the construction of various oligo- and polymers, in order to study their chiroptical properties in terms of exciton chirality. The quaternary carbon atom at the 3-position of the indolenine subunit, as well as the alkyl side chain attached to the indolenine nitrogen were selected as the most suitable site for chiral functionalization.

The first step of this project was the development of a synthetic methodology that enabled the preparation of these types of chirally substituted squaraines. For the C(3)-chiral derivatives, two routes depending on the desired substitution at the stereogenic center were established. In order to introduce a phenyl substituent at this position, an asymmetric synthesis of C(3)-chiral oxindoles developed by Smith et al.[239] was employed, where the reaction of a nitrone and a ketene in a percicyclic reaction cascade led to the formation of the desired oxindoles in a high enantiomeric purity of > 97%. This route further proved to be very efficient, as most of the reaction steps resulted in sufficiently high yields of 70% or greater. Due to the ketene only being stable when bearing aromatic residues, a different method was

required for the synthesis of the analogous *n*-propyl substituted derivatives. Here, the indolenine was prepared racemically and was subsequently resolved. This was achieved by kinetic resolution using an asymmetric hydrogenation developed by Fan et al.,[243] as well as resolution by preparative HPLC using a chiral stationary phase. In this case, the latter proved to be superior due to the low selectivity of the hydrogenation reaction, which resulted in low yields of 16-20%. Nevertheless, both methods afforded the indolenine in a high enantiomeric purity of > 98%. The chiral side chains **R^{2*}** and **R^{3*}** were prepared via Evans asymmetric alkylation of the respective carbamates,[268] where the resulting branching point at the 2-position constituted the chiral center.

While the chiral substitution only had minor effects on the linear optical properties and geometric structure of the chromophore (introduction of a phenyl group at the 3-position led to bathochromic shift of absorption and emission band, as well as a slight curvature of the chromophore structure, although these two observations were proven to be not causally linked), all compounds exhibited a distinct and measurable CD signal. It was found that an increasing distance of the chiral perturbation to the chromophore led to a decrease of the aforementioned CD signal as previously discussed by Moscowitz and Snatzke.[12, 14, 274] Furthermore, it was proven by TD-DFT calculations that the electric and magnetic transition moments are generally quite large, but almost mutually orthogonal. The proven synthetic methodology may enable the synthesis of different derivatives, e.g., different aromatic residues at C(3) bearing electron donating or withdrawing groups, in order to systematically vary the chiroptical properties by changing the magnitude and orientation of the electric and magnetic transition moments, which then can in turn be used to design oligo- and polymers with specific properties, since this greatly affects the R_{mon} and $R_{e\text{-}m}$ terms in eq. (42).

As SQB-homooligo- and polymers adopt helical conformations in solution,[91-92] the use of chiral side chains was tested as a means for the induction of a twist-sense bias. Therefore, various polymers bearing chiral side chains, where the size of the substituent and the position of the chiral center were systematically varied, were prepared via Yamamoto-homocoupling of the respective dibrominated monomer compounds. As for the previously studied achiral analogues, absorption spectroscopy revealed a solvent dependent H- or J-type behavior, that was ascribed to the formation of a helix or random coil superstructure, respectively. Interestingly, the side chains had an impact on the conformations in solution, as moving the branching point closer to the chromophore and increasing its size significantly favored the

formation of the J-type structure in **p(SQB-R^{3}*)** in most solvents. Indeed, CD spectroscopy revealed that the resulting helices possessed a twist-sense bias, as large $\Delta\varepsilon$ and g_{abs}-values were found for all of the chiral polymers in solvents which facilitated the formation of helices. In order to quantify the thermodynamic parameters of the (*M*- and *P*-) helix-coil equilibrium, temperature dependent UV-Vis-NIR absorption and CD spectroscopy was performed in PhCN and DMF. As expected, increasing the temperature led to an unfolding of the helix, which was apparent by the diminishing intensity of the H-band (along with the concomitant emergence of the J-band), as well as the decreasing CD signal. Fitting the temperature dependent absorption data enabled the determination of the thermodynamic parameters, which revealed the presence of independent helical sections, where the length increased throughout the investigated series from **p(SQB-R^{0})** to **p(SQB-R^{3}*)**. Comparison of the CD and absorption data showed a varying solvent-dependent degree of homohelicity, which was also dependent on the side chain. While the random coil conformations displayed fluorescence from the lowest-lying energetic state according to Kasha's rule, the helical conformation unexpectedly exhibited a sharp fluorescence signal at 11 800 cm^{-1} in toluene. CPL spectroscopy then revealed a large g_{lum}-value of 0.053 cgs, which further rigidified this assignment. In future studies, the chiroptical properties could further be tailored by variation of the geometrical parameters (pitch, diameter) of the helix, e.g., by inserting linkers (such as *m*-phenyl or thiophene) in between the squaraine units or by squeezing the SQB chromophores through introduction of a methyl group at the methine bridge in order to reduce the diameter of the resulting helix.

The **Ph-SQB*** moiety was selected for the incorporation into various alternating cooligo- and polymers (**SQA-SQB*** and **SQB-SQB***), as well as **Ph-SQB*** homooligo- and polymers. The oligomers were synthesized following the well-established semisquaraine route via Suzuki-coupling of the respective mono- and dibrominated and borylated monomers. [91, 96, 260, 299-300] Copolymers were synthesized by copolymerization via Suzuki coupling, whereas the **pSQB***-homopolymer was synthesized via Yamamoto-homocoupling. While the linear absorption and fluorescence properties of the di- and trimers were basically identical to their achiral counterparts, all of the polymers exclusively displayed a solvent-independent J-type absorption behavior, indicating the presence of only random coil type conformations, which is in contrast to the solvent-dependent adoption of helix (type) conformations of their tetramethyl-substituted analougues. Interestingly, in contrast to the absorption behavior, the

CD spectra possessed a pronounced solvent dependency, where the shape and magnitude greatly varied when comparing those obtained in different solvents. As the shape of the CD spectra was similar in all cases when comparing the dimer to the trimer and the polymer, TD-DFT calculations on the dimers were performed in order to elucidate the underlying reasons for this peculiar observation. Geometry optimizations revealed four main conformations possessing different dihedral angles θ, which can be classified as *cis*/*trans* (regarding the mutual orientation of the chromophores) and *syn*/*anti* (with respect to the adjacent phenyl group). Due to the mutual orientation of the chromophores being similar in all cases, the absorption properties remained largely unchanged, while different solvents led to the favoring of either the *syn*- or the *anti*-conformers. In chloroform, the *syn*-conformers were clearly favored, as evident by the sign and shape of the CD spectra, whereas in toluene a very slight bias towards the *anti*-conformations was observed, along with a much lesser degree of chiral discrimination overall in **SQA-SQB*** and **SQB-SQB***. This was not the case for **dSQB***, as here the anti-conformation was clearly favored, which indicates that the large phenyl groups influence the conformations in solution, possibly by exerting a larger degree of steric hindrance. No explanation regarding the reason for this specific solvent dependency can be put forward at this point. In future studies, the problem of the varying dihedral angle can be circumvented by fixating it using certain bridge/linker units, as similarly done with the anthracene-bridged dimer in Figure 57c. This may enable the systematic study of the dihedral angle dependence of R and the isolation/quantification of the three main contributions R_{mon}, $R_{e\text{-}m}$ and R_{ex} of the Rosenfeld-equation (42). Furthermore, the steric hindrance of the phenyl groups may be used to construct conformationally stable axially chiral squaraine dimers, which are linked via the *meta*-position, such as the one depicted in Figure 73.

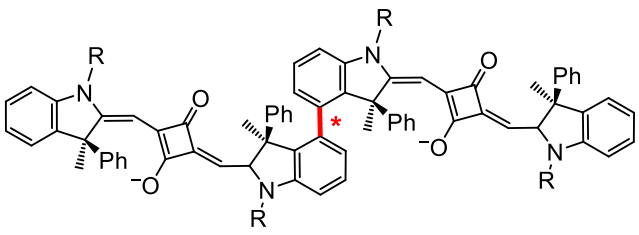

Figure 73. Axially chiral Ph-SQA*-dimer.

The last chapter dealt with the **Pr-SQB*** homopolymer, which was synthesized via Yamamoto-homocoupling of **Br_2-Pr-SQB***. Here, absorption spectroscopy revealed the exclusive formation of random coil conformations, which cements the claim that substituents larger

than a methyl group at C(3) definitively preclude the helix folding in SQB-polymers. In this case, smaller substituents, such as the replacement of a methyl group by a fluorine atom, may be tested in future studies. The CD spectra showed a constant shape and a variation in magnitude when changing the solvent. The rotational strengths and g_{abs}-values were significantly increased compared to the monomer, which is a direct result of exciton coupling according to eq. (42). Contrarily to the phenyl substituted derivatives, the *anti*-conformers were favored in all solvents, as revealed by TD-DFT calculations.

7.2 Deutsch

In der vorliegenden Arbeit wurden verschiedene chiral substituierte Indolenin-Squarain-Monomere des SQB-Typs erfolgreich synthetisiert und für den Aufbau verschiedener Oligo- und Polymere verwendet, um deren chiroptischen Eigenschaften im Rahmen der Exzitonenchiralität zu untersuchen. Sowohl das quartäre Kohlenstoffatom an der 3-Position der Indolenineinheit sowie die Alkylkette, die an das Stickstoffatom des Indolenins gebunden ist, wurden als geeignete Stellen für die chirale Funktionalisierung ausgewählt.

Der erste Schritt dieses Projekts war die Entwicklung einer Synthesestrategie für die chiral substituierten Squaraine. Für die C(3)-chiralen Derivate wurden zwei Routen in Abhängigkeit der Art der Substituenten am Chiralitätszentrum etabliert. Um eine Phenylgruppe an dieser Position einzuführen wurde eine von Smith et al.[239] entwickelte asymmetrische Synthese von C(3)-chiralen Oxindolen eingesetzt, bei der die Reaktion eines Nitrons mit einem Keten in einer Kaskade aufeinanderfolgenden pericyclischen Reaktionen zur Bildung der Oxindole in hoher Enantiomerenreinheit (> 97 %) führte. Diese Methode erwies sich zudem als sehr effizient, da die meisten Reaktionsschritte in ausreichend hohen Ausbeuten von über 70 % erfolgten. Da jedoch diese Ketenderivate nur mit aromatischen Resten ausreichend stabilisiert sind, musste eine alternative Methode für die Darstellung der *n*-Propyl substituierten Derivate verwendet werden. In diesem Fall wurde das Indolenin als Racemat hergestellt, welches darauffolgend getrennt wurde. Dies gelang mittels einer von Fan et al.[243] entwickelten asymmetrischen Hydrierung oder durch Trennung mittels HPLC an chiraler stationärer Phase. In diesem Fall erwies sich Letzteres als besser geeignet, da die Hydrierung wenig selektiv war und daher nur in niedrigen Ausbeuten von 16-20 % resultierte. Dennoch führten beide Methoden der Racemattrennung zu einer hohen stereochemischen Reinheit von > 98 %. Die chiralen

Seitenketten **R^{2*}** und **R^{3*}** wurden mithilfe der asymmetrischen Evans-Alkylierung der entsprechenden Carbamate[268] synthetisiert, bei der die resultierende Verzweigung an der 2-Position das Chiralitätszentrum darstellte.

Während sich die chirale Substitution kaum auf die linearen optischen Eigenschaften und die geometrische Struktur der Chromophore auswirkte (der Einbau einer Phenylgruppe führte zu einer bathochromen Verschiebung der Hauptabsorptionsbande sowie einer leichten Krümmung des Squarainchromophors, obwohl diese Beobachtungen nicht kausal zusammenhängten), zeigten alle Verbindungen ein deutlich messbares CD-Signal. Es wurde festgestellt, dass eine zunehmende Entfernung des Chiralitätszentrums zum Chromophor zu einer Abnahme des CD-Signals führte, wie zuvor von Moscowitz und Snatzke diskutiert.[12, 14, 274] Weiterhin wurde durch TD-DFT-Rechnungen bewiesen, dass die elektrischen und magnetischen Übergangsmomente im Allgemeinen recht groß, aber nahezu orthogonal zueinander sind. Die erwiesene Synthesemethodik könnte weiterhin die Darstellung verschiedener Derivate ermöglichen, wie beispielsweise verschiedene aromatische Reste am C(3)-Atom mit zusätzlichen elektronenziehenden oder -schiebenden Gruppen. Dies ermöglicht die systematische Variation der chiroptischen Eigenschaften durch Veränderung des Betrags und der Orientierung der elektrischen und magnetischen Übergangsmomente. Dadurch könnten gezielt Oligo- und Polymere mit spezifischen Eigenschaften konstruiert werden, da dies die R_{mon} und $R_{e\text{-}m}$ Terme von Gleichung (42) signifikant beeinflusst.

Da SQB-Homooligo- und -polymere in Lösung helikale Konformationen ausbilden können,[91-92] wurde die Verwendung chiraler Seitenketten als Methode der Induktion einer bevorzugten Windungsrichtung getestet. Deshalb wurden verschiedene Polymere mit unterschiedlichen Seitenketten mittels Yamamoto-Homokupplung der entsprechenden dibromierten Monomerverbindungen synthetisiert, bei welchen die Größe des Substituenten und die Position des Chiralitätszentrum systematisch variiert wurden. Wie im Falle der analogen achiralen Verbindungen konnte durch Absorptionsspektroskopie ein lösungsmittelabhängiges J- oder H-Typ-Verhalten beobachtet werden, was auf die Ausbildung von Helices und Random-Coil Konformationen zurückzuführen ist. Interessanterweise wirkten sich die Seitenketten auf die gebildeten Konformationen aus, da ein größerer Substituent mit einem an dem Chromophor näheren Verzweigungspunkt die Ausbildung einer Random-Coil Superstruktur im Falle von **p(SQB-R^{3*})** in den meisten Lösungsmitteln begünstigte. Mittels CD Spektroskopie konnte die Homohelizität bewiesen werden, da alle chiralen Verbindungen in Lösungsmitteln,

die eine Helixfaltung begünstigen, große $\Delta\varepsilon$ und g_{abs}-Werte aufwiesen. Um die thermodynamischen Parameter des (*M*- und *P*-) Helix-Coil Gleichgewichts zu quantifizieren, wurde temperaturabhängige Absorptions- und CD-Spektroskopie in DMF und PhCN durchgeführt. Wie erwartet führte eine Erhöhung der Temperatur zu einer Entfaltung der Helix, was durch die Abnahme der Intensität der H-Bande (und einhergehendem Aufkommen der J-Bande) und des CD Signals bestätigt wurde. Durch Fitten der temperaturabhängigen Absorptionsdaten konnten die thermodynamischen Parameter daraus ermittelt werden, welche auf das Vorhandensein unabhängiger helikaler Segmente, deren Länge innerhalb der Serie von **p(SQB-R^0)** nach **p(SQB-R^3*)** zunahm, deutete. Der Vergleich dieser Daten mit den temperaturabhängigen CD Daten zeigte einen lösungsmittelabhängigen Grad der Homohelizität, welcher auch abhängig von der verwendeten Seitenkette war. Während die Random-Coil Strukturen Fluoreszenz vom energetisch niedrigsten Zustand zeigten, zeigte die Helix unerwarteterweise ein scharfes Fluoreszenzsignal bei 11 800 cm^{-1} in Toluol. Anhand von CPL-Spektroskopie, durch welche ein g_{lum} -Wert von 0.053 cgs ermittelt wurde, konnte diese Zuordnung nochmals bestätigt werden. In weiteren Studien könnten die chiroptischen Eigenschaften durch Veränderung der geometrischen Parameter (Durchmesser, Ganghöhe) der Helix angepasst werden, wie z.B. durch das Einführen von Linkern (wie *m*-phenyl oder Thiophen) zwischen den Squaraineinheiten oder alternativ durch das „Quetschen“ der Squarainchromophore (wie z.B. das Anbringen von Methylgruppen an der Methinbrücke), um den Durchmesser der daraus resultierenden Helix zu verkleinern.

Die **Ph-SQB***-Einheit wurde für den Einbau in verschiedene alternierende Cooligo- und -polymere (**SQA-SQB*** und **SQB-SQB***) sowie **Ph-SQB*** Homooligo- und -polymere gewählt. Die Oligomere wurden über die literaturbekannte Semisquarain-Route mittels Suzuki-Kupplung der jeweiligen mono- und dibromierten und borylierten Monomere synthetisiert. [91, 96, 260, 299-300] Copolymere wurden über die Suzuki-Kreuzkupplung dargestellt, während Homopolymere mittels Yamamoto-Hokokupplung synthetisiert wurden. Während die linearen Absorptions- und Fluoreszenzeigenschaften der Di- und Trimere im Wesentlichen identisch mit denen der jeweiligen achiralen Derivate waren, zeigten alle Polymere eine lösungsmittelunabhängige J-Typ Absorption, was auf das ausschießliche Vorhandensein von Random-Coil Konformationen hinweist. Dies ist im Gegensatz zu den jeweiligen analogen tetramethylsubstituierten Polymeren, welche abhängig vom eingesetzten Lösungsmittel helix(artige) Strukturen ausbilden. Interessanterweise zeigten diese Verbindungen im

Gegensatz zur Absorption deutlich lösungsmittelabhängige CD Spektren, bei denen die Bandenform und deren Intensität sich beim Verwenden unterschiedlicher Lösungsmittel deutlich unterschied. Weil die CD Spektren der Dimere in allen Fällen denen der Tri- und Polymere ähnelten, wurden TD-DFT Rechnungen von den Dimeren durchgeführt, um die Ursache für diese merkwürdige Beobachtung zu ermitteln. Geometrieoptimierungen ergaben vier Hauptkonformationen mit unterschiedlichen Diederwinkeln θ, die als *cis*/*trans* (in Bezug auf die Anordnung der Chromophore zueinander) und *syn*/*anti* (in Bezug auf die benachbarte Phenylgruppe) klassifiziert werden konnten. Aufgrund der in allen Fällen ähnlicher gegenseitiger Anordnung der Chromophore blieb das Absorptionsverhalten unverändert, während in unterschiedlichen Lösungsmittel jeweils *syn*- oder *anti*-Konformationen bevorzugt eingenommen wurden. In Chloroform waren die *syn*-Konformere eindeutig bevorzugt, wie aus dem Vorzeichen und der Form der CD-Spektren hervorgeht, während in Toluol eine sehr leichte Tendenz zu den *anti*-Konformationen beobachtet wurde, zusammen mit einer insgesamt viel geringeren chiralen Diskriminierung in **SQA-SQB*** und **SQB-SQB***. Dies war bei **dSQB*** nicht der Fall, da hier die *anti*-Konformation eindeutig begünstigt war, was darauf hindeutet, dass die großen Phenylgruppen die Konformation in Lösung beeinflussen, möglicherweise durch eine stärker ausgeprägte sterische Hinderung. Zum jetzigen Stand konnte bisher keine Erklärung dieser spezifischen Lösungsmittelabhängigkeit gefunden werden. In zukünftigen Projekten könnte das Problem der variablen Diederwinkel durch Fixierung mittels geeigneter Linker/Brückeneinheiten umgangen werden, ähnlich wie beim Anthracen-verbrückten Dimer, dargestellt in Abbildung 57c. Dies würde die systematische Untersuchung der Winkelabhängigkeit der Rotationsstärke R und die Isolierung/Quantifizierung der einzelnen Beiträge R_{mon}, $R_{e\text{-}m}$ und R_{ex} der Rosenfeldgleichung (42) ermöglichen. Darüber hinaus könnte die sterische Hinderung durch die Phenylgruppen dazu verwendet werden, um konformativ stabile axial chirale Squaraindimere, welche *meta*-verknüpft sind, herzustellen (siehe Abbildung 73).

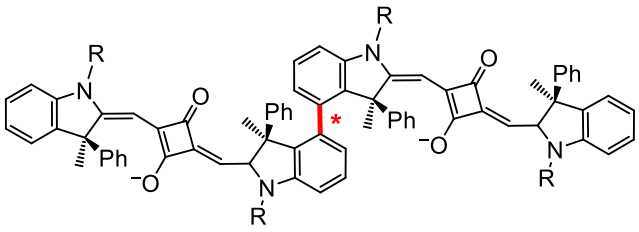

Abbildung 73. Axial chirales Ph-SQA*-Dimer.

Das letzte Kapitel befasste sich mit dem **Pr-SQB***-Homopolymer, welches durch Yamamoto-Homokupplung von **Br_2-Pr-SQB*** synthetisiert wurde. Hier konnte durch Absorptionsspektroskopie die ausschließliche Bildung von Random-Coil Konformationen gezeigt werden, was zur Behauptung führt, dass größere Substituenten als eine Methylgruppe am C(3)-Atom definitiv die Helixfaltung von SQB-Polymeren verhindern. In diesem Fall können in zukünftigen Studien kleinere Substituenten, wie der Ersatz einer Methylgruppe durch ein Fluoratom getestet werden. Die CD-Spektren zeigten eine konstante Bandenform und eine lösungsmittelabhängige Intensität. Die Rotationsstärken und g_{abs}-Werte waren im Vergleich zum Monomer signifikant erhöht, was eine direkte Folge der Exzitonenkopplung nach Gleichung (42) ist. Im Gegensatz zu den phenylsubstituierten Derivaten waren die *anti*-Konformere allen Lösungsmitteln bevorzugt, wie TD-DFT-Rechnungen zeigten.

8 EXPERIMENTAL SECTION

8.1 Materials and methods

Absorption spectroscopy

- JASCO V670 UV-Vis-NIR spectrophotometer
- Agilent Technologies Cary 5000 UV-Vis-NIR spectrophotometer

Solvents for spectroscopic studies were of spectroscopic grade und used as received. Absorption spectra were measured in quartz cuvettes with path lengths of 10 mm at 293 K with concentrations ranging from ca. 10^{-6} to 10^{-5} M and referenced against the pure solvent. Variable temperature absorption measurements were executed with an external cryostat OptistatDN (Oxford Instruments Nanoscience, England). The cryostat was accurately placed into the beam path of the Agilent Technologies Cary 5000 UV/vis/NIR spectrophotometer. The temperature was manually regulated with an electronic temperature control unit. The measuring cell was purged with argon prior to inserting the sample and sealed with a cuff to exclude moisture.

Fluorescence spectroscopy

- Edinburgh Instruments FLS980 fluorescence lifetime spectrometer 450 W Xenon lamp/ PMT (R5509-42)

Steady-state emission spectra were recorded at 298 K in 10 mm quarts cells from Starna (Pfungstadt, Germany). The emission and excitation spectra were measured with strongly diluted samples (OD @ λ_{max} < 0.05) in order to prevent self-absorption. The fluorescence quantum yields were determined with optically dense samples in an integrating sphere. The observed fluorescence quantum yields were afterwards corrected for self-absorption applying the method of Bardeen et al.[304] Fluorescence lifetimes were determined by time-correlated single-photon counting (TCSPC). The samples were excited by a pulsed laser diode under magic angle conditions and the fluorescence was detected with a high-speed PMT detector (H10720). Deconvolution of the data (4096 channels) was conducted by measuring the instrument response function with a scatterer solution consisting of colloidal silicon in

deionised water (LUDOX). The FAST software (version 3.4.2) was used to fit the decay curves with exponential decay functions.

CD spectroscopy

- Jasco 300 CD – CPL Hybrid spectrometer
- Jasco J-810 CD spectrometer

Solvents for spectroscopic studies were of spectroscopic grade und used as received from Acros Organics. Absorption spectra were measured in quartz cuvettes with path lengths of 1 mm or 10 mm at 293 K with concentrations ranging from ca. 10^{-6} to 10^{-5} M and referenced against the pure solvent. Variable temperature absorption measurements were executed with a CDF-426S Peltier element.

CPL spectroscopy

- Jasco 300 CD – CPL Hybrid spectrometer

CPL spectra were recorded with a customized JASCO CPL-300/J-1500 hybrid spectrometer. The CPL measurements were performed at 20 °C at different optical densities (OD @ λ_{max} = 1.5, 0.9, 0.6, 0.2). The values for g_{lum} were obtained from the integrated analysis software and the obtained CPL spectra were further smoothed for better quality. The spectra were corrected for self-absorption by a method developed by Castiglioni et al.,[139, 294] which is further described in section 11.6.

Flash chromatography

- Interchim PF 450 Flash-chromatography-system with a photodiode array UV-Vis-NIR detector (175-840 nm) and a fraction collector

Flash chromatography was performed using pre-packed Interchim PuriFlash PF-30SIHP (40 g or 25 g) columns.

GPC/HPLC

- Shimadzu instrument set: SPD-M20A diode array detector, CBM-20A system controller, LC-20AD solvent delivery unit, DGU 20A9 online degasser.
- Jasco instrument set 1: PU-1580 pump, DG-2080-53 three-line degasser unit, LC-980-025 ternary gradient unit, AS-2055 Plus automatic sampler, CO-1560 column oven, MD-2010 Plus diode-array detector.
- Jasco instrument set 2: LC-NetII ADC interface box, PU-2080 plus pump, DG-2080-53 online degasser, LV-2080-03 solvent selection valve unit, UV-2077 UV/vis detector.

Analytical HPLC measurements were performed on all of the instruments mentioned above using the conditions specified in the characterization data. Preparative HPLC was performed using a preparative Phenomenex LUX i-Amylose 3 column on the Jasco instrument set 2, preparative GPC on the Shimadzu or Jasco instrument set 2 using two SDV columns (50 Å, 500 Å; particle size 10 µm, 20 × 600 mm) from PSS.

X-ray crystallography

- Bruker D8 Quest Kappa Diffractometer with a Photon100 CMOS or CPAD PhotonII detector and multi-layered mirror monochromated CuKα radiation.
- Rigaku XtaLAB Synergy, Dualflex Diffractometer with a HyPix detector and multi-layered mirror monochromated CuKα radiation.
- Rigaku OD XtaLAB Synergy-S diffractometer with a HPAD area detector and multi-layer mirror monochromated CuK$_\alpha$ radiation.

X-ray diffraction data were collected at 100 K on one of the systems mentioned above. The structure was solved using direct methods or the intrinsic phasing method ShelXT,[305] expanded with Fourier techniques and refined with the ShelX or ShelXL[306] software package. All non-hydrogen atoms were refined anisotropically. Hydrogen atoms were included in the structure factor calculation on geometrically idealized positions. Plots were done using the software package OLEX2.[307]

NMR spectroscopy

- Avance III HD 400 FT-Spectrometer (^{1}H: 400.13 MHz, ^{13}C: 100.61 MHz) with a Bruker Ultrashield magnet
- Avance III HD 400 FT-Spectrometer (^{1}H: 400.03 MHz, ^{13}C: 100.59 MHz) with a Bruker Ascend magnet
- Avance III HD 600 FT-Spectrometer (^{1}H: 600.13 MHz, ^{13}C: 150.90 MHz) with an Oxford Instrument magnet
- Avance III HD 600 FT-Spectrometer (^{1}H: 600.43 MHz, ^{13}C: 150.98 MHz) with a Bruker Ascend magnet

^{1}H and ^{13}C NMR spectra were recorded with one of the spectrometers above. Standard commercially available deuterated solvents were used without further purification. The 400 MHz spectrometers run at 300 K, while the 600 MHz spectrometers use different temperatures for specific solvents, e.g. 303.6 K for $CDCl_3$ or 293.5 K for CD_2Cl_2. Chemical shifts are given in ppm relative to the frequency of tetramethylsilane and the solvent signal (for ^{1}H NMR the respective residual proton signal)[308] (^{1}H: $CDCl_3$: δ 7.26 ppm, CD_2Cl_2: δ 5.32 ppm, CD_3OD: δ 3.31 ppm, $(CD_3)_2CO$: δ 2.05 ppm; ^{13}C: δ $CDCl_3$: δ 77.16 ppm, CD_2Cl_2: δ 53.84 ppm, CD_3OD: δ 49.00 ppm, $(CD_3)_2CO$: δ 29.84 ppm) was used as an internal standard. The abbreviations used for declaration of the spin multiplicities and C-atom depictions are: s = singlet, d = doublet, dd = doublet of doublet, t = triplet, q = quartet, sept = septet, m = multiplet, br = broad, prim. = primary, sec. = secondary, tert. = tertiary, quart. = quaternary. Overlapping signals of chemically non-equivalent protons in proton NMR spectra that could not be assigned to first-order couplings are given as m'.

Mass spectrometry

- Bruker Daltonics autoflex II (MALDI)
- Bruker Daltonics microTOF focus (ESI, APCI)
- Finnigan MAT90 (EI)

Mass spectra were recorded with a Bruker Daltonics autoflex II (MALDI) in positive mode (POS) using a DCTB (trans-2-[3-(4-tert-butylphenyl)-2-methyl-2-propenyl-idene]malononitrile) matrix, with a Bruker Daltonic microTOF focus (ESI, APCI) or a Finnigan MAT90 (EI). All mass

spectrometry peaks are reported as m/z. For calculation of the respective mass values of the isotopic distribution, the software module “Bruker Daltonics IsotopePattern” from the software Compass 1.1 from Bruker Daltonics GmbH, Bremen was used. Calculated (calc.) and measured (found) peak values always correspond to the most intense peak of the isotopic distribution unless stated otherwise.

8.2 Synthesis

All reactions were performed in standard glass ware and chemicals that were obtained from commercial suppliers were used without further purification. For reactions under nitrogen atmosphere, the nitrogen was dried with Sicapent® from Merck, oxygen was removed with a cupric oxide catalyst R3-11 from BASF and standard Schlenk techniques were used. Solvents for oxygen- and/or moisture-sensitive reactions were purified and dried using a solvent purifying system from Inert and sparged with nitrogen prior to use. A conventional oil bath was used for heating. All reactions were monitored by analytical thin-layer chromatography (unless stated otherwise), which was performed on Macherey-Nagel ALUGRAM® Xtra SIL G/UV_{254} plates. Visualization was achieved using UV light, iodine vapor or submersion in either a solution containing $KMnO_4$ or ammonium molybdate/cerium sulfate (Henessian’s Stain). Column chromatography was performed on silica gel (Macherey-Nagel “Silica 60 M”, 40 – 63 µm).

The compounds phenylhydroxylamine,[309-310] 4-bromophenylhydroxylamine,[309-310] triethylammonium 3-(dicyanomethylene)-2-ethoxy-4-oxocyclobut-1-en-1-olate (**CN**),[90, 311] 5-bromo-2-methyl-3-propylindole (**12**),[312-313] 2-methyl-3-propylindole (**11**),[312-313] *N*-((1*R*,2*R*)-2-amino-1,2-diphenylethyl)-4-(trifluoromethyl)benzenesulfonamide (**15**),[314] compound (**16**),[315] **Cat***,[315] 5-bromo-2,3,3-trimethyl-3*H*-indole,[316] 2,3,3-trimethyl-3*H*-indole,[316] 7-methyloctanol (**25**),[269] (*S*)-1-iodo-3,7-dimethyloctane (**31b**),[265] (*S*)-5-bromo-1-(3,7-dimethyloctyl)-2,3,3-trimethyl-3*H*-indol-1-ium iodide (**34b**)[89, 92, 94, 260] and 5-bromo-3,3-dimethylindolin-2-one (**32**)[273] were synthesized according to the reported literature procedures. **SQA** and **SQB** were thankfully provided by Dr. A. Turkin.

The reported yields and characterization data for enantiomeric compounds were similar and showed no systematic deviations in all cases. Chromatograms, as well as tables containing the documentation of stereochemical purity of the various batches of the precursor compounds

9, **10**, **13** and **14**, as well as **Ph-SQB***, **Pr-SQB***, **Ph-SQA***, **Pr-SQA***, **Br_2-Ph-SQB***, **Br_2-Pr-SQB***, **Br-SQB*-C6**, **Br-SQB*-C16** can be found in the appendix.

8.2.1 General procedures

General procedure for the N-Alkylation of 3,3-disubstituted oxindoles and isatine derivatives (GP I):[90, 242]

To a solution of the oxindole (1.0 eq, 200 µmol/mL) in anhydrous DMF was added dry K_2CO_3 (10.0 eq) under nitrogen atmosphere. The reaction mixture was then stirred for 30 min, after which the alkyl iodide (1.0-2.0 eq) was added dropwise and the reaction stirred at 85-100 °C for 18-64 hours. The mixture was then poured onto water and extracted with EA, dried over Na_2SO_4 and concentrated under reduced pressure. The residue was purified by column chromatography.

General procedure for the synthesis of 3,3-disubstituted N-alkyl-2-methylindol-1-ium chlorides from the respective oxindoles via nucleophilic addition of MeMgBr and subsequent acidic elimination with HCl (GP II):[90]

The N-alkylated oxindole (1.0 eq, 10.0 µmol/mL) was dissolved in anhydrous THF under nitrogen atmosphere. A solution of MeMgBr (4.0 eq, 3 M in Et_2O) was added dropwise and the reaction mixture stirred for 60 min at 65 °C. The reaction mixture was then quenched with MeOH and HCl (3 M in MeOH), before the solvent was removed in HV. The residue was dissolved in HCl (3 M in MeOH) and the mixture then stirred for 30 min, before being extracted with DCM and dried over $MgSO_4$. The solvent was then removed under reduced pressure and the residue was used immediately for further synthesis without purification. The yield was assumed to be quantitative.

General procedure for the Knoevenagel condensation of semisquaraine esters and malonic acid dinitrile using triethylamine (GP III):[299]

The semisquaraine ester (1.0 eq, 250 µmol/mL) and malonic acid dinitrile (1.1 eq) were dissolved in EtOH. NEt_3 (2.0 eq) was then added dropwise and the reaction stirred for 2-4 h at RT. The solvent was removed under reduced pressure and the crude product purified by column chromatography or used crude without further purification.

General procedure for the Miyaura borylation of bromo-substituted squaraines (GP IV):[96]

The brominated squaraine monomer (1.0 eq, 70.0 µmol/mL), bis(pinacolato)diboron (1.5-2.8 eq), potassium acetate (3.2 eq), $Pd(PhCN)_2Cl_2$ (5 mol%) and 1,1'-bis(diphenylphosphino)ferrocen (5 mol%) were suspended in anhydrous degassed 1,4-dioxane under nitrogen atmosphere. The mixture was stirred for 18 h at 85-100 °C. The solvent was then removed under reduced pressure and the crude product purified by column chromatography.

General procedure for the Suzuki coupling of bromo- and pinacolborato-substituted squaraine monomers using XPhos G2 and $CsCO_3$ (GP V):[91]

The brominated squaraine monomer (1.0 eq, 10.0 µmol/mL), the borylated squaraine monomer (2.0-3.5 eq), $CsCO_3$ (10.0 eq) and XPhos Pd G2 (3-6 mol%) were dissolved in a degassed mixture of THF/H_2O (4:1). The mixture was stirred for 18 h at 65 °C, before being extracted with DCM and dried over Na_2SO_4. The solvent was removed under reduced pressure and the crude product purified by flash chromatography followed by preparative GPC (DCM).

General procedure for the polymerization of dibromo-substituted squaraine monomers via Yamamoto homocoupling (GP VI):[92]

$Ni(COD)_2$ (2.4 eq, 140 µmol/mL), COD (2.4 eq) and 1,1'-bipyridine (2.4 eq) were dissolved in a degassed mixture of anhydrous DMF/toluene (1:1) and stirred at 65 °C for 30 min. A solution of the dibrominated squaraine monomer (1.0 eq, 0.04 mmol/mL) in DMF/toluene was then slowly added and the reaction mixture stirred for 10 d at 65 °C under the exclusion of light. The reaction mixture was then poured in a mixture of MeOH/HCl (20% in H_2O) (4:1) and the green precipitate filtered off. The crude product was placed in an extraction thimble and washed successively with *n*-hexane, MeOH and acetone (or DCM) using a Soxhlet extractor, until the solvent ceased to be colored. The *n*-hexane and MeOH extracts were discarded and the acetone (or DCM) extract was concentrated under reduced pressure, before being fractionated by preparative GPC (DCM). The final step was precipitation from either hexane or MeOH/H_2O (4:1). To evaluate the chain lengths and the molecular weight distribution, analytical GPC was performed using a PSS Linear S column and chloroform as an eluent.

General procedure for the synthesis of semisquaraine ethyl esters (GP VII):[96, 300]

The indolium salt (1.2 eq) was dissolved in EtOH/NEt_3 (4:1) and heated to reflux. Squaric acid diethylester (1.0 eq, 1.05 mmol/mL) was then added dropwise and the mixture stirred for 4 h. The solvent was removed and the residue purified by column chromatography.

General procedure for the nucleophilic addition of MeMgBr to N-alkylated isatine derivatives (GP VIII):[317]

The isatine derivative (1.0 eq, 200 µmol/mL) was dissolved in anhydrous THF under nitrogen atmosphere and cooled to -78 °C. A solution of MeMgBr (1.1 eq) was then added dropwise and the reaction mixture stirred for 1 h at -78 °C, before being slowly warmed up to 0 °C over 1 h. The reaction was then quenched with water and NH_4Cl, before being extracted with EA. and dried over Na_2SO_4. The solvent was removed under reduced pressure and the crude product purified by precipitation from pentane at -35 °C.

General procedure for the racemic synthesis of 3-methyl-3-phenyl substituted oxindoles using trifluoromethanesulfonic acid (GP IX):[90, 318]

A mixture of the 3-methyl-3-hydroxy substituted N-alkylated oxindole (1.0 eq), benzene (50 eq) and TfOH (100 eq) was stirred at RT overnight. The reaction mixture was then poured onto ice and extracted with $CHCl_3$. The organic phase was washed with water and brine, dried over $MgSO_4$, and the solvent removed under reduced pressure. The crude product was then purified by flash chromatography.

8.2.2 Side chain precursors

7-Methyloctanoic acid (26)

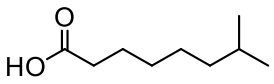

CAS: 693-19-6

Synthesis based on given literature.[270]

7-Methyloctanol (**25**) (8.07 g, 55.9 mmol) was dissolved in DCM (140 mL) and the solution cooled to 0 °C, before 4-MeO-TEMPO (104 mg, 559 µmol), Adogen464 (1.13 g, 2.80 mmol) and KBr (11.2 mL, 5.59 mmol, 0.5 M in H_2O) were added. A mixture of NaOCl (400 mL, 140 mmol, 0.35 M in H_2O) and $NaHCO_3$ (20.0 g, 238 mmol) was then slowly added under vigorous stirring (1300 rpm). The reaction mixture was then stirred for 40 min at 0 °C, before being basified with NaOH (pH < 12). The organic layer was removed and the aqueous phase was acidified with 6 M HCl (pH > 2), before being extracted with DCM and dried over $MgSO_4$. The solvent was then removed under reduced pressure and the crude product used without further purification.

Yield: 8.18 g (51.7 mmol, 92%) of a colorless oil.

$C_9H_{18}O_2$ [158.24]

^{1}H NMR (400.1 MHz, CD_2Cl_2):[1]

δ [ppm] = 2.34 (t, 2H, ^3J = 7.7 Hz, C-H$_2$), 1.67-1.57 (m, 2H, C-H$_2$), 1.52 (sept, 1H, ^3J = 6.6 Hz, C-H), 1.35-1.25 (m', 4H, C-H$_2$), 1.21-1.13 (m, 2H, C-H$_2$), 0.86 (d, 6H, ^3J = 6.6 Hz, C-H$_3$).

[1] The signal for the O-H proton was not observed due to rapid proton exchange.

7-Methyloctanoyl chloride (27)

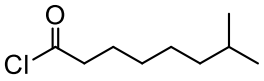

CAS: 122876-14-6

7-Methyloctanoic acid (**26**) (6.07 g, 38.4 mmol) was dissolved in thionyl chloride (80.0 mL, 131 g, 1.10 mol) and the reaction mixture heated to reflux for 1.5 h. The excess thionyl chloride was removed in HV and the crude product purified by fractionated distillation in HV.

Yield: 4.59 g (26.0 mmol, 68%) of a colorless oil.

$C_9H_{17}OCl$ [176.68]

Boiling Point: 63 °C (5.4×10^{-1} mbar)

^{1}H NMR (400.1 MHz, CD_2Cl_2):

δ [ppm] = 2.90 (t, 2H, ^3J = 7.4 Hz, C-H_2), 1.75-1.65 (m, 2H, C-H_2), 1.52 (sept, 1H, ^3J = 6.6 Hz, C-H), 1.37-1.25 (m', 4H, C-H_2), 1.21-1.13 (m, 2H, C-H_2), 0.87 (d, 6H, ^3J = 6.6 Hz, C-H_3).

(*R*)-4-Benzyl-3-(7-methyloctanoyl)oxazolidin-2-one (28)

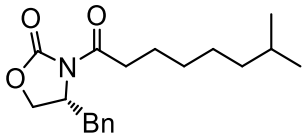

CAS: -

Synthesis based on given literature.[319]

(*R*)-4-Benzyloxazolidin-2-one (5.91 g, 33.3 mmol) was dissolved in dry THF (70 mL) and the solution cooled to -78 °C, before a solution of *n*BuLi (22.9 mL, 1.6 M in hexane, 36.6 mmol) was added dropwise. The reaction mixture was then stirred for 30 min at -78 °C, before 7-methylocanoyl chloride (**27**) (7.66 g, 43.4 mmol) was added dropwise. After stirring the

reaction mixture for 60 min at -78 °C, it was poured onto a saturated aqueous solution of $NaHCO_3$ and extracted with EA. The organic layer was washed with brine and dried over Na_2SO_4, before the solvent was removed under reduced pressure. The residue was purified by column chromatography (silica, EA/PE 1:9).

Yield: 8.30 g (26.1 mmol, 78%) of a colorless crystalline solid.

$C_{19}H_{27}NO_3$ [317.42]

^{1}H NMR (400.0 MHz, $CDCl_3$):

δ [ppm] = 7.36-7.25 (m', 3H, C_{Ar}-H), 7.24-7.19 (m', 2H, C_{Ar}-H), 4.71-4.63 (m, 1H, C-H), 4.23-4.14 (m, 2H, C-H_2), 3.30 (dd, 1H, ^2J = 13.2 Hz, ^3J = 3.2 Hz, C-H_2), 3.02-2.85 (m, 2H, C-H_2), 2.76 (dd, 1H, ^2J = 13.2 Hz, ^3J = 9.6 Hz, C-H_2), 1.75-1.63 (m, 2H, C-H_2), 1.53 (sept, 1H, ^3J = 6.7 Hz, C-H), 1.43-1.25 (m', 4H, C-H_2), 1.22-1.13 (m, 2H, C-H_2), 0.87 (d, 6H, ^3J = 6.7 Hz, C-H_3).

^{13}C(^{1}H) NMR (100.6 MHz, $CDCl_3$):

δ [ppm] = 173.6 (quart.), 153.6 (quart.), 135.5 (quart.), 129.6 (tert.), 129.1 (tert.), 127.5 (tert.), 66.3 (sec.), 55.3 (tert.), 38.9 (sec.), 38.1 (sec.), 35.7 (sec.), 29.5 (sec.), 28.1 (tert.), 27.3 (sec.), 24.4 (sec.), 22.8 (2 × prim.).

HRMS (ESI, pos.): $[M + Na]^{\bullet+}$

calcd: 340.18832

found: 340.18815 Δ = 0.49 ppm

(*R*)-4-Benzyl-3-((*R*)-2,7-dimethyloctanoyl)oxazolidin-2-one (29a)

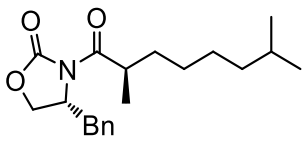

CAS: -

Synthesis based on given literature.[271]

A solution of NaHMDS (59.1 mL, 1 M in THF, 59.1 mmol) was cooled to -78 °C, before a solution of (*R*)-4-benzyl-3-(7-methyloctanoyl)oxazolidin-2-one (**28**) (3.75 g, 11.8 mmol) in dry THF (50 mL) was added dropwise. The reaction mixture was then stirred for 75 min, after which MeI (8.38 g, 3.68 mL, 59.1 mmol) was added dropwise. The reaction mixture was then further stirred for 4 h at -78 °C. After warming to ca. -15 °C, the reaction was quenched with sat. aq. NH_4Cl and warmed to RT, before being extracted with Et_2O. The organic layer was washed with brine and dried over Na_2SO_4. The solvent was removed under reduced pressure and the residue purified by column chromatography (silica, EA/PE 3:22).

Yield: 1.98 g (5.97 mmol, 51%) of a colorless, viscous oil.

$C_{20}H_{29}NO_3$ [331.45]

^{1}H NMR (400.1 MHz, CD_2Cl_2):

δ [ppm] = 7.37-7.19 (m', 5H, C_{Ar}-H), 4.72-4.63 (m, 1H, C-H), 4.24-4.12 (m', 2H, C-H_2), 3.72-3.62 (m, 1H, C-H), 3.19 (dd, 1H, ^2J = 13.5 Hz, ^3J = 3.2 Hz, C-H_2), 2.83 (dd, 1H, ^2J = 13.5 Hz, ^3J = 9.1 Hz, C-H_2), 1.79-1.66 (m, 1H, C-H_2), 1.52 (sept, 1H, ^3J = 6.6 Hz, C-H), 1.46-1.12 (m', 10H, C-H_2, C-H_2, C-H_3), 0.87 (d, 6H, ^3J = 6.6 Hz, 2×C-H_3).

^{13}C(^{1}H) NMR (100.6 MHz, CD_2Cl_2):

δ [ppm] = 177.4 (quart.), 153.5 (quart.), 136.0 (quart.), 129.9 (tert.), 129.2 (tert.), 127.5 (tert.), 66.5 (sec.), 55.6 (tert.), 39.2 (sec.), 38.11 (sec.), 38.05 (tert.), 33.8 (sec.), 28.3 (tert.), 27.88 (sec.), 27.83 (sec.), 22.78 (prim.), 22.76 (prim.), 17.5 (prim.).

HRMS (ESI, pos.): $[M + Na]^{\bullet+}$

calcd: 354.20397

found: 354.20451 Δ = 1.52 ppm

(*R*)-4-Benzyl-3-((*R*)-2-ethyl-7-methyloctanoyl)oxazolidin-2-one (29b)

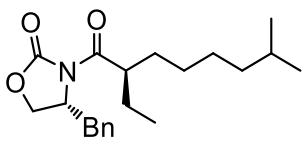

CAS: -

Synthesis based on given literature.[319]

A solution of NaHMDS (25.4 mL, 1 M in THF, 25.4 mmol) was cooled to -78 °C, before a solution of (*R*)-4-benzyl-3-(7-methyloctanoyl)oxazolidin-2-one (**28**) (3.22 g, 10.1 mmol) in dry THF (25 mL) was added dropwise. The solution was then stirred for 1.5 h, after which EtI (4.75 g, 2.45 mL, 30.4 mmol) was added dropwise. The reaction mixture was then gradually warmed up to -25 °C and stirred for 24 h. After warming to ca. -15 °C, the reaction was quenched with sat. aq. NH_4Cl and warmed to RT, before the organic solvent was removed under reduced pressure. The mixture was then extracted with DCM. The organic layer was dried over Na_2SO_4 and the solvent removed under reduced pressure, before the residue was purified by flash chromatography (silica, PE → EA/PE 15:85).

Yield: 1.30 g (3.76 mmol, 37%) of a colorless, viscous oil.

$C_{21}H_{31}NO_3$ [345.48]

^{1}H NMR (400.0 MHz, $CDCl_3$):

δ [ppm] = 7.34-7.21 (m', 5H, C_{Ar}-H), 4.74-4.66 (m, 1H, C-H), 4.20-4.12 (m, 2H, C-H_2), 3.77-3.68 (m, 1H, C-H), 3.34 (dd, 1H, ^2J = 13.3 Hz, ^3J = 3.4 Hz, C-H_2), 2.70 (dd, 1H, ^2J = 13.3 Hz, ^3J = 10.0 Hz, C-H_2), 1.82-1.43 (m', 5H, C-H_2, C-H), 1.32-1.21 (m', 4H, C-H_2,), 1.19-1.10 (m, 2H, C-H_2), 0.96 (t, 3H, ^3J = 7.4 Hz, C-H_3), 0.85 (d, 6H, ^3J = 6.6 Hz, C-H_3).

^{13}C(^{1}H) NMR (100.6 MHz, $CDCl_3$):

δ [ppm] = 177.0 (quart.), 153.3 (quart.), 135.6 (quart.), 129.5 (tert.), 129.1 (tert.), 127.4 (tert.), 66.0 (sec.), 55.6 (tert.), 44.2 (tert.), 38.9 (sec.), 38.2 (sec.), 31.7 (sec.), 28.0 (tert.), 27.8 (sec.), 27.7 (sec.), 25.6 (sec.), 22.78 (prim.), 22.73 (prim.), 11.6 (prim.).

HRMS (ESI, pos.): $[M + Na]^{\bullet+}$

calcd: 368.21962

found: 368.22058 Δ = 2.61 ppm

(*R*)-2,7-Dimethyloctanol (30a)

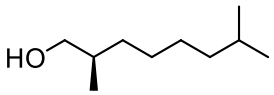

CAS: 15250-22-3 (racemic mixture)

Synthesis based on given literature.[319]

A mixture of (*R*)-4-benzyl-3-((*R*)-2,7-dimethyloctanoyl)oxazolidin-2-one (**29a**) (1.80 g, 5.43 mmol), absolute ethanol (381 µL, 300 mg, 6.52 mmol) and dry Et_2O (20 mL) was cooled to 0 °C, before $LiBH_4$ (4.07 mL, 2 M in Et_2O, 8.15 mmol) was added dropwise. The reaction was stirred for 3.5 h at 0 °C, after which it was quenched with sat. aq. NaCl. The layers were separated and the aqueous layer was extracted with Et_2O. The combined organic layers were washed with water and dried over Na_2SO_4, before the solvent was removed under reduced pressure. The residue was purified by column chromatography (silica, EA/PE 3:7).

Yield: 758 mg (4.79 mmol, 88%) of a colorless, viscous oil.

$C_{10}H_{22}O$ [158.28]

^{1}H NMR (400.1 MHz, $CDCl_3$):

δ [ppm] = 3.51 (dd, 1H, ^2J = 10.4 Hz, ^3J = 5.8 Hz, C-$\underline{H}_2$), 3.42 (dd, 1H, ^2J = 10.4 Hz, ^3J = 6.6 Hz, C-$\underline{H}_2$), 1.67-1.46 (m', 2H, C-$\underline{H}$), 1.44-1.05 (m', 9H, C-$\underline{H}_2$, O-$\underline{H}$), 0.91 (d, 3H, ^3J = 6.7 Hz, C-$\underline{H}_3$), 0.91 (d, 3H, ^3J = 6.7 Hz, C-$\underline{H}_3$), 0.86 (d, 3H, ^3J = 6.7 Hz, C-$\underline{H}_3$).

(*R*)-2-Ethyl-7-methyloctanol (30b)

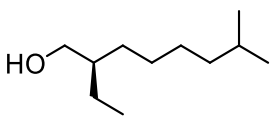

CAS: -

Synthesis based on given literature.[319]

A mixture of (*R*)-4-benzyl-3-((*R*)-2-ethyl-7-methyloctanoyl)oxazolidin-2-one (**29b**) (1.67 g, 4.83 mmol), absolute ethanol (339 µL, 267 mg, 5.80 mmol) and dry Et_2O (15 mL) was cooled to 0 °C, before $LiBH_4$ (4.23 mL, 2 M in Et_2O, 8.46 mmol) was added dropwise. The reaction was stirred for 4.5 h at 0 °C, after which it was quenched with sat. aq. NaCl. The layers were separated and the aqueous layer was extracted with Et_2O. The combined organic layers were washed with water and dried over Na_2SO_4, before the solvent was removed under reduced pressure. The residue was purified by column chromatography (silica, EA/PE 3:7).

Yield: 479 mg (2.78 mmol, 58%) of a colorless, viscous oil.

$C_{11}H_{24}O$ [172.31]

^{1}H NMR (400.0 MHz, $CDCl_3$):

δ [ppm] = 3.58-3.50 (m', 2H, C-$\underline{H_2}$), 1.51 (sept, ^3J = 6.6 Hz, 1H, C-$\underline{H}$), 1.45-1.21 (m', 10H, C-$\underline{H_2}$, O-$\underline{H}$), 1.20-1.12 (m, 2H, C-$\underline{H_2}$), 0.89 (t, 3H, ^3J = 7.4 Hz, C-$\underline{H_3}$), 0.86 (d, 6H, ^3J = 6.6 Hz, C-$\underline{H_3}$).

^{13}C(^{1}H) NMR (100.6 MHz, $CDCl_3$):

δ [ppm] = 65.4 (sec.), 42.1 (tert.), 39.1 (sec.), 30.6 (sec.), 28.1 (tert.), 28.0 (sec.), 27.3 (sec.), 23.5 (sec.), 22.8 (2 × prim.), 11.2 (prim).

HRMS (APCI, pos.): $[M + Na]^{\bullet+}$

calcd: 155.17943

found: 155.17920 Δ = 1.46 ppm

1-Iodo-7-methyloctane (31a)

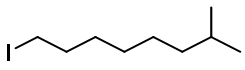

CAS: 10266-06-5

Synthesis based on given literature.[265]

Triphenylphosphane (8.00 g, 30.5 mmol), 7-methyloctanol (**25**) (4.00 g, 27.7 mmol) and 1*H*-imidazole (2.27 g, 33.3 mmol) were suspended in toluene (95 mL). Iodine (9.15 g,

36.0 mmol) was then added and the reaction stirred for 96 h at RT. The reaction was then washed with 10% aq. $Na_2S_2O_3$ until the mixture was colorless. The organic layer was then dried over Na_2SO_4 and the solvent removed under reduced pressure. The residue was then suspended in hexane and stored at 4 °C for 1 h, whereupon the impurities precipitated. The suspension was then filtered and the filtrate concentrated under reduced pressure. The crude product was purified by fractionated distillation in HV.

Yield: 6.31 g (24.8 mmol, 90%) of a colorless oil.

$C_9H_{19}I$ [254.15]

Boiling Point: 85 °C (2.0×10^{-1} mbar)

^{1}H NMR (400.1 MHz, $CDCl_3$):

δ [ppm] = 3.19 (t, 2H, ^3J = 7.0 Hz, C-H_2), 1.86-1.78 (m, 2H, C-H_2), 1.51 (sept, 1H, ^3J = 6.6 Hz, C-H), 1.44-1.34 (m, 2H, C-H_2), 1.32-1.23 (m', 4H, C-H_2), 1.20-1.11 (m, 2H, C-H_2), 0.86 (d, 6H, ^3J = 6.6 Hz, C-H_3).

(*R*)-1-Iodo-2,7-dimethyloctane (31c)

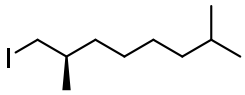

CAS: -

Synthesis based on given literature.[265]

Triphenylphosphane (1.28 g, 4.88 mmol), (*R*)-2,7-dimethyloctanol (**30a**) (700 mg, 4.42 mmol) and 1*H*-imidazole (361 mg, 5.31 mmol) were suspended in toluene (15 mL). Iodine (1.46 g, 5.75 mmol) was then added and the reaction stirred for 72 h at RT. The reaction was then washed with 5% aq. $Na_2S_2O_3$ until the mixture was colorless. The organic layer was then dried over Na_2SO_4 and the solvent removed under reduced pressure. The residue was then suspended in hexane and stored at 4 °C for 1 h, whereupon the impurities precipitated. The suspension was then filtered and the filtrate concentrated under reduced pressure. The residue was purified by column chromatography (silica, PE).

Yield: 762 mg (2.84 mmol, 64%) of a colorless oil.

$C_{10}H_{21}I$ [268.18]

^{1}H NMR (400.1 MHz, $CDCl_3$):

δ [ppm] = 3.23 (dd, 1H, ^{2}J = 9.5 Hz, ^{3}J = 4.6 Hz, C-$\underline{H}_2$), 3.15 (dd, 1H, ^{2}J = 9.5 Hz, ^{3}J = 6.0 Hz, C-$\underline{H}_2$), 1.56-1.11 (m', 10H, C-$\underline{H}_2$, C-$\underline{H}$), 0.91 (d, 3H, ^{3}J = 6.7 Hz, C-$\underline{H}_3$), 0.97 (d, 3H, ^{3}J = 6.5 Hz, C-$\underline{H}_3$), 0.86 (d, 3H, ^{3}J = 6.6 Hz, C-$\underline{H}_3$).

^{13}C(^{1}H) NMR (100.6 MHz, $CDCl_3$):

δ [ppm] = 39.1 (sec.), 36.6 (sec.), 34.9 (tert.), 28.1 (tert.), 27.6 (sec.), 27.3 (sec.), 22.79 (prim.), 22.78 (prim.), 20.8 (prim.), 18.2 (sec.).

HRMS (APCI, pos.): $[M - I]^{\bullet+}$

calcd: 141.16378

found: 141.16419 Δ = 2.90 ppm

(*R*)-1-Iodo-2-ethyl-7-methyloctane (31d)

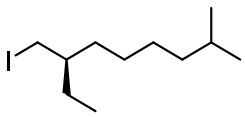

CAS: -

Synthesis based on given literature.[265]

Triphenylphosphane (703 mg, 2.68 mmol), (*R*)-2-ethyl-7-methyloctanol (**30b**) (420 mg, 2.44 mmol) and 1*H*-imidazole (199 mg, 2.92 mmol) were suspended in toluene (10 mL). Iodine (804 mg, 3.17 mmol) was then added and the reaction stirred for 72 h at RT. The reaction was then washed with 5% aq. $Na_2S_2O_3$ until the mixture was colorless. The organic layer was then dried over Na_2SO_4 and the solent removed under reduced pressure. The residue was then directly purified by column chromatography (silica, PE).

Yield: 591 mg (2.09 mmol, 86%) of a colorless oil.

$C_{11}H_{23}I$ [282.21]

^{1}H NMR (400.0 MHz, $CDCl_3$):

δ [ppm] = 3.31-3.23 (m, 2H, C-$\underline{H}_2$), 1.52 (sept, ^{3}J = 6.6 Hz, 1H, C-$\underline{H}$), 1.45-1.12 (m', 10H, C-$\underline{H}_2$), 1.12-0.99 (m, 1H, C-$\underline{H}$), 0.89-0.84 (m', 9H, C-$\underline{H}_3$).

^{13}C(^{1}H) NMR (100.6 MHz, $CDCl_3$):

δ [ppm] = 40.5 (tert.), 39.1 (sec.), 34.2 (sec.), 28.1 (tert.), 27.6 (sec.), 27.2 (sec.), 27.0 (sec.), 22.80 (prim.), 22.78 (prim.), 16.4 (sec.), 11.0 (prim).

Various attempts at measuring a mass spectrum using different methods (ESI, APCI) were not successful.

8.2.3 Squaraine precursors

Compound 1

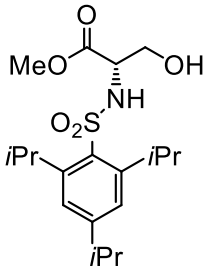

***S*-1**

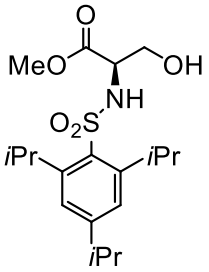

***R*-1**

CAS: 159155-12-1

Synthesis according to literature.[239]

A solution of *D*- or *L*-serine methyl ester hydrochloride (5.32 g, 34.2 mmol) in DCM (70 mL) was cooled to 0 °C, before triethylamine (11.4 mL, 8.30 g, 82.0 mmol) was added dropwise. After stirring for 5 min at 0 °C, 2,4,6-triisopropylbenzenesulfonyl chloride (10.9 g, 36.0 mmol) was added in one portion and the reaction stirred for 16 h allowing to warm to RT. The reaction was quenched with H_2O (100 mL) before being extracted with DCM (3 × 120 mL). The combined organic layers were then washed in succession with sat. aq. $NaHCO_3$ (100 mL), aq. HCl (2.5%, 100 mL), H_2O (100 mL) and brine (100 mL) before being dried over $MgSO_4$, filtered and concentrated under reduced pressure. The crude product was then recrystallized from

MeOH/H_2O. Using *D*-serine methyl ester hydrochloride led to the formation of *R*-1, using the *L*-enantiomer led to ***S*-1**.

Yield: 12.0 g (31.1 mmol, 91%) of a colorless crystalline solid.

$C_{19}H_{31}NO_5S$ [385.52]

^{1}H NMR (400 MHz, CD_2Cl_2):

δ [ppm] = 7.19 (s, 2H, C_{Ar}-H), 5.50 (d, 1H, ^3J = 7.6 Hz, N-H), 4.10-3.99 (m', 3H, C-H), 3.91-3.81 (m, 2H, C-H_2) 3.60 (s, 3H, C-H_3), 2.91 (sept, 1H, ^3J = 7.0 Hz, C-H), 2.09 (t, 1H, ^3J = 7.0 Hz, O-H), 1.28-1.22 (m', 18H, C-H_3).

Compound 2

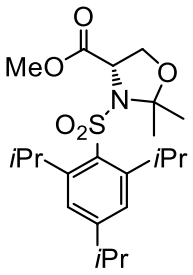

***S*-2**

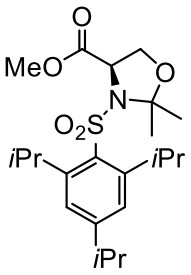

***R*-2**

CAS: 1352790-93-2

Synthesis according to literature.[239]

To a solution of compound **1** (12.9 g, 33.5 mmol) and pyridinium *para*-toluenesulfonate (2.10 g, 8.36 mmol) in toluene (450 mL) was added 2,2-dimethoxypropane (61.4 mL, 52.2 g, 501 mmol) and the reaction stirred at 80 °C for 16 h. After cooling to RT, the solvent was removed under reduced pressure to yield a crude light-brown oil which was purified by column chromatography (silica, EA/PE 1:9 → EA/PE 3:17).

Yield: 8.81 g (20.7 mmol, 62%) of an off-white crystalline solid.

$C_{22}H_{35}NO_5S$ [425.58]

^{1}H NMR (400 MHz, CD_2Cl_2):

δ [ppm] = 7.17 (s, 2H, C_{Ar}-H), 4.37 (dd, 1H, ^3J = 7.6 Hz, ^2J = 2.2 Hz, C-H_2), 4.29-4.18 (m', 3H, C-H), 4.04 (dd, 1H, ^3J = 9.3 Hz, ^2J = 2.2 Hz, C-H_2), 3.20 (s, 3H, C-H_3), 2.89 (sept, 1H, ^3J = 7.0 Hz, C-H), 1.77 (s, 3H, C-H_3), 1.73 (s, 3H, C-H_3), 1.28-1.22 (m', 18H, C-H_3).

Compound 3

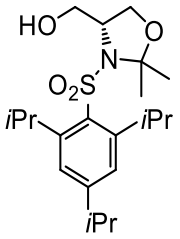

***S*-3**

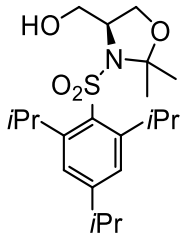

***R*-3**

CAS: 1352790-94-3

Synthesis according to literature.[239]

To a stirred solution of compound **2** (2.91 g, 6.84 mmol) in THF (20 mL) was added dropwise a solution of $LiAlH_4$ (2.0 M in THF, 5.13 mL, 10.3 mmol) at 0 °C and the reaction stirred at 0 °C for 30 min. The reaction was then quenched with dropwise addition of H_2O (1 mL), followed by addition of 40% KOH (1 mL), H_2O (3 mL) and EA (5 mL). The resulting slurry was then stirred vigorously for 1 h allowing to warm to RT, before being filtered through a celite plug and the residue washed with EA (30 mL). The reaction mixture was then dried over $MgSO_4$ and the solvent was removed under reduced pressure. The crude product was used without further purification.

Yield: 2.92 g (7.34 mmol, quant.)[1] of a colorles viscous oil.

$C_{21}H_{35}NO_4S$ [397.57]

^{1}H NMR (400 MHz, CD_2Cl_2):

δ [ppm] = 7.20 (s, 2H, C_{Ar}-H), 4.30 (sept, 2H, ^3J = 6.9 Hz, C-H), 4.13-4.02 (m', 2H, C-H_2), 3.85-3.79 (m, 1H, C-H), 3.14-3.07 (m, 1H, C-H_2), 2.92 (sept, 1H, ^3J = 6.9 Hz, C-H), 2.87-

[1] Due to the product containing impurities and/or solvent residues the reported yield is greater than 100%.

2.81 (m, 1H, C-H$_2$), 1.75 (s, 3H, C-H$_3$), 1.68 (s, 3H, C-H$_3$), 1.38 (t, 1H, ^3J = 5.3 Hz, O-H), 1.27-1.23 (m', 18H, C-H$_3$).

Compound 4

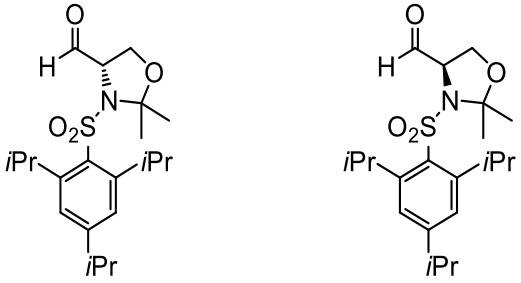

***S*-4** ***R*-4**

CAS: 1352790-95-4

Synthesis according to literature.[239]

A solution of DMSO (4.43 mL, 4.87 g, 62.3 mmol) in DCM (95 mL) was added dropwise to a stirred solution of oxalyl chloride (2.67 mL, 3.96 g, 31.2 mmol) in DCM (50 mL), which was cooled to -78 °C. The mixture then stirred for 15 min. A solution of compound **3** (6.20 g, 15.6 mmol) in DCM (80 mL) was then added dropwise and the reaction stirred for 35 min, before DIPEA (16.3 mL, 12.1 g, 93.6 mmol) was added dropwise and the reaction mixture stirred allowing to warm to RT, before being quenched with sat. aq. NH_4Cl (50 mL). The organic phase was then separated and washed with sat. aq. $NaHCO_3$ (60 mL) and brine (2 × 60 mL), before being dried over Na_2SO_4. The solvent was removed under reduced pressure and the crude product used without further purification.

Yield: 7.31 g (18.5 mmol, quant.) of a light-brown viscous oil.[1]

$C_{21}H_{33}NO_4S$ [395.56]

[1] Due to the product containing impurities and/or solvent residues the reported yield is greater than 100%.

^{1}H NMR (400.1 MHz, CD_2Cl_2):

δ [ppm] = 8.95 (m, 1H, C-H), 7.19 (s, 2H, C_{Ar}-H), 4.33-4.21 (m', 3H, C-H), 4.15-4.08 (m', 2H, C-H, C-H_2), 2.90 (sept, 1H, ^3J = 6.9 Hz, C-H), 1.78 (s, 3H, C-H_3), 1.76 (s, 3H, C-H_3), 1.27-1.22 (m', 18H, C-H_3).

Compound 5

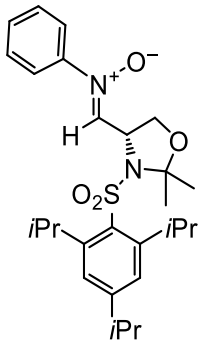

***S*-5**

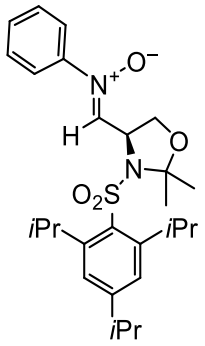

***R*-5**

CAS: 1352790-96-5

Synthesis according to literature.[239]

To a solution of compound **4** (3.50 g, 8.85 mmol) in DCM (35 mL) was added $MgSO_4$ (1.60 g, 13.3 mmol) and the reaction mixture stirred for 5 min at RT. After this time, phenylhydroxylamine (1.93 g, 17.7 mmol) was added and the reaction stirred for 26 h at RT. The mixture was filtered to remove $MgSO_4$ and the solvent was removed under reduced pressure. The crude product was purified by column chromatography (silica, Acetone/PE 1:4) followed by precipitation from PE.

Yield: 2.75 g (5.65 mmol, 64%) of a colorless solid.

$C_{27}H_{38}N_2O_4S$ [486.67]

^{1}H NMR (400 MHz, CD_2Cl_2):

δ [ppm] = 7.40-7.35 (m, 1H, C_{Ar}-H), 7.32-7.26 (m, 2H, C_{Ar}-H), 7.21 (s, 2H, C_{Ar}-H), 7.03-6.99 (m, 2H, C_{Ar}-H), 6.68 (d, 1H, ^3J = 5.3 Hz, C-H), 5.08-5.02 (m, 1H, C-H), 4.45 (dd, 1H, ^2J = 9.4 Hz, ^3J = 7.3 Hz, C-H_2), 4.33 (sept, 2H, ^3J = 6.8 Hz, C-H), 4.18 (dd, 1H, ^2J = 9.4 Hz, ^3J = 2.2 Hz, C-H_2), 2.87 (sept, 1H, ^3J = 6.9 Hz, C-H), 1.80 (s, 3H, C-H_3), 1.79 (s, 3H, C-H_3), 1.27-1.17 (m', 18H, C-H_3).

Compound 6

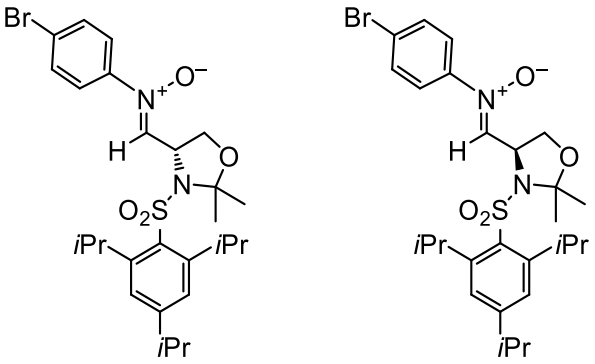

***S*-6** ***R*-6**

CAS: -

Synthesis based on given literature.[239]

To a solution of compound **4** (3.81 g, 9.63 mmol) in DCM (40 mL) was added $MgSO_4$ (1.05 g, 8.72 mmol) and the reaction mixture stirred for 5 min at RT. After this time, (4-bromophenyl)hydroxylamine (1.81 g, 9.63 mmol) was added and the reaction stirred for 18 h at RT. The mixture was filtered to remove $MgSO_4$ and the solvent was removed under reduced pressure. The crude product was purified by column chromatography (silica, acetone/PE 1:4) followed by precipitation from PE.

Yield: 3.24 g (5.73 mmol, 66%) of a colorless solid.

$C_{27}H_{37}BrN_2O_4S$ [565.56]

^{1}H NMR (400 MHz, CD_2Cl_2):

δ [ppm] = 7.43 (AA', 2H, C_{Ar}-H), 7.20 (s, 2H, C_{Ar}-H), 6.92 (BB', 2H, C_{Ar}-H), 6.67 (d, 1H, ^3J = 5.4 Hz, C-H), 5.05-5.00 (m, 1H, C-H), 4.44 (dd, 1H, ^2J = 9.4 Hz, ^3J = 7.3 Hz, C-H_2), 4.32 (sept, 2H, ^3J = 6.8 Hz, C-H), 4.16 (dd, 1H, ^2J = 9.4 Hz, ^3J = 2.2 Hz, C-H_2), 2.87 (sept, 1H, ^3J = 7.0 Hz, C-H), 1.80 (s, 3H, C-H_3), 1.78 (s, 3H, C-H_3), 1.27-1.17 (m', 18H, C-H_3).

^{13}C(^{1}H) NMR (100.1 MHz, CD_2Cl_2):

δ [ppm] = 154.7 (quart.), 152.0 (quart.), 145.7 (quart.), 139.1 (tert.), 132.8 (quart.), 132.5 (tert.), 124.7 (tert.), 124.5 (quart.), 122.9 (tert.), 100.5 (quart.), 68.2 (sec.), 56.4

(tert.), 34.6 (tert.), 29.4 (tert.), 28.2 (prim.), 25.1 (2 × prim.), 24.8 (2 × prim.), 24.7 (prim.), 23.7 (2 × prim.).

MS (APCI, pos): $[M + H]^{\bullet+}$

calcd: 567.1713

found: 567.1717

2-Phenylpropanoic acid chloride (7)

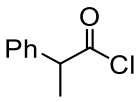

CAS: 22414-26-2

2-Phenylpropanoic acid (5.92 g, 39.4 mmol) was dissolved in thionyl chloride (40 mL) and the reaction mixture was heated to reflux for 1.5 h. The excess thionyl chloride was removed in HV and the crude product purified by fractionated distillation under HV.

Yield: 5.92 g (35.1 mmol, 89%) of a colorless liquid.

C_9H_9ClO [168.62]

Boiling Point: 60 °C (2.5×10^{-2} mbar)

^{1}H NMR (400 MHz, CD_3OD):

δ [ppm] = 7.28-7.15 (m', 5H, C_{Ar}-H), 3.69 (q, 1H, ^3J = 7.2 Hz, C-H), 1.38 (d, 3H, ^3J = 7.2 Hz, C-H_3).

Phenylmethylketene (8)

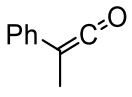

CAS: 3156-07-8

Synthesis based on given literature.[240-241]

2-Phenylpropanoic acid chloride (**7**) (3.03 g, 18.0 mmol) was dissolved in dry Et_2O (20 mL) under nitrogen atmosphere and the solution cooled to -2 °C, before dry NEt_3 (2.49 mL, 1.82 g, 18.0 mmol) was added dropwise (ca. 30 min). The reaction mixture was then stirred for 18 h at -2 °C under the exclusion of light. The formed precipitate was filtered off under nitrogen and the solvent was removed under reduced pressure. The residue was then purified by fractionated distillation under reduced pressure.

Yield: 1.61 g (12.2 mmol, 68%) of a yellow-orange liquid.

C_9H_8O [132.16]

Boiling Point: 28 °C (1.0×10^{-1} mbar)

^{1}H NMR (400 MHz, $CDCl_3$):

δ [ppm] = 7.35-7.29 (m, 2H, C_{Ar}-H), 7.10-7.00 (m', 3H, C_{Ar}-H), 2.01 (s, 3H, C-H_3).

3-Methyl-3-phenylindolin-2-one (9)

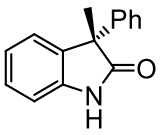

***S*-9**

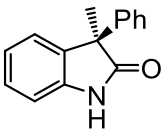

***R*-9**

CAS: 1185154-68-0

Synthesis according to literature.[239]

A solution of compound **5** (715 mg, 1.47 mmol) in dry THF (10 mL) under nitrogen atmosphere was cooled to -78 °C. A solution of phenylmethylketene (**8**) (330 mg, 2.50 mmol) in dry THF (1 mL) was then added dropwise and the reaction stirred at -78 °C until analysis by TLC showed consumption of nitrone. The reaction was quenched with aq. HCl (2M) and stirred for 30 min, allowing to warm to RT before being extracted with Et_2O (3 × 10 mL). The combined organic phases were washed with sat. aq. $NaHCO_3$ and dried over Na_2SO_4, before the solvent was removed under reduced pressure. The crude product was purified by column chromatography

(silica, EA/PE 1:4 → EA/PE 1:3). Using ***R*-5** led to the formation of ***R*-9**, using the *S*-enantiomer led to ***S*-9**.

Yield: 314 mg (1.41 mmol, 96%) of a colorless viscous oil.

$C_{15}H_{13}NO$ [223.27]

HPLC (Phenomenex LUX Cellulose-4, *n*-hexane/*i*PrOH 9:1, 1 mL min^{-1}):
8.9 min (*S*-enantiomer), 18.1 min (*R*-enantiomer).

^{1}H NMR (400.1 MHz, CD_2Cl_2):
δ [ppm] = 7.82-7.65 (br, 1H, N-H), 7.34-7.22 (m', 6H, C_{Ar}-H), 7.14-7.11 (m, 1H, C_{Ar}-H), 7.08-7.03 (m, 1H, C_{Ar}-H), 6.98-6.95 (m, 1H, C_{Ar}-H), 1.78 (s, 3H, C-H_3).

5-Bromo-3-methyl-3-phenylindolin-2-one (10)

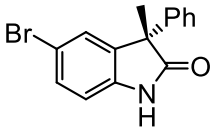

***S*-10**

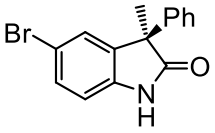

***R*-10**

CAS: -

Synthesis based on given literature.[239]

A solution of compound **6** (2.45 g, 4.32 mmol) in dry THF (30 mL) under nitrogen atmosphere was cooled to -78 °C. A solution of phenylmethylketene (**8**) (1.00 g, 7.57 mmol) in dry THF (2 mL) was then added dropwise and the reaction stirred at -78 °C until analysis by TLC showed consumption of nitrone. The reaction was quenched with aq. 2M HCl and stirred for 30 min, allowing to warm to RT before being extracted with Et_2O (3 × 10 mL). The combined organic phases were washed with sat. aq. $NaHCO_3$ and dried over Na_2SO_4, before the solvent was removed under reduced pressure. The crude product was purified by column chromatography (silica, EA/PE 1:3 → EA/PE 7:15) and recrystallization from MeCN/H_2O (1:1). Using ***R*-6** led to the formation of ***R*-10**, using the *S*-enantiomer led to ***S*-10**.

Yield: 643 mg (2.13 mmol, 49%) of an off-white crystalline solid.

$C_{15}H_{12}BrNO$ [302.17]

HPLC (Phenomenex LUX Cellulose-1, *n*-hexane/*i*PrOH 9:1, 1 mL min^{-1}):

8.1 min (*S*-enantiomer), 12.2 min (*R*-enantiomer).

^{1}H NMR (400 MHz, $CDCl_3$):

δ [ppm] = 8.61 (s, 1H, N-H), 7.39-7.22 (m', 7H, C_{Ar}-H), 6.86 (d, 1H, ^{3}J = 8.3 Hz, C_{Ar}-H), 1.79 (s, 3H, C-H_3).

^{13}C(^{1}H) NMR (100 MHz, CD_2Cl_2):

δ [ppm] = 181.5 (quart.), 140.4 (quart.), 139.9 (quart.), 138.3 (quart.), 131.3 (tert.), 129.0 (tert.), 127.9 (tert.), 127.8 (tert.), 126.9 (tert.), 115.5 (quart.), 112.0 (tert.), 53.2 (quart.), 23.2 (prim.).

MS (EI): $[M + H]^{\bullet+}$

calcd: 302.0175

found: 302.0175

2,3-Dimethyl-3-propyl-3*H*-indole (*rac*-13)

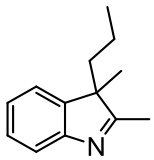

CAS: 1429431-74-2

Synthesis based on given literature.[244]

A solution of MeMgBr (15.2 mL, 3 M in Et_2O, 45.6 mmol) was dilluted to a total volume of 100 mL with anhydrous Et_2O, before a solution of 2-methyl-3-propylindole (**11**) (7.20 g, 41.6 mmol) in anhydrous Et_2O (20 mL) was added dropwise. After stirring for 1 h at RT, a solution of MeI (25.9 mL, 59.1 g, 416 mmol) in anhydrous Et_2O (20 mL) was added dropwise and the reaction was stirred for 20 h at RT under the exclusion of light. The reaction was then quenched with sat. aq. NH_4Cl, before being extracted with DCM. The combined organic layers

were dried over $MgSO_4$, before the solvent was removed under reduced pressure. The crude product was then purified by fractionated distillation under vacuum.

Yield: 5.37 g (28.7 mmol, 69%) of a colorless oil.

$C_{13}H_{17}N$ [187.29]

Boiling Point: 54 °C (1.0×10^{-1} mbar)

^{1}H NMR (400.1 MHz, $CDCl_3$):

δ [ppm] = 7.54-7.50 (m, 1H, C_{Ar}-H), 7.32-7.27 (m, 1H, C_{Ar}-H), 7.25-7.22 (m, 1H, C_{Ar}-H), 7.21-7.16 (m, 1H, C_{Ar}-H), 2.41 (s, 3H, C-H_3), 1.89-1.79 (m, 1H, C-H_2), 1.76-1.67 (m, 1H, C-H_2), 1.28 (s, 3H, C-H_3), 0.83-0.58 (m', 5H, C-H_2, C-H_3).

5-Bromo-2,3-dimethyl-3-propyl-3*H*-indole (*rac*-14)

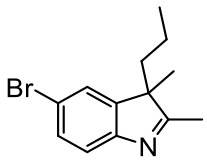

CAS: -

Synthesis based on given literature.[244]

A solution of MeMgBr (13.2 mL, 3 M in Et_2O, 39.6 mmol) was diluted to a total volume of 95 mL with anhydrous Et_2O, before a solution of 5-bromo-3-propyl-2-methylindiole (**12**) (10.0 g, 39.7 mmol) in anhydrous Et_2O (20 mL) was added dropwise. After stirring for 1 h at RT, a solution of MeI (24.7 mL, 56.3 g, 397 mmol) in anhydrous Et_2O (20 mL) was added dropwise and the reaction was stirred for 20 h at RT under the exclusion of light. The reaction was then quenched with sat. aq. NH_4Cl, before being extracted with DCM. The combined organic layers were dried over $MgSO_4$, before the solvent was removed under reduced pressure. The crude product was then purified by column chromatography (silica, EA/PE 1:4).

Yield: 6.61 g (24.8 mmol, 63%) of a pale-yellow oil.

$C_{13}H_{16}BrN$ [266.18]

^{1}H NMR (400.1 MHz, $CDCl_3$):

δ [ppm] = 7.42 (dd, 1H, ^{3}J = 8.2 Hz, ^{3}J = 1.9 Hz, C_{Ar}-H), 7.38 (d, 1H, ^{3}J = 8.2 Hz C_{Ar}-H), 7.35 (dd, 1H, ^{4}J = 1.9 Hz, ^{5}J = 0.5 Hz, C_{Ar}-H), 2.24 (s, 3H, C-H_3), 1.87-1.77 (m, 1H, C-H_2), 1.77-1.67 (m, 1H, C-H_2), 1.27 (s, 3H, C-H_3), 0.91-0.59 (m', 5H, C-H_2, C-H_3).

^{13}C(^{1}H) NMR (100.6 MHz, $CDCl_3$):

δ [ppm] = 188.1 (quart.), 153.3 (quart.), 146.3 (quart.), 130.7 (tert.), 125.1 (tert.), 121.2 (tert.), 119.0 (quart.), 58.7 (quart.), 39.5 (sec.), 22.7 (prim.), 17.6 (sec.), 15.8 (prim.), 14.3 (prim.).

HRMS (APCI, pos.): $[M + H]^{\bullet+}$

calcd: 266.05389

found: 266.05447 Δ = 2.18 ppm

(*S*)-2,3-dimethyl-3-propyl-3*H*-indole (*S*-13)

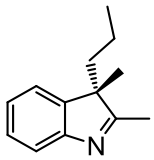

CAS: -

Synthesis based on given literature.[243]

A solution of ***rac*-13** (1.20 g, 6.41 mmol) and **Cat*** (386 mg, 480 µmol, 7.5 mol%) in 1,1,1,3,3,3-hexafluoroisopropanol (20 mL) was degassed for 10 min before being placed in an autoclave. The autoclave was purged with hydrogen, before the hydrogen pressure was adjusted to 10 bar. The reaction was stirred at RT and monitored by ^{1}H NMR. After 19 h, the reaction was terminated and the solvent removed under reduced pressure. The residue was purified by flash chromatography (silica, EA/PE 1:3) to obtain the enantiomerically enriched indolenine ***S*-13.**

Yield: 193 mg (480 µmol, 16%) of a colorless oil.

$C_{13}H_{17}N$ [187.29]

HPLC (Phenomenex LUX Cellulose-4, *n*-hexane/*i*PrOH 99:1, 1 mL min^{-1}):
13.6 min (*S*-enantiomer), 12.4 min (*R*-enantiomer).

(*S*)-5-Bromo-2,3-dimethyl-3-propyl-3*H*-indole (*S*-14)

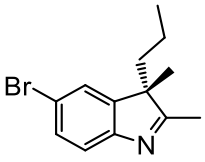

CAS: -

Synthesis based on given literature.[243]

A solution of ***rac*-14** (1.13 g, 4.25 mmol) and **Cat*** (295 mg, 367 µmol, 8.6 mol%) in 1,1,1,3,3,3-hexafluoroisopropanol (21 mL) was degassed for 10 min before being placed in an autoclave. The autoclave was purged with hydrogen, before the hydrogen pressure was adjusted to 10 bar. The reaction was stirred at RT and monitored by ^{1}H NMR. After 19 h, the reaction was terminated and the solvent removed under reduced pressure. The residue was purified by flash chromatography (silica, EA/PE 1:4) to obtain the enantiomerically enriched indolenine ***S*-14.**

Yield: 210 mg (789 µmol, 19%) of a colorless oil.

$C_{13}H_{16}BrN$ [266.18]

HPLC (Phenomenex LUX Cellulose-4, *n*-hexane/*i*PrOH 99:1, 1 mL min^{-1}):
11.5 min (*S*-enantiomer), 8.9 min (*R*-enantiomer).

1-Butylindoline-2,3-dione (15a)

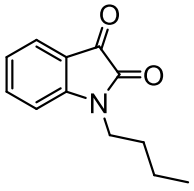

CAS: -

Synthesis following GP I: Isatin (500 mg, 3.40 mmol), dry K_2CO_3 (4.70 g, 34.0 mmol), *n*-butyl iodide (763 µL, 1.25 g, 6.79 mmol) in anhydrous DMF (10 mL). 18 h at 85 °C Purification by column chromatography (silica, DCM).

Yield: 677 mg (3.33 mmol, 98%) of a deep red viscous oil.

$C_{12}H_{13}NO_2$ [203.24]

^{1}H NMR (400.0 MHz, $CDCl_3$):

δ [ppm] = 7.60-7.55 (m', 2H, C_{Ar}-H), 7.12-7.07 (m, 1H, C_{Ar}-H), 6.91-6.88 (m, 1H, C_{Ar}-H), 3.71 (t, 2H, ^3J = 7.4 Hz, C-H_2), 1.71-1.63 (m, 2H, C-H_2), 1.45-1.34 (m, 2H, C-H_2), 0.95 (t, 3H, ^3J = 7.3 Hz, C-H_3).

^{13}C(^{1}H) NMR (100.6 MHz, $CDCl_3$):

δ [ppm] = 183.8 (quart.), 158.2 (quart.), 151.2 (quart.), 138.4 (tert.), 125.5 (tert.), 123.7 (tert.), 117.6 (quart.), 110.3 (tert.), 40.1 (sec.), 29.4 (sec.), 20.2 (sec.), 13.8 (prim.).

HRMS (APCI, pos.): $[M + H]^{\bullet+}$

calcd: 204.1019

found: 204.1025 Δ = 2.94 ppm

1-Hexylindoline-2,3-dione (15b)

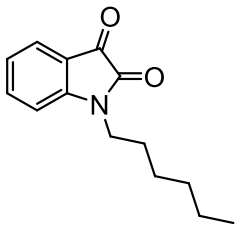

CAS: -

Synthesis following GP I: Isatin (2.00 g, 13.6 mmol), dry K_2CO_3 (18.8 g, 136 mmol), *n*-hexyl iodide (3.40 mL, 4.90 g, 23.1 mmol) in anhydrous DMF (42 mL). 18 h at 85 °C. Purification by column chromatography (silica, DCM).

Yield: 1.57 g (6.79 mmol, 50%) of a red solid.

$C_{14}H_{17}NO_2$ [231.29]

^{1}H NMR (400.0 MHz, $CDCl_3$):

δ [ppm] = 7.62-7.56 (m', 2H, C_{Ar}-H), 7.14-7.08 (m, 1H, C_{Ar}-H), 6.91-6.87 (m, 1H, C_{Ar}-H), 3.71 (t, 2H, ^3J = 7.4 Hz, C-H_2), 1.74-1.66 (m, 2H, C-H_2), 1.43-1.25 (m', 6H, C-H_2), 0.89 (t, 3H, ^3J = 7.0 Hz, C-H_3).

^{13}C(^{1}H) NMR (100.6 MHz, $CDCl_3$):

δ [ppm] = 183.8 (quart.), 158.2 (quart.), 151.2 (quart.), 138.4 (tert.), 125.6 (tert.), 123.7 (tert.), 117.7 (quart.), 110.3 (tert.), 40.4 (sec.), 31.5 (sec.), 27.3 (sec.), 26.7 (sec.), 22.6 (sec.), 14.1 (prim.).

MS (ESI, pos.): $[M + Na]^{\bullet+}$

calcd: 254.115

found: 254.116

1-Hexadecylindoline-2,3-dione (15c)

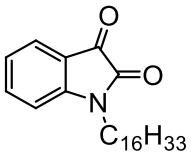

CAS: -

Synthesis following GP I: Isatin (2.00 g, 13.6 mmol), dry K_2CO_3 (18.8 g, 136 mmol), *n*-hexadecyl iodide (7.26 mL, 8.14 g, 23.1 mmol) in anhydrous DMF (42 mL). 18 h at 85 °C Purification by column chromatography (silica, DCM).

Yield: 808 mg (2.17 mmol, 16%) of a red solid.

$C_{24}H_{37}NO_2$ [371.56]

^{1}H NMR (400.0 MHz, $CDCl_3$):

δ [ppm] = 7.62-7.55 (m', 2H, C_{Ar}-H), 7.14-7.08 (m, 1H, C_{Ar}-H), 6.91-6.86 (m, 1H, C_{Ar}-H), 3.71 (t, 2H, ^{3}J = 7.5 Hz, C-H_2), 1.74-1.64 (m, 2H, C-H_2), 1.38-1.21 (m', 26H, C-H_2), 0.88 (t, 3H, ^{3}J = 6.9 Hz, C-H_3).

^{13}C(^{1}H) NMR (100.6 MHz, $CDCl_3$):

δ [ppm] = 183.8 (quart.), 158.2 (quart.), 151.2 (quart.), 138.4 (tert.), 125.6 (tert.), 123.7 (tert.), 117.7 (quart.), 110.3 (tert.), 40.4 (sec.), 32.1 (sec.), 29.83 (2 × sec.), 29.82 (sec.), 29.80 (2 × sec.), 29.74 (sec.), 29.68 (sec.), 29.6 (sec.), 29.5 (sec.), 29.4 (sec.), 27.4 (sec.), 27.0 (sec.), 22.8 (sec.), 14.3 (prim.).

MS (ESI, pos.): $[M + Na]^{\bullet+}$

calcd: 394.272

found: 394.273

5-Bromo-1-hexylindoline-2,3-dione (16a)

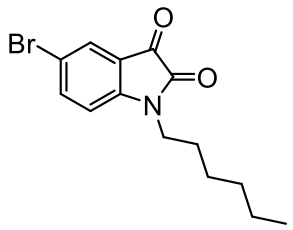

CAS: -

Synthesis following GP I: 5-Bromoisatin (2.00 g, 8.85 mmol), dry K_2CO_3 (12.2 g, 88.3 mmol), *n*-hexyl iodide (2.22 mL, 3.19 g, 15.0 mmol) in anhydrous DMF (27 mL). 18 h at 85 °C Purification by column chromatography (silica, DCM).

Yield: 779 mg (2.51 mmol, 28%) of a red solid.

$C_{14}H_{16}BrNO_2$ [310.19]

^{1}H NMR (400.0 MHz, $CDCl_3$):

δ [ppm] = 7.72-7.68 (m', 2H, C_{Ar}-H), 6.82-6.79 (m, 1H, C_{Ar}-H), 3.70 (t, 2H, ^{3}J = 7.4 Hz, C-H_2), 1.73-1.63 (m, 2H, C-H_2), 1.41-1.25 (m', 6H, C-H_2), 0.88 (t, 3H, ^{3}J = 7.1 Hz, C-H_3).

$^{13}C(^{1}H)$ NMR (100.6 MHz, $CDCl_3$):

δ [ppm] = 182.6 (quart.), 157.5 (quart.), 149.8 (quart.), 140.6 (tert.), 128.4 (tert.), 118.8 (quart.), 116.5 (quart.), 112.0 (tert.), 40.5 (sec.), 31.4 (sec.), 27.2 (sec.), 26.6 (sec.), 22.6 (sec.), 14.0 (prim.).

MS (ESI, pos.): $[M + Na]^{\bullet+}$

calcd: 332.026

found: 332.027

5-Bromo-1-hexadecylindoline-2,3-dione (16b)

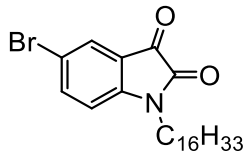

CAS: -

Synthesis following GP I: 5-Bromoisatin (5.00 g, 22.1 mmol), dry K_2CO_3 (30.6 g, 221 mmol), *n*-hexadecyl iodide (11.8 mL, 13.3 g, 37.7 mmol) in anhydrous DMF (75 mL). 18 h at 85 °C. Purification by column chromatography (silica, DCM).

Yield: 5.41 g (12.0 mmol, 54%) of a deep red viscous oil.

$C_{24}H_{36}BrNO_2$ [450.45]

^{1}H NMR (400.0 MHz, $CDCl_3$):

δ [ppm] = 7.71-7.67 (m', 2H, C_{Ar}-H), 6.82-6.79 (m, 1H, C_{Ar}-H), 3.69 (t, 2H, ^{3}J = 7.5 Hz, C-H_2), 1.72-1.62 (m, 2H, C-H_2), 1.40-1.18 (m', 26H, C-H_2), 0.87 (t, 3H, ^{3}J = 7.1 Hz, C-H_3).

$^{13}C(^{1}H)$ NMR (100.6 MHz, $CDCl_3$):

δ [ppm] = 182.6 (quart.), 157.5 (quart.), 149.9 (quart.), 140.6 (tert.), 128.3 (tert.), 118.9 (quart.), 116.5 (quart.), 112.0 (tert.), 40.6 (sec.), 32.1 (sec.), 29.83 (sec.), 29.82 (sec.), 29.80 (sec.), 29.78 (sec.), 29.77 (sec.), 29.73 (sec.), 29.65 (sec.), 29.6 (sec.), 29.5 (sec.), 29.3 (sec.), 27.3 (sec.), 27.0 (sec.), 22.8 (sec.), 14.3 (prim.).

MS (MALDI, pos.): $[M + Na]^{\bullet+}$

calcd: 474.180

found: 474.196

1-Butyl-3-hydroxy-3-methylindolin-2-one (17a)

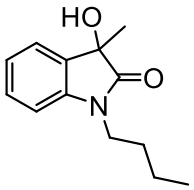

CAS: -

Synthesis following GP VIII: Compound **15a** (1.06 g, 5.22 mmol), MeMgBr (1.86 mL, 3 M in Et_2O, 5.58 mmol) in anhydrous THF (26 mL).

Yield: 817 mg (3.73 mmol, 71%) of a yellow-orange solid.

$C_{13}H_{17}NO_2$ [219.28]

^{1}H NMR (400.1 MHz, $CDCl_3$):

δ [ppm] = 7.43-7.40 (m, 1H, C_{Ar}-H), 7.33-7.28 (m, 1H, C_{Ar}-H), 7.12-7.06 (m, 1H, C_{Ar}-H), 6.89-6.84 (m, 1H, C_{Ar}-H), 3.77-3.59 (m, 2H, C-H_2), 3.06-1.93 (br, 1H, O-H), 1.71-1.61 (m, 2H, C-H_2), 1.60 (s, 3H, C-H_3), 1.44-1.32 (m, 2H, C-H_2), 0.95 (t, 3H, ^3J = 7.5 Hz, C-H_3).

^{13}C(^{1}H) NMR (100.6 MHz, $CDCl_3$):

δ [ppm] = 178.6 (quart.), 142.4 (quart.), 131.6 (quart.), 129.7 (tert.), 123.7 (tert.), 123.1 (tert.), 109.0 (tert.), 73.7 (quart.), 39.9 (sec.), 29.5 (sec.), 25.1 (prim.), 20.2 (sec.), 13.9 (prim.).

MS (APCI, pos.): $[M + H]^{\bullet+}$

calcd: 204.133

found: 220.135

1-Hexyl-3-hydroxy-3-methylindolin-2-one (17b)

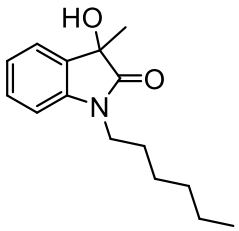

CAS: -

Synthesis following GP VIII: Compound **15b** (1.40 g, 6.05 mmol), MeMgBr (2.16 mL, 3 M in Et_2O, 6.48 mmol) in anhydrous THF (30 mL).

Yield: 1.01 g (4.08 mmol, 67%) of a yellow-orange solid.

$C_{15}H_{21}NO_2$ [247.34]

^{1}H NMR (400.1 MHz, $CDCl_3$):[1]

δ [ppm] = 7.43-7.39 (m, 1H, C_{Ar}-H), 7.34-7.29 (m, 1H, C_{Ar}-H), 7.11-7.06 (m, 1H, C_{Ar}-H), 6.88-6.83 (m, 1H, C_{Ar}-H), 3.76-3.59 (m, 2H, C-H_2), 1.72-1.63 (m, 2H, C-H_2), 1.59 (s, 3H, C-H_3), 1.39-1.25 (m', 6H, C-H_2), 0.88 (t, 3H, ^3J = 7.4 Hz, C-H_3).

^{13}C(^{1}H) NMR (100.6 MHz, $CDCl_3$):

δ [ppm] = 178.7 (quart.), 142.3 (quart.), 131.8 (quart.), 129.6 (tert.), 123.7 (tert.), 123.1 (tert.), 108.9 (tert.), 73.7 (quart.), 40.1 (sec.), 31.5 (sec.), 27.4 (sec.), 26.6 (sec.), 25.1 (prim.), 22.6 (sec.), 14.1 (prim.).

MS (ESI, pos.): $[M + Na]^{\bullet+}$

calcd: 270.146

found: 270.147

[1] The signal for the O-H proton was not observed due to rapid proton exchange.

1-Hexadecyl-3-hydroxy-3-methylindolin-2-one (17c)

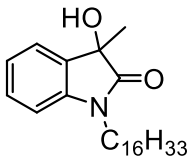

CAS: -

Synthesis following GP VIII: Compound **15c** (690 mg, 1.86 mmol), MeMgBr (662 µL, 3 M in Et_2O, 1.99 mmol) in anhydrous THF (10 mL).

Yield: 509 mg (1.31 mmol, 70%) of a yellow-orange solid.

$C_{25}H_{41}NO_2$ [387.60]

^{1}H NMR (400.1 MHz, $CDCl_3$):[1]

δ [ppm] = 7.43-7.39 (m, 1H, C_{Ar}-H), 7.34-7.28 (m, 1H, C_{Ar}-H), 7.11-7.06 (m, 1H, C_{Ar}-H), 6.88-6.83 (m, 1H, C_{Ar}-H), 3.75-3.59 (m, 2H, C-H_2), 1.72-1.63 (m, 2H, C-H_2), 1.59 (s, 3H, C-H_3), 1.39-1.21 (m', 26H, C-H_2), 0.88 (t, 3H, ^3J = 7.1 Hz, C-H_3).

^{13}C(^{1}H) NMR (100.6 MHz, $CDCl_3$):

δ [ppm] = 178.4 (quart.), 142.4 (quart.), 131.6 (quart.), 129.7 (tert.), 123.7 (tert.), 123.1 (tert.), 109.0 (tert.), 73.7 (quart.), 40.2 (sec.), 32.1 (sec.), 29.84 (2 × sec.), 29.83 (sec.), 29.81 (2 × sec.), 29.75 (sec.), 29.71 (sec.), 29.6 (sec.), 29.5 (sec.), 29.4 (sec.), 27.4 (sec.), 27.0 (sec.), 25.1 (prim.), 22.8 (sec.), 14.3 (prim.).

MS (ESI, pos.): $[M + Na]^{\bullet+}$

calcd: 410.303

found: 410.301

[1] The signal for the O-H proton was not observed due to rapid proton exchange.

5-Bromo-1-hexyl-3-hydroxy-3-methylindolin-2-one (18a)

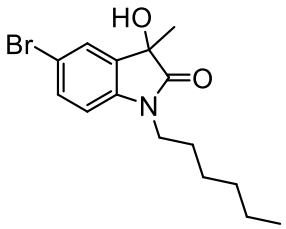

CAS: -

Synthesis following GP VIII: Compound **16a** (750 mg, 2.42 mmol), MeMgBr (862 µL, 3 M in Et_2O, 2.59 mmol) in anhydrous THF (12 mL).

Yield: 785 mg (2.41 mmol, quant.)[1] of a yellow-orange viscous oil.

$C_{15}H_{20}BrNO_2$ [326.23]

^{1}H NMR (400.1 MHz, $CDCl_3$):[2]

δ [ppm] = 7.52 (d, 1H, ^4J = 2.0 Hz, C_{Ar}-H), 7.43 (dd, 1H, ^3J = 8.3 Hz, ^4J = 2.0 Hz, C_{Ar}-H), 6.73 (d, 1H, ^3J = 8.3 Hz, C_{Ar}-H), 3.73-3.56 (m, 2H, C-H_2), 1.69-1.56 (m', 5H, C-H_2, C-H_3), 1.38-1.25 (m', 6H, C-H_2), 0.87 (t, 3H, ^3J = 7.1 Hz, C-H_3).

^{13}C(^{1}H) NMR (100.6 MHz, $CDCl_3$):

δ [ppm] = 178.1 (quart.), 141.4 (quart.), 133.6 (quart.), 132.4 (tert.), 127.2 (tert.), 115.8 (quart.), 110.5 (tert.), 73.7 (quart.), 40.3 (sec.), 31.5 (sec.), 27.3 (sec.), 26.6 (sec.), 25.1 (prim.), 22.6 (sec.), 14.1 (prim.).

HRMS (ESI, pos.): [$M^{\bullet+}$ + Na]

calcd: 348.05696

found: 348.05678 Δ = 0.52 ppm

[1] Due to the product containing impurities and/or solvent residues the reported yield is greater than 100%.
[2] The signal for the O-H proton was not observed due to rapid proton exchange.

5-Bromo-1-hexadecyl-3-hydroxy-3-methylindolin-2-one (18b)

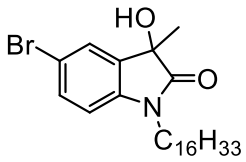

CAS: -

Synthesis following GP VIII: Compound **16b** (4.33 g, 9.61 mmol), MeMgBr (7.35 mL, 1.4 M in THF/toluene, 10.3 mmol) in anhydrous THF (48 mL).

Yield: 3.59 g (7.70 mmol, 80%) of a pale-yellow solid.

$C_{25}H_{40}BrNO_2$ [466.50]

^{1}H NMR (400.1 MHz, $CDCl_3$):[1]

δ [ppm] = 7.52 (d, 1H, ^4J = 2.0 Hz, C_{Ar}-H), 7.42 (dd, 1H, ^3J = 8.3 Hz, ^4J = 2.0 Hz, C_{Ar}-H), 6.72 (d, 1H, ^3J = 8.3 Hz, C_{Ar}-H), 3.73-3.55 (m, 2H, C-H_2), 1.68-1.53 (m', 5H, C-H_2, C-H_3), 1.34-1.20 (m', 26H, C-H_2), 0.87 (t, 3H, ^3J = 7.1 Hz, C-H_3).

^{13}C(^{1}H) NMR (100.6 MHz, $CDCl_3$):

δ [ppm] = 178.3 (quart.), 141.3 (quart.), 133.8 (quart.), 132.4 (tert.), 127.2 (tert.), 115.6 (quart.), 110.4 (tert.), 73.7 (quart.), 40.3 (sec.), 32.1 (sec.), 29.83 (2 × sec.), 29.82 (sec.), 29.79 (2 × sec.), 29.75 (sec.), 29.7 (sec.), 29.6 (sec.), 29.5 (sec.), 29.4 (sec.), 27.3 (sec.), 26.9 (sec.), 25.1 (prim.), 22.8 (sec.), 14.3 (prim.).

MS (MALDI, pos.): $[M - H_2O]^{\bullet+}$

calcd: 449.211

found: 449.255

[1] The signal for the O-H proton was not observed due to rapid proton exchange.

1-Butyl-3-methyl-3-phenylindolin-2-one (19a)

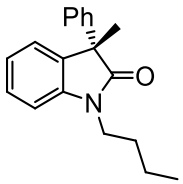

***S*-19a**

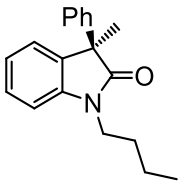

***R*-19a**

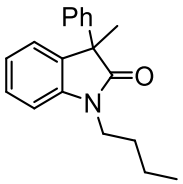

***rac*-19a**

CAS: -

Asymmetric synthesis following GP I: ***R/S*-9** (200 mg, 896 µmol), dry K_2CO_3 (1.24 g, 8.98 mmol), *n*-butyl iodide (201 µL, 325 mg, 1.77 mmol) in anhydrous DMF (3 mL). 18 h at 85 °C Purification by column chromatography (silica, DCM).

Racemic synthesis following GP IX: Compound **17a** (817 mg, 3.73 mmol), benzene (16.6 mL, 14.6 g, 187 mmol), TfOH (29.6 mL, 50.3 g, 335 mmol). 18 h at RT. Purification by column chromatography (silica, DCM).

Yield: GP I: 108 mg (387 µmol, 43%)
GP IX: 470 mg (1.68 mmol, 45%) of a pale-yellow viscous oil.

$C_{19}H_{21}NO$ [279.38]

^{1}H NMR (400.0 MHz, CD_2Cl_2):

δ [ppm] = 7.32-7.21 (m', 6H, C_{Ar}-H), 7.14-7.11 (m, 1H, C_{Ar}-H), 7.07-7.02 (m, 1H, C_{Ar}-H), 6.97-6.93 (m, 1H, C_{Ar}-H), 3.79-3.65 (m, 2H, C-H_2), 1.74 (s, 3H, C-H_3), 1.72-1.63 (m, 2H, C-H_2), 1.42-1.31 (m, 2H, C-H_2), 0.94 (t, 3H, ^3J = 7.4 Hz, C-H_3).

^{13}C(^{1}H) NMR (100.6 MHz, CD_2Cl_2):

δ [ppm] = 179.5 (quart.), 143.1 (quart.), 141.7 (quart.), 135.8 (quart.), 128.8 (tert.), 128.3 (tert.), 127.5 (tert.), 126.9 (tert.), 124.4 (tert), 122.7 (tert.), 109.0 (tert.), 52.3 (quart.), 40.2 (sec.), 29.9 (sec.), 23.5 (prim.), 20.5 (sec.), 13.9 (prim.).

HRMS (ESI, pos.): $[M + Na]^{\bullet+}$

calcd: 302.15154

found: 302.15230 Δ = 2.53 ppm

1-Hexyl-3-methyl-3-phenylindolin-2-one (19b)

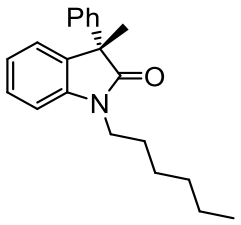

***S*-19b**

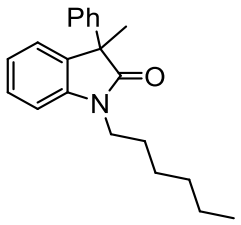

***rac*-19b**

CAS: -

Asymmetric synthesis following GP I: ***S*-9** (812 mg, 3.64 mmol), dry K_2CO_3 (5.03 g, 36.4 mmol), *n*-hexyl iodide (1.07 mL, 1.54 g, 7.26 mmol) in anhydrous DMF (18 mL). 18 h at 85 °C. Purification by column chromatography (silica, DCM).

Racemic synthesis following GP IX: Compound **17b** (1.00 g, 4.04 mmol), benzene (18.0 mL, 15.8 g, 202 mmol), TfOH (32.2 mL, 55.1 g, 367 mmol). 18 h at RT. Purification by column chromatography (silica, DCM/PE 2:1).

Yield: GP I: 940 mg (3.06 mmol, 84%)
GP IX: 1.22 g (3.97 mmol, 98%) of a pale-yellow viscous oil.

$C_{21}H_{25}NO$ [307.43]

^{1}H NMR (400.0 MHz, CD_2Cl_2):

δ [ppm] = 7.33-7.21 (m', 6H, C_{Ar}-H), 7.15-7.12 (m, 1H, C_{Ar}-H), 7.07-7.03 (m, 1H, C_{Ar}-H), 6.97-6.93 (m, 1H, C_{Ar}-H), 3.79-3.64 (m, 2H, C-H_2), 1.74 (s, 3H, C-H_3), 1.73-1.64 (m, 2H, C-H_2), 1.38-1.24 (m', 6H, C-H_2), 0.86 (t, 3H, ^3J = 6.9 Hz, C-H_3).

^{13}C(^{1}H) NMR (100.6 MHz, CD_2Cl_2):

δ [ppm] = 179.5 (quart.), 143.1 (quart.), 141.7 (quart.), 135.8 (quart.), 128.8 (tert.), 128.3 (tert.), 127.5 (tert.), 126.9 (tert.), 124.4 (tert), 122.7 (tert.), 109.0 (tert.), 52.3 (quart.), 40.4 (sec.), 31.8 (sec.), 27.7 (sec.), 26.9 (sec.), 23.5 (prim.), 22.9 (sec.), 14.1 (prim.).

MS (EI, pos.): $[M + H]^{\bullet+}$

calcd: 308.201

found: 308.201

1-Hexadecyl-3-methyl-3-phenylindolin-2-one (19c)

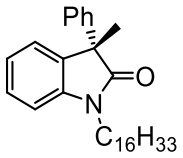

***S*-19c**

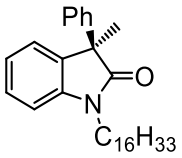

***R*-19c**

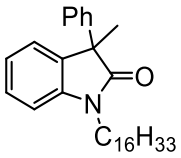

***rac*-19c**

CAS: -

Asymmetric synthesis following GP I: ***R/S*-9** (108 mg, 484 µmol), dry K_2CO_3 (669 mg, 4.84 mmol), 1-iodohexadecane (304 µL, 341 mg, 968 µmol) in anhydrous DMF (3 ml). 18 h at 85 °C. Purification by column chromatography (silica, DCM/PE 3:2).

Racemic synthesis following GP IX: Compound **17c** (450 mg, 1.16 mmol), benzene (5.16 mL, 4.53 g, 58.0 mmol), TfOH (9.25 mL, 15.7 g, 105 mmol). 18 h at RT. Purification by column chromatography (silica, DCM/PE 2:1).

Yield: GP I: 190 mg (424 µmol, 88%)
GP IX: 170 mg (380 µmol, 33%) of a colorless viscous oil.

$C_{31}H_{45}NO$ [447.71]

^{1}H NMR (400.0 MHz, $CDCl_3$):

δ [ppm] = 7.34-7.26 (m', 5H, C_{Ar}-H), 7.25-7.20 (m, 1H, C_{Ar}-H), 7.19-7.15 (m, 1H, C_{Ar}-H), 7.09 - 7.04 (m, 1H, C_{Ar}-H), 6.94-6.91 (m, 1H, C_{Ar}-H), 3.80-3.64 (m, 2H, C-H_2), 1.78 (s, 3H, C-H_3), 1.74-1.61 (m, 2H, C-H_2), 1.36-1.19 (m', 26H, C-H_2), 0.88 (t, 3H, ^3J = 7.0 Hz, C-H_3).

^{13}C(^{1}H) NMR (100.6 MHz, $CDCl_3$):

δ [ppm] = 179.4 (quart.), 142.8 (quart.), 141.1 (quart.), 135.3 (quart.), 128.7 (tert.), 128.1 (tert.), 127.3 (tert.), 126.7 (tert.), 124.4 (tert), 122.6 (tert.), 108.7 (tert.), 52.2 (quart.), 40.2 (sec.), 32.1 (sec.), 29.84 (2 × sec.), 29.83 (sec.), 29.80 (2 × sec.), 29.77

(sec.), 29.7 (sec.), 29.6 (sec.), 29.5 (sec.), 29.4 (sec.), 27.5 (sec.), 27.0 (sec.), 23.8 (prim.), 22.8 (sec.), 14.3 (prim.).

MS (MALDI, pos.): $[M]^{\bullet+}$

calcd: 447.350

found: 447.347

5-Bromo-1-hexyl-3-methyl-3-phenylindolin-2-one (20a)

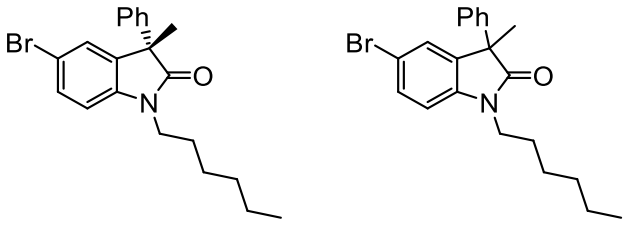

***S*-20a** ***rac*-20a**

CAS: -

Asymmetric synthesis following GP I: ***S*-10** (385 mg, 1.27 mmol), dry K_2CO_3 (1.76 g, 12.7 mmol), 1-iodohexane (375 µL, 540 mg, 2.55 mmol) in anhydrous DMF (6 ml). 64 h at 85 °C. Purification by column chromatography (silica, DCM).

Racemic synthesis following GP IX: Compound **18a** (660 mg, 2.02 mmol), benzene (8.99 mL, 7.90 g, 101 mmol), TfOH (16.1 mL, 27.3 g, 182 mmol). 18 h at RT. Purification by column chromatography (silica, DCM/PE 2:1).

Yield: GP I: 449 mg (1.16 mmol, 91%)
GP IX: 529 mg (1.37 mmol, 68%) of a colorless viscous oil.

$C_{21}H_{24}BrNO$ [386.33]

^{1}H NMR (400.1 MHz, CD_2Cl_2):

δ [ppm] = 7.43 (dd, 1H, ^{3}J = 8.3 Hz, ^{4}J = 2.0 Hz, C_{Ar}-H), 7.34-7.21 (m', 6H, C_{Ar}-H), 6.84 (d, 1H, ^{3}J = 8.4 Hz, C_{Ar}-H), 3.78-3.62 (m, 2H, C-H_2), 1.74 (s, 3H, C-H_3), 1.72-1.62 (m, 2H, C-H_2), 1.37-1.22 (m', 6H, C-H_2), 0.86 (t, 3H, ^{3}J = 7.0 Hz, C-H_3).

^{13}C(^{1}H) NMR (100.6 MHz, CD_2Cl_2):

δ [ppm] = 179.0 (quart.), 142.3 (quart.), 140.9 (quart.), 137.9 (quart.), 131.2 (tert.), 129.0 (tert.), 127.8 (tert.), 127.6 (tert.), 126.9 (tert), 115.2 (quart.), 110.6 (tert.), 52.5 (quart.), 40.5 (sec.), 31.8 (sec.), 27.6 (sec.), 26.8 (sec.), 23.3 (prim.), 22.9 (sec.), 14.1 (prim.).

HRMS (ESI, pos.): $[M + H]^{\bullet+}$

calcd: 388.10960

found: 388.10985 Δ = 0.64 ppm

5-Bromo-1-hexadecyl-3-methyl-3-phenylindolin-2-one (20b)

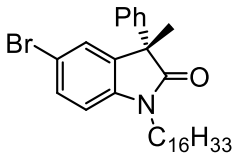

***S*-20b**

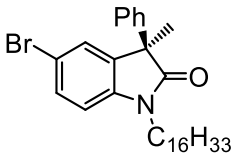

***R*-20b**

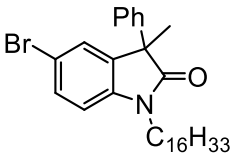

***rac*-20b**

CAS: -

Asymmetric synthesis following GP I: ***R/S*-10** (217 mg, 718 µmol), dry K_2CO_3 (992 mg, 7.18 mmol), 1-iodohexadecane (451 µL, 506 mg, 1.44 mmol) in anhydrous DMF (4 ml). 42 h at 85 °C. Purification by column chromatography (silica, DCM/PE 3:2).

Racemic synthesis following GP IX: Compound **18b** (3.59 g, 7.70 mmol), benzene (32.0 mL, 28.0 g, 358 mmol), TfOH (64.0 mL, 109 g, 726 mmol). 18 h at RT. Purification by column chromatography (silica, DCM/PE 2:3 → DCM/PE 7:3).

Yield: GP I: 360 mg (684 µmol, 95%)
GP IX: 3.48 g (6.61 mmol, 86%) of a colorless viscous oil.

$C_{31}H_{44}BrNO$ [526.59]

^{1}H NMR (400.0 MHz, CD_2Cl_2):

δ [ppm] = 7.43 (dd, 1H, ^{3}J = 8.3 Hz, ^{4}J = 2.0 Hz, C_{Ar}-H), 7.34-7.21 (m', 6H, C_{Ar}-H), 6.84 (d, 1H, ^{3}J = 8.3 Hz, C_{Ar}-H), 3.79-3.65 (m, 2H, C-H_2), 1.74 (s, 3H, C-H_3), 1.72-1.62 (m, 2H, C-H_2), 1.35-1.21 (m', 26H, C-H_2), 0.88 (t, 3H, ^{3}J = 6.9 Hz, C-H_3).

^{13}C(^{1}H) NMR (100.6 MHz, CD_2Cl_2):

δ [ppm] = 179.0 (quart.), 142.3 (quart.), 140.9 (quart.), 137.9 (quart.), 131.2 (tert.), 129.0 (tert.), 127.8 (tert.), 127.6 (tert.), 126.9 (tert), 115.2 (quart.), 110.6 (tert.), 52.5 (quart.), 40.5 (sec.), 32.3 (sec.), 30.10 (2 × sec.), 30.09 (sec.), 30.07 (2 × sec.), 30.04 (sec.), 29.93 (sec), 29.89 (sec.), 29.8 (sec.), 29.6 (sec.), 27.7 (sec.), 27.2 (sec.), 23.4 (prim.), 23.1 (sec.), 14.3 (prim.).

MS (EI, pos.): $[M + H]^{\bullet+}$

calcd: 528.2664

found: 528.2659

(*R*)-5-bromo-1-(2,7-dimethyloctyl)-3,3-dimethylindolin-2-one (33a)

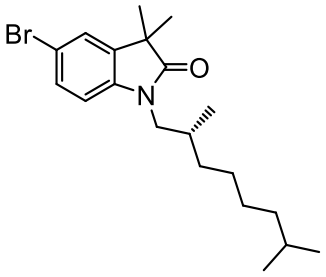

CAS: -

Synthesis following GP I: 5-bromo-3,3-dimethylindolin-2-one (**32**) (259 mg, 1.08 mmol), dry K_2CO_3 (1.49 g, 10.8 mmol), (*R*)-1-iodo-2,7-dimethyloctane (**31c**) (434 mg, 1.62 mmol) in anhydrous DMF (5 mL). 64 h at 100 °C. Purification by column chromatography (silica, DCM/PE 4:1).

Yield: 225 mg (592 µmol, 55%) of a colorless, viscous oil.

$C_{20}H_{30}BrNO$ [380.36]

^{1}H NMR (400.1 MHz, $CDCl_3$):

δ [ppm] = 7.35 (dd, 1H, ^{3}J = 8.3 Hz, ^{4}J = 2.0 Hz, C_{Ar}-H), 7.31 (d, 1H, ^{4}J = 2.0 Hz, C_{Ar}-H), 6.71 (d, 1H, ^{3}J = 8.3 Hz, C_{Ar}-H), 3.57-3.45 (m, 2H, C-H_2), 2.01-1.98 (m, 1H, C-H), 1.49 (sept, 1H, ^{3}J = 6.6 Hz, C-H), 1.40-1.10 (m', 14H, C-H_2, C-H_3), 0.89-0.82 (m', 9H, C-H_3).

^{13}C(^{1}H) NMR (100.6 MHz, $CDCl_3$):

δ [ppm] = 181.0 (quart.), 141.6 (quart.), 138.1 (quart.), 130.5 (tert.), 125.9 (tert.), 115.0 (quart.), 110.2 (tert.), 46.3 (sec.), 44.4 (quart.), 39.0 (sec.), 34.5 (sec.), 31.6 (tert.), 28.0 (tert.), 27.7 (sec.), 27.2 (sec.), 24.6 (prim.), 24.5 (prim.), 22.78 (prim.), 22.73 (prim.), 17.6 (prim.).

HRMS (ESI, pos.): $[M + Na]^{\bullet+}$

calcd: 402.14030

found: 402.14083 Δ = 1.32 ppm

(*R*)-5-bromo-1-(2-ethyl-7-methyloctyl)-3,3-dimethylindolin-2-one (33b)

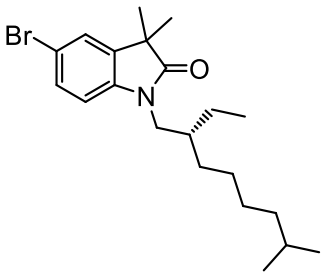

CAS: -

Synthesis following GP I: 5-bromo-3,3-dimethylindolin-2-one (**32**) (533 mg, 2.22 mmol), dry Na_2CO_3 (2.14 g, 20.2 mmol), (*R*)-1-iodo-2,7-dimethyloctane (**31d**) (570 mg, 2.02 mmol) in anhydrous DMF (10 mL). 48 h at 100 °C. Purification by column chromatography (silica, DCM/PE 9:1).

Yield: 232 mg (588 µmol, 29%) of a colorless, viscous oil.

$C_{21}H_{32}BrNO$ [394.39]

^{1}H NMR (400.1 MHz, $CDCl_3$):

δ [ppm] = 7.35 (dd, 1H, ^{3}J = 8.3 Hz, ^{4}J = 2.0 Hz, C_{Ar}-H), 7.31 (d, 1H, ^{4}J = 2.0 Hz, C_{Ar}-H), 6.71 (d, 1H, ^{3}J = 8.3 Hz, C_{Ar}-H), 3.62-3.51 (m, 2H, C-H_2), 1.85-1.74 (m, 1H, C-H), 1.49 (sept, 1H, ^{3}J = 6.6 Hz, C-H), 1.39-1.18 (m', 14H, C-H_2, C-H_3), 1.17-1.11 (m, 2H, C-H_2), 0.91 (t, 3H, ^{3}J = 7.4 Hz, C-H_3), 0.85-0.82 (m', 6H, C-H_3).

^{13}C(^{1}H) NMR (100.6 MHz, $CDCl_3$):

δ [ppm] = 181.1 (quart.), 141.6 (quart.), 138.2 (quart.), 130.5 (tert.), 125.9 (tert.), 115.0 (quart.), 110.2 (tert.), 44.4 (quart.), 44.0 (sec.), 39.0 (sec.), 37.3 (tert.), 31.3 (sec.), 28.1 (tert.), 27.8 (sec.), 26.8 (sec.), 24.6 (2 × prim.), 24.1 (sec.), 22.8 (2 × prim.), 10.7 (prim.).

HRMS (ESI, pos.): $[M + Na]^{\bullet+}$

calcd: 418.15414

found: 418.15422 Δ = 0.19 ppm

1-Butyl-2,3-dimethyl-3-phenyl-3*H*-indol-1-ium chloride (21a)

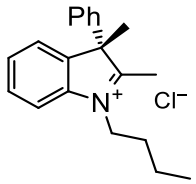

S-**21a**

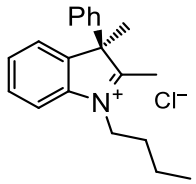

R-**21a**

CAS: -

Synthesis following GP II: ***R/S*-19a** (108 mg, 387 µmol), MeMgBr (515 µL, 3 M in Et_2O, 1.55 mmol) in anhydrous THF (4 mL). Crude product was used without further purification or characterization.

$C_{20}H_{24}NCl$ [313.86]

(*S*)-1-Hexyl-2,3-dimethyl-3-phenyl-3*H*-indol-1-ium chloride (21b)

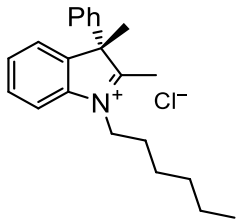

CAS: -

Synthesis following GP II: ***S*-19b** (927 mg, 3.02 mmol), MeMgBr (4.02 mL, 3 M in Et_2O, 12.1 mmol) in anhydrous THF (30 mL). Crude product was used without further purification or characterization.

$C_{22}H_{28}ClN$ [341.92]

1-Hexadecyl-2,3-dimethyl-3-phenyl-3*H*-indol-1-ium chloride (21c)

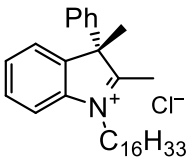

S-**21c**

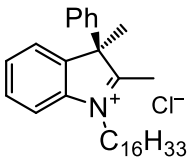

R-**21c**

CAS: -

Synthesis following GP II: ***R*/*S*-19c** (190 mg, 424 µmol), MeMgBr (566 µL, 3 M in Et_2O, 1.70 mmol) in anhydrous THF (5 mL). Crude product used without further purification or characterization.

$C_{32}H_{48}NCl$ [482.18]

(*S*)-5-Bromo-1-hexyl-2,3-dimethyl-3-phenyl-3*H*-indol-1-ium chloride (22a)

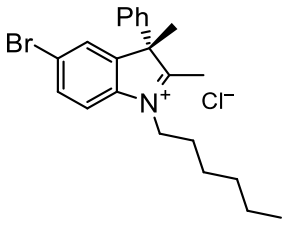

CAS: -

Synthesis following GP II: **20a** (87.0 mg, 225 µmol), MeMgBr (300 µL, 3 M in Et_2O, 900 µmol) in anhydrous THF (2 mL). Crude product used without further purification or characterization.

$C_{22}H_{227}BrNCl$ [420.81]

5-Bromo-1-hexadecyl-2,3-dimethyl-3-phenyl-3*H*-indol-1-ium chloride (22b)

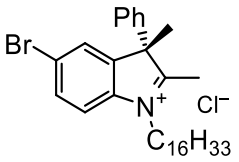

S-**22b**

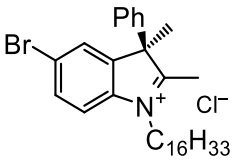

R-**22b**

CAS: -

Synthesis following GP II: ***R/S*-20b** (334 mg, 634 µmol), MeMgBr (515 µL, 1.4 M in THF/toluene 1:3, 721 µmol) in anhydrous THF (6 mL). Crude product used without further purification or characterization.

$C_{32}H_{47}BrNCl$ [561.08]

(*S*)-1-Butyl-2,3-dimethyl-3-propyl-3*H*-indol-1-ium iodide (23)

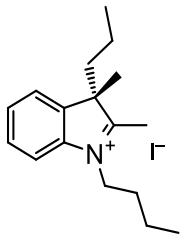

CAS: -

Synthesis based on given literature.[89, 92, 94, 260]

S-2,3-Dimethyl-3-propyl-3*H*-indole (***S*-13**) (200 mg, 1.07 mmol) and 1-iodobutane (425 µL, 688 mg, 3.74 mmol) were dissolved in $MeNO_2$ (2 mL) and the mixture heated to reflux for 18 h. The solvent was then removed under reduced pressure and the residue was used for further synthesis without purification or characterization. The yield was assumed to be quantitative.

$C_{17}H_{26}NI$ [371.30]

(*S*)-5-Bromo-2,3-dimethyl-1-(7-methyloctyl)-3-propyl-3*H*-indol-1-ium iodide (24)

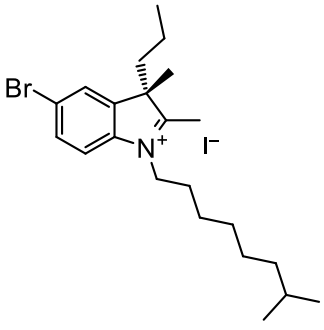

CAS: -

Synthesis based on given literature.[89, 92, 94, 260]

S-5-Bromo-2,3-dimethyl-3-propyl-3*H*-indole (***S*-14**) (448 mg, 1.68 mmol) and 1-iodo-7-methyloctane (**31a**) (1.28 g, 5.04 mmol) were dissolved in MeNO2 (3 mL) and the mixture

heated to reflux for 8 h. The solvent was then removed under reduced pressure, the residue suspended in Et_2O and stored at 4 °C for 2 h. The precipitated solid was filtered off and generously washed with Et_2O. The hereby obtained crude product was used without further purification.

Yield: 644 mg (1.24 mmol, 74%) of an off-white solid.

$C_{22}H_{35}BrNI$ [520.33]

^{1}H NMR (400.0 MHz, CD_2Cl_2):

δ [ppm] = 7.77 (dd, 1H, ^3J = 8.5 Hz, ^4J = 1.7 Hz, C_{Ar}-H), 7.73 (d, 1H, ^4J = 1.7 Hz, C_{Ar}-H), 7.62 (d, 1H, ^3J = 8.5 Hz, C_{Ar}-H), 4.75-4.65 (m, 1H, C-H_2), 4.64-4.53 (m, 1H, C-H_2), 3.02 (s, 3H, C-H_3), 2.18-2.01 (m, 2H, C-H_2), 2.00-1.80 (m, 2H, C-H_2), 1.67 (s, 3H, C-H_3), 1.56-1.41 (m', 3H, C-H_2, C-H), 1.40-1.23 (m', 4H, C-H_2), 1.19-1.11 (m, 2H, C-H_2), 0.88-0.67 (m', 11H, C-H_2, C-H_3).

^{13}C(^{1}H) NMR (100.6 MHz, CD_2Cl_2):

δ [ppm] = 196.2 (quart.), 142.6 (quart.), 141.2 (quart.), 133.1 (tert.), 127.5 (tert.), 124.9 (quart.), 117.2 (tert.), 59.6 (quart.), 50.9 (sec.), 40.4 (sec.), 39.1 (sec.), 29.7 (sec.), 28.5 (sec.), 28.3 (tert.), 27.4 (sec.), 27.2 (sec.), 22.7 (2 × prim.), 22.4 (prim.), 18.1 (sec.), 17.2 (prim.), 14.0 (prim.).

HRMS (ESI, pos.): $[M - I]^+$

calcd: 394.19294

found: 394.19270 Δ = 0.61 ppm

5-Bromo-2,3,3-trimethyl-1-(7-methyloctyl)-3*H*-indol-1-ium iodide (34a)

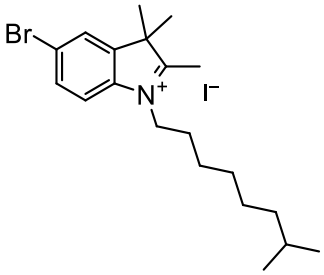

CAS: -

Synthesis based on given literature. [89, 92, 94, 260]

1-Iodo-7-methyloctane (**31a**) (650 mg, 2.56 mmol) and 5-bromo-2,3,3-trimethyl-3*H*-indole (500 mg, 2.10 mmol) were dissolved in $MeNO_2$ (5 mL). The mixture was heated to reflux for 18 h. The solvent was then removed under reduced pressure, the residue suspended in Et_2O and stored at 4 °C for 2 h. The precipitated solid was filtered off and generously washed with Et_2O. The hereby obtained crude product was used without further purification.

Yield: 677 mg (1.38 mmol, 66%) of an off-white solid.

$C_{20}H_{31}BrNI$ [492.28]

^{1}H NMR (400.0 MHz, CD_2Cl_2):

δ [ppm] = 7.79-7.73 (m', 2H, C_{Ar}-H), 7.62-7.58 (m, 1H, C_{Ar}-H), 4.59 (t, 2H, ^3J = 7.8 Hz, C-H_2), 3.01 (s, 3H, C-H_3), 1.98-1.86 (m, 2H, C-H_2), 1.64 (s, 6H, C-H_3), 1.56-1.41 (m', 3H, C-H_2, C-H), 1.40-1.24 (m, 4H, C-H_2), 1.19-1.11 (m, 2H, C-H_2), 0.85 (d, 6H, ^3J = 6.6 Hz, C-H_3).

^{13}C(^{1}H) NMR (100.6 MHz, CD_2Cl_2):

δ [ppm] = 196.2 (quart.), 143.9 (quart.), 140.5 (quart.), 133.0 (tert.), 127.4 (tert.), 124.8 (quart.), 117.3 (tert.), 55.2 (quart.), 50.7 (sec.), 39.1 (sec.), 29.7 (sec.), 28.23 (tert.), 28.17 (sec.), 27.4 (sec.), 27.1 (sec.), 23.2 (prim.), 22.7 (prim.), 17.0 (prim.).

HRMS (ESI, pos.): [M^+]

calcd: 364.16344

found: 364.16335 Δ = 0.25 ppm

(*R*)-5-bromo-1-(2,7-dimethyloctyl)-2,3,3-trimethylindol-1-ium chloride (34c)

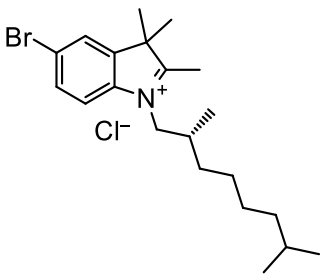

CAS: -

Synthesis following GP II: **33a** (225 mg, 592 µmol), MeMgBr (789 µL, 3 M in Et_2O, 2.37 mmol) in anhydrous THF (6 mL). Crude product used without further purification or characterization.

$C_{21}H_{33}BrNCl$ [414.85]

(*R*)-5-bromo-1-(2-ethyl-7-methyloctyl)-2,3,3-trimethylindol-1-ium chloride (34d)

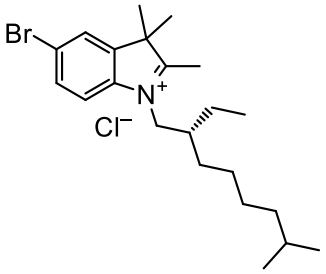

CAS: -

Synthesis following GP II: **33b** (225 mg, 571 µmol), MeMgBr (789 µL, 3 M in Et_2O, 2.37 mmol) in anhydrous THF (6 mL). Crude product used without further purification or characterization.

$C_{22}H_{35}BrNCl$ [428.88]

1-Hexyl-2,3,3-trimethyl-3*H*-indol-1-ium iodide (35a)

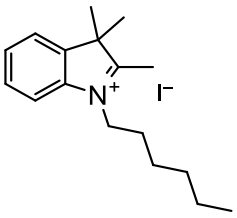

CAS: -

Synthesis based on given literature.[89, 92, 94, 260]

1-Iodohexane (9.55 mL, 13.8 g, 65.1 mmol) and 2,3,3-trimethyl-3*H*-indole (2.95 g, 18.5 mmol) were dissolved in $MeNO_2$ (37 mL). The mixture was heated to reflux for 18 h. The solvent was then removed under reduced pressure, the residue suspended in Et_2O and stored at 4 °C for 2 h. The precipitated solid was filtered off and generously washed with Et_2O. The hereby obtained crude product was used without further purification.

Yield: 5.71 g (15.4 mmol, 83%) of a brown solid.

$C_{17}H_{26}NI$ [371.30]

^{1}H NMR (400.0 MHz, CD_2Cl_2):

δ [ppm] = 7.71-7.66 (m, 1H, C_{Ar}-H), 7.65-7.58 (m', 3H, C_{Ar}-H), 4.59 (t, 2H, ^3J = 7.8 Hz, C-H_2), 3.03 (s, 3H, C-H_3), 1.99-1.89 (m, 2H, C-H_2), 1.63 (s, 6H, C-H_3), 1.52-1.41 (m, 2H, C-H_2,), 1.41-1.26 (m', 4H, C-H_2), 0.88 (t, 3H, ^3J = 7.1 Hz, C-H_3).

^{13}C(^{1}H) NMR (100.6 MHz, CD_2Cl_2):

δ [ppm] = 195.9 (quart.), 142.0 (quart.), 141.3 (quart.), 130.5 (tert.), 129.8 (tert.), 123.8 (tert.), 115.6 (tert.), 55.0 (quart.), 50.2 (sec.), 31.5 (sec.), 28.2 (sec.), 26.7 (sec.), 23.2 (prim.), 22.7 (sec.), 16.8 (prim.), 14.0 (prim.).

MS (ESI, pos.): $[M - I]^+$

calcd: 244.206

found: 244.207

1-Hexadecyl-2,3,3-trimethyl-3*H*-indol-1-ium iodide (35b)

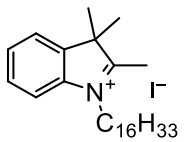

CAS: -

Synthesis based on given literature.[89, 92, 94, 260]

1-Iodohexadecane (12.3 mL, 13.8 g, 39.2 mmol) and 2,3,3-trimethyl-3*H*-indole (2.50 g, 15.7 mmol) were dissolved in $MeNO_2$ (30 mL). The mixture was heated to reflux for 18 h. The

solvent was then removed under reduced pressure, the residue suspended in Et_2O and stored at 4 °C for 2 h. The precipitated solid was filtered off and generously washed with Et_2O. The hereby obtained crude product was used without further purification.

Yield: 6.74 g (13.2 mmol, 84%) of an off-white solid.

$C_{27}H_{46}NI$ [511.57]

^{1}H NMR (400.1 MHz, CD_2Cl_2):

δ [ppm] = 7.70-7.65 (m, 1H, C_{Ar}-H), 7.64-7.58 (m', 3H, C_{Ar}-H), 4.60 (t, 2H, ^3J = 7.9 Hz, C-H_2), 3.03 (s, 3H, C-H_3), 1.99-1.89 (m, 2H, C-H_2), 1.63 (s, 6H, C-H_3), 1.51-1.19 (m', 26H, C-H_2,), 0.87 (t, 3H, ^3J = 7.0 Hz, C-H_3).

^{13}C(^{1}H) NMR (100.6 MHz, CD_2Cl_2):

δ [ppm] = 195.9 (quart.), 142.0 (quart.), 141.3 (quart.), 130.5 (tert.), 129.8 (tert.), 123.8 (tert.), 115.6 (tert.), 55.0 (quart.), 50.3 (sec.), 32.2 (sec.), 30.01 (sec.), 30.00 (sec.), 29.99 (sec.), 29.97 (sec.), 29.96 (sec.), 29.9 (sec), 29.8 (sec.), 29.7 (sec.), 29.6 (sec.), 29.4 (sec.), 28.4 (sec.), 27.1 (sec.), 23.2 (prim.), 23.0 (sec.), 16.8 (prim.), 14.2 (prim.).

MS (ESI, pos.): $[M - I]^+$

calcd: 384.362

found: 384.364

5-Bromo-1-hexyl-2,3,3-trimethyl-3*H*-indol-1-ium iodide (36a)

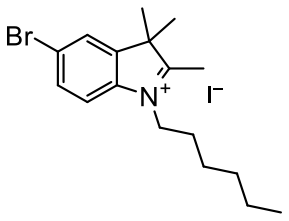

CAS: -

Synthesis based on given literature.[89, 92, 94, 260]

1-Iodohexane (6.52 mL, 9.38 g, 44.2 mmol) and 5-bromo-2,3,3-trimethyl-3*H*-indole (3.01 g, 12.6 mmol) were dissolved in $MeNO_2$ (25 mL). The mixture was heated to reflux for 18 h. The solvent was then removed under reduced pressure, the residue suspended in Et_2O and stored at 4 °C for 2 h. The precipitated solid was filtered off and generously washed with Et_2O. The hereby obtained crude product was used without further purification.

Yield: 4.48 g (9.95 mmol, 79%) of a brown solid.

$C_{17}H_{25}BrNI$ [450.20]

^{1}H NMR (400.0 MHz, CD_2Cl_2):

δ [ppm] = 7.79-7.72 (m', 2H, C_{Ar}-H), 7.65 (d, 1H, ^3J = 8.6 Hz, C_{Ar}-H), 4.58 (t, 2H, ^3J = 7.8 Hz, C-H_2), 3.02 (s, 3H, C-H_3), 1.96-1.86 (m, 2H, C-H_2), 1.64 (s, 6H, C-H_3), 1.50-1.40 (m, 2H, C-H_2,), 1.39-1.25 (m', 4H, C-H_2), 0.88 (t, 3H, ^3J = 7.1 Hz, C-H_3).

^{13}C(^{1}H) NMR (100.6 MHz, CD_2Cl_2):

δ [ppm] = 196.1 (quart.), 143.9 (quart.), 140.4 (quart.), 132.9 (tert.), 127.3 (tert.), 124.7 (quart.), 117.3 (tert.), 55.1 (quart.), 50.6 (sec.), 31.5 (sec.), 28.1 (sec.), 26.7 (sec.), 23.1 (prim.), 22.6 (sec.), 17.1 (prim.), 14.0 (prim.).

MS (ESI, pos.): $[M - I]^+$

calcd: 322.116

found: 322.118

5-Bromo-1-hexadecyl-2,3,3-trimethyl-3*H*-indol-1-ium iodide (36b)

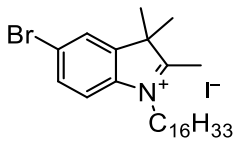

CAS: 1227384-10-2

Synthesis based on given literature.[89, 92, 94, 260]

1-Iodohexadecane (14.4 mL, 15.9 g, 45.1 mmol) and 5-bromo-2,3,3-trimethyl-3*H*-indole (3,06 g, 12.9 mmol) were dissolved in $MeNO_2$ (25 mL). The mixture was heated to reflux for

18 h. The solvent was then removed under reduced pressure, the residue suspended in Et_2O and stored at 4 °C for 2 h. The precipitated solid was filtered off and generously washed with Et_2O. The hereby obtained crude product was used without further purification.

Yield: 4.03 g (6.83 mmol, 53%) of an off-white solid.

$C_{27}H_{45}BrNI$ [590.46]

^{1}H NMR (400.1 MHz, CD_2Cl_2):

δ [ppm] = 7.78-7.74 (m', 2H, C_{Ar}-H), 7.58-7.54 (m, 1H, C_{Ar}-H), 4.59 (t, 2H, ^3J = 7.7 Hz, C-H_2), 3.01 (s, 3H, C-H_3), 1.97-1.87 (m, 2H, C-H_2), 1.65 (s, 6H, C-H_3), 1.50-1.20 (m', 26H, C-H_2,), 0.87 (t, 3H, ^3J = 7.0 Hz, C-H_3).

Compound 37a

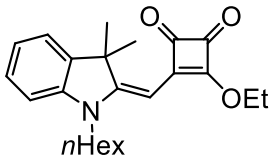

CAS: 457961-79-4

Synthesis following GP VII: **35a** (5.71 g, 15.4 mmol), squaric acid diethylester (1.90 mL, 2.18 mg, 12.8 mmol) in EtOH/NEt_3 (4:1, 11 mL). 4 h at 80 °C. Purification by column chromatography (silica, EA/PE 3:17).

Yield: 2.32 g (6.31 mmol, 49%) of an orange solid.

$C_{23}H_{29}NO_3$ [367.48]

^{1}H NMR (400.1 MHz, CD_2Cl_2):

δ [ppm] = 7.31-7.24 (m', 2H, C_{Ar}-H), 7.09-7.04 (m, 1H, C_{Ar}-H), 6.93-6.89 (m, 1H, C_{Ar}-H), 5.41 (s, 1H, C-H), 4.86 (q, 2H, ^3J = 7.1 Hz, C-H_2), 3.81 (t, 2H, ^3J = 8.2 Hz, C-H_2), 1.79-1.69 (m, 2H, C-H_2), 1.61 (s, 6H, C-H_3), 1.51 (t, 3H, ^3J = 7.1 Hz, C-H_3), 1.46-1.25 (m', 6H, C-H_2), 0.90 (t, 3H, ^3J = 7.0 Hz, C-H_3).

Compound 37b

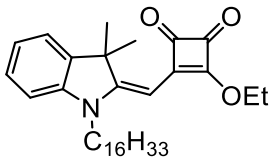

CAS: 1570368-74-9

Synthesis following GP VII: **35b** (6.00 g, 11.7 mmol), squaric acid diethylester (1.45 mL, 1.66 g, 9.76 mmol) in EtOH/NEt_3 (4:1, 9 mL). 4 h at 80 °C. Purification by column chromatography (silica, EA/PE 3:17).

Yield: 2.26 g (4.45 mmol, 46%) of an orange solid.

$C_{33}H_{49}NO_3$ [507.75]

^{1}H NMR (400.1 MHz, CD_2Cl_2):

δ [ppm] = 7.31-7.24 (m', 2H, C_{Ar}-H), 7.09-7.04 (m, 1H, C_{Ar}-H), 6.93-6.89 (m, 1H, C_{Ar}-H), 5.41 (s, 1H, C-H), 4.86 (q, 2H, ^3J = 7.1 Hz, C-H_2), 3.81 (t, 2H, ^3J = 7.7 Hz, C-H_2), 1.79-1.68 (m, 2H, C-H_2), 1.61 (s, 6H, C-H_3), 1.52 (t, 3H, ^3J = 7.1 Hz, C-H_3), 1.46-1.33 (m', 4H, C-H_2), 1.32-1.21 (m', 22H, C-H_2), 0.88 (t, 3H, ^3J = 7.0 Hz, C-H_3).

Compound 38a

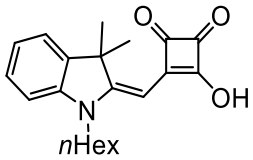

CAS: 457961-82-9

Synthesis based on given literature.[260, 300]

Compound **37a** (2.00 g, 5.44 mmol) was dissolved in acetone (200 mL) and heated to reflux, before aq. HCl (200 mL, 2M) was added. The mixture was further heated to reflux for 2 h. The

solvent was removed under reduced pressure and the crude product used without further purification.

Yield: 1.87 g (5.50 mmol, quant.)[1] of a dark yellow oil.

$C_{21}H_{25}NO_3$ [339.43]

^{1}H NMR (400.1 MHz, acetone-d_6):

δ [ppm] = 7.44-7.36 (m, 1H, C_{Ar}-H), 7.33-7.24 (m, 1H, C_{Ar}-H), 7.15-7.01 (m', 2H, C_{Ar}-H), 5.59 (s, 1H, C-H), 6.00-4.81 (br, 1H, O-H), 4.02-3.92 (m, 2H, C-H_2), 1.82-1.72 (m, 2H, C-H_2), 1.63 (s, 6H, C-H_3), 1.51-1.41 (m, 2H, C-H_2), 1.41-1.26 (m', 4H, C-H_2), 0.87 (t, 3H, ^3J = 7.2 Hz, C-H_3).

Compound 38b

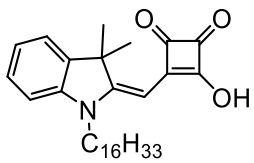

CAS: 1570368-79-4

Synthesis based on given literature.[260, 300]

Compound **37b** (840 mg, 1.65 mmol) was dissolved in acetone (60 mL) and heated to reflux, before aq. HCl (60 mL, 2M) was added. The mixture was further heated to reflux for 2 h. The solvent was removed under reduced pressure and the crude product used without further purification.

Yield: 784 mg (1.63 mmol, 99%) of a dark yellow oil.

$C_{31}H_{45}NO_3$ [479.70]

[1] Due to the product containing impurities and/or solvent residues the reported yield is greater than 100%.

^{1}H NMR (400.0 MHz, CD_2Cl_2):

δ [ppm] = 9.95-9.38 (br, 1H, O-H), 7.39-7.27 (m', 2H, C_{Ar}-H), 7.19-7.10 (m, 1H, C_{Ar}-H), 7.04-6.97 (m, 1H, C_{Ar}-H), 5.68 (s, 1H, C-H), 4.00-3.87 (m, 2H, C-H_2), 1.84-1.73 (m, 2H, C-H_2), 1.66 (s, 6H, C-H_3), 1.47-1.19 (m', 26H, C-H_2), 0.87 (t, 3H, ^3J = 7.0 Hz, C-H_3).

Compound 39a

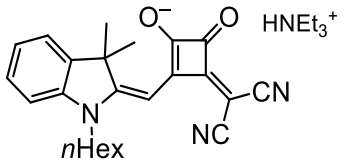

CAS: -

Synthesis following GP III: Compound **37a** (446 mg, 1.21 mmol), malonic acid dinitrile (87.0 mg, 1.32 mmol), NEt_3 (328 µL, 239 mg, 2.36 mmol) in EtOH (5 mL). 3 h at RT. Crude product used without further purification.

Yield: 612 mg (1.25 mmol, quant.)[1] of a brown solid.

$C_{30}H_{40}N_4O_2$ [488.67]

^{1}H NMR (400.1 MHz, CD_2Cl_2):[2]

δ [ppm] = 7.27-7.20 (m', 2H, C_{Ar}-H), 7.02-6.96 (m, 1H, C_{Ar}-H), 6.87-6.83 (m, 1H, C_{Ar}-H), 6.08 (s, 1H, C-H), 3.78 (t, 2H, ^3J = 7.7 Hz, C-H_2), 3.23 (q, 6H, ^3J = 7.3 Hz, C-H_2), 1.77-1.68 (m, 2H, C-H_2), 1.63 (s, 6H, C-H_3), 1.47-1.38 (m, 2H, C-H_2), 1.38-1.28 (m', 13H, C-H_2, C-H_3), 0.88 (t, 3H, ^3J = 7.2 Hz, C-H_3).

^{13}C(^{1}H) NMR (100.6 MHz, CD_2Cl_2):

δ [ppm] = 191.7 (quart.), 185.2 (quart.), 177.7 (quart.), 168.6 (quart.), 165.8 (quart.), 143.7 (quart.), 141.3 (quart.), 127.9 (tert.), 122.0 (tert.), 121.9 (tert.), 119.0 (quart.), 118.6 (quart.), 108.3 (tert.), 85.2 (tert.), 47.6 (quart.), 47.1 (sec.), 43.5 (sec.), 39.7

[1] Due to the product containing impurities and/or solvent residues the reported yield is greater than 100%.
[2] The signal for the N-H proton was not observed due to rapid proton exchange.

(quart.), 32.0 (sec.), 27.4 (prim.), 26.84 (sec.), 26.80 (sec.), 22.9 (sec.), 14.2 (prim.), 9.2 (prim.).

MS (ESI, neg.): $[M - HNEt_3]^-$

calcd: 386.187

found: 386.188

Compound 39b

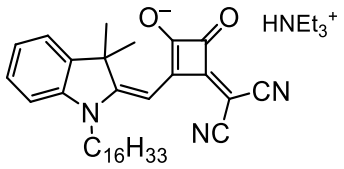

CAS: -

Synthesis following GP III: Compound **37b** (1.00 g, 1.97 mmol), malonic acid dinitrile (141 mg, 2.13 mmol), NEt_3 (532 µL, 389 mg, 3.84 mmol) in EtOH (8 mL). 4 h at RT. Crude product used without further purification.

Yield: 1.07 g (1.70 mmol, 86%) of a brown solid.

$C_{40}H_{60}N_4O_2$ [628.93]

^{1}H NMR (400.1 MHz, CD_2Cl_2):

δ [ppm] = 10.23-9.79 (br, 1H, N-H), 7.26-7.19 (m', 2H, C_{Ar}-H), 7.02-6.96 (m, 1H, C_{Ar}-H), 6.87-6.82 (m, 1H, C_{Ar}-H), 6.08 (s, 1H, C-H), 3.78 (t, 2H, ^3J = 7.7 Hz, C-H_2), 3.27 (q, 6H, ^3J = 7.3 Hz, C-H_2), 1.78-1.67 (m, 2H, C-H_2), 1.62 (s, 6H, C-H_3), 1.45-1.22 (m', 35H, C-H_2, C-H_3), 0.87 (t, 3H, ^3J = 7.0 Hz, C-H_3).

The ^{13}C NMR analysis was precluded due to significant signal broadening

HRMS (ESI, neg.): $[M^-]$

calcd: 526.34390

found: 526.34364 Δ = 0.49 ppm

Compound 40a

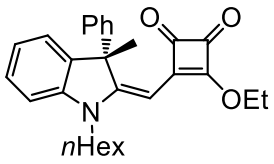

CAS: -

Synthesis following GP VII: ***S*-21b** (1.03 g, 3.01 mmol), squaric acid diethylester (446 µL, 513 mg, 3.01 mmol) in EtOH/NEt_3 (4:1, 3 mL). 4 h at 80 °C. Purification by column chromatography (silica, Acetone/DCM 3:97).

Yield: 674 mg (1.57 mmol, 52%) of an orange solid.

$C_{28}H_{31}NO_3$ [429.55]

^{1}H NMR (400.1 MHz, CD_2Cl_2):

δ [ppm] = 7.32-7.15 (m', 6H, C_{Ar}-H), 7.12-7.09 (m, 1H, C_{Ar}-H), 6.96-6.90 (m', 2H, C_{Ar}-H), 5.67 (s, 1H, C-H), 4.56 (dq, 1H, ^2J = 10.4 Hz, ^3J = 7.1 Hz, C-H_2), 4.43 (dq, 1H, ^2J = 10.4 Hz, ^3J = 7.1 Hz, C-H_2), 3.95 (t, 2H, ^3J = 7.7 Hz, C-H_2), 1.97 (s, 3H, C-H_3), 1.91-1.81 (m, 2H, C-H_2), 1.53-1.43 (m', 2H, C-H_2), 1.44-1.32 (m', 4H, C-H_2), 1.24 (t, 3H, ^3J = 7.1 Hz, C-H_3), 0.92 (t, 3H, ^3J = 7.2 Hz, C-H_3).

^{13}C(^{1}H) NMR (100.6 MHz, CD_2Cl_2):

δ [ppm] = 193.3 (quart.), 188.5 (quart.), 186.9 (quart.), 173.1 (quart.), 166.5 (quart.), 143.4 (quart.), 142.6 (quart.), 140.5 (quart.), 128.7 (tert.), 128.2 (tert.), 126.9 (tert.), 126.4 (tert.), 123.3 (tert.), 122.8 (tert.), 109.0 (tert.), 82.1 (tert.), 69.6 (sec.), 56.0 (quart.), 43.6 (sec.), 31.9 (sec.), 27.1 (sec.), 26.7 (sec.), 26.6 (prim.), 22.9 (sec.), 15.8 (prim.), 14.2 (prim.).

MS (ESI, pos.): $[M]^{\bullet+}$

calcd: 429.230

found: 429.228

Compound 40b

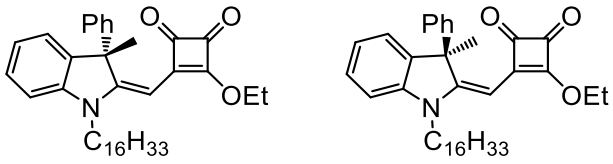

***S*-40b** ***R*-40b**

CAS: -

Synthesis following GP VII: ***R/S*-21c** (204 mg, 423 µmol), squaric acid diethylester (62.8 µL, 72.2 mg, 424 µmol) in EtOH/NEt_3 (4:1, 1 mL). 4 h at 80 °C. Purification by column chromatography (silica, EA/PE 1:4).

Yield: 101 mg (177 µmol, 42%) of an orange solid.

$C_{38}H_{51}NO_3$ [569.82]

^{1}H NMR (600.1 MHz, CD_2Cl_2):

δ [ppm] = 7.32-7.15 (m', 6H, C_{Ar}-H), 7.11-7.09 (m, 1H, C_{Ar}-H), 6.95-6.90 (m', 2H, C_{Ar}-H), 5.67 (s, 1H, C-H), 4.47 (dq, 1H, ^2J = 10.4 Hz, ^3J = 7.1 Hz, C-H_2), 4.44 (dq, 1H, ^2J = 10.4 Hz, ^3J = 7.1 Hz, C-H_2), 3.95 (t, 2H, ^3J = 7.7 Hz, C-H_2), 1.97 (s, 3H, C-H_3), 1.89-1.83 (m, 2H, C-H_2), 1.52-1.46 (m', 2H, C-H_2), 1.45-1.38 (m', 2H, C-H_2), 1.35-1.22 (m', 25H, C-H_2, C-H_3), 0.88 (t, 3H, ^3J = 7.0 Hz, C-H_3).

^{13}C(^{1}H) NMR (150.9 MHz, CD_2Cl_2):

δ [ppm] = 193.3 (quart.), 188.5 (quart.), 186.9 (quart.), 173.1 (quart.), 166.5 (quart.), 143.4 (quart.), 142.6 (quart.), 140.6 (quart.), 128.7 (tert.), 128.2 (tert.), 126.9 (tert.), 126.4 (tert.), 123.3 (tert.), 122.8 (tert.), 109.0 (tert.), 82.1 (tert.), 69.6 (sec.), 56.0 (quart.), 43.6 (sec.), 32.3 (sec.), 30.09 (2 × sec.), 30.08 (sec.), 30.07 (sec.), 30.05 (sec.), 30.02 (sec.), 29.97 (sec.), 29.9 (sec.), 29.8 (2 × sec.), 27.5 (sec.), 26.8 (sec.), 26.6 (prim.), 23.1 (sec.), 15.8 (prim.), 14.3 (prim.).

HRMS (ESI, pos.): $[M + Na]^{\bullet+}$

calcd: 592.37612

found: 592.37632 Δ = 0.34 ppm

Compound 41a

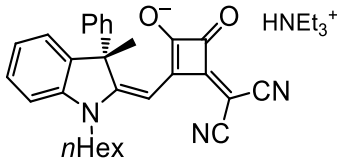

CAS: -

Synthesis following GP III: Compound **40a** (600 mg, 1.40 mmol), malonic acid dinitrile (100 mg, 1.51 mmol), NEt_3 (378 µL, 276 mg, 2.72 mmol) in EtOH (6 mL). 3 h at r.t. Purification by column chromatography (silica, MeOH/DCM 1:9).

Yield: 638 mg (1.16 mmol, 83%) of a brown solid.

$C_{35}H_{42}N_4O_2$ [550.75]

The ^1H and ^{13}C NMR analyses were precluded due to significant signal broadening.

MS (ESI, pos.): $[M - HNEt_3 + Na]^+$

calcd: 471.192

found: 471.190

Compound 41b

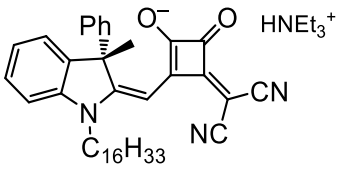

***S*-41b**

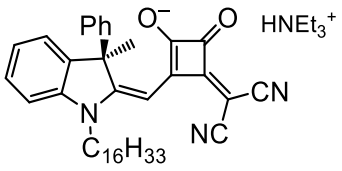

***R*-41b**

CAS: -

Synthesis following GP III: Compound ***R*/*S*-40b** (100 mg, 175 µmol), malonic acid dinitrile (12.5 mg, 189 µmol), NEt_3 (48.9 µL, 35.5 mg, 351 µmol) in EtOH (1 mL). 3 h at RT. Crude product used without further purification.

Yield: 105 mg (152 µmol, 87%) of a dark yellow solid.

$C_{45}H_{62}N_4O_2$ [691.00]

^{1}H NMR (400.1 MHz, acetone-d_6):[1]

δ [ppm] = 7.40-7.36 (m‘, 2H, C_{Ar}-H), 7.22-7.13 (m‘, 3H, C_{Ar}-H), 7.10-7.04 (m‘, 2H, C_{Ar}-H), 7.01-6.97 (m, 1H, C_{Ar}-H), 6.84-6.79 (m, 1H, C_{Ar}-H), 6.27 (s, 1H, C-H), 4.03-3.86 (m, 2H, C-H_2), 3.36 (q, 6H, ^3J = 7.3 Hz, C-H_2), 2.15 (s, 3H, C-H_3), 1.94-1.79 (m, 2H, C-H_2), 1.58-1.48 (m, 2H, C-H_2), 1.48-1.39 (m, 2H, C-H_2), 1.45-1.32 (m’, 31H, C-H_2, C-H_3), 0.88 (t, 3H, ^3J = 7.1 Hz, C-H_3).

^{13}C(^{1}H) NMR (100.6 MHz, acetone-d_6):

δ [ppm] = 193.0 (quart.), 186.1 (quart.), 178.8 (quart.), 167.5 (quart.), 162.3 (quart.), 145.4 (quart.), 144.0 (quart.), 141.3 (quart.), 128.7 (tert.), 128.4 (tert.), 127.6 (tert.), 126.7 (tert.), 123.9 (tert.), 121.8 (tert.), 119.8 (quart.), 118.6 (quart.), 108.7 (tert.), 86.9 (tert.), 55.5 (quart.), 47.7 (sec.), 43.7 (sec.), 38.7 (quart.), 32.7 (sec.), 30.5-30.3 (10 × sec)[2], 27.6 (sec.), 27.4 (prim.), 27.3 (sec.), 23.4 (sec.), 14.5 (prim.), 9.4 (prim.).

HRMS (ESI, pos.): $[M + Na]^{\bullet+}$

calcd: 611.34822

found: 611.34826 *Δ* = 0.07 ppm

[1] The signal for the N-H proton was not observed due to rapid proton exchange.

[2] An accurate determination was not possible due to superposition with the solvent signal (*δ*(CD_3OCD_3) = 29.84 ppm).Lit

8.2.4 Squaraine monomers

Ph-SQB*

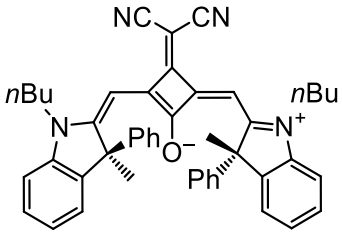

S*-Ph-SQB

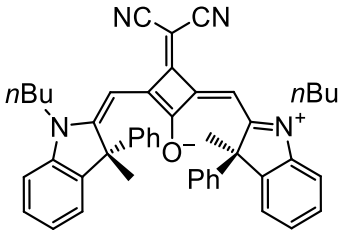

R*-Ph-SQB

CAS: -

Synthesis based on given literature.[92]

A solution of 1-butyl-3-methyl-3-phenyl-3*H*-indol-1-ium chloride ***R/S*-21a** (118 mg, 376 µmol), triethylammonium 3-(dicyanomethylene)-2-ethoxy-4-oxocyclobut-1-en-1-olate (**CN**) (54.8 mg, 188 µmol) and pyridine (333 µL, 326 mg, 4.12 mmol) in *n*BuOH/toluene 1:1 (35 mL) was heated to reflux using a Dean-Stark trap for 18 h. The solvent was removed under reduced pressure and the residue was purified by column chromatography (silica, EA/DCM 1:19) followed by recrystallization from EtOH/*n*-hexane. Single crystals were obtained by layering a DCM solution with *n*-hexane followed by slow evaporation at RT.

Yield: 98.9 mg (145 µmol, 77%) of a ruby-colored crystalline solid.

$C_{47}H_{44}N_4O$ [680.88]

HPLC (Phenomenex LUX i-Amylose-3, *n*-hexane/DCM/*i*PrOH 250:80:1, 1 mL min^{-1}):
34.5 min (*RS*-diastereomer), 37.0 min (*SS*-diastereomer), 52.3 min (*RR*-diastereomer).

^{1}H NMR (400.0 MHz, CD_2Cl_2):

δ [ppm] = 7.32-7.22 (m', 6H, C_{Ar}-H), 7.19-7.13 (m', 6H, C_{Ar}-H), 7.13-7.02 (m', 6H, C_{Ar}-H), 6.43-6.22 (br, 2H, C-H), 4.19-3.93 (br, 4H, C-H_2), 1.90-1.72 (m', 10H, C-H_2, C-H_3), 1.50-1.40 (m, 4H, C-H_2), 0.98 (t, 6H, ^3J = 7.4 Hz, C-H_3).

^{13}C(^{1}H) NMR (100.6 MHz, CD_2Cl_2):

δ [ppm] = 171.4 (quart.), 171.1 (quart.), 168.1 (quart.), 166.2 (quart.), 142.3 (quart.), 142.2 (quart.), 142.1 (quart.), 128.6 (tert.), 128.4 (tert.), 127.1 (tert.), 126.7 (tert.), 125.0

(tert.), 123.7 (tert.), 119.3 (quart.), 110.8 (tert.), 90.0 (tert.), 57.5 (quart.), 45.1 (sec.), 39.3 (quart.), 29.7 (sec.), 25.3 (prim.), 20.6 (sec.), 14.1 (prim.).

HRMS (ESI, pos.): $[M]^{\bullet+}$

calcd: 680.35096

found: 680.35073 Δ = 0.34 ppm

Crystal data ($C_{47}H_{44}N_4O$):

M_r = 680.86, 0.368 × 0.250 × 0.101 mm^3, monoclinic space group $P2_1$, a = 9.5514(13) Å, α = 90°, b = 10.8418(15) Å, β = 102.372(5)°, c = 18.966(3) Å, γ = 90°, V = 1918.4(5) Å^3, Z = 2, ρ(calcd)= 1.179 g cm^{-3}, μ = 0.547 mm^{-1}, F(000)= 724.0, GooF(F^2) = 1.042, Flack = 0.05(5), R1= 0.0368, wR2= 0. 1009 for I > 2sigma(I), R1= 0.0377,wR2= 0. 1019 for all data, 7542 unique reflections [θ = 67.679°] with a completeness of 100.0 % and 506 parameters, 5 restraints.

Ph-SQA*

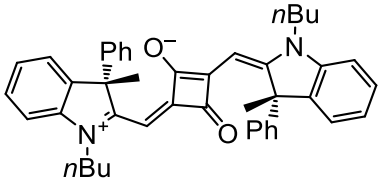

CAS: -

Synthesis based on given literature.[90, 94, 96]

A solution of (*S*)-1-butyl-3-methyl-3-phenyl-3*H*-indol-1-ium chloride ***S*-21a** (121 mg, 386 µmol), squaric acid (22.0 mg, 193 µmol) and pyridine (500 µL, 489 mg, 6.18 mmol) in *n*BuOH/toluene 1:1 (10 mL) was heated to reflux using a Dean-Stark trap for 18 h. The solvent was removed under reduced pressure and the residue was purified by column chromatography (silica, MeOH/DCM 1:99) followed by recrystallization from MeOH/H_2O.

Yield: 80.0 mg (126 µmol, 65%) of a green crystalline solid.

$C_{44}H_{44}N_2O_2$ [632.83]

HPLC (Phenomenex LUX i-Amylose-3, EA/DCM 9:1, 1 mL min^{-1}):

10.7 min (*SS*-diastereomer), 15.1 min (*RS*-diastereomer).

^{1}H NMR (400.0 MHz, CD_3OD):

δ [ppm] = 7.33-7.27 (m, 2H, C_{Ar}-H), 7.25-7.19 (m', 10H, C_{Ar}-H), 7.18-7.11 (m', 4H, C_{Ar}-H), 7.09-7.03 (m, 2H, C_{Ar}-H), 5.77 (s, 2H, C-H), 4.32-4.16 (br, 4H, C-H_2), 2.06 (s, 6H, C-H_3), 1.87-1.77 (m, 4H, C-H_2), 1.57-1.46 (m, 4H, C-H_2), 1.02 (t, 6H, ^{3}J = 7.4 Hz, C-H_3).

^{13}C(^{1}H) NMR (150.9 MHz, CD_3OD):

δ [ppm] = 183.6 (quart.), 177.3 (quart.), 171.0 (quart.), 143.7 (quart.), 143.4 (quart), 143.1 (quart.), 129.3 (tert.), 129.2 (tert.), 127.8 (tert.), 127.5 (tert.), 125.4 (tert.), 124.5 (tert.), 111.6 (tert.), 88.2 (tert.), 58.2 (quart.), 45.0 (sec.), 30.4 (sec.), 26.0 (prim.), 21.3 (sec.), 14.3 (prim.).

HRMS (ESI, pos.): $[M]^{\bullet+}$

calcd: 632.33973

found: 632.33969 Δ = 0.06 ppm

Pr-SQB*

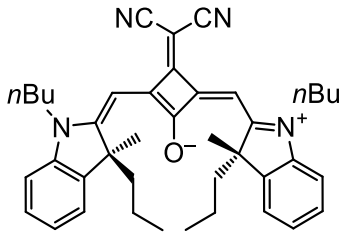

CAS: -

Synthesis based on given literature.[92]

A solution of (*S*)-1-butyl-2,3-dimethyl-3-propyl-3*H*-indol-1-ium iodide ***S*-23** (831 mg, 2.24 mmol), triethylammonium 3-(dicyanomethylene)-2-ethoxy-4-oxocyclobut-1-en-1-olate (**CN**) (326 mg, 1.12 mmol) and pyridine (1.98 mL, 1.94 g, 24.5 mmol) in *n*BuOH/toluene 1:1 (35 mL) was heated to reflux using a Dean-Stark trap for 18 h. The solvent was removed under reduced pressure and the residue was purified by column chromatography (silica, DCM) and

crystallization from a concentrated DCM/*n*-hexane solution at 4 °C. The hereby obtained crystals were single crystals.

Yield: 422 mg (689 µmol, 62%) of a shiny green crystalline solid.

$C_{41}H_{48}N_4O$ [612.85]

HPLC (Phenomenex LUX i-Amylose-3, *n*-hexane/DCM/*i*PrOH 95:27:3, 1 mL min^{-1}):
6.0 min (*SS*-diastereomer), 7.6 min (*RS*-diastereomer).

^{1}H NMR (400.0 MHz, CD_2Cl_2):

δ [ppm] = 7.40-7.33 (m', 4H, C_{Ar}-H), 7.25-7.18 (m, 2H, C_{Ar}-H), 7.11-7.05 (m, 2H, C_{Ar}-H), 6.64-6.39 (br, 2H, C-H), 4.12-3.92 (m, 4H, C-H_2), 2.93-2.80 (m, 2H, C-H_2), 2.02-1.92 (m, 2H, C-H_2), 1.85-1.71 (m', 10H, C-H_2, C-H_3), 1.55-1.44 (m, 4H, C-H_2), 0.98 (t, 6H, ^3J = 7.4 Hz, C-H_3), 0.90-0.76 (m, 2H, C-H_2), 0.70 (t, 6H, ^3J = 7.1 Hz, C-H_2), 0.62-0.48 (m, 2H, C-H_2).

^{13}C(^{1}H) NMR (100.6 MHz, CD_2Cl_2):

δ [ppm] = 173.4 (quart.), 171.2 (quart.), 167.9 (quart), 166.7 (quart.), 143.4 (quart.), 141.1 (quart.), 128.3 (tert.), 124.7 (tert.), 122.7 (tert.), 119.4 (quart.), 110.3 (tert.), 89.6 (tert.), 54.2 (quart.), 44.7 (sec.), 42.5 (sec.), 40.2 (quart.), 29.8 (sec.), 26.5 (prim.), 20.5 (sec.), 18.2 (sec.), 14.4 (prim.), 14.1 (prim.).

HRMS (ESI, pos.): $[M]^{\bullet+}$

calcd: 612.38226

found: 612.38266 Δ = 0.65 ppm

Crystal data ($C_{41}H_{48}N_4O$):

M_r = 612.83, 0.239 × 0.182 × 0.094 mm^3, monoclinic space group $P2_1$, a = 12.5152(11) Å, α = 90°, b = 8.1909(7) Å, β = 109.467(2)°, c = 18.3478(16) Å, γ = 90°, V = 1773.3(3) $Å^3$, Z = 2, ρ(calcd)= 1.148 g cm^{-3}, µ = 0.532 mm^{-1}, F(000)= 660.0, GooF(F^2) = 1.030, Flack = 0.00(5), $R1$ = 0.0392, w$R2$= 0. 1034 for I > 2sigma(I), $R1$= 0.0397,w$R2$= 0. 1041 for all data, 6912 unique reflections [θ = 67.679°] with a completeness of 99.9% and 421 parameters, 1 restraint.

Pr-SQA*

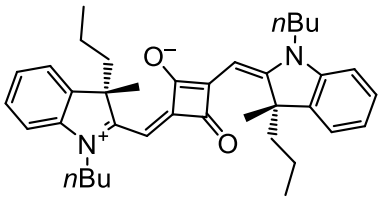

CAS: -

Synthesis based on given literature.[94, 96]

A solution of (*S*)-1-butyl-2,3-dimethyl-3-propyl-3*H*-indol-1-ium iodide ***S*-23** (397 mg, 1.07 mmol), squaric acid (61.0 mg, 535 µmol) and pyridine (1.59 mL, 1.56 g, 19.7 mmol) in *n*BuOH/toluene 1:1 (19 mL) was heated to reflux using a Dean-Stark trap for 18 h. The solvent was removed under reduced pressure and the residue was purified by column chromatography (silica, MeOH/DCM 1:99) and crystallization from a concentrated DCM/*n*-hexane solution at 4 °C. Single crystals were obtained by layering a DCM solution with MeOH followed by slow evaporation at 4 °C.

Yield: 217 mg (384 µmol, 72%) of a bronze-colored crystalline solid.

$C_{38}H_{48}N_2O_2$ [564.80]

HPLC (Phenomenex LUX i-Amylose-3, EA/DCM 9:1, 1 mL min^{-1}):
7.4 min (*SS*-diastereomer), 10.4 min (*RS*-diastereomer).

^{1}H NMR (400.0 MHz, CD_2Cl_2):

δ [ppm] = 7.36-7.28 (m', 4H, C_{Ar}-H), 7.17-7.12 (m, 2H, C_{Ar}-H), 7.03-6.99 (m, 2H, C_{Ar}-H), 6.00-5.89 (br, 2H, C-H), 4.10-3.89 (m, 4H, C-H_2), 3.05-2.75 (m, 2H, C-H_2), 2.00-1.90 (m, 2H, C-H_2), 1.84-1.69 (m', 10H, C-H_2, C-H_3), 1.54-1.42 (m, 4H, C-H_2), 1.00 (t, 6H, ^3J = 7.4 Hz, C-H_3), 0.92-0.78 (m, 2H, C-H_2), 0.71 (t, 6H, ^3J = 7.1 Hz, C-H_3), 0.62-0.48 (m, 2H, C-H_2).

^{13}C(^{1}H) NMR (100.6 MHz, CD_2Cl_2):

δ [ppm] = 182.1 (quart.), 180.3 (quart.), 169.0 (quart.), 143.9 (quart.), 140.8 (quart.), 128.0 (tert.), 123.8 (tert.), 122.6 (tert.), 109.6 (tert.), 87.1 (tert.), 54.0 (quart.), 43.8 (sec.),

42.9 (sec.), 29.5 (sec.), 26.9 (prim.), 20.8 (sec.), 18.2 (sec.), 14.5 (prim.), 14.0 (prim.).

HRMS (ESI, pos.): $[M]^{\bullet+}$

calcd: 564.37103

found: 564.37135 Δ = 0.57 ppm

Crystal data ($C_{38}H_{48}N_2O_2$):

M_r = 564.78, 0.515 × 0.072 × 0.069 mm^3, tetragonal space group $P4_1$, a = 20.40883(7) Å, α = 90°, b = 20.40883(7) Å, β = 90°, c = 9.19586(5) Å, γ = 90°, V = 3830.27(3) Å^3, Z = 4, ρ(calcd)= 0.979 g·cm^{-3}, μ = 0.460 mm^{-1}, F(000)= 1224.0, GooF(F^2) = 1.064, Flack = 0.07(7), R1= 0.0345, wR2 = 0.0866 for I > 2sigma(I), R1= 0.0354, wR2= 0.0871 for all data, 7961 unique reflections [θ = 68.1328°] with a completeness of 100.0 % and 385 parameters, 1 restraint.

Br_2-SQB-R^0

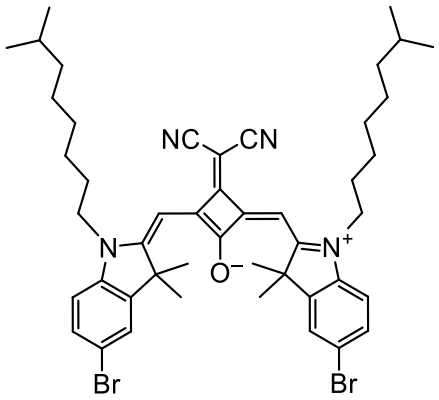

CAS: -

Synthesis based on given literature.[92]

5-Bromo-2,3,3-trimethyl-1-(7-methyloctyl)-3*H*-indol-1-ium iodide (**34a**) (500 mg, 1.02 mmol), triethylammonium 3-(dicyanomethylene)-2-ethoxy-4-oxocyclobut-1-en-1-olate (**CN**) (148 mg, 508 µmol) and pyridine (900 µL, 884 mg, 11.2 mmol) were suspended in toluene/*n*-BuOH (1:1, 20 mL) and the mixture heated to reflux for 18 h using a Dean-Stark trap. The solvent was then removed under reduced pressure and the residue purified by column chromatography (silica,

DCM/PE 17:3) followed by precipitation from DCM/MeOH. Single crystals were obtained by layering a DCM solution with MeOH followed by slow evaporation at 4 °C.

Yield: 274 mg (321 µmol, 63%) of a ruby-colored solid.

$C_{47}H_{58}Br_2N_4O$ [854.80]

^{1}H NMR (400.0 MHz, CD_2Cl_2):

δ [ppm] = 7.53-7.45 (m', 4H, C_{Ar}-H), 6.97 (d, 2H, ^3J = 8.3 Hz, C_{Ar}-H), 6.50 (s, 2H, C-H), 3.97 (t, 4H, ^3J = 7.7 Hz, C-H_2), 1.84-1.71 (m', 16H, C-H_2, C-H_3), 1.56-1.39 (m', 6H, C-H, C-H_2), 1.38-1.23 (m', 8H, C-H_2), 1.19-1.11 (m, 4H, C-H_2), 0.85 (d, 12H, ^3J = 6.6 Hz, C-H_3).

^{13}C(^{1}H) NMR (100.6 MHz, CD_2Cl_2):

δ [ppm] = 173.2 (quart.), 171.2 (quart.), 168.0 (quart.), 167.2 (quart), 144.8 (quart.), 141.6 (quart.), 131.3 (tert.), 126.1 (tert.), 119.0 (quart.), 117.7 (quart.), 112.0 (tert.), 89.9 (tert.), 49.8 (quart.), 45.0 (sec.), 40.9 (quart.), 39.2 (sec.), 30.0 (sec.), 28.3 (tert.), 27.5 (2 × sec.), 27.0 (sec.), 26.7 (prim), 22.8 (prim.).

HRMS (ESI, pos.): $[M]^{\bullet+}$

calcd: 854.29571

found: 854.29807 Δ = 2.76 ppm

Crystal data ($C_{47}H_{58}Br_2N_4O$):

M_r = 854.79, 0.221×0.157×0.013 mm^3, space group $P2_1/c$, a = 8.97291(17) Å, b = 16.4669(4) Å, c = 29.9186(8) Å, α = 90°, β = 96.063(2)°, γ = 90°, V = 4395.93(19) Å^3, Z = 4, ρ_{calcd} = 1.292 g·cm^{-3}, μ = 2.626 mm^{-1}, F(000) = 1784, T = 100.00(11) K, R_1 = 0.0717, wR^2 = 0.1354, 9069 independent reflections [2θ≤155.578°] and 535 parameters.

Br_2-SQB-R^1*

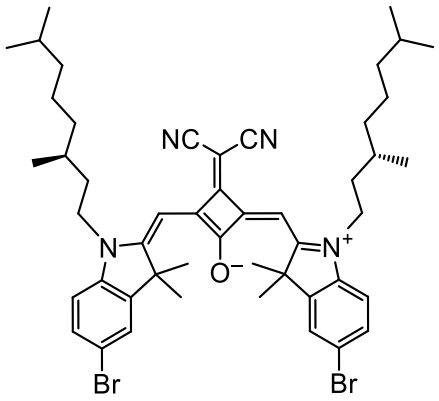

CAS: -

Synthesis according to literature.[92]

S-5-Bromo-1-(3,7-dimethyloctyl)-2,3,3-trimethyl-3*H*-indol-1-ium iodide (**34b**) (1.80 g, 3.56 mmol), triethylammonium 3-(dicyanomethylene)-2-ethoxy-4-oxocyclobut-1-en-1-olate (**CN**) (518 mg, 1.78 mmol) and pyridine (3.15 mL, 3.09 mg, 39.1 mmol) were suspended in toluene/*n*-BuOH (1:1, 70 mL) and the mixture heated to reflux for 20 h using a Dean-Stark trap. The solvent was then removed under reduced pressure and the residue purified by column chromatography (silica, DCM) followed by precipitation from *n*-hexane. Single crystals were obtained by layering a DCM solution with *n*-hexane followed by slow evaporation at 4 °C.

Yield: 1.29 g (1.46 mmol, 82%) of a ruby-colored crystalline solid.

$C_{49}H_{62}Br_2N_4O$ [882.85]

^{1}H NMR (600.1 MHz, CD_2Cl_2):

δ [ppm] = 7.50 (d, 2H, ^4J = 1.9 Hz C_{Ar}-H), 7.48 (dd, 2H, ^3J = 8.3 Hz, ^4J = 1.9 Hz C_{Ar}-H), 6.96 (d, 2H, ^3J = 8.4 Hz, C_{Ar}-H), 6.46 (s, 2H, C-H), 4.06-3.93 (m, 4H, C-H_2), 1.80-1.71 (m‘, 14H, C-H_2, C-H_3), 1.67-1.55 (m’, 4H, C-H_2), 1.55-1.47 (m, 2H, C-H), 1.41-1.30 (m, 4H, C-H_2), 1.29-1.10 (m’, 8H, C-H_2), 1.01 (d, 6H, ^3J = 6.5 Hz, C-H_3), 0.86 (d, 12H, ^3J = 6.6 Hz, C-H_3).

^{13}C(^{1}H) NMR (150.9 MHz, CD_2Cl_2):

δ [ppm] = 173.2 (quart.), 171.6 (quart.), 167.9 (quart.), 167.2 (quart), 144.8 (quart.), 141.4 (quart.), 131.2 (tert.), 126.0 (tert.), 118.9 (quart.), 117.7 (quart.), 111.8 (tert.), 89.7

(tert.), 49.8 (quart.), 43.4 (sec.), 40.9 (quart.), 39.4 (sec.), 37.4 (sec.), 34.2 (sec.), 31.2 (tert.), 28.3 (tert.), 26.61 (prim), 26.57 (prim), 25.0 (sec.), 22.8 (prim.), 22.7 (prim), 19.7 (prim).

HRMS (ESI, pos.):[1] $[M]^{\bullet+}$

calcd: 880.32904

found: 880.32851 Δ = 0.60 ppm

Crystal data ($C_{49}H_{62}Br_2N_4O$):

M_r = 882.84, 0.679×0.485×0.040 mm^3, space group *C*2, a = 22.54173(16) Å, b = 13.65826(10) Å, c = 30.13980(19) Å, α = 90°, β = 99.2043(6)°, γ = 90°, V = 9159.98(11) Å^3, Z = 8, ρ_{calcd} = 1.280 g·cm^{-3}, μ = 2.536 mm^{-1}, F(000) = 3696, T = 100.00(10) K, R_1 = 0.0373, wR_2 = 0.0952, Flack parameter = 0.006(8), 19142 independent reflections [2θ≤160.406°] and 1208 parameters.

Br_2-SQB-R^2*

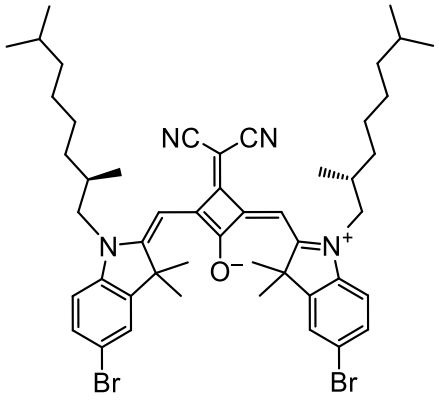

CAS: -

Synthesis based on given literature.[92]

R-5-Bromo-1-(2,7-dimethyloctyl)-2,3,3-trimethyl-3*H*-indol-1-ium chloride (**34c**) (245 mg, 591 µmol), triethylammonium 3-(dicyanomethylene)-2-ethoxy-4-oxocyclobut-1-en-1-olate (**CN**) (86.0 mg, 295 µmol) and pyridine (523 µL, 514 mg, 6.50 mmol) were suspended in

[1] Monoisotopic mass

toluene/*n*-BuOH (1:1, 12 mL) and the mixture heated to reflux for 20 h using a Dean-Stark trap. The solvent was then removed under reduced pressure and the residue purified by column chromatography (silica, DCM/PE 17:3) followed by precipitation from DCM/MeOH. Single crystals were obtained by layering a DCM solution with MeOH followed by slow evaporation at RT.

Yield: 243 mg (275 µmol, 93%) of a ruby-colored crystalline solid.

$C_{49}H_{62}Br_2N_4O$ [882.85]

^{1}H NMR (400.1 MHz, CD_2Cl_2):

δ [ppm] = 7.53-7.44 (m', 4H, C_{Ar}-H), 6.96 (d, 2H, ^3J = 8.4 Hz, C_{Ar}-H), 6.52 (s, 2H, C-H), 3.92-3.77 (m, 4H, C-H_2), 2.24-2.09 (m, 2H, C-H), 1.78-1.74 (m, 12H, C-H_3), 1.54-1.33 (m', 6H, C-H, C-H_2) 1.32-1.18 (m', 8H, C-H_2), 1.18-1.08 (m, 4H, C-H_2), 0.96 (d, 6H, ^3J = 6.6 Hz, C-H_3), 0.86-0.81 (m, 12H, C-H_3).

^{13}C(^{1}H) NMR (100.6 MHz, CD_2Cl_2):

δ [ppm] = 173.3 (quart.), 172.3 (quart.), 168.1 (quart.), 167.0 (quart), 144.7 (quart.), 142.2 (quart.), 131.2 (tert.), 126.0 (tert.), 119.1 (quart.), 117.7 (quart.), 112.5 (tert.), 90.6 (tert.), 50.8 (sec.), 49.8 (quart.), 41.0 (quart.), 39.2 (sec.), 34.3 (sec.), 32.5 (tert.), 28.3 (tert.), 27.7 (sec.), 27.4 (sec.), 26.8 (2 × prim), 22.8 (prim.), 22.7 (prim), 17.1 (prim).

HRMS (ESI, pos.): $[M]^{\bullet+}$

calcd: 882.32706

found: 882.32917 Δ = 2.39 ppm

Crystal data ($C_{49}H_{62}Br_2N_4O$):

M_r = 882.84, 0.512×0.043×0.034 mm^3, space group $P2_12_12_1$, a = 9.23400(9) Å, b = 16.14579(15) Å, c = 30.2628(4) Å, α = 90°, β = 90°, γ = 90°, V = 4511.89(8) Å^3, Z = 4, ρ_{calcd} = 1.300 g·cm^{-3}, μ = 2.575 mm^{-1}, F(000) = 1848, T = 100.00(10) K, R_1 = 0.0305, wR_2 = 0.0725, Flack parameter = -0.017(6), 9705 independent reflections [2θ≤160.208°] and 516 parameters.

Br_2-SQB-R^3*

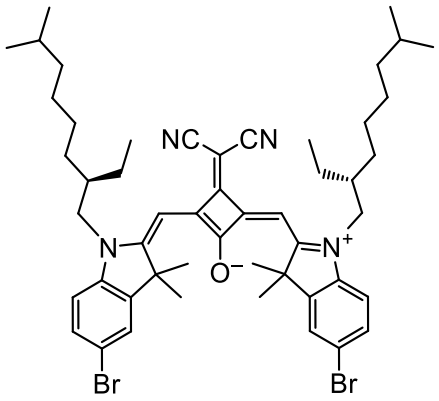

CAS: -

Synthesis based on given literature.[92]

R-5-bromo-1-(2-ethyl-7-methyloctyl)-2,3,3-trimethyl-3*H*-indol-1-ium chloride (**34d**) (239 mg, 557 µmol), triethylammonium 3-(dicyanomethylene)-2-ethoxy-4-oxocyclobut-1-en-1-olate (**CN**) (81.0 mg, 278 µmol) and pyridine (494 µL, 485 mg, 6.13 mmol) were suspended in toluene/*n*-BuOH (1:1, 12 mL) and the mixture heated to reflux for 20 h using a Dean-Stark trap. The solvent was then removed under reduced pressure and the residue purified by column chromatography (silica, EA/DCM 1:39). Freeze drying from benzene afforded the product as a solid. Single crystals were obtained by slow evaporation from a concentrated solution of *n*-hexane at RT.

Yield: 239 mg (262 µmol, 94%) of a green solid.

$C_{51}H_{66}Br_2N_4O$ [910.91]

^{1}H NMR (400.0 MHz, acetone-d_6):

δ [ppm] = 7.75 (d, 2H, ^4J = 2.0 Hz, C_{Ar}-H), 7.57 (dd, 2H, ^3J = 8.5 Hz, ^4J = 2.0 Hz, C_{Ar}-H), 7.35 (d, 2H, ^3J = 8.5 Hz, C_{Ar}-H), 6.56 (s, 2H, C-H), 4.13-4.02 (m, 4H, C-H_2), 2.19-2.10 (m, 2H, C-H), 1.85-1.80 (m, 12H, C-H_3), 1.54-1.18 (m‘, 18H, C-H, C-H_2) 1.16-1.07 (m, 4H, C-H_2), 0.96 (t, 6H, ^3J = 7.5 Hz, C-H_3), 0.82-0.78 (m, 12H, C-H_3).

$^{13}C(^{1}H)$ NMR (100.6 MHz, CD_2Cl_2):

δ [ppm] = 173.1 (quart.), 172.3 (quart.), 167.8 (quart.), 166.7 (quart), 144.5 (quart.), 141.8 (quart.), 130.9 (tert.), 125.7 (tert.), 118.8 (quart.), 117.5 (quart.), 112.2 (tert.), 90.3 (tert.), 49.6 (quart.), 48.7 (sec.), 40.8 (quart.), 38.9 (sec.), 37.9 (tert.), 30.4 (sec.), 28.0 (tert.), 27.7 (sec.), 26.60 (sec.), 26.57 (prim.), 26.5 (prim.), 23.9 (sec.), 22.5 (prim.), 22.4 (prim), 10.7 (prim).

HRMS (ESI, pos.): $[M]^{\bullet+}$

calcd: 910.35840

found: 910.35869 Δ = 0.32 ppm

Crystal data ($C_{51}H_{66}Br_2N_4O$):

M_r = 910.89, 0.306×0.298×0.039 mm^3, space group *C*2, a = 15.7519(2) Å, b = 9.67420(7) Å, c = 18.1575(2) Å, α = 90°, β = 120.4788(17)°, γ = 90°, V = 2384.62(6) Å^3, Z = 2, ρ_{calcd} = 1.269 g·cm^{-3}, μ = 2.451 mm^{-1}, F(000) = 956, T = 100.01(10) K, R_1 = 0.0252, wR_2 = 0.0625, Flack parameter = -0.037(7), 5085 independent reflections [2θ≤160.528°] and 269 parameters.

Br_2-Pr-SQB*

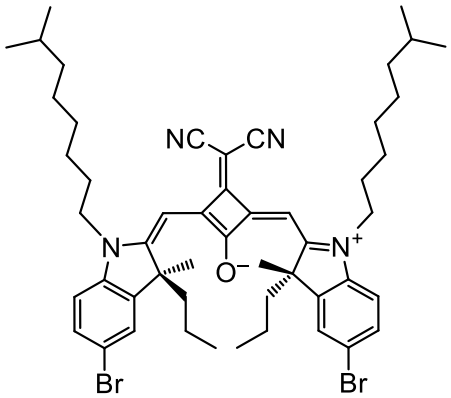

CAS: -

Synthesis based on given literature.[92]

(*S*)-5-Bromo-2,3-dimethyl-1-(7-methyloctyl)-3-propyl-3H-indol-1-ium iodide (**24**) (200 mg, 384 µmol), triethylammonium 3-(dicyanomethylene)-2-ethoxy-4-oxocyclobut-1-en-1-olate (**CN**) (56.0 mg, 192 µmol) and pyridine (341 µL, 334 mg, 4.22 mmol) were suspended in

toluene/*n*-BuOH (1:1, 2 mL). The solution was thoroughly degassed before being heated at 120 °C for 18 h. The solvent was then removed under reduced pressure and the residue purified by column chromatography (silica, DCM) and precipitation from MeOH.

Yield: 99.2 mg (109 µmol, 57%) of a dark green solid.

$C_{51}H_{66}Br_2N_4O$ [910.91]

HPLC (Phenomenex LUX i-Amylose-3, *n*-hexane/DCM/*i*PrOH 40:9:1, 1 mL min^{-1}):
6.3 min (*RS*-diastereomer), 5.4 min (*SS*-diastereomer).

^{1}H NMR (400.0 MHz, CD_2Cl_2):

δ [ppm] = 7.49-7.46 (m', 4H, C_{Ar}-H), 6.98-6.92 (m, 2H, C_{Ar}-H), 6.52 (s, 2H, C-H), 4.07-3.90 (m, 4H, C-H_2), 2.93-2.80 (m, 2H, C-H_2), 1.99-1.87 (m, 2H, C-H_2), 1.83-1.70 (m', 10H, C-H_2, C-H_3), 1.55-1.39 (m', 6H, C-H, C-H_2), 1.38-1.23 (m, 8H, C-H_2), 1.19-1.10 (m, 4H, C-H_2), 0.90-0.76 (m', 14H, C-H_2, C-H_3), 0.72 (t, 6H, ^3J = 7.0 Hz, C-H_3), 0.66-0.52 (m, 2H, C-H_2).

^{13}C(^{1}H) NMR (100.6 MHz, CD_2Cl_2):

δ [ppm] = 173.2 (quart.), 170.7 (quart.), 168.1 (quart.), 167.1 (quart), 143.2 (quart.), 142.6 (quart.), 131.3 tert.), 126.1 (tert.), 119.1 (quart.), 117.7 (quart.), 111.8 (tert.), 90.2 (tert.), 54.4 (quart.), 45.0 (sec.), 42.5 (sec.), 40.8 (quart.), 39.2 (sec.), 30.0 (sec.), 28.3 (tert.), 27.65 (sec.), 27.55 (sec.), 27.1 (sec.), 26.5 (prim.), 22.7 (2 × prim.), 18.2 (sec.), 14.4 (prim.).

MS (MALDI, pos.): $[M]^{\bullet+}$

calcd: 910.358

found: 910.382

Br_2-Ph-SQB*

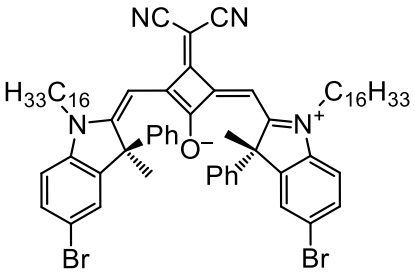

S*-Br_2-Ph-SQB

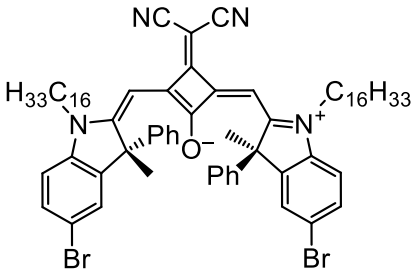

R*-Br_2-Ph-SQB

CAS: -

Synthesis based on given literature.[90]

Triethylammonium 3-(dicyanomethylene)-2-ethoxy-4-oxocyclobut-1-en-1-olate (**CN**) (55.3 mg, 190 µmol) and 5-bromo-1-hexadecyl-2,3-dimethyl-3-phenyl-3H-indol-1-ium chloride ***R*/*S*-22b** (213 mg, 380 µmol) were dissolved in a mixture of *n*BuOH/toluene (1:1, 8 mL), before pyridine (336 µL, 330 mg, 4.17 mmol) was added. The solution was thoroughly degassed before being heated at 120 °C for 18 h. The solvent was then removed under reduced pressure and the residue purified by column chromatography (silica, DCM).

Yield: 158 mg (134 µmol, 71%) of a dark green solid.

$C_{71}H_{90}Br_2N_4O$ [1175.31]

HPLC (Phenomenex LUX i-Amylose-3, *n*-hexane/DCM/*i*PrOH 250:80:1, 1 mL min^{-1}):
17.3 min (*RS*-diastereomer), 19.4 min (*SS*-diastereomer), 23.9 min (*RR*-diastereomer).

^{1}H NMR (400.0 MHz, CD_2Cl_2):

δ [ppm] = 7.41 (dd, 2H, ^{3}J = 8.4 Hz, ^{4}J = 1.9 Hz, C_{Ar}-H), 7.31-7.24 (m', 4H, C_{Ar}-H), 7.24-7.13 (m', 8H, C_{Ar}-H), 6.95 (d, 2H, ^{3}J = 8.4 Hz, C_{Ar}-H), 6.36 (s, 2H, C-H), 4.09-3.98 (m, 4H, C-H_2), 1.91-1.76 (m', 10H, C-H_2, C-H_3), 1.48-1.21 (m', 52H, C-H_2), 0.89 (t, 6H, ^{3}J = 6.8 Hz, C-H_3).

^{13}C(^{1}H) NMR (100.6 MHz, CD_2Cl_2):

δ [ppm] = 171.1 (quart.), 170.5 (quart.), 168.6 (quart.), 166.4 (quart.), 144.3 (quart.), 141.5 (quart.), 141.2 (quart.), 131.4 (tert.), 128.7 (tert.), 127.4 (tert.), 127.0 (tert.), 126.7 (tert.), 119.1 (quart.), 117.8 (quart.), 112.2 (tert.), 90.6 (tert.), 57.4 (quart.), 45.4 (sec.), 39.8 (quart.), 32.3 (sec.), 30.11 (3 × sec.), 30.09 (sec.), 30.08 (sec.), 30.05 (sec.), 29.97 (sec.), 29.9 (sec.), 29.77 (sec.), 29.76 (sec.), 27.6 (sec.), 27.2 (sec.), 25.4 (prim.), 23.1 (sec.), 14.3 (prim.).

HRMS (ESI, pos.): $[M]^{\bullet+}$

calcd: 1174.54673

found: 1174.54721 Δ = 0.41 ppm

Br_2-SQB

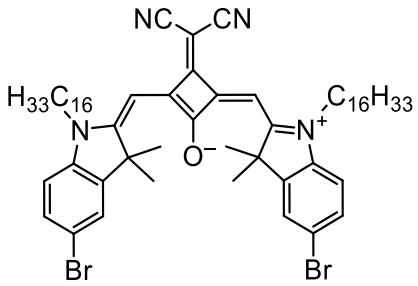

CAS: -

Synthesis based on given literature.[90]

5-Bromo-1-hexadecyl-2,3,3-trimethyl-3*H*-indol-1-ium iodide (**36b**) (1.00 g, 1.69 mmol), triethylammonium 3-(dicyanomethylene)-2-ethoxy-4-oxocyclobut-1-en-1-olate (**CN**) (247 mg, 848 µmol) and pyridine (750 µL, 737 mg, 9.32 mmol) were suspended in toluene/*n*-BuOH (1:1,

35 mL) and the mixture heated to reflux for 20 h using a Dean-Stark trap. The solvent was then removed under reduced pressure and the residue purified by column chromatography (silica, DCM/PE 7:3).

Yield: 884 mg (841 µmol, 99%) of a dark green viscous oil.

$C_{61}H_{86}Br_2N_4O$ [1051.17]

^{1}H NMR (400.1 MHz, CD_2Cl_2):

δ [ppm] = 7.52-7.45 (m', 4H, C_{Ar}-H), 6.96 (d, 2H, ^3J = 8.3 Hz, C_{Ar}-H), 6.49 (s, 2H, C-H), 4.04-3.89 (m, 4H, C-H_2), 1.83-1.71 (m', 16H, C-H_2, C-H_3), 1.47-1.20 (m', 52H, C-H_2), 0.87 (t, 6H, ^3J = 6.8 Hz, C-H_3).

^{13}C(^{1}H) NMR (150.9 MHz, $CDCl_3$):

δ [ppm] = 172.9 (quart.), 171.3 (quart.), 167.9 (quart.), 167.0 (quart.), 144.4 (quart.), 141.1 (quart.), 131.0 (tert), 125.7 (tert), 118.1 (quart.), 117.6 (quart.), 111.4 (tert.), 89.6 (tert.), 49.4 (quart.), 44.6 (sec.), 41.2 (quart.), 31.9 (sec.), 29.69 (sec.), 29.68 (sec.), 29.67 (sec.), 29.65 (sec.), 29.65 (sec.), 29.60 (sec.), 29.54 (sec.), 29.40 (sec.), 29.36 (sec.), 29.35 (sec.), 27.3 (sec.), 26.7 (sec.), 26.6 (prim.), 22.7 (sec.), 14.1(prim.).

HRMS (ESI, pos.): $[M^{\bullet+}]$[1]

calcd: 1048.51684

found: 1048.51633 Δ = 0.47 ppm

Bpin$_2$-SQB

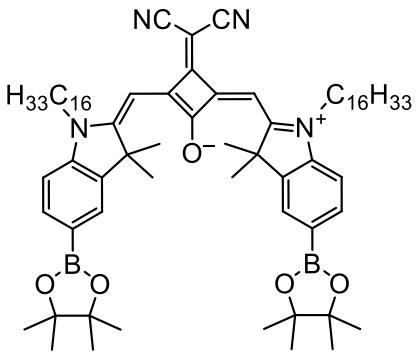

[1] Monoisotopic mass

CAS: -

Synthesis following GP IV: **Br_2-SQB** (2.21 g, 2.10 mmol), B_2Pin_2 (1.50 g, 5.91 mmol), KOAc (660 mg, 6.73 mmol), dppf (58.0 mg, 105 µmol), $Pd(PhCN)_2Cl_2$ (40.0 mg, 104 µmol) in anhydrous 1,4-dioxane (60 mL). 18 h at 100 °C. Purification by column chromatography (silica, DCM/PE 3:7).

Yield: 687 mg (600 µmol, 29%) of a dark green solid.

$C_{73}H_{110}B_2N_4O_5$ [1145.30]

^{1}H NMR (400.1 MHz, CD_2Cl_2):

δ [ppm] = 7.81-7.75 (m', 4H, C_{Ar}-H), 7.09 (d, 2H, ^3J = 7.9 Hz, C_{Ar}-H), 6.54 (s, 2H, C-H), 4.08-3.97 (m, 4H, C-H_2), 1.86-1.75 (m', 16H, C-H_2, C-H_3), 1.50-1.17 (m', 76H, C-H_2, C-H_3), 0.87 (t, 6H, ^3J = 6.7 Hz, C-H_3).

^{13}C(^{1}H) NMR (100.6 MHz, CD_2Cl_2):

δ [ppm] = 173.3 (quart.), 172.4 (quart.), 168.1 (quart.), 167.3 (quart.), 145.0 (quart.), 142.1 (quart.), 135.5 (tert.), 128.5 (tert.), 125.5 (quart.), 119.2 (quart.), 110.0 (tert.), 90.0 (tert.), 84.3 (quart.), 49.6 (quart.), 44.9 (sec.), 40.7 (quart.), 32.3 (sec.), 30.11 (sec.), 30.10 (2 × sec.), 30.08 (2 × sec.), 29.97 (sec.), 29.9 (sec.), 29.8 (2 × sec.), 27.7 (sec.), 27.0 (sec.), 26.8 (prim.), 25.1 (prim.), 23.1 (sec.), 14.3 (prim.).

MS (MALDI, pos.): $[M]^{\bullet+}$

calcd: 1144.868

found: 1144.868

Br_2-SQA

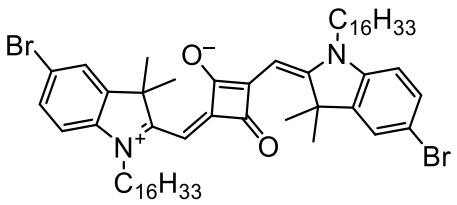

CAS: -

Synthesis based on given literature.[94, 96]

5-Bromo-1-hexadecyl-2,3,3-trimethyl-3H-indol-1-ium iodide (**36b**) (1.50 g, 2.54 mmol), squaric acid (116 mg, 1.02 mmol) and pyridine (6.00 mL, 5.89 g, 74.5 mmol) were suspended in toluene/*n*-BuOH (1:1, 70 mL) and the mixture heated to reflux for 20 h using a Dean-Stark trap. The solvent was then removed under reduced pressure and the residue purified by column chromatography (silica, MeOH/DCM 1:199 → MeOH/DCM 3:197).

Yield: 931 mg (928 µmol, 91%) of a dark blue solid.

$C_{58}H_{86}Br_2N_2O_2$ [1003.12]

^{1}H NMR (400.1 MHz, CD_2Cl_2):

δ [ppm] = 7.47 (d, 2H, ^4J = 2.0 Hz, C_{Ar}-H), 7.43 (dd, 2H, ^3J = 8.4 Hz, ^4J = 2.0 Hz, C_{Ar}-H), 6.87 (d, 2H, ^3J = 8.4 Hz, C_{Ar}-H), 5.91 (s, 2H, C-H), 4.07-3.84 (br, 4H, C-H_2), 1.83-1.70 (m', 16H, C-H_2, C-H_3), 1.46-1.19 (m', 52H, C-H_2), 0.87 (t, 6H, ^3J = 6.7 Hz, C-H_3).

^{13}C(^{1}H) NMR (150.9 MHz, $CDCl_3$):

δ [ppm] = 182.2 (quart.), 180.1 (quart.), 169.4 (quart.), 144.2 (quart.), 141.5 (quart.), 130.7 (tert.), 125.7 (tert.), 116.6 (quart.), 110.7 (tert.), 87.1 (tert.), 49.3 (quart.), 43.9 (sec.), 31.9 (sec.), 29.68 (sec.), 29.66 (sec.), 29.65 (sec.), 29.63 (sec.), 29.61 (sec.), 29.56 (sec.), 29.49 (sec.), 29.44 (sec.), 29.33 (sec.), 29.32 (sec.), 27.01 (sec.), 27.00 (prim.), 26.9 (sec.), 22.6 (sec.), 14.1 (prim.).

HRMS (ESI, pos.): $[M^{\bullet+}]$[1]

calcd: 1000.50561

found: 1000.50589 Δ = 0.28 ppm

[1] Monoisotopic mass

$Bpin_2$-SQA

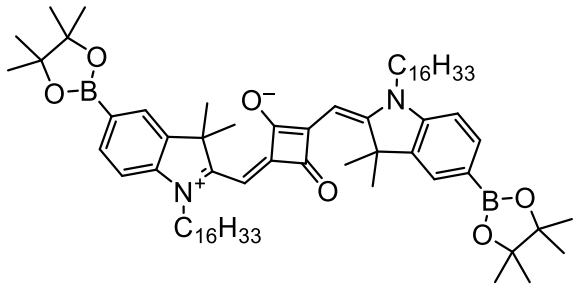

CAS: -

Synthesis following GP IV: **Br_2-SQA** (931 mg, 928 µmol), B_2Pin_2 (660 mg, 2.60 mmol), KOAc (291 mg, 2.97 mmol), dppf (25.7 mg, 46.4 µmol), $Pd(PhCN)_2Cl_2$ (17.8 mg, 46.4 µmol) in anhydrous 1,4-dioxane (25 mL). 18 h at 75 °C. Purification by column chromatography (silica, EA/DCM 1:24 → EA/DCM 4:6) and precipitation from *n*-hexane.

Yield: 501 mg (457 µmol, 49%) of a shiny green solid.

$C_{70}H_{110}B_2N_2O_6$ [1097.26]

^{1}H NMR (400.0 MHz, CD_2Cl_2):

δ [ppm] = 7.78-7.72 (m', 4H, C_{Ar}-H), 7.02 (d, 2H, ^3J = 8.4 Hz, C_{Ar}-H), 5.95 (s, 2H, C-H), 4.13-3.87 (br, 4H, C-H_2), 1.85-1.72 (m', 16H, C-H_2, C-H_3), 1.47-1.21 (m', 76H, C-H_2, C-H_3), 0.87 (t, 6H, ^3J = 6.8 Hz, C-H_3).

^{13}C(^{1}H) NMR (100.6 MHz, CD_2Cl_2):

δ [ppm] = 182.0 (quart.), 181.3 (quart.), 170.4 (quart.), 145.6 (quart.), 141.8 (quart.), 135.3 (tert.), 128.4 (tert.), 124.3 (quart.), 109.3 (tert.), 87.6 (tert.), 84.2 (quart.), 49.4 (quart.), 44.1 (sec.), 32.3 (sec.), 30.09 (3 × sec.), 30.06 (2 × sec.), 30.02 (sec.), 29.95 (sec.), 29.9 (sec.), 29.8 (2 × sec.), 27.4 (2 × sec.), 27.2 (prim.), 25.1 (prim.), 23.1 (sec.), 14.3 (prim.).

MS (MALDI, pos.): $[M]^{\bullet+}$

calcd: 1096.857

found: 1096.865

Br-SQB*-C6

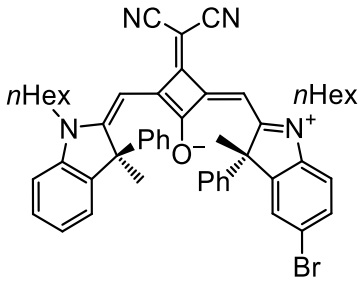

CAS: -

Synthesis based on given literature.[96]

Compound **41a** (70.7 mg, 128 µmol) and (*S*)-5-bromo-1-hexyl-2,3-dimethyl-3-phenyl-3*H*-indol-1-ium chloride (**22a**) (54.0 mg, 128 µmol) were dissolved in a mixture of *n*BuOH/toluene (1:1, 3 mL), before pyridine (228 µL, 223 mg, 2.82 mmol) was added. The solution was heated to reflux using a Dean-Stark trap for 18 h. The solvent was then removed under reduced pressure and the residue purified by column chromatography (silica, DCM) and precipitation from *n*-hexane.

Yield: 36.2 mg (44.4 µmol, 35%) of a ruby colored crystalline solid.

$C_{51}H_{51}BrN_4O$ [815.88]

HPLC (Phenomenex LUX i-Amylose-3, *n*-hexane/DCM/*i*PrOH 250:80:1, 1 mL min^{-1}):[1]
23.9 min (*RS*-diastereomer), 25.1 min (*SR*-diastereomer), 27.1 min (*SS*-diastereomer), 36.9 min (*RR*-diastereomer).

^{1}H NMR (400.0 MHz, CD_2Cl_2):

δ [ppm] = 7.39 (dd, 1H, ^3J = 8.4 Hz, ^4J = 1.7 Hz, C_{Ar}-H), 7.35-7.06 (m', 15H, C_{Ar}-H), 6.91 (d, 1H, ^3J = 8.4 Hz, C_{Ar}-H), 6.44-6.23 (m', 2H, C-H), 4.14-3.95 (m', 4H, C-H_2), 1.91-1.75 (m', 10H, C-H_2, C-H_3), 1.47-1.27 (m', 12H, C-H_2), 0.90 (m', 6H, C-H_3).

[1] Due to the asymmetry of the molecule, the *RS* and *SR* diastereomer are not identical. The assignment was arbitrary.

$^{13}C(^{1}H)$ NMR (100.6 MHz, CD_2Cl_2):

δ [ppm] = 172.3 (quart.), 171.3 (quart.), 169.3 (2 × quart.), 167.3 (quart.), 166.3 (quart.), 144.1 (quart.), 142.5 (quart.), 141.9 (3 × quart.), 141.5 (quart.), 131.2 (tert.), 128.7 (2 × tert.), 128.5 (tert.), 127.3 (2 × tert.), 126.9 (tert.), 126.8 (tert.), 126.7 (tert.), 125.5 (tert.), 123.8 (tert.), 119.2 (2 × quart.), 117.2 (quart.), 111.9 (tert.), 111.3 (tert.), 90.5 (tert.), 90.1 (tert.), 57.8 (quart.), 57.1 (quart.), 45.6 (sec.), 45.2 (sec.), 39.5 (quart.), 31.89 (sec.), 31.87 (sec.), 27.7 (sec.), 27.4 (sec.), 26.8 (2 × sec.), 25.5 (prim.), 25.1 (prim.), 22.87 (2 × sec.), 14.2 (2 × prim.).

MS (MALDI, pos.): $[M]^{\bullet+}$

calcd: 816.323

found: 816.343

Br-SQB*-C16

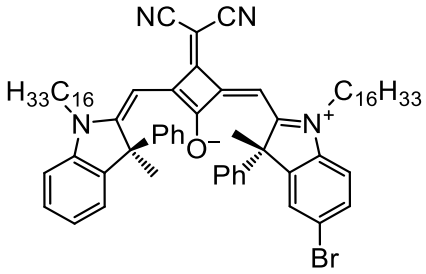

***S*-Br-SQB*-C16**

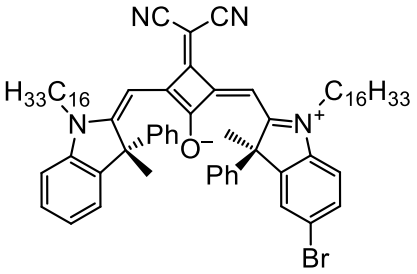

***R*-Br-SQB*-C16**

CAS: -

Synthesis based on given literature.[96]

Compound ***R*/*S*-41b** (183 mg, 265 µmol) and 5-bromo-1-hexadecyl-2,3-dimethyl-3-phenyl-3*H*-indol-1-ium chloride ***R*/*S*-22b** (174 mg, 310 µmol) were dissolved in a mixture of *n*BuOH/toluene (1:1, 12 mL), before pyridine (541 mg, 6.41 mmol) was added. The solution was thoroughly degassed before being heated at 120 °C for 18 h. The solvent was then removed under reduced pressure and the residue purified by column chromatography (silica, DCM).

Yield: 189 mg (172 µmol, 65%) of a green viscous oil.

$C_{71}H_{91}BrN_4O$ [1096.41]

HPLC (Phenomenex LUX i-Amylose-3, *n*-hexane/DCM/*i*PrOH 250:80:1, 1 mL min^{-1}):[1]

12.5 min (*RS*-diastereomer), 13.2 min (*SR*-diastereomer), 14.4 min (*SS*-diastereomer), 19.3 min (*RR*-diastereomer).

^{1}H NMR (400. MHz, CD_2Cl_2):

δ [ppm] = 7.39 (dd, 1H, ^3J = 8.5 Hz, ^4J = 1.7 Hz, C_{Ar}-H), 7.35-7.06 (m', 15H, C_{Ar}-H), 6.91 (d, 1H, ^3J = 8.5 Hz, C_{Ar}-H), 6.44-6.23 (m', 2H, C-H), 4.14-3.95 (m', 4H, C-H_2), 1.91-1.75 (m', 10H, C-H_2, C-H_3), 1.48-1.21 (m', 52H, C-H_2), 0.88 (t, 6H, ^3J = 6.8 Hz, C-H_3).

^{13}C(^{1}H) NMR (100.6 MHz, CD_2Cl_2):

δ [ppm] = 172.3 (quart.), 171.3 (quart.), 169.3 (2 × quart.), 167.3 (quart.), 166.3 (quart.), 144.1 (quart.), 142.5 (quart.), 141.9 (3 × quart.), 141.5 (quart.), 131.2 (tert.), 128.7 (2 × tert.), 128.5 (tert.), 127.3 (2 × tert.), 126.9 (tert.), 126.8 (tert.), 126.7 (tert.), 125.5 (tert.), 123.8 (tert.), 119.2 (2 × quart.), 117.2 (quart.), 111.9 (tert.), 111.3 (tert.), 90.5 (tert.), 90.1 (tert.), 57.8 (quart.), 57.1 (quart.), 45.6 (sec.), 45.2 (sec.), 39.6 (quart.), 32.3 (2 × sec.), 30.11 (8 × sec.), 30.09 (2 × sec.), 30.07 (2 × sec.), 30.04 (2 × sec.), 29.98 (2 × sec.), 29.9 (2 × sec.), 29.8 (4 × sec.), 27.7 (sec.), 27.5 (sec.), 27.2 (2 × sec.), 25.5 (prim.), 25.1 (prim.), 23.1 (2 × prim.).

MS (MALDI, pos.): $[M]^{\bullet+}$

calcd: 1096.637

found: 1096.652

[1] Due to the asymmetry of the molecule, the *RS* and *SR* diastereomer are not identical. The assignment was arbitrary.

Bpin-SQB*-C6

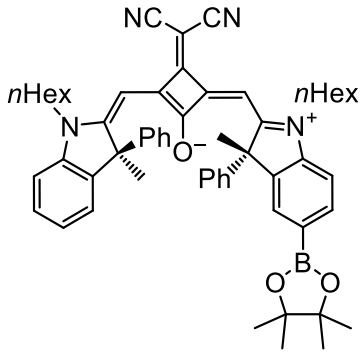

CAS: -

Synthesis following GP IV: **Br-SQB*-C6** (20.0 mg, 24.2 µmol), B_2Pin_2 (8.71 mg, 34.3 µmol), KOAc (7.70 mg, 78.5 µmol), dppf (679 µg, 1.22 µmol), $Pd(PhCN)_2Cl_2$ (470 µg, 1.23 µmol) in anhydrous 1,4-dioxane (1 mL). 18 h at 100 °C. Purification by column chromatography (silica, DCM → EA/DCM 1:9).

Yield: 12.3 mg (14.3 µmol, 59%) of a green solid.

$C_{57}H_{63}BN_4O_3$ [862.95]

^{1}H NMR (600.1 MHz, acetone-d_6):

δ [ppm] = 7.71 (dd, 1H, ^3J = 8.0 Hz, ^4J = 1.1 Hz, C_{Ar}-H), 7.46-7.43 (m', 2H, C_{Ar}-H), 7.39-7.35 (m', 2H, C_{Ar}-H), 7.29-7.23 (m', 9H, C_{Ar}-H), 7.18-7.13 (m', 3H, C_{Ar}-H), 6.45 (s, 1H, C-H), 6.41 (s, 1H, C-H), 4.28-4.13 (m', 4H, C-H_2), 1.95-1.82 (m', 10H, C-H_2, C-H_3), 1.53-1.47 (m', 4H, C-H_2), 1.40-1.26 (m', 20H, C-H_2, C-H_3), 0.90-0.87 (m', 6H, C-H_3).

^{13}C(^{1}H) NMR (150.9 MHz, acetone-d_6):

δ [ppm] = 172.7 (quart.), 171.2 (quart.), 170.9 (quart.), 169.3 (quart.), 167.6 (quart.), 166.3 (quart.), 145.3 (quart.), 143. 2 (quart.), 143.1 (quart.), 142.6 (quart.), 142.5 (quart.), 142.3 (quart.), 136.0 (tert.), 129.8 (tert.), 129.1 (tert), 129.0 (tert.), 128.9 (tert.), 127.6 (tert.), 127.5 (tert.), 127.4 (tert.), 127.3 (tert.), 126.1 (tert.), 125.7 (quart.), 124.3 (tert.), 119.4 (2 × quart.), 112.2 (tert.), 111.0 (tert.), 90.6 (tert.), 90.4 (tert.), 84.6 (quart.), 58.3 (quart.), 57.5 (quart.), 45.7 (sec.), 45.2 (sec.), 39.1 (quart.), 32.28 (sec), 32.24 (sec.), 28.1 (sec.), 27.9 (sec.), 27.07 (sec.), 27.06 (sec.),

25.5 (prim.), 25.23 (prim.), 25.21 (prim.), 25.1 (prim.), 23.18 (sec.), 23.17 (sec.), 14.27 (prim.), 14.26 (prim.).

MS (MALDI, pos.): $[M]^{\bullet+}$

calcd: 862.500

found: 862.498

Bpin-SQB*-C16

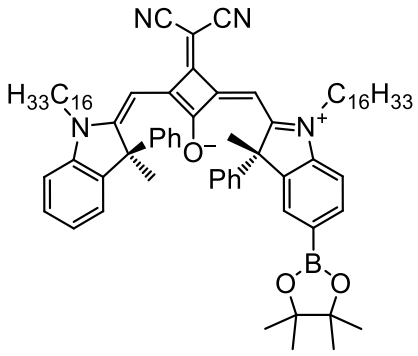

CAS:-

Synthesis following GP IV: **Br-SQB*-C16** (141 mg, 129 µmol), B_2Pin_2 (45.7 mg, 180 µmol), KOAc (40.4 mg, 42 µmol), dppf (3.56 mg, 6.42 µmol), $Pd(PhCN)_2Cl_2$ (2.47 mg, 6.44 µmol) in anhydrous 1,4-dioxane (2 mL). 18 h at 100 °C. Purification by column chromatography (silica, DCM → EA/DCM 1:9).

Yield: 90.4 mg (79.1 µmol, 61%) of a green solid.

$C_{77}H_{103}BN_4O_3$ [1143.51]

^{1}H NMR (400.0 MHz, acetone-d_6):

δ [ppm] = 7.71 (dd, 1H, ^3J = 8.0 Hz, ^4J = 1.1 Hz, C_{Ar}-H), 7.47-7.41 (m', 2H, C_{Ar}-H), 7.39-7.33 (m', 2H, C_{Ar}-H), 7.30-7.11 (m', 12H, C_{Ar}-H), 6.45 (s, 1H, C-H), 6.42 (s, 1H, C-H), 4.29-4.13 (m', 4H, C-H_2), 1.96-1.82 (m', 10H, C-H_2, C-H_3), 1.55-1.44 (m', 4H, C-H_2), 1.44-1.20 (m', 60H, C-H_2, C-H_3), 0.91-0.84 (m', 6H, C-H_3).

$^{13}C(^{1}H)$ NMR (100.6 MHz, acetone-d_6):

δ [ppm] = 172.8 (quart.), 171.3 (quart.), 171.0 (quart.), 169.4 (quart.), 167.6 (quart.), 166.4 (quart.), 145.4 (quart.), 143.22 (quart.), 143.16 (quart.), 142.61 (quart.), 142.57 (quart.), 142.4 (quart.), 136.0 (tert.), 129.9 (tert.), 129.13 (tert), 129.09 (tert.), 129.0 (tert.), 127.6 (tert.), 127.52 (tert.), 127.49 (tert.), 127.3 (tert.), 126.1 (tert.), 125.7 (quart.), 124.4 (tert.), 119.4 (2 × quart.), 112.3 (tert.), 111.1 (tert.), 90.7 (tert.), 90.5 (tert.), 84.6 (quart.), 58.3 (quart.), 57.5 (quart.), 45.7 (sec.), 45.3 (sec.), 39.3 (quart.), 32.7 (2 × sec), 29.6-29.1 (20 × sec.)[1], 28.2 (sec.), 28.0 (sec.), 27.4 (2 × sec.), 25.6 (prim.), 25.4 (prim.), 25.3 (prim.), 25.2 (prim.), 23.4 (2 × sec.), 14.5 (2 × prim.).

MS (MALDI, pos.): $[M]^{\bullet+}$

calcd: 1142.813

found: 1142.813

Br-SQB-C6

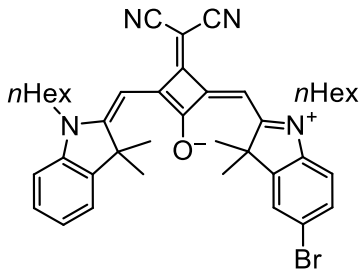

CAS: -

Synthesis based on given literature.[96]

Compound **39a** (466 mg, 954 µmol) and 5-bromo-1-hexyl-2,3,3-trimethyl-3*H*-indol-1-ium iodide (**36a**) (429 mg, 953 µmol) were dissolved in a mixture of toluene/*n*-BuOH (1:1, 40 mL) and pyridine (1.69 mL, 1.66 g, 21.0 mmol) was added. The mixture was heated to reflux for 18 h using a Dean-Stark trap. The solvent was then removed and the crude product purified by column chromatography (silica, EA/DCM 1:19).

[1] An accurate determination was not possible due to superposition with the solvent signal ($\delta(CD_3OCD_3)$ = 29.84 ppm)Lit.

Yield: 579 mg (837 µmol, 88%) of a purple solid.

$C_{41}H_{47}BrN_4O$ [691.74]

^{1}H NMR (400.0 MHz, acetone-d_6):

δ [ppm] = 7.71 (d, 1H, ^4J = 1.9 Hz, C_{Ar}-H), 7.58-7.52 (m', 2H, C_{Ar}-H), 7.46-7.39 (m', 2H, C_{Ar}-H), 7.34-7.28 (m', 2H, C_{Ar}-H), 6.59 (s, 1H, C-H), 6.49 (s, 1H, C-H), 4.16 (t, 2H, ^3J = 7.6 Hz, C-H_2), 4.08 (t, 2H, ^3J = 7.6 Hz, C-H_2), 1.88-1.76 (m', 16H, C-H_2, C-H_3), 1.56-1.45 (m', 4H, C-H_2), 1.41-1.26 (m', 8H, C-H_2), 0.90-0.85 (m', 6H, C-H_3).

^{13}C(^{1}H) NMR (100.6 MHz, acetone-d_6):

δ [ppm] = 173.9 (quart.), 173.7 (quart.), 171.4 (quart.), 168.1 (quart.), 168.0 (quart.), 166.2 (quart.), 145.5 (quart.), 143.6 (quart.), 142.9 (quart.), 142.6 (quart.), 131.9 (tert.), 129.2 (tert.), 126.5 (tert.), 126.1 (tert.), 123.3 (tert.), 119.35 (quart.), 119.33 (quart.), 117.6 (quart.), 113.2 (tert.), 112.2 (tert.), 90.2 (tert.), 89.6 (tert.), 50.7 (quart.), 50.3 (quart.), 45.4 (sec.), 45.1 (sec.), 40.7 (quart.), 32.39 (sec.), 32.37 (sec.), 28.2 (sec.), 27.9 (sec.), 27.02 (sec.), 27.01 (sec.), 27.0 (2 × prim.), 26.7 (2 × prim.), 23.29 (sec.), 23.28 (sec.), 14.4 (2 × prim.).

MS (MALDI, pos.): $[M]^{\bullet+}$

calcd: 692.292

found: 692.318

Br-SQB-C16

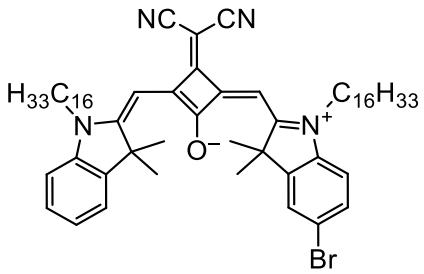

CAS: -

Synthesis based on given literature.[96]

Compound **39b** (1.07 g, 1.70 mmol) and 5-bromo-1-hexadecyl-2,3,3-trimethyl-3*H*-indol-1-ium iodide (**36b**) (1.01 g, 1.71 mmol) were dissolved in a mixture of toluene/*n*-BuOH (1:1, 70 mL) and pyridine (3.02 mL, 2.96 g, 37.4 mmol) was added. The mixture was heated to reflux for 18 h using a Dean-Stark trap. The solvent was then removed under reduced pressure and the crude product purified by column chromatography (silica, DCM).

Yield: 1.22 g (1.25 mmol, 74%) of a green solid.

$C_{61}H_{87}BrN_4O$ [972.28]

^{1}H NMR (400.0 MHz, CD_2Cl_2):

δ [ppm] = 7.50-7.34 (m', 4H, C_{Ar}-H), 7.27-7.21 (m, 1H, C_{Ar}-H), 7.15-7.11 (m, 1H, C_{Ar}-H), 6.93 (d, 1H, ^3J = 8.4 Hz, C_{Ar}-H), 6.55 (s, 1H, C-H), 6.45 (s, 1H, C-H), 4.04 (t, 2H, ^3J = 7.8 Hz, C-H_2), 3.95 (t, 2H, ^3J = 7.9 Hz, C-H_2), 1.87-1.72 (m', 16H, C-H_2, C-H_3), 1.51-1.20 (m', 52H, C-H_2), 0.87 (m', 6H, C-H_3).

^{13}C(^{1}H) NMR (100.6 MHz, CD_2Cl_2):

δ [ppm] = 173.3 (quart.), 173.1 (quart.), 170.6 (quart.), 168.0 (quart.), 167.9 (quart.), 166.1 (quart.), 144.7 (quart.), 143.0 (quart.), 142.3 (quart.), 141.8 (quart.), 131.2 (tert.), 128.4 (tert.), 126.0 (tert.), 125.3 (tert.), 122.7 (tert.), 119.13 (quart.), 119.11 (quart.), 117.2 (quart.), 111.7 (tert.), 110.9 (tert.), 90.0 (tert.), 89.4 (tert.), 50.1 (quart.), 49.6 (quart.), 45.0 (sec.), 44.8 (sec.), 40.8 (quart.), 32.3 (2 × sec.), 30.10 (6 × sec.), 30.07 (4 × sec.), 30.04 (2 × sec.), 29.96 (2 × sec.), 29.9 (2 × sec.), 29.8 (4 × sec.), 27.7 (sec.), 27.5 (sec.), 27.0 (2 × sec.), 26.9 (prim.), 26.6 (prim.), 23.1 (2 × sec.), 14.3 (2 × prim.).

HRMS (ESI, pos.): $[M]^{\bullet+}$

calcd: 972.60538

found: 972.60611 Δ = 0.75 ppm

Bpin-SQB-C6

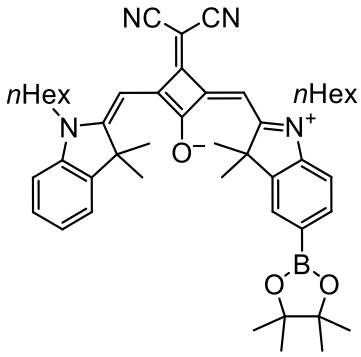

CAS: -

Synthesis following GP IV: **Br-SQB-C6** (200 mg, 289 µmol), B_2Pin_2 (103 mg, 406 µmol), KOAc (91.0 mg, 927 µmol), dppf (8.01 mg, 14.4 µmol), $Pd(PhCN)_2Cl_2$ (5.54 mg, 14.4 µmol) in anhydrous 1,4-dioxane (4 mL). 18 h at 100 °C. Purification by column chromatography (silica, EA/DCM 3:17).

Yield: 92.3 mg (125 µmol, 43%) of a green solid.

$C_{47}H_{59}BN_4O_3$ [738.81]

^{1}H NMR (400.0 MHz, acetone-d_6):

δ [ppm] = 7.82-7.76 (m', 2H, C_{Ar}-H), 7.59-7.55 (m, 1H, C_{Ar}-H), 7.46-7.41 (m', 2H, C_{Ar}-H), 7.39-7.35 (m, 1H, C_{Ar}-H), 7.34-7.27 (m, 1H, C_{Ar}-H), 6.59 (s, 1H, C-H), 6.54 (s, 1H, C-H), 4.20-4.09 (m', 4H, C-H_2), 1.88-1.75 (m', 16H, C-H_2, C-H_3), 1.56-1.46 (m', 4H, C-H_2), 1.41-1.26 (m', 20H, C-H_2, C-H_3), 0.90-0.86 (m', 6H, C-H_3).

^{13}C(^{1}H) NMR (100.6 MHz, acetone-d_6)[1]:

δ [ppm] = 173.73 (quart.), 173.68 (quart.), 172.3 (quart.), 168.2 (quart.), 167.9 (quart.), 166.4 (quart.), 145.8 (quart.), 143.6 (quart.), 143.0 (quart.), 142.6 (quart.), 136.2 (tert.), 129.2 (tert.), 128.9 (tert.), 126.1 (tert.), 123.3 (tert.), 119.38 (quart.), 119.35 (quart.), 112.1 (tert.), 111.0 (tert), 90.1 (tert.), 89.8 (tert.), 84.7 (quart.), 50.6 (quart.), 50.0 (quart.), 45.3 (sec.), 45.0 (sec.), 40.6 (quart.), 32.40 (sec.), 32.37

[1] Due to quadrupolar interactions, the signal for the carbon atom adjacent to the boron atom was not visible.

(sec.), 28.2 (sec.), 28.1 (sec.), 27.1 (prim.), 27.0 (2 × sec.), 26.7 (prim.), 25.3 (prim.), 23.27 (sec.), 23.26 (sec.), 14.4 (2 × prim.).

MS (MALDI, pos.): $[M]^{\bullet+}$

calcd: 738.468

found: 738.468

Bpin-SQB-C16

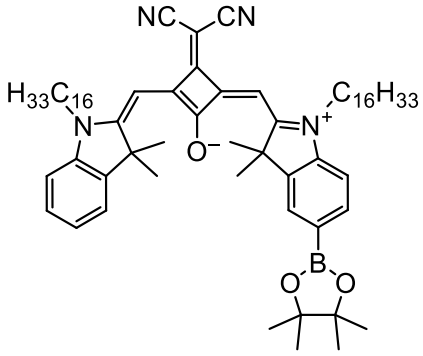

CAS: -

Synthesis following GP IV: **Br-SQB-C16** (1.15 g, 1.18 mmol), B_2Pin_2 (419 mg, 1.65 mmol), KOAc (369 mg, 3.76 mmol), dppf (32.7 mg, 59.0 µmol), $Pd(PhCN)_2Cl_2$ (22.6 mg, 59.0 µmol) in anhydrous 1,4-dioxane (170 mL). 18 h at 105 °C. Purification by column chromatography (silica, DCM → EA/DCM 1:19).

Yield: 833 mg (817 µmol, 69%) of a green solid.

$C_{67}H_{99}BN_4O_3$ [1019.34]

^{1}H NMR (400.0 MHz, CD_2Cl_2):

δ [ppm] = 7.80-7.72 (m', 2H, C_{Ar}-H), 7.43-7.39 (m, 1H, C_{Ar}-H), 7.39-7.34 (m, 1H, C_{Ar}-H), 7.27-7.21 (m, 1H, C_{Ar}-H), 7.14-7.09 (m, 1H, C_{Ar}-H), 7.07 (d, 1H, ^3J = 8.0 Hz, C_{Ar}-H), 6.53 (s, 1H, C-H), 6.49 (s, 1H, C-H), 4.08-3.94 (m', 4H, C-H_2), 1.87-1.72 (m', 16H, C-H_2, C-H_3), 1.51-1.18 (m', 64H, C-H_2), 0.87 (m', 6H, C-H_3).

$^{13}C(^{1}H)$ NMR (100.6 MHz, CD_2Cl_2):[1]

δ [ppm] = 173.4 (quart.), 172.8 (quart.), 171.8 (quart.), 168.0 (quart.), 167.6 (quart.), 166.5 (quart.), 145.1 (quart.), 143.0 (quart.), 142.4 (quart.), 142.0 (quart.), 135.4 (tert.), 128.4 (2 × tert.), 125.1 (tert.), 122.6 (tert.), 119.21 (quart.), 119.17 (quart.), 110.8 (tert.), 109.8 (tert.), 89.8 (tert.), 89.7 (tert.), 84.3 (quart.), 50.0 (quart.), 49.4 (quart.), 44.9 (sec.), 44.7 (sec.), 40.6 (quart.), 32.3 (2 × sec.), 30.09 (6 × sec.), 30.06 (4 × sec.), 30.03 (2 × sec.), 29.95 (2 × sec.), 29.84 (2 × sec.), 29.76 (4 × sec.), 27.7 (sec.), 27.6 (sec.), 27.0 (2 × sec.), 26.8 (prim.), 26.6 (prim.), 25.1 (prim.), 23.1 (2 × sec.), 14.3 (2 × prim.).

MS (MALDI, pos.): $[M]^{\bullet+}$

calcd: 1018.782

found: 1018.783

Br-SQA-C6

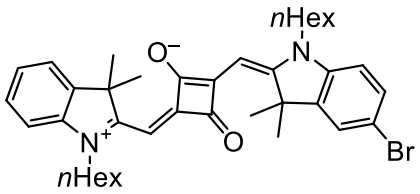

CAS: 426233-27-4

Synthesis based on given literature.[96]

Compound **38a** (1.85 g, 5.45 mmol), 5-bromo-1-hexyl-2,3,3-trimethyl-3*H*-indol-1-ium iodide (**36a**) (2.45 g, 5.44 mmol) and pyridine (25.0 mL, 24.6 g, 311 mmol) were suspended in toluene/*n*-BuOH (1:1, 250 mL) and the mixture heated to reflux for 18 h using a Dean-Stark trap. The solvent was then removed under reduced pressure and the residue purified by column chromatography (silica, MeOH/DCM 1:99).

Yield: 3.02 g (4.69 mmol, 86%) of a copper-colored solid.

[1] Due to quadrupolar interactions, the signal for the carbon atom adjacent to the boron atom was not visible.

$C_{38}H_{47}BrN_2O_2$ [643.70]

^{1}H NMR (400.0 MHz, CD_2Cl_2):

δ [ppm] = 7.47-7.30 (m', 4H, C_{Ar}-H), 7.20-7.15 (m, 1H, C_{Ar}-H), 7.07-7.03 (m, 1H, C_{Ar}-H), 6.86 (d, 1H, ^3J = 8.4 Hz, C_{Ar}-H), 5.95 (s, 1H, C-H), 5.88 (s, 1H, C-H), 4.12-3.83 (m', 4H, C-H_2), 1.86-1.70 (m', 16H, C-H_2, C-H_3), 1.50-1.26 (m', 12H, C-H_2), 0.93-0.86 (m', 6H, C-H_3).

Br-SQA-C16

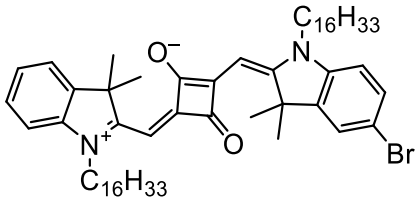

CAS: -

Synthesis based on given literature.[96]

Compound **38b** (770 mg, 1.61 mmol), 5-bromo-1-hexadecyl-2,3,3-trimethyl-3H-indol-1-ium iodide (**36b**) (948 mg, 1.61 mmol) and pyridine (7.30 mL, 7.14 g, 90.3 mmol) were suspended in toluene/*n*-BuOH (1:1, 75 mL) and the mixture heated to reflux for 18 h using a Dean-Stark trap. The solvent was then removed under reduced pressure and the residue purified by column chromatography (silica, EA/DCM 1:19).

Yield: 1.17 g (1.27 mmol, 79%) of a blue solid.

$C_{58}H_{87}BrN_2O_2$ [924.23]

^{1}H NMR (400.1 MHz, CD_2Cl_2):

δ [ppm] = 7.47-7.30 (m', 4H, C_{Ar}-H), 7.20-7.15 (m, 1H, C_{Ar}-H), 7.07-7.03 (m, 1H, C_{Ar}-H), 6.86 (d, 1H, ^3J = 8.4 Hz, C_{Ar}-H), 5.95 (s, 1H, C-H), 5.88 (s, 1H, C-H), 4.10-3.86 (m', 4H, C-H_2), 1.87-1.70 (m', 16H, C-H_2, C-H_3), 1.49-1.17 (m', 52H, C-H_2), 0.87 (m', 6H, C-H_3).

$^{13}C(^{1}H)$ NMR (100.6 MHz, CD_2Cl_2):

δ [ppm] = 182.0 (3 × quart.), 179.5 (quart.), 171.2 (quart.), 168.5 (quart.), 144.6 (quart.), 142.8 (quart.), 142.7 (quart.), 142.4 (quart.), 130.9 (tert.), 128.2 (tert.), 125.9 (tert.), 124.3 (tert.), 122.6 (tert.), 116.1 (quart.), 111.0 (tert.), 110.2 (tert.), 87.2 (tert.), 87.1 (tert.), 49.8 (quart.), 49.4 (quart.), 44.2 (sec.), 44.0 (sec.), 32.3 (2 × sec.), 30.10 (6 × sec.), 30.06 (4 × sec.), 30.0 (2 × sec.), 29.94 (2 × sec.), 29.89 (2 × sec.), 29.8 (4 × sec.), 27.5 (sec.), 27.4 (2 × sec.), 27.2 (sec., prim.), 27.0 (prim.), 23.1 (2 × sec.), 14.3 (2 × prim.).

MS (MALDI, pos.): $[M]^{\bullet+}$

calcd: 924.594

found: 924.611

Bpin-SQA-C6

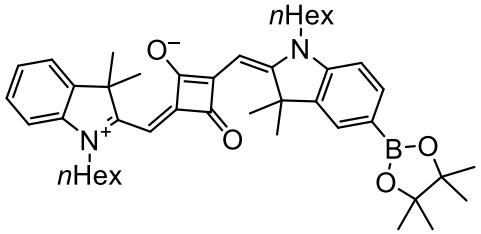

CAS: -

Synthesis following GP IV: **Br-SQA-C6** (500 mg, 777 µmol), B_2Pin_2 (280 mg, 1.10 mmol), KOAc (243 mg, 2.48 mmol), dppf (22.0 mg, 39.7 µmol), $Pd(PhCN)_2Cl_2$ (15.2 mg, 39.6 µmol) in anhydrous 1,4-dioxane (11 mL). 18 h at 85 °C. Purification by column chromatography (silica, EA/DCM 1:9) and precipitation from *n*-hexane.

Yield: 518 mg (750 µmol, 97%) of an indigo-colored solid.

$C_{44}H_{59}BN_2O_4$ [690.76]

^{1}H NMR (400.0 MHz, CD_2Cl_2):

δ [ppm] = 7.75-7.71 (m', 2H, C_{Ar}-H), 7.40-7.36 (m, 1H, C_{Ar}-H), 7.35-7.30 (m', 1H, C_{Ar}-H), 7.20-7.14 (m, 1H, C_{Ar}-H), 7.07-7.02 (m, 1H, C_{Ar}-H), 7.02-6.97 (m, 1H, C_{Ar}-H), 5.95 (s, 1H, C-H), 5.92 (s, 1H, C-H), 4.13-3.86 (m', 4H, C-H_2), 1.85-1.72 (m', 16H, C-H_2, C-H_3), 1.50-1.23 (m', 24H, C-H_2), 0.93-0.86 (m', 6H, C-H_3).

^{13}C(^{1}H) NMR (100.6 MHz, CD_2Cl_2)[1]:

δ [ppm] = 182.1 (2 × quart.), 181.7 (quart.), 180.0 (quart.), 170.9 (quart.), 169.6 (quart.), 145.7 (quart.), 142.9 (quart.), 142.6 (quart.), 141.7 (quart.), 135.2 (tert.), 128.4 (tert.), 128.1 (tert.), 124.2 (tert.), 122.6 (tert.), 110.1 (tert.), 109.1 (tert), 87.3 (tert.), 87.1 (tert.), 84.2 (quart.), 49.8 (quart.), 49.2 (quart.), 44.2 (sec.), 44.0 (sec.), 31.9 (2 × sec.), 27.4 (sec.), 27.31 (sec.), 27.26 (prim.), 27.1 (2 × sec, prim.), 25.1 (prim.), 22.9 (2 × sec.), 14.1 (2 × prim.).

MS (MALDI, pos.): $[M]^{\bullet+}$

calcd: 690.457

found: 690.457

Bpin-SQA-C16

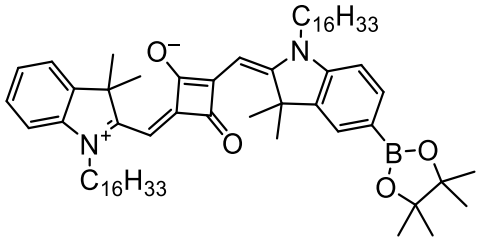

CAS: -

Synthesis following GP IV: **Br-SQA-C16** (1.15 g, 1.24 mmol), B_2Pin_2 (449 mg, 1.77 mmol), KOAc (390 mg, 3.97 mmol), dppf (35.2 mg, 63.4 µmol), $Pd(PhCN)_2Cl_2$ (24.3 mg, 63.5 µmol) in anhydrous 1,4-dioxane (180 mL). 18 h at 85 °C. Purification by column chromatography (silica, EA/DCM 1:19 → EA/DCM 3:17).

[1] Due to quadrupolar interactions, the signal for the carbon atom adjacent to the boron atom was not visible.

Yield: 1.07 g (1.10 mmol, 89%) of a copper-colored solid.

$C_{64}H_{99}BN_2O_4$ [971.32]

^{1}H NMR (400.0 MHz, CD_2Cl_2):

δ [ppm] = 7.75-7.71 (m', 2H, C_{Ar}-H), 7.40-7.36 (m, 1H, C_{Ar}-H), 7.35-7.30 (m', 1H, C_{Ar}-H), 7.19-7.14 (m, 1H, C_{Ar}-H), 7.06-7.02 (m, 1H, C_{Ar}-H), 7.02-6.97 (m, 1H, C_{Ar}-H), 5.95 (s, 1H, C-H), 5.92 (s, 1H, C-H), 4.13-3.86 (m', 4H, C-H_2), 1.85-1.72 (m', 16H, C-H_2, C-H_3), 1.48-1.21 (m', 64H, C-H_2, C-H_3), 0.87 (m', 6H, C-H_3).

^{13}C(^{1}H) NMR (100.6 MHz, CD_2Cl_2)[1]:

δ [ppm] = 182.1 (2 × quart.), 181.7 (quart.), 180.0 (quart.), 170.9 (quart.), 169.6 (quart.), 145.7 (quart.), 142.9 (quart.), 142.6 (quart.), 141.7 (quart.), 135.3 (tert.), 128.4 (tert.), 128.1 (tert.), 124.2 (tert.), 122.6 (tert.), 110.1 (tert.), 109.1 (tert), 87.3 (tert.), 87.1 (tert.), 84.2 (quart.), 49.8 (quart.), 49.2 (quart.), 44.2 (sec.), 44.0 (sec.), 32.3 (2 × sec.), 30.09 (6 × sec.), 30.06 (4 × sec.), 30.02 (2 × sec.), 29.96 (2 × sec.), 29.9 (2 × sec.), 29.8 (4 × sec.), 27.44 (sec.), 27.42 (2 × sec.), 27.37 (sec.), 27.3 (prim.), 27.1 (prim.), 25.1 (prim.), 23.1 (2 × sec.), 14.3 (2 × prim.).

MS (MALDI, pos.): $[M]^{\bullet+}$

calcd: 970.770

found: 970.771

[1] Due to quadrupolar interactions, the signal for the carbon atom adjacent to the boron atom was not visible.

8.2.5 Squaraine oligomers

_S_-SQA-SQB*

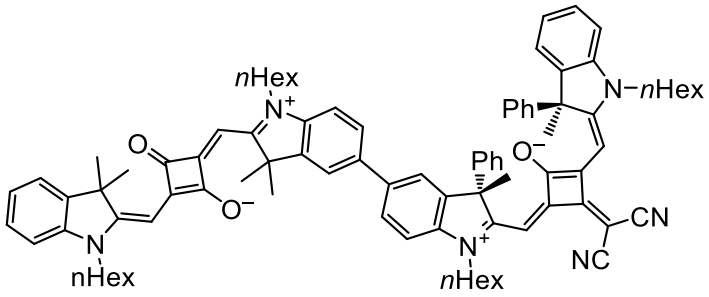

CAS: -

Synthesis following GP VI: **Br-SQA-C6** (42.7 mg, 66.3 µmol), ***S*-Bpin-SQB*-C6** (38.2 mg, 44.3 µmol), Cs_2CO_3 (144 mg, 442 µmol), XPhos G2 (1.05 mg, 1.33 µmol). 18 h at 65 °C Purification by flash chromatography (silica, PE → acetone/PE 2:3), preparative GPC (DCM) and precipitation from DCM/*n*-hexane.

Yield: 15.5 mg (11.9 µmol, 27%) of a teal solid.

$C_{89}H_{98}N_6O_3$ [1299.77]

^{1}H NMR (600.1 MHz, CD_2Cl_2):

δ [ppm] = 7.56-7.52 (m, 1H, C_{Ar}-H), 7.47-7.41 (m', 2H, C_{Ar}-H), 7.39-7.36 (m, 1H, C_{Ar}-H), 7.35-7.21 (m', 9H, C_{Ar}-H), 7.20-7.13 (m', 6H, C_{Ar}-H), 7.13-7.06 (m', 3H, C_{Ar}-H), 7.05-7.00 (m', 2H, C_{Ar}-H), 6.44-6.24 (m', 2H, C-H), 6.00-5.83 (m', 2H, C-H), 4.18-3.88 (m', 8H, C-H_2), 1.95 (s, 3H, C-H_3), 1.91-1.73 (m', 23H, C-H_2, C-H_3), 1.50-1.40 (m', 8H, C-H_2), 1.40-1.29 (m', 16H, C-H_2), 0.93-0.87 (m', 12H, C-H_3).

^{13}C(^{1}H) NMR (150.9 MHz, CD_2Cl_2):

δ [ppm] = 182.1 (2 × quart.), 180.1 (quart.), 179.8 (quart.), 171.5 (quart.), 171.2 (quart.), 170.5 (2 × quart.), 169.4 (quart.), 168.2 (quart.), 167.7 (quart.), 166.2 (quart.), 143.3 (quart.), 143.1 (quart.), 142.9 (quart.), 142.6 (2 × quart.), 142.4 (quart.), 142.2 (2 × quart.), 142.1 (quart.), 141.5 (quart.), 138.0 (quart.), 136.2 (quart.), 128.7 (tert.), 128.6 (tert), 128.4 (tert.), 128.1 (tert.), 127.20 (tert.), 127.16 (tert.), 127.13 (tert.), 126.9 (tert.), 126.8 (tert.), 126.7 (tert.), 125.1 (tert.), 124.1 (tert.),

123.7 (tert.), 122.6 (tert.), 122.1 (tert.), 121.1 (tert.), 119.3 (2 × quart.), 111.2 (tert.), 110.9 (tert.), 110.0 (2 × tert.), 90.3 (tert.), 90.2 (tert.), 87.2 (tert.), 87.0 (tert.), 57.5 (2 × quart.), 49.7 (quart.), 49.5 (quart.), 45.4 (sec.), 45.3 (sec.), 44.1 (2 × sec.), 39.4 (quart.), 31.92 (sec.), 31.90 (3 × sec.), 27.7 (sec.), 27.6 (sec.), 27.5-27.0 (2 × sec., 6 × prim.), 26.88 (sec.), 26.86 (sec.), 25.5 (sec.), 25.3 (sec.), 22.93 (2 × sec.), 22.90 (sec.), 22.88 (sec.), 14.18 (prim.), 14.16 (prim.), 14.14 (2 × prim.).

HRMS (ESI, pos.): $[M]^{\bullet+}$

calcd: 1298.76949

found: 1298.76768 Δ = 1.39 ppm

R*-SQA-SQB

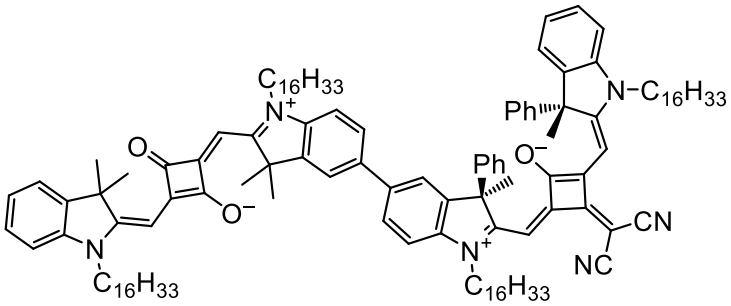

CAS: -

Synthesis following GP VI: ***R*-Br-SQB*-C16** (21.0 mg, 19.2 µmol), **Br-SQA-C16** (37.2 mg, 40.2 µmol), Cs_2CO_3 (62.4 mg, 192 µmol), XPhos G2 (904 µg, 1.15 µmol). 18 h at 65 °C Purification by flash chromatography (silica, PE → acetone/PE 1:1) and preparative GPC (DCM). Freeze-drying from benzene afforded the product as a solid.

Yield: 15.4 mg (8.28 µmol, 43%) of a teal solid.

$C_{129}H_{178}N_6O_3$ [1860.84]

^{1}H NMR (600.1 MHz, CD_2Cl_2):

δ [ppm] = 7.56-7.52 (m, 1H, C_{Ar}-H), 7.47-7.41 (m', 2H, C_{Ar}-H), 7.39-7.36 (m, 1H, C_{Ar}-H), 7.35-7.21 (m', 9H, C_{Ar}-H), 7.20-7.13 (m', 6H, C_{Ar}-H), 7.13-7.06 (m', 3H, C_{Ar}-H), 7.05-6.99 (m', 2H, C_{Ar}-H), 6.44-6.24 (m', 2H, C-H), 5.96-5.88 (m', 2H, C-H), 4.18-3.88

(m', 8H, C-$\underline{H}_2$), 1.95 (s, 3H, C-$\underline{H}_3$), 1.91-1.73 (m', 23H, C-$\underline{H}_2$, C-$\underline{H}_3$), 1.48-1.40 (m', 8H, C-$\underline{H}_2$), 1.40-1.33 (m', 8H, C-$\underline{H}_2$), 1.33-1.20 (m', 88H, C-$\underline{H}_2$), 0.90-0.85 (m', 12H, C-$\underline{H}_3$).

^{13}C(^{1}H) NMR (150.9 MHz, CD_2Cl_2):

δ [ppm] = 182.1 (2 × quart.), 180.1 (quart.), 179.8 (quart.), 171.5 (quart.), 171.2 (quart.), 170.5 (2 × quart.), 169.4 (quart.), 168.2 (quart.), 167.7 (quart.), 166.2 (quart.), 143.3 (quart.), 143.1 (quart.), 142.9 (quart.), 142.6 (2 × quart.), 142.4 (quart.), 142.2 (3 × quart.), 141.6 (quart.), 138.0 (quart.), 136.2 (quart.), 128.7 (tert.), 128.6 (tert), 128.4 (tert.), 128.1 (tert.), 127.20 (tert.), 127.16 (tert.), 127.14 (tert.), 126.9 (tert.), 126.8 (tert.), 126.7 (tert.), 125.1 (tert.), 124.1 (tert.), 123.7 (tert.), 122.6 (tert.), 122.1 (tert.), 121.1 (tert.), 119.3 (2 × quart.), 111.2 (tert.), 110.9 (tert.), 110.0 (2 × tert.), 90.3 (tert.), 90.2 (tert.), 87.2 (tert.), 87.0 (tert.), 57.6 (2 × quart.), 49.7 (quart.), 49.5 (quart.), 45.4 (sec.), 45.3 (sec.), 44.1 (2 × sec.), 39.4 (quart.), 32.3 (4 × sec.), 30.10 (6 × sec.), 30.09 (4 × sec.), 30.08 (4 × sec.), 30.06 (8 × sec.), 30.02 (2 × sec.), 30.00 (sec.), 29.99 (sec.), 29.95 (2 × sec.), 29.00 (3 × sec.), 29.88 (sec.), 29.80 (sec.), 29.78 (2 × sec.), 29.76 (5 × sec.), 27.71 (sec.), 27.67 (sec.), 27.4 (4 × sec.), 27.30 (prim.), 27.25 (sec., prim.), 27.22 (sec.), 27.1 (2 × prim.), 25.5 (prim.), 25.3 (prim.), 23.1 (4 × sec.), 14.3 (4 × prim.).

HRMS (ESI, pos.): [M^{2+}]

calcd: 930.19912

found: 930.20106 Δ = 2.09 ppm

S*-SQB-SQB

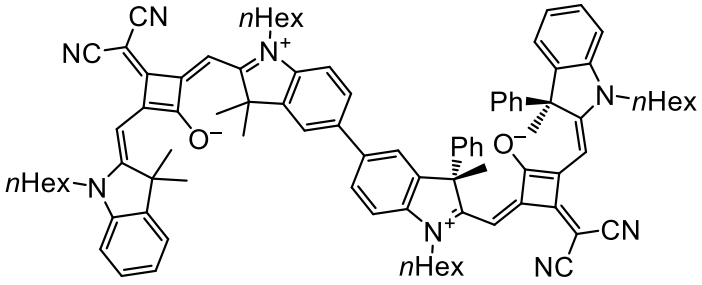

CAS: -

Synthesis following GP VI: ***S*-Br-SQB*-C6** (15.0 mg, 18.4 µmol), **Bpin-SQB-C6** (40.7 mg, 55.1 µmol), Cs_2CO_3 (59.9 mg, 184 µmol), XPhos G2 (868 µg, 1.10 µmol). 18 h at 65 °C Purification by column chromatography (silica, acetone/PE 2:7), preparative GPC (DCM) and precipitation from MeOH.

Yield: 14.2 mg (10.5 µmol, 57%) of a green solid.

$C_{92}H_{98}N_8O_2$ [1347.82]

^{1}H NMR (600.1 MHz, CD_2Cl_2):

δ [ppm] = 7.56-7.53 (m, 1H, C_{Ar}-H), 7.48-7.45 (m', 2H, C_{Ar}-H), 7.42-7.39 (m, 1H, C_{Ar}-H), 7.38-7.35 (m, 1H, C_{Ar}-H), 7.32-7.07 (m', 19H, C_{Ar}-H), 6.44-6.51 (s, 1H, C-H), 6.49 (s, 1H, C-H), 6.35 (m', 2H, C-H), 4.14-3.97 (m', 8H, C-H_2), 1.95 (s, 3H, C-H_3), 1.90-1.74 (m', 23H, C-H_2, C-H_3), 1.50-1.41 (m', 8H, C-H_2), 1.39-1.29 (m', 16H, C-H_2), 0.92-0.87 (m', 12H, C-H_3).

^{13}C(^{1}H) NMR (150.9 MHz, CD_2Cl_2):

δ [ppm] = 173.5 (quart.), 172.5 (quart.), 171.4 (3 × quart.), 170.4 (quart.), 168.4 (quart.), 168.0 (quart.), 167.6 (quart.), 167.1 (quart.), 166.3 (2 × quart.), 143.6 (quart.), 143.1 (quart.), 142.9 (quart.), 142.4 (2 × quart.), 142.2 (quart.), 142.1 (2 × quart.), 142.0 (quart.), 141.8 (quart.), 137.7 (quart.), 137.2 (quart.), 128.7 (tert.), 128.6 (tert.), 128.44 (tert.), 128.38 (tert.), 127.3 (tert.), 127.2 (3 × tert.), 126.8 (tert.), 126.7 (tert.), 125.2 (tert.), 125.0 (tert.), 123.7 (tert.), 122.6 (tert.), 122.2 (tert.), 121.1 (tert.), 119.3 (2 × quart.), 119.2 (2 × quart.), 111.2 (tert.), 111.0 (tert.), 110.72 (tert.), 110.71 (tert.), 90.29 (tert.), 90.24 (tert.), 89.6 (2 × tert.), 57.6 (quart.), 57.5 (quart.), 49.9 (quart.), 49.7 (quart.), 45.4 (2 × sec.), 44.9 (2 × sec.), 40.5 (quart.), 39.4 (quart.), 31.93 (sec.), 31.91 (sec.), 31.90 (2 × sec.), 27.7 (3 × sec.), 27.6 (sec.), 26.89 (sec.), 26.86 (sec., prim.), 26.8 (prim.), 26.73 (sec.), 26.72 (sec.), 26.6 (2 × prim.), 25.5 (prim.), 25.3 (prim.), 22.90 (sec.), 22.88 (sec.), 22.87 (2 × sec.), 14.18 (prim.), 14.16 (prim.), 14.15 (prim.), 14.14 (prim.).

HRMS (ESI, pos.): $[M]^{\bullet+}$

calcd: 1347.78393

found: 1347.78059 *Δ* = 2.48 ppm

R*-SQB-SQB

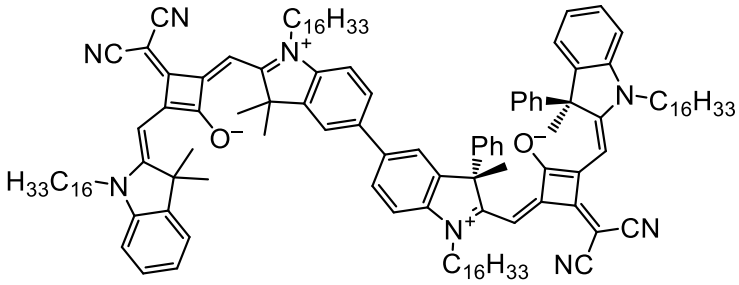

CAS: -

Synthesis following GP VI: ***R*-Br-SQB*-C16** (19.5 mg, 17.8 µmol), **Bpin-SQB-C16** (36.6 mg, 37.6 µmol), $CsCO_3$ (57.9 mg, 178 µmol), XPhos G2 (840 µg, 1.07 µmol). 18 h at 65 °C Purification by flash chromatography (silica, PE → acetone/PE 6:4), preparative GPC (DCM) and precipitation from MeOH.

Yield: 19.7 mg (10.3 µmol, 58%) of a green solid.

$C_{132}H_{178}N_8O_2$ [1908.88]

^{1}H NMR (600.1 MHz, CD_2Cl_2):

δ [ppm] = 7.57-7.52 (m, 1H, C_{Ar}-H), 7.48-7.45 (m', 2H, C_{Ar}-H), 7.42-7.39 (m, 1H, C_{Ar}-H), 7.38-7.35 (m, 1H, C_{Ar}-H), 7.32-7.06 (m', 19H, C_{Ar}-H), 6.44-6.51 (s, 1H, C-H), 6.49 (s, 1H, C-H), 6.35 (s, 2H, C-H), 4.14-3.97 (m', 8H, C-H_2), 1.95 (s, 3H, C-H_3), 1.91-1.75 (m', 23H, C-H_2, C-H_3), 1.49-1.41 (m', 8H, C-H_2), 1.40-1.33 (m', 8H, C-H_2), 1.33-1.21 (m', 88H, C-H_2), 0.89-0.86 (m', 12H, C-H_3).

^{13}C(^{1}H) NMR (150.9 MHz, CD_2Cl_2):

δ [ppm] = 173.4 (quart.), 172.5 (quart.), 171.4 (3 × quart.), 170.4 (quart.), 168.4 (quart.), 168.0 (quart.), 167.6 (quart.), 167.1 (quart.), 166.26 (quart.), 166.25 (quart.), 143.6 (quart.), 143.1 (quart.), 142.9 (quart.), 142.43 (quart.), 142.39 (quart.), 142.2 (quart.), 142.1 (2 × quart.), 142.0 (quart.), 141.8 (quart.), 137.7 (quart.), 137.2 (quart.), 128.7 (tert.), 128.6 (tert.), 128.44 (tert.), 128.38 (tert.), 127.3 (tert.), 127.2 (3 × tert.), 126.8 (tert.), 126.7 (tert.), 125.2 (tert.), 125.0 (tert.), 123.7 (tert.), 122.6 (tert.), 122.2 (tert.), 121.1 (tert.), 119.3 (2 × quart.), 119.2 (2 × quart.), 111.2 (tert.), 111.0 (tert.), 110.73 (tert.), 110.72 (tert.), 90.32 (tert.), 90.25 (tert.), 89.7

(2 × tert.), 57.6 (quart.), 57.5 (quart.), 49.9 (quart.), 49.7 (quart.), 45.4 (2 × sec.), 44.9 (2 × sec.), 40.6 (quart.), 39.5 (quart.), 32.3 (4 × sec.), 30.10 (6 × sec.), 30.09 (8 × sec.), 30.06 (8 × sec.), 30.03 (2 × sec.), 30.00 (sec.), 29.99 (sec.), 29.95 (2 × sec.), 29.90 (sec.), 29.87 (sec.), 29.84 (2 × sec.), 29.81 (sec.), 29.76 (7 × sec.), 27.69 (3 × sec.), 27.65 (sec.), 27.25 (sec.), 27.22 (sec.), 27.1 (sec.), 27.0 (sec.), 26.9 (prim.), 26.8 (prim.), 26.6 (2 × prim.), 25.5 (prim.), 25.3 (prim.), 23.1 (4 × sec.), 14.3 (4 × prim.).

HRMS (ESI, pos.): $[M]^{2+}$

calcd: 954.20473

found: 954.20669 Δ = 2.05 ppm

SQA-SQB*-SQA

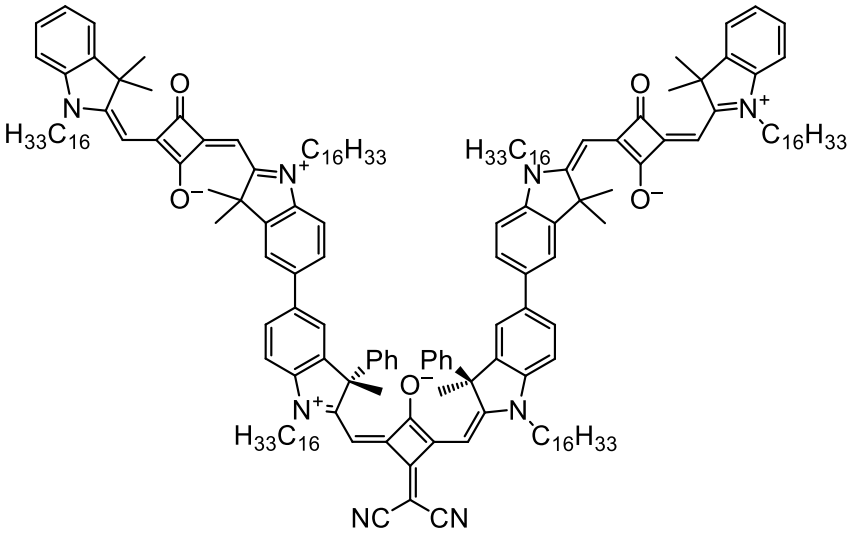

***S*-SQA-SQB*-SQA**

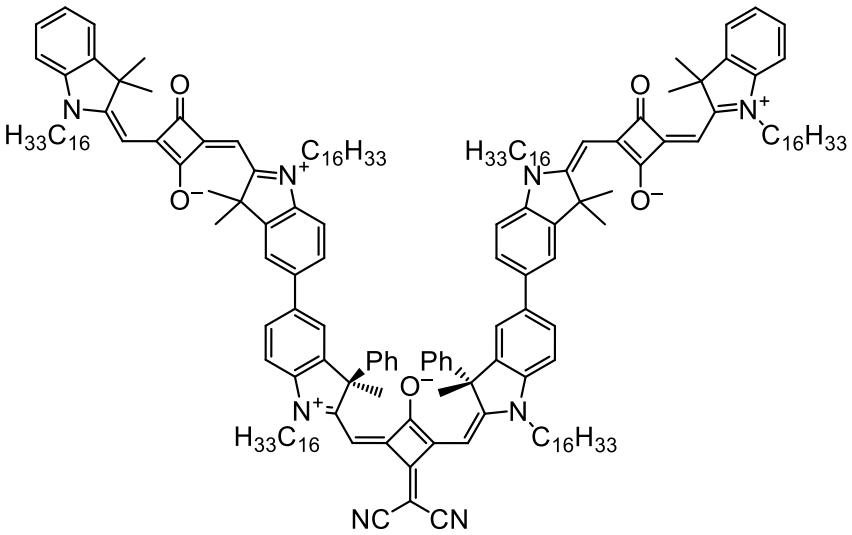

***R*-SQA-SQB*-SQA**

CAS: -

Synthesis following GP VI: ***R/S*-Br$_2$-Ph-SQB*** (8.90 mg, 7.57 µmol), **Bpin-SQA-C16** (22.1 mg, 22.8 µmol), Cs_2CO_3 (24.7 mg, 75.8 µmol), XPhos G2 (357 µg, 454 nmol). 18 h at 65 °C Purification by flash chromatography (silica, PE → acetone/PE 2:3) and preparative GPC (DCM). Freeze-drying from benzene afforded the product as a solid.

Yield: 15.1 mg (5.58 µmol, 74%) of a dark blue-green solid.

$C_{187}H_{264}N_8O_5$ [2704.15]

^{1}H NMR (600.1 MHz, CD_2Cl_2):

δ [ppm] = 7.57-7.52 (m, 2H, C_{Ar}-H), 7.48-7.41 (m', 4H, C_{Ar}-H), 7.39-7.35 (m, 2H, C_{Ar}-H), 7.35-7.22 (m', 12H, C_{Ar}-H), 7.22-7.12 (m', 6H, C_{Ar}-H), 7.05-6.99 (m', 4H, C_{Ar}-H), 6.47-6.24 (br, 2H, C-H), 5.98-5.87 (m', 4H, C-H), 4.18-4.08 (m, 4H, C-H_2), 4.08-3.86 (br, 8H, C-H_2), 1.97 (s, 6H, C-H_3), 1.90-1.71 (m', 36H, C-H_2, C-H_3), 1.49-1.40 (m', 12H, C-H_2), 1.40-1.18 (m', 144H, C-H_2), 0.89-0.84 (m', 18H, C-H_3).

^{13}C(^{1}H) NMR (150.9 MHz, CD_2Cl_2):

δ [ppm] = 182.1 (2 × quart.), 181.0 (quart.), 179.8 (quart.), 171.7 (quart.), 170.6 (2 × quart.), 169.4 (quart.), 167.7 (quart.), 166.3 (quart.), 143.3 (quart.), 143.2 (quart.), 142.9 (quart.), 142.6 (2 × quart.), 142.2 (quart.), 141.5 (quart.), 138.1 (quart.), 136.2 (quart.), 128.7 (tert.), 128.1 (tert.), 127.2 (2 × tert.), 127.0 (tert.), 126.8 (tert.), 124.1 (tert.), 122.6 (tert.), 122.2 (tert.), 121.1 (tert.), 119.3 (quart.), 111.3 (tert.),

110.0 (2 × tert.), 90.5 (tert.), 87.2 (tert.), 87.0 (tert.), 57.6 (quart.), 49.7 (quart.), 45.5 (sec.), 44.1 (2 × sec.), 39.5 (quart.), 32.3 (3 × sec.), 30.11 (2 × sec.), 30.10 (4 × sec.), 30.09 (2 × sec.), 30.08 (2 × sec.), 30.06 (6 × sec.), 30.02 (3 × sec.), 29.96 (sec.), 29.95 (sec.), 29.90 (3 × sec.), 29.81 (sec.), 29.78 (sec.), 29.76 (4 × sec.), 27.7 (sec.), 27.4 (3 × sec.), 27.30 (prim.), 27.26 (2 × sec.), 27.1 (3 × prim.), 25.5 (prim.), 23.1 (3 × sec.), 14.3 (3 × prim.).

HRMS (ESI, pos.): [M^{2+}]

calcd: 1352.03524

found: 1352.03737 Δ = 1.58 ppm

SQB-SQB*-SQB

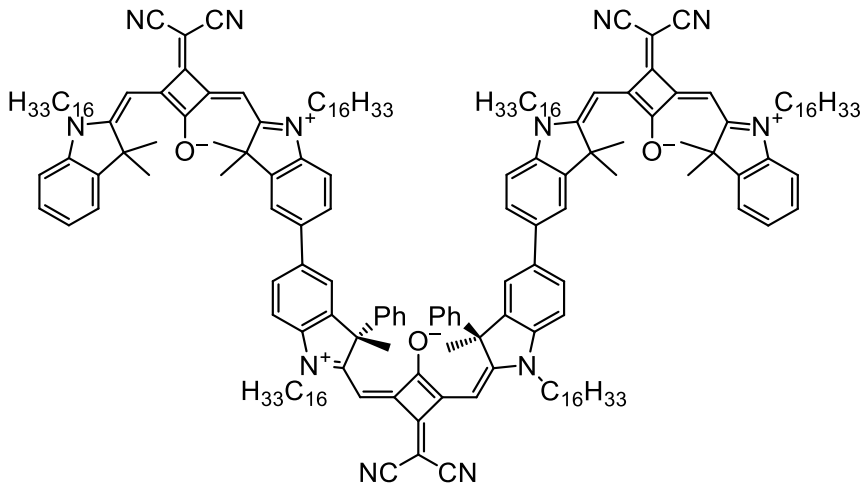

***S*-SQB-SQB*-SQB**

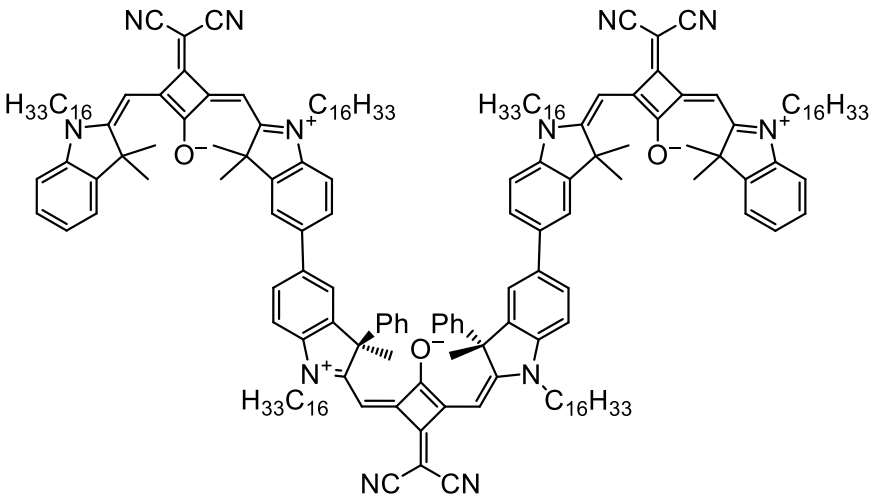

***R*-SQB-SQB*-SQB**

CAS: -

Synthesis following GP VI: ***R/S*-Br$_2$-Ph-SQB*** (19.5 mg, 16.6 µmol), **Bpin-SQB-C16** (50.7 mg, 49.7 µmol), Cs_2CO_3 (54.1 mg, 166 µmol), XPhos G2 (783 µg, 995 nmol). 18 h at 65 °C. Purification by flash chromatography (silica, PE → acetone/PE 9:11), preparative GPC (DCM) and precipitation from MeOH.

Yield: 19.7 mg (7.04 µmol, 42%) of a green solid.

$C_{193}H_{264}N_{12}O_3$ [2800.25]

^{1}H NMR (600.1 MHz, CD_2Cl_2):

δ [ppm] = 7.58-7.54 (m, 2H, C_{Ar}-H), 7.49-7.45 (m', 4H, C_{Ar}-H), 7.42-7.39 (m, 2H, C_{Ar}-H), 7.38-7.34 (m, 2H, C_{Ar}-H), 7.33-7.15 (m', 16H, C_{Ar}-H), 7.12-7.08 (m', 4H, C_{Ar}-H), 6.52 (s, 2H, C-H), 6.49 (s, 2H, C-H), 6.45-6.30 (br, 2H, C-H), 4.16-4.08 (m, 4H, C-H_2), 4.06-3.97 (m', 8H, C-H_2), 1.97 (s, 6H, C-H_3), 1.90-1.74 (m', 36H, C-H_2, C-H_3), 1.49-1.42 (m', 12H, C-H_2), 1.40-1.21 (m', 144H, C-H_2), 0.89-0.85 (m', 18H, C-H_3).

^{13}C(^{1}H) NMR (150.9 MHz, CD_2Cl_2):

δ [ppm] = 173.4 (quart.), 172.5 (quart.), 171.6 (quart.), 171.4 (quart.), 170.7 (quart.), 168.0 (quart.), 167.8 (quart.), 167.1 (quart.), 166.4 (quart.), 166.2 (quart.), 143.6 (quart.), 143.2 (quart.), 142.9 (quart.), 142.4 (quart.), 142.2 (quart.), 142.1 (quart.), 141.7 (quart.), 137.9 (quart.), 137.2 (quart.), 128.7 (tert.), 128.4 (tert.), 127.32 (tert.), 127.25 (tert.), 127.2 (tert.). 126.8 (tert.), 125.0 (tert.), 122.6 (tert.), 122.2 (tert.), 121.1 (tert.), 119.2 (3 × quart.), 111.3 (tert.), 110.7 (2 × tert.), 90.5 (tert.), 89.7 (2 × tert.), 57.6 (quart.), 49.9 (quart.), 49.7 (quart.), 45.5 (sec.), 44.9 (2 × sec.), 40.6 (quart.), 39.6 (quart.), 32.3 (3 × sec.), 30.11 (3 × sec.), 30.10 (3 × sec.), 30.09 (4 × sec.), 30.06 (6 × sec.), 30.03 (2 × sec.), 30.01 (sec.), 29.95 (2 × sec.), 29.89 (sec.), 29.85 (sec.), 29.84 (sec.), 29.81 (sec.), 29.75 (5 × sec.), 27.75 (sec.), 27.68 (sec.), 27.65 (sec.), 27.3 (sec.), 27.1 (sec.), 27.0 (sec.), 26.9 (prim.), 26.8 (prim.), 26.6 (2 × prim.), 25.5 (prim.), 23.1 (3 × sec.), 14.3 (3 × prim.).

HRMS (ESI, pos.): $[M]^{2+}$

calcd: 1400.04644

found: 1400.04808 *Δ* = 1.17 ppm

S*-dSQB

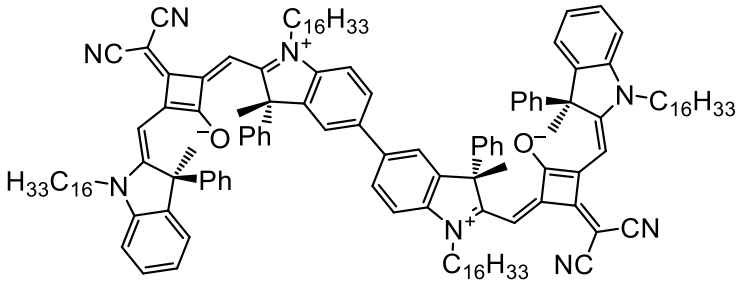

CAS: -

Synthesis following GP VI: ***S*-Br-SQB*-C16** (16.9 mg, 15.4 µmol), ***S*-Bpin-SQB*-C16** (41.0 mg, 35.9 µmol), Cs_2CO_3 (46.7 mg, 143 µmol), XPhos G2 (1.35 mg, 1.72 µmol). 18 h at 65 °C. Purification by flash chromatography (silica, PE → acetone/PE 7:12) and preparative GPC (DCM). Freeze-drying from benzene afforded the product as a solid.

Yield: 25.5 mg (12.5 µmol, 81%) of a green solid.

$C_{142}H_{182}N_8O_2$ [2033.02]

^{1}H NMR (600.1 MHz, CD_2Cl_2):

δ [ppm] = 7.43-7.39 (m, 2H, C_{Ar}-H), 7.32-7.28 (m, 2H, C_{Ar}-H), 7.27-7.21 (m', 8H, C_{Ar}-H), 7.20-7.13 (m', 14H, C_{Ar}-H), 7.13-7.06 (m', 8H, C_{Ar}-H), 6.46-6.20 (m', 4H, C-H), 4.11-4.02 (m', 8H, C-H_2), 1.94-1.76 (m', 20H, C-H_2, C-H_3), 1.47-1.39 (m', 8H, C-H_2), 1.39-1.32 (m', 8H, C-H_2), 1.33-1.22 (m', 88H, C-H_2), 0.90-0.85 (m', 12H, C-H_3).

^{13}C(^{1}H) NMR (150.9 MHz, CD_2Cl_2):

δ [ppm] = 171.4 (2 × quart.), 170.3 (quart.), 168.4 (quart.), 167.5 (quart.), 166.3 (quart.), 143.0 (quart.), 142.4 (quart.), 142.1 (3 × quart.), 141.7 (quart.), 137.4 (quart.), 128.6 (2 × tert.), 128.4 (tert.), 127.2 (tert.), 127.1 (2 × tert.), 126.8 (tert.), 126.7 (tert.), 125.2 (tert.), 123.7 (tert.), 122.2 (tert.), 119.2 (2 × quart.), 111.0 (2 × tert.), 90.28 (tert.), 90.25 (tert.), 57.6 (quart.), 57.4 (quart.), 45.4 (2 × sec.), 39.5 (quart.), 32.3 (2 × sec.), 30.10 (6 × sec.), 30.08 (2 × sec.), 30.06 (2 × sec.), 30.04 (2 × sec.), 30.00 (sec.), 29.99 (sec.), 29.88 (sec.), 29.87 (sec.), 29.79 (sec.), 29.76 (3 × sec.), 27.69 (sec.), 27.66 (sec.), 27.23 (sec.), 27.21 (sec.), 25.5 (prim.), 25.3 (prim.), 23.1 (2 × sec.), 14.3 (2 × prim.).

HRMS (ESI, pos.): $[M]^{2+}$

calcd: 1016.22038

found: 1016.22159 Δ = 1.19 ppm

S*-tSQB

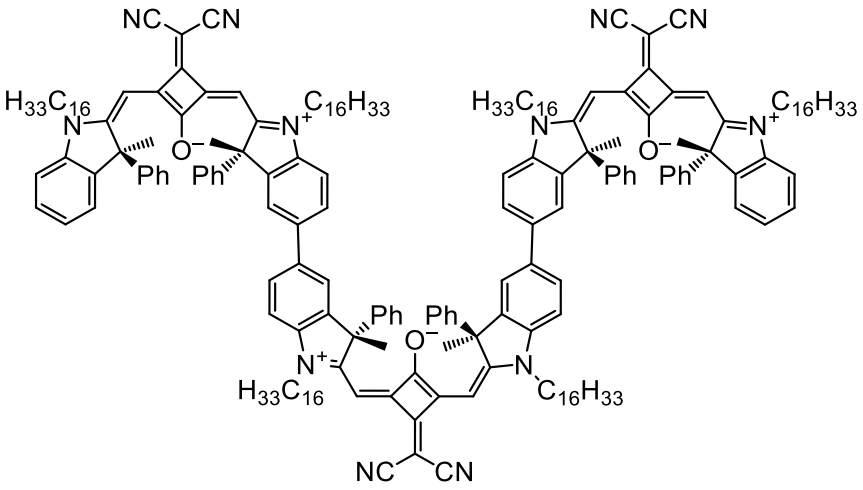

CAS: -

Synthesis following GP VI: ***S*-Br$_2$-Ph-SQB*** (20.2 mg, 17.2 µmol), ***S*-Bpin-SQB*-C16** (49.0 mg, 42.9 µmol), Cs_2CO_3 (55.8 mg, 171 µmol), XPhos G2 (1.62 µg, 2.06 nmol). 18 h at 65 °C Purification by flash chromatography (silica, PE → acetone/PE 3:7) and preparative GPC (DCM). Freeze-drying from benzene afforded the product as a solid.

Yield: 40.4 mg (13.3 µmol, 77%) of a green solid.

$C_{213}H_{272}N_{12}O_3$ [3048.53]

^{1}H NMR (600.1 MHz, CD_2Cl_2):

δ [ppm] = 7.43-7.39 (m', 4H, C_{Ar}-H), 7.32-7.28 (m, 2H, C_{Ar}-H), 7.28-7.21 (m', 12H, C_{Ar}-H), 7.20-7.13 (m', 22H, C_{Ar}-H), 7.12-7.06 (m', 10H, C_{Ar}-H), 6.48-6.20 (m', 6H, C-H), 4.15-4.02 (m', 12H, C-H_2), 1.96-1.76 (m', 30H, C-H_2, C-H_3), 1.47-1.39 (m', 12H, C-H_2), 1.39-1.32 (m', 12H, C-H_2), 1.32-1.21 (m', 132H, C-H_2), 0.89-0.86 (m', 18H, C-H_3).

$^{13}C(^{1}H)$ NMR (150.9 MHz, CD_2Cl_2):

δ [ppm] = 171.4 (2 × quart.), 170.6 (quart.), 170.2 (quart.), 168.4 (quart.), 167.7 (quart.), 167.5 (quart.), 166.34 (quart.), 166.26 (quart.), 143.1 (2 × quart.), 142.4 (quart.), 142.1 (4 × quart.), 141.7 (3 × quart.), 137.6 (quart.), 137.4 (quart.), 128.6 (3 × tert.), 128.4 (tert.), 127.28 (tert.), 127.25 (tert.), 127.1 (3 × tert.), 126.8 (2 × tert.), 126.7 (tert.), 125.2 (tert.), 123.7 (tert.), 122.2 (2 × tert.), 119.2 (3 × quart.), 111.2 (tert.), 111.0 (2 × tert.), 90.5 (tert.), 90.3 (2 × tert.), 57.6 (quart.), 57.5. (quart.), 57.4 (quart.), 45.4 (3 × sec.), 39.6 (quart.), 39.5 (2 × quart.), 32.3 (3 × sec.), 30.10 (9 × sec.), 30.08 (3 × sec.), 30.06 (3 × sec.), 30.04 (3 × sec.), 29.99 (3 × sec.), 29.9 (3 × sec.), 29.79 (2 × sec.), 29.76 (4 × sec.), 27.69 (2 × sec.), 27.66 (sec.), 27.23 (2 × sec.), 27.21 (sec.), 25.5 (prim.), 25.4 (prim.), 25.3 (prim.), 23.1 (3 × sec.), 14.30 (2 × prim.), 14.29 (prim.).

HRMS (ESI, pos.):[1] $[M]^{2+}$

calcd: 1523.07502

found: 1523.07788 *Δ* = 1.88 ppm

[1] Monoisotopic mass

8.2.6 Squaraine polymers

p(SQB-R^0)

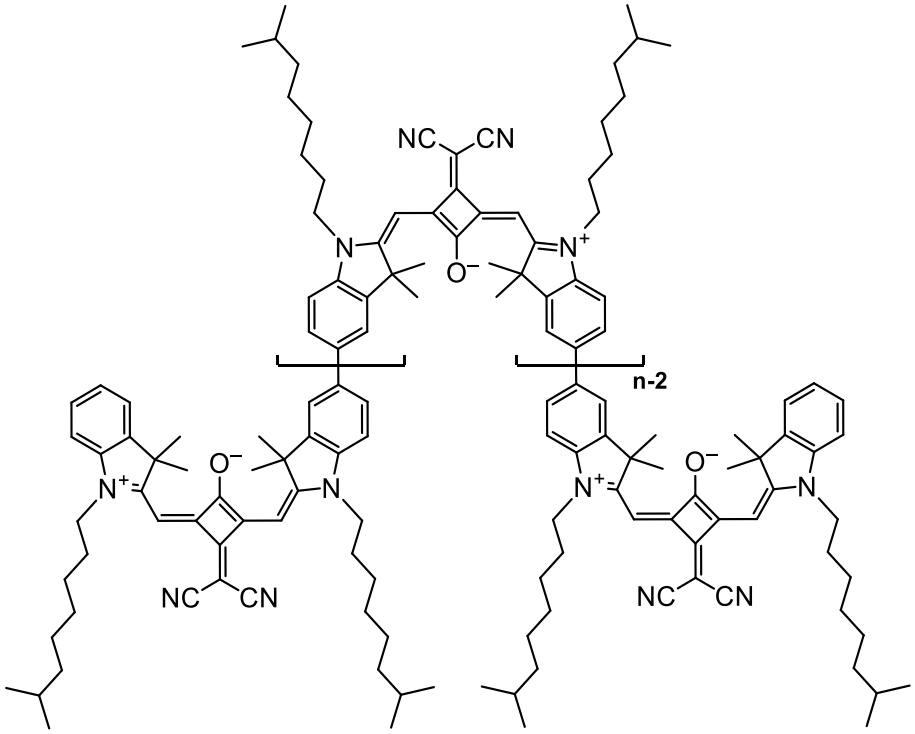

CAS: -

Synthesis following GP VI: $Ni(COD)_2$ (116 mg, 422 µmol), COD (51.6 µL, 45.5 mg, 421 µmol), 2,2'-bipyridine (65.7 mg, 421 µmol) in DMF/toluene (1:1, 3 mL), 30 min at 65 °C. **Br$_2$-SQB-R^0** (150 mg, 175 µmol) in DMF/toluene (1:1, 5 mL) added, 10 d at 65 °C. Washed successively with *n*-hexane, MeOH and DCM using a Soxhlet extractor. Fractionation by preparative GPC (DCM). The final step was precipitation from MeOH/H_2O (4:1) (F1) or freeze drying from benzene (F2).

Yield: F1: 20.3 mg (29.2 µmol, 17%)
F2: 25.2 mg (36.3 µmol, 21%)
F3: 37.1 mg (53.4 µmol, 31%) of a green solid.

$(C_{47}H_{58}N_4O)_n$ [n × 694.99]

^{1}H NMR (400.1 MHz, CD_2Cl_2):

δ [ppm] = 7.73-7.43 (m', 4H, C_{Ar}-H), 7.26-7.07 (m, 2H, C_{Ar}-H), 6.50 (s, 2H, C-H), 4.24-3.79 (br, 4H, C-H_2), 1.96-1.65 (m', 16H, C-H_2, C-H_3), 1.58-1.43 (m', 6H, C-H, C-H_2), 1.40-1.25 (m', 8H, C-H_2), 1.21-1.11 (m, 4H, C-H_2), 0.85 (d, 12H, ^3J = 6.6 Hz, C-H_3).

p(SQB-R^{1}*)

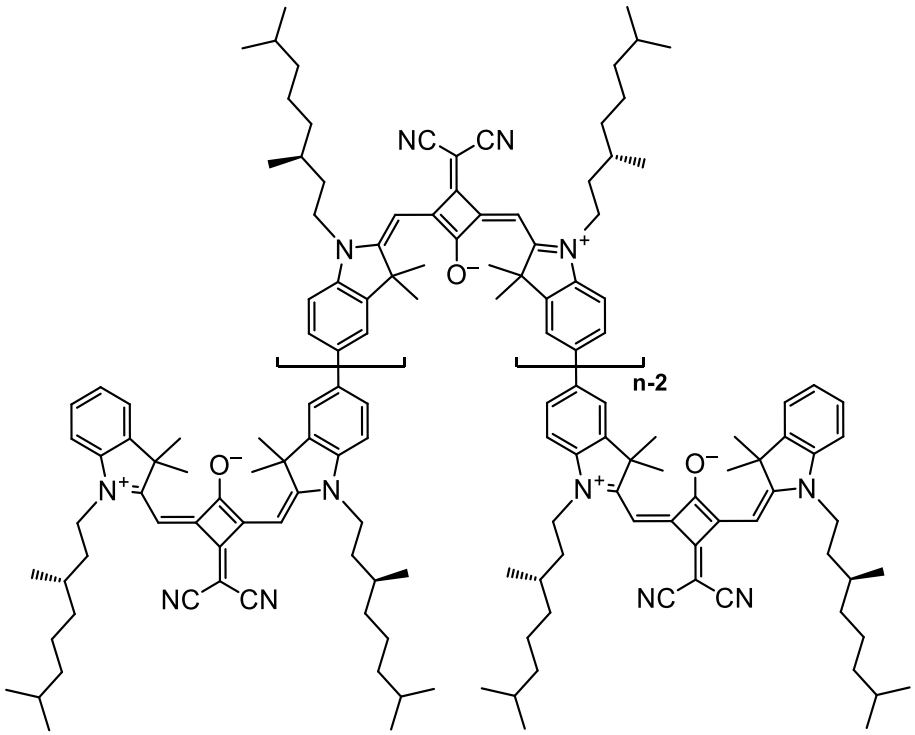

CAS: -

Synthesis following GP VI: $Ni(COD)_2$ (149 mg, 542 µmol), COD (66.6 µL, 58.7 mg, 543 µmol), 2,2'-bipyridine (85.0 mg, 544 µmol) in DMF/toluene (1:1, 4 mL), 30 min at 65 °C. **Br_2-SQB-R^{1}*** (200 mg, 227 µmol) in DMF/toluene (1:1, 6 mL) added, 10 d at 65 °C. Washed successively with *n*-hexane, MeOH and acetone using a Soxhlet extractor. Fractionated by preparative GPC (DCM). The final step was precipitation from MeOH/H_2O (4:1) (F1) or freeze drying from benzene (F2).

Yield: F1: 33.5 mg (46.3 µmol, 20%)
F2: 30.3 mg (41.9 µmol, 18%)
F3: 33.9 mg (46.9 µmol, 21%) of a green solid.

$(C_{49}H_{62}N_4O)_n$ [n × 723.04]

^{1}H NMR (400.0 MHz, CD_2Cl_2):

δ [ppm] = 7.69-7.52 (m', 4H, C_{Ar}-H), 7.20-7.09 (m, 2H, C_{Ar}-H), 6.51 (s, 2H, C-H), 4.22-3.92 (br, 4H, C-H_2), 1.96-1.73 (m', 14H, C-H_3, C-H), 1.72-1.59 (m, 4H, C-H_2), 1.46-1.12 (m', 14H, C-H, C-H_2), 1.04 (d, 6H, ^{3}J = 6.1 Hz C-H_3), 0.86 (d, 12H, ^{3}J = 6.6 Hz, C-H_3).

p(SQB-R²*)

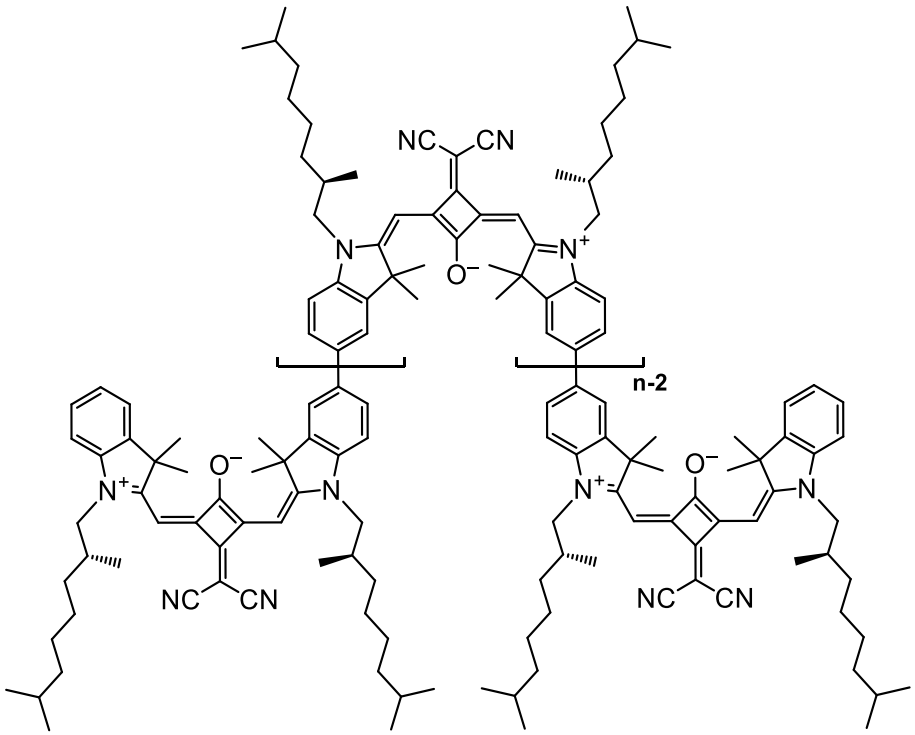

CAS: -

Synthesis following GP VI: $Ni(COD)_2$ (87.4 mg, 318 µmol), COD (39.0 µL, 34.4 mg, 318 µmol), 2,2'-bipyridine (49.6 mg, 318 µmol) in DMF/toluene (1:1, 2 mL), 30 min at 65 °C. **Br_2-SQB-R²*** (117 mg, 133 µmol) in DMF/toluene (1:1, 4 mL) added, 10 d at 65 °C. Washed successively with *n*-hexane, MeOH and acetone using a Soxhlet extractor. Fractionated by preparative GPC (DCM). The final step was precipitation from hexane (F1) or freeze drying from benzene (F2).

Yield: F1: 25.7 mg (35.5 µmol, 27%)
F2: 23.8 mg (32.9 µmol, 25%)
F3: 28.8 mg (39.8 µmol, 30%) of a green solid.

$(C_{49}H_{62}N_4O)_n$ [n × 723.04]

^{1}H NMR (400.1 MHz, CD_2Cl_2):

δ [ppm] = 7.67-7.51 (m', 4H, C_{Ar}-H), 7.21-7.10 (m, 2H, C_{Ar}-H), 6.56 (s, 2H, C-H), 4.03-3.83 (br, 4H, C-H_2), 2.32-2.15 (br, 2H, C-H), 1.92-1.74 (m, 12H, C-H_3), 1.52-1.39 (m', 6H, C-H, C-H_2) 1.34-1.21 (m', 8H, C-H_2), 1.19-1.09 (m, 4H, C-H_2), 1.00 (d, 6H, ^3J = 6.6 Hz, C-H_3), 0.86-0.80 (m, 12H, C-H_3).

p(SQB-R^3*)

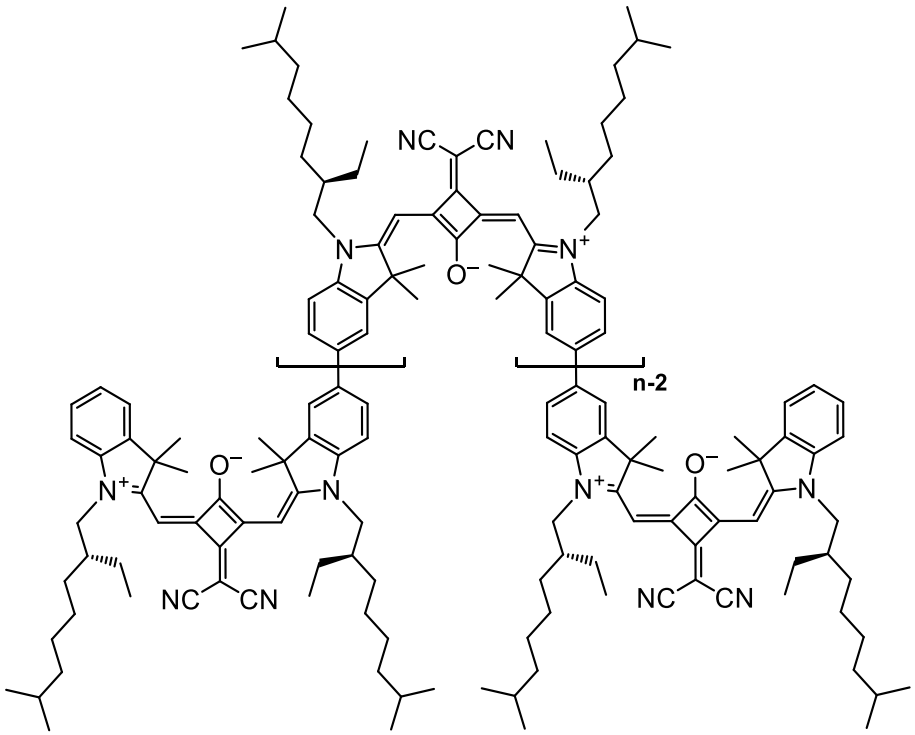

CAS: -

Synthesis following GP VI: $Ni(COD)_2$ (87.6 mg, 318 µmol), COD (39.0 µL, 34.4 mg, 318 µmol), 2,2'-bipyridine (49.7 mg, 318 µmol) in DMF/toluene (1:1, 2 mL), 30 min at 65 °C. **Br_2-SQB-R^3*** (121 mg, 133 µmol) in DMF/toluene (1:1, 4 mL) added, 10 d at 65 °C. Washed successively with *n*-hexane, MeOH and DCM using a Soxhlet extractor. Fractionated by preparative GPC (DCM). The final step was freeze drying from benzene (F1, F2).

Yield: F1: 20.3 mg (27.0 µmol, 20%)
F2: 19.4 mg (25.8 µmol, 19%)
F3: 41.2 mg (54.9 µmol, 41%) of a green solid.

$(C_{51}H_{66}N_4O)_n$ [n × 751.10]

^{1}H NMR (400.0 MHz, CD_2Cl_2):

δ [ppm] = 7.70-7.51 (m', 4H, C_{Ar}-H), 7.22-7.11 (m, 2H, C_{Ar}-H), 6.65-6.45 (br, 2H, C-H), 4.12-3.85 (br, 4H, C-H_2), 2.16-2.01 (br, 2H, C-H), 1.84 (s, 12H, C-H_3), 1.66-1.54 (br,

4H, C-$\underline{H}_2$), 1.52-1.42 (m, 2H, C-$\underline{H}$),[1] 1.41-1.19 (m', 12H, C-$\underline{H}_2$), 1.17-1.08 (m, 4H, C-$\underline{H}_2$), 1.01-0.93 (m, 6H, C-$\underline{H}_3$), 0.85-0.78 (m', 12H, C-$\underline{H}_3$).

p(Pr-SQB*)

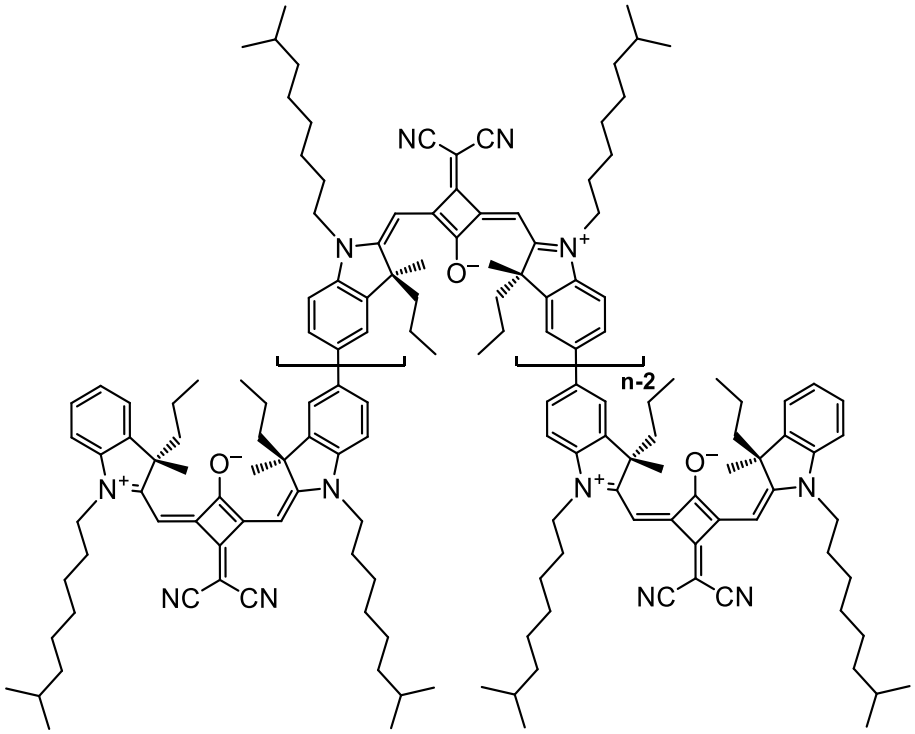

CAS: -

Synthesis following GP VI: $Ni(COD)_2$ (109 mg, 396 µmol), COD (48.4 µL, 42.7 mg, 395 µmol), 2,2'-bipyridine (61.6 mg, 394 µmol) in DMF/toluene (1:1, 3 mL), 30 min at 65 °C. **Br_2-Pr-SQB*** (150 mg, 165 µmol) in DMF/toluene (1:1, 4 mL) added, 10 d at 65 °C. Washed successively with *n*-hexane, MeOH and DCM using a Soxhlet extractor. Fractionated by preparative GPC (DCM). The final step was freeze drying from benzene (F1, F2).

Yield: F1: 32.9 mg (43.8 µmol, 27%)
F2: 31.1 mg (41.4 µmol, 25%)
F3: 28.9 mg (38.5 µmol, 23%) of a green solid.

$(C_{51}H_{66}N_4O)_n$ [n × 751.10]

[1] Signal superimposed by water signal ($\delta(H_2O)$ = 1.52 ppm)[1]

^{1}H NMR (400.0 MHz, CD_2Cl_2):

δ [ppm] = 7.72-7.49 (m', 4H, C_{Ar}-H), 7.24-7.07 (m, 2H, C_{Ar}-H), 6.57 (s, 2H, C-H), 4.30-3.85 (br, 4H, C-H_2), 3.07-2.77 (br, 2H, C-H_2), 2.12-1.96 (m, 2H, C-H_2), 1.90-1.73 (m', 10H, C-H_2, C-H_3), 1.56-1.43 (m', 6H, C-H, C-H_2), 1.41-1.24 (m, 8H, C-H_2), 1.21-1.11 (m, 4H, C-H_2), 0.93-0.61 (m', 22H, C-H_2, C-H_3).

p(Ph-SQB*)

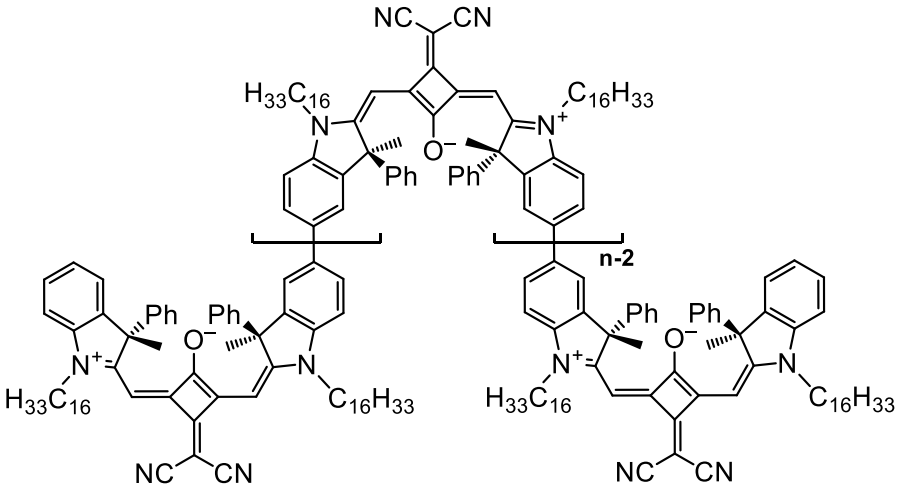

CAS: -

Synthesis following GP VI: $Ni(COD)_2$ (65.0 mg, 236 µmol), COD (28.7 µL, 25.3 mg, 234 µmol), 2,2'-bipyridine (36.5 mg, 234 µmol) in DMF/toluene (1:1, 2 mL), 30 min at 65 °C. **Br_2-Ph-SQB*** (115 mg, 97.8 µmol) in DMF/toluene (1:1, 3 mL) added, 10 d at 65 °C. Washed successively with *n*-hexane, MeOH and DCM using a Soxhlet extractor. Fractionated by preparative GPC (DCM). The final step was freeze drying from benzene (F1, F2).

Yield: F1: 11.0 mg (10.8 µmol, 11%)
F2: 22.8 mg (22.5 µmol, 23%)
F3: 19.8 mg (19.5 µmol, 20%) of a green solid.

$(C_{71}H_{90}N_4O)_n$ [n × 1015.50]

^{1}H NMR (400.0 MHz, CD_2Cl_2):

δ [ppm] = 7.46-7.38 (m, 2H, C_{Ar}-H), 7.28-7.05 (m', 14H, C_{Ar}-H), 6.47-6.19 (br, 2H, C-H), 4.23-3.94 (br, 4H, C-H_2), 1.98-1.74 (m', 10H, C-H_2, C-H_3), 1.47-1.18 (m', 52H, C-H_2), 0.90-0.83 (m', 6H, C-H_3).

_S_-p(SQA-SQB*)

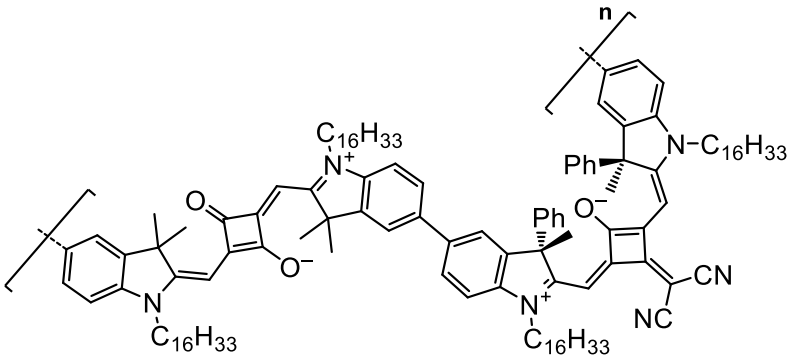

CAS: -

Synthesis based on given literature.[87]

S-**Br_2-Ph-SQB*** (50.0 mg, 42.5 µmol), **$Bpin_2$-SQA** (46.7 mg, 42.6 µmol) and $NaHCO_3$ (143 mg, 1.70 mmol) were dissolved in a degassed mixture of THF/H_2O (4:1, 4 mL), before $Pd(PPh_3)_4$ (983 µg, 851 nmol) was added. The reaction was stirred at 105 °C for 6 d. The reaction mixture was then diluted with $CHCl_3$ (20 mL) and washed successively with water and brine. The organic layer was dried over Na_2SO_4 and the solvent removed under reduced pressure. The crude product was precipitated from MeOH/HCl (20% in H_2O) (4:1), before being placed in an extraction thimble and washed successively with *n*-hexane, MeOH and DCM using a Soxhlet extractor, until the solvent ceased to be colored. The *n*-hexane and MeOH extracts were discarded and the DCM extract was concentrated under reduced pressure, before being fractionated by preparative GPC ($CHCl_3$). The final step was precipitation from MeOH/H_2O (4:1). To evaluate the chain lengths and the molecular weight distribution, analytical GPC was performed using a PSS Linear S column and chloroform as an eluent.

Yield: F1: 10.8 mg (5.81 µmol, 14%)
F2: 5.70 mg (3.07 µmol, 7%)
F3: 11.2 mg (6.03 µmol, 14%)
F4: 23.0 mg (12.4 µmol, 29%)
F5: 8.10 mg (4.36 µmol, 10%) of a teal solid.

$(C_{129}H_{176}N_6O_3)_n$ [n × 1858.82]

^{1}H NMR (400.0 MHz, CD_2Cl_2):

δ [ppm] = 7.58-7.52 (m', 2H, C_{Ar}-H), 7.49-7.41 (m', 4H, C_{Ar}-H), 7.34-7.13 (m', 14H, C_{Ar}-H), 7.07-7.00 (m, 2H, C_{Ar}-H), 6.47-6.22 (br, 2H, C-H), 5.99-5.88 (m', 2H, C-H), 4.23-3.89 (m', 8H, C-H_2), 2.01-1.72 (m', 26H, C-H_2, C-H_3), 1.50-1.17 (m', 104H, C-H_2), 0.90-0.83 (m', 12H, C-H_3).

***S*-p(SQB-SQB*)**

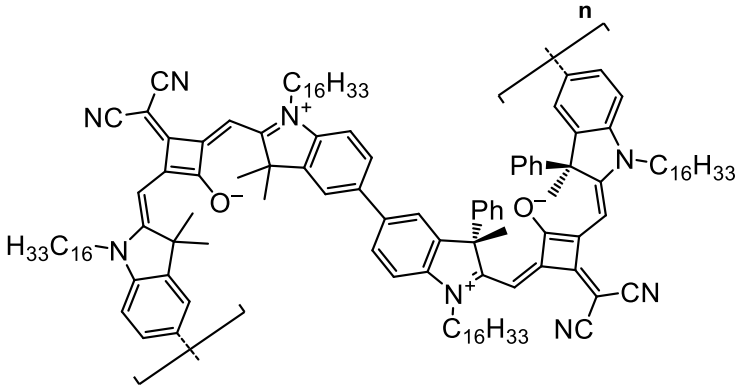

CAS: -

Synthesis based on given literature.[87]

S-**Br_2-Ph-SQB*** (219 mg, 186 µmol), **$Bpin_2$-SQB** (213 mg, 186 µmol) and $NaHCO_3$ (626 mg, 7.45 mmol) were dissolved in a degassed mixture of THF/H_2O (4:1, 18 mL), before $Pd(PPh_3)_4$ (4.31 mg, 3.73 µmol) was added. The reaction was stirred at 105 °C for 6 d. The reaction mixture was then diluted with $CHCl_3$ (50 mL) and washed successively with water and brine. The organic layer was dried over Na_2SO_4 and the solvent removed under reduced pressure. The crude product was precipitated from MeOH/HCl (20% in H_2O) (4:1), before being placed in an extraction thimble and washed successively with *n*-hexane, MeOH and DCM using a

Soxhlet extractor, until the solvent ceased to be colored. The *n*-hexane and MeOH extracts were discarded and the DCM extract was concentrated under reduced pressure, before being fractionated by preparative GPC ($CHCl_3$). The final step was precipitation from MeOH/H_2O (4:1). To evaluate the chain lengths and the molecular weight distribution, analytical GPC was performed using a PSS Linear S column and chloroform as an eluent.

Yield: F1: 47.8 mg (25.1 µmol, 13%)
F2: 24.4 mg (12.8 µmol, 7%)
F3: 13.0 mg (6.82 µmol, 4%) of a green solid.

$(C_{132}H_{176}N_8O_2)_n$ [n × 1906.87]

^{1}H NMR (400.0 MHz, CD_2Cl_2):

δ [ppm] = 7.59-7.53 (m', 2H, C_{Ar}-H), 7.50-7.43 (m', 4H, C_{Ar}-H), 7.33-7.06 (m', 16H, C_{Ar}-H), 6.51 (m', 2H, C-H), 6.36 (m', 2H, C-H), 4.29-3.89 (m', 8H, C-H_2), 2.06-1.71 (m', 26H, C-H_2, C-H_3), 1.50-1.18 (m', 104H, C-H_2), 0.89-0.83 (m', 12H, C-H_3).

9 LITERATURE

[1] J. Fabian, R. Zahradník, *Angew. Chem. Int. Edit.* **1989**, *28*, 677-694.
[2] C. Tsopelas, R. Sutton, *J. Nucl. Med.* **2002**, *43*, 1377-1382.
[3] L. L. Munn, T. P. Padera, *Microvasc. Res.* **2014**, *96*, 55-63.
[4] A. Hagfeldt, G. Boschloo, L. Sun, L. Kloo, H. Pettersson, *Chem. Rev.* **2010**, *110*, 6595-6663.
[5] H. Uoyama, K. Goushi, K. Shizu, H. Nomura, C. Adachi, *Nature* **2012**, *492*, 234-238.
[6] U. Mitschke, P. Bäuerle, *J. Mater. Chem.* **2000**, *10*, 1471-1507.
[7] J.-M. Zhang, Y. Liu, *Eur. J. Phys.* **2016**, *37*.
[8] L. Zhang, *Introduction to Light-Matter Interaction: The Typical Models and Methods*, **2020**.
[9] K. Dolgaleva, in *Synthesis Lectures on Materials and Optics, Vol. 1*, Morgan & Claypool Publishers, **2020**, pp. 1-111.
[10] J. Mun, M. Kim, Y. Yang, T. Badloe, J. Ni, Y. Chen, C.-W. Qiu, J. Rho, *Light: Sci. Appl.* **2020**, *9*, 139.
[11] S. Yoo, Q. H. Park, *Phys. Rev. Lett.* **2015**, *114*, 203003.
[12] A. Moscowitz, *Tetrahedron* **1961**, *13*, 48-56.
[13] J. A. Schellman, *Chem. Rev.* **1975**, *75*, 323-331.
[14] G. Snatzke, *Angew. Chem. Int. Edit.* **1979**, *18*, 363-377.
[15] L. L. Whyte, *Nature* **1958**, *182*, 198-198.
[16] L. Pauling, R. B. Corey, H. R. Branson, *P. Natl. Acad. Sci. U.S.A.* **1951**, *37*, 205-211.
[17] J. D. Watson, F. H. C. Crick, *Nature* **1953**, *171*, 737-738.
[18] J. E. McMurry, *Organic Chemistry*, Cengage Learning, **2015**.
[19] L. A. Nguyen, H. He, C. Pham-Huy, *Int J Biomed Sci* **2006**, *2*, 85-100.
[20] W. H. Brooks, W. C. Guida, K. G. Daniel, *Curr Top Med Chem* **2011**, *11*, 760-770.
[21] L. E. MacKenzie, P. Stachelek, *Nat. Chem.* **2021**, *13*, 521-522.
[22] M.-C. Schanne-Klein, T. Boulesteix, E. Beaurepaire, M.-P. Sauviat, *Chiral Chromophores for Second Harmonic Microscopy, Vol. 5139*, SPIE, **2003**.
[23] Y. Kubo, S. y. Maeda, S. Tokita, M. Kubo, *Nature* **1996**, *382*, 522-524.
[24] D. Walaszek, K. Maximova, K. Rybicka-Jasińska, A. Lipke, D. Gryko, *J. Porphyrins Phthalocyanines* **2014**, *18*, 493-505.
[25] X. Shang, I. Song, H. Ohtsu, Y. H. Lee, T. Zhao, T. Kojima, J. H. Jung, M. Kawano, J. H. Oh, *Adv. Mater.* **2017**, *29*, 1605828.
[26] M. Schulz, M. Mack, O. Kolloge, A. Lützen, M. Schiek, *Phys. Chem. Chem. Phys.* **2017**, *19*, 6996-7008.
[27] S. K. Jung, J. H. Heo, D. W. Lee, S. H. Lee, S. C. Lee, W. Yoon, H. Yun, D. Kim, J. H. Kim, S. H. Im, O. P. Kwon, *ChemSusChem* **2019**, *12*, 224-230.
[28] J. R. Brandt, X. Wang, Y. Yang, A. J. Campbell, M. J. Fuchter, *J. Am. Chem. Soc.* **2016**, *138*, 9743-9746.
[29] Y. Yang, R. C. da Costa, D.-M. Smilgies, A. J. Campbell, M. J. Fuchter, *Adv. Mater.* **2013**, *25*, 2624-2628.
[30] P. Osswald, M. Reichert, G. Bringmann, F. Würthner, *J. Org. Chem.* **2007**, *72*, 3403-3411.
[31] X. Shang, I. Song, J. H. Lee, M. Han, J. C. Kim, H. Ohtsu, J. Ahn, S. K. Kwak, J. H. Oh, *J. Mater. Chem. C* **2019**, *7*, 8688-8697.

[32] C. Kulkarni, P. A. Korevaar, K. K. Bejagam, A. R. A. Palmans, E. W. Meijer, S. J. George, *J. Am. Chem. Soc.* **2017**, *139*, 13867-13875.
[33] F. Zinna, T. Bruhn, C. A. Guido, J. Ahrens, M. Bröring, L. Di Bari, G. Pescitelli, *Chem. Eur. J.* **2016**, *22*, 16089-16098.
[34] T. Bruhn, G. Pescitelli, S. Jurinovich, A. Schaumloffel, F. Witterauf, J. Ahrens, M. Broring, G. Bringmann, *Angew. Chem. Int. Edit.* **2014**, *53*, 14592-14595.
[35] E. M. Sánchez-Carnerero, F. Moreno, B. L. Maroto, A. R. Agarrabeitia, M. J. Ortiz, B. G. Vo, G. Muller, S. d. l. Moya, *J. Am. Chem. Soc.* **2014**, *136*, 3346-3349.
[36] M. J. Hodgson, V. V. Borovkov, Y. Inoue, D. P. Arnold, *J. Organomet. Chem.* **2006**, *691*, 2162-2170.
[37] C. Schies, A. B. Alemayehu, H. Vazquez-Lima, K. E. Thomas, T. Bruhn, G. Bringmann, A. Ghosh, *Chem. Commun.* **2017**, *53*, 6121-6124.
[38] G. Bringmann, D. C. G. Götz, T. A. M. Gulder, T. H. Gehrke, T. Bruhn, T. Kupfer, K. Radacki, H. Braunschweig, A. Heckmann, C. Lambert, *J. Am. Chem. Soc.* **2008**, *130*, 17812-17825.
[39] A. C. Gehrold, T. Bruhn, H. Schneider, U. Radius, G. Bringmann, *J. Org. Chem.* **2015**, *80*, 12359-12378.
[40] D. C. G. Gotz, A. C. Gehrold, S. J. Dorazio, P. Daddario, L. Samankumara, G. Bringmann, C. Bruckner, T. Bruhn, *Eur. J. Org. Chem.* **2015**, *2015*, 3913-3922.
[41] D. M. Răsădean, T. M. Gianga, A. H. Swan, G. Kociok-Köhn, G. D. Pantoş, *Org. Lett.* **2018**, *20*, 2645-2648.
[42] M. Á. Revuelta-Maza, T. Torres, G. d. l. Torre, *Org. Lett.* **2019**, *21*, 8183-8186.
[43] C. Schaack, L. Arrico, E. Sidler, M. Górecki, L. Di Bari, F. Diederich, *Chem. Eur. J.* **2019**, *25*, 8003-8007.
[44] C. Shen, E. Anger, M. Srebro, N. Vanthuyne, K. K. Deol, T. D. Jefferson, G. Muller, J. A. G. Williams, L. Toupet, C. Roussel, J. Autschbach, R. Réau, J. Crassous, *Chem. Sci.* **2014**, *5*, 1915-1927.
[45] L. J. Prins, C. Thalacker, F. Würthner, P. Timmerman, D. N. Reinhoudt, *P. Natl. Acad. Sci. U.S.A.* **2001**, *98*, 10042-10045.
[46] L. Eggers, K. Kolster, V. Buss, *Chirality* **1997**, *9*, 243-249.
[47] J. R. Brandt, F. Salerno, M. J. Fuchter, *Nat. Rev. Chem.* **2017**, *1*, 0045.
[48] M. Liu, L. Zhang, T. Wang, *Chem. Rev.* **2015**, *115*, 7304-7397.
[49] A. R. A. Palmans, E. W. Meijer, *Angew. Chem. Int. Edit.* **2007**, *46*, 8948-8968.
[50] L. Pu, *Acta Polym.* **1997**, *48*, 116-141.
[51] E. Yashima, N. Ousaka, D. Taura, K. Shimomura, T. Ikai, K. Maeda, *Chem. Rev.* **2016**, *116*, 13752-13990.
[52] A. Ajayaghosh, P. Chithra, R. Varghese, *Angew. Chem. Int. Edit.* **2007**, *46*, 230-233.
[53] F. Balzer, M. F. Schumacher, S. Mattiello, M. Schulz, J. Zablocki, M. Schmidtmann, K. Meerholz, N. Serdar Sariciftci, L. Beverina, A. Lützen, M. Schiek, *Isr. J. Chem.* **2021**, *n/a*.
[54] H. Chen, M. S. Farahat, K.-Y. Law, D. G. Whitten, *J. Am. Chem. Soc.* **1996**, *118*, 2584-2594.
[55] P. Chithra, R. Varghese, K. P. Divya, A. Ajayaghosh, *Chem. Asian J.* **2008**, *3*, 1365-1373.
[56] C. Geiger, M. Stanescu, L. Chen, D. G. Whitten, *Langmuir* **1999**, *15*, 2241-2245.
[57] K. Jyothish, M. Hariharan, D. Ramaiah, *Chem. Eur. J.* **2007**, *13*, 5944-5951.
[58] M. Schulz, J. Zablocki, O. S. Abdullaeva, S. Brück, F. Balzer, A. Lützen, O. Arteaga, M. Schiek, *Nat. Commun.* **2018**, *9*, 2413.
[59] M. Stanescu, H. Samha, J. Perlstein, D. G. Whitten, *Langmuir* **2000**, *16*, 275-281.
[60] R. S. Stoll, N. Severin, J. P. Rabe, S. Hecht, *Adv. Mater.* **2006**, *18*, 1271-1275.

[61] A. H. Schmidt, *Synthesis (Stuttg.)* **1980**, 961-994.
[62] K. Ilina, W. M. MacCuaig, M. Laramie, J. N. Jeouty, L. R. McNally, M. Henary, *Bioconjugate Chem.* **2020**, *31*, 194-213.
[63] U. Mayerhöffer, M. Gsänger, M. Stolte, B. Fimmel, F. Würthner, *Chem. Eur. J.* **2013**, *19*, 218-232.
[64] L. Beverina, P. Salice, *Eur. J. Org. Chem.* **2010**, *2010*, 1207-1225.
[65] U. Mayerhöffer, B. Fimmel, F. Würthner, *Angew. Chem. Int. Edit.* **2012**, *51*, 164-167.
[66] S. Sreejith, P. Carol, P. Chithra, A. Ajayaghosh, *J. Mater. Chem.* **2008**, *18*, 264-274.
[67] A. Ajayaghosh, *Acc. Chem. Res.* **2005**, *38*, 449-459.
[68] L. Hu, Z. Yan, H. Xu, *RSC Adv.* **2013**, *3*, 7667-7676.
[69] G. Lee, J. Kim, S. Y. Kim, D. E. Kim, T. Joo, *ChemPhysChem* **2017**, *18*, 670-676.
[70] J. L. Richards, S. A. Rice, *J. Chem. Phys.* **1971**, *54*, 2014-2023.
[71] T. H. Keil, *Phys. Rev.* **1965**, *140*, A601-A617.
[72] T. Brixner, R. Hildner, J. Köhler, C. Lambert, F. Würthner, *Adv. Energy Mater.* **2017**, *7*, 1700236.
[73] M. H. Schreck, *Julius-Maximilians-Universität Würzburg* **2018**.
[74] M. Kasha, *Radiat. Res.* **1963**, *20*, 55-&.
[75] M. Kasha, H. R. Rawls, M. A. El-Bayoumi, *Pure Appl. Chem.* **1965**, *11*, 371-392.
[76] H. Van Amerongen, L. Valkunas, R. van Grondelle, *Photosynthetic Excitons*, **2000**.
[77] G. Chen, H. Sasabe, W. Lu, X.-F. Wang, J. Kido, Z. Hong, Y. Yang, *J. Mater. Chem. C* **2013**, *1*, 6547-6552.
[78] C.-A. Shen, D. Bialas, M. Hecht, V. Stepanenko, K. Sugiyasu, F. Würthner, *Angew. Chem. Int. Edit.* **2021**, *60*, 11949-11958.
[79] A. J. McKerrow, E. Buncel, P. M. Kazmaier, *Can. J. Chem.* **1995**, *73*, 1605-1615.
[80] F. Balzer, H. Kollmann, M. Schulz, G. Schnakenburg, A. Lützen, M. Schmidtmann, C. Lienau, M. Silies, M. Schiek, *Cryst. Growth Des.* **2017**, *17*, 6455–6466.
[81] F. Balzer, M. Schiek, A. Osadnik, A. Lützen, H.-G. Rubahn, *Organic Nanofibers from Squarylium Dyes: Local Morphology, Optical, and Electrical Properties, Vol. 8258*, SPIE, **2012**.
[82] U. Mayerhöffer, F. Würthner, *Chem. Sci.* **2012**, *3*, 1215-1220.
[83] Y. Xu, Z. Li, A. Malkovskiy, S. Sun, Y. Pang, *J. Phys. Chem. B* **2010**, *114*, 8574-8580.
[84] A. S. Tatikolov, S. l. M. B. Costa, *J. Photoch. Photobio. A* **2001**, *140*, 147-156.
[85] C. Lambert, J. Hoche, M. H. Schreck, M. Holzapfel, A. Schmiedel, J. Selby, A. Turkin, R. Mitric, *J. Phys. Chem. A* **2021**, *125*, 2504-2511.
[86] C. Lambert, F. Koch, S. F. Völker, A. Schmiedel, M. Holzapfel, A. Humeniuk, M. I. S. Röhr, R. Mitric, T. Brixner, *J. Am. Chem. Soc.* **2015**, *137*, 7851-7861.
[87] P. Malý, J. Lüttig, A. Turkin, J. Dostál, C. Lambert, T. Brixner, *Chem. Sci.* **2020**, *11*, 456-466.
[88] M. I. S. Röhr, H. Marciniak, J. Hoche, M. H. Schreck, H. Ceymann, R. Mitric, C. Lambert, *J. Phys. Chem. C* **2018**, *122*, 8082-8093.
[89] D. Scherer, R. Dörfler, A. Feldner, T. Vogtmann, M. Schwoerer, U. Lawrentz, W. Grahn, C. Lambert, **2002**.
[90] M. H. Schreck, L. Breitschwerdt, H. Marciniak, M. Holzapfel, D. Schmidt, F. Würthner, C. Lambert, *Phys. Chem. Chem. Phys.* **2019**, *21*, 15346-15355.
[91] A. Turkin, M. Holzapfel, M. Agarwal, D. Fischermeier, R. Mitric, R. Schweins, F. Gröhn, C. Lambert, *Chem. Eur. J.* **2021**, *27*, 8380-8389.
[92] S. F. Völker, C. Lambert, *Chem. Mater.* **2012**, *24*, 2541-2553.

[93] S. F. Völker, A. Schmiedel, M. Holzapfel, K. Renziehausen, V. Engel, C. Lambert, *J. Phys. Chem. C* **2014**, *118*, 17467-17482.
[94] S. F. Völker, S. Uemura, M. Limpinsel, M. Mingebach, C. Deibel, V. Dyakonov, C. Lambert, *Macromol. Chem. Phys.* **2010**, *211*, 1098-1108.
[95] A. Ajayaghosh, *Chem. Soc. Rev.* **2003**, *32*, 181-191.
[96] S. F. Völker, T. Dellermann, H. Ceymann, M. Holzapfel, C. Lambert, *J. Polym. Sci. A Polym. Chem.* **2014**, *52*, 890-911.
[97] T. Maeda, T. V. Nguyen, Y. Kuwano, X. Chen, K. Miyanaga, H. Nakazumi, S. Yagi, S. Soman, A. Ajayaghosh, *J. Phys. Chem. C* **2018**, *122*, 21745-21754.
[98] B. Radaram, T. Mako, M. Levine, *Dalton T.* **2013**, *42*, 16276-16278.
[99] A. Ajayaghosh, E. Arunkumar, J. Daub, *Angew. Chem. Int. Edit.* **2002**, *41*, 1766-+.
[100] B. A. Rao, H. Kim, Y. A. Son, *Sensor Actuat. B-Chem.* **2013**, *188*, 847-856.
[101] J. V. Ros-Lis, R. Martinez-Manez, J. Soto, *Chem. Commun.* **2002**, 2248-2249.
[102] K. D. Volkova, V. B. Kovalska, A. L. Tatarets, L. D. Patsenker, D. V. Kryvorotenko, S. M. Yarmoluk, *Dyes Pigments* **2007**, *72*, 285-292.
[103] A. L. Tatarets, I. A. Fedyunyayeva, T. S. Dyubko, Y. A. Povrozin, A. O. Doroshenko, E. A. Temetschnig, L. D. Patsenker, *Anal. Chim. Acta* **2006**, *570*, 214-223.
[104] V. Rapozzi, L. Beverina, P. Salice, G. A. Pagani, M. Camerin, L. E. Xodo, *J. Med. Chem.* **2010**, *53*, 2188-2196.
[105] J. R. Johnson, N. Fu, E. Arunkumar, W. M. Leevy, S. T. Gammon, D. Piwnica-Worms, B. D. Smith, *Angew. Chem. Int. Edit.* **2007**, *46*, 5528-5531.
[106] S. L. Luo, E. L. Zhang, Y. P. Su, T. M. Cheng, C. M. Shi, *Biomaterials* **2011**, *32*, 7127-7138.
[107] K. Y. Law, *Chem. Rev.* **1993**, *93*, 449-486.
[108] J. Fabian, H. Nakazumi, M. Matsuoka, *Chem. Rev.* **1992**, *92*, 1197-1226.
[109] M. Emmelius, G. Pawlowski, H. W. Vollmann, *Angew. Chem. Int. Edit.* **1989**, *28*, 1445-1471.
[110] V. B. Jipson, C. R. Jones, *J. Vac. Sci. Technol.* **1981**, *18*, 105-109.
[111] S. A. Odom, S. Webster, L. A. Padilha, D. Peceli, H. Hu, G. Nootz, S.-J. Chung, S. Ohira, J. D. Matichak, O. V. Przhonska, A. D. Kachkovski, S. Barlow, J.-L. Brédas, H. L. Anderson, D. J. Hagan, E. W. Van Stryland, S. R. Marder, *J. Am. Chem. Soc.* **2009**, *131*, 7510-7511.
[112] S. Webster, S. A. Odom, L. A. Padilha, O. V. Przhonska, D. Peceli, H. Hu, G. Nootz, A. D. Kachkovski, J. Matichak, S. Barlow, H. L. Anderson, S. R. Marder, D. J. Hagan, E. W. Van Stryland, *J. Phys. Chem. B* **2009**, *113*, 14854-14867.
[113] C. Toro, L. D. Boni, S. Yao, J. P. Ritchie, A. E. Masunov, K. D. Belfield, F. E. Hernandez, *J. Chem. Phys.* **2009**, *130*, 214504.
[114] B. Stender, S. F. Völker, C. Lambert, J. Pflaum, *Adv. Mater.* **2013**, *25*, 2943-2947.
[115] K. Strassel, W.-H. Hu, S. Osbild, D. Padula, D. Rentsch, S. Yakunin, Y. Shynkarenko, M. Kovalenko, F. Nüesch, R. Hany, M. Bauer, *Sci. Technol. Adv. Mat.* **2021**, *22*, 194-204.
[116] D. J. Harkin, K. Broch, M. Schreck, H. Ceymann, A. Stoy, C.-K. Yong, M. Nikolka, I. McCulloch, N. Stingelin, C. Lambert, H. Sirringhaus, *Adv. Mater.* **2016**, *28*, 6378-6385.
[117] U. Mayerhöffer, K. Deing, K. Gruß, H. Braunschweig, K. Meerholz, F. Würthner, *Angew. Chem. Int. Edit.* **2009**, *48*, 8776-8779.
[118] F. Silvestri, M. D. Irwin, L. Beverina, A. Facchetti, G. A. Pagani, T. J. Marks, *J. Am. Chem. Soc.* **2008**, *130*, 17640-17641.
[119] S. Wang, L. Hall, V. V. Diev, R. Haiges, G. Wei, X. Xiao, P. I. Djurovich, S. R. Forrest, M. E. Thompson, *Chem. Mater.* **2011**, *23*, 4789-4798.
[120] W. Kylberg, Y. Zhang, A. Aebersold, F. A. d. Castro, T. Geiger, J. Heier, S. Kuster, C.-Q. Ma, P. Bäuerle, F. Nüesch, J.-N. Tisserant, R. Hany, *Org. Electron.* **2012**, *13*, 1204-1212.

[121] M. Gsänger, E. Kirchner, M. Stolte, C. Burschka, V. Stepanenko, J. Pflaum, F. Würthner, *J. Am. Chem. Soc.* **2014**, *136*, 2351-2362.
[122] A. Laskarakis, S. Logothetidis, E. Pavlopoulou, M. Gioti, *Thin Solid Films* **2004**, *455-456*, 43-49.
[123] R. P. L. R. B. S. M. L. Feynman, *The Feynman Lectures on Physics*, Addison-Wesley Pub. Co., Reading, Mass., **1963**.
[124] R. de L. Kronig, *J. Opt. Soc. Am.* **1926**, *12*, 547-557.
[125] M. Beck, I. A. Walmsley, J. D. Kafka, *IEEE J. Quantum. Electron.* **1991**, *27*, 2074-2081.
[126] V. Lucarini, J. Saarinen, K. Peiponen, E. Vartiainen, *Kramers-Kronig Relations in Optical Materials Research, Vol. 110*, **2005**.
[127] A. Eisfeld, R. Kniprath, J. S. Briggs, *J. Chem. Phys.* **2007**, *126*, 104904.
[128] I. Warnke, F. Furche, *WIREs Comput. Mol. Sci.* **2012**, *2*, 150-166.
[129] F. W. Lichtenthaler, *Angew. Chem. Int. Edit.* **1992**, *31*, 1541-1556.
[130] J. H. Eberly, L. Mandel, E. Wolf, *Coherence and Quantum Optics Vii: Proceedings of the Seventh Rochester Conference on Coherence and Quantum Optics, Held at the University of Rochester, June 7–10, 1995*, Springer US, **2013**.
[131] H. Tanaka, Y. Inoue, T. Mori, *ChemPhotoChem* **2018**, *2*, 386-402.
[132] M. Wakabayashi, S. Yokojima, T. Fukaminato, K.-i. Shiino, M. Irie, S. Nakamura, *J. Phys. Chem. A* **2014**, *118*, 5046-5057.
[133] F. B. Silsbee, *J. Res. Natl. Bur. Stand.* **1962**, *66C*, 137-183.
[134] H. Kubo, T. Hirose, T. Nakashima, T. Kawai, J.-y. Hasegawa, K. Matsuda, *J. Phys. Chem. Lett.* **2021**, *12*, 686-695.
[135] N. Lehtinen, **2010**.
[136] P. R. Surjan, M. Kertesz, *Theor. Chim. Acta* **1980**, *55*, 103-115.
[137] R. R. Gould, R. Hoffmann, *J. Am. Chem. Soc.* **1970**, *92*, 1813-1818.
[138] J. Kumar, T. Nakashima, T. Kawai, *J. Phys. Chem. Lett.* **2015**, *6*, 3445-3452.
[139] G. Longhi, E. Castiglioni, J. Koshoubu, G. Mazzeo, S. Abbate, *Chirality* **2016**, *28*, 696-707.
[140] F. C. Spano, Z. Zhao, S. C. J. Meskers, *J. Chem. Phys.* **2004**, *120*, 10594-10604.
[141] F. C. Spano, S. C. J. Meskers, E. Hennebicq, D. Beljonne, *J. Am. Chem. Soc.* **2007**, *129*, 7044-7054.
[142] F. C. Spano, S. C. J. Meskers, E. Hennebicq, D. Beljonne, *J. Chem. Phys.* **2008**, *129*, 024704.
[143] R. Tempelaar, A. Stradomska, J. Knoester, F. C. Spano, *J. Phys. Chem. B* **2011**, *115*, 10592-10603.
[144] L. Arrico, L. Di Bari, F. Zinna, *Chem. Eur. J.* **2021**, *27*, 2920-2934.
[145] W. W. Parson, *Modern Optical Spectroscopy: With Exercises and Examples from Biophysics and Biochemistry*, Springer Berlin Heidelberg, **2015**.
[146] N. Berova, P. L. Polavarapu, K. Nakanishi, R. W. Woody, *Comprehensive Chiroptical Spectroscopy, Volume 2: Applications in Stereochemical Analysis of Synthetic Compounds, Natural Products, and Biomolecules*, Wiley, **2012**.
[147] J. Gawronski, P. Skowronek, *Curr. Org. Chem.* **2004**, *8*, 65-82.
[148] S. Castro-Fernández, Á. Peña-Gallego, R. A. Mosquera, J. L. Alonso-Gómez, *Molecules* **2019**, *24*, 141.
[149] A. Cotton, *J. Phys. Theor. Appl.* **1896**, *5*, 237-244.
[150] E. L. Eliel, S. H. Wilen, *Stereochemistry of Organic Compounds*, Wiley, **1994**.
[151] L. Di Bari, G. Pescitelli, P. Salvadori, *J. Am. Chem. Soc.* **1999**, *121*, 7998-8004.
[152] S. F. Mason, R. H. Seal, D. R. Roberts, *Tetrahedron* **1974**, *30*, 1671-1682.

[153] N. Harada, K. j. Nakanishi, *Circular Dichroic Spectroscopy : Exciton Coupling in Organic Stereochemistry*, University Science Books, Mill Valley, CA, **1983**.
[154] S.-M. L. Chen, N. Harada, K. Nakanishi, *J. Am. Chem. Soc.* **1974**, *96*, 7352-7354.
[155] N. Harada, S.-M. L. Chen, K. Nakanishi, *J. Am. Chem. Soc.* **1975**, *97*, 5345-5352.
[156] N. Harada, K. Nakanishi, *Acc. Chem. Res.* **1972**, *5*, 257-263.
[157] N. Harada, M. Ohashi, K. Nakanishi, *J. Am. Chem. Soc.* **1968**, *90*, 7349-7351.
[158] A. I. Levin, I. T. Jr., *J. Chem. Phys.* **1977**, *66*, 3491-3497.
[159] W. Moffitt, *J. Chem. Phys.* **1956**, *25*, 467-478.
[160] T. Ando, *Prog. Theor. Phys.* **1968**, *40*, 471-485.
[161] F. M. Loxsom, *J. Chem. Phys.* **1969**, *51*, 4899-4905.
[162] C. Didraga, J. A. Klugkist, J. Knoester, *J. Phys. Chem. B* **2002**, *106*, 11474-11486.
[163] C. W. Deutsche, *J. Chem. Phys.* **1970**, *52*, 3703-3714.
[164] D. A. Rabenold, W. Rhodes, *J. Chem. Phys.* **1984**, *80*, 3866-3872.
[165] F. Bloch, *Z. Physik* **1929**, *52*, 555-600.
[166] C. B. Anfinsen, *Science* **1973**, *181*, 223-230.
[167] T. Nakano, Y. Okamoto, *Chem. Rev.* **2001**, *101*, 4013-4038.
[168] J. J. L. M. Cornelissen, A. E. Rowan, R. J. M. Nolte, N. A. J. M. Sommerdijk, *Chem. Rev.* **2001**, *101*, 4039-4070.
[169] D. J. Hill, M. J. Mio, R. B. Prince, T. S. Hughes, J. S. Moore, *Chem. Rev.* **2001**, *101*, 3893-4011.
[170] E. Yashima, K. Maeda, T. Nishimura, *Chem. Eur. J.* **2004**, *10*, 42-51.
[171] E. Yashima, K. Maeda, H. Iida, Y. Furusho, K. Nagai, *Chem. Rev.* **2009**, *109*, 6102-6211.
[172] D. S. Poland, *Theory of Helix-Coil Transitions in Biopolymers*, Academic Press, **1970**.
[173] B. H. Zimm, J. K. Bragg, *J. Chem. Phys.* **1959**, *31*, 526-535.
[174] H. Qian, J. A. Schellman, *J. Phys. Chem.* **1992**, *96*, 3987-3994.
[175] D. C. Poland, H. A. Scheraga, *J. Chem. Phys.* **1965**, *43*, 2071-&.
[176] V. Dehm, M. Büchner, J. Seibt, V. Engel, F. Würthner, *Chem. Sci.* **2011**, *2*, 2094-2100.
[177] R. B. Prince, J. G. Saven, P. G. Wolynes, J. S. Moore, *J. Am. Chem. Soc.* **1999**, *121*, 3114-3121.
[178] B. M. W. Langeveld-Voss, M. P. T. Christiaans, R. A. J. Janssen, E. W. Meijer, *Macromolecules* **1998**, *31*, 6702-6704.
[179] F. Sanda, K. Terada, T. Masuda, *Macromolecules* **2005**, *38*, 8149-8154.
[180] E. Kolomiets, V. Berl, J. M. Lehn, *Chem.-Eur. J.* **2007**, *13*, 5466-5479.
[181] K.-C. Sham, C.-C. Yee, Y. Pan, K.-C. Lau, S.-M. Yiu, H.-L. Kwong, *RSC Adv.* **2014**, *4*, 14513-14526.
[182] N. Sakamoto, C. Ikeda, M. Yamamura, T. Nabeshima, *Chem. Commun.* **2012**, *48*, 4818-4820.
[183] K. Maeda, K. Morino, E. Yashima, *J. Polym. Sci. A Polym. Chem.* **2003**, *41*, 3625-3631.
[184] M. Waki, H. Abe, M. Inouye, *Chem.-Eur. J.* **2006**, *12*, 7839-7847.
[185] J. M. Lehn, A. Rigault, J. Siegel, J. Harrowfield, B. Chevrier, D. Moras, *P. Natl. Acad. Sci. U.S.A.* **1987**, *84*, 2565-2569.
[186] L. Allouche, A. Marquis, J. M. Lehnl, *Chem.-Eur. J.* **2006**, *12*, 7520-7525.
[187] A. Zhu, M. J. Mio, J. S. Moore, H. G. Drickamer, *J. Phys. Chem. B* **2001**, *105*, 12374-12377.
[188] M. T. Stone, J. S. Moore, *Org. Lett.* **2004**, *6*, 469-472.
[189] M. T. Stone, J. M. Fox, J. S. Moore, *Org. Lett.* **2004**, *6*, 3317-3320.
[190] R. B. Prince, J. S. Moore, L. Brunsveld, E. W. Meijer, *Chem. Eur. J.* **2001**, *7*, 4150-4154.

[191] R. B. Prince, L. Brunsveld, E. W. Meijer, J. S. Moore, *Angew. Chem. Int. Edit.* **2000**, *39*, 228-230.
[192] M. S. Gin, T. Yokozawa, R. B. Prince, J. S. Moore, *J. Am. Chem. Soc.* **1999**, *121*, 2643-2644.
[193] M. S. Gin, J. S. Moore, *Org. Lett.* **2000**, *2*, 135-138.
[194] L. Brunsveld, R. B. Prince, E. W. Meijer, J. S. Moore, *Org. Lett.* **2000**, *2*, 1525-1528.
[195] L. Brunsveld, E. W. Meijer, R. B. Prince, J. S. Moore, *J. Am. Chem. Soc.* **2001**, *123*, 7978-7984.
[196] Z. Yu, S. Weidner, T. Risse, S. Hecht, *Chem. Sci.* **2013**, *4*, 4156-4167.
[197] H. Goto, Y. Yokochi, E. Yashima, *Chem. Commun.* **2012**, *48*, 3291-3293.
[198] F. Wang, K. Nakano, H. Segawa, K. Tajima, *ACS Appl. Mater. Inter.* **2021**, *13*, 7510-7516.
[199] M. M. Bouman, E. W. Meijer, *Adv. Mater.* **1995**, *7*, 385-387.
[200] G. Bidan, S. Guillerez, V. Sorokin, *Adv. Mater.* **1996**, *8*, 157-160.
[201] Z.-B. Zhang, M. Fujiki, M. Motonaga, H. Nakashima, K. Torimitsu, H.-Z. Tang, *Macromolecules* **2002**, *35*, 941-944.
[202] J.-m. Suk, D. A. Kim, K.-S. Jeong, *Org. Lett.* **2012**, *14*, 5018-5021.
[203] H.-P. Yi, X.-B. Shao, J.-L. Hou, C. Li, X.-K. Jiang, Z.-T. Li, *New J. Chem.* **2005**, *29*, 1213-1218.
[204] C. Dolain, H. Jiang, J.-M. Léger, P. Guionneau, I. Huc, *J. Am. Chem. Soc.* **2005**, *127*, 12943-12951.
[205] D. Sánchez-García, B. Kauffmann, T. Kawanami, H. Ihara, M. Takafuji, M.-H. Delville, I. Huc, *J. Am. Chem. Soc.* **2009**, *131*, 8642-8648.
[206] Y. Ferrand, A. M. Kendhale, B. Kauffmann, A. Grélard, C. Marie, V. Blot, M. Pipelier, D. Dubreuil, I. Huc, *J. Am. Chem. Soc.* **2010**, *132*, 7858-7859.
[207] C. Ikeda, Z. S. Yoon, M. Park, H. Inoue, D. Kim, A. Osuka, *J. Am. Chem. Soc.* **2005**, *127*, 534-535.
[208] Y. Inai, K. Tagawa, A. Takasu, T. Hirabayashi, T. Oshikawa, M. Yamashita, *J. Am. Chem. Soc.* **2000**, *122*, 11731-11732.
[209] S. Kwon, H. S. Shin, J. Gong, J.-H. Eom, A. Jeon, S. H. Yoo, I. S. Chung, S. J. Cho, H.-S. Lee, *J. Am. Chem. Soc.* **2011**, *133*, 17618-17621.
[210] Y. Furusho, H. Goto, K. Itomi, H. Katagiri, T. Miyagawa, E. Yashima, *Chem. Commun.* **2011**, *47*, 9795-9797.
[211] W. Zarges, J. Hall, J.-M. Lehn, C. Bolm, *Helv. Chim. Acta* **1991**, *74*, 1843-1852.
[212] B. Hasenknopf, J.-M. Lehn, *Helv. Chim. Acta* **1996**, *79*, 1643-1650.
[213] M. Ikeda, Y. Tanaka, T. Hasegawa, Y. Furusho, E. Yashima, *J. Am. Chem. Soc.* **2006**, *128*, 6806-6807.
[214] W. Makiguchi, S. Kobayashi, Y. Furusho, E. Yashima, *Polym. J.* **2012**, *44*, 1071-1076.
[215] M. M. Green, N. C. Peterson, T. Sato, A. Teramoto, R. Cook, S. Lifson, *Science* **1995**, *268*, 1860-1866.
[216] M. M. Green, C. Khatri, N. C. Peterson, *J. Am. Chem. Soc.* **1993**, *115*, 4941-4942.
[217] M. M. Green, B. A. Garetz, B. Munoz, H. P. Chang, S. Hoke, R. G. Cooks, *J. Am. Chem. Soc.* **1995**, *117*, 4181-4182.
[218] M. M. Green, C. Andreola, B. Munoz, M. P. Reidy, K. Zero, *J. Am. Chem. Soc.* **1988**, *110*, 4063-4065.
[219] S. Lifson, M. M. Green, C. Andreola, N. C. Peterson, *J. Am. Chem. Soc.* **1989**, *111*, 8850-8858.
[220] E. Ramos, J. Bosch, J. L. Serrano, T. Sierra, J. Veciana, *J. Am. Chem. Soc.* **1996**, *118*, 4703-4704.

[221] K. Onitsuka, T. Mori, M. Yamamoto, F. Takei, S. Takahashi, *Macromolecules* **2006**, *39*, 7224-7231.
[222] H.-Z. Tang, B. M. Novak, J. He, P. L. Polavarapu, *Angew. Chem. Int. Edit.* **2005**, *44*, 7298-7301.
[223] H. Nakashima, M. Fujiki, J. R. Koe, M. Motonaga, *J. Am. Chem. Soc.* **2001**, *123*, 1963-1969.
[224] M. Fujiki, *Macromol. Rapid. Comm.* **2001**, *22*, 539-563.
[225] F. Ciardelli, S. Lanzillo, O. Pieroni, *Macromolecules* **1974**, *7*, 174-179.
[226] J. S. Moore, C. B. Gorman, R. H. Grubbs, *J. Am. Chem. Soc.* **1991**, *113*, 1704-1712.
[227] K. Morino, K. Maeda, E. Yashima, *Macromolecules* **2003**, *36*, 1480-1486.
[228] T. Takata, Y. Furusho, K.-i. Murakawa, T. Endo, H. Matsuoka, T. Hirasa, J. Matsuo, M. Sisido, *J. Am. Chem. Soc.* **1998**, *120*, 4530-4531.
[229] H.-C. Zhang, L. Pu, *Macromolecules* **2004**, *37*, 2695-2702.
[230] Y. Okamoto, K. Suzuki, K. Ohta, K. Hatada, H. Yuki, *J. Am. Chem. Soc.* **1979**, *101*, 4763-4765.
[231] K. Maeda, S. Wakasone, K. Shimomura, T. Ikai, S. Kanoh, *Macromolecules* **2014**, *47*, 6540-6546.
[232] N. Chandramouli, Y. Ferrand, G. Lautrette, B. Kauffmann, C. D. Mackereth, M. Laguerre, D. Dubreuil, I. Huc, *Nat. Chem.* **2015**, *7*, 334-341.
[233] Y. Okamoto, T. Nakano, *Chem. Rev.* **1994**, *94*, 349-372.
[234] V. Jain, K.-S. Cheon, K. Tang, S. Jha, M. M. Green, *Isr. J. Chem.* **2011**, *51*, 1067-1074.
[235] A. J. Bur, L. J. Fetters, *Chem. Rev.* **1976**, *76*, 727-746.
[236] J. C. Nelson, J. G. Saven, J. S. Moore, P. G. Wolynes, *Science* **1997**, *277*, 1793-1796.
[237] R. B. Prince, S. A. Barnes, J. S. Moore, *J. Am. Chem. Soc.* **2000**, *122*, 2758-2762.
[238] H. Ceymann, A. Rosspeintner, M. H. Schreck, C. Mützel, A. Stoy, E. Vauthey, C. Lambert, *Phys. Chem. Chem. Phys.* **2016**, *18*, 16404-16413.
[239] E. Richmond, K. B. Ling, N. Duguet, L. B. Manton, N. Çelebi-Ölçüm, Y.-H. Lam, S. Alsancak, A. M. Z. Slawin, K. N. Houk, A. D. Smith, *Org. Boimol. Chem.* **2015**, *13*, 1807-1817.
[240] C. Concellon, N. Duguet, A. D. Smith, *Adv. Synth. Catal.* **2009**, *351*, 3001-3009.
[241] J. J. Douglas, G. Churchill, A. M. Z. Slawin, D. J. Fox, A. D. Smith, *Chem. Eur. J.* **2015**, *21*, 16354-16358.
[242] T. Maeda, S. Nitta, Y. Sano, S. Tanaka, S. Yagi, H. Nakazumi, *Dyes Pigments* **2015**, *122*, 160-167.
[243] Z. S. Yang, F. Chen, Y. M. He, N. F. Yang, Q. H. Fan, *Angew. Chem. Int. Edit.* **2016**, *55*, 13863-13866.
[244] J. G. Rodríguez, A. Urrutia, *J. Heterocyclic Chem.* **1999**, *36*, 129-135.
[245] M. Yamakawa, I. Yamada, R. Noyori, *Angew. Chem. Int. Edit.* **2001**, *40*, 2818-2821.
[246] M. Yamakawa, H. Ito, R. Noyori, *J. Am. Chem. Soc.* **2000**, *122*, 1466-1478.
[247] Y.-E. Luo, Y.-M. He, Q.-H. Fan, *Chem. Rec.* **2016**, *16*, 2697-2711.
[248] R. E. Gawley, *J. Org. Chem.* **2006**, *71*, 2411-2416.
[249] S. Bellemin-Laponnaz, J. Tweddell, J. C. Ruble, F. M. Breitling, G. C. Fu, *Chem. Commun.* **2000**, 1009-1010.
[250] A. H. Hoveyda, R. R. Schrock, *Chemistry - A European Journal* **2001**, *7*, 945-950.
[251] John M. Keith, Jay F. Larrow, Eric N. Jacobsen, *Adv. Synth. Catal.* **2001**, *343*, 5-26.
[252] S. Chen, Y.-H. Shi, M. Wang, *Chem. Asian J.* **2018**, *13*, 2184-2194.
[253] M. Matsui, M. Fukushima, Y. Kubota, K. Funabiki, M. Shiro, *Tetrahedron* **2012**, *68*, 1931-1935.

[254] D. E. Lynch, K. A. Byriel, *Cryst. Eng.* **1999**, *2*, 225-239.
[255] D. Lynch, *Acta Crystallogr. E* **2002**, *58*, o1025-o1027.
[256] S. Parsons, *Tetrahedron Asymmetry* **2017**, *28*, 1304-1313.
[257] H. D. Flack, G. Bernardinelli, *Chirality* **2008**, *20*, 681-690.
[258] D. J. Watkin, R. I. Cooper, *Chemistry* **2020**, *2*, 796-804.
[259] K. M. Barkigia, M. D. Berber, J. Fajer, C. J. Medforth, M. W. Renner, K. M. Smith, *J. Am. Chem. Soc.* **1990**, *112*, 8851-8857.
[260] H. Marciniak, N. Auerhammer, S. Ricker, A. Schmiedel, M. Holzapfel, C. Lambert, *J. Phys. Chem. C* **2019**, *123*, 3426-3432.
[261] H. Ceymann, A. Rosspeintner, M. H. Schreck, C. Mutzel, A. Stoy, E. Vauthey, C. Lambert, *Phys. Chem. Chem. Phys.* **2016**, *18*, 16404-16413.
[262] J.-H. Yum, P. Walter, S. Huber, D. Rentsch, T. Geiger, F. Nüesch, F. De Angelis, M. Grätzel, M. K. Nazeeruddin, *J. Am. Chem. Soc.* **2007**, *129*, 10320-10321.
[263] K. Srinivas, C. Prabhakar, C. L. Devi, K. Yesudas, K. Bhanuprakash, V. J. Rao, *J. Phys. Chem. A* **2007**, *111*, 3378-3386.
[264] H. Feki, A. B. Ahmed, N. Fourati, Y. Abid, C. Minot, *J. Mol. Struc.-Theochem* **2009**, *895*, 21-25.
[265] C. J. Bennett, S. T. Caldwell, D. B. McPhail, P. C. Morrice, G. G. Duthie, R. C. Hartley, *Bioorg. Med. Chem.* **2004**, *12*, 2079-2098.
[266] E. J. Alvarez-Manzaneda, R. Chahboun, E. Cabrera Torres, E. Alvarez, R. Alvarez-Manzaneda, A. Haidour, J. M. Ramos López, *Tetrahedron Lett.* **2005**, *46*, 3755-3759.
[267] D. A. Evans, J. Bartroli, T. L. Shih, *J. Am. Chem. Soc.* **1981**, *103*, 2127-2129.
[268] D. A. Evans, M. D. Ennis, D. J. Mathre, *J. Am. Chem. Soc.* **1982**, *104*, 1737-1739.
[269] J. Klimentová, P. Kosák, K. Vávrová, T. Holas, A. Hrabálek, *Bioorg. Med. Chem.* **2006**, *14*, 7681-7687.
[270] P. Lucio Anelli, C. Biffi, F. Montanari, S. Quici, *J. Org. Chem.* **1987**, *52*, 2559-2562.
[271] M. Richardson, S. Williams, *Beilstein J. Org. Chem.* **2013**, *9*, 1807-1812.
[272] G. M. Loudon, J. Parise, *Organic Chemistry*, **2016**.
[273] A. Fensome, W. R. Adams, A. L. Adams, T. J. Berrodin, J. Cohen, C. Huselton, A. Illenberger, J. C. Kern, V. A. Hudak, M. A. Marella, E. G. Melenski, C. C. McComas, C. A. Mugford, O. D. Slayden, M. Yudt, Z. Zhang, P. Zhang, Y. Zhu, R. C. Winneker, J. E. Wrobel, *J. Med. Chem.* **2008**, *51*, 1861-1873.
[274] G. Snatzke, in *Optical Activity and Chiral Discrimination* (Ed.: S. F. Mason), Springer Netherlands, **1979**, pp. 25-41.
[275] A. Turkin, P. Malý, C. Lambert, *Phys. Chem. Chem. Phys.* **2021**.
[276] A. Turkin, *Julius-Maximilians-Universität Würzburg* **2022**.
[277] C. M. Hansen, *Hansen Solubility Parameters : A User's Handbook*, CRC Press, Boca Raton, **2007**.
[278] S. Grimme, *Angew. Chem. Int. Edit.* **2008**, *47*, 3430-3434.
[279] T. Steiner, *Angew. Chem. Int. Edit.* **2002**, *41*, 48-76.
[280] F. Würthner, *Acc. Chem. Res.* **2016**, *49*, 868-876.
[281] G. W. Longman, G. D. Wignall, R. P. Sheldon, *Polymer* **1979**, *20*, 1063-1069.
[282] F. Hinderer, R. May, S.-S. Jester, S. Höger, *Macromolecules* **2016**, *49*, 1816-1821.
[283] S. Wang, J. Shaw, Y. Han, Z. Fei, F. Glöcklhofer, M. Heeney, *Chem. Commun.* **2020**, *56*, 12138-12141.
[284] T. Pullerits, M. Chachisvilis, V. Sundström, *J. Phys. Chem.* **1996**, *100*, 10787-10792.
[285] E. Rousseau, M. M. Koetse, M. Van der Auweraer, F. C. De Schryver, *Photochem. Photobio. Sci.* **2002**, *1*, 395-406.

[286] L. J. Patalag, L. P. Ho, P. G. Jones, D. B. Werz, *J. Am. Chem. Soc.* **2017**, *139*, 15104-15113.
[287] Z. Chen, Y. Liu, W. Wagner, V. Stepanenko, X. Ren, S. Ogi, F. Würthner, *Angew. Chem. Int. Edit.* **2017**, *56*, 5729-5733.
[288] G. Longhi, E. Castiglioni, C. Villani, R. Sabia, S. Menichetti, C. Viglianisi, F. Devlin, S. Abbate, *J. Photoch. Photobio. A* **2016**, *331*, 138-145.
[289] S. Kitamura, K. Nakabayashi, T. Wakabayashi, N. Tajima, M. Fujiki, Y. Imai, *RSC Adv.* **2015**, *5*, 67449-67453.
[290] T. Amako, T. Kimoto, N. Tajima, M. Fujiki, Y. Imai, *Tetrahedron* **2013**, *69*, 2753-2757.
[291] Y. Nagata, T. Nishikawa, M. Suginome, *Chem. Commun.* **2014**, *50*, 9951-9953.
[292] M. Kasha, *Discuss. Faraday Soc.* **1950**, 14-19.
[293] E. W. Knapp, *Chem. Phys.* **1984**, *85*, 73-82.
[294] E. Castiglioni, S. Abbate, F. Lebon, G. Longhi, *Chirality* **2012**, *24*, 725-730.
[295] E. Michail, M. H. Schreck, M. Holzapfel, C. Lambert, *Phys. Chem. Chem. Phys.* **2020**, *22*, 18340-18350.
[296] C. Lambert, T. Scherpf, H. Ceymann, A. Schmiedel, M. Holzapfel, *J. Am. Chem. Soc.* **2015**, *137*, 3547-3557.
[297] P. Ottiger, S. Leutwyler, *J. Chem. Phys.* **2012**, *137*, 204303.
[298] P. Ottiger, H. Koppel, S. Leutwyler, *Chem. Sci.* **2015**, *6*, 6059-6068.
[299] A. L. Tatarets, I. A. Fedyunyaeva, E. Terpetschnig, L. D. Patsenker, *Dyes Pigments* **2005**, *64*, 125-134.
[300] M. Matsui, H. Mase, J.-Y. Jin, K. Funabiki, T. Yoshida, H. Minoura, *Dyes Pigments* **2006**, *70*, 48-53.
[301] J. V. Ros-Lis, B. García, D. Jiménez, R. Martínez-Máñez, F. Sancenón, J. Soto, F. Gonzalvo, M. C. Valldecabres, *J. Am. Chem. Soc.* **2004**, *126*, 4064-4065.
[302] P. B. Walczak, A. Eisfeld, J. S. Briggs, *J. Chem. Phys.* **2008**, *128*.
[303] C. Zhong, D. Bialas, C. J. Collison, F. C. Spano, *J. Phys. Chem. C* **2019**, *123*, 18734-18745.
[304] T.-S. Ahn, R. O. Al-Kaysi, A. M. Müller, K. M. Wentz, C. J. Bardeen, *Rev. Sci. Instrum.* **2007**, *78*, 086105.
[305] G. Sheldrick, *Acta Crystallogr. A* **2015**, *71*, 3-8.
[306] G. Sheldrick, *Acta Crystallogr. A* **2008**, *64*, 112-122.
[307] O. V. Dolomanov, L. J. Bourhis, R. J. Gildea, J. A. K. Howard, H. Puschmann, *J. Appl. Crystallogr.* **2009**, *42*, 339-341.
[308] G. R. Fulmer, A. J. M. Miller, N. H. Sherden, H. E. Gottlieb, A. Nudelman, B. M. Stoltz, J. E. Bercaw, K. I. Goldberg, *Organometallics* **2010**, *29*, 2176-2179.
[309] K. N. Lee, Z. Lei, C. A. Morales-Rivera, P. Liu, M.-Y. Ngai, *Org. Boimol. Chem.* **2016**, *14*, 5599-5605.
[310] I. Nakamura, M. Owada, T. Jo, M. Terada, *Org. Lett.* **2017**, *19*, 2194-2196.
[311] R. I. Zubatyuk, V. N. Baumer, A. L. Tatarets, L. D. Patsenker, O. V. Shishkin, *Acta Crystallographica Section E-Crystallographic Communications* **2004**, *60*, O2252-O2254.
[312] M. López-Iglesias, E. Busto, V. Gotor, V. Gotor-Fernández, *J. Org. Chem.* **2012**, *77*, 8049-8055.
[313] N. T. Patil, A. Konala, *Eur. J. Org. Chem.* **2010**, *2010*, 6831-6839.
[314] M. A. Ariger, E. M. Carreira, *Org. Lett.* **2012**, *14*, 4522-4524.
[315] F. Chen, Z. Ding, Y. He, J. Qin, T. Wang, Q.-H. Fan, *Tetrahedron* **2012**, *68*, 5248-5257.
[316] M. V. Reddington, *Bioconjugate Chem.* **2007**, *18*, 2178-2190.
[317] X. Dou, W. Yao, S. Wen, Y. Lu, *Chem. Commun.* **2014**, *50*, 9469-9472.
[318] D. A. Klumpp, K. Y. Yeung, G. K. S. Prakash, G. A. Olah, *J. Org. Chem.* **1998**, *63*, 4481-4484.

[319] R. B. Zerdan, N. T. Shewmon, Y. Zhu, J. P. Mudrick, K. J. Chesney, J. Xue, R. K. Castellano, *Adv. Funct. Mater.* **2014**, *24*, 5993-6004.
[320] A. D. McNaught, A. Wilkinson, I. U. o. Pure, A. Chemistry, *Compendium of Chemical Terminology: Iupac Recommendations*, Blackwell Science, **1997**.
[321] J. E. Lewis, M. Maroncelli, *Chem. Phys. Lett.* **1998**, *282*, 197-203.
[322] N. W. Tschoegl, in *Fundamentals of Equilibrium and Steady-State Thermodynamics* (Ed.: N. W. Tschoegl), Elsevier Science, Amsterdam, **2000**, pp. 49-61.
[323] E. Fišerová, M. Kubala, *J. Lumin.* **2012**, *132*, 2059-2064.
[324] U. Mayerhöffer, M. Gsänger, M. Stolte, B. Fimmel, F. Würthner, *Chemistry - A European Journal* **2013**, *19*, 218-232.
[325] S. Boros, Z. Gáspári, G. Batta, in *Annual Reports on Nmr Spectroscopy, Vol. 94* (Ed.: G. A. Webb), Academic Press, **2018**, pp. 1-39.

10 TABLE OF FORMULAS

10.1 Precursors

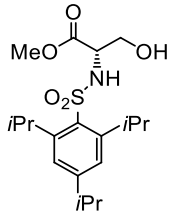

***S*-1**

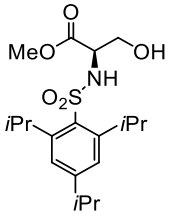

***R*-1**

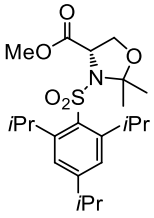

***S*-2**

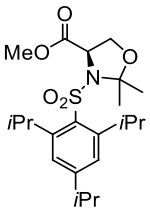

***R*-2**

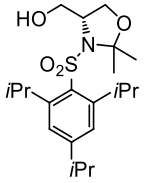

***S*-3**

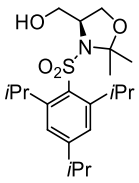

***R*-3**

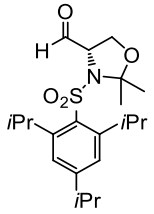

***S*-4**

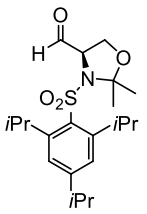

***R*-4**

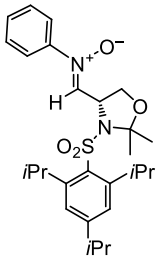

***S*-5**

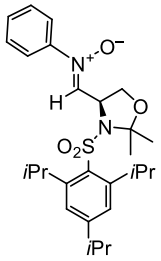

***R*-5**

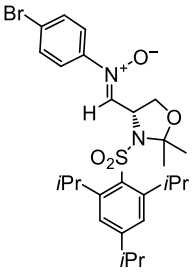

***S*-6**

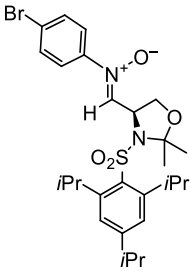

***R*-6**

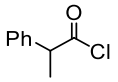

7

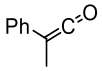

8

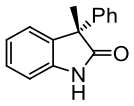

***S*-9**

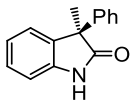

***R*-9**

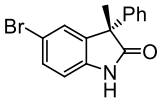

***S*-10**

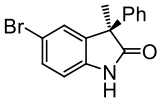

***R*-10**

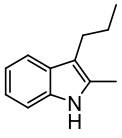

11

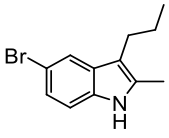

12

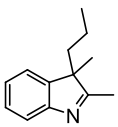

***rac*-13**

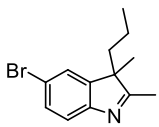

***rac*-14**

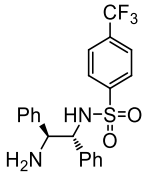

15

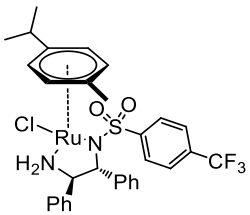

16

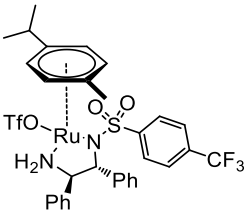

Cat*

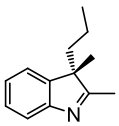

***S*-13**

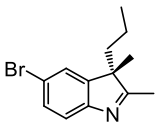

***S*-14**

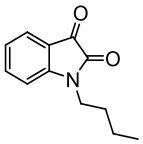

15a

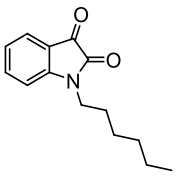

15b

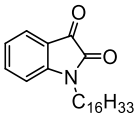

15c

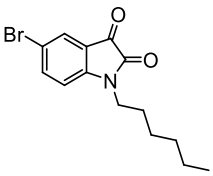

16a

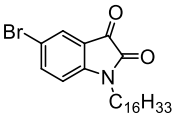

16b

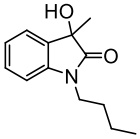

17a

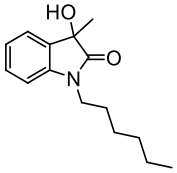

17b

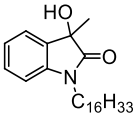

17c

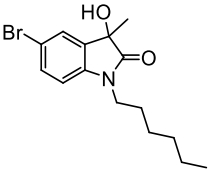

18a

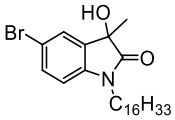

18b

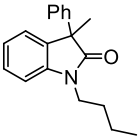

***rac*-19a**

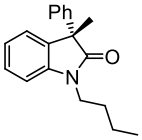

***S*-19a**

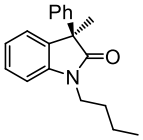

***R*-19a**

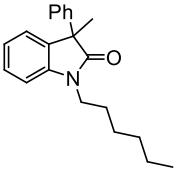

***rac*-19b**

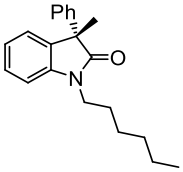

***S*-19b**

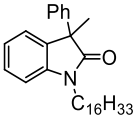

***rac*-19c**

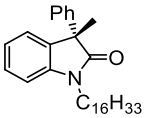

***S*-19c**

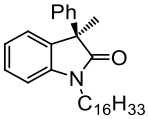

***R*-19c**

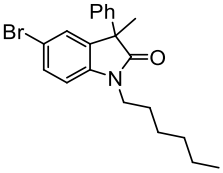

***rac*-20a**

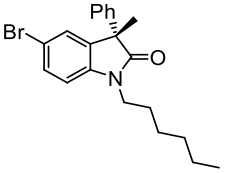

***S*-20a**

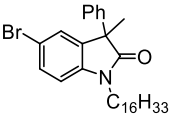

***rac*-20b**

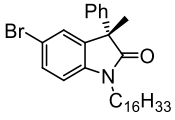

***S*-20b**

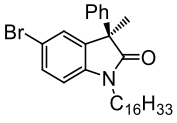

***R*-20b**

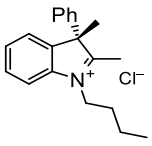

***S*-21a**

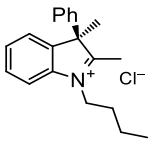

***R*-21a**

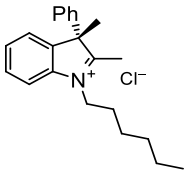

***S*-21b**

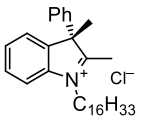

***S*-21c**

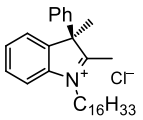

***R*-21c**

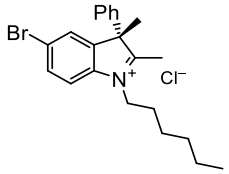

***S*-22a**

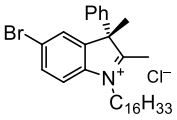

***S*-22b**

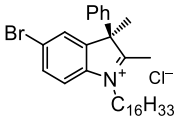

***R*-22b**

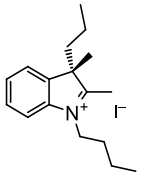

23

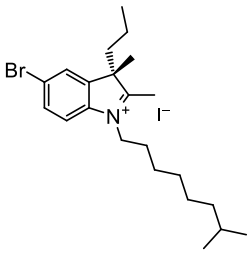

24

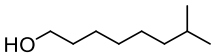

25

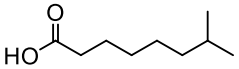

26

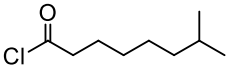

27

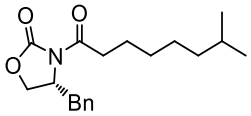

28

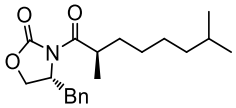

29a

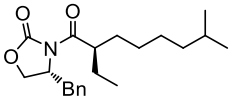

29b

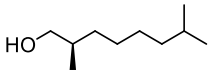

30a

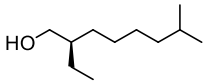

30b

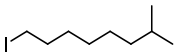

31a

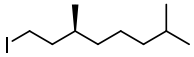

31b

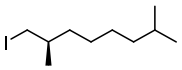

31c

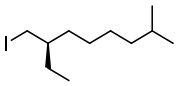

31d

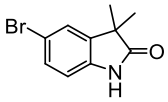

32

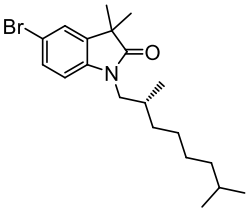

33a

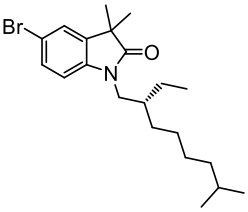

33b

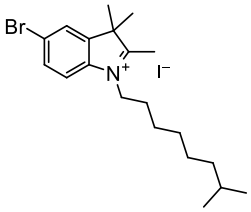

34a

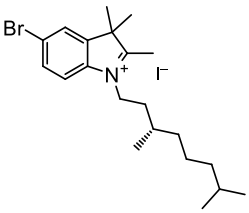

34b

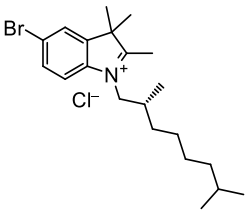

34c

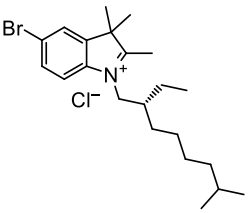

34d

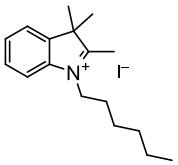

35a

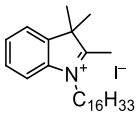

35b

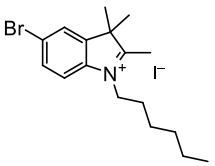

36a

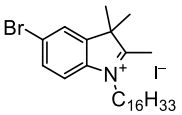

36b

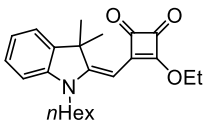

37a

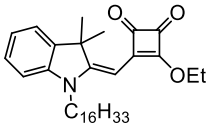

37b

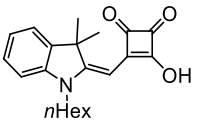

38a

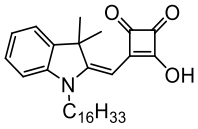

38b

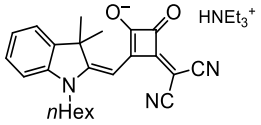

39a

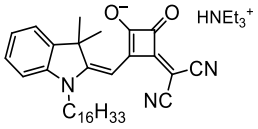

39b

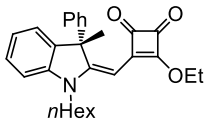

***S*-40a**

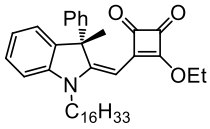

***S*-40b**

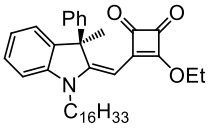

***R*-40b**

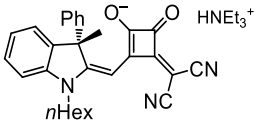

***S*-41a**

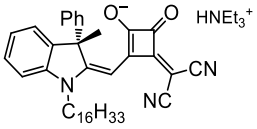

***S*-41b**

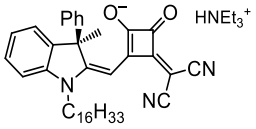

***R*-41b**

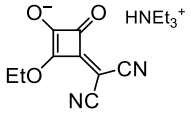

CN

10.2 Squaraine monomers

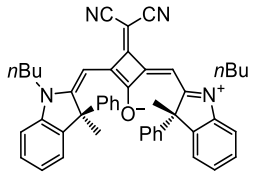

S*-Ph-SQB

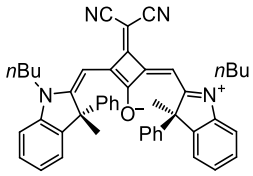

R*-Ph-SQB

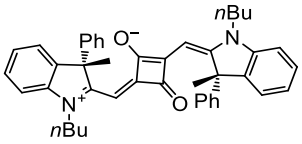

Ph-SQA*

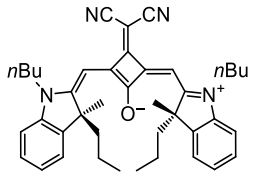

Pr-SQB*

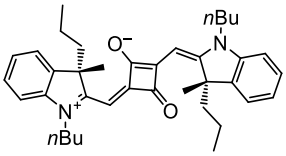

Pr-SQA*

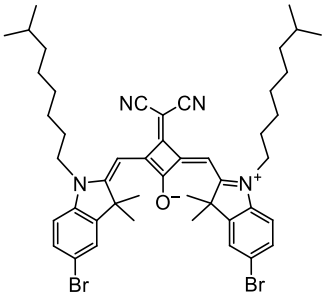

Br_2-SQB-R^0

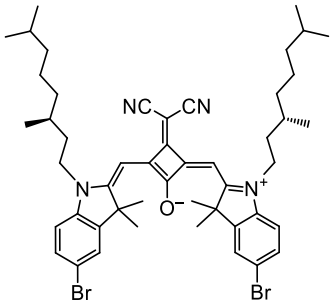

Br_2-SQB-R^1*

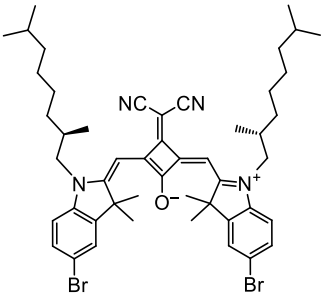

Br_2-SQB-R^2*

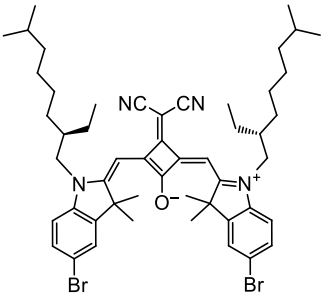

Br_2-SQB-R^3*

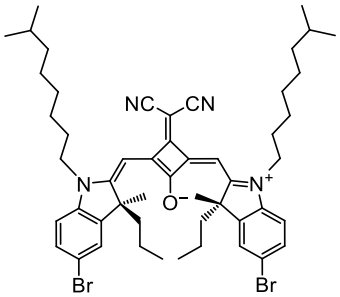

Br_2-Pr-SQB*

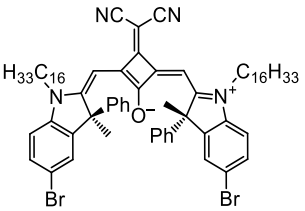

S*-Br_2-Ph-SQB

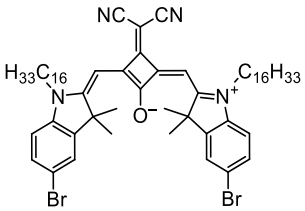

R*-Br_2-Ph-SQB

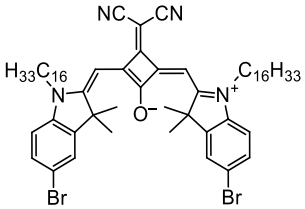

Br_2-SQB

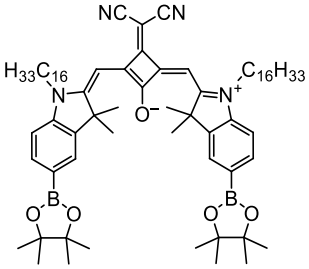

$Bpin_2$-SQB

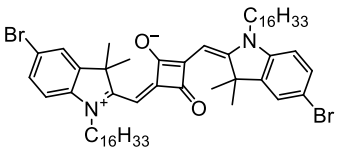

Br_2-SQA

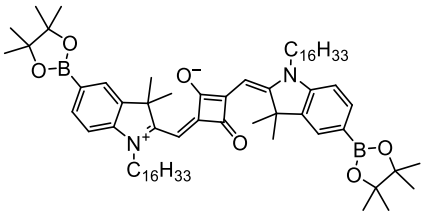

Bpin$_2$-SQA

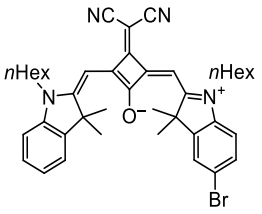

Br-SQB-C6

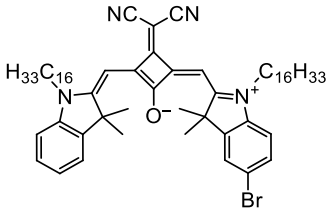

Br-SQB-C16

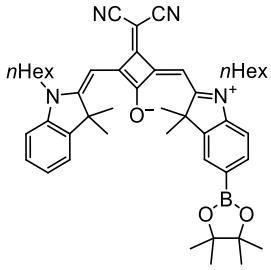

Bpin-SQB-C6

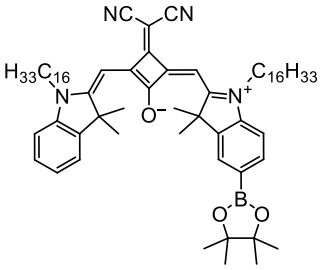

Bpin-SQB-C16

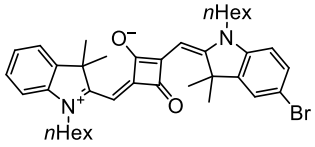

Br-SQA-C6

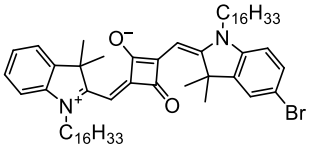

Br-SQA-C16

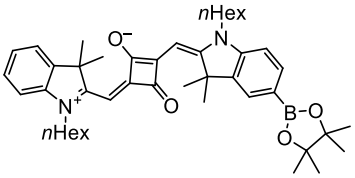

Bpin-SQA-C6

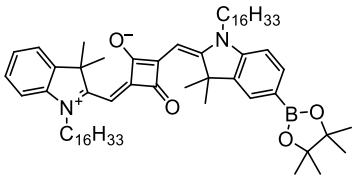

Bpin-SQA-C16

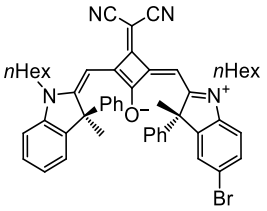

***S*-Br-SQB*-C6**

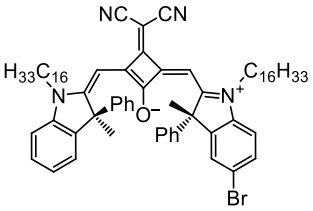

***S*-Br-SQB*-C16**

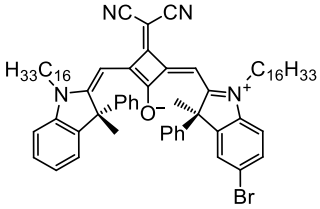

***R*-Br-SQB*-C16**

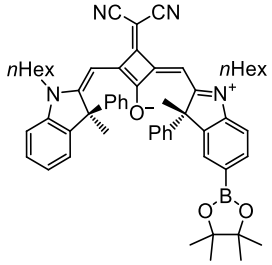

***S*-Bpin-SQB*-C6**

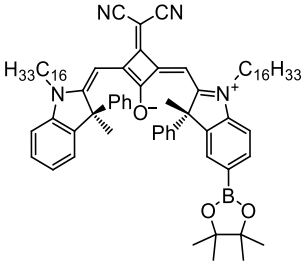

***S*-Bpin-SQB*-C16**

10.3 Squaraine oligomers

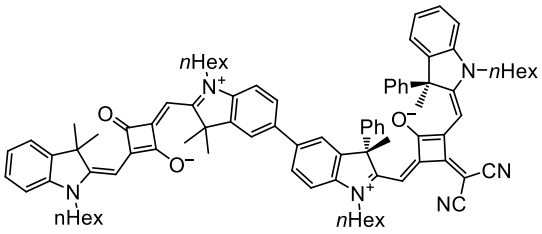

S*-SQA-SQB

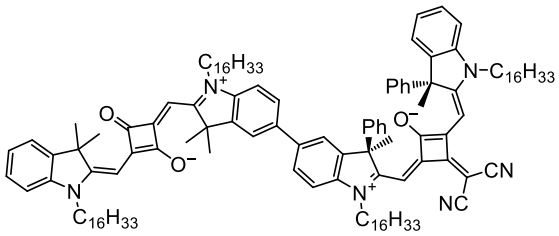

R*-SQA-SQB

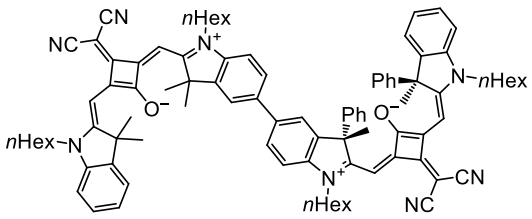

S*-SQB-SQB

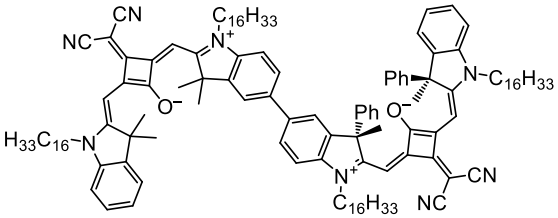

R*-SQB-SQB

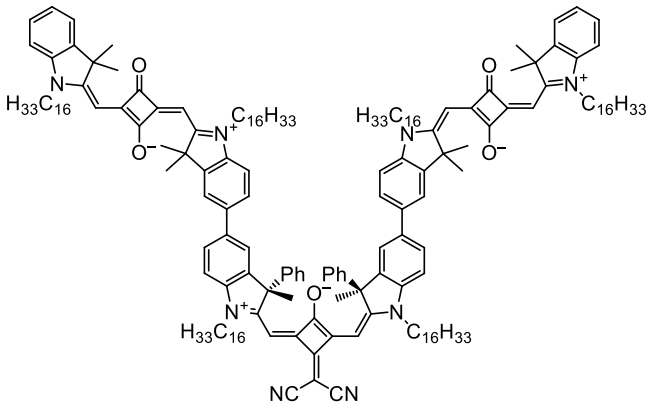

***S*-SQA-SQB*-SQA**

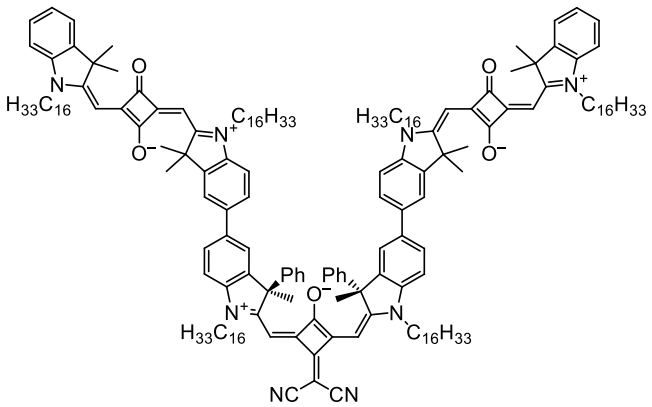

***R*-SQA-SQB*-SQA**

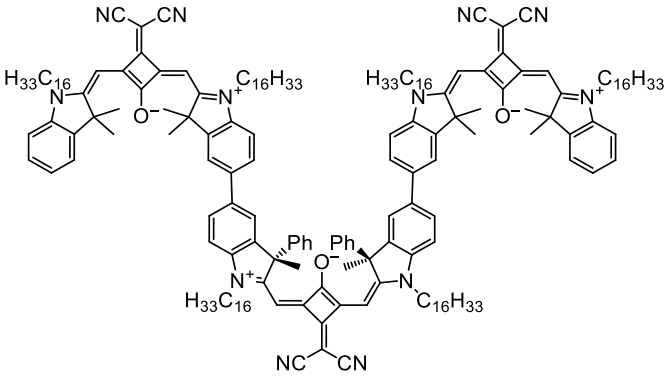

***S*-SQB-SQB*-SQB**

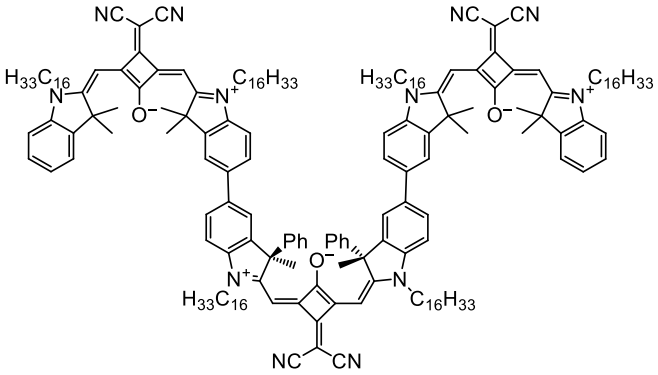

***R*-SQB-SQB*-SQB**

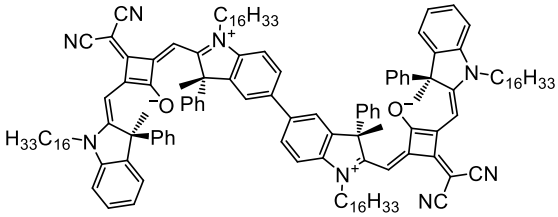

dSQB*

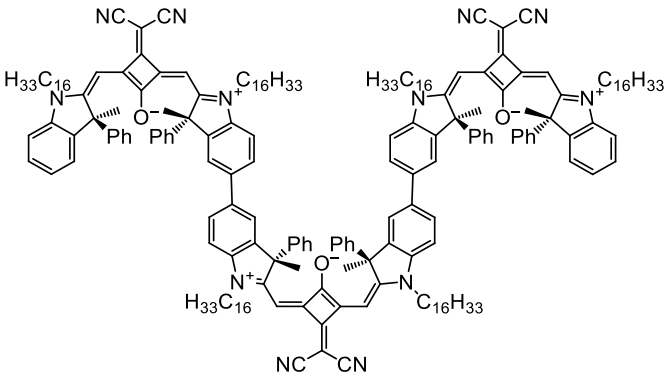

tSQB*

10.4 Squaraine polymers

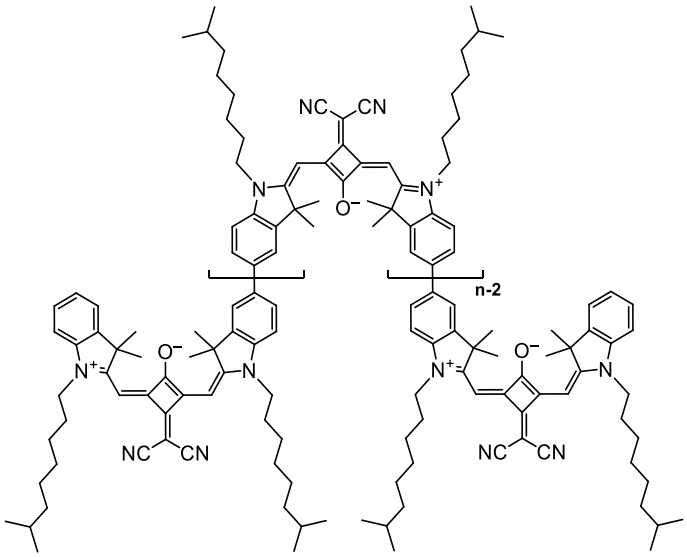

p(SQB-R^0)

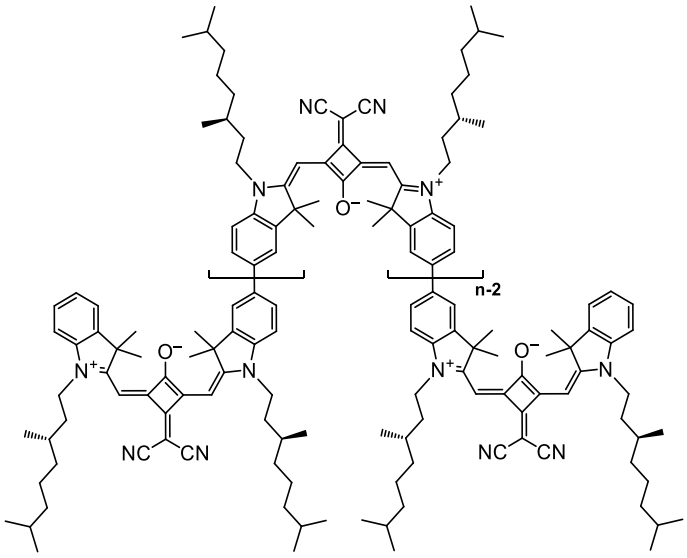

p(SQB-R^1*)

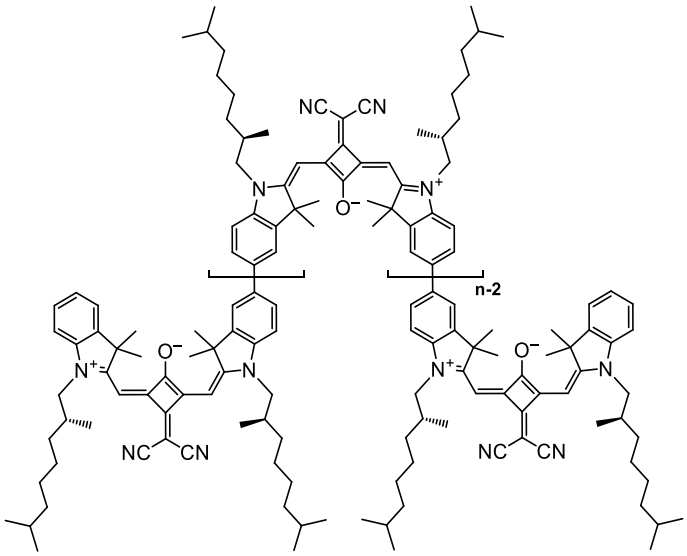

p(SQB-R^{2}*)

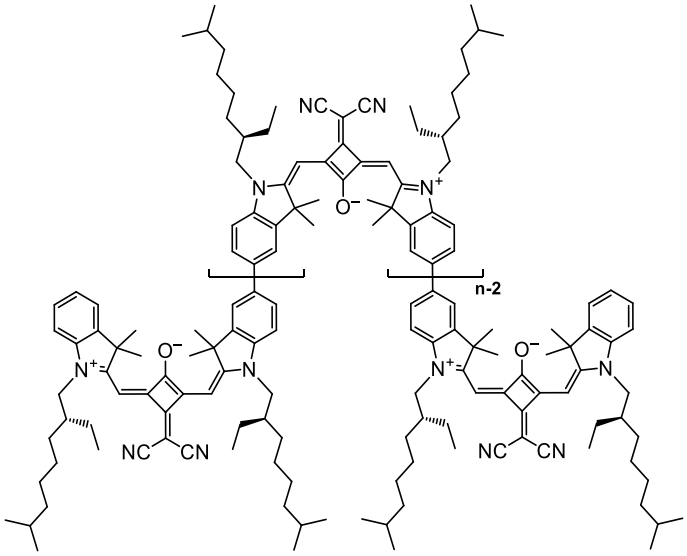

p(SQB-R^{3}*)

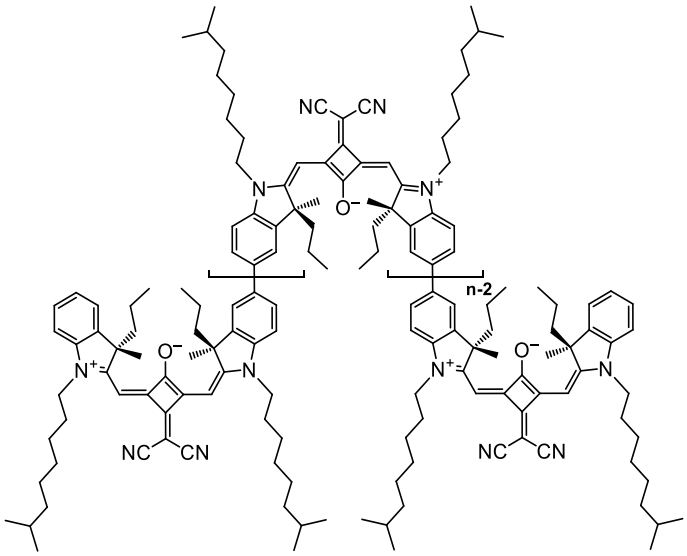

p(Pr-SQB*)

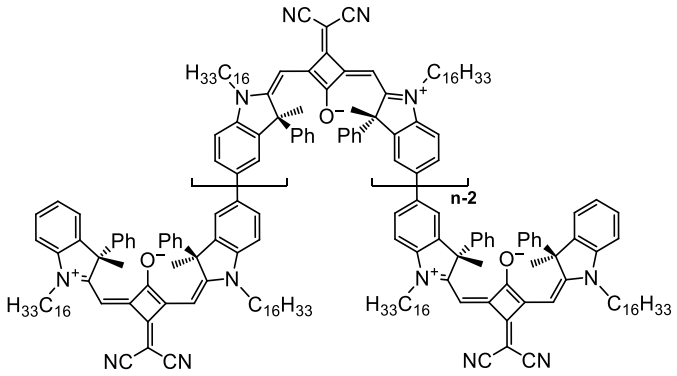

pSQB*

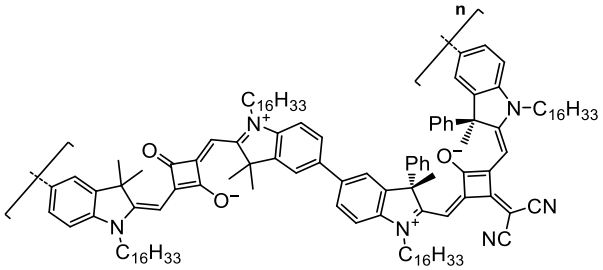

p(SQA-SQB*)

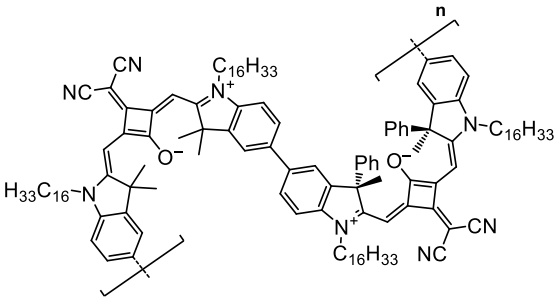

p(SQB-SQB*)

11 APPENDIX

11.1 Liquid chromatography

11.1.1 Analytical HPLC

Compound 9

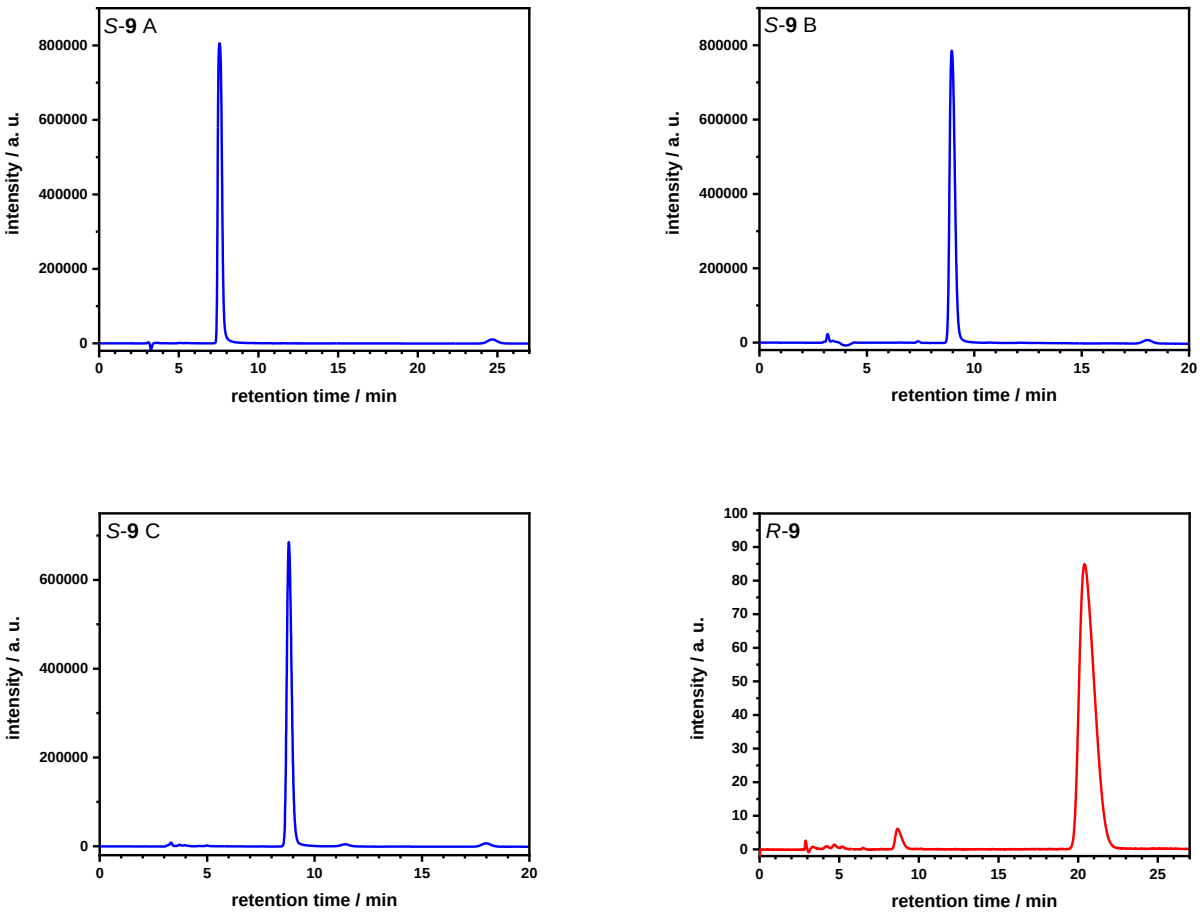

Figure 74. Analytical HPLC chromatograms of the batches of compound **9** which were used for further synthesis.

Detection at 225 nm, eluent: *n*Hex/iPrOH 9:1, flow rate: 1 mL/min, Phenomenex® LUX cellulose-1 (***R*-9**), LUX cellulose-2 (***S*-9** A), LUX cellulose-4 (***S*-9** B, ***S*-9** C).

Table 19. Data obtained from analytical HPLC of compound **9.**

Batch	*t*(R) / min	*t*(S) / min	%R[a]	%S[a]	For synthesis of
S-**9** A	24.7	7.5	2.6	97.4	*S*-**Ph-SQB***, *S*-**SQA-SQB***, *S*-**SQB-SQB***
S-**9** B	18.1	8.9	0.8	99.2	**Ph-SQA***
S-**9** C	18.0	8.8	1.4	98.6	**dSQB***, **tSQB***
R-**9**	20.4	8.7	97.0	3.0	*R*-**Ph-SQB***, *R*-**SQA-SQB***, *R*-**SQB-SQB***

[a] ratio of the area of the peak in the chromatogram to the sum of the areas of all relevant peaks.

Compound 10

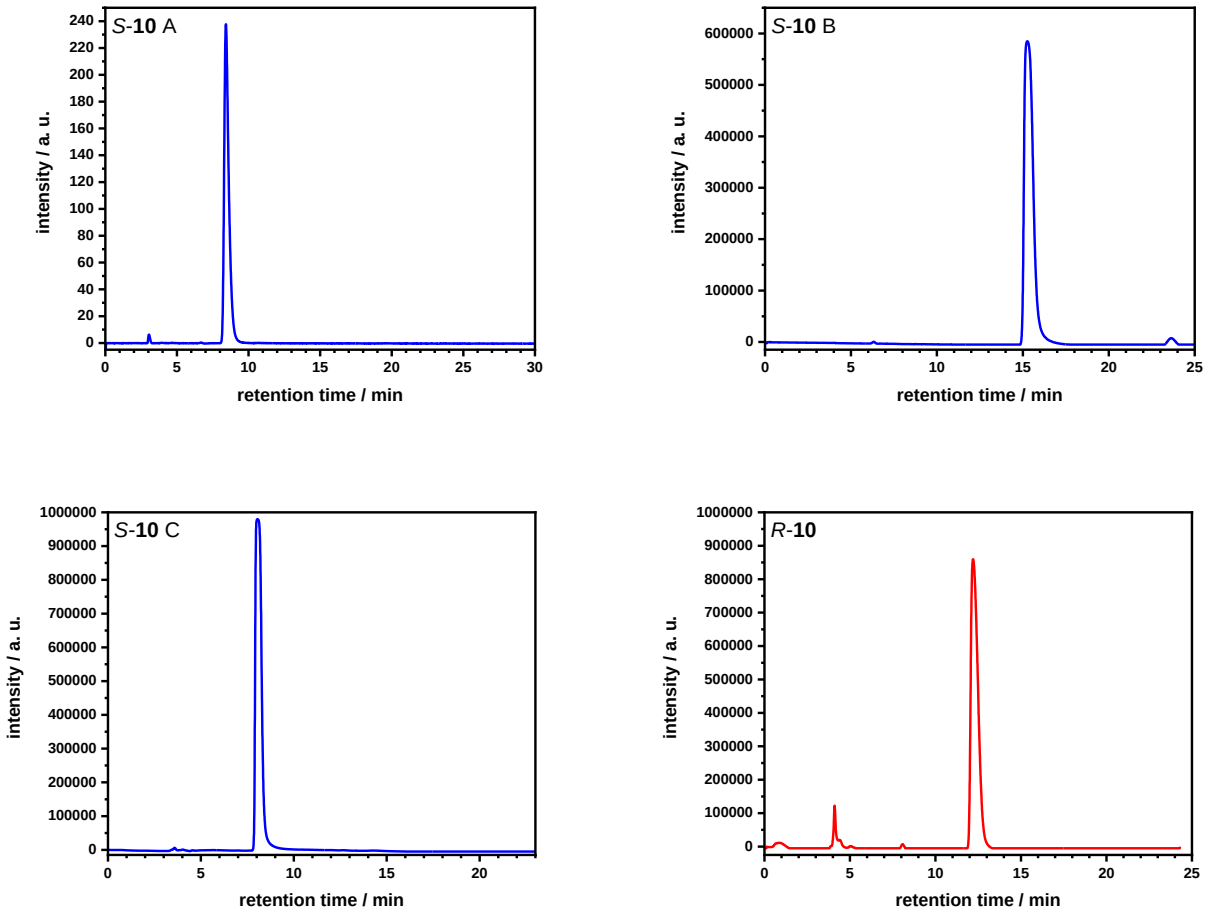

Figure 75. Analytical HPLC chromatograms of the batches of compound **10** which were used for further synthesis.

Detection at 254 nm, eluent: *n*Hex/iPrOH 9:1, flow rate: 1 mL/min, Phenomenex® LUX cellulose-2 (*S*-**10** A, *S*-**10** B), LUX cellulose-4 (*S*-**10** C, *R*-**10**).

Table 20. Data obtained from analytical HPLC of compound **10.**

Batch	*t*(R) / min	*t*(S) / min	%R[a]	%S[a]	For synthesis of
S-**10** A	-	8.4	-	>99.9	**p(SQA-SQB*), p(SQB-SQB*)**, *S*-**SQA-SQB*-SQA**, *S*-**SQB-SQB*-SQB**
S-**10** B[b]	23.6	15.3	0.4	99.6	*S*-**SQB-SQB***, *S*-**SQA-SQB***
S-**10** C	-	8.1	-	>99.9	**tSQB***, **pSQB***
R-**10**	12.2	8.1	99.7	0.3	*R*-**SQB-SQB***, *R*-**SQA-SQB***, *R*-**SQA-SQB*-SQA**, *R*-**SQB-SQB*-SQB**

[a] ratio of the area of the peak in the chromatogram to the sum of the areas of all relevant peaks [b] larger retention time due to instrument malfunction.

Compound 13

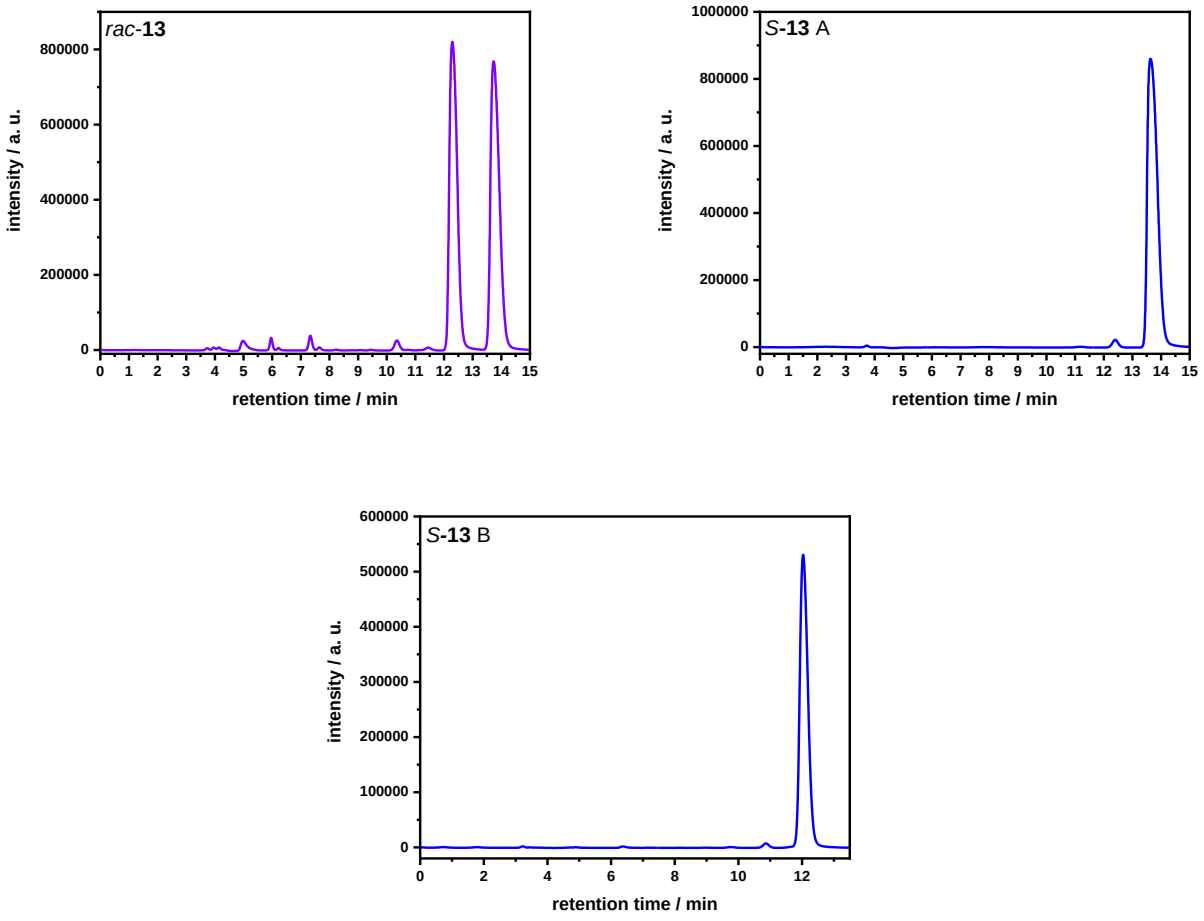

Figure 76. Analytical HPLC chromatograms of the batches of compound **13** which were used for further synthesis.

Detection at 254 nm, eluent: *n*Hex/iPrOH 99:1, flow rate: 1 mL/min, Phenomenex® LUX cellulose-2 (**13** B), LUX cellulose-4 (*rac*-**13**, **13** A).

Table 21. Data obtained from analytical HPLC of compound **13.**

Batch	*t*(R) / min	*t*(S) / min	%R[a]	%S[a]	For synthesis of
S-**13** A	12.4	13.6	1.4	98.6	**Pr-SQB***
S-**13** B	10.9	12.0	0.8	99.2	**Pr-SQA***

[a] ratio of the area of the peak in the chromatogram to the sum of the areas of all relevant peaks.

Compound 14

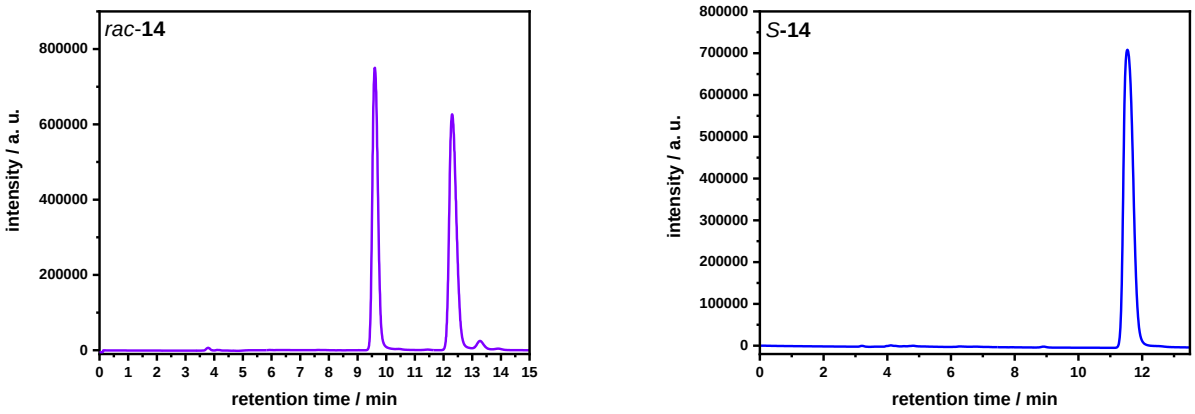

Figure 77. Analytical HPLC chromatograms of the batch of compound **14** which was used for further synthesis.

Detection at 254 nm, eluent: *n*Hex/iPrOH 99:1, flow rate: 1 mL/min, Phenomenex® LUX cellulose-4.

Table 22. Data obtained from analytical HPLC of compound **14.**

Batch	*t*(R) / min	*t*(S) / min	%R[a]	%S[a]	For synthesis of
S-**14**	8.9	11.5	0.5	99.5	**p(Pr-SQB*)**

[a] ratio of the area of the peak in the chromatogram to the sum of the areas of all relevant peaks.

Ph-SQB*

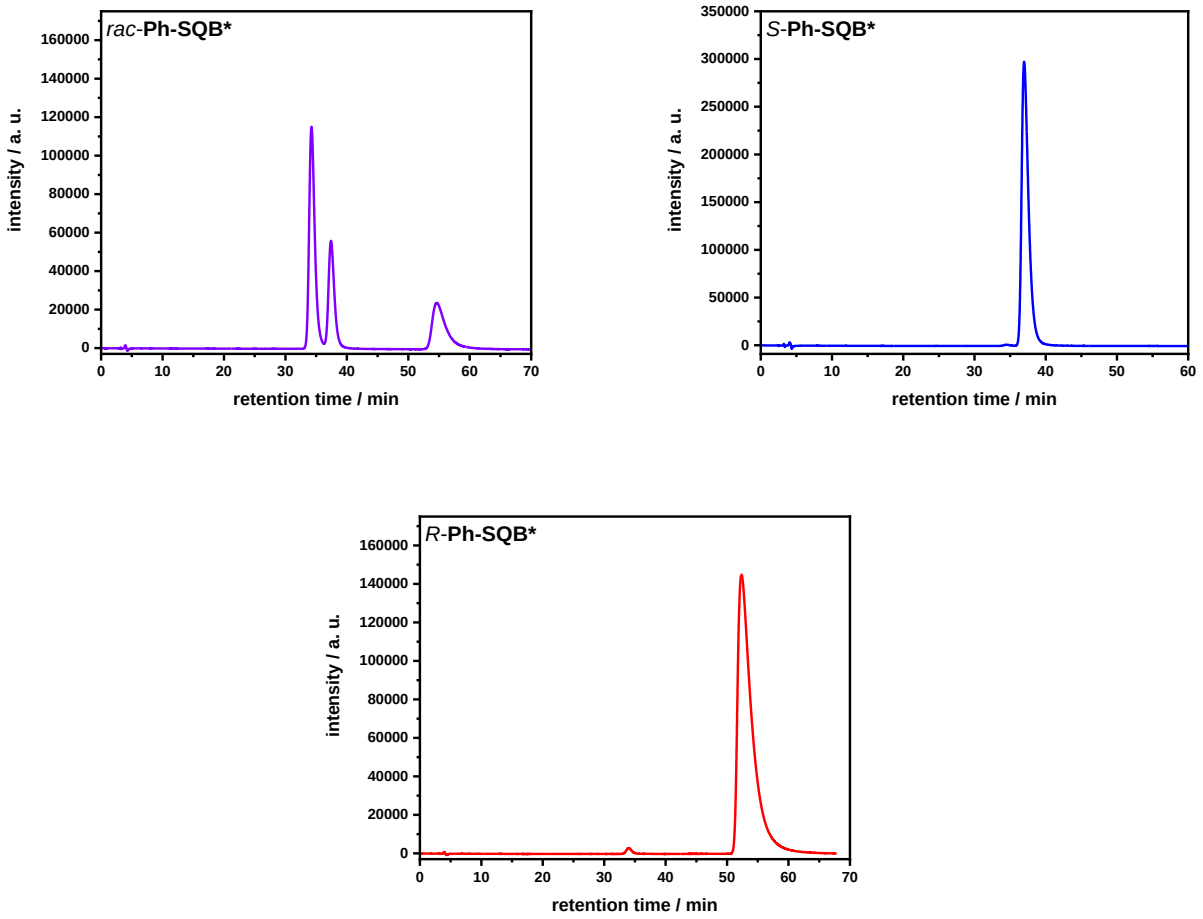

Figure 78. Analytical HPLC chromatograms of **Ph-SQB***.

Detection at 710 nm, eluent: *n*Hex/DCM/iPrOH 250:80:1, flow rate: 1 mL/min, Phenomenex® LUX iAmylose-3.

Table 23. Data obtained from analytical HPLC of **Ph-SQB*.**

	***t*(SS) / min**	***t*(RR) / min**	**t(RS) / min**	**%SS[a]**	**%RR[a]**	**%RS[a]**
S	37.0	-	34.5	99.7	-	0.3
R	-	52.3	34.0	-	99.4	0.6

[a] ratio of the area of the peak in the chromatogram to the sum of the areas of all relevant peaks.

Ph-SQA*

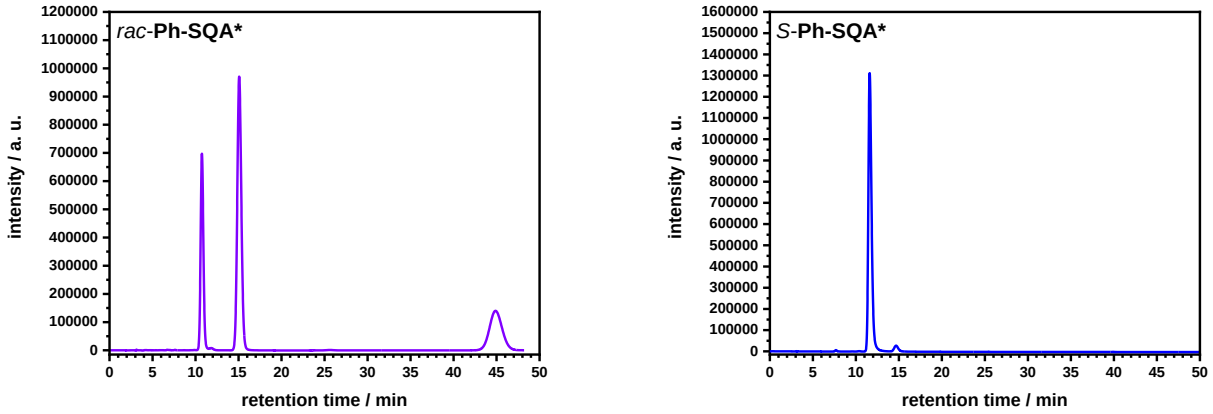

Figure 79. Analytical HPLC chromatograms of **Ph-SQA***.

Detection at 640 nm, eluent: EA/DCM 9:1, flow rate: 1 mL/min, Phenomenex® LUX iAmylose-3.

Table 24. Data obtained from analytical HPLC of **Ph-SQA*.**

	***t*(SS) / min**	***t*(RR) / min**	**t(RS) / min**	**%SS[a]**	**%RR[a]**	**%RS[a]**
S	10.7	-	15.1	97.5	-	2.5

[a] ratio of the area of the peak in the chromatogram to the sum of the areas of all relevant peaks.

Pr-SQB*

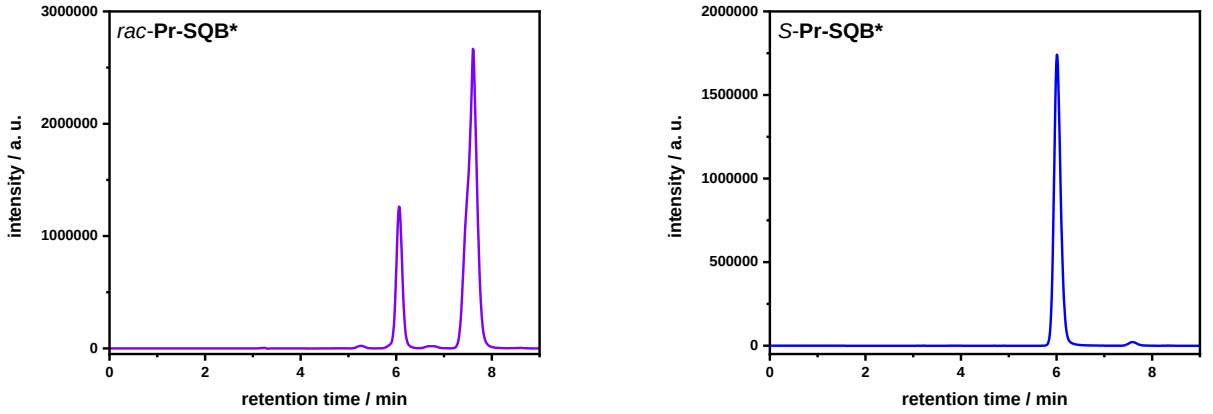

Figure 80. Analytical HPLC chromatograms of **Pr-SQB***.

Detection at 640 nm, eluent: *n*Hex/DCM/*i*PrOH 95:27:3, flow rate: 1 mL/min, Phenomenex® LUX iAmylose-3.

Table 25. Data obtained from analytical HPLC of **Pr-SQB*.**

	***t*(SS) / min**	***t*(RR) / min**	**t(RS) / min**	**%SS[a]**	**%RR[a]**	**%RS[a]**
S	6.0	-	7.6	98.5	-	1.5

[a] ratio of the area of the peak in the chromatogram to the sum of the areas of all relevant peaks.

Pr-SQA*

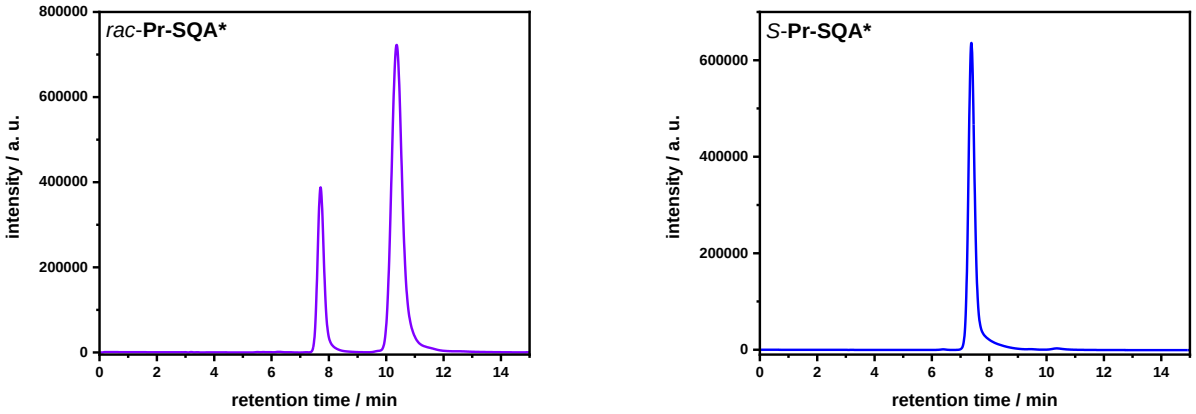

Figure 81. Analytical HPLC chromatograms of **Pr-SQB***.

Detection at 640 nm, eluent: EA/DCM 9:1, flow rate: 1 mL/min, Phenomenex® LUX iAmylose-3.

Table 26. Data obtained from analytical HPLC of **Pr-SQA*.**

	***t*(SS) / min**	***t*(RR) / min**	**t(RS) / min**	**%SS[a]**	**%RR[a]**	**%RS[a]**
S	7.4	-	10.4	99.3	-	0.7

[a] ratio of the area of the peak in the chromatogram to the sum of the areas of all relevant peaks.

Br_2-Ph-SQB*

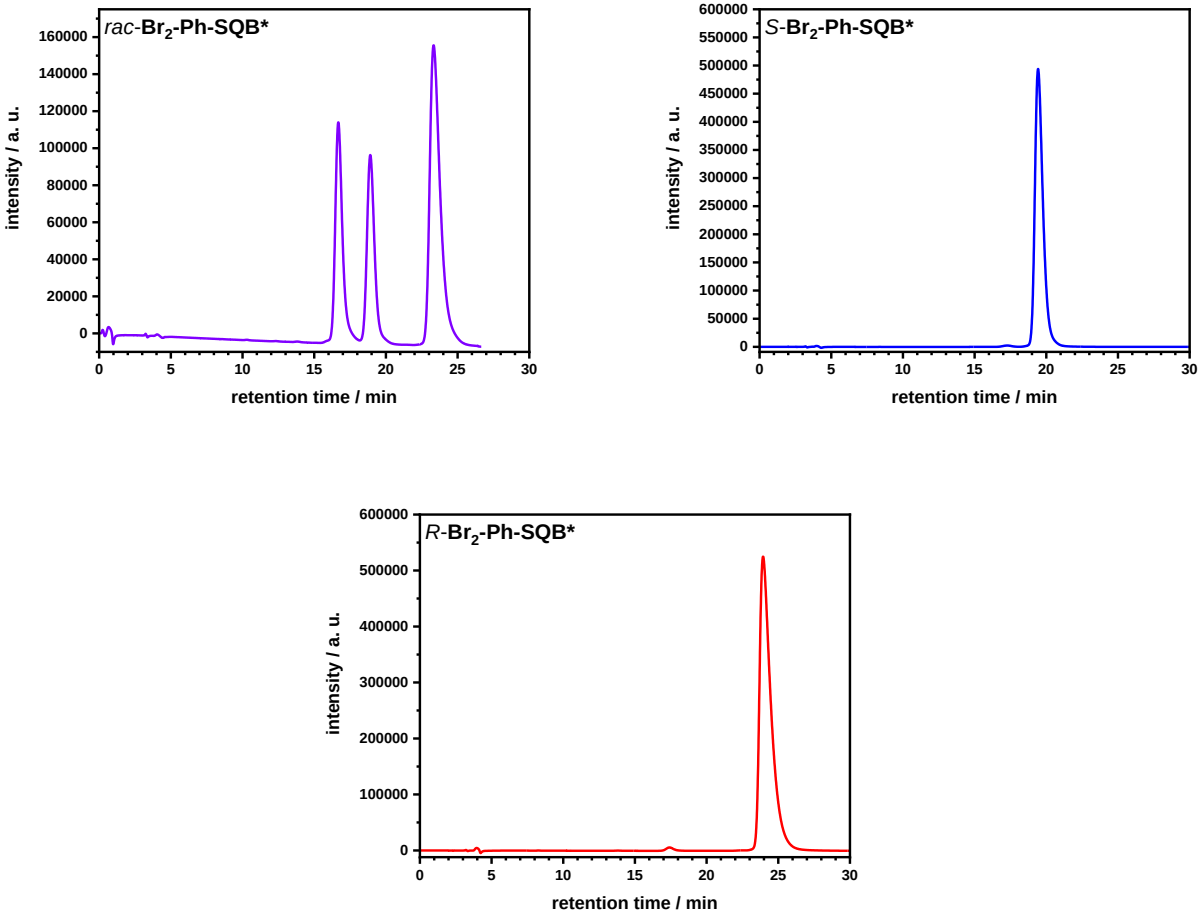

Figure 82. Analytical HPLC chromatograms of **Br_2-Ph-SQB***.

Detection at 720 nm, eluent: *n*Hex/DCM/iPrOH 250:80:1, flow rate: 1 mL/min, Phenomenex® LUX iAmylose-3. The diastereomeric mixture was prepared by mixing the individual diastereomers, which led to the intensity ratios being not representative.

Table 27. Data obtained from analytical HPLC of **Br_2-Ph-SQB*.**

	***t*(SS) / min**	***t*(RR) / min**	**t(RS) / min**	**%SS[a]**	**%RR[a]**	**%RS[a]**
S	19.4	-	17.3	99.5	-	0.5
R	-	23.9	17.4	-	99.5	0.5

[a] ratio of the area of the peak in the chromatogram to the sum of the areas of all relevant peaks.

Br_2-Pr-SQB*

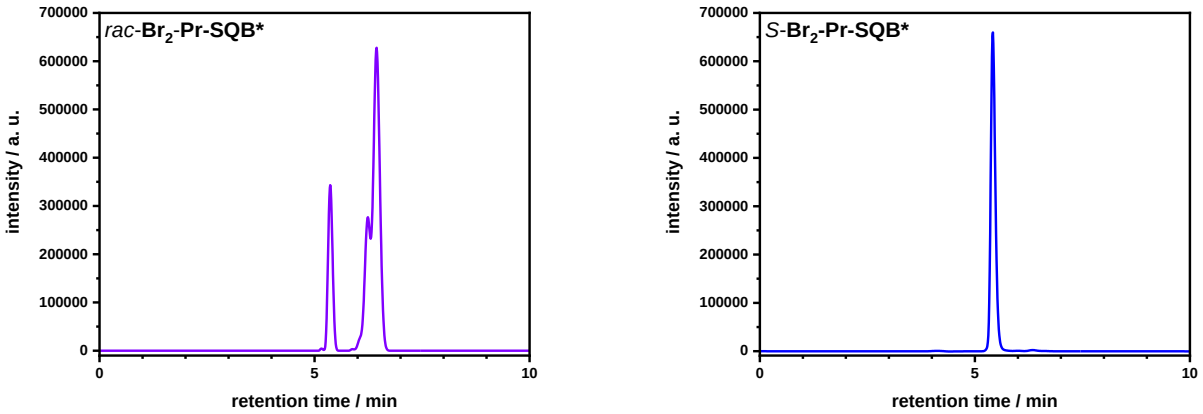

Figure 83. Analytical HPLC chromatograms of **Br_2-Pr-SQB*** used for the synthesis of **p(Pr-SQB*)**.

Detection at 665 nm, eluent: *n*Hex/DCM/iPrOH 40:9:1, flow rate: 1 mL/min, Phenomenex® LUX iAmylose-3.

Table 28. Data obtained from analytical HPLC of **Br_2-Pr-SQB*.**

	***t*(SS) / min**	***t*(RR) / min**	***t*(RS) / min**	**%SS[a]**	**%RR[a]**	**%RS[a]**
S	5.4	-	6.3	99.3	-	0.7

[a] ratio of the area of the peak in the chromatogram to the sum of the areas of all relevant peaks.

Br-SQB*-C6

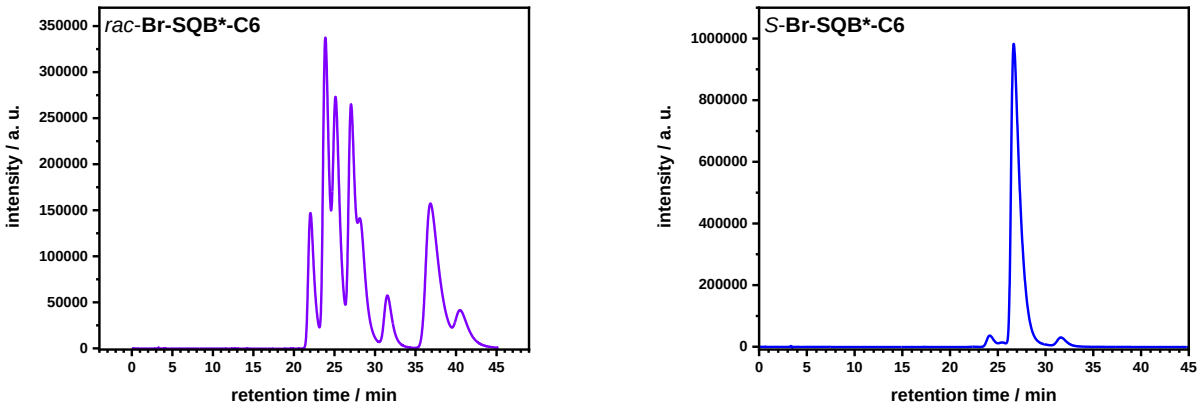

Figure 84. Analytical HPLC chromatograms of **Br-SQB*-C6**.

Detection at 715 nm, eluent: *n*Hex/DCM/iPrOH 250:80:1, flow rate: 1 mL/min, Phenomenex® LUX iAmylose-3. The diastereomeric mixture was obtained after column chromatography of *rac*-**Br-SQB*-C6** and contains impurities – mainly the dibrominated derivative. The relevant peaks were identified by their absorption spectra and intensity ratios.

Table 29. Data obtained from analytical HPLC of **Br-SQB*-C6.**

	***t*(SS) / min**	***t*(RR) / min**	***t*(RS) / min**	***t*(SR) / min**	**%SS[a]**	**%RR[a]**	**%RS[a]**	**%SR[a]**
S	26.7	-	24.2	-	96.7	-	3.3	-

[a] ratio of the area of the peak in the chromatogram to the sum of the areas of all relevant peaks.

Br-SQB*-C16

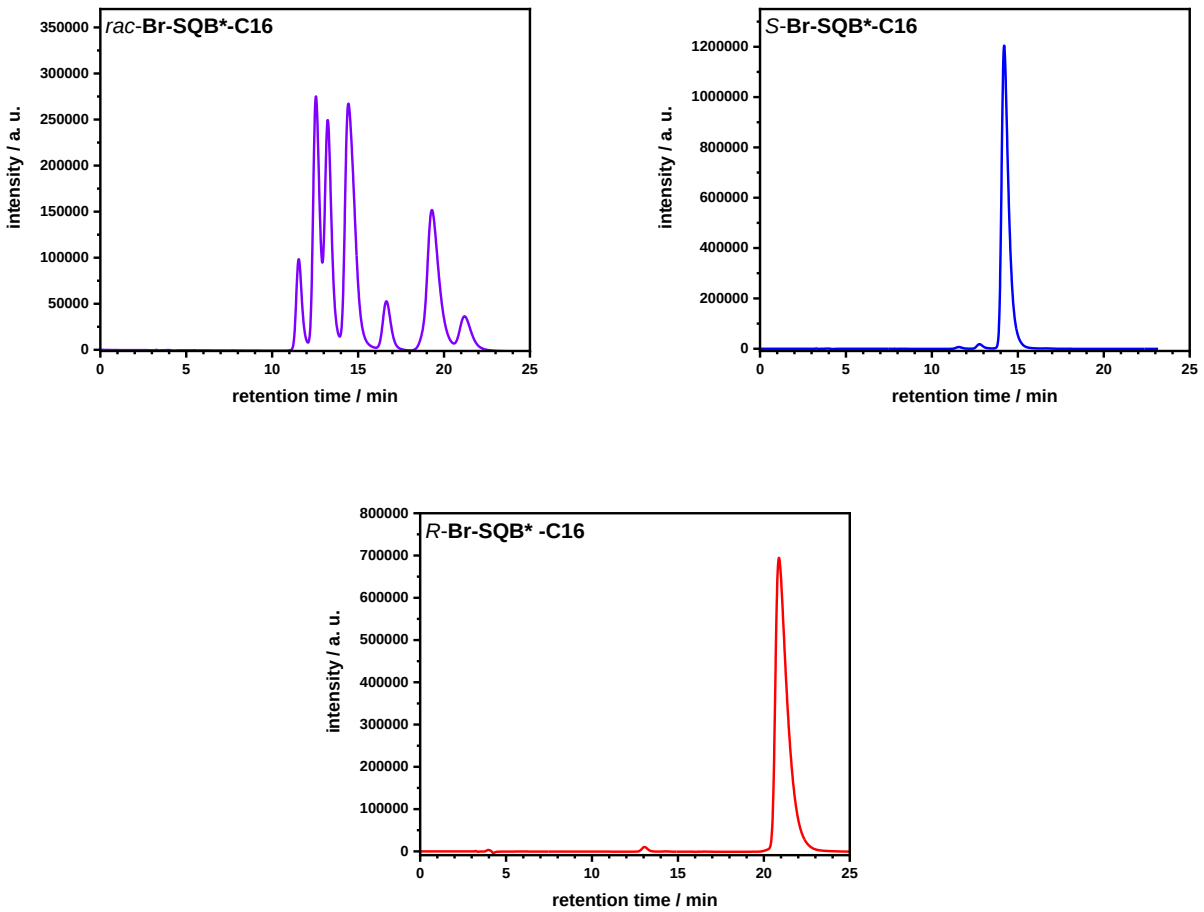

Figure 85. Analytical HPLC chromatograms of **Br-SQB*-C16**.

Detection at 715 nm, eluent: *n*Hex/DCM/iPrOH 250:80:1, flow rate: 1 mL/min, Phenomenex® LUX iAmylose-3. The diastereomeric mixture was obtained after column chromatography of *rac*-**Br-SQB*-C6** and contains impurities – mainly the dibrominated derivative. The relevant peaks were identified by their absorption spectra and intensity ratios.

Table 30. Data obtained from analytical HPLC of **Br-SQB*-C16.**

	***t*(SS) / min**	***t*(RR) / min**	***t*(RS) / min**	***t*(SR) / min**	**%SS[a]**	**%RR[a]**	**%RS[a]**	**%SR[a]**
S	14.2	-	12.7	-	98.8	-	1.2	-
R[b]	-	20.9	-	13.0	-	99.3	-	0.7

[a] ratio of the area of the peak in the chromatogram to the sum of the areas of all relevant peaks [b] slight deviation of retention times due to minor errors in the preparation of the eluent mixture.

11.1.2 Analytical GPC

11.1.2.1 Calibration curve

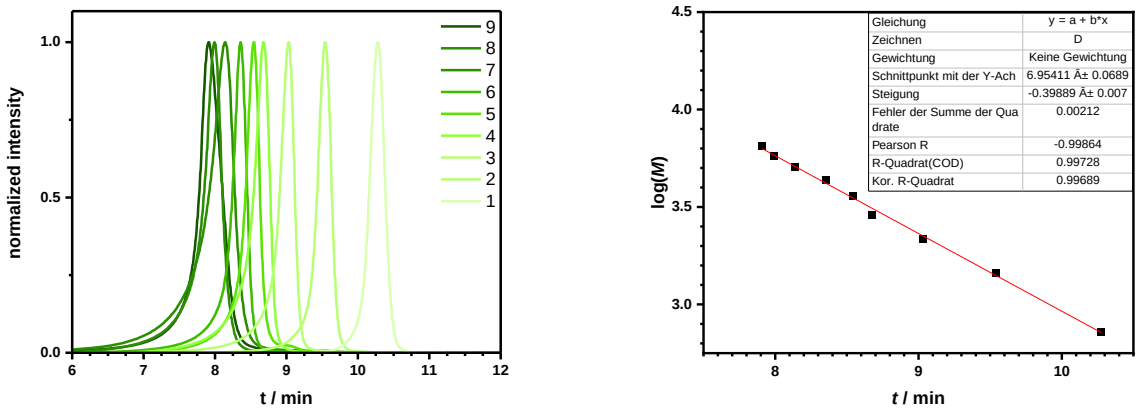

Figure 86. Left: Chromatograms of the series of defined squaraine oligomers **SQB$_{1\text{-}9}$**,[91] right: calibration curve obtained from the peak data.

Table 31. Peak data (retention time *t*, molecular weight *M*, number average molecular weight (polystyrene) M_n) of the series of defined squaraine oligomers.

	t **/ min**	***M*** **/ g mol^{-1}**	***M*$_n$**[a]
oSQ$_1$	10.275	725.08	716
oSQ$_2$	9.538	1448.14	1414
oSQ$_3$	9.028	2171.20	2278
oSQ$_4$	8.674	2894.26	3143
oSQ$_5$	8.542	3617.32	3544
oSQ$_6$	8.355	4340.38	4229
oSQ$_7$	8.137	5063.44	5180
oSQ$_8$	7.988	5786.50	5857
oSQ$_9$	7.909	6509.56	6285

[a] Number average molecular weight determined by referencing with a polystyrene standard.

11.1.2.2 Chromatograms and data

p(SQB-R^0)

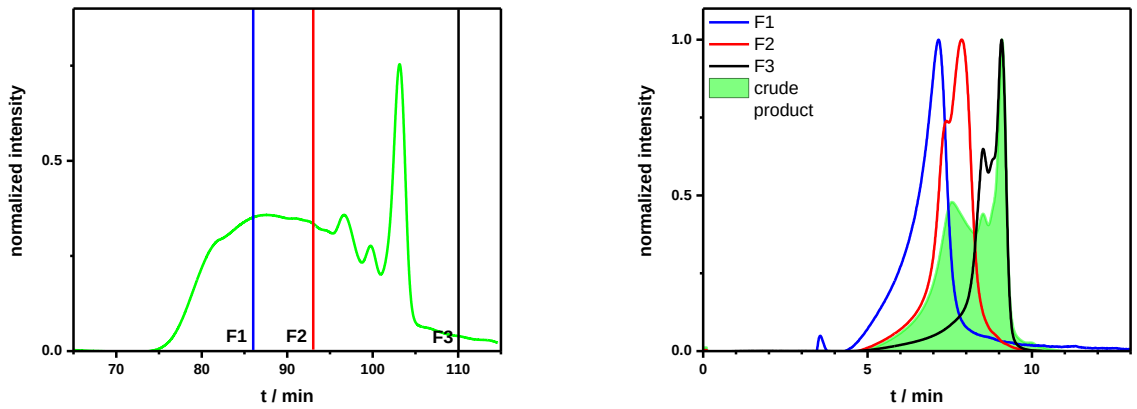

Figure 87. GPC of **p(SQB-R^0)**. Left: chromatogram of the preparative GPC run. Lines represent the time of fraction change. Right: chromatograms of the analytical GPC of the individual fractions and the crude product.

Table 32. Data obtained from analytical GPC of **p(SQB-R^0)**.

	X_n[a]	M_n	M_W	M_z	PDI[b]
Crude	5.5	3844	7873	19099	2.05
F1	22.8	15851	23269	39234	1.47
F2	10.9	7564	9495	13049	1.26
F3	4.1	2870	3440	4628	1.35

[a] M_n/M(monomer) [b] M_w/M_n

p(SQB-R^{1}*)

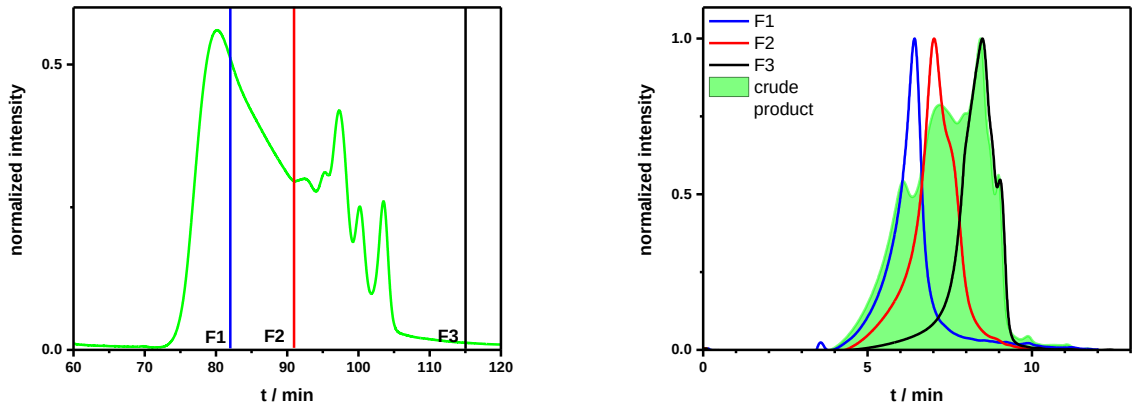

Figure 88. GPC of **p(SQB-R^{1}*)**. Left: chromatogram of the preparative GPC run. Lines represent the time of fraction change. Right: chromatograms of the analytical GPC of the individual fractions and the crude product.

Table 33. Data obtained from analytical GPC of **p(SQB-R^{1}*)**.

	X_n[a]	M_n	M_W	M_z	PDI[b]
Crude	9.8	7080	19054	50548	2.69
F1	38.5	27823	36315	52236	1.31
F2	16.1	11636	19271	37959	1.66
F3	5.2	3761	4345	5650	1.21

[a] M_n/M(monomer) [b] M_w/M_n

p(SQB-R^{2}*)

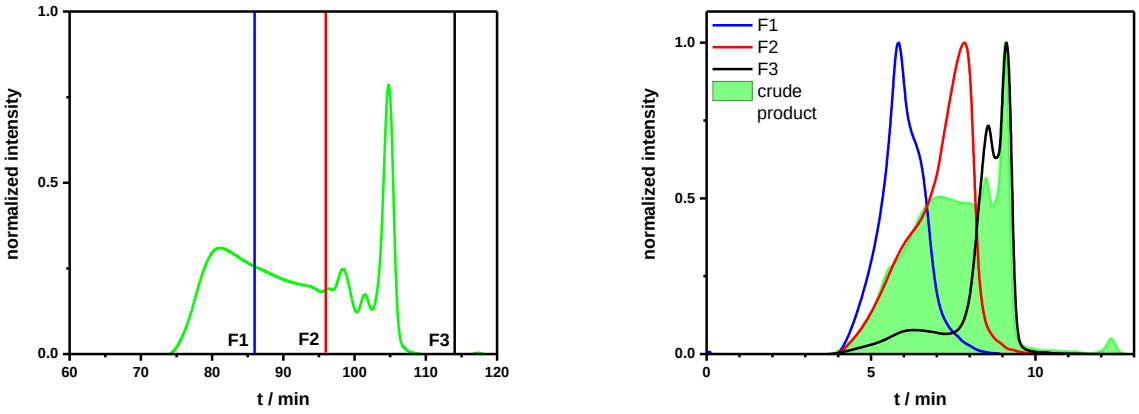

Figure 89 GPC of **p(SQB-R^{2}*)**. Left: chromatogram of the preparative GPC run. Lines represent the time of fraction change. Right: chromatograms of the analytical GPC of the individual fractions and the crude product.

Table 34. Data obtained from analytical GPC of **p(SQB-R²*)**.

	X_n[a]	M_n	M_W	M_z	PDI[b]
Crude	7.9	5684	18804	52876	3.31
F1	44.1	31875	47174	68821	1.48
F2	14.5	10481	22104	53442	2.11
F3	4.2	3052	6071	23677	1.99

[a] M_n/M(monomer) [b] M_w/M_n

p(SQB-R³*)

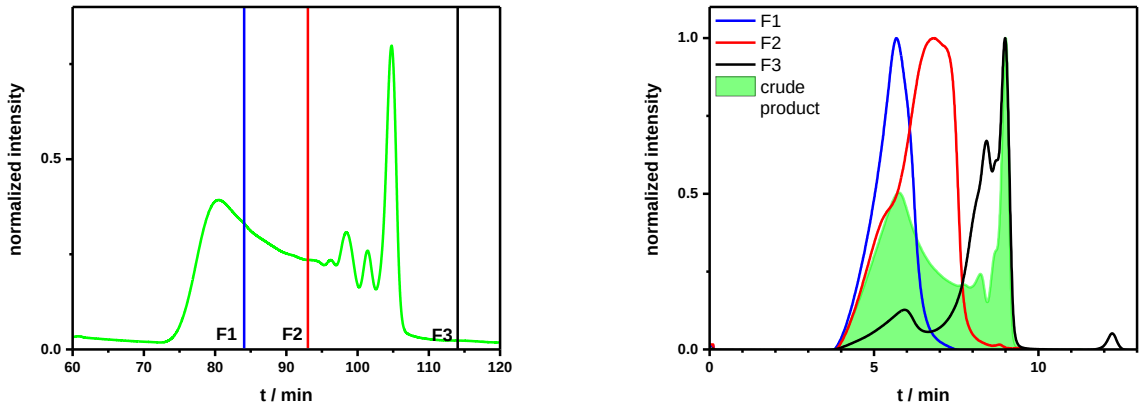

Figure 90. GPC of **p(SQB-R³*)**. Left: chromatogram of the preparative GPC run. Lines represent the time of fraction change. Right: chromatograms of the analytical GPC of the individual fractions and the crude product.

Table 35. Data obtained from analytical GPC of **p(SQB-R³*)**.

	X_n[a]	M_n	M_W	M_z	PDI[b]
Crude	10.1	7617	37059	85288	4.87
F1	65.3	49082	64425	86241	1.34
F2	27.3	20542	36193	68590	1.76
F3	5.3	4016	12051	54476	3.00

[a] M_n/M(monomer) [b] M_w/M_n

p(Pr-SQB*)

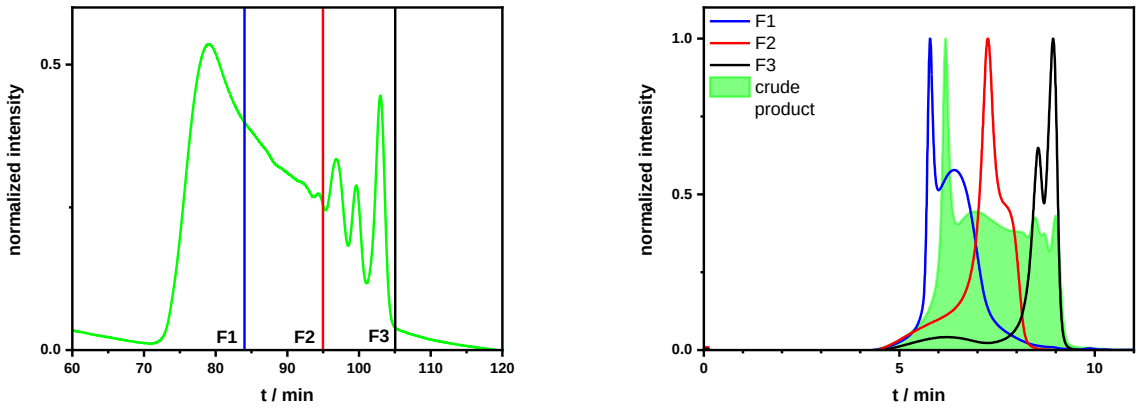

Figure 91. GPC of **p(Pr-SQB*)**. Left: chromatogram of the preparative GPC run. Lines represent the time of fraction change. Right: chromatograms of the analytical GPC of the individual fractions and the crude product.

Table 36. Data obtained from analytical GPC of **p(Pr-SQB*)**.

	X_n[a]	M_n	M_W	M_z	PDI[b]
Crude	9.5	7110	16008	29139	2.25
F1	32.4	24370	29710	34941	1.22
F2	14.6	10936	16148	31109	1.48
F3	4.3	3215	5636	21426	1.75

[a] M_n/M(monomer) [b] M_w/M_n

pSQB*

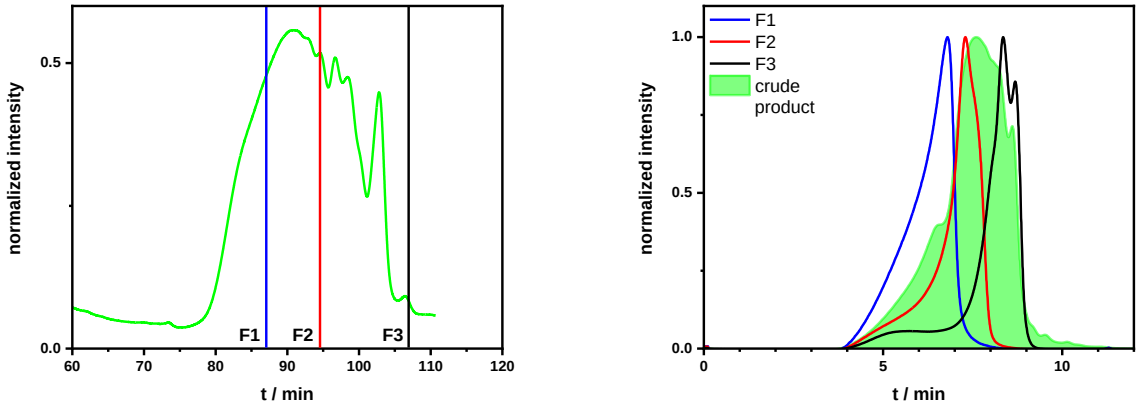

Figure 92. GPC of **pSQB***. Left: chromatogram of the preparative GPC run. Lines represent the time of fraction change. Right: chromatograms of the analytical GPC of the individual fractions and the crude product.

Table 37. Data obtained from analytical GPC of **pSQB***.

	X_n[a]	M_n	M_W	M_z	PDI[b]
Crude	7.1	7173	15245	41375	2.13
F1	26.0	26357	39344	66314	1.49
F2	12.6	12753	21740	53594	1.70
F3	4.7	4741	10618	49234	2.24

[a] M_n/M(monomer) [b] M_w/M_n

p(SQA-SQB*)

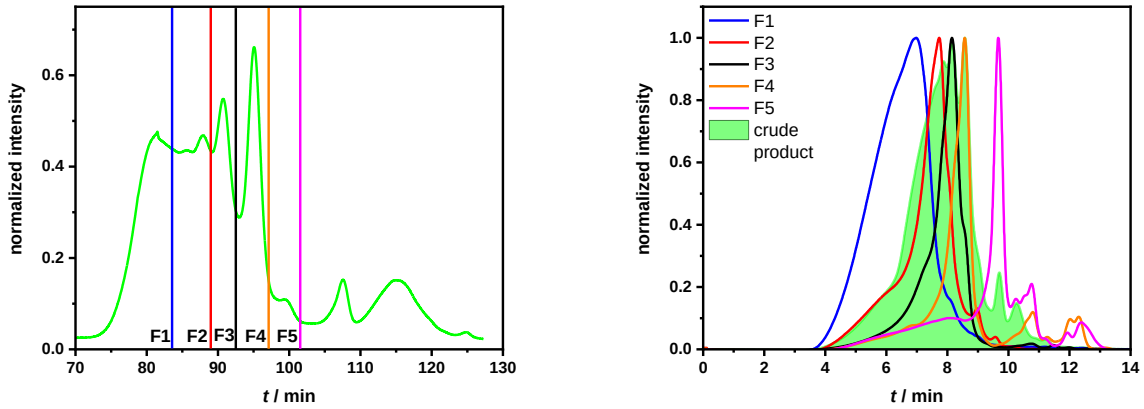

Figure 93. GPC of **p(SQA-SQB*)**. Left: chromatogram of the preparative GPC run. Lines represent the time of fraction change. Right: chromatograms of the analytical GPC of the individual fractions and the crude product.

Table 38. Data obtained from analytical GPC of **p(SQA-SQB*)**.

	X_n[a]	M_n	M_W	M_z	PDI[b]
Crude	2.4	4474	11698	33469	2.61
F1	9.5	17746	35530	69762	2.00
F2	4.8	8862	17556	46142	1.98
F3	3.3	6042	9766	24894	1.62
F4	2.4	4373	6848	18130	1.57
F5	0.7	1345	1884	8032	1.40

[a] M_n/M(monomer) [b] M_w/M_n

p(SQB-SQB*)

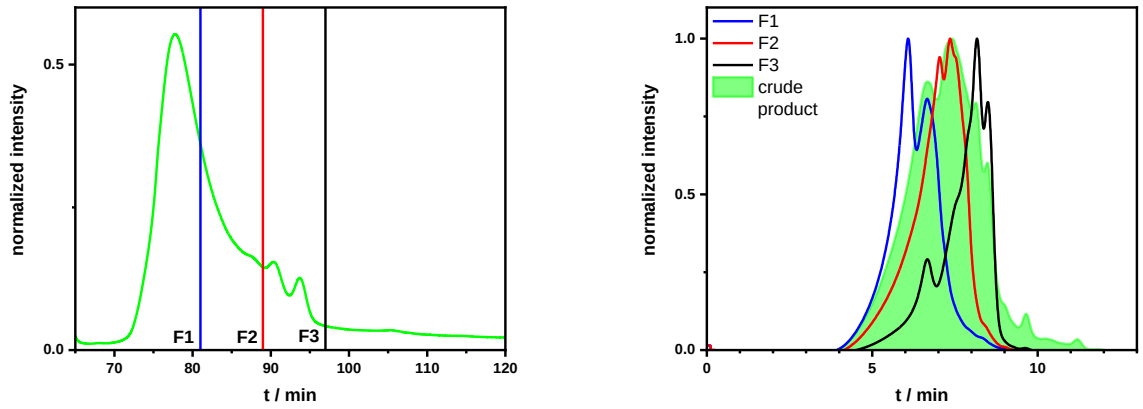

Figure 94. GPC of **p(SQB-SQB*)**. Left: chromatogram of the preparative GPC run. Lines represent the time of fraction change. Right: chromatograms of the analytical GPC of the individual fractions and the crude product.

Table 39. Data obtained from analytical GPC of **p(SQB-SQB*)**.

	X_n[a]	M_n	M_W	M_z	PDI[b]
Crude	4.7	8876	20338	46656	2.29
F1	12.0	22876	35106	54358	1.53
F2	6.5	12452	21257	43957	1.71
F3	3.3	6222	10395	22676	1.67

[a] M_n/M(monomer) [b] M_w/M_n

11.2 Additional equations

Beer-Lambert law[13, 320]

$$OD = -\log T = \log\frac{I}{I_0} = \varepsilon c d \tag{71}$$

$$\varepsilon = \frac{N_A}{2303}\frac{u}{I} \tag{72}$$

Where *OD* is the absorbance, I is the intensity measured after passing through the sample, I_0 the intensity of the incident light, *T* the transmittance, *c* the concentration, *d* the path length of the sample, ε the molar extinction coefficient, N_A Avogadro's constant, and *u* the absorption rate.

Radiation intensity[13]

$$I = \frac{cnE_0^2}{8\pi} = \frac{cH_0E_0}{8\pi} = c\frac{H_0^2}{n8\pi} \tag{73}$$

Where *I* is the intensity, *c* the speed of light in vacuum, *n* the refractive index, E_0 the electric field strength, and H_0 the magnetic field strength.

Calculation of transition moments and rotatory strengths by integration of spectral bands

The following equations were used to calculate the transition moment μ_{eg}^2[321] and rotatory strength R_{eg}[13]:

$$\mu_{\mathrm{eg}}^2 = \frac{3hc\varepsilon_0}{2000\pi^2}\frac{\ln(10)}{N_{\mathrm{A}}}\frac{9n}{(n^2+2)^2}\int\frac{\varepsilon(\tilde{\nu})}{\tilde{\nu}}\mathrm{d}\tilde{\nu} \tag{74}$$

$$R_{eg} = \frac{3(2303)\hbar c}{16\pi^2 N_{\mathrm{A}}}\int\frac{\Delta\varepsilon(\tilde{\nu})}{\tilde{\nu}}\mathrm{d}\tilde{\nu} \tag{75}$$

Where *h* is Planck's constant, $\hbar$ is the reduced Planck's constant, *c* is the speed of light in vacuum, ε_0 is the vacuum permittivity, N_{A} is Avogadro's constant, *n* is the refractive index of the solvent, $\tilde{\nu}$ is the wavenumber, $\varepsilon(\tilde{\nu})$ is the absorption coefficient dependent on the wavenumber (absorption spectrum) and $\varepsilon(\tilde{\nu})$ the difference of the absorption coefficient of left and right circularly polarized light dependent on the wavenumber (CD spectrum).

Gibbs-Helmholtz equation[322]

$$\Delta G = \Delta H - T\Delta S \tag{76}$$

Where ΔG is the change in Gibbs free energy, ΔH the change of enthalpy, T the temperature and ΔS the change of entropy.

Intensity-weighed mean fluorescence lifetime[323]

$$\bar{\tau}_{\mathrm{fl}} = \frac{\sum a_{\mathrm{i}}\tau_{\mathrm{i}}^2}{\sum a_{\mathrm{i}}\tau_{\mathrm{i}}} \tag{77}$$

Where $\bar{\tau}_{\mathrm{fl}}$ is the intensity-weighed mean fluorescence lifetime, a_{i} the amplitude of component i and τ_{i} the lifetime component i.

11.3 X-ray crystallography

11.3.1 C(3)-chiral squaraine monomers

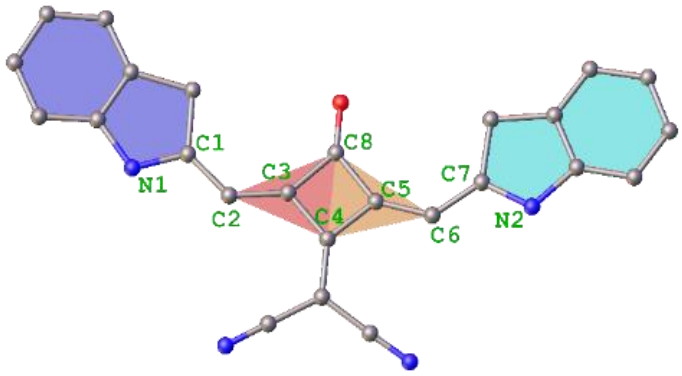

Figure 95. General structure with the numbered polymethine chain N1-C(1-7)-N2. Selected planes I_1 and I_2 (indolenine rings), and A_1 and A_2 (one half of the central squaric acid moiety) are marked in color.

Table 40. Bond lengths of the polymethine chains of various indolenine squaraines.

	N1-C1/ Å	C1-C2/ Å	C2-C3/ Å	C3-C4/ Å	C4-C5/ Å	C5-C6/ Å	C6-C7/ Å	C7-N2/ Å
SQB[324]	1.351	1.389	1.386	1.439	1.433	1.399	1.379	1.360
Pr-SQB*	1.367	1.383	1.404	1.439	1.453	1.383	1.405	1.348
SQA-C4[253]	1.365	1.382	1.398	1.468	1.483	1.404	1.384	1.366
SQA-C6[254]	1.361	1.384	1.390	1.464	1.474	1.390	1.384	1.361
SQA-C8[255]	1.352	1.379	1.399	1.464	1.466	1.399	1.379	1.352
Pr-SQA*	1.368	1.379	1.399	1.458	1.482	1.396	1.384	1.358
Ph-SQB* Crystal	1.353	1.392	1.385	1.439	1.437	1.394	1.375	1.362
Ph-SQB* Calcd	1.370	1.388	1.400	1.451	1.451	1.400	1.388	1.370
Ph-SQA* Calcd	1.375	1.382	1.402	1.474	1.479	1.402	1.382	1.375
TPh-SQB[90]	1.303	1.429	1.365	1.435	1.424	1.396	1.395	1.339

11.3.2 Dibrominated monomers with chiral side chains

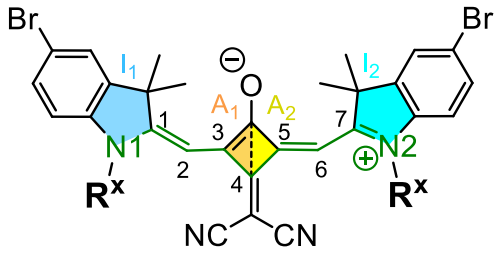

Figure 96. General monomer structure with the polymethine chain N1-C(1-7)-N2 marked in green. Selected planes I_1 and I_2 (indolenine rings), and A_1 and A_2 (one half of the central squaric acid moiety) are marked in color.

Table 41. Bond lengths of the polymethine chain of the dibrominated squaraine monomers.

	N1-C1 / Å	C1-C2 / Å	C2-C3 / Å	C3-C4 / Å	C4-C5 / Å	C5-C6 / Å	C6-C7 / Å	C7-N2 / Å
Br_2-mSQ-R^0	1.36	1.39	1.40	1.45	1.44	1.40	1.39	1.37
Br_2-mSQ-R^{1*}	1.36	1.39	1.39	1.45	1.45	1.40	1.39	1.36
Br_2-mSQ-R^{2*}	1.37	1.39	1.40	1.44	1.44	1.40	1.38	1.37
Br_2-mSQ-R^{3*}	1.36	1.39	1.40	1.44	1.44	1.40	1.39	1.36

Table 42. Bond angles around the atoms of the polymethine chain of the dibrominated squaraine monomers.

	N1-C1-C2	C1-C2-C3	C2-C3-C4	C3-C4-C5	C4-C5-C6	C5-C6-C7	C6-C7-N2
Br_2-mSQ-R^0	120.6°	132.0°	128.0°	92.5°	128.1°	132.2°	120.5°
Br_2-mSQ-R^{1*}	120.7°	133.0°	128.4°	92.6°	127.6°	130.7°	121.0°
Br_2-mSQ-R^{2*}	121.5°	132.4°	128.1°	92.6°	128.2°	132.7°	121.4°
Br_2-mSQ-R^{3*}	121.2°	131.3°	129.3°	92.7°	129.3°	131.3°	121.2°

Table 43. Plain dihedral angles in the dibrominated squaraine monomers.

	I_1-A_1	I_2-A_2	A_1-A_2	I_1-I_2
Br_2-mSQ-R^0	7.7°	4.6°	4.2°	16.1°
Br_2-mSQ-R^1*	15.2°	13.1°	4.6°	29.0°
Br_2-mSQ-R^2*	10.7°	3.1°	5.1°	16.5°
Br_2-mSQ-R^3*	7.2°	7.2°	0.0°	13.4°

11.4 NOESY-NMR spectroscopy of Ph-SQA*

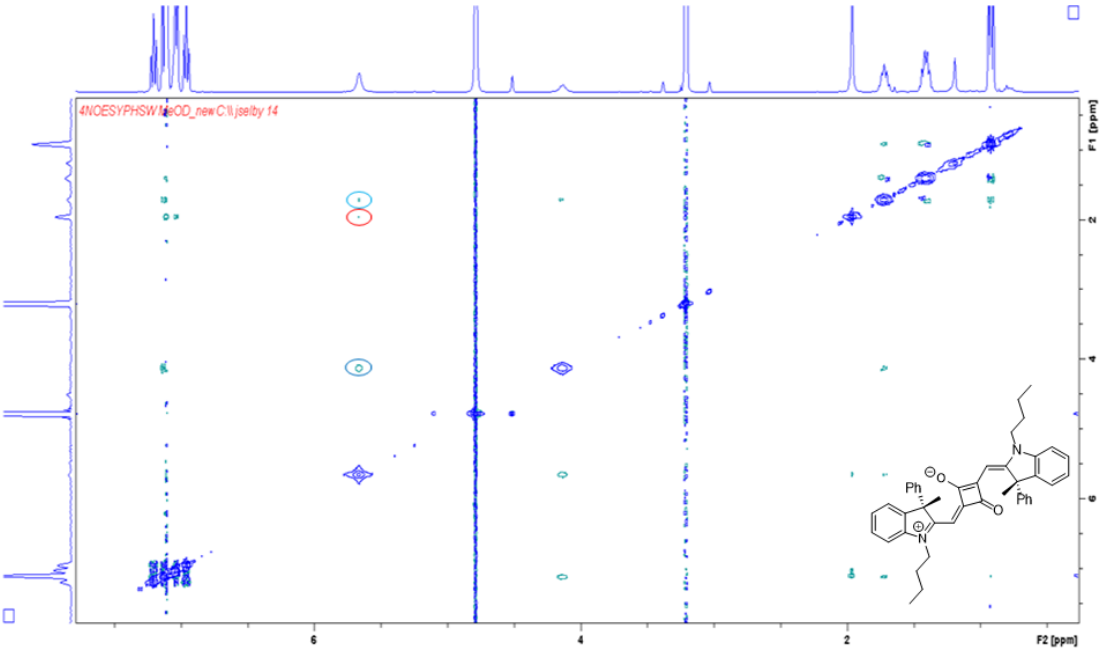

Figure 97. Full NOESY-NMR spectrum of **Ph-SQA*** (400 MHz, methanol-d_5, mixing time = 0.6 s).

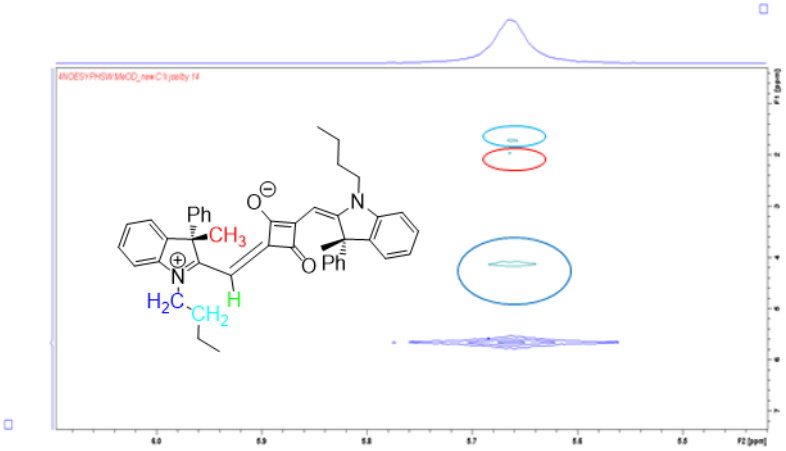

Figure 98. Magnified section of the NOESY-spectrum of **Ph-SQA*** showing the cross peaks of the methine proton (green) with the methyl group at C(3) (red), as well as the first (dark blue) and second (light blue) methylene groups of the alkyl side chain.

The proton distances were calculated using the following equation:[325]

$$d = d_{\mathrm{ref}}\left(\frac{a_{\mathrm{ref}}}{a}\right) \tag{78}$$

Where d is the distance between two protons, d_{ref} is the reference distance, a_{ref} the relative integral of the reference NOESY cross signal and a the relative integral of the NOESY cross signal corresponding to the proton distance to be determined.

Table 44. Atom distances in the crystal structure and the DFT-optimized structure of Ph-SQB*, relative NOESY cross-signal intensities and calculated atom distances using eq.(78).

	d(**Ph-SQB*** cryst) / Å	*d*(**Ph-SQB*** calcd) / Å	Rel. Integral NOESY	*d*(**Ph-SQA***)$_{\mathrm{NOESY}}$ / Å
H - CH_3	3.87	4.23	0.1438	3.08
H - CH_2	2.07	2.18	1.0000	2.13*
H - CH_2	2.51	-	0.2414	2.69

* used as the reference distance (average of crystal structure and calculated structure)

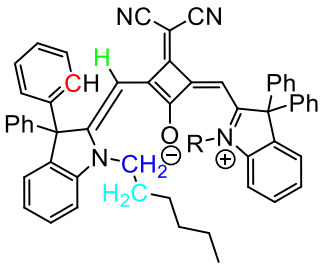

Figure 99. Structure of **TPh-SQB** with the relevant protons marked in color.

Table 45. Atom distances in the crystal structure of **TPh-SQB.**

	d (**TPh-SQB** cryst) / Å
H - CH	2.75, 3.85*
H - CH_2	3.83
H - CH_2	3.49

*because of structural torsion, different values were obtained for the carbon atoms of the phenyl groups.

For the evaluation of proton distances, the bridge methine group (green in Figure 98 and Figure 99) was chosen as the main reference point. As can be seen in Table 44, the calculated proton distances using eq. (78 match the distances in the crystal structure and the DFT-optimized structure for **Ph-SQB*** (which is known to have the expected geometry) quite well for the first two methylene groups of the alkyl side chain. Also, the NOESY data indicates that the distance of the methyl group protons at the 3-position is significantly larger than that of the aforementioned alkyl chain portons, which is also true for both of the **Ph-SQB*** structures. When examining the data from the crystal structure of **TPh-SQB** (Table 45), it can be seen that the distances of the alkyl chain protons are markedly larger than those in **Ph-SQB***. Also, the distances of the phenyl group (attached at C(3)) carbon atoms are roughly the same or even shorter compared to the first two methylene groups of the alkyl chain. It can be therefore concluded that **Ph-SQA*** possesses the same standard squaraine geometry.

11.5 Supporting spectra

11.5.1 C(3)-chiral squaraine monomers

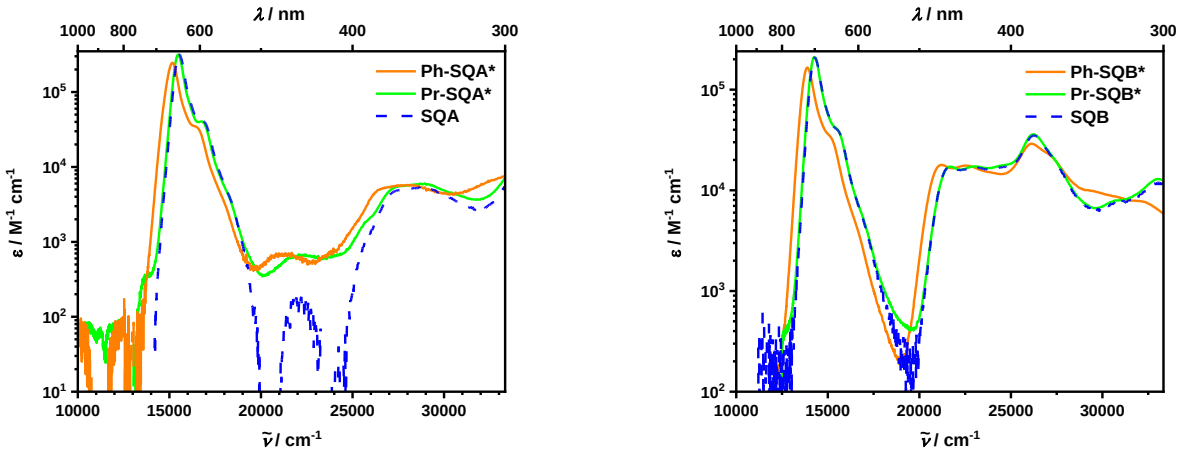

Figure 100. Full range (1000-300 nm) logarithmic plots of the UV-Vis-NIR spectra of the SQA- (left) **Pr-SQA*** and **Ph-SQA*,** and SQB-type squaraines (right) **Pr-SQB*** and **Ph-SQB*** in toluene.

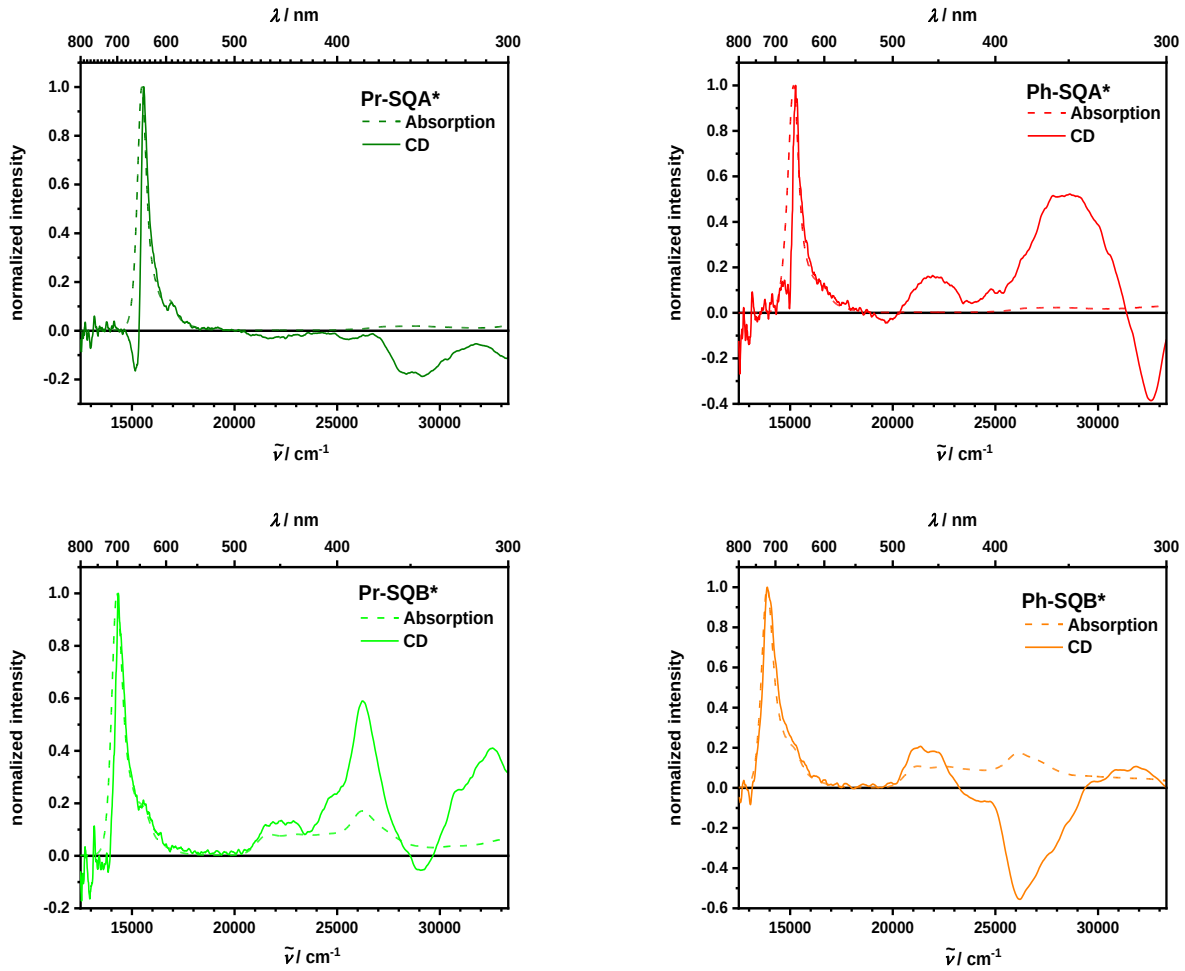

Figure 101. Normalized absorption and CD spectra of **Pr-SQA***, **Ph-SQA***, **Pr-SQB*** and **Ph-SQB*** in toluene. Top: SQA-type squaraines, bottom: SQB-type squaraines; left: propyl-substituted derivatives, right: phenyl-substituted derivatives.

11.5.2 SQB polymers bearing chiral side chains

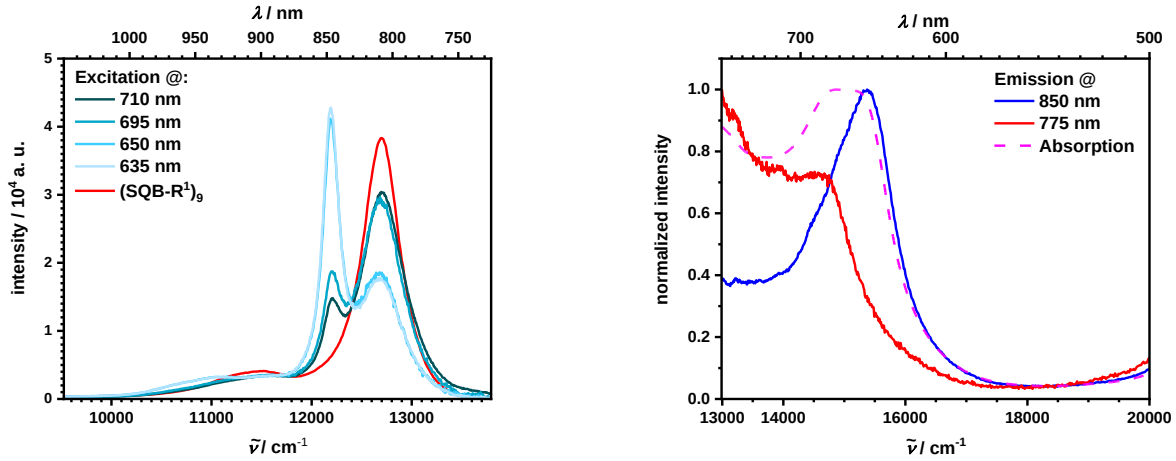

Figure 102. Left: Emission spectra of **p(SQB-R^1*)** at different excitation wavelengths compared to the emission spectrum of **(SQB-R^1)$_9$**.[91] Right: normalized excitation spectra and absorption spectrum of **p(SQB-R^1*)** in toluene.

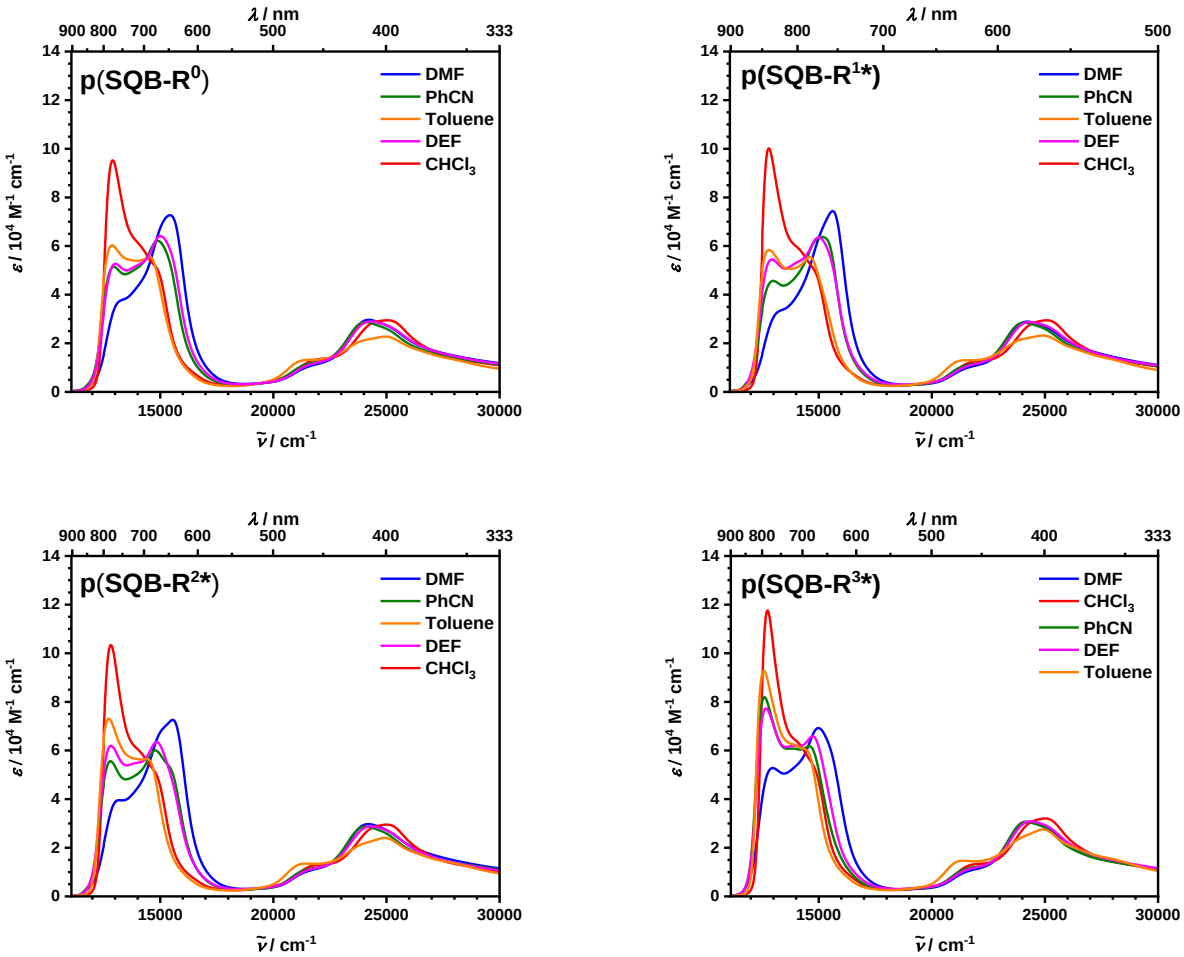

Figure 103. Full range UV-Vis-NIR absorption spectra of **p(SQB-R⁰)**, **p(SQB-R¹*)**, **p(SQB-R²*)** and **p(SQB-R³*)** (F2) in various solvents. Absorption coefficients are reported per monomer unit.

Table 46. Optical spectroscopic data (absorption maxima $\tilde{\nu}_{abs}$, extinction coefficients ε_{max}, squared transition moments μ_{eg}) of the F2 fractions of the squaraine polymers.

		$\tilde{\nu}_{abs}$ (λ_{abs})[a] / cm^{-1} (/ nm)	ε_{max}[a b] / M^{-1} cm^{-1}	μ_{eg}^2[b c] / D^2
p(SQB-R⁰) F2	$CHCl_3$	12 900 (776)	9.52×10^4	111.3
	toluene	12 900 (777)	6.03×10^4	90.1
	DEF	15 000 (666)	6.41×10^4	109.7
	PhCN	14 900 (672)	6.22×10^4	98.4
	DMF	15 400 (648)	7.27×10^4	104.1
p(SQB-R¹*) F2	$CHCl_3$	12 800 (782)	1.00×10^5	113.4
	toluene	12 800 (781)	5.84×10^4	93.0
	DEF	15 000 (667)	6.35×10^4	113.1
	PhCN	15 200 (660)	6.37×10^4	98.0

	DMF	15 600 (641)	7.44×10^4	102.5
	$CHCl_3$	12 800 (781)	1.03×10^5	115.3
	toluene	12 700 (786)	7.31×10^4	97.3
p(SQB-R²*) F2	DEF	14 800 (674)	6.35×10^4	116.5
	PhCN	14 800 (677)	6.01×10^4	102.3
	DMF	15 500 (644)	3.72×10^4	110.2
	$CHCl_3$	12 700 (785)	1.18×10^5	126.1
	toluene	12 600 (795)	9.28×10^4	113.6
p(SQB-R³*) F2	DEF	12 700 (790)	7.73×10^4	128.1
	PhCN	12 600 (794)	8.19×10^4	114.7
	DMF	15 000 (668)	6.92×10^4	119.6

[a] values for global maximum. [b] values per monomer unit [c] determined by integration of the main absorption band and calculated using eq. (75).

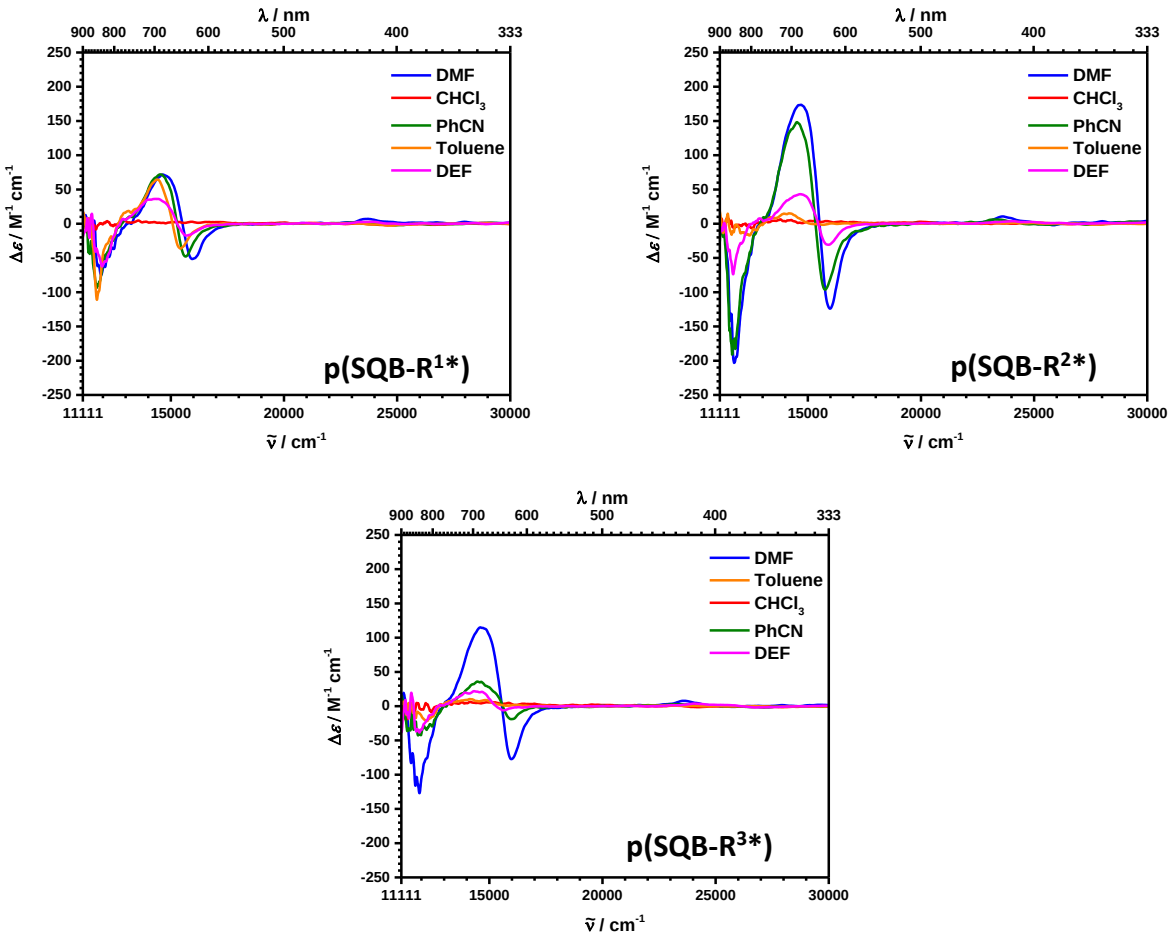

Figure 104. Full range CD spectra of **p(SQB-R⁰)**, **p(SQB-R¹*)**, **p(SQB-R²*)** and **p(SQB-R³*)** (F2) in various solvents. Values for Δε are reported per monomer unit.

Table 47. Temperature dependent spectroscopic data (temperature T, absorption maxima $\tilde{\nu}_{abs}$, extinction coefficients ε_{max}, squared transition moments per monomer μ_{eg}^2) of **p(SQB-R⁰)**, **p(SQB-R¹*)**, **p(SQB-R²*)** and **p(SQB-R³*)** in benzonitrile.

	T / °C	$\tilde{\nu}_{abs}$ (λ_{abs}) / cm^{-1} (/ nm)	ε_{max} / M^{-1} cm^{-1}	$\mu_{eg}^{2\,a}$ / D²
p(SQB-R⁰)	-5	15 400 (648)	4.99×10^4	63.2
	160	12 700 (788)	4.92×10^4	69.3
p(SQB-R¹*)	-5	15 500 (646)	7.72×10^4	91.9
	150	12 600 (792)	7.53×10^4	104.1
p(SQB-R²*)	-5	15 600 (639)	7.32×10^4	87.5
	110	12 600 (796)	7.38×10^4	97.3
p(SQB-R³*)	-10	15 700 (637)	7.31×10^4	103.9
	35	12 500 (799)	8.78×10^4	117.0

[a] determined by integration of the main absorption band and calculated using eq. (74). The refractive index of PhCN at RT was used for the calculation.

Table 48. Exact wavenumbers and wavelengths of the corresponding values used for the fits of the temperature dependent data. The values are those of the respective band at the lowest measured temperature.

	$\tilde{\nu}_{abs}$ (λ_{abs}) [1] / cm^{-1} (/ nm)	$\tilde{\nu}_{CD}$ (λ_{CD}) [2] / cm^{-1} (/ nm)	$\tilde{\nu}_{abs}$ (λ_{abs}) [3] / cm^{-1} (/ nm)
p(SQB-R⁰)	15 440 (647.5)	-	-
p(SQB-R¹*)	15 490 (645.5)	PhCN 15 710 (636.5) DMF 16 140 (619.5)	PhCN 15 410 (649.0) DMF 15 740 (635.5)
p(SQB-R²*)	15 640 (639.5)	PhCN 15 910 (628.5) DMF 16 120 (620.0)	PhCN 15 560 (642.5) DMF 15 770 (634.0)
p(SQB-R³*)	15 710 (636.5)	PhCN 15 960 (626.5) DMF 11 660 (857.5)	PhCN 15 630 (640.0) DMF 15 580 (642.0)

[1] Temperature dependent UV-Vis-NIR absorption spectroscopy (Figure 49 and Figure 50, Agilent Technologies Cary 5000) [2] Temperature dependent CD spectroscopy (CD values, Figure 52 and Figure 53, Jasco J-800) [3] Temperature dependent CD spectroscopy (Absorption coefficients values, Figure 53 and Figure 105, Jasco J-800).

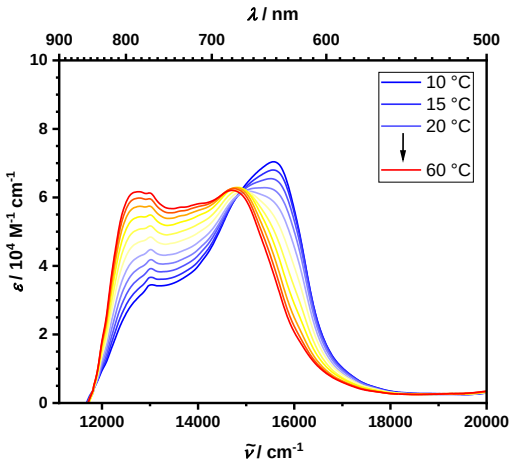

Figure 105. Temperature dependent absorption spectra in DMF of **p(SQB-R^{3}*)** recorded on a Jasco-810 CD spectrometer. Absorption coefficient reported per monomer unit.

11.5.3 SQA-SQB cooligo- and polymers*

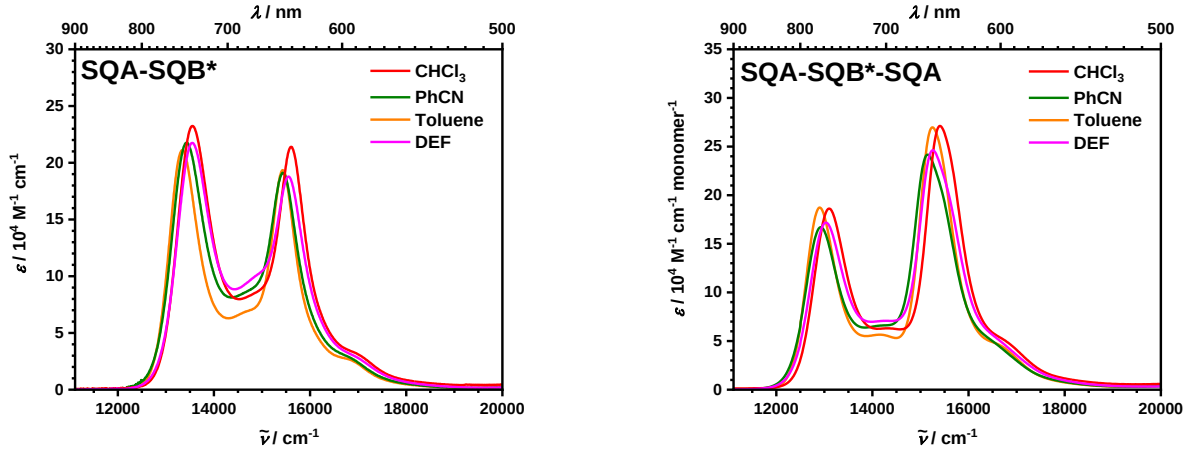

Figure 106. Absorption spectra of **SQA-SQB*** (left) and **SQA-SQB*-SQA** (right) in various solvents.

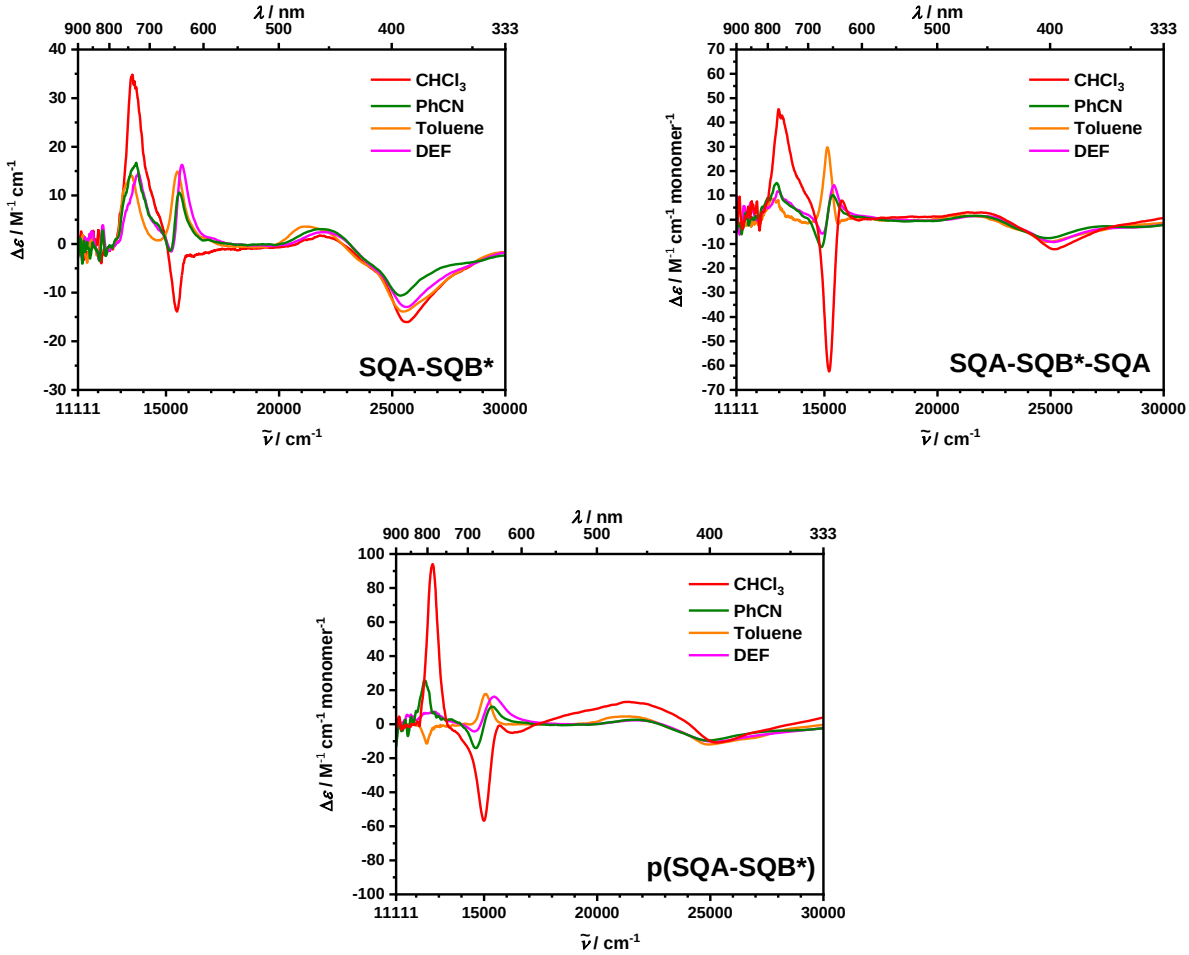

Figure 107. CD spectra (*S*-enantiomers) of **SQA-SQB*** (left), **SQA-SQB*-SQA** (right) and **p(SQA-SQB*)** in various solvents.

11.5.4 SQB-type (co)oligo- and polymers

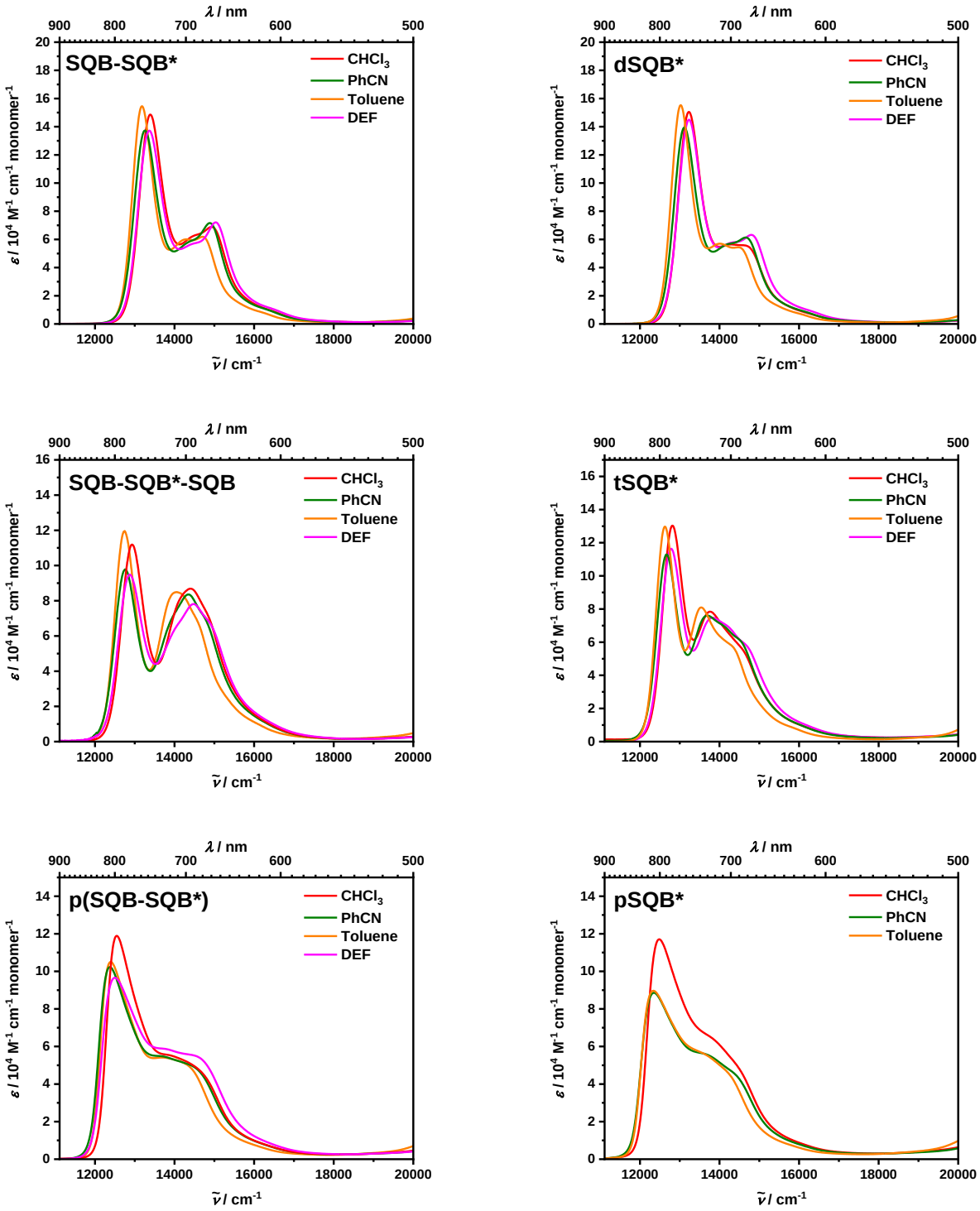

Figure 108. Absorption spectra of **SQB-SQB*** (upper left), **SQB-SQB*-SQB** (middle left), **p(SQB-SQB*)** (lower left)**, dSQB*** (upper right)**, tSQB*** (middle right) and **pSQB*** (lower right) in various solvents.

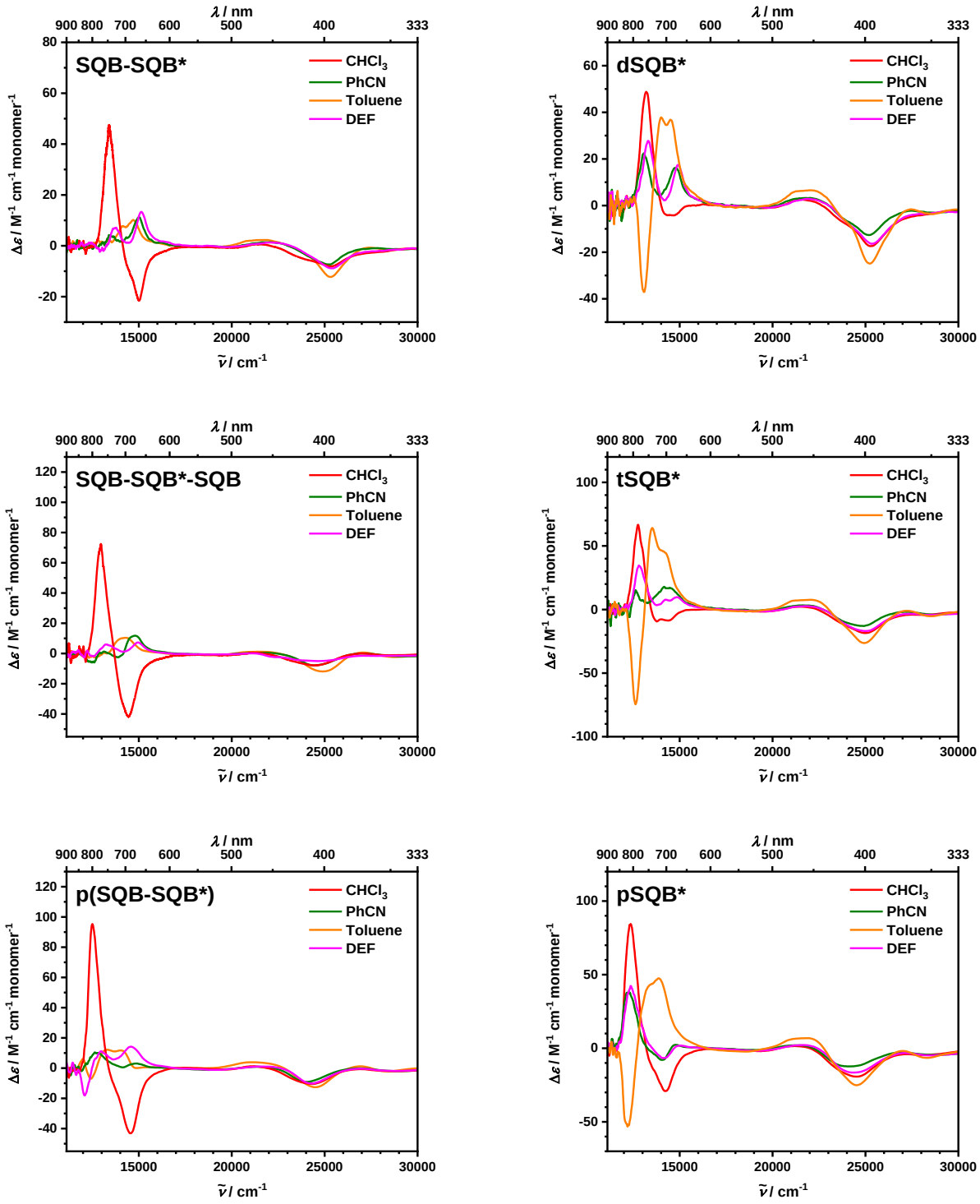

Figure 109. CD spectra (*S*-enantiomers) of **SQB-SQB*** (upper left), **SQB-SQB*-SQB** (middle left), **p(SQB-SQB*)** (lower left), **dSQB*** (upper right), **tSQB*** (middle right) and **pSQB*** (lower right) in various solvents.

11.6 Ph-SQB*-doped SQB homopolymers

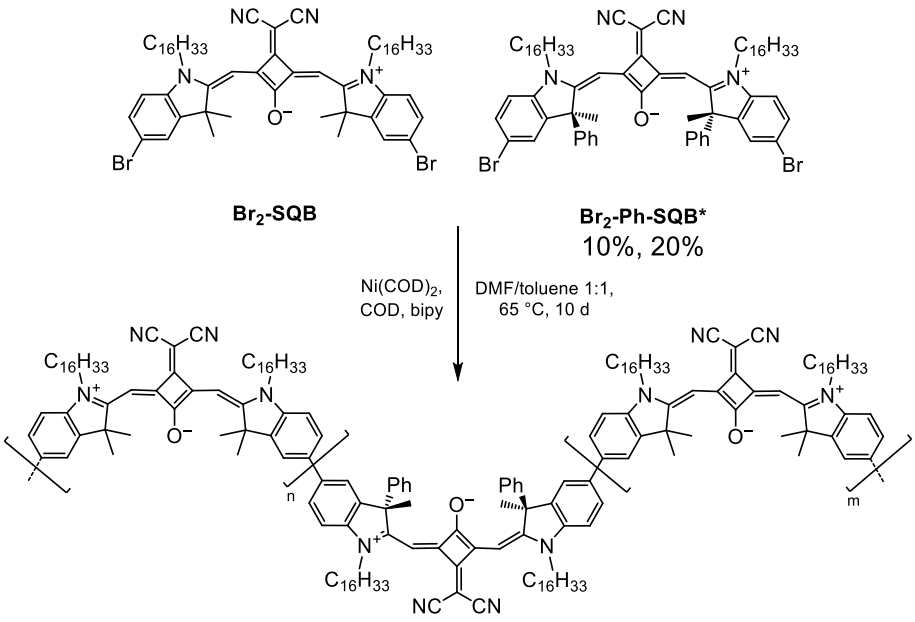

Scheme 23. Synthesis of the **Ph-SQB*** doped SQB homopolymers.

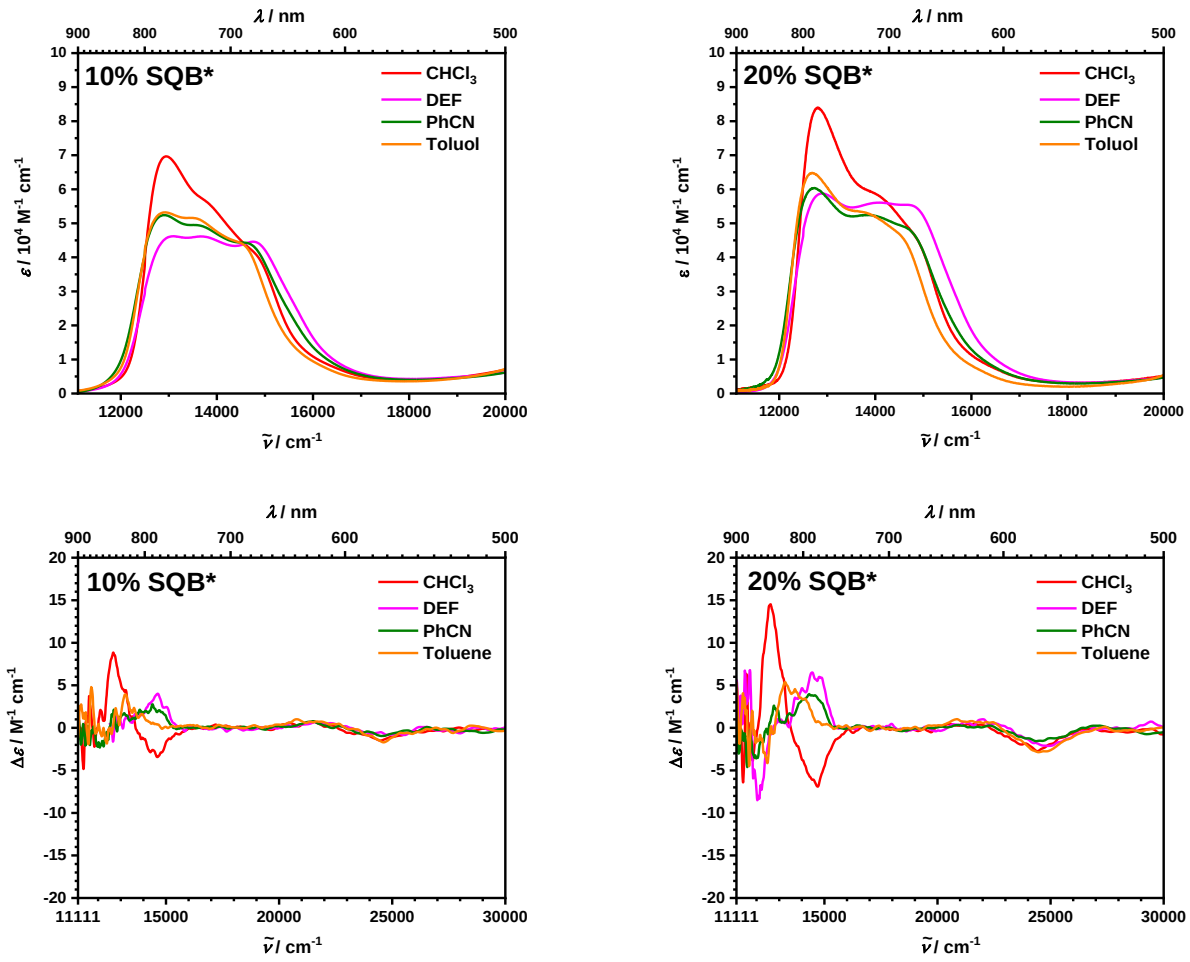

Figure 110. Absorption (top) and CD (bottom) spectra of the **Ph-SQB*** doped SQB homopolymers.

The synthesis of these polymers is shown in Scheme 23, the absorption and CD spectra are shown in Figure 110. The absence of helical conformations can be proven by the exclusive J-type absorption behavior, as well as the absence of the previously described CD fingerprint of the SQB helix (see sections 4.3 and 6.3), along with an overall small magnitude of the CD signal that roughly correlates with the number of **SQB*** units incorporated into the main chain. The shapes of the CD spectra are similar to those of **SQB-SQB*-SQB** (see Figure 109), which further points to the signal originating from such SQB-SQB*-SQB sequences within the polymer strand.

11.7 Self-absorption correction of the CPL spectrum of p(SQB-R[1]*)

The following equations were used for the self-absorption correction:[139, 294]

$$Fl_{\mathrm{corr}} = \frac{Fl_{\mathrm{obs}}}{T} \tag{79}$$

$$CPL_{\mathrm{corr}} = \frac{Fl_{\mathrm{obs}} * \alpha * \ln(10) * \Delta OD}{T} + \frac{CPL_{\mathrm{obs}}}{T} = \text{CD Term} + \text{CPL Term} \tag{80}$$

$$g_{lum,corr} = \frac{CPL_{\mathrm{corr}}}{Fl_{\mathrm{corr}}} = \alpha * \ln(10) * \Delta OD + \frac{CPL_{\mathrm{obs}}}{Fl_{\mathrm{obs}}} = \alpha * \ln(10) * \Delta OD + g_{\mathrm{lum,obs}} \tag{81}$$

Table 49. Quantities used for the calculation of the self-absorption correction according to eq. (79)-(81).

Fl_{corr}	corrected fluorescence intensity	fluorescence intensity corrected for self-absorption (eq. S3)
CPL_{corr}	corrected CPL intensity	CPL intensity corrected for self-absorption (eq. S4)
$g_{lum,corr}$	corrected dissymmetry factor	dissymmetry factor corrected for self-absorption (eq. S5)
Fl_{obs}	observed fluorescence intensity	2 * DC-component of the signal of the CPL measurement $2U_{DC}$
CPL_{obs}	observed CPL intensity	AC-component of the signal of the CPL measurement U_{AC}
$g_{lum,obs}$	observed dissymmetry factor	measured dissymetry factor ($U_{AC}/2U_{DC}$)
ΔOD	measured CD signal	CD signal in ΔOD (CD [mdeg]/32980)
α	geometrical factor	α=0.5, path length for CD measurement was 10 mm, the effective self-absorption path length in the CPL experiment was 5 mm
T	transmittance of sample for CPL measurement	path length for transmittance measurement using a UV-Vis spectrometer was 10 mm, the effective self-absorption path length in the CPL experiment was 5 mm, therefore $T = \sqrt{T_{\text{UV-Vis}}}$

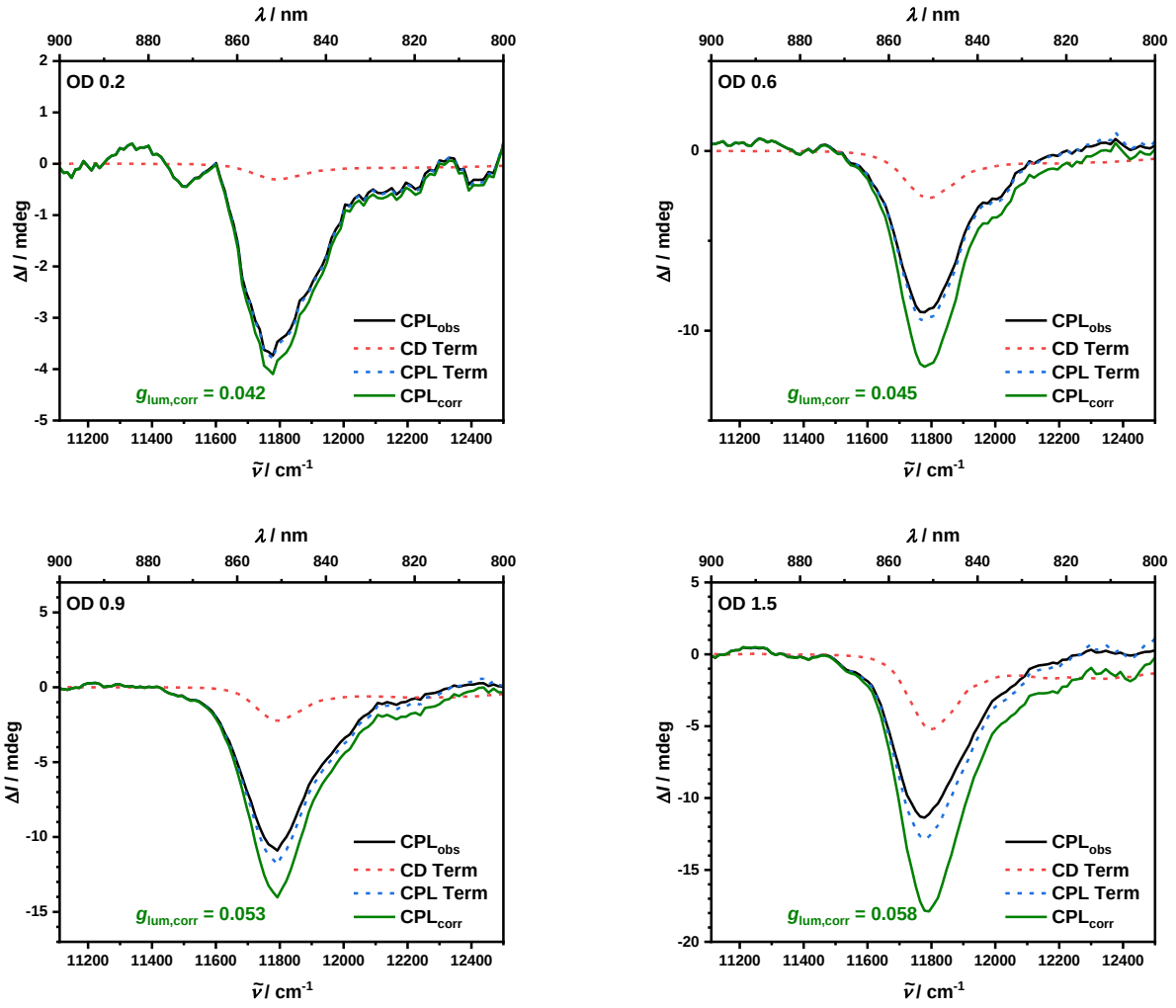

Figure 111. Self-absorption correction using eq. (80) of the measured CPL spectra of **p(SQB-R^1*)** (green traces) at different concentrations (OD of λ_{max} at 676 nm denoted in the top left corner of the respective spectra). The black traces are the corresponding measured CPL spectra, the dotted red and blue lines are the individual terms of eq. (80) that contribute to the correction. The corrected values for the dissymmetry factors $g_{lum,corr}$ were calculated using eq. (81).

11.8 List of publications and conference contributions

Talks

1. Workshop der DFG Forschergruppe 1809, Mai **2018**, Rückersbach, Deutschland.
2. Workshop der DFG Forschergruppe 1809, Mai **2019**, Rückersbach, Deutschland.
3. SolTech II Conference, Oktober **2020**, Würzburg, Deutschland.

Posters

1. Conjugated Oligomers and Polymers (KOPO 2017), August **2017**, Bad Honnef, Deutschland.
2. Workshop der DFG Forschergruppe 1809, April **2018**, Rückersbach, Deutschland.

Publications

1. *Chiroptical Properties of Indolenine Squaraines with a Stereogenic Center at Close Proximity*, J. Selby, M. Holzapfel, B. K. Lombe, D. Schmidt, A.-M. Krause, F. Würthner, G. Bringmann, C. Lambert *J. Org. Chem.* **2020**, *85*, 12227-122242.
2. *Polymeric Indolenine-Squaraine Foldamers with a Preferred Helix Twist Sense and their Chiroptical Absorption and Emission Properties*, J. Selby, M. Holzapfel, K. Radacki, A. Swain, H. Braunschweig, C. Lambert *Macromolecules* **2022**, *55*, 421-436.
3. *Ultrafast Energy Transfer Dynamics in a Squaraine Heterotriad*, C. Lambert, J. Hoche, M. H. Schreck, M. Holzapfel, A. Schmiedel, J. Selby, A. Turkin, R. Mitric *J. Phys. Chem. A* **2021**, *125*, 2504-2511.

11.9 Danksagung

An dieser Stelle möchte ich mich bei allen Personen bedanken, die am Gelingen dieser Arbeit ihren Beitrag geleistet haben.

Allen voran möchte der Gruppe um Prof. Dr. Lambert bedanken:

Dr. Marco Holzapfel, Michael Moos, Alexander Schmiedel und Christel Wendiger für jegliche Experimente, Auswertungen und Hilfestellungen. Den restlichen Doktoranden, Masteranden und Bacheloranden für die angenehme Atmosphäre im Laboralltag. Schließlich noch Manuel Buckel und Silas Gröger für die Durchführung ihrer Bachelorarbeiten unter meiner Aufsicht.

Weiterhin möchte ich meinen Kooperationspartnern danken:

Dr. David Schmidt, Ana-Maria Krause und Dr. Krysztof Radacki für das Messen der Kristallstrukturen und der damit verbundenen Mitarbeit an den Publikationen.

Dr. Dieudonné Tschitenge, Dr. Blaise Kimbadi Lombe und Prof. Gerhard Bringmann für die Durchführung und Hilfestellung bei der Analyse der chiralen Verbindungen mittels HPLC, sowie der Mitarbeit an der damit verbundenen Publikation.

David Fischermeier für die theoretische Berechnung und Modellierung der Squaraindi- und -trimere.

Jun.-Prof. Dr. Ann-Christin-Pöppler für die Hilfestellung bei NMR-Experimenten.

Abschließend danke ich noch:

Dr. Matthias Grüne sowie dem Service-Team Dr. Juliane Adelmann, Patricia Altenberger und Stefanie Schmitt für die unzähligen Messungen und Hilfestellung bei jedwedem Problem.

Joachim Ultsch, Bernd Brunner, Markus Braun, Jonathan Landeck, Bálint Klink, Michael Ramold, Matthias Fromm und dem Technischen Betrieb für die Versorgung und Instandhaltung aller Chemikalien, Apparaturen, Geräte und dem allgemeinen Erhalt des Instituts.

Dr. Christian Stadler, Dr. Alfons Ledermann, Dr. Michael Büchner, Christiana Toussaint, Anette Krug, Eleonore Kraus, Uschi Rüppel und Sarah Bullnheimer für die Verwaltung der Bürokratie und sonstige infrastrukturellen Arbeiten.